PART I. COMPARATIVE PETROLOGY OF THE APOLLO 11 MARE BASALTS

PART II. THE OXYGEN ISOTOPE GEOCHEMISTRY OF THE ABITIBI GREENSTONE BELT

Thesis by

David Wayne Beaty

In Partial Fulfillment of the Requirements

for the Degree of

Doctor of Philosophy

California Institute of Technology

Pasadena, California

1980

(Submitted May 6, 1980)

DEDICATION

This thesis is dedicated to the Higgins clan, and especially to the Big Hig, who made my stay in Pasadena quite memorable.

ACKNOWLEDGEMENTS

I am most grateful to my two thesis advisors, Drs. Arden L. Albee and Hugh P. Taylor, Jr., for allowing me the freedom to pursue my own interests in the form of a two-part thesis. Dr. Albee, who suffered through countless examples of bad exposition before finally teaching me how to write, remains in excellent mental health, and even more surprising, still likes to read. Dr. Taylor taught me the value of organization.

Drs. George R. Rossman and Leon T. Silver can also take credit for a significant part of my education. Discussions with fellow students W.S. Baldridge, R.E. Criss, R.F. Dymek, R.T. Gregory, S.M.R. Hill, T.C. Labotka, P. Larson, R.E. Powell, and J.E. Quick have been of great value. Field assistance in Canada from W.T. Jolly, P. Coad, W.A. Hogg, and L. Gelinas is much appreciated. I.E.M. Smith, A. Hynes, W.T. Jolly, and R. Whitehead provided some of the samples which were analyzed in Part II. During my stay at Caltech I have benefitted from the assistance and instruction of A.A. Chodos, J. Coulson, and J. Goris, who operate and maintain some of the analytical equipment used in this research. Claudia Beaty, Lou Ann Cordell, Betty Robinson and Jnay Buffington did most of the typing, and Pat Lee and Jan Mayne did most of the drafting. Financial support was provided by NASA grant NGL-05-002-338, NSF grants EAR-76-21310 and EAR-78-16874 and the Department of Energy grant EX-76-G-03-1305.

I wish to thank my coauthors for the help they gave me in completing the work presented in the Appendix to Part I. Written permission has been received from the publishers to reproduce those manuscripts in unmodified form.

ABSTRACT

PART I. Over the past decade a wealth of geochemical and petrological information has been accumulated on the Apollo 11 basalts. These data indicate that the 73 thus far identified basalts can be divided into five petrologic groups which must represent at least five separate igneous cooling units. These five igneous bodies range in age from 3.90 b.y. to 3.60 b.y. Photogeologic studies of the landing site indicate that three mare units are present, and that the lunar module set down on the oldest of the three. The exposure age data suggest that the high-K flow(s) is the surficial rock type at the landing area, and is therefore probably the oldest of the three mare units. The three low-K groups of samples are older than (and underlie) the high-K basalts, and were apparently excavated by West Crater. By studying the size frequency distribution and the inferred cooling rates of the individual samples, it is possible to calculate the formation thicknesses within the 30 m-deep West Crater. This suggests that A=9 m, B1=2 m (and may be an ejecta blanket), B2=>8 m and B3=6 m. Because the Group D samples have not been dated, it is not known whether they lie above or below the high-K unit. They may, however, represent one of the two younger mare units present near the landing site.

PART II. A variety of petrologic, geochemical and geophysical evidence indicates that the modern oceanic crust interacts on a massive scale with seawater. To evaluate whether or not similar processes were taking place in the Archean, the well preserved Abitibi greenstone belt was studied using oxygen isotopes and the petrographic microscope. In thin section, all of the volcanic rocks in the Abitibi area are found to have been subjected to a hydrothermal process of some sort. The original

igneous minerals have been largely replaced by secondary hydrous minerals such as chlorite, epidote and actinolite. The metamorphic assemblages range from the prehnite-pumpellyite facies in the core of the Blake River syncline to greenschist facies adjacent to the large Kenoran granitic batholiths. The structural relations are such that the metamorphic grade decreases in a general way with structural height; the lowest temperature rocks are those which are highest in the volcanic pile.

$\delta^{18}O$ is also correlated with structural height. In each of five widely separated traverses (Benoit, Ben Nevis, Noranda, Skead, Timmins), $\delta^{18}O$ increases upwards through the stratigraphic section (typically +6 to +10 from base to top). In the Benoit area $\delta^{18}O$ and structural height also correlate with the silica content of the volcanic rocks. Silica content and the degree of petrographic recrystallization are not correlated, however, whereas $\delta^{18}O$ and the degree of recrystallization are. This indicates that the gradient in SiO_2 is a relic igneous feature and that the gradient in $\delta^{18}O$ is a hydrothermal alteration feature. Additional evidence that these rocks have undergone isotopic exchange comes from the mineral separate data. Relic clinopyroxene in the basalts has $\delta^{18}O \approx +5.5$, and quartz phenocrysts in the rhyolites are +7.6, indicating that these lavas were not erupted as high-^{18}O magmas; they have undergone subsolidus enrichments in $\delta^{18}O$ of 0-4 per mil. Using temperatures inferred from the metamorphic assemblages, $\delta^{18}O$ of the fluid responsible for producing these $\delta^{18}O$ shifts can be calculated. Assuming an open system, water flux within 100°C of the final metamorphic temperature, and using the feldspar geothermometer, the hydrothermal fluid has $\delta^{18}O = 0 \pm 2$ and alteration took place under conditions of high water/rock ratio. The oxygen isotopic effects are associated with the prehnite-pumpellyite

facies burial metamorphism, which is thought to have taken place during the formation of the volcanic pile. Since the pile formed in a marine environment the only logical source for such large amounts of fluid is seawater itself.

Oxygen isotopic study of the Amulet "A" massive sulfide deposit indicates that it was formed by a fluid with a similar $\delta^{18}O$ (0.5 ± 1.0). Similar deposits in the Phanerozoic (Cyprus, Kuroko, Gulf of California) are thought to have originated from heated seawater circulating through the oceanic crust. The fact that the Amulet ore fluid is indistinguishable from the inferred Archean seawater indicates that analagous hydrothermal processes were taking place in the Archean. At the Kidd Creek mine, however, the ore-forming solution is thought to have had $\delta^{18}O$ between +6 and +9. This fluid could either have been derived from normal-^{18}O seawater through evaporation or exchange with high-^{18}O country rocks, or it could have been some sort of metamorphic fluid. This indicates that massive sulfide ore deposits have formed by more than one mechanism, and that the simple seawater-hydrothermal model may not be generally applicable.

Less extensive data from other greenstone belts throughout the world indicate that like Abitibi, all have undergone ^{18}O-enrichments relative to primary igneous values. By mass balance, these ^{18}O-enrichments must have caused a complementary ^{18}O-depletion in some other oxygen reservoir. That reservoir was apparently not seawater, nor has it been discovered in the geologic record. Because the oxygen isotopic exchange process is self-buffering, the consistent ^{18}O-enrichments in greenstone belts throughout history suggests that they were not the dominant form of submarine volcanism in the Archean. This, combined with the apparent destruction of the low-^{18}O reservoir, suggests that seafloor spreading

volcanism was also taking place in the early Precambrian. This is consistent with a variety of geological, geophysical, geochemical, isotopic and petrologic data which indicate that greenstone belts resemble modern island arcs in a number of important respects.

TABLE OF CONTENTS

DEDICATION. ii

ACKNOWLEDGMENTS iii

ABSTRACT. iv

PART I. COMPARATIVE PETROLOGY OF THE APOLLO 11 MARE BASALTS. 1

1. INTRODUCTION TO PART I 2

2. THE GEOLOGY AND PETROLOGY OF THE APOLLO 11 LANDING SITE. 3

APPENDIX TO PART I. 25

1. COMPARATIVE PETROLOGY AND POSSIBLE GENETIC RELATIONS AMONG THE APOLLO 11 BASALTS. (Co-authored with A.L. Albee; published in Proceedings of the Ninth Lunar and Planetary Science Conference, Geochim. et Cosmochim. Acta, Suppl. 10, p. 359-463, 1978). 26

2. THE PETROLOGY AND CHEMISTRY OF BASALTIC FRAGMENTS FROM THE APOLLO 11 SOIL, PART I. (Co-authored with S.M.R. Hill, A.L. Albee, M.-S. Ma, and R.A. Schmitt; Published in Proceedings of the Tenth Lunar and Planetary Science Converence, Geochim. et Cosmochim. Acta, Suppl. 11, p. 41-75, 1979). 131

3. THE PETROGRAPHY OF BASALTIC FRAGMENTS IN APOLLO 11 DRIVE TUBES 10004 AND 10005. (Co-authored with A.L. Albee; published in Lunar and Planetary Science XI, the Lunar and Planetary Institute, Houston, p. 64-66, 1980). 166

4. SILICA SOLID SOLUTION AND ZONING IN NATURAL PLAGIOCLASE (Co-authored with A.L. Albee; published in American Mineralogist, 65, p. 63-74, 1980) 169

5. APOLLO 12 FELDSPATHIC BASALTS 12031, 12038 and 12072; PETROLOGY, COMPARISON AND INTERPRETATIONS. (Co-authored with S.M.R. Hill, A.L. Albee, and W.S. Baldridge; published in Proceedings of the Tenth Lunar and Planetary Science Conference, Geochim. et Cosmochim. Acta, Suppl. 11, p. 115-139, 1979). 181

6. THE PETROLOGY OF A PYROXENITE XENOLITH IN MARE BASALT 10050. (Co-authored with A.L. Albee; published in Lunar and Planetary Science XI, the Lunar and Planetary Institute, Houston, p. 67-69, 1980). 206

PART II. THE OXYGEN ISOTOPE GEOCHEMISTRY OF THE ABITIBI GREENSTONE BELT 209

CHAPTER 1. INTRODUCTION 210

A. BACKGROUND AND PURPOSE. 210

B. METHOD OF STUDY 214

CHAPTER 2. GEOLOGIC SETTING OF THE ABITIBI GREENSTONE BELT. 219

CHAPTER 3. $^{18}O/^{16}O$ RATIOS IN VOLCANIC ROCKS 225

A. GENERAL STATEMENT 225

B. BEN NEVIS TRAVERSE. 229

I. GEOLOGY. 229

II. PETROLOGY. 232

III. OXYGEN ISOTOPIC DATA 233

IV. FLUID COMPOSITION. 236

C. BENOIT SYNCLINE 250

I. GEOLOGY. 250

II. PETROLOGY. 250

III. OXYGEN ISOTOPIC DATA 253

IV. FLUID COMPOSITION. 265

D. NORANDA AREA 267

I. GEOLOGY. 267

II. PETROLOGY. 271

III. OXYGEN ISOTOPIC DATA 271

IV. FLUID COMPOSITION. 275

E. SKEAD VOLCANICS. 277

I. GEOLOGY. 277

II. PETROLOGY. 277

III. OXYGEN ISOTOPIC DATA 279

IV. FLIUD COMPOSITION. 282

F. MUNRO TOWNSHIP. 284

I. INTRODUCTION 284

II. SAMPLING 286

III. METAMORPHIC PETROLOGY. 286

IV. OXYGEN ISOTOPIC DATA 292

1. Isotopic Structure of the Flow. 292

2. $\delta^{18}O$ of Fresh Komatiites. 295

3. Source Region 297

4. $\delta^{18}O$ of Secondary Minerals. 298

5. Fluid Composition and Water/Rock Ratio. 299

6. Komatiites from Other Areas 301

V. CONCLUSIONS. 304

G. TIMMINS AREA. 306

I. GEOLOGY. 306

II. PETROLOGY. 309

III. OXYGEN ISOTOPE DATA. 309

IV. FLUID COMPOSITION. 315

CHAPTER 4. $^{18}O/^{16}O$ RATIOS IN MASSIVE SULFIDE ORE DEPOSITS 320

A. GENERAL STATEMENT 320

B. THE KIDD CREEK MINE 322

I. GEOLOGY. 322

II. PETROLOGY. 326

III. OXYGEN ISOTOPE DATA. 327

1. Andesite/diorite. 327

2. Dacite Sequence 327

3. Quartz Porphyry 329

4. Carbonaceous Horizon. 330

6. Rhyolites 330

a). DDH J-628 330

b). East outcrop. 338

c). 1600 Level, N. Orebody. 341

7. Nearby Rhyolites. 342

IV. SUMMARY OF THE OXYGEN ISOTOPE DISTRIBUTION 344

V. HYDROTHERMAL HISTORY 344

VI. $\delta^{18}O$ OF THE HYDROTHERMAL FLUIDS. 349

VII. SOURCE OF THE ORE-FORMING SOLUTION 351

VIII. CONCLUSIONS. 357

C. THE AMULET "A" MINE 360

I. GEOLOGY AND STRUCTURE. 360

II. PETROLOGY. 368

III. OXYGEN ISOTOPE DATA. 373

1. Whole-Rock Data 373

2. Mineral Data. 374

3. The Effect of Contact Metamorphism. 374

4. Oxygen Isotopic Effect of Dehydration 376

5. Fluid Composition 377

6. Water/Rock Ratio. 379

IV. CONCLUSIONS. 381

D. COMPARATIVE STABLE ISOTOPE GEOCHEMISTRY OF MASSIVE SULFIDE DEPOSITS. 383

I. OXYGEN ISOTOPES. 383

II. HYDROGEN ISOTOPES. 387

III. DISCUSSION 387

IV. IMPLICATIONS FOR EXPLORATION 392

CHAPTER 5. NON-VOLCANIC ROCKS 396

I. GRANITIC ROCKS 396

1. Round Lake Batholith. 396

2. Otto Stock and Lake Dufault Granodiorite. 403

3. Comparison with Other Archean Granitoids. 403

II. KAMISKOTIA GABBRO. 405

1. GEOLOGY 405

2. OXYGEN ISOTOPIC DATA. 406

3. FLUID COMPOSITION 406

III. MIGMATITIC GNEISSES. 407

IV. SEDIMENTARY ROCKS. 411

CHAPTER 6. OTHER GREENSTONE BELTS 413

CHAPTER 7. SUMMARY AND CONCLUSIONS. 420

I. SUMMARY OF THE ABITIBI GREENSTONE BELT DATA. 420

1. General Statement 420

2. Seafloor Burial Metamorphism. 426

3. Source of the Fluid 428

II. COMPARISON WITH OPHIOLITES AND ISLAND ARCS 431

1. General Statement 431

2. Tectonic Setting. 431

3. Granitic Rocks. 432

4. Stratigraphy. 434

5. Stratigraphic Thickness 436

6. Metamorphic Style 436

7. Oxygen Isotopes 438

III. IMPLICATIONS FOR THE EVOLUTION OF THE OCEANIC CRUST. 440

IV. THE SIGNIFICANCE OF GREENSTONE BELTS 450

REFERENCES 452

PART I. COMPARATIVE PETROLOGY OF THE APOLLO 11 MARE BASALTS.

INTRODUCTION TO PART I

This part of the thesis seeks to answer the question, "How many igneous cooling units are represented by the Apollo 11 basalt suite, and what is the significance of those igneous units?" To answer this question, a comparative study was made of each of the 73 basalt fragments thus far identified from the Apollo 11 site. Detailed microprobe studies were undertaken on about 30 of the coarsest samples. New INAA trace element data were collected in collaboration with Ma and Schmitt, and the isotopic and chemical data for these rocks from the literature was reviewed. This work led to the subdivision of the 73 basalt fragments into 5 petrologic groups. This conclusion was then considered in view of the field relations at the Apollo 11 site, and a model for the geology and petrology of the landing site was developed.

The text of Part I contains an abbreviated summary of this work, which includes most of the important conclusions. The detailed descriptive and analytic material which led to these conclusions is presented in the Appendix to Part I.

I. INTRODUCTION

For several years prior to man's first visit to the moon, intensive effort was put into mapping the surface of the moon. One of the primary functions of these maps was to help in the selection of the landing sites. After the first samples were returned, however, scientific interest focused on laboratory studies of the returned rocks, and much of the mapping work was seemingly forgotten. This is particularly true of the Apollo 11 landing site. There has been a full decade of detailed study of individual specimens, but no attempt has been made to relate these rocks to the various geologic formations present in the sampled area. This research attempts to bridge that gap by considering together the important features of these two data sets, and has led to the development of a detailed model of the geology and petrology of the Apollo 11 landing site.

II. GEOLOGY OF THE LANDING SITE

The Apollo 11 Lunar Module (LM) landed in the southwestern part of Mare Tranquillitatis, 42 km NNE of the western promontory of the Kant Plateau, the nearest highland region. Mare Tranquillitatis is a "blue" mare of irregular form, and several features suggest that the mare fill is relatively thin (Apollo 11 Preliminary Science Report, 1969). On the basis of differences in albedo and crater density, three mare units have been mapped in the vicinity of the landing site (Fig. 1). The LM landed on the most densely cratered, and presumably the oldest, of these three units. Gentle, sinuous scarps, which are presumed to be flow fronts, can be traced for several kilometers across the second of the three units (Fig. 1). Close to the landing site are six "dimple" craters. These

features are nearly rimless craters having convex upward walls, which are interpreted to be either small volcanic vents or "impact craters in which the fragmental layer has drained through narrow fractures or openings into the underlying substrate" (Grolier, 1970). Superimposed on this volcanic terrain is a multitude of craters, which have been divided into eight age groups. For cartographic simplicity the three youngest and five oldest groups of craters are shown together on Figure 1. For additional details, see Grolier (1970).

III. PETROLOGY AND AGES OF THE BASALT SAMPLES

The samples returned by the Apollo 11 astronauts were classified by LSPET (1969) into four types: Fine-grained basalts, coarse-grained basalts, breccias, and soil samples. Most of the rock fragments in the soils and the breccias are basalts which are similar to the large samples, although scattered highlands fragments are present (e.g., Luny Rock 1; Albee and Chodos, 1970). Thus all of the returned sample types are dominated by a basaltic component. This is consistent with the volcanic features observed by Grolier (1970) in photographs of the landing site, and suggests that most of the returned sample may be of local derivation.

Our comparative studies of the Apollo 11 basalts have resulted in five principal subdivisions (Beaty and Albee, 1978; Beaty et al., 1979; Ma et al., 1980) that have been confirmed by Rhodes and Blanchard (1980). The high-K (type A) basalts show a range of textures (Grove and Beaty, 1980), but are unique chemically and isotopically. The low-K (type B) basalts can be divided into three groups, named B1, B2 and B3 for reference, which have distinctive textures, mineral chemistries, bulk compositions and ages. The Group D basalts (which are also low-K) are

also unique chemically. This five-way classification is summarized in Figure 2. Of the 73 basalt samples which we have analyzed from Apollo 11, 70 can be uniquely assigned to one of these five petrologic groups. The remaining three rocks are not classified because the data are insufficient to clearly distinguish between B2 and B3.

Also shown on Figure 2 are the ages and the number of samples available for each group. Most of the samples (64 of 70) are members of three of the groups, A, B2 and B3, whereas groups B1 and D contain only three samples each. The high-K (A) samples are the youngest of the Apollo 11 basalts, with an age of about 3.60 b.y. (Guggisberg et al., 1979; Papanastassiou et al., 1977). Group B1 has a well-defined age of about 3.72 b.y. (Guggisberg et al., 1979). Group B3 has been dated at 3.76 b.y., but the data are from intermediate temperature Ar-release plateaus, and are considered less reliable (Geiss et al., 1977). Group B2 is the oldest of the Apollo 11 mare basalts, with an Ar-Ar age of about 3.90 b.y. (Guggisberg et al., 1979). Group D remains undated.

A variety of arguments have been advanced to indicate that these five groups represent at least five separate igneous cooling units (Beaty and Albee, 1978; Beaty et al., 1979; Rhodes and Blanchard, 1980). Not only do they have different ages, the bulk compositions cannot be related to one another by crystal-liquid fractionation. What is the significance of these five groups and how do they relate to the three mare units shown in Figure 1? To answer this question, the size-frequency distribution of the five rock types must be considered along with the sampling procedure used and the nature of the cratering events.

IV. SIGNIFICANCE OF THE PETROLOGIC GROUPS

A. Size frequency distribution

The size frequency distribution of the 70 classified Apollo 11 basalt samples is shown in Figure 3. The rocks are divided into three populations on the basis of mass, and the proportions of the different petrologic groups compared. The two coarsest size fractions have a similar constitution. Each consists about 55% of Group A, about 10% of B2 and about 20% of B3. These three rock types constitute 91% of the returned sample (Fig. 2), so the similarities are significant. An important difference, however, is that the >1 gm fraction contains 15% B1 and 0% D, and vice versa in the 25 mg - 1.0 gm fraction.

By contrast, the finest size fraction contains less group A (35%), and more B2 (20%) and B3 (45%). Groups B1 and D are not present in this set of samples. The explanation for this difference probably lies in the sampling procedure, although care must be taken in dealing with the statistics of small populations such as this. Twenty-nine of the 31 samples in the <25 mg fraction were obtained from the two drive tubes, 10004 and 10005. The remaining two samples are 10085,844 (B3) and clast δ, a high-K vitrophyre in soil breccia 10060. The two coarse size fractions were obtained from the documented sample (isolated rocks), the bulk sample (collected with a scoop) and the contingency sample (also using a scoop). The two coarsest size fractions were therefore obtained from the uppermost part of the lunar regolith; the large rocks in the documented sample were resting on top of the regolith. The two drive tubes, however, penetrated a short distance into the regolith (10 cm and 13.5 cm), so they contain deeper and possibly older regolith material. Before evaluating this deeper regolith material, the source of the surficial debris will be considered.

B. Source of the coarse debris

Prior to the landing event, it was recognized that the southern part of Mare Tranquillitatis was crossed by two sets of rays which were thought to be associated with Theophilus and either Tycho or Alfraganus (Apollo 11 PSR, 1969). All three of these craters are in the highlands, however, and could not have supplied the mare material. Another possible source is the crater Moltke, 40 km SE of the landing site. Consideration of Figure 1, however, indicates a much more likely source for the coarse debris at the landing site. The LM landed about 400 m west of a sharp-rimmed, rayed crater approximately 180 m in diameter and 30 m deep known as West Crater. Surrounding West Crater is a continuous blocky ejecta apron which extends outwards about 250 m from the rim crest, and is more extensive in the direction of the landing site (Fig. 1). Rays of blocky ejecta with many coarse fragments, (1/2 to 2 m in width), extend beyond the ejecta apron past the landing point. The astronauts approached this area from the east and were originally targeted to land within the boulder field surrounding West Crater. Because of the extremely rough topography, however, they overflew the boulder field and landed on the first smooth area they found, which was an opening between two of the rays at the western edge of the continuous ejecta blanket. From the ground they could observe the ray to the north of the LM (Fig. 4), which was described as a "long boulder field with many boulders averaging at least two feet in diameter" (Apollo 11 PSR, 1969; p. 35). It is probable, therefore, that many of the rocks lying about the landing site were derived from West Crater. Thus, one would anticipate a clustering of exposure ages at some young value, and then conclude that these rocks had been excavated by West Crater.

C. Exposures ages

The ^{37}Ar-^{38}Ar exposure ages of most of the large Apollo 11 rocks have been measured by the Berne group (Guggisberg et al., 1979; Geiss et al., 1977). These data indicate that seven of the eight low-K basalts analyzed have been exposed at close to the lunar surface for 100±20 m.y. The lone exception is 10050 (exposure age ≈500 m.y.; Guggisberg et al., 1979) which could not be classified. Analyzed samples of groups B1, B2 and B3 appear to have been excavated together, and that excavation event is presumed to be West Crater. The high-K basalts have exposure ages ranging from 20 to 520 m.y. and $^{131}Xe/^{126}Xe$ ratios of 6-8. This indicates that at least some irradiation was received at depth (Geiss et al., 1977), prior to exposure at the lunar surface. This suggests that the high-K flow(s) is the surficial mare unit in this region. In that position it would have had a long history of pre-excavation irradiation, while shielding the underlying low-K basalts (which received no irradiation at depth). This is also consistent with the fact that the high-K basalts are the youngest samples in the collection.

Thus if West Crater is 100 m.y. old, then some of the high-K basalts were excavated after that event. Most of the high-K samples, however, also could have been excavated by West Crater. In fact, because the high-K samples are apparently from the uppermost lava flow or flows in this region (based both on the exposure history and on the age), it is inevitable that they would have been included in the ejecta from West Crater.

In summary, the field relations at the landing site and the exposure data both suggest that most of the coarse samples returned by Apollo 11 were excavated by West Crater. In this regard it is important

to note that the two coarsest size fractions on Figure 3 show the same distribution of rock types, but the fine-grained samples from the core tubes show a different distribution. This suggests the possibility that the two coarse fractions are derived from West Crater, and that the core tubes contain a significant fraction of the pre-West Crater regolith.

D. West Crater

By making the following assumptions, it is possible to make some interesting calculations concerning the geology of West Crater.

1. All of the samples in the two coarse fractions are derived from West Crater.
2. Layer-cake geologic structure at West Crater.
3. The ejecta sampled by Apollo 11 is representative of the total excavated volume.
4. 5 m of regolith (Apollo 11 PSR, 1969, p. 46).

West Crater is 30 m deep and 180 m in diameter; so the volume of ejected bedrock is about 2.7×10^5 m^3. The radiometric age data indicate that the rock types increase in age in the order A<B1<B3<B2. Group D is undated and cannot be considered in this calculation. If the ejected volume is 60% Group A, the observed frequency in the returned sample, then the high-K stratum is 9 m thick. Underlying that are successively 2 m of B1, 6 m of B3 and at least 8 m of B2 (Fig. 5).

It is possible to calculate independently the minimum thickness of the lava flows within which these samples are presumed to have crystallized. Provost and Bottinga (1972) have solved the heat flow equation for a lava flow cooling at the lunar surface and have found that the rate of heat loss by radiation from the upper surface is only slightly faster than that by conduction through the base. The most

slowly-cooled and coarsest-grained portion of any given flow is located between one-third and one-half of the distance from the base to the top. The cooling rate of each of the samples can be calculated from the plagioclase size (Grove, 1977), and from that the distance to the nearest surface of conductive heat loss can be calculated (Jaegar, 1957). The largest of these distances is multiplied by three to arrive at the flow thickness.

The flow thicknesses calculated assuming that each of the petrologic groups represents exactly one lava flow are listed in Table 1. Also shown are the formation thicknesses calculated for West Crater. For Group A, the two values are similar. For B1, the samples are too coarse-grained to have crystallized in a 2 m lava flow. This indicates that they are either inadequately represented in the returned sample for some reason, or they did not crystallize at West Crater. It is possible, for example, that the B1 samples were part of an ejecta blanket which lies between A and B3. For B2 and B3 the flow thicknesses calculated using the cooling rate are less than the formation thicknesses in West Crater. This admits the possibility that there are multiple B2 and B3 flows. The group D samples cannot be placed in this stratigraphic section because of the uncertainty in age.

As suggested by Beaty and Albee (1978), it is possible that all of the low-K samples were contained in ejecta blankets beneath a high-K flow. However this now seems unlikely in view of the fact that although the total number of samples studied since 1978 has been quadrupled, the number of petrologic groups (and presumably lava flows) has been increased only from 4 to 5. If a 16 m thick ejecta blanket underlay the high-K flow(s), one might anticipate the presence of a

wide variety of rock types. The restriction of the returned sample to five sample basalt types suggests that these basalts are actually in place in West Crater. Thus the most reasonable geological model for the structure of the Apollo 11 landing site is shown in Figure 5. A, B2 and B3 represent formations of one or two flows each, and B1 represents an interlayered ejecta blanket. Alternatively, if the constraints used to deny a genetic relationship between B1 and B3 are relaxed (see Beaty and Albee, 1978), it is possible that B1 and B3 represent different portions of a single lava flow.

The validity of this discussion depends, of course, on the validity of the assumptions upon which it is based, and at least two of the assumptions are open to question. It is assumed that all of the large samples are derived from West Crater, but at least two of the high-K rocks are younger than West Crater. More serious is the assumption that the returned sample is representative of the excavated volume. Detailed study of Meteor Crater, Arizona indicates that a well-defined inverted stratigraphy is present within the ejected blanket (Shoemaker, 1963). At any given point within the ejecta apron, a randomly collected set of samples would not represent the entire excavated volume. The same situation probably holds for the rays. Overlying the entire impact feature, however, is a layer of mixed debris which was thrown to great height, and which may be more nearly geologically representative. Because of the location of the Apollo 11 site, it seems likely that the returned samples were part of the mixed debris shower, and hence may be quite representative of the entire excavated volume.

E. Group D

Group D has been consistently ignored throughout the above discussion

because of the absence of isotopic data. Note, however, that West Crater impacted the oldest of the three mare units shown on Figure 1. The exposure data suggest that the high-K samples outcrop close to the surface in this area, and hence represent mare unit 1 (Fig. 1). The low-K flows are all older than that, and do not outcrop on the area shown on Figure 1. There are two younger mare units close to the landing site, however. It is possible that one of these units is composed of Group D basalts. This would be consistent with the calculations of Beaty et al. (1979) who concluded that B2 and D were probably derived from the same source region, and are related by different degrees of partial meltig. Particularly attractive is mare unit 2, which was penetrated by a relatively large (600 m), young rayed crater 3.4 km from the landing site (Fig. 1). It is entirely reasonable that some of the ejecta from this impact may be present at the landing site.

F. Drive tubes

The drive tubes contain more B2 and B3, and less A than the presumed West Crater-derived large samples. The drive tubes are probably different because they contain a component of pre-West Crater regolith. If so, then the source of that regolith was richer in low-K and poorer in high-K basalts than West Crater. This suggests either a greater contribution of deep craters (consistent with an increased B2 abundance), or a thickening of B3 relative to A away from West Crater. In any case, the data suggest that like other mare sites (Vaniman et al., 1979), the upper part of the regolith is composed principally of locally-derived material.

V. CONCLUSIONS

Using the wealth of chemical, petrologic, geologic and isotopic data which have been collected at the Apollo 11 landing site during the past 15 years, an attempt has been made to construct a geological model for this portion of Mare Tranquillitatis which satisfies all of the available constraints. This model is neither unique nor detailed -- the lack of field control precludes such luxuries. The essential features of this model, along with possible alternative explanations, are outlined below.

The southern part of Mare Tranquillitatis is covered by three different mare units which can be distinguished on the basis of different albedo and crater density. The oldest of these units (upon which the LM landed) is the high-K basalts, which are presumed to be present as one or more flows. The volcanic vents from which these high-K basalts were erupted may be the dimple craters which are close to the landing site. The two younger mare units have not yet been identified in the returned sample. One of them (probably the second) may be the source of the Group D basalts, but this cannot be established without geochronologic data.

The Apollo 11 LM landed close to an extremely young crater, West Crater, which impacted the oldest of the three mare units. West Crater excavated 30 m of material, and most of the large rocks returned by the astronauts are part of that ejecta. The three low-K basalt types, B1, B2 and B3 underlie the high-K unit, and are present in the upper 30 m of stratigraphy in Mare Tranquillitatis. Assuming a stratified geologic structure, it is possible to use the frequency distribution of the various basalt types to calculate the formation thicknesses in West Crater: A = 9 m, B1 = 2m, B2 = >8 m, B3 = 6 m. In three of these four cases the grain sizes of the samples are appropriate for lava flows of the

stated size. In B1, however, a 7 m thick flow is required to produce the coarse-grained samples observed, hence B1 may be from an ejecta blanket which is interlayered between flows. It is possible that B2 and B3 are also present as ejecta blankets, but the low number of rock types in the returned sample suggests that they are in place in West Crater.

VI. ACKNOWLEDGEMENTS

This research constitutes the summary of a portion of the senior author's Ph.D. thesis at Caltech. Lou Ann Cordell, our overworked and underloved secretary, typed the manuscript. Financial support was provided by NASA grant NGL-05-002-338.

REFERENCES

Albee A.L. and Chodos A.A. (1970) Microprobe investigations on Apollo 11 samples. Proc. Apollo 11 Lunar Sci. Conf., p. 135-157.

Apollo 11 Preliminary Science Report (1969) NASA SP-214, 204 p.

Beaty D.W. and Albee A.L. (1978) Comparative petrology and possible genetic relations among the Apollo 11 basalts. Proc. Lunar Planet. Sci. Conf. 9th, p. 359-463.

Beaty D.W., Hill S.M.R., Albee A.L., Ma M.-S. and Schmitt R.A. (1979) The petrology and chemistry of basaltic fragments from the Apollo 11 soil, Part I. Proc. Lunar Planet. Sci. Conf. 10th, p. 41-75.

Geiss J., Eberhardt P. Grogler N., Guggisberg S., Maurer P. and Stettler A. (1977) Absolute time scale of lunar mare formation and filling. Phil. Trans. Roy. Soc. London A285, p. 151-158.

Grolier M.J. (1970) Geologic map of Apollo landing site 2 (Apollo 11). U.S. Geol. Sur. Map I-619 [ORB II-6 (25)].

Grove T.L. (1977) Cooling histories of Apollo 15 quartz normative basalts (Abs.). In Lunar Science VIII, p. 380-382. The Lunar Science Institute, Houston.

Grove T.L. and Beaty D.W. (1980) Origin of textural diversity in Apollo 11 high-K basalts (abs.). In Lunar and Planetary Science XI, p. 371-373. The Lunar and Planetary Institute, Houston.

Guggisberg S., Eberhardt P., Geiss J., Grogler N., Stettler A., Brown G.M. and Peckett A. (1979) Classification of the Apollo 11 mare basalts according to ^{39}Ar-^{40}Ar ages and petrological properties. Proc. Lunar Planet Sci. Conf. 10th, p. 1-39.

Jaeger J.C. (1957) The temperature in the neighborhood of a cooling intrusive sheet. Amer. Jour. Sci. 225, p. 306-318.

LSPET (Lunar Sample Preliminary Examination Team) (1969) Preliminary examination of lunar samples from Apollo 11. Science 165, p. 1211-1227.

Ma M.-S., Schmitt R.A., Beaty D.W. and Albee A.L. (1980). The petrology and chemistry of basaltic fragments from the Apollo soil: Drive tubes 10004 and 10005. Proc. Lunar Planet. Sci. Conf. 11th (this volume).

Papanastassiou D.A., DePaolo D.J. and Wasserburg G.J. (1977) Rb-Sr and Sm-Nd chronology and genealogy of mare basalts from the Sea of Tranquillity. Proc. Lunar Sci. Conf. 8th, p. 1639-1672.

Provost A. and Bottinga Y. (1972) Rates of solidification of Apollo 11 basalt and Hawaiian tholeiite. Earth and Planet. Sci. Lett. 15, p. 325-337.

Rhodes J.M. and Blanchard D.P. (1980) Chemistry of Apollo 11 low-K mare basalts. (Abs.) In Lunar and Planetary Science XI, p. 926-928. The Lunar and Planetary Institute, Houston.

Shoemaker E.M. (1963) Impact mechanics at Meteor Crater, Arizona. In The Solar System, v. 4, pt. 2 (G.P. Kuiper, ed.), p. 303-336, University of Chicago Press, Chicago.

Vaniman D.T., Labotka T.C., Papike J.J., Simon S.B. and Laul J.C. (1979) The Apollo 17 drill core: Petrologic systematics and the identification of a possible Tycho component. Proc. Lunar Planet. Sci. Conf. 10th, p. 1185-1227.

Table 1.

CALCULATED FLOW THICKNESSES (M.)

	Cooling Rate	Frequency Distribution
A	9	9
B1	7	2
B3	4	6
B2	3	>8
D	3	--

FIGURE CAPTIONS

Figure 1. Geology of the area around the Apollo 11 landing site, modified from Grolier (1970). The three youngest groups of Copernican craters have been grouped as very young craters, and the three oldest sets of Copernican craters have been grouped with the Eratosthenean craters as old craters. Note the proximity of the landing site to West Crater.

Figure 2. Simplified summary of the petrologic and geochemical data on the Apollo 11 basalts. The 70 basalt samples can be divided into five groups which are presumed to represent at least five separate lava flows.

Figure 3. Size-frequency distribution of the Apollo 11 basalt samples. The two coarse fractions are similarly distributed (with the exception of B1 and D) whereas the fine fraction is obviously different. Twenty-nine of the 31 fragments in the fine fraction are from the core tubes, and all of the other samples were collected either by hand or by using the scoop.

Figure 4. Hasselblad photograph from the window of the LM, showing the blocky ray from West Crater which passes to the north of the landing site.

Figure 5. Interpretive cross section through West Crater. Using the coarse ejecta composition from Figure 3, and assuming a stratified geologic structure, it is possible to calculate the formation thicknesses in the

30 m thick West Crater section. The crater shape is assumed to be parabolic for ease of integration. Comparison of the thicknesses calculated in this manner with the thicknesses calculated from cooling rate studies (Table 1) suggests that B1 may be an ejecta blanket.

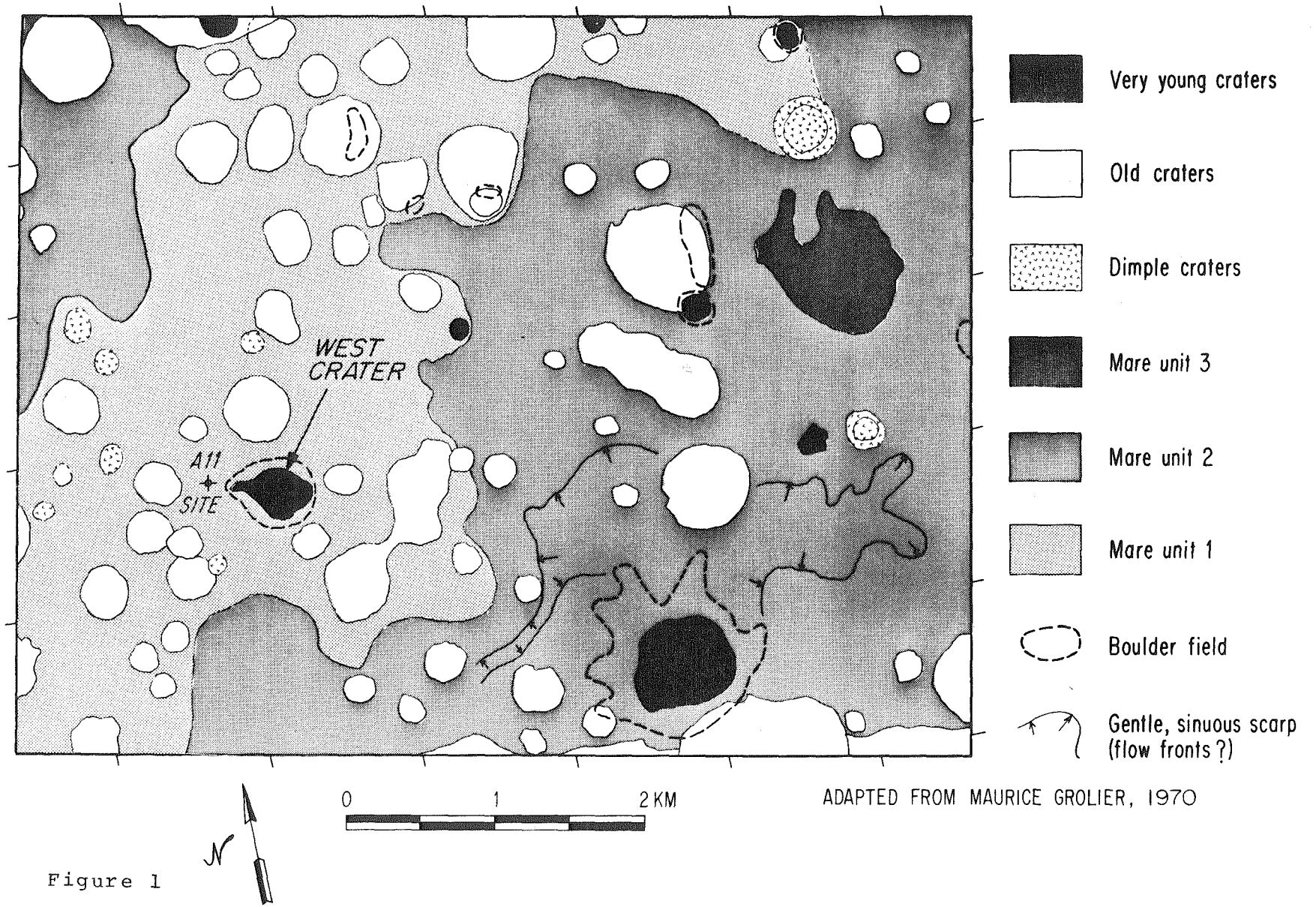
WEST
CRATER
A11
SITE
Very young craters
Old craters
Dimple craters
Mare unit 3
Mare unit 2
Mare unit 1
Boulder field
Gentle, sinuous scarp
(flow fronts ?)
0
1
2 KM
N
ADAPTED FROM MAURICE GROLIER, 1970

Figure 1

APOLLO 11 BASALTS

Rock Type	400 μm	No. of Samples	Age (Æ)
A	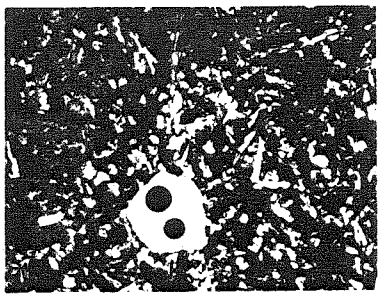	33	3.60
B1	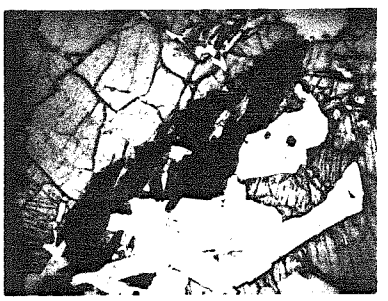	3	3.72
B2	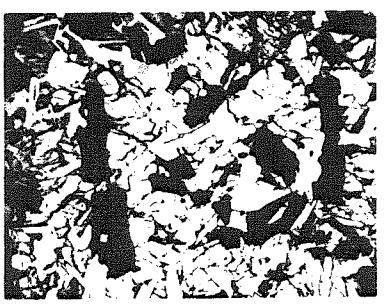	10	3.90
B3	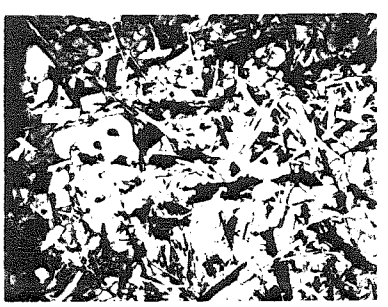	21	3.76
D		3	?

Figure 2

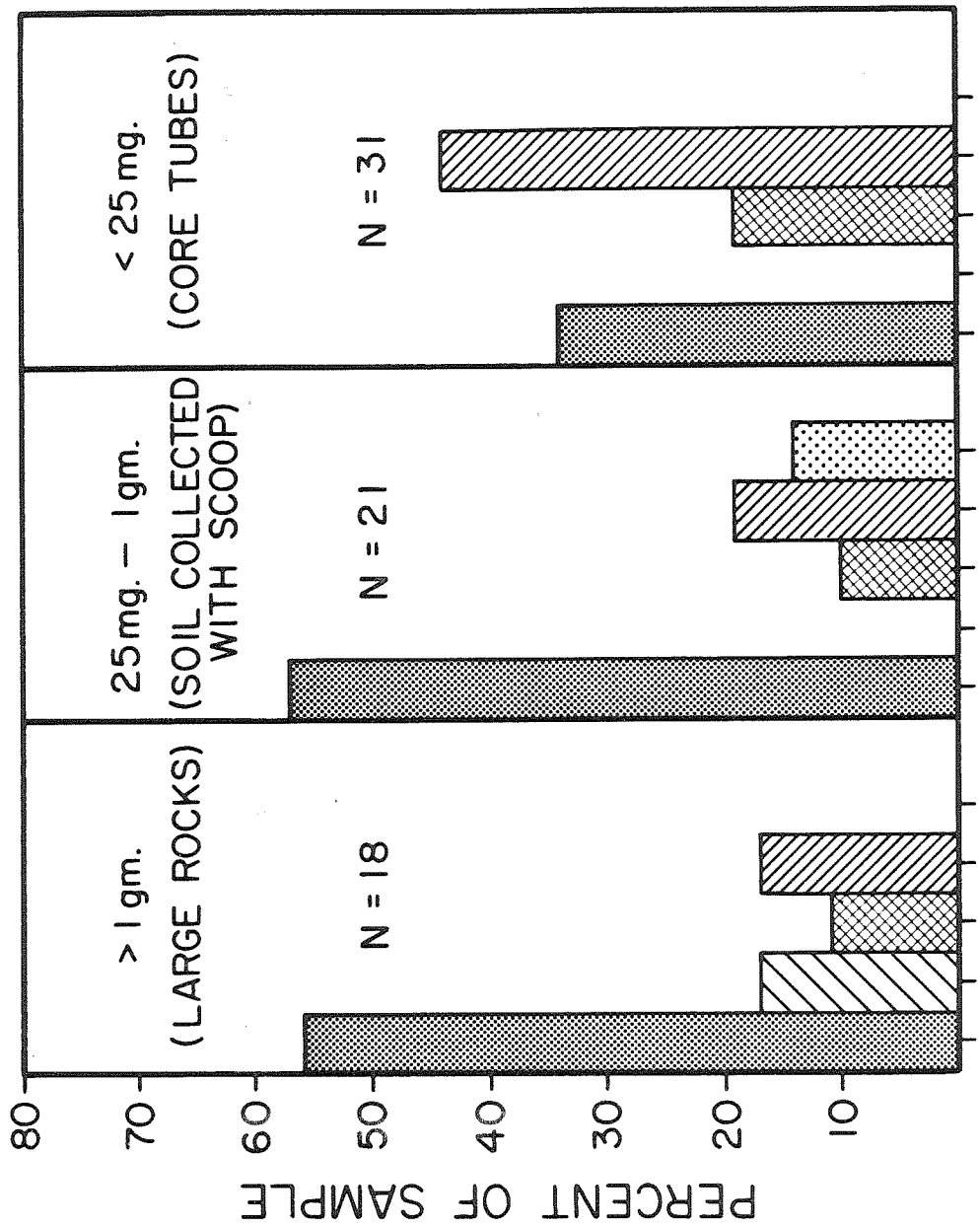
APOLLO 11 BASALT FRAGMENTS
> 1 gm.
(LARGE ROCKS)
N = 18
25 mg. – 1 gm.
(SOIL COLLECTED WITH SCOOP)
N = 21
< 25 mg.
(CORE TUBES)
N = 31
PERCENT OF SAMPLE
80
70
60
50
40
30
20
10
A B1 B2 B3 D
A B1 B2 B3 D
A B1 B2 B3 D
ROCK TYPE

Figure 3

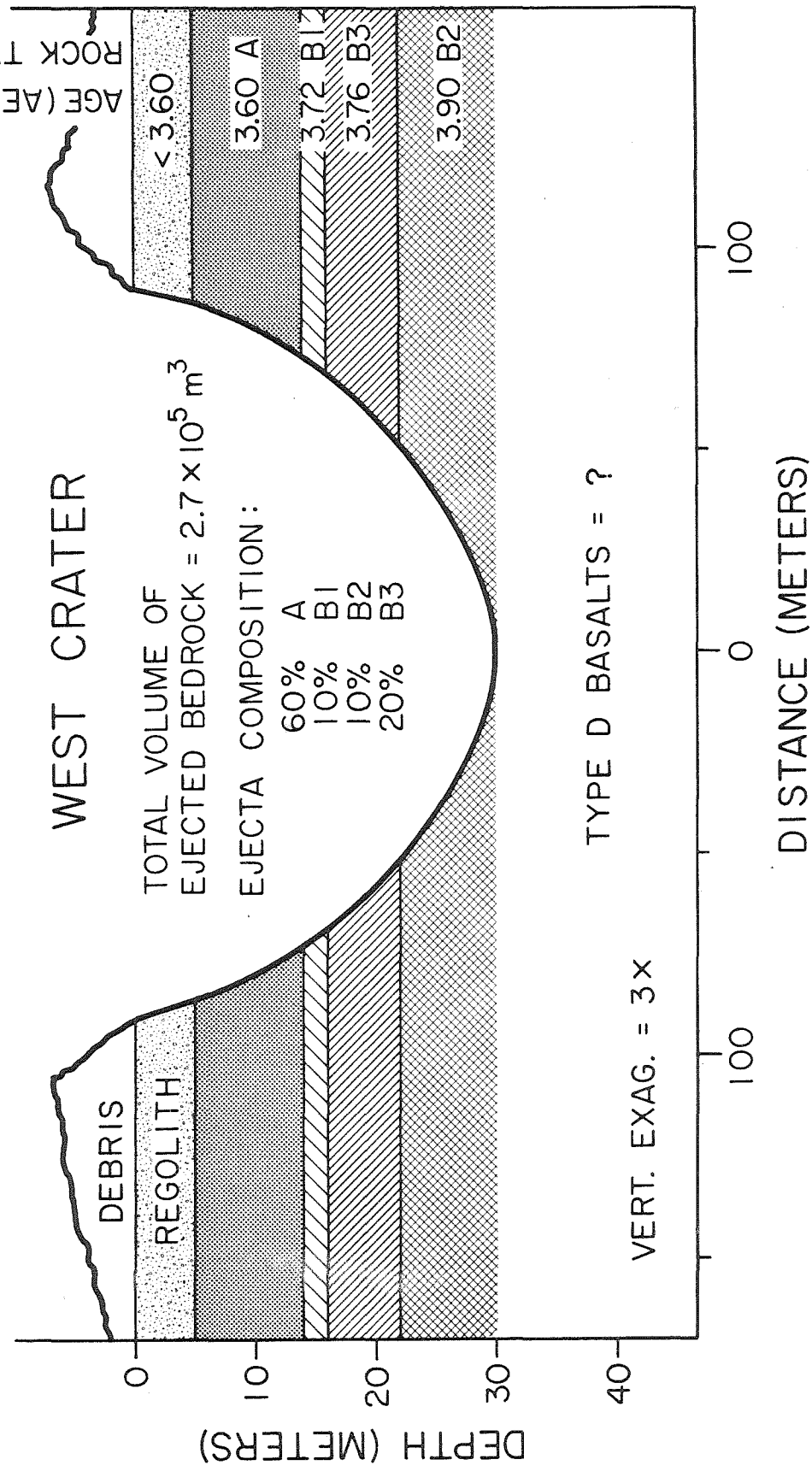
WEST CRATER
TOTAL VOLUME OF
EJECTED BEDROCK = 2.7 × 10^5 m^3
EJECTA COMPOSITION:
60% A
10% B1
10% B2
20% B3
TYPE D BASALTS = ?
VERT. EXAG. = 3×
DEBRIS
REGOLITH
< 3.60
3.60 A
3.72 B1
3.76 B3
3.90 B2
AGE (AE)
ROCK TYPE
DEPTH (METERS)
DISTANCE (METERS)
0
10
20
30
40
100
0
100

Figure 5

APPENDIX TO PART I.

Proc. Lunar Planet. Sci. Conf. 9th (1978), p. 359–463.
Printed in the United States of America

Comparative petrology and possible genetic relations among the Apollo 11 basalts

D. W. BEATY and A. L. ALBEE

Division of Geological and Planetary Sciences* California Institute of Technology, Pasadena, California 91125

Abstract—A comparative petrologic study has been made of the 19 large Apollo 11 basalt fragments, as well as two smaller vitrophyres, to answer the question, "How many igneous bodies are represented by this suite of rocks?" On each sample, we have made detailed petrographic and mineral chemical studies and performed an electron microprobe point count, which gives the mode, the range and distribution of all mineral zonation, and the bulk composition. These data confirm the twofold division of the Apollo 11 basalts into high-K (type A) and low-K (type B) basalts.

The ten low-K basalts may be divided into three groups, among which most textural, petrologic, compositional and isotopic properties are similar. These groups have been named B1, B2 and B3 as subdivisions of LSPET's type B basalt. Two samples, 10062 and 10050, do not simply fit into this framework and have not been classified. 10062 is similar texturally and petrologically to B3, but isotopically and chemically to B2. 10050 is similar petrologically to B2, but chemically to either B1 or B3. Bulk compositional and isotopic data indicate that B1, B2 and B3 cannot be related to each other by crystal-liquid fractionation and must represent three different igneous cooling units which span 200 m.y. in age.

The nine high-K basalt and two vitrophyre samples are similar compositionally and do not show any groupings, such as those for the low-K basalts. Six samples define what is termed here as the main series of basalts, a set of samples which define a linear differentiation trend on most variation diagrams. The most evolved sample (10049) can be derived from the most primitive (10024) by fractionation of about 10% armalcolite and/or ilmenite along with olivine and/or pyroxene. The fact that the cooling rate (determined by grain size) is independent of position in this fractionation series indicates that differentiation took place prior to the final emplacement of the lava flow. The simplest model is that of a high-level magma chamber, which was continuously fractionating during eruption. If these six high-K rocks are from the same lava flow, they, therefore, represent a sampling of lateral variation away from the vent. Two other high-K basalts can be related to this igneous system through mineralogic inhomogeneities. The remaining three high-K samples are porphyritic and may represent a batch of magma produced by the same differentiating magma chamber but which underwent a two-stage cooling history. Alternatively, they may represent the products of a meteorite collision with a partially crystalline high-K flow.

The exposure data of Geiss *et al.* (1977) strongly indicate that the high-K samples came from a lava flow (or flows) at the surface of Mare Tranquillitatis, and that the low-K basalts, which were all excavated in the same cratering event, came from beneath that flow. The most likely source of the low-K samples was West Crater, a sharp-rimmed, rayed crater 30m deep and located 400m east of the landing site. Two possible end member geologic histories for this portion of the mare may then be inferred: 1) Early rapid volcanism filled all but the last 30m of the basin, which was then filled by sporadic eruptions over the next 300 m.y. 2) The low-K samples are derived from an ejecta blanket (or blankets) which was covered by the high-K flow.

*Contribution No. 3070

INTRODUCTION

When the Apollo 11 basalts were first examined in hand sample by LPSET, they were divided into two types: fine-grained vesicular rocks (type A) and coarse-grained vuggy rocks (type B). Subsequent analytic work by Gast and Hubbard (1970), Compston *et al.* (1970a,b), and many others showed that there is a dichotomy of chemical compositions which corresponded closely to the hand sample classification. Most obviously, the type A basalts are high in K_2O (~0.30 wt.%); whereas, the type B basalts are low in K_2O (~0.05 wt.%). It was tacitly concluded for several years, therefore, (e.g., Papike *et al.*, 1976) that these rocks had sampled two lava flows of different compositions.

The detailed K-Ar work of Geiss and his coworkers (summarized in Geiss *et al.*, 1977) has now established that the type B samples have a range in age of ~200 m.y., a result confirmed by Rb-Sr studies (Papanastassiou *et al.*, 1977). Since such an age span demands multiple igneous cooling units, we have attempted to determine how many such units there were and which samples are genetically related to each other. The same consideration was given to the type A basalts, which all have about the same age. For each sample we have made detailed petrographic observations, undertaken electron microprobe studies of all phases, and performed a microprobe point count to provide the mode, the range and distribution of all mineral zonation, and the bulk chemical composition. Since the purpose of this paper is essentially comparative, all of the descriptive petrography, as well as most of the analytic work reported here, is original data collected on the same instruments by the same operator (DWB). However, most of these samples have been studied previously by a number of researchers, and their ideas have also been incorporated to some extent.

For the low-K suite, we conclude that there are three textural, petrologic and compositional groups, which have been named B1, B2 and B3 as subdivisions of LSPET's type B basalt. The characteristics of these groups are summarized in Table 1. These groupings will be compared, first petrographically, and then isotopically and chemically, to evaluate the possible genetic relations. Although a unique solution is not possible, these three petrologic groups may be adequately explained by three igneous cooling units, presumably separate lava flows. For the high-K rocks, there are no groupings which are coincident on both textural and compositional grounds, and hence, the suite has not been subdivided. These rocks also have been compared petrographically, isotopically, and chemically, and we conclude that they may be reasonably related to a single magma chamber that was differentiating during eruption. Finally, using the exposure histories determine by Geiss *et al.* (1977), astronaut observations, and photo interpretation, possible geologic histories of this portion of Mare Tranquillitatis are presented.

ANALYTICAL TECHNIQUES

The data points plotted on the various diagrams represent analyses performed consecutively on a single spot for 8–16 elements in groups of three using a MAC-5-SA3 electron microprobe interfaced

to a PDP-8/L computer for control and on-line data processing. Operating conditions were uniformly 15 kV accelerating voltage and 0.05 or 0.005 μA sample current (on brass) with beam current integration and pulse height selection. Elements with peak to background ratios greater than five (about 1 wt.% of the oxide) are counted to a precision of 1% or better. Minor elements (<1% abundances) are usually counted for 90 seconds which yields counting statistics of better than 10% for elements present in amounts greater than ~0.1 wt.%. Reproducibility (1σ) on two "known unknowns" over a 13-month period ranged from 1-½% (for elements with abundances >1%) to 3% of the amount present (for elements with abundances >0.1%) (Champion *et al.*, 1975).

Microprobe point counts were performed using a 161 eV Si(Li) detector interfaced to a NS-880 multichannel analyser with a dual floppy disk. For each sample we have measured the abundance, average composition, and range of composition of each mineral and calculated the bulk composition from the mass balance equations. Basically, the procedure is to analyse for 10 elements with 5 second counts at grid points on a polished thin section, identify the phase at each point to obtain the phase abundances, and accumulate an average spectrum for each phase. The critical factor in automated point count analysis is the correct and rapid phase identification at each grid point. Identification is accomplished by a transformation of the spectrum from compositional space to phase space, using pre-inverted compositional matrices for minerals observed in the rock. For a typical basalt, about 3000 grid points are analysed on an area of about 1 cm^2 with >99% of the points identified. The unknowns are discarded. The spectrum and identification for each point are stored sequentially on a floppy disk for subsequent reprocessing, editing, statistical analysis, or graphical display. Details of this procedure are given by Albee *et al.* (1978).

Each of the "average" mineral compositions given in the tables is actually a "representative" analysis. It is a complete wavelength dispersive analysis of a single point (or an average of several such points) that was selected from all the analyses as the best fit to the average values obtained by the point count. Only the major components of the average (such as Mg, Ca and Fe in pyroxene) were used in selecting the analysis. A computer printout of all the analyses may be obtained from A. L. Albee. The calculated chemical compositions for the bulk rocks in Table 3 are compared with values obtained by chemical analysis in Tables A1–A22. In most cases the values are very similar.

The reported uncertainty in the mode was calculated by dividing the points from each point count into groups of 100 and using these groups to compute the standard deviation of the mean for each phase. The standard deviation of the mean is a statistical parameter, which describes the uncertainty in a property of an infinite population (such as a lava flow) based on measurements of a finite subset (such as a thin section). There is a 68% probability that the "true" unknown value lies within the limits so derived. Note that point counting is the only technique which can place such constraints on the geologic body as a whole. Comparison of this uncertainty with that predicted using Bernoulli statistics (see Neilson and Brockman, 1977) gives a measure of the adequacy of a given thin section as a sample of the "infinite" body of rock. This is exceedingly important as a means to determine the statistical validity of each point count. For instance, if the olivine crystals are very large and clumped together in a given thin section, the modal olivine will have a much higher standard deviation of the mean than that of plagioclase, which may be small and evenly distributed. By comparison, these two phases might have identical Bernoulli uncertainties. Note that the standard deviation of the mean does *not* represent the error in the mode; it represents the confidence limits on the larger population. The error in each mode is *always* smaller than this. By assigning uncertainties to the average phase compositions, it is possible to calculate how the error propagates to the bulk composition. In all cases, the reported errors are absolute, referring to the "true", unknown value. However, two samples can be compared more accurately than we can absolutely determine either one. For comparative purposes, therefore, the reported errors in the bulk composition are overestimated.

All formula compositions and elemental ratios used in the text and in diagrams are in molecular proportions. Pyroxene formulae were calculated by assuming Fe^{2+}, Ti^{4+} and Cr^{3+}, normalizing the sum of the cations to four and sequentially calculating $Fe_2Si_2O_6$, $Mg_2Si_2O_6$, $CaCrAlSiO_6$, $CaTiAl_2O_6$, $NaAlSi_2O_6$, $CaAl_2SiO_6$, and $Ca_2Si_2O_6$ end members. The major components not shown on the pyroxene quadrilateral are represented on an inset diagram for Ti-Al-Cr. This triangular diagram includes the $RAl(AlSiO_6)$, $RCr^{3+}(AlSiO_6)$, $RTi^{3+}(AlSiO_6)$, and $RTi^{4+}(Al_2O_6)$ end members. The

stoichiometry of those analyses falling in the lower division of the triangle indicates that they contain Ti^{3+}. Those analyses falling below the 0.5 Ti–.5 Cr line may contain Cr^{2+}, octahedral vacancies, or tetrahedral Ti or Fe.

Feldspar formulae were calculated by normalizing the sum of the cation charges to 16 and sequentially calculating $KAlSi_3O_8$, $NaAlSi_3O_8$, $BaAl_2Si_2O_8$, $CaAl_2Si_2O_8$, (Fe, Mg)$Al_2Si_2O_8$, Ca(Fe, Mg) Si_3O_8, and [ ] Si_4O_8, in accordance with the findings of Longhi and Hays (1978). Feldspars were calculated in some earlier-studied samples (10044, 10003, 10050, 10045, 10072) by normalizing the sum of the cations to five and assuming no tetrahedral Fe. All other mineral formulae were calculated by normalization of the cation sums to appropriate values.

PART I. LOW-K BASALTS

1. CLASSIFICATION OF LOW-K BASALTS

LSPET originally distinguished the type B basalt on the basis of grain size and vesicularity, as being "medium-grained, vuggy, crystalline igneous rocks." Cristobalite was recognized, but olivine was not recognized in hand sample. Hence, these samples originally were called cristobalite basalts or microgabbros (Apollo 11 PSR, p. 124–126). A preliminary comparative study was made by James and Jackson (1970), who split the low-K basalts on the basis of grain size.

To subdivide the ten type B basalts, we have relied primarily on texture and mode. Although these two parameters are not necessarily indicative of different lava flows, they are directly observable and allow ready classification of additional samples. These divisions have been retained because the bulk compositional and isotopic groupings coincide with the textural and modal groupings. Table 1 summarizes the textural, chemical and isotopic characteristics of the type B basalts. Note that 10050 and 10062 have not been grouped because their textures, mineralogies, and isotopic and chemical compositions do not all match any one of the three groups.

One of the most significant characteristics in Table 1 is the relation between modal cristobalite and modal olivine, shown in Fig. 1. Because olivine and cristobalite are an incompatible pair, the diagram reflects both bulk composition (silica saturation) and cooling rate. The boundary between olivine normative and quartz normative rocks and the approximate limit of the olivine liquidus field, based on the experimental work of Walker *et al.* (1975), are shown for reference. The clustering of the modal data is pronounced and is one of the essential elements of the classification system. The isochemical lines on this figure are parallel to the pyroxene-forming reaction line ($Fo_{70} + SiO_2 = En_{70}$). Group B1 has a drastically different composition from any of the other groups. In terms of silica saturation 10092 seems to have a similar composition to group B2. However, both compositional and mineral-chemical data (see below) indicate that it differs from the rest of B3 by olivine accumulation and that it has a fundamentally different bulk composition from B2. Sample 10062 is like group B3, but sample 10050 has a silica saturation like group B3 and a cooling rate like group B2.

Having thus defined the three subdivisions of the low-K basalts, we may now examine each group in detail.

Table 1. Textural, compositional, and isotopic characteristics of the Apollo 11 low-K basalts.

	Group B1			Group B2		?*	Group B3			?**
	(10044	10047	10058)	(10003	10029)	(10050)	(10020	10045	10092)	(10062)
Overall texture	subophitic			ophitic			ophitic-intergranular			
Average grain size	coarse grained (800μ)			medium grained (500μ)			fine grained (200μ)			
Max plag ⊥ (010) (μm)†	250	290	280	100	120	190	50	70	60	70
Ilmenite morphology	cockscomb intergrowths w. pyroxene, anhedral			blocky, equant, and subhedral to euhedral			acicular and skeletal, also equant forms common in 10045, 10092			
Mode: Mg-olivine	0	0	0.02	0.40	0.26	0.73	4.71	3.50	4.91	4.98
cristobalite	6.71	6.22	4.77	1.06	0.58	2.31	4.64	3.13	2.59	4.64
% pyx = pigeonite	0	0	0	15.3	19.2	11.3	0.9	4.4	6.6	1.5
Olivine habit	absent			small, anhedral, mantled			porphyritic to glomeroporphyritic			
$\frac{Fe}{Mg}_{ol.}$ $\frac{Fe}{Mg}_{Rock}$ Bulk	—	—	0.25	0.38	0.41	0.38	0.28	0.25	0.33	0.27
Olivine composition	Fa_{99}	Fa_{99}	Fa_{32}	$Fa_{35} \rightarrow Fa_{97}$ intermediate		$Fa_{31\text{-}60}$	$Fa_{27} \rightarrow Fa_{50}$; Fa_{95} low			
LIL concentrations		high								
Bulk comp.: MgO	5.95	5.51	5.80	7.60	7.53	7.90	7.97	7.67	8.90	6.81
FeO	17.88	19.32	19.64	19.92	20.49	17.83	18.29	19.27	18.38	18.04
TiO_2	10.25	9.19	10.60	10.46	12.15	11.12	10.61	11.02	12.74	10.57
Ar-Ar age (b.y.)[1]	3.71	3.74	(3.71)	3.91	(3.89)	3.75	(3.77)	(3.75)		3.82
Rb-Sr age (b.y.)[2]	3.71		3.63	3.84						4.01
Sm-Nd age (b.y.)[2]										3.88
Exposure age (m.y.)[1]	70	110	65	130		400	120	110		85
($^{131}Xe/^{126}Xe$)[1]	3.8	3.4	3.6	3.4		9.6	3.7	4.5		
Interpretation	10044 and 10047 are identical, 10058 is less differentiated. All three may be fragments of the same block.			10003 and 10029 from same unit; 10050 may be from either B1 or B3.			10020 and 10045 ≈ liquid composition; 10062 has lost and 10092 gained olivine and ilmenite. 10062 probably from same unit as B2.			

*10050 is distinguished from B2 on the basis of bulk composition and age.

**10062 is distinguished from B3 on the basis of its rare earth pattern.

Ages in parentheses are from intermediate temperature plateaus and are considered less reliable.

†According to the experiments of Grove (1977) and Walker *et al.* (1978) this parameter is related to the cooling rate through $\log_{10}$ [cooling rate] (°C/hr)$=-1.6 \log_{10}$ [plag width] (μm) + 3.2

[1]Geiss *et al.* (1977)

[2]Papanastassiou *et al.* (1977)

2. PETROGRAPHIC CHARACTERISTICS

A. Group B1

Group B1 consists of samples 10044, 10047, and 10058. They are so similar to one another that it seems quite likely that these rocks are fragments of a larger block that broke either at the landing site, or less likely, in the bulk sample container. There are measurable differences among these three samples, but the grain size is so coarse compared to the sample size that these are attributed to centimeter-scale inhomogeneities.

Texturally, these rocks are coarse-grained (800 μm), subophitic basalts (Fig. 2) comprised of anhedral grains of ilmenite (11–13%), lath-shaped plagioclase (34–35%), equant pyroxene (45–47%), interstitial cristobalite (6%), and minor amounts of troilite, Fe-metal, ulvöspinel, fayalite, apatite, tranquillityite, residual glass, and K,Ba-feldspar. A single crystal of Mg-olivine was observed in 10058,46. The phase abundances, average phase compositions and bulk compositions of these three samples are listed in Tables 2, 3, A8, A10, and A14. The overall subophitic texture is characterized by large (1–2 mm), subhedral,

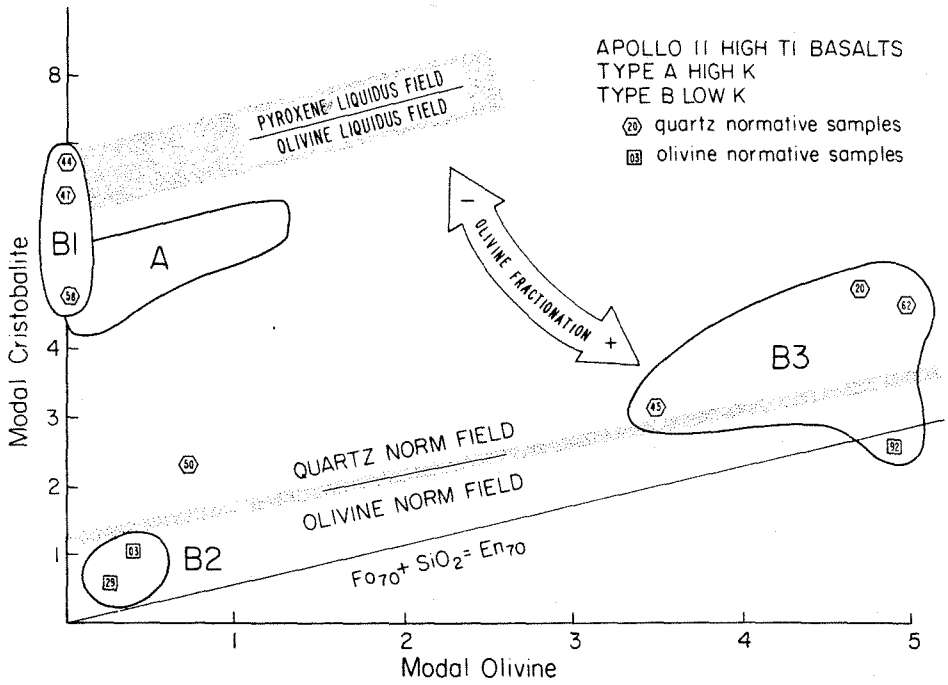

Fig. 1. Modal cristobalite and modal olivine for the low-K basalts. Field of high-K basalts is shown for comparison. Note both the obvious clustering of the data and the fact that B1 has a clearly different composition than the other samples. Boundaries of the olivine normative field and the olivine liquidus field for this composition are shown for reference.

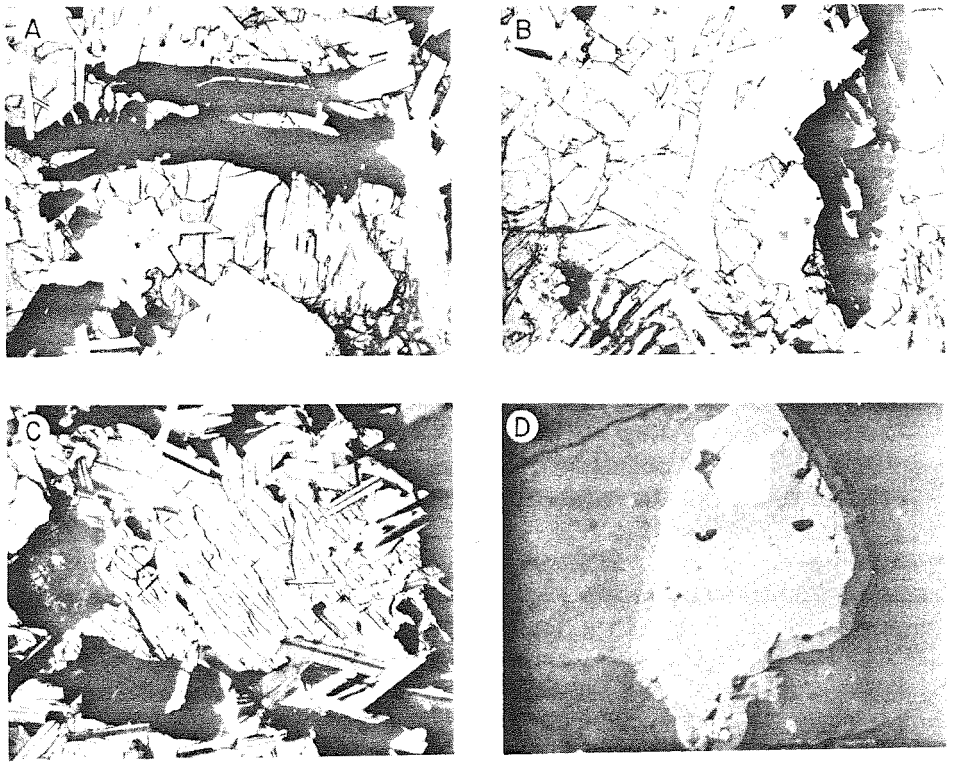

Fig. 2. Photomicrographs of Group B1. (A) 10044, transmitted light; 2.0 mm full scale. (B) 10047, transmitted light; 2.0 mm full scale. (C) 10058, crossed polars; 2.0 mm full scale. In A,B,C three minerals are visible: plagioclase (white laths), ilmenite (opaque), pyroxene (gray with cleavage). Note the distinctive ilmenite morphology in A,B and the segregation of feldspars to the margins of the pyroxene in C. (D) 10044, reflected light; 100 μm full scale. Intergrowth of troilite (white), ulvöspinel (light gray), and ilmenite (medium gray), mantled by a thin rim of fayalite (dark gray).

sector-zoned pyroxene crystals whose rims are intergrown with randomly-oriented laths of plagioclase (Fig. 2c). Ilmenite is evenly dispersed, but most of the plagioclase has been segregated into clumps interstitial to the large pyroxenes. Cristobalite occurs in coarse patches, and the residual phases occupy the angular interstices between plagioclase, pyroxene, and ilmenite.

Ilmenite is typically anhedral and occurs in characteristic lobate intergrowths with pyroxene and plagioclase (Fig. 2a,b). Many grains show a tendency towards a bladed habit. Larger ilmenite grains may poikilitically enclose plagioclase laths, which commonly transect pyroxene-ilmenite grain contacts. Zoning within individual ilmenite grains is insignificant, but a small amount of intergranular variation is present. In all cases, the total range of zonation (expressed as mole % geikielite, $MgTiO_3$) is from Gi_4 to Gi_0, with an average ilmenite composition of Gi_{2-3}. Although ilmenite is usually absent from the cores of the large sector-zoned

pyroxene grains, the pyroxene that occurs in lobate intergrowths with ilmenite (Fig. 2a,b) is a magnesian augite. This indicates that ilmenite co-crystallized with the earliest pyroxene. The Cr_2O_3 content of the ilmenite ranges from 0.1 to 0.6 wt.% and shows a consistent decrease with decreasing MgO. Al_2O_3 and SiO_2 are usually less than 0.1%; V_2O_3 can rarely be detected; and Nb_2O_5 and ZrO_2 each range up to 0.4 wt.%. The highest Nb and Zr contents are found in the mesostasis ilmenite.

One rounded, anhedral olivine grain is mantled by a large zoned pyroxene crystal in 10058,46. The olivine is compositionally zoned from end to end (Fa_{32} to Fa_{42}), the adjacent pyroxene changing its iron to magnesium ratio sympathetically. This is consistent with continuous reaction of the olivine with the melt as the pyroxene mantled it from one end to the other. The presence of olivine in 10058 confirms its more mafic nature as indicated by the relative abundance of cristobalite (Fig. 1). 10047 and 10044 both have about 6.5 vol.% cristobalite; whereas, 10058 has only 4.8%. It therefore "remembers" the prior presence of some olivine that has now reacted out. Late stage olivine occurs as isolated interstitial grains (Fa_{99}) in the mesostasis areas in all three samples, as rims around late stage ilmenite and ulvöspinel grains (Fig. 2d) and in intricate, wormy mixtures with ferrohedenbergite and SiO_2. The olivine rims on ilmenite resemble the olivine rims on magnetite in the Skaergaard (A. R. McBirney, pers. comm., 1978). Unfortunately, these rims, as well as the wormy intergrowths (which are the subsolidus breakdown products of pyroxferroite), are too small for microprobe analysis. Both primary magmatic crystallization and a subsolidus origin therefore are indicated.

Plagioclase predominantly occurs as euhedral to subhedral, well-twinned laths (Fig. 2c). The latest plagioclase to form, however, tends to be coarser, anhedral, poorly-twinned, and poikilitically encloses earlier plagioclase laths and ilmenite. Both early and late plagioclase are inclusion-free. Compositionally, the three B1 samples all zone from An_{94} to around An_{70} (Figs. 3–5), with the average plagioclase in the range An_{85-86}. The K content of the plagioclase steadily increased with increasing Ab content until the liquid composition entered the two feldspar field in the final stages of crystallization. At that point, Ba had been many-fold concentrated in the melt such that the second feldspar was extremely Ba-rich, containing 74 mole percent orthoclase and 13 mole percent celsian. The FeO content of the plagioclase (0.24–0.89 wt.%) increases with increasing albite content, while the MgO content decreases. Stoichiometry suggests that most of the iron is tetrahedral. The excess silica substitution [ ] Si_4O_8 increases in a very regular way with both sodium and iron content (Figs. 4, 5), reaching a maximum of 4.6 mole% in the most sodic feldspars.

Pyroxene occurs as anhedral to subhedral, equant crystals with a fairly restricted size distribution centered about 1.2 mm. Sector zoning is prominent and visible in both plane- and cross-polarized transmitted light. Discontinuous rims of pyroxferroite are common. The color of the pyroxene ranges from light brown to rose, while the pyroxferroite is light yellowish-green. Brown *et al.* (1970) reported optically-visible pigeonite exsolution lamellae 1–2 μm thick in

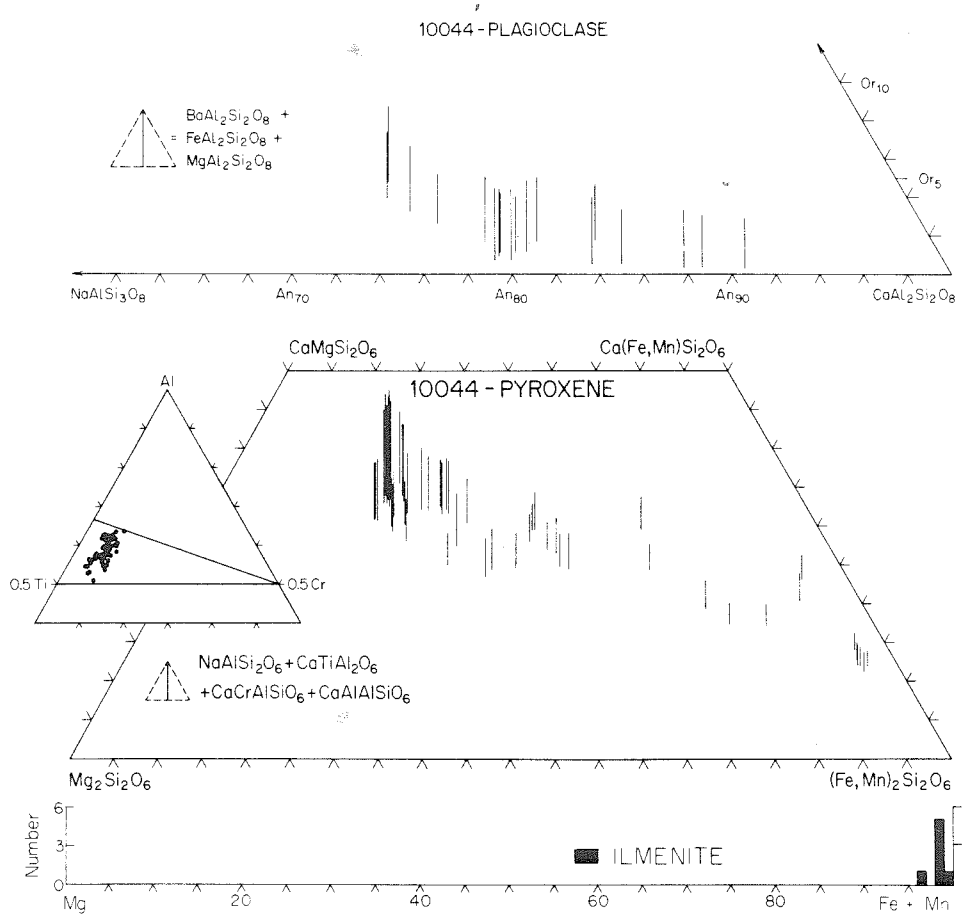

Fig. 3. Composition of pyroxene, plagioclase and ilmenite in 10044.

10058 but were unable to confirm their identification with the microprobe. Bailey *et al.* (1970) presented a convincing argument for exsolution in the form of a single crystal X-ray diffraction study on 10044 and concluded that the pigeonite lamellae average about 0.025 μm wide. In this study, no pigeonite was observed either optically or sampled by the point count (~4500 analyses with a 1 μm diameter beam), a result consistent with the work of Bailey *et al.* (1970). Most pyroxene crystals have relatively inclusion-free cores, but towards their margins the amounts of included plagioclase, ilmenite, troilite and ulvöspinel increase. The pyroxferroite rims locally contain large (50 μm) inclusions of apatite.

Pyroxene zoning is relatively simple because only a single pyroxene phase crystallized. Augite cores zone with steadily increasing Fe and decreasing Ca to about $Wo_{20}En_{10}Fs_{70}$, and are then surrounded by discontinuous pyroxferroite

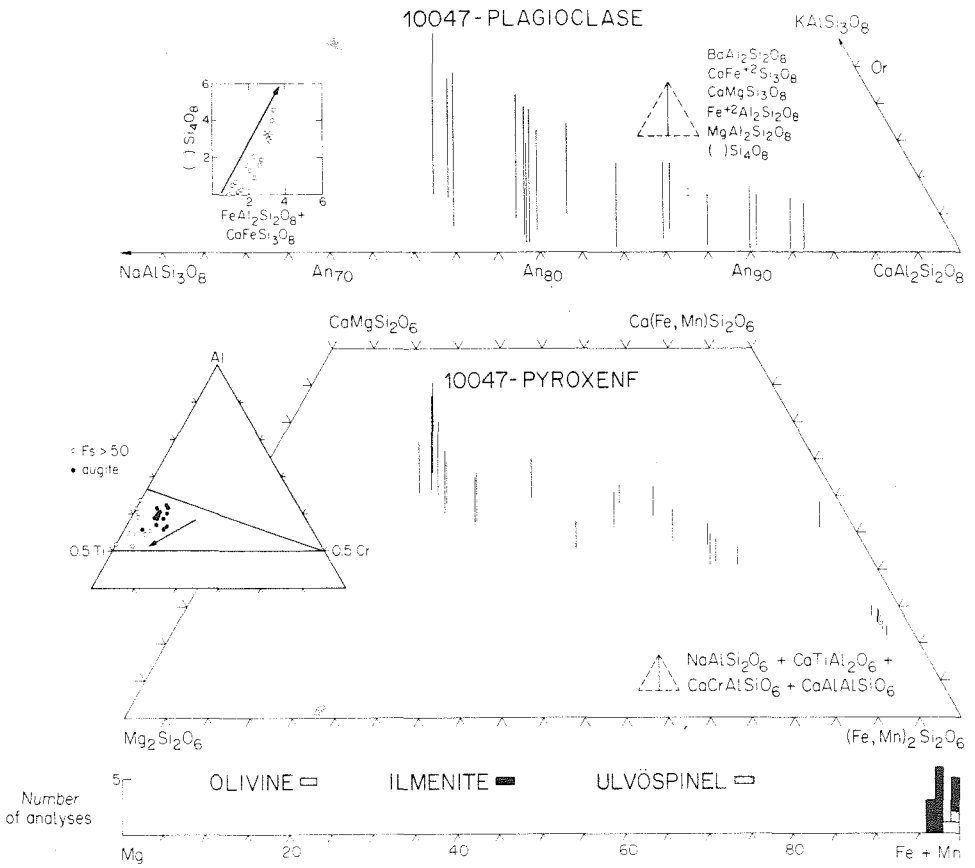

Fig. 4. Composition of pyroxene, plagioclase and ilmenite in 10047.

rims (Figs. 3–5). All sectors of the pyroxene show this trend, but the (001) sector is less calcic by about 5 mole percent than the (010) sector. The difference in color between the two sectors is due to the lower abundances of Al, Ti and Cr in the (001) sector (Albee and Chodos, 1970). A trend towards ferrohedenbergite ($Wo_{30}En_5Fs_{65}$) is present locally in these samples, especially in the mesostasis areas which contain magmatic fayalite. Differentiation locally followed a Skaergaard-type ferrohedenbergite trend, but in most cases it followed the metastable pyroxferroite trend.

The metastable nature of pyroxferroite (Chao *et al.*, 1970) is indicated by the presence of its breakdown products—fayalite, silica and pyroxene—in micron-scale intergrowths similar to those found in devitrified glass. Defocused beam analyses of these intricate mixtures have pyroxene compositions and are shown in Fig. 5. The original structure of the areas cannot be determined, but both pyroxferroite and pyroxene are unstable in this compositional range. It is

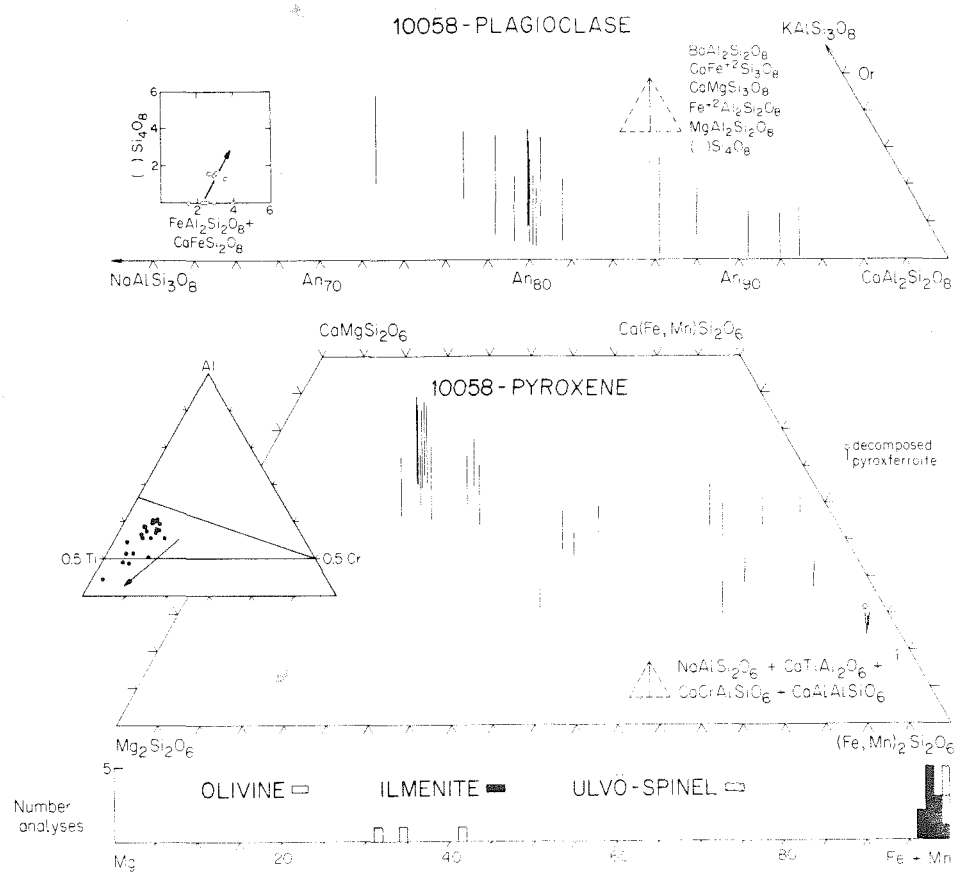

Fig. 5. Composition of pyroxene, plagioclase, olivine and ilmenite in 10058.

noteworthy that the decomposed areas are usually roughly circular in shape; whereas, crystalline pyroxferroite forms either irregular grains in the mesostasis areas or rims on pyroxene. This suggests that the parent for these areas was pyroxene rather than pyroxferroite.

Al, Ti, Cr, and Na contents all decrease continuously with increasing Fe content. The earliest and most aluminous pyroxenes contain 4.1 wt.% Al_2O_3 and 3.3 wt.% TiO_2, but both rapidly fall to less than 2 wt.% each. The relative proportions of Al, Ti, and Cr (Figs. 3–5) lie in a field which indicates the presence of trivalent Ti. Zoning is towards the Ti corner and slightly away from Cr, with some analyses extending below the 0.5 Ti-0.5 Cr join (Fig. 5). This may indicate the presence of tetrahedral Ti or octahedral vacancies.

Cristobalite is fairly coarse (up to 400 μm) and typically anhedral, although subhedral morphologies are present. Inversion twinning due to the transformation from high to low cristobalite at 280°C (Nord *et al.*, 1974) is abundant.

Tridymite is known to be present (e.g., Dence *et al.*, 1970, Bailey *et al.*, 1970) both in B1 and in some of the other low-K basalts. However, in this study all SiO_2 is reported as cristobalite.

Ulvöspinel usually occurs as isolated, equant anhedra poikilitically enclosed by pyroxene in the mesostasis areas. It also occurs intergrown with ilmenite in a probable eutectic relationship (Fig. 2d). The proportion of ilmenite to ulvöspinel in the intergrowths ranges from 1:3 to 1:1. The ulvöspinel has a relatively constant composition of about $Ulv_{93.4}Chr_{0.6}Her_{6.0}$ with Fe/(Fe + Mg) in excess of 0.99. The stoichiometry provides no evidence for a $FeTi_2^{3+}O_4$ component. Other mesostasis phases present include tranquillityite, fluorapatite, baddelyite, and troilite and amoeboid Fe-metal. The tranquillityite contains 2.0 wt.% Y_2O_3, 0.3% Nb_2O_5, 1.0% Al_2O_3 and 1.0% CaO in addition to the major components Si, Ti, Fe, and Zr. Fluorapatite contains about 1.4 wt.% SiO_2, 1–2 wt.% FeO, 1 wt.% Y_2O_3 and about 1 wt.% REE oxides. Baddelyite contains 2.8 wt.% TiO_2, 0.2 wt.% MgO, 0.1 wt.% Cr_2O_3, and little else besides ZrO_2. A K, Si-rich residual glass ($Qtz_{45}Fld_{54}Pyx_{0.2}$ $Other_1$) is present but sparse, and silicate liquid immiscibility is indicated by the divitrified remains of a high-Fe glass. Roedder and Weiblen (1977) in their exhaustive study of silicate melt inclusions in these samples found not only the above two glasses but also an enigmatic high SiO_2 (76%), low K_2O (0.03%) glass. They have postulated 13 mechanisms for the origin of this melt, all of which are unsatisfactory to some degree.

Other phases known to be present in B1 include whitlockite (Albee and Chodos, 1970), Cr-ulvöspinel (Brown *et al.*, 1970), monazite (Lovering *et al.*, 1974) and zirconolite (Wark *et al.*, 1973). The presence of whitlockite indicates that the B1 rocks were oversaturated in phosphate with respect to fluorine, and, although the whitlockite/apatite ratio is not known in the other groups due to their fine grain size, the same condition probably held. In addition, Gay *et al.* (1970) chipped a dark green clinoamphibole from a vug in 10058.

We interpret the crystallization sequence as follows: Plagioclase, pyroxene and ilmenite appeared on the liquidus together, i.e., the liquid was multiply saturated. In 10058 olivine formed before pyroxene but soon reacted out. This property of multiple saturation is very characteristic of near surface fractionation at low pressure as pointed out by O'Hara *et al.* (1974). These three major minerals then co-crystallized all the way to the solidus, being joined ultimately by cristobalite and the mesostasis minerals. Both sulfide and silicate liquid immiscibility occurred, but neither can be placed very accurately in the paragenetic sequence due to obliteration of the evidence by subsequent crystallization. However, sulfide immiscibility probably occurred fairly early and silicate immiscibility fairly late.

B. Group B2

Group B2 consists of two samples, 10003 and 10029. Both samples are very old, 3.91 and 3.89 b.y. (Geiss *et al.*, 1977), and their bulk compositions, textures, and petrology are so similar that it is very reasonable to assume that they came

from the same lava flow. Several characteristics, however, indicate that 10029 cooled somewhat more slowly than 10003.

These samples are relatively medium-grained (~500 μ), spectacularly-ophitic basalts comprised of equant, blocky grains of ilmenite (13–16%), small, anhedral, mantled olivine (0.3%), and small plagioclase laths (34–35%) set in much coarser pyroxene (47–50%) (Fig. 6a,b). Also present are late cristobalite, apatite, troilite, Fe-metal, ulvöspinel, and tranquillityite. One grain of K, Ba-feldspar was found in 10003, and a few grains of Cr-spinel poikilitically enclosed in olivine were observed in 10029.

The overall texture of B2 is characterized by randomly oriented laths of plagioclase that, although locally occurring in clusters, tend to be evenly distributed through the sample without forming an interlocking network (Fig. 6a,b). Instead they are suspended in the much coarser pyroxene. The abundance of plagioclase inclusions in the margins of the pyroxenes is greater than in the cores, indicating the beginnings of igneous segregation. Ilmenite is distributed randomly while olivine is generally confined to the cores of pyroxene grains (Fig. 6d). All of the other phases are restricted to the interstitial mesostasis areas.

Ilmenite typically occurs as blocky, straight-sided, subhedral grains, rarely euhedral, with a seriate size distribution up to a maximum of 400 μm (Fig. 6a, b). In 10003, many of the ilmenite grains contain rutile lamellae along $(10\bar{1}2)$ and Cr-spinel lamellae along (0001), and these grains tend to have higher Mg-values than those without exsolution. The lesser abundance of these features in 10029 is directly attributable to cooling rate: The ilmenite in 10029 was able to equilibrate to a lower temperature than the ilmenite in 10003. Although individual ilmenite crystals are essentially unzoned, intergranular variation is extensive. Both samples have ilmenite compositions that range from Gi_{20} in the cores of pyroxenes to Gi_0 in the mesostasis areas (Figs. 7–8). In 10003, the most magnesian ilmenite is found in vermicular intergrowths with olivine in which the olivine acts as the host, and the ilmenite occurs as micron-sized wormy blebs. This is interpreted as heterogeneous nucleation of ilmenite on the growing olivine crystal. These vermicular intergrowths are less abundant in 10029. Plagioclase laths commonly invade ilmenite grain boundaries, but it cannot unambiguously be determined which began to crystallize first. Circular glass inclusions are common in ilmenite and are typically partially crystalline with incipient sheaves of pyroxene crystallites. Although the ilmenite locally has an acicular habit, particularly the late ilmenite, it does not form skeletal grains. Lobate intergrowths with pyroxene, characteristic of Group B1, are also present but rare.

There is a good positive correlation between Mg and Cr content in ilmenite. The Gi_{20} grains contain about 0.7 wt.% Cr_2O_3, while Gi_1 grains have only about 0.4 wt.%. Al_2O_3, V_2O_3 and Nb_2O_5 rarely exceed 0.05 wt.% (our detection level), but in the most Fe-rich grains, Nb_2O_5 ranges up to 0.1 wt.%. ZrO_2, however, increases in a non-linear way with FeO content. From Gi_{20} to Gi_4, ZrO_2 rarely exceeds 0.1 wt.%, but from Gi_4 to Gi_1, it ranges up to 0.4 wt.%. One analysis of the exsolved rutile was obtained, and it contained 1.1 wt.% FeO, 0.3 wt.% Cr_2O_3, and trace amounts of Zr, Mg, Mn, and Nb. The high-Ti, Al (as evidenced by

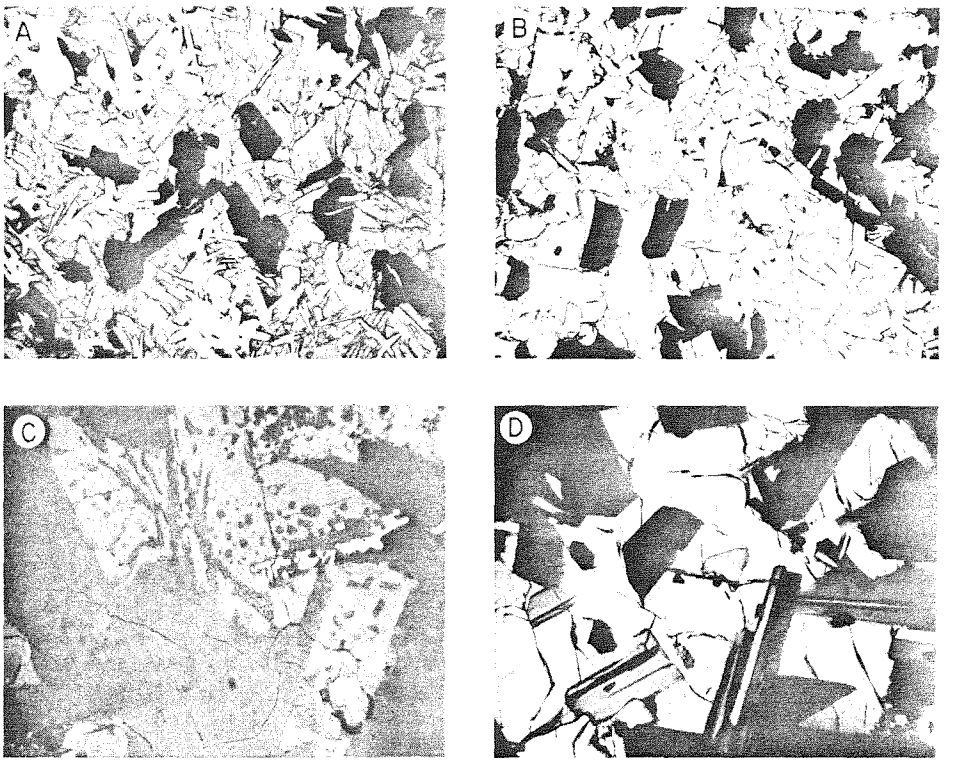

Fig. 6. Photomicrographs of Group B2. (A) 10003 transmitted light; 2.0 mm full scale. (B) 10029 transmitted light; 2.0 mm full scale. Ilmenite (opaque) and plagioclase (white) ophitically enclosed in pyroxene (gray with cleavage). (C) 10003 reflected light; 200 μm full scale. Late-stage fayalite (medium gray) enclosing spheres of plagioclase (dark gray). Texture probably formed because of liquid immiscibility. (D) 10029 crossed plars; 500 μm full scale. Olivine (center, dark gray), twinned plagioclase laths, and ilmenite (opaque) opitically enclosed in pyroxene.

rutile and spinel exsolutions), and Cr contents of the early ilmenite have been interpreted as evidence of previously existing armalcolite (Beaty *et al.*, 1977). Textural evidence for this is lacking, however, and there is no armalcolite presently remaining in these or any of the other low-K samples.

Plagioclase occurs as euhedral to subhedral laths with a very limited size range (0.1 to 0.4 mm long). Individual crystals are well-twinned and typically have a core (60–80 percent of the grain) that is relatively unzoned (An_{93}-An_{88}), which is surrounded by a strongly zoned rim (to An_{70}) (Figs. 7–8). The calcic cores locally contain minute ($<5\mu$) ilmenite platelets aligned along (010). Rare, subrounded to elongate, olivine inclusions and tiny pyroxene inclusions occur in both core and rim. In a few cases, plagioclase is intergrown on a fine scale with cristobalite in the mesostasis areas. Rows of glass spheres are incorporated in the rims of many

laths, a feature interpreted by Roedder and Weiblen (1970) as due to the onset of silicate liquid immiscibility. One crystal of K,Ba-feldspar was detected in 10003 ($Or_{75}An_1Ab_9Cel_{15}$) indicating late-stage entry into the two feldspar field.

There are two important minor component substitutions in B2 plagioclase, Fe^{2+} either as $Fe(Al_2Si_2O_8)$ or $Ca(FeSi_3O_8)$, and excess Si as $[\ ]Si_4O_8$. In 10029 both iron and excess silica increase consistently with increasing Ab content (Fig. 8). In the last stages of crystallization, the feldspar has about 6 mole percent $[\ ]Si_4O_8$ and 5 mole percent of Fe feldspar. By comparing the total aluminum to the sum of the contents of the distorted 8-fold site and assuming all Fe is divalent, it is possible to calculate the apparent distribution of iron between the two sites. This calculation indicates most of the iron is tetrahedral and that the ratio Fe^{VIII}/Fe^{IV} is reasonably constant at about 0.6 throughout the crystallization history.

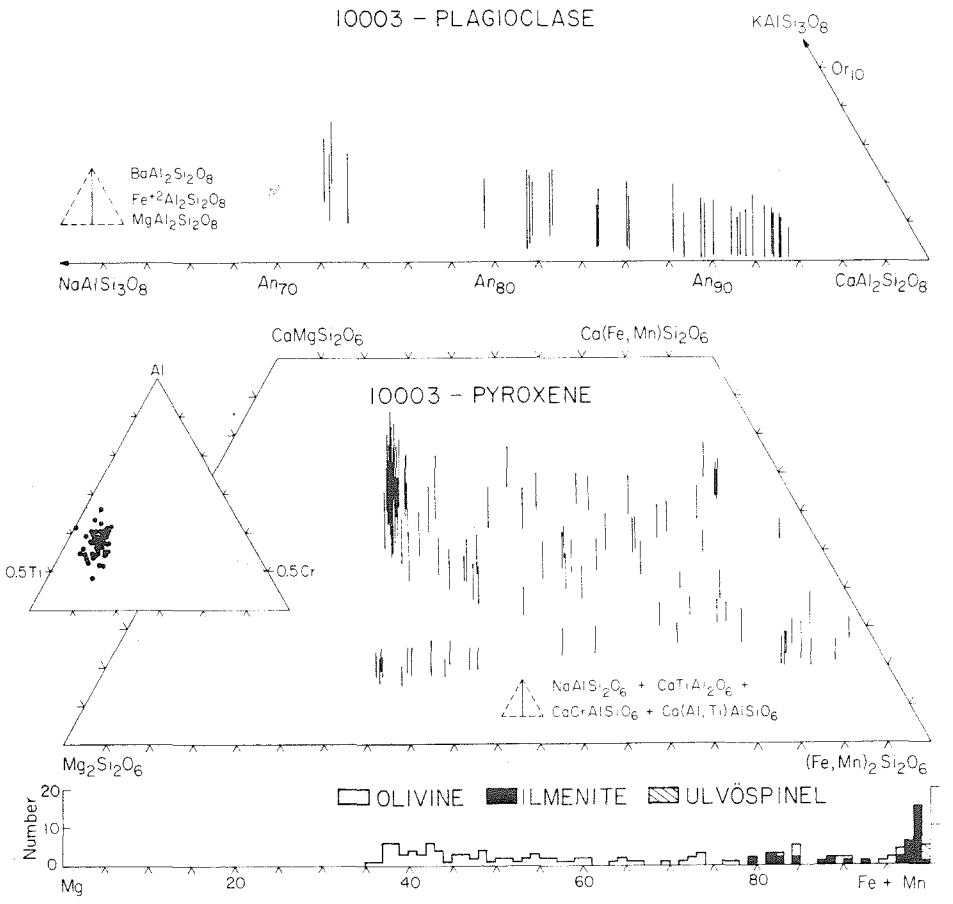

Fig. 7. Composition of pyroxene, plagioclase, olivine and ilmenite in 10003.

Olivine grains are subrounded and anhedral, ranging in size up to 380μm, but most grains are smaller than 100μm. Typically olivine is located in the cores of pyroxene crystals where it has rounded or embayed outlines. The zoning is frequently not concentric but rather longitudinal from one end of the grain to the other. This indicates either resorption or continued equilibration with the melt as the olivine was being mantled from one end to the other. There are no inclusions of either plagioclase or spinel in olivine in 10003, but spinel inclusions are present in 10029. Rare subhedral to euhedral ilmenite inclusions are present in both samples and have straight or gently curved grain contacts against the enclosing olivine. Where the edge of the olivine grain is in contact with external ilmenite, however, the boundary is characterized by the vermicular intergrowths discussed above.

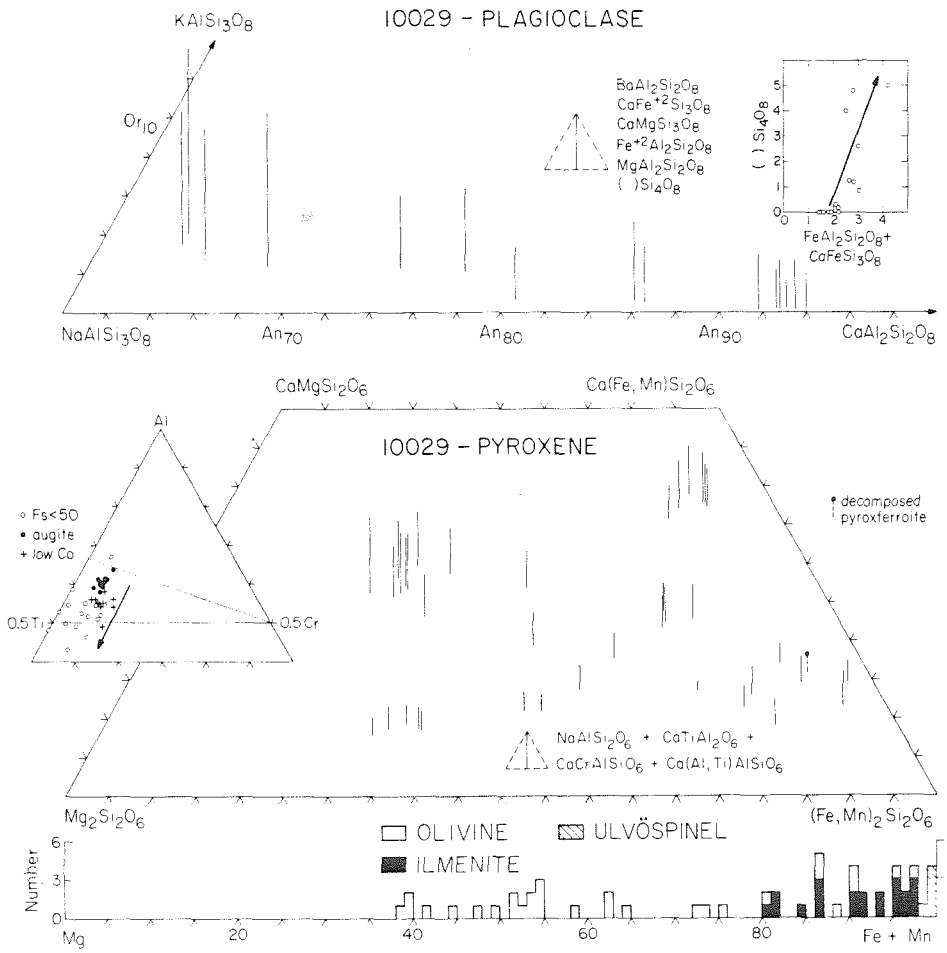

Fig. 8. Composition of pyroxene, plagioclase, olivine and ilmenite in 10029.

As with ilmenite, chemical zoning within individual olivine crystals is small (<5 mole percent), but intercrystalline variation spans the range Fo_{63} to Fo_3 (Figs. 7–8). The fact that olivine zones continuously to fayalite is a particularly striking feature and clearly marks 10003 and 10029 as similar to each other and different from the other samples (Fig. 9). In spite of this range, the most magnesian olivine in both samples is clearly out of equilibrium with a liquid of the composition of the bulk samples (Fig. 10). The earliest olivines, therefore, have not been preserved. The composition of the average olivine is difficult to estimate from individual analyses, but the point count indicates that it is Fo_{52}. Ca, Al, Cr, and Ti are all present in small amounts (<0.30 wt.% of the oxide) in olivine; whereas, Ni can rarely be detected.

The pyroxene in B2 is very complex optically, chemically and crystallographically. Color ranges from light pink in the cores to light green in the rims. Compositional zonation spans most of the pyroxene quadrilateral. Sector zoning is rarely visible, but single crystals may be zoned optically through 130° of extinction. Discontinuous rims of pyroxferroite are not present, and although

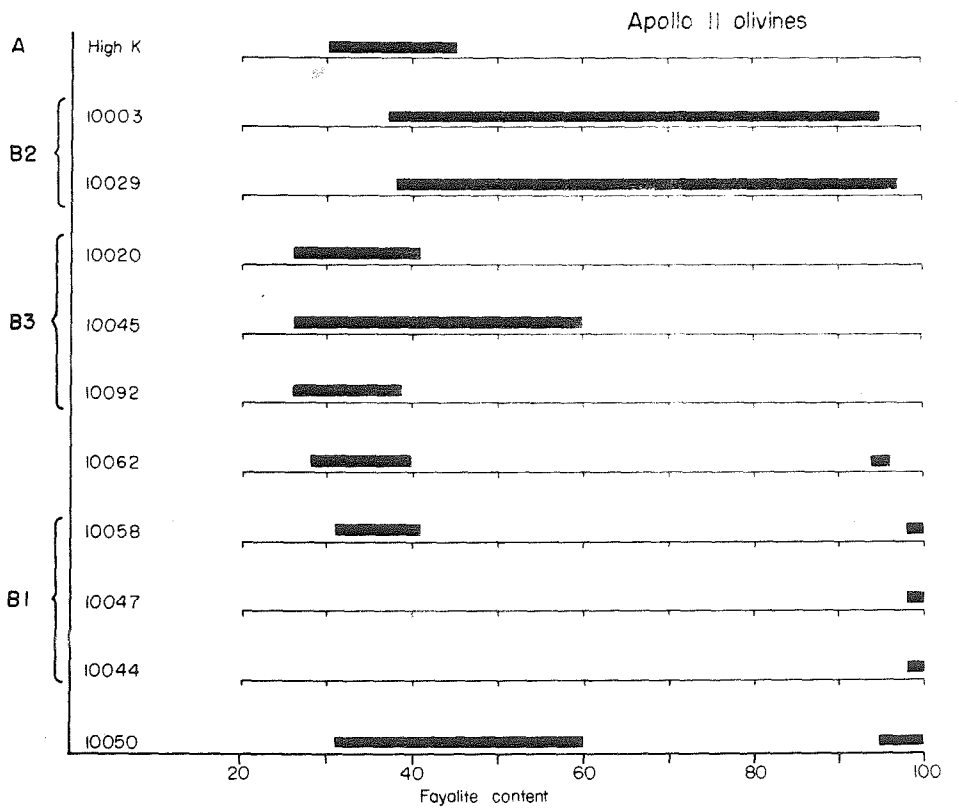

Fig. 9. Olivine zonation in Apollo 11 basalts.

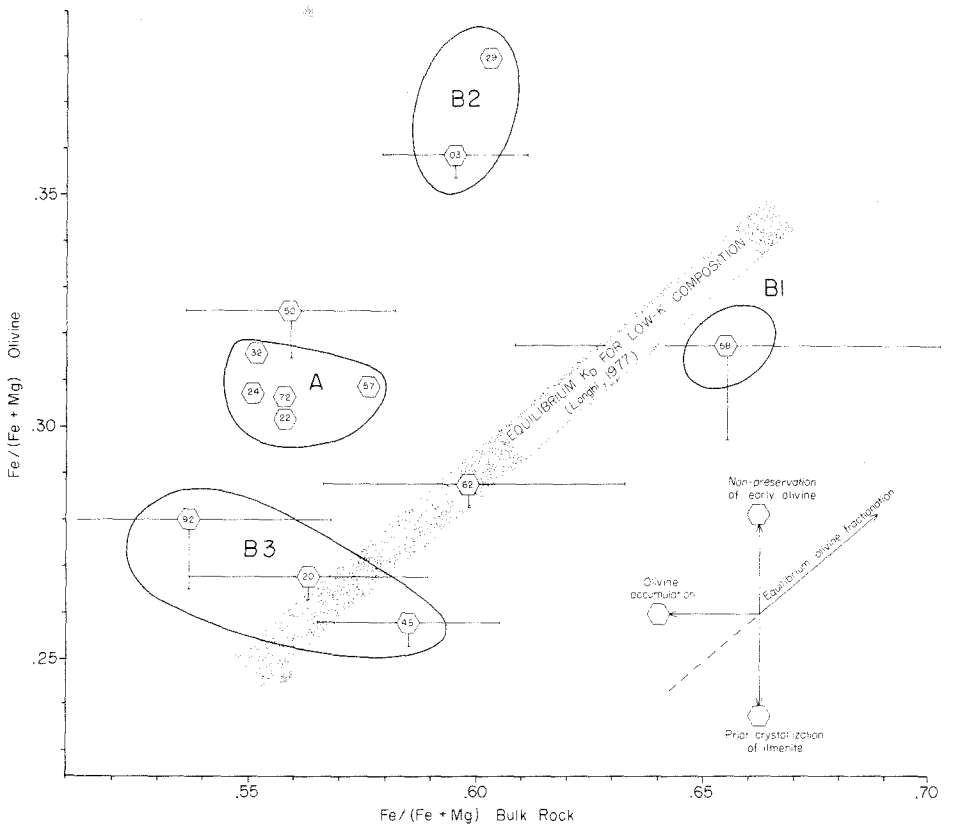

Fig. 10. Most magnesian olivine as a function of bulk Fe/(Fe + Mg). Stippled area has boundaries of K_D = 0.27 and 0.29, the equilibrium values calculated (Longhi, 1977) for low-K compositions.

zoning extends to extremely Fe-rich compositions, there is no evidence for a pyroxenoid.

Chemically, the pyroxene shows growth on both branches of the two-pyroxene field, a high-Ca augite and a low-Ca pyroxene (Figs. 7, 8). Much of the previous work on 10003 (Beaty *et al.*, 1977, Gamble *et al.*, 1978) suggested that intermediate-Ca pyroxenes are present, which fall in the area of the two-pyroxene field. Careful beam scans, however, indicate that *all* such points are resolvable mixtures of low and high-Ca pyroxenes. This conclusion extends to most of the other Apollo 11 basalts as well. Both low and high-Ca branches zone towards higher Fe, and where they meet on the iron-rich end, there is a very complicated region where a wide variety of compositions are possible (Figs. 7–8). The final zoning has one trend up towards ferrohedenbergite and another down towards ferrosilite. The ferrohedenbergite grains are associated with fayalite, so, as in B1, both stable and metastable crystallization trends are indicated. The

optically-discontinuous pyroxferroite from Group B1 has a very restricted range of zoning ($Wo_{14}En_4Fs_{82}$ to $Wo_{12}En_3Fs_{85}$), along with low abundances of Al, Cr and Ti (Fig. 4); whereas, in B2 the high-Fe pyroxene has variable composition, higher Al, Cr and Ti abundances, and may be traced continuously to the earlier, more Mg-rich compositions (Fig. 7). The high-Fe, low-Ca pyroxene is metastable, and the subsolidus breakdown reaction, pyroxene → ferroheedenbergite + fayalite + SiO_2, is present in both samples.

The normalized amounts of Al, Ti and Cr fall in the field which indicates that the major substitutions are probably $R^{2+}Cr^{3+}AlSiO_6$, $R^{2+}Ti^{4+}Al_2O_6$, and $R^{2+}Ti^{3+}AlSiO_6$ (Figs. 7–8). Low-Ca pyroxene has more Cr and Ti relative to Al than augite, while high-Fe pyroxene has relatively more Ti but equal Cr (Fig. 8). Thus, there is a trend towards Ti and away from Al during crystallization. Several points fall below the 0.5 Ti-0.5 Cr join, indicating the presence of quite different substitutions. This Ti enrichment trend may be related to the fact that once silicate liquid immiscibility is reached, the Al goes into the "granitic" melt while the Ti goes into "high-Fe" melt. Since the latest pyroxenes grow from the "high-Fe" melt, they see a much higher Ti/Al than the earlier pyroxene. Na_2O in pyroxene is very minor, decreasing from 0.10 wt.% in augite to 0.00 wt.% in the high-Fe pyroxenes.

Cristobalite occurs in the interstices between pyroxene, plagioclase and ilmenite and is usually associated with the other mesostasis phases. Euhedral plagioclase may be found surrounded by cristobalite, and occasionally they form a "myrmekitic" intergrowth (James and Jackson, 1970).

Troilite occurs as interstitial, irregularly-shaped grains, rarely intergrown with either plagioclase or pyroxene. Amoeboid native iron inclusions are abundant (about 10%) in the troilite, and contain 0.2–0.6 wt.% Co but less than 0.1 wt.% Ni. Application of the troilite-ilmenite geothermometer (Taylor *et al.*, 1973) indicates that in 10003 these two minerals equilibrated down to 650–675°C. Fine-grained crystals of tranquillityite, zirconolite, K,Ba-feldspar, ulvöspinel and apatite all occur scattered throughout the mesostasis areas. Tranquillityite, zirconolite and apatite typically are enclosed poikilitically by iron-rich pyroxene. Zirconolite contains 12.6 wt.% Y_2O_3, 9.0% FeO, 1.3% Nb_2O_5, 0.5% La_2O_3 and 2.6% Nd_2O_3, and apatite contains 1.0 wt.% SiO_2, 4.2% F, about 2% REE oxides, and traces of Fe, Y, and Cl. Ulvöspinel occurs as small, isolated, rounded grains, typically in pyroxene but also intergrown with ilmenite. The composition of the ulvöspinel is fairly constant in both samples at about $Ulv_{95.3}Chr_{1.5}Her_{3.2}$. One unusual grain of ulvöspinel intergrown with ilmenite in 10029, however, was much more Cr-rich (11.3 wt.% Cr_2O_3 = $Chr_{18.3}$), a feature also observed by Gamble *et al.* (1978).

Evidence for late-stage silicate liquid immiscibility is extensive, as pointed out by Roedder and Weiblen (1970). In 10029 the low- and high-index glasses have normative compositions of $Qtz_{34}Fld_{61}Pyx_4Other_1$ and $Fld_5Pyx_{49}Oliv_{32}Ilm_7Other_6$, respectively. The low-index glass occurs both interstitially and as spheres incorporated in the rims of plagioclase laths. There are also spectacular spherical inclusions (5μm) of low-index glass and troilite in large grains (70μm) of fayalite.

In Figure 6c, it appears that the high-index melt crystallized directly to fayalite with minor apatite and ilmenite. The high-Si melt, or its crystalline products, occur as spheres in fayalite. Residual low-index glass is colorless to light brown and is very well preserved in B2, with only incipient crystallization of feldspar.

The paragenetic sequence in B2 is interpreted as follows: Cr-spinel and olivine were the first phases to crystallize. Ilmenite then began nucleating heterogeneously on the growing olivine crystals, forming the olivine-ilmenite symplectites. Plagioclase began to crystallize at or slightly after the time of ilmenite saturation, and olivine, ilmenite and plagioclase then coprecipitated. Cr-spinel stopped crystallizing very early, perhaps reacting to ilmenite. When the melt was about 10% solidified, pyroxene began to crystallize, and the four major minerals olivine, pyroxene, plagioclase and ilmenite coprecipitated all the way to the solidus. Sulfide immiscibility occurred fairly early in this sequence and silicate liquid immiscibility fairly late. In the final stages of crystallization, the mesostasis assemblage formed, consisting of cristobalite, fayalite, apatite, ulvöspinel, tranquillityite, zirconolite, and K-feldspar. The petrologic evidence indicates, therefore, that the B2 samples were not multiply saturated at their liquidi and, consequently, could not have undergone extensive low-pressure fractionation.

C. Group B3

Group B3 consists of three samples, 10020, 10045, and 10092, which are all relatively fine-grained (200μ), porphyritic to glomeroporphyritic, intergranular-ophitic basalts (Fig. 11a,b,c). 10062 is indistinguishable in terms of texture but has a somewhat different mode and bulk composition, which require separate discussion. They are composed of dominantly acicular ilmenite (12–15%), lath-like plagioclase (31–34%), equant pyroxene (45–46%), olivine phenocrysts (3–5%) and interstitial cristobalite (3–5%). Minor phases include Cr-ulvöspinel, usually as inclusions in olivine, and late-stage apatite, fayalite, ulvöspinel, troilite, Fe-metal, tranquillityite and two immiscible residual glasses. 10062 has more plagioclase (38%) and less pyroxene (39%) but also high cristobalite (5%) and olivine (5%). However, because of the textural and petrologic similarities of 10062 and B3, they will be discussed together.

The overall texture is characterized by an open network of randomly-oriented plagioclase laths and ilmenite platelets (Fig. 11a,b,c). Pyroxene occurs either as small grains between the plagioclase framework (intergranular texture) or as coarser grains enclosing it (ophitic texture). The amount of ophitic pyroxene increases directly with grain size in the order 10020<10062<10045 = 10092. Except for olivine, however, the major minerals are roughly equigranular. Olivine phenocrysts are up to three times as large as the other major minerals and are commonly clumped together in glomeroporphyritic texture. This suggests that olivine was mobile in the crystallizing magma, and raises the possibility of crystal-liquid fractionation. This possibility will be fully evaluated later.

The ilmenite in these four samples ranges from dominantly acicular forms in 10020 and 10062 to dominantly equant, blocky forms in 10045 (Fig. 11a,b,c).

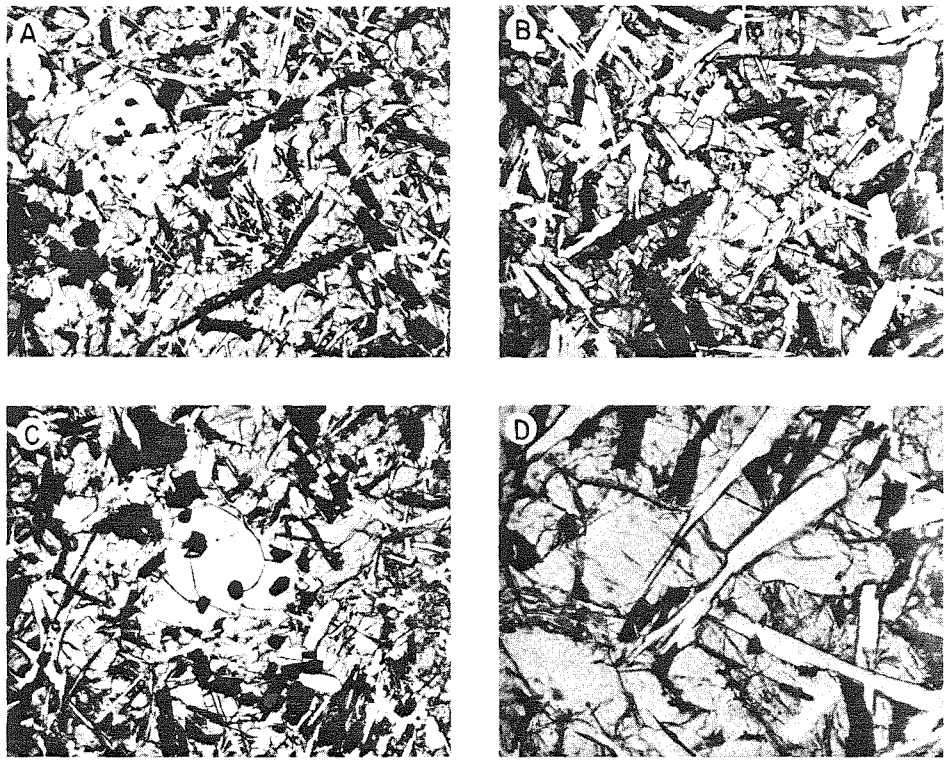

Fig. 11. Photomicrographs of Group B3. (A) 10020, transmitted light; 2.0 mm full scale. (B) 10062, transmitted light; 2.0 mm full scale. (C) 10045, transmitted light; 2.0 mm full scale. Olivine phenocrysts (light) contain Cr-ulvöspinel inclusions (opaque). Plagioclase (white) and ilmenite (opaque) laths form a network which pyroxene (gray) either encloses (ophitic texture) or is interstitial to (intergranular texture). (D) 10062, transmitted light; 500 μm full scale. Olivine (light gray, outlined by dashed line) "ophitically" enclosing plagioclase laths (white).

There is also a scattering of grains with the lobate intergrowths with pyroxene so characteristic of Group B1. As in the other low-K samples, individual ilmenite grains are essentially unzoned. Grain to grain variation is extensive, however, ranging from $Gi_{\sim 20}$ to Gi_0 in the three B3 samples (Figs. 12–14). Sample 10062 ranges from Gi_{12} to Gi_0 and has indications of a bimodal compositional distribution with peaks centered at Gi_8 and Gi_1 (Fig. 15).

Ilmenite has several habits and both composition and morphology changed continuously as crystallization proceeded. In 10020, the earliest grains (Gi_{23-16}) are euhedral and enclosed poikilitically by olivine. Ilmenite in the olivine-ilmenite symplectites is subequant and subhedral (Gi_{10-14}). The acicular grains and those forming lobate intergrowths with pyroxene range from Gi_{10}–Gi_6. Finally, euhedral, acicular ilmenite needles (Gi_1) are associated with the mesostaisis areas.

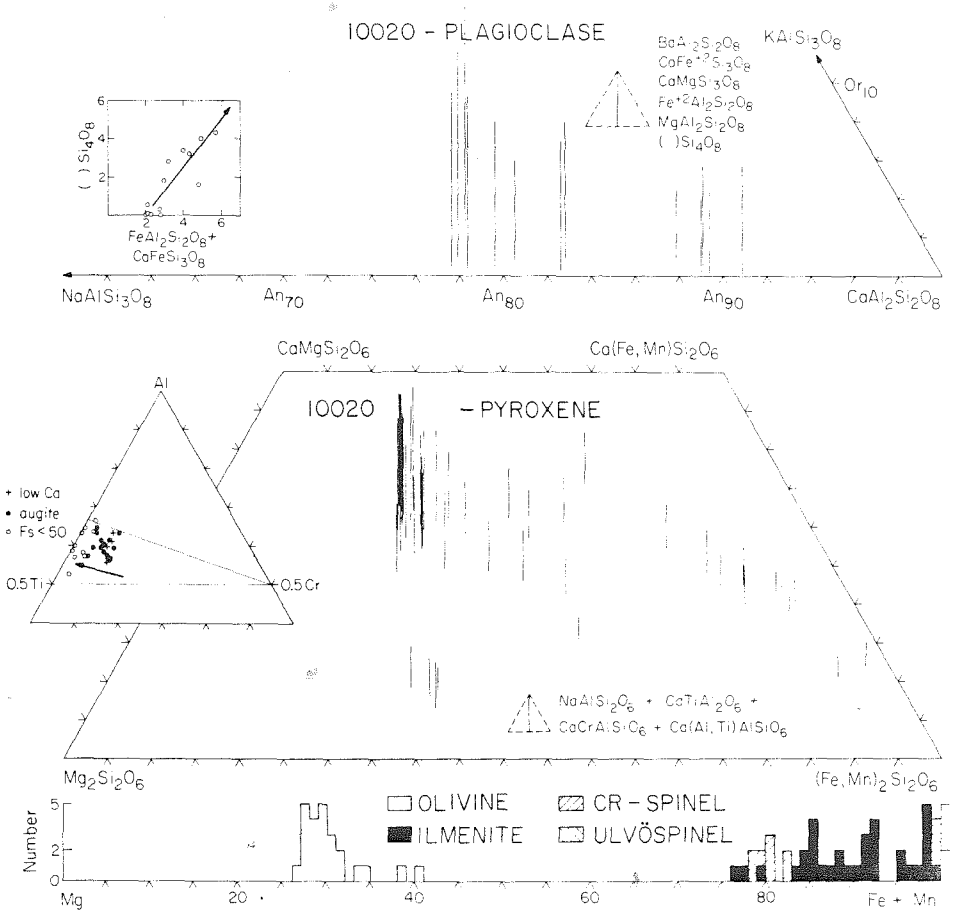

Fig. 12. Composition of pyroxene, plagioclase, olivine and ilmenite in 10020.

In 10062, ilmenite ranges from equant, anhedral grains that poikilitically enclose plagioclase, to subhedral, acicular needles. Although the equant forms tend to be more Fe-rich than the acicular forms, there is a continuous gradation between them in texture and the apparent bimodality in composition may not be real. Rutile and Cr-spinel exsolution lamellae are present in all samples, but as in B2, only in the more magnesian grains. An analysis of a spinel lamellae in ilmenite showed $Ulv_{15}Her_{32}Chr_{53}$ (James and Jackson, 1970), which is considerably more aluminous than the spinel enclosed in olivine ($Ulv_{55}Her_{15}Chr_{30}$). The lack of ilmenite more magnesian than Gi_{12} in 10062 is a very real difference between 10062 and the samples of Group B3 (Fig. 15). For instance, ilmenite poikilitically included in olivine in 10062 is only Gi_{12}; whereas, in the other samples such grains would be at least Gi_{20}.

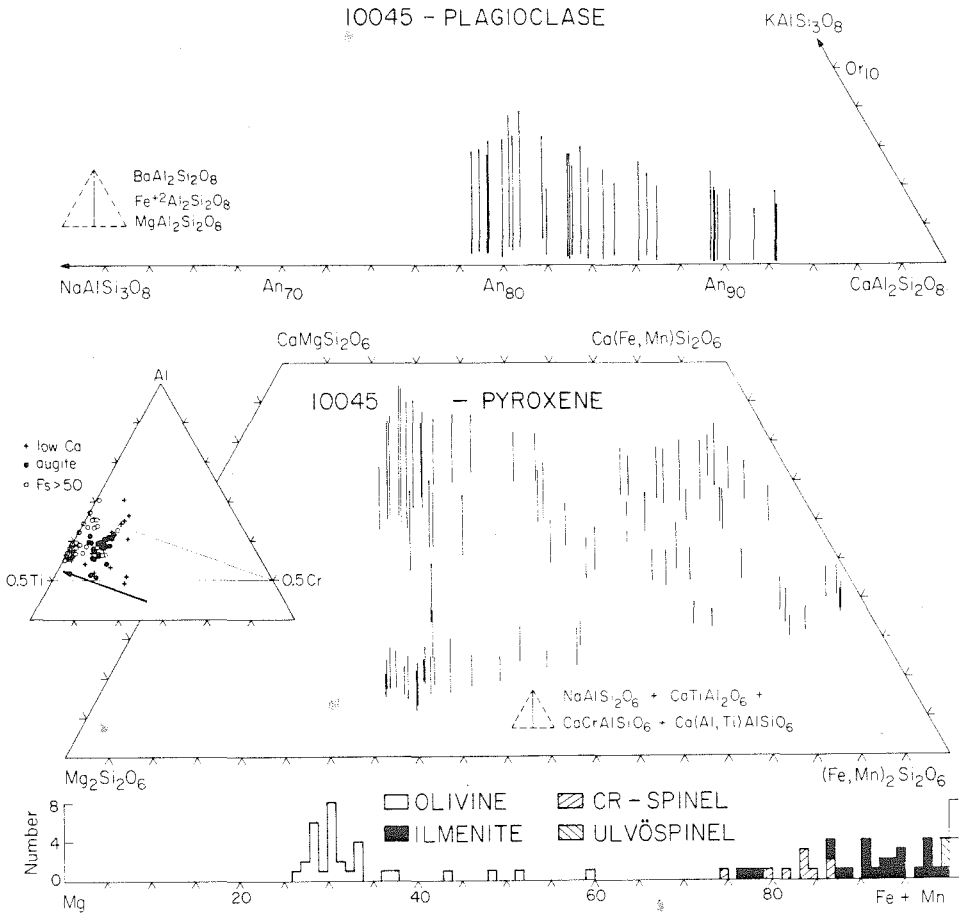

Fig. 13. Composition of pyroxene, plagioclase, olivine and ilmenite in 10045.

Cr is the most important minor constituent in the ilmenite and shows a positive correlation with Mg content. In 10020, most grains contain from 0.8 to 1.5 wt.% Cr_2O_3; in 10045, 0.3 to 1.0 wt.%; while in 10062, the range is 0.1 to 0.7 wt.%. 10092 has a range similar to that of 10045. The higher values in 10020 as compared to 10045 and 10092 may be attributed to the slower cooling rate of 10045 and 10092, while the absence of Cr-rich ilmenite in 10062 is caused by the absence of Mg-rich ilmenite.

Olivine has a seriate size distribution up to 800μm, but most grains are within the 100–300μm range. Although euhedral morphologies are preserved locally, most grains are anhedral, rounded, and rarely contain hollow cores. The smaller grains are mantled by pyroxene, and the numerous rounded embayments clearly suggest resorption. Inclusions in olivine consist of euhedral (octrahedra) to

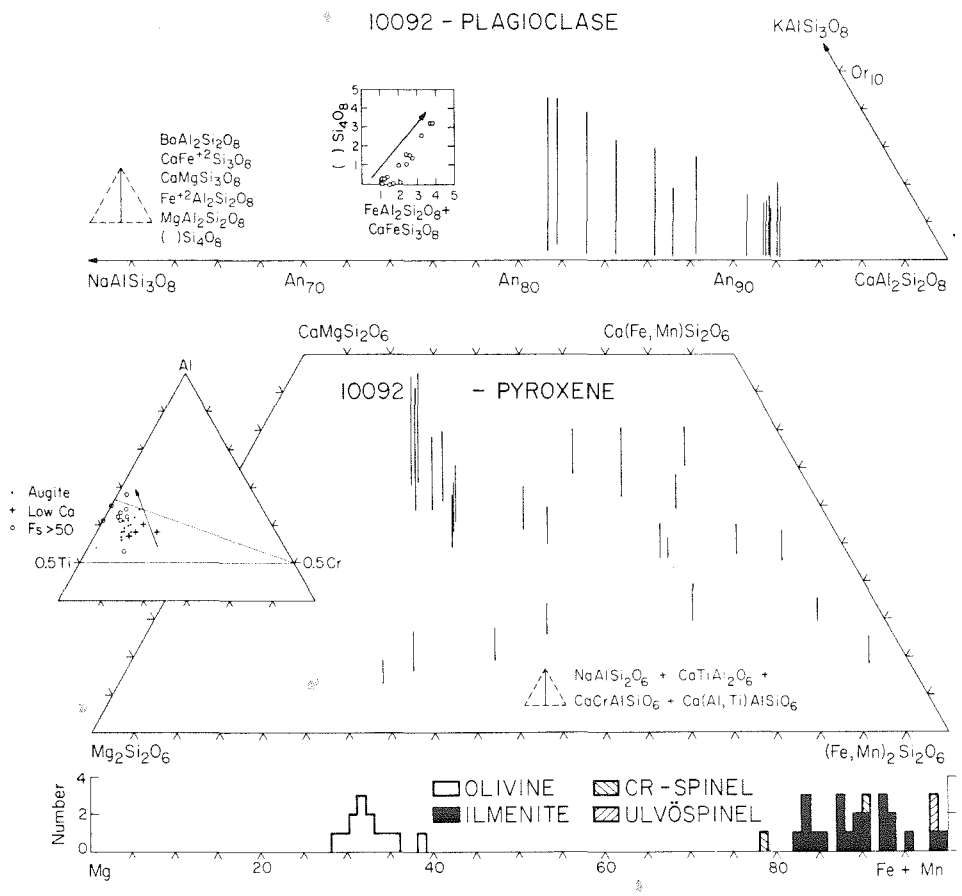

Fig. 14. Composition of pyroxene, plagioclase, olivine and ilmenite in 10092.

anhedral (equant) Cr-ulvöspinel up to 110μm in diameter. Euhedral ilmenite inclusions are present also and are the most magnesian ilmenite present. Plagioclase also may be found entirely enclosed by olivine (Fig. 11d), generally as poorly-formed laths 100–200μm in length. More typically, however, ilmenite and plagioclase laths penetrate only a short distance into the olivine grains. There are also numerous rounded glass inclusions, with daughter crystals of ilmenite, plagioclase, troilite, and feathery pyroxene. These melt inclusions have been studied extensively by Roedder and Weiblen (1977) and used to determine the liquid line of descent for lunar magmas. Vermicular intergrowths of olivine and ilmenite similar to those found in B2 are present, and in one case the ilmenite occurs as parallel elongate blebs that extend into the olivine. The blebs are parallel to (0001) of the ilmenite and not obviously crystallographically oriented with respect to the olivine.

Zoning in olivine is similar in all four samples. The most magnesian cores are

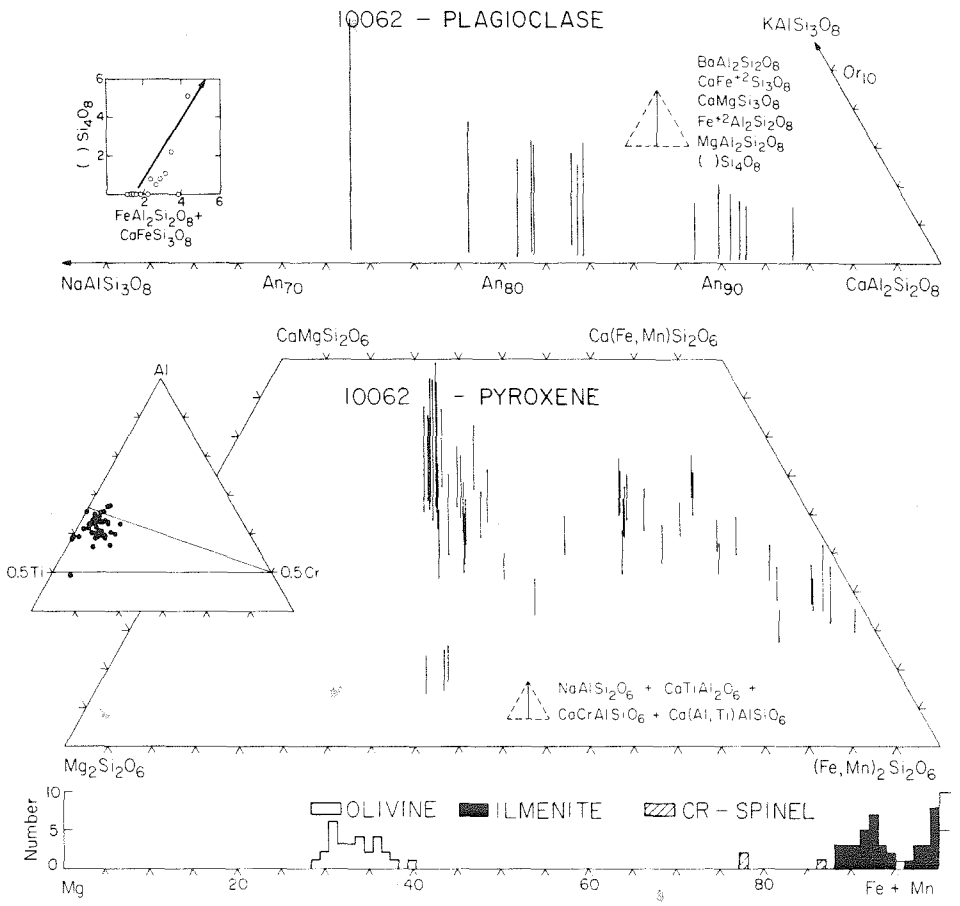

Fig. 15. Composition of pyroxene, plagioclase, olivine and ilmenite in 10069.

about Fa_{27} and the most iron-rich rims about Fa_{45-50} (Figs. 9, 12–15). Most of this range can be found in single crystals, but more commonly, the olivines are weakly zoned. There is a gap in olivine composition from Fa_{50} to Fa_{95}, followed by discrete grains of Fa_{95} in the mesostasis areas. Only one crystal of fayalite was actually analysed (Fig. 9), but its presence was confirmed optically in *all* samples. The most magnesian olivine present in three of the four samples is in apparent equilibrium with the bulk Fe/(Fe + Mg) ratio (Fig. 10). This indicates that the early olivines crystallized from liquids of the same composition as the samples themselves. The bulk composition of 10092, on the other hand, is too Mg-rich to be in equilibrium with its earliest olivine. This, combined with the fact the most magnesian olivine in 10092 (Fa_{28}) is similar to that found in 10020 (Fa_{27}) suggests that 10092 was derived from 10020 by accumulation of olivine. The trace constituents in olivine are Cr, Ti and Ca, none of which exceeds

0.4 wt.% of the oxide. The Cr and Ti contents decrease towards the rims, commensurate with the early crystallization of Cr-spinel and ilmenite; whereas, the Ca content remains constant. Isolated analyses show some Ni, but more typically NiO is <0.05 wt.%.

Most of the plagioclase occurs as well-twinned, euhedral laths, which are both optically and compositionally zoned. Late-stage plagioclase is subhedral to anhedral, however, and in the mesostasis areas it may occur in "myrmekitic" intergrowths with cristobalite. Although plagioclase is virtually inclusion-free, some grains have micron-sized ilmenite in their cores. Rows of low-index glass spheres are common along the margins of some grains, possibly due to the onset of silicate liquid immiscibility (Roedder and Weiblen, 1970). No K-feldspar was observed or has been reported from these four samples. This may be a function of cooling rate—the K-feldspar that would have formed in a more slowly cooled sample is quenched in the residual glass in these rapidly cooled samples.

Compositionally, the B3 and 10062 feldspars range from An_{94} to An_{80} (Figs. 12–15). The absence of feldspars more sodic than An_{80} was confirmed by systematically searching 10045 with the microprobe (Fig. 13) and also by examination of histograms of An content generated from the point count data. The average An content ranges from An_{86} to An_{89} (Table 2), while the peak in the An content histogram tends to be marginally higher than the average. The K_2O content is very low, increasing to only about 0.15 wt.% or 0.8 mole percent orthoclase in the most sodic feldspars. As in the other low-K samples, [ ] Si_4O_8 and iron feldspar are the two major substitutions. Of the four B3 + 10062 samples, all but 10045 have been normalized to calculate excess silica. There is a strong positive correlation (Figs. 12, 14, 15) between excess silica and Fe content and between both of those and albite content. As [ ] Si_4O_8 ranges up to 5.2 mole percent, the total iron feldspar increases to 4.2 mole percent. Stoichiometric considerations suggest that 80–100% of the iron is tetrahedral.

Pyroxene ranges from reddish brown to light greenish brown and is characterized by patchy to irregular extinction. Sector zoning was observed only in 10045. Chemical zoning is prominent, and single grains have a compositional range as large as that spanned by each rock. Neither discontinuous rims of pyroxferroite nor its subsolidus breakdown products were observed. Although most pyroxene grains are small and contain at most one or two plagioclase or ilmenite laths, a few mm-sized crystals ophitically enclose large portions of the plagioclase-ilmenite network, especially in the coarser samples 10045 and 10092.

Zoning is similar to that found in B2; primary crystallization on both branches of the two pyroxene field, followed by iron enrichment to either ferrohedenbergite or pyroxferroite (Figs. 12–15). Most of the pyroxene is augite (58–71 vol.%), and medium-Fe pyroxene (20–32 vol.%), along with lesser amounts of low-Ca pyroxene (1–7 vol.%), high-Fe pyroxene (2–8 vol.%) and ferrohedenbergite (<0.1 vol.%) (Table 2). Al_2O_3 and TiO_2 in augite average about 3.7 and 3.2 wt.% respectively, and may range as high as 5.7 and 4.7 wt.% respectively. These high values are consistent with the higher cooling rates of Group B3 (Grove, 1978). The relative abundances of Al, Ti and Cr (Figs. 12–15) indicate

that the major substitutions are probably $R^{2+}TiAl_2O_6$, $R^{2+}Cr^{3+}AlSiO_6$, and $R^{2+}Ti^{3+}AlSiO_6$. Zoning trends either directly away from Cr as in 10020 and 10045 or slightly towards Al as in 10092. The low-Ca pyroxenes show a great deal of scatter due to the low abundances of these minor elements but tend to have more Cr than the coexisting augite and follow a similar Cr-depletion, Al-enrichment trend. Na_2O, as usual, decreases with increasing FeO. Note that the Al-enrichment trend is the reverse of the Ti-enrichment trends of B1 and B2.

Cr-spinel ranges up to 0.22 vol.% in Group B3, usually as anhedral inclusions in olivine (see Fig. 11a,c), but also as distinct grains in the main body of the rock. Some grains have dendritic inclusions and thin, discontinuous rims of ilmenite. This is evidence of a reaction relationship with the melt. Individual crystals are only slightly zoned, but slight variation is present from grain to grain. The earliest spinels have a composition of $Ulv_{49}Chr_{34}Her_{17}$ with Fe/(Fe + Mg) of 0.75 and these range continuously to $Ulv_{59}Chr_{30}Her_{11}$ with Fe/(Fe + Mg) of 0.86. There is a compositional gap between these spinels and the late stage ulvöspinel, which has a very uniform composition in all samples of about $Ulv_{96}Chr_{0.2}Her_4$.

Mesostasis areas contain cristobalite—sometimes in "myrmekitic" intergrowths with plagioclase—Ca-phosphate, troilite with ~10% metal inclusions, tranquillityite, rare fayalite, vermicular ulvöspinel, and two glasses—a high-index, dark-brown glass, and a low-index colorless glass. The coexisting low- and high-refractive index glasses in 10092 have normative compositions of $Qtz_{43}Fld_{50}Pyx_6Other_1$ and $Oliv_{13}Fld_{10}Pyx_{60}Ilm_7Ap_9Other_1$ respectively (Table A21). Although most of the late-stage ulvöspinel is in vermicular intergrowths with iron-rich pyroxene, some is intergrown with ilmenite in a texture similar to that shown in Fig. 2d but on a much finer scale. None of the phosphate grains were analysed because of their small size, but by analogy with Group B1, both whitlockite and apatite are probably present (Albee and Chodos, 1970).

Preservation of the early olivine in Group B3 enables a much more detailed understanding of the paragenetic sequence. Ilmenite and Cr-spinel are contained in the earliest olivine, whereas plagioclase is contained only in the margins of olivine. This indicates that the crystallization sequence must have been as follows: Cr-spinel was on the liquidus followed by olivine. The spinel the began reacting with the melt to form ilmenite, and olivine and ilmenite coprecipitated. Plagioclase then began to crystallize, and after that olivine reacted with the melt to form pyroxene. After olivine ceased to grow, plagioclase, pyroxene, and ilmenite coprecipitated for the entire cystallization history of the melt, to be joined, ultimately, by the mesostasis minerals. The experimental work of O'Hara *et al.* (1974) indicates that for 10020 the saturation temperatures are spinel (1163°C), olivine (1160°C), plagioclase and ilmenite (1151°C), and pyroxene (1145°C). For 10062, they found olivine (1170°C), spinel (1163°C), plagioclase (1142°C), and pyroxene, ilmenite and possibly armalcolite (1133°C). Note that both of these sequences differ in detail from that observed in the natural samples. Texturally and experimentally, therefore, it is clear that these samples were not

multiply saturated at the start of crystallization. This precludes extensive low pressure fractionation.

D. Sample 10050

10050 is a unique sample among the ten low-K rocks studied. Texturally and petrologically it is similar to B2; the rock is medium grained and has blocky ilmenite (Fig. 16a). Lath shaped plagioclase (34%) tends to be segregated into interstitial clumps (Fig. 16a,b). Ilmenite (14%) is equant and blocky into small anhedral olivine (0.7%) is mantled by the coarser pyroxene (49%). 10050 is coarser than either of the B2 samples (Table 1), and the greater degree of igneous segregation shown by the plagioclase clumps (Fig. 16a,b) may be attributed to a slower cooling rate. The mineral chemistries in 10050 are generally similar to those in B2. As in B2, the earliest-formed olivines have not been preserved (Fig. 10). Note, however, that in contrast to B2, the olivine does not zone continuously to fayalite (Fig. 9) but has the ranges $Fa_{31} \rightarrow Fa_{60}$ and $Fa_{95} \rightarrow Fa_{99}$. The maximum Al_2O_3 and TiO_2 contents of pyroxene are 3.4 and 2.8 wt.% respectively, which are distinctly less than those found in B2. This is another reflection of the slower cooling rate of 10050 (Grove, 1978). An unusual feature of the pyroxene in 10050 is that the Fe-rich compositions do not zone to pyroxferroite but are lower in Ca, trending directly towards ferrosilite (Fig. 17). The most iron-rich pyroxene analyzed was $Wo_5En_3Fs_{89}Other_3$. The ilmenite ranges from 0.8 to 0.1 wt.% Cr_2O_3 as it zones from Gi_{17} to Gi_3. Spinel inclusions in olivine are $Ulv_{55}Her_{15}Chr_{30}$ with Fe/(Fe + Mg) of 0.84, and the late stage ulvöspinel is $Ulv_{96}Her_4Chr_{0.5}$ (Table A12). The crystallization history of 10050, as closely as it can be determined, is identical to that of B2.

An interesting feature of thin section 10050,31 is the presence of a xenolith, so

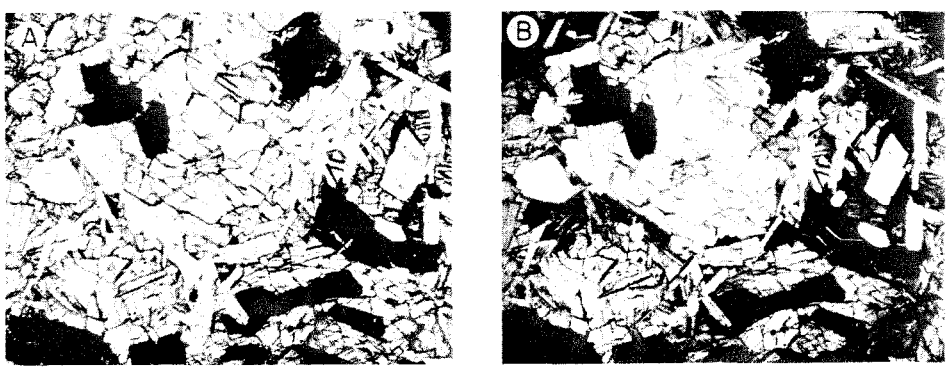

Fig. 16. Photomicrographs of 10050. (A) Transmitted light; 2.0 mm full scale. Blocky ilmenite (opaque), plagioclase (white) and fractured pyroxene (gray). Abundance of fractures indicates that 10050 has undergone the most severe shock of all Apollo 11 basalts. (B) Same view, crossed polars. Note the segregation of plagioclase laths to clumps interstitial to pyroxene grains.

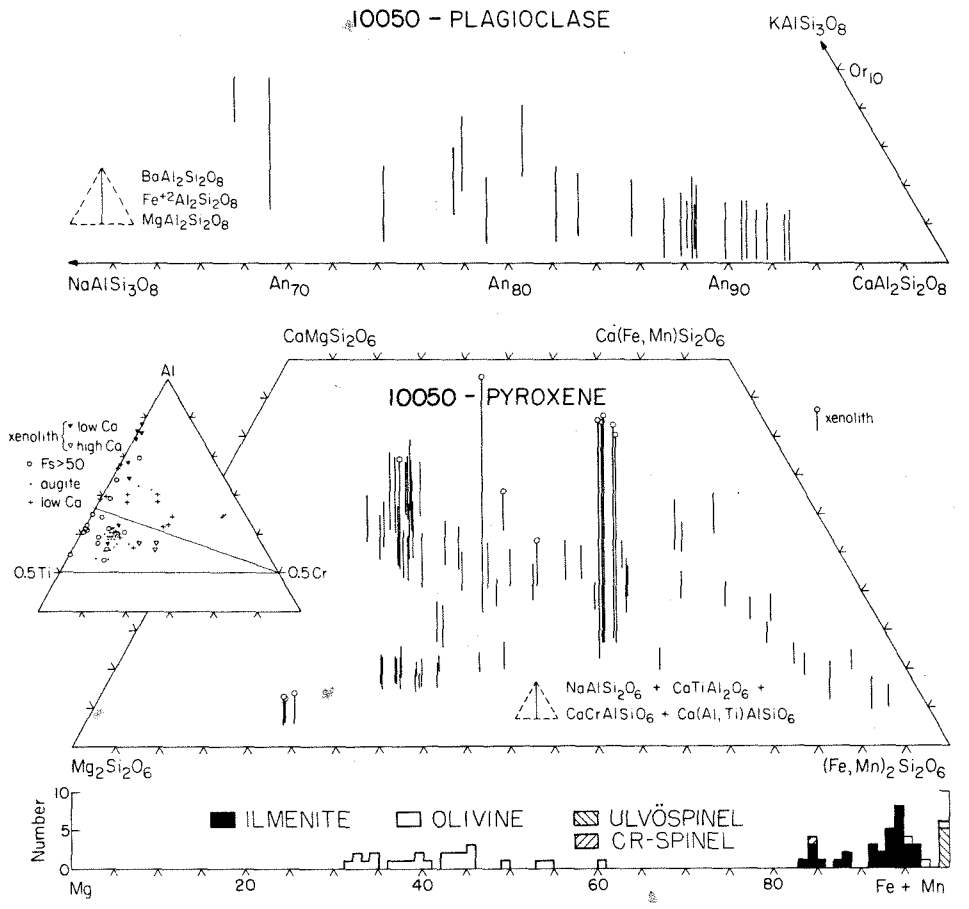

Fig. 17. Composition of pyroxene, plagioclase, olivine and ilmenite in 10050.

described because the minerals are totally out of equilibrium with the bulk of the rock. The xenolith is a polycrystalline aggregate, 170μm × 80μm in size, containing 16 plagioclase laths, 2 Mg-pyroxene grains and 2 anhedral ilmenite grains set in a matrix of clinopyroxene. The average grain size of all minerals except the clinopyroxene is 10 microns. Plagioclase has an average composition of An_{91} and show no apparent zoning. All plagioclase analyses are much more Mg-rich (0.6 wt.%) than those from the host (0.2 wt.%) and contain appreciable excess silica (4 mole %). Mg-pyroxene has a composition of $Wo_3En_{73}Fs_{21}Other_3$ (Fig. 17), with 0.9 wt.% Al_2O_3, 0.7 wt.% TiO_2 and 0.3 wt.% Cr_2O_3. The relative abundance of Cr (Fig. 17, inset) is significantly higher than that in the host. Most of the clinopyroxene has a composition of $Wo_{11}En_{19}Fs_{34}Other_{31}$ with 10.8 wt.% Al_2O_3 and 2.1 wt.% TiO_2 (Fig. 17). Both the absolute and relative amounts of Al are far higher than that in 10050 pyroxene. This xenolith is

potentially very important, as it may be a sample of the conduit along which the magma ascended.

In spite of the many similarities between 10050 and Group B2, they have been separated for two fundamental reasons. First, they have different ages (Table 1), a fact which precludes their being derived from the same lava flow. Secondly, they have different bulk compositions. As shown in a later section, 10050 is more nearly similar in composition to 10020, a member of Group B3, than to the B2 samples. A final unique feature of 10050, which serves to distinguish it from all of the other low-K samples, is its exposure history (Table 1). Six of the seven samples measured had identical exposure histories; whereas, 10050 had been exposed for about four times as long and at a different depth (Geiss *et al.*, 1977). An obvious interpretation is excavation by two separate cratering events, and since 10050 is the lone sample of the first cratering event, it is a unique specimen.

3. COMPARATIVE PETROLOGY

The textural and petrologic differences between samples must be due to either differences in bulk composition or to different physical conditions of crystallization. Although the bulk compositions of the three groups are measurably different, they are similar enough that there cannot be a strong effect on the petrology. Since they all probably crystallized at or near the surface, the only physical condition which changed from sample to sample was the cooling rate. As a first approximation, therefore, we assume that all of the textural and petrologic variations are due to variations in cooling rate. Any property which does not show a consistent variation with cooling rate then indicates either unusual physical conditions of crystallization or somewhat anomalous compositions. As a measure of the cooling rate, we have used the inverse correlation with plagioclase size demonstrated by Grove (1977) and Walker *et al.* (1978). Cooling rate decreases in the order 10020>10092>10045≈10062>10003>10029>10050>10044≈10047≈10058 (Table 1).

A. Texture

The overall texture changes from intergranular to ophitic to subophitic across this sequence. This is due entirely to a dramatic coarsening of the pyroxene, which first is interstitial, then encloses, then segregates plagioclase. Sympathetically plagioclase forms an evenly distributed interlocking network in the fine-grained samples, then becomes increasingly segregated to interstitial clumps by the growing pyroxene. Olivine, naturally enough, is preserved as phenocrysts only in the fine-grained rocks, and is small and mantled where preserved in the coarser samples. Ilmenite continuously changes morphology from elongate bladed grains to equant blocky grains to equant anhedral grains with lobate intergrowths with pyroxene. Pyroxene displays better crystal form with slower cooling; subhedral

Table 2. Point count summary: Apollo 11 low-K basalts.

	B1						B2				B3									
	10044		10047		10058		10003		10029		10020		10045		10092		10050		10062	
Mode	Vol.%	σ	Vol.%	σ	Vol.%	σ	Vol.%	σ	Vol.%	σ	Vol.%	σ	Vol.%	σ	Vol.%	σ	Vol.%	σ	Vol.%	σ
Plagioclase	35.06	1.29	34.91	1.58	33.89	1.82	34.18	0.82	35.01	1.09	31.36	1.13	33.32	1.24	30.64	1.55	33.65	1.47	37.58	1.58
Pyroxene	44.83	1.42	46.53	2.12	47.01	2.02	50.00	1.09	47.48	1.21	45.69	1.64	45.03	1.27	45.66	2.06	48.77	1.85	38.98	1.31
Ilmenite	12.56	1.20	11.20	1.25	12.94	1.39	13.28	0.53	15.76	0.87	12.45	0.84	13.49	0.64	15.59	1.26	14.21	0.70	12.48	1.09
Cristobalite	6.71	0.78	6.22	0.78	4.77	0.58	1.06	0.25	0.58	0.14	4.86	0.54	3.13	0.46	2.59	0.33	2.31	0.39	4.64	0.85
Mg-Olivine	absent	—	absent	—	absent	—	0.40	0.14	0.26	0.09	4.71	0.73	3.47	0.48	4.91	0.72	0.73	0.18	4.98	0.62
Fayalite	0.13	0.07	<.05	—	0.43	0.14	0.12	0.06	0.06	0.04	<.05	—	<.04	—	<.05	—	<.05	—	<.05	—
Troilite	0.43	0.12	0.43	0.15	0.42	0.14	0.68	0.13	0.47	0.12	0.47	0.15	0.30	0.10	0.23	0.10	0.23	0.10	0.33	0.12
Phosphate	0.10	0.06	0.36	0.14	0.38	0.14	0.25	0.08	0.25	0.09	0.17	0.09	0.07	0.05	0.06	0.05	0.05	0.05	0.23	0.10
Ulvöspinel	0.08	0.05	0.05	0.05	0.05	0.05	0.01	0.01	0.03	0.03	0.05	0.05	0.05	0.04	0.04	0.04	<.05	—	0.06	0.05
Glass	0.10	0.06	0.10	0.07	0.10	0.07	0.03	0.03	0.03	0.03	0.18	0.09	0.68	0.16	0.14	0.08	0.07	0.06	0.62	0.17
Cr-spinel	absent	—	absent	—	absent	—	absent	—	0.03	0.03	0.05	0.05	0.22	0.09	0.05	0.05	<.01	—	0.10	0.07
Fe-metal	<.03	—	0.10	0.07	<.05	—	<.01	—	0.03	0.03	<.05	—	<.04	—	0.05	0.05	<.05	—	<.05	—
Phase Chemistries																				
Ave. Plag (An)	85.0		85.4		86.3		87.4		88.1		87.3		85.8		88.7		89.4		86.8	
Ave. Px Wo	28.2		25.9		26.9		22.2		20.8		28.1		25.7		26.6		24.8		27.5	
En	35.3		31.5		32.5		39.9		41.2		34.6		35.5		39.9		41.8		32.4	
Fs	30.7		36.4		33.6		32.7		33.1		28.2		30.1		24.5		26.8		30.4	
Other	5.8		6.2		7.0		5.2		4.9		9.1		8.7		9.0		6.6		9.7	
Ave. Mg-01 (Fo)	absent		absent		65.2		52.4		52.2		69.5		66.4		68.0		63.0		67.9	
Ave. Ilm (Fe)	98.5		97.4		97.4		96.1		93.8		93.7		94.2		90.6		95.1		95.6	
% Pyx[1] = LoCa	—		—		—		15.3		19.2		0.9		4.4		6.6		11.3		1.5	
Augite	59.7		45.8		52.1		42.8		35.6		68.0		58.3		71.4		60.7		58.4	
MedFe	30.9		35.2		32.0		36.6		40.8		24.1		30.9		20.1		25.2		31.8	
HiFe	9.4		18.6		15.6		5.2		4.3		7.0		6.4		1.8		2.9		8.2	
Ferrohed	—		0.4		0.3		0.1		—		—		—		0.1		—		0.1	
ρ calc	3.29		3.30		3.33		3.38		3.41		3.33		3.38		3.38		3.35		3.29	

Notes:

All values were measured by computer-controlled microprobe point count. The quoted errors are the standard deviation of the mean (SDM), a statistical parameter which describes the uncertainty in an infinite population (lava flow) based on measurements of a finite subset (hand sample). The mode of each thin section considered alone is more precise than this (see Analytical Techniques).

[1]Pyroxenes were subdivided using K-values. For LoCaPx MgO/CaO >1.75; boundaries of the others are at approximately Fs_{30}, Fs_{60}, and En_{10}, Wo_{33} (ferrohed).

morphologies and sector zoning become prominent in B1. The modes, as shown in Fig. 1, change from large amounts of the incompatible pair olivine and cristobalite at rapid cooling rates, to lower amounts of both as cooling rate is decreased. We conclude that all the textural features indicative of cooling rate do correlate well with the change in grain size.

B. Mineral chemistry

Several aspects of mineral chemistry show interesting variations, namely the compositions of the cores of each phase, the range and distribution of mineral zonation, and the minor element contents. The magnesium content of the first pyroxene to form in each sample shows an inverse correlation with cooling rate and no correlation with bulk composition. The most magnesian pyroxene is in B1, the slowest cooled and most Fe-rich samples. This indicates that the composition of the first pyroxene is controlled by the amount of under-cooling, which may be proportional to cooling rate. Similar results have been obtained experimentally by Usselman *et al.* (1975). The amount of low-Ca pyroxene is inversely correlated with the amount of olivine for all samples except Group B1 which contains none of either. This is significant in that when olivine and cristobalite are added to the average pyroxene, it drives the composition away from wollastonite and into the two pyroxene field. Thus, resorption of olivine should increase the amount of low-Ca pyroxene which crystallizes. This explains the relative abundances of olivine and low-Ca pyroxene in B2, B3, and 10050. The absence of both low-Ca pyroxene and olivine in B1 suggests that if B1 is at all similar to the other low-K basalts, then early olivine was not resorbed, but instead was fractionated and lost from the system. In this way the composition of the average pyroxene was not driven into the two pyroxene field. Note that this conclusion agrees with Fig. 1, which shows that if B1 crystallized from a magma similar to B2 or B3, it must have lost significant amounts of olivine. The amount of high-Fe pyroxene should be a measure of the efficiency of *in situ* fractional crystallization, but no consistent trend with cooling rate is observed.

The most calcic plagioclase in each sample is the same (An_{94}) within sampling and analytical uncertainty. The constancy of the earliest plagioclase composition indicates that these feldspars all crystallized from melts of similar composition and that plagioclase was close to the liquidus. Na, Ca and Al, the components of plagioclase, are all incompatible in olivine and ilmenite. Fractionation of those phases will not change the composition of the first plagioclase, but rather the total abundance of plagioclase. Prior crystallization of pyroxene, however, would affect Ca and the *first* crystallized plagioclase would be different. Plagioclase, therefore, preceeded pyroxene in all samples. On the other hand, the composition of the *average* plagioclase is not constant but changes consistently with Fe content of the average pyroxene (Fig. 18). The more differentiated the sample, the more sodic the feldspar. Since the melts are inferred to have had the same initial Ca, Al, and Na compositions due to similarity of the first-formed plagioclase, this suggests either augite or plagioclase fractionation. Only in this

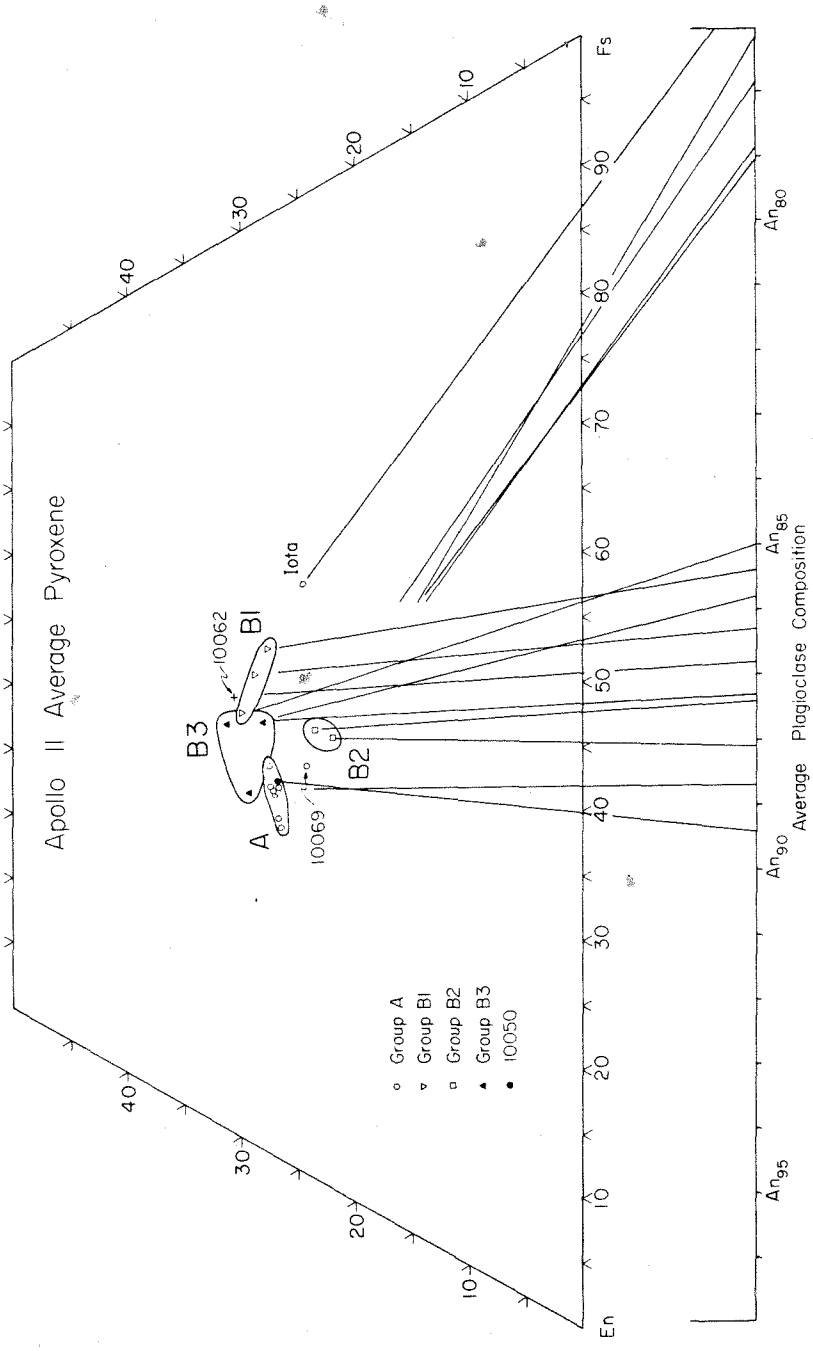

Fig. 18. Average pyroxene and average plagioclase in Apollo 11 basalts. Note the correlation with rock type and the consistent tie lines defined by the low-K (type B) basalts. The high-K basalts (type A) show a consistent iron enrichment in the average pyroxene and are petrologically distinct from the low-K basalts.

way can the albite component of the melt be enriched over the anorthite component. The concomitant increase of Fe in the average pyroxene reflects the fact that olivine probably accompanied the above fractionation. Once again, then, there is an indication that B1 was derived from a parent magma similar to B2 or B3 through fractionation of olivine and an unknown amount of augite and/or plagioclase.

Where preserved, the most magnesian olivine is a function only of Fe/(Fe + Mg) of the bulk sample in all cases except 10092, in which the sample is too magnesian. The olivine, however, is similar in composition to those from 10020 (Fig. 10), suggesting the derivation of 10092 by olivine accumulation. This conclusion is supported (see below) by the bulk compositional data.

The extensive zoning of olivine in B2 as compared with the more normal zoning found in B3 and 10050 obviously cannot be related to cooling rate. Slower cooling of B3 would result in the preservation of smaller amounts of olivine, until at equilibrium no olivine at all would be present because the B3 samples are quartz normative. This should not affect the composition of the olivine, however. One of the two initial assumptions of this discussion, therefore, must be wrong: either B2 crystallized under different physical conditions or B2 crystallized from a magma of fundamentally different chemistry. The latter condition is known to be present from the bulk compostional data, one manifestation of which is the fact that B2 is olivine normative. This different bulk compostion was in apparent equilibrium with olivine along the entire liquid line of descent.

The most magnesian ilmenite in many samples is Gi_{20-23}. If this was the liquidus ilmenite, then its absence in the slowly cooled samples is due to later equilibration at lower temperatures. The absence of high-Mg ilmenite in 10062, however, cannot be explained in this manner and remains an unexplained anomaly.

The only minor element contents that vary with cooling rate are Al, Ti and Cr in pyroxene. These three decrease together with cooling rate, a speedometer that has been calibrated experimentally for a Luna 24 composition by Grove (1978). In addition, the trends on the normalized Al, Ti, Cr pyroxene diagrams change from Ti-enrichment trends with slow cooling to Al-enrichment trends with more rapid cooling. Other minor components such as Cr in ilmenite, and [ ] Si_4O_8 in plagioclase also seem to decrease in abundance with slower cooling.

The absolute value of the cooling rate may be determined in several ways. Using the Al substitution in pyroxene (Grove, 1978), one finds that 10020 cooled at about 30°C/hr, 10003 at about 2°C/hr, and all of Group B1 at 1°C/hr or less. Using the maximum plagioclase width cooling indicator developed by Grove (1977) and Walker *et al.* (1978) (see Table 1), 10020 cooled at about 3°C/hr., 10003 at 1°C/hr., and Group B1 at 0.2°C/hr. Although these experiments may not be applicable because the charges were low-Ti in composition, both results are in general agreement with the work of Usselman *et al.* (1975) on high-Ti basalts. Although the textures and mineral morphologies reported by Usselman *et al.* (1975) do not match those observed in the low-K suite, the ilmenite morphology in B3 resembles that produced at 18°/hr. and 7°/hr., while that in

B2 is similar to 2°/hr. Group B1 is somewhere off their calibrated scale, having cooled slower than 2°/hr.

4. Genetic Relations

If one makes the reasonable assumption that B1 has fractionated from a composition similar to B2 or B3, then as shown above, most of the textural, petrologic, mineralogic and mineral chemical features present could be related to cooling rate. The major exception is the extensive olivine zonation in B2 which cannot be so explained. Although the above properties are important, other data must also be considered to fully evaluate possible genetic relationships. In particular, rocks from the same igneous cooling unit must have the same age, and they must either have the same bulk composition or be relatable to each other by logical crystal-liquid fractionation.

A. Isotopic constraints

It has been shown by several workers (Geiss *et al.*, 1977; Papanastassiou *et al.*, 1977) that the samples of B1 and B2 differ in age by about 200 m.y. (Table 1) and, therefore, cannot be related. B3 and 10050 both lie between these extremes in age. B3 apparently has an age of about 3.76 b.y., slightly older than B1 (3.72 b.y.), but none of the B3 samples have been reliably dated (Table 1). 10050 (3.75 b.y.) possibly overlaps B1 or B3 in age, but not B2 (3.90 b.y.). 10062 is as old as B2, and is clearly older than B1. In conclusion, the ages indicate that B1 $\neq$ B2 + 10062 and 10050 $\neq$ B2. Hence, it is necessary to evaluate two possible associations: B2-B3-10062 and B1-B3-10050. These will be treated in order.

B. Bulk compositional constraints

On all variation diagrams involving the major elements, the petrologic groups translate directly to compositional groups. Although important, this in itself does not indicate that the different groups are from different lava flows. It is perfectly possible for a sample from the core of a flow to have lost olivine, thereby changing its composition, as well as having a different texture from the rim of the same flow. In these rocks, olivine and ilmenite may reasonably be expected to fractionate, as they are both early-crystallizing, dense phases. Augite will probably be only slightly denser than the melt and should not fractionate strongly. Plagioclase is also at or near the liquidus and might float. Thus, from a possible parent magma, we should expect loss of olivine and ilmenite and possibly addition of plagioclase to derive the others. If fractionation is extensive enough, of course, augite will become involved.

Table 3. Compositional summary: Apollo 11 low-K basalts

	B1						B2				B3									
	10044	σ	10047	σ	10058	σ	10003	σ	10029	σ	10020	σ	10045	σ	10092	σ	10050	σ	10062	σ
P_2O_5	0.04	0.02	0.13	.05	0.16	0.06	0.10	.04	0.09	0.03	0.07	0.03	0.03	0.02	0.03	0.02	0.02	0.02	0.10	0.04
SiO_2	42.21	1.07	42.51	1.37	40.24	1.33	39.70	.69	37.89	0.76	40.47	1.06	39.83	0.91	38.05	1.24	40.05	1.14	40.23	1.13
TiO_2	10.25	0.91	9.21	.92	10.60	1.19	10.46	.40	12.15	0.64	10.61	0.64	11.02	0.48	12.74	0.94	11.12	0.54	10.57	0.83
Al_2O_3	10.35	0.38	10.54	.46	10.34	0.51	10.23	.27	10.32	0.32	9.73	0.33	10.03	0.36	9.66	0.44	10.49	0.43	11.21	0.44
Cr_2O_3	0.24	0.02	0.23	.03	0.22	0.02	0.23	.03	0.27	0.03	0.38	0.03	0.41	0.04	0.44	0.04	0.34	0.03	0.31	0.03
MgO	5.95	0.23	5.51	.27	5.80	0.28	7.60	.18	7.53	0.21	7.97	0.36	7.67	0.29	8.90	0.42	7.90	0.31	6.81	0.28
CaO	12.08	0.33	11.82	.40	12.18	0.44	11.06	.21	10.47	0.24	12.04	0.34	11.13	0.28	11.38	0.40	11.67	0.36	11.91	0.33
FeO	17.88	0.86	19.31	.99	19.60	1.15	19.92	.44	20.49	0.61	18.29	0.66	19.27	0.52	18.38	0.85	17.83	0.58	18.04	0.79
MnO	0.27	0.02	0.26	.02	0.29	0.02	0.26	.02	0.23	0.02	0.25	0.02	0.28	0.02	0.23	0.02	0.28	0.03	0.23	0.02
Na_2O	0.50	0.03	0.48	.03	0.42	0.06	0.42	.03	0.39	0.03	0.37	0.03	0.44	0.03	0.33	0.03	0.36	0.03	0.50	0.04
K_2O	0.03	0.03	0.02	.03	0.06	0.04	0.03	.02	0.03	0.03	0.04	0.03	0.04	0.03	0.02	0.02	0.04	0.01	0.06	0.02
BaO	<.01	—	<.01	—	0.03	0.02	0.02	.01	<.01	—	0.01	0.01	<.01	—	<.01	—	<.01	—	0.03	0.02
S	0.22	0.06	0.22	.08	0.20	0.07	0.36	.07	0.23	0.06	0.24	0.08	0.15	0.05	0.11	0.01	0.12	0.05	0.17	0.06
Σ	100.02		100.20		100.15		100.40		100.09		100.48		100.30		100.28		100.36		100.21	
Barth-Niggli norm (cation %)																				
Qtz	4.65		3.87		2.34		—		—		0.96		0.56		—		1.19		1.14	
Oliv	—		—		—		0.27		1.09		—		—		1.29		—		—	
An	27.89		29.34		26.71		27.79		28.42		26.40		27.06		26.52		28.69		30.13	
Ab	4.83		3.67		5.33		4.04		3.78		3.54		4.23		3.17		3.45		4.80	
Or	0.19		0.38		0.32		0.19		0.19		0.25		0.25		0.13		0.25		0.38	
Di	29.06		26.99		28.91		24.26		21.61		29.43		25.46		26.87		26.34		25.93	
Hy	17.44		21.17		19.65		27.01		25.91		22.85		25.33		22.38		23.01		21.10	
Ilm	15.36		13.79		15.93		15.61		18.27		15.75		16.41		18.96		16.52		15.74	
Chr	0.28		0.27		0.26		0.27		0.32		0.45		0.48		0.52		0.40		0.36	
Py	0.21		0.21		0.19		0.34		0.22		0.22		0.14		0.10		0.11		0.16	
Ap	0.09		0.32		0.36		0.22		0.20		0.16		0.07		0.07		0.05		0.22	
Fe/ (Fe + Mg)	.628		.663		.655		.595		.604		.563		.585		.537		.559		.598	

Notes

All bulk compositions calculated from point count data. The quoted errors are the standard deviation of the mean (SDM), a statistical parameter which describes the uncertainty in an infinite population (lava flow) based on measurements of a finite subset (hand sample). The composition of each thin section considered alone is considerably more precise than this (see Analytical Techniques).

C. B2–B3–10062

It can be seen from Fig. 19b (Al_2O_3) and Fig. 19c (CaO) that the amounts of olivine and ilmenite that must be removed from B3 to derive B2 have opposite signs. Figure 19b indicates that olivine and ilmenite loss would be necessary to move from B3 to B2; whereas, in Fig. 19c, olivine and ilmenite addition is required. Involvement of plagioclase and pyroxene does not help this dilemma, and we are forced to the conclusion that B3 and B2 are not related by simple crystal-liquid fractionation. Another strong, simple argument is that olivine must be removed from B3 to increase the bulk Fe/(Fe+Mg) to that seen in B2. This would involve separation of olivine from a quartz-normative magma to produce an olivine-normative magma, which is clearly impossible. Thus, we conclude that B2 must represent a distinctly different igneous event from B3.

10062 is texturally and petrologically similar to group B3 but, more importantly for this discussion, chemically and isotopically similar to group B2. For example, on Fig. 20 it can be seen that 10062 has the same rare earth pattern as B2 sample 10003 and that neither is parallel to either B1 or B3. They are enriched in the light REE, especially La, a property used by Schmitt (pers. comm.) to distinguish them from the other low-K basalts. All of Fig. 19, as well as Fig. 10, indicate that 10062 may be simply related to 10045 and 10020 by loss of about 3 wt.% olivine and gain of about 3% plagioclase. Alternatively, 10062 may be related to B2 by loss of small amounts of olivine and ilmenite [maintaining a constant Fe/(Fe + Mg)] along with accumulation of about 3 wt.% plagioclase. Because of this non-uniqueness and the uncertainty in age of group B3, 10062 has not been classified. The rare earth data, however, strongly suggest that 10062 should be associated with B2.

D. B1–B3–10050

Of the four plots shown in Fig. 19, 10050 falls interior to group B3 on three. Only in Al_2O_3 (Fig. 19b) is 10050 measurably different from group B3. In particular 10050 is similar chemically to 10020 and 10045, the two B3 samples that represent magmatic compositions. Thus, despite the textural similarities of B2 and 10050, 10050 is compositionally like B3, and they may be derived from different parts of the same flow.

Group B1 on all four diagrams (Fig. 19) can apparently be related to B3 and B4 by fractionation of about 6 wt.% olivine and 2 wt.% ilmenite. This process would enrich the incompatible elements, such as the REE, by about 9%. As shown in Fig. 20, however, the rare earths in group B1 are enriched by about 80% over 10045 (B3). This is outside the range currently identified by Haskin *et al.* (1977) as being spanned by samples from a single flow, and we conclude that B1 $\neq$ B3. Note that 10050, which is intermediate in REE between B1 and B3, could be related to either group. Because of this ambiguity, we have not classified 10050 with either group, but like 10062, it does not extend beyond three the minimum number of lava flows required.

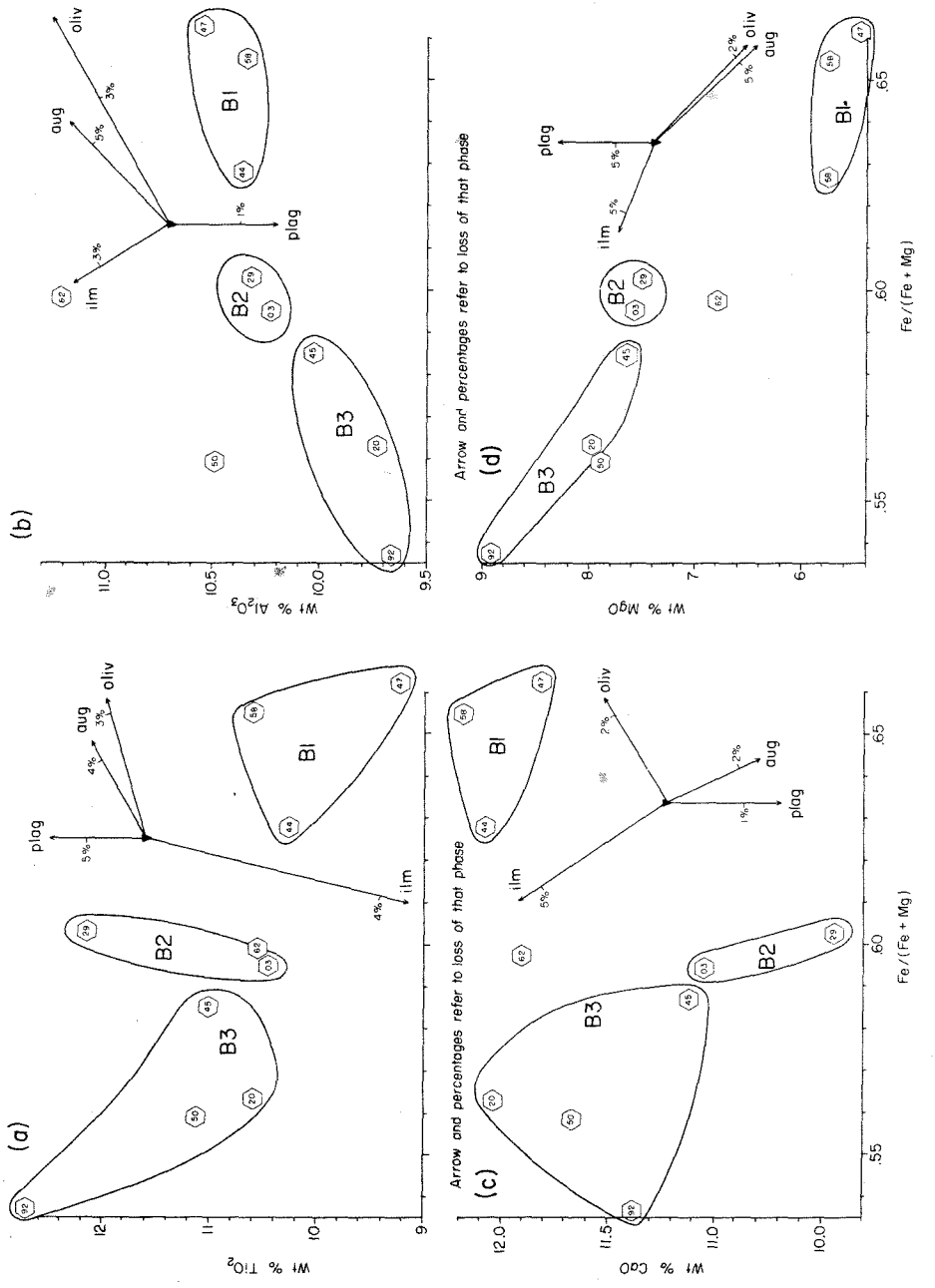

Fig. 19. Bulk compositions of low-K basalts.

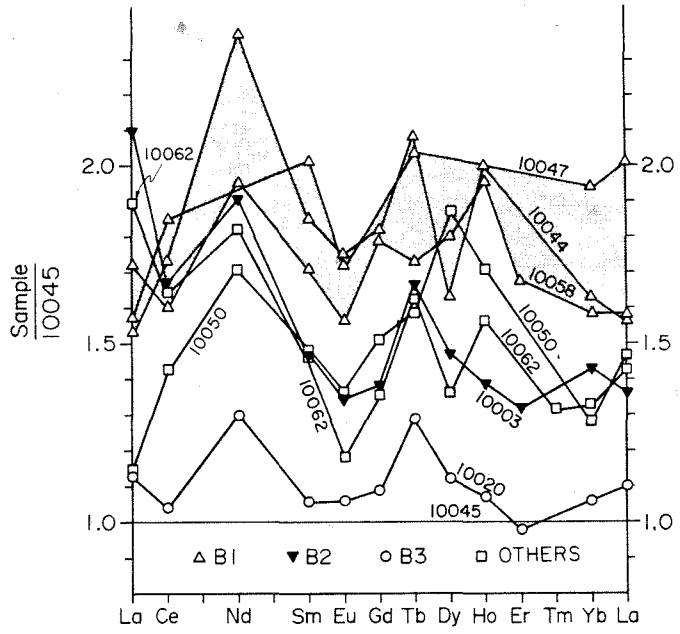

Fig. 20. Rare earth abundances in low-K basalts normalized to 10045. Best data in the literature was averaged to improve sampling. Data from Gast *et al.*, Goles *et al.*, Haskin *et al.*, Wakita *et al.*, Turekian *et al.*, Wänke *et al.*, Annell *et al.*, and Philpotts *et al.*, all of which are in *Proc. Apollo 11 Lunar Sci Conf.* (1970).

In summary, eight of the ten low-K basalts can be divided into three well-defined groups which represent three separate igneous cooling units. The other two samples cannot uniquely be classified, but each can be related to one or another of the above cooling units. Naturally, the three flow model is not the only one possible—there could have been 10 flows which provided the 10 samples. Three lava flows, however, simply explain all of the observed data.

Part II. High-K Basalts

1. Introduction

The Apollo 11 high-K basalts (type A basalt of LSPET) are completely distinct from the low-K suite isotopically, petrologically, chemically, and texturally. Their petrologic and bulk compositional differences are emphasized on Fig. 7, which shows the average pyroxene and the average plagioclase for all of the Apollo 11 basalts. Note that the tie lines for the low-K basalts form a consistent array, as do the tie lines for the high-K basalts, but considered together the two suites are greatly divergent. The Rb-Sr systematics indicate that the high-K basalts came from a different source region than the low-K basalts (Papanastassiou *et al.*, 1977) and by all techniques they have different ages.

Texturally, James and Jackson (1970) classified all of the high-K basalts as intersertal, and all of the low-K basalts as ophitic. Compositionally Gast and Hubbard (1970), Compston *et al.* (1970a, b) and Tera *et al.* (1970) noted the dichotomy of K contents, the low-K basalts having about 0.05 wt.% K_2O, and the high-K basalts containing about 0.30 wt.% K_2O. There can be no doubt, therefore, that the high-K basalts represent a completely separate magmatic system.

In this section we report extensive petrologic studies on the nine large high-K basalt samples, as well as two high-K vitrophyres, in an attempt to resolve the genetic relationships in this suite. It will be shown that, although textural variation is dramatic, the bulk compositions are very similar to one another. Although samples representative of the most pristine magma are identified and fractionation schemes to derive the other samples are suggested, it must be remembered that the differences being examined are very small. Compared to the other basalt suites returned from the moon, all of the Apollo 11 high-K samples are far and away more similar to each other than to any other samples.

2. Petrography and Petrology

LSPET (1969) originally distinguished the type A basalts using the criteria that they are "fine-grained, vesicular, crystalline igneous rocks". In thin section, a wide range in texture is present, although there are no major differences in mode. The average grain size varies by an order of magnitude, with the mineral morphologies changing continuously with grain size. Of the eleven high-K samples examined, eight fall into a textural sequence which is presumably related to differences in cooling rate. Three samples, 10022, 10085,12-7 and 10060,71 clast δ, are porphyritic. The descriptions, therefore, will treat first the major group of eight, then secondly compare these samples to the three porphyritic ones.

A. Non-porphyritic samples

The main textural sequence consists of eight samples: 10017, 10024, 10032, 10049, 10057, 10069, 10071 and 10072. These rocks are composed of subhedral to anhedral plagioclase (22–24%), euhedral to subhedral equant ilmenite (14–16%), subhedral pyroxene (48–53%), and a residual mesostasis (7–11%), which is composed of a fine-grained mixture of plagioclase, cristobalite and a potassic glass. Minor phases include olivine (0–1%), which is always partially resorbed and mantled, granular cristobalite (1–2%), troilite (0.4–0.7%), Ca-phosphate(s), ulvöspinel, tranquillityite and Fe-metal. In addition, armalcolite was found in two samples. No early Cr-spinels were observed optically or sampled by the point count. The phase abundances, average phase compositions, and bulk compositions of these samples are listed in Tables A1 through A22, and summarized in Tables 4 and 5.

Table 4. Point count summary: Apollo 11 high-K basalts

	MAIN SERIES																PORPHYRITIC SERIES					
Mode	10024 Vol.%	σ	10032 Vol.%	σ	10071 Vol.%	σ	10017 Vol.%	σ	10057 Vol.%	σ	10049 Vol.%	σ	Iota[1] Vol.%	σ	10072 Vol.%	σ	10069 Vol.%	σ	10022 Vol.%	σ	Clast δ[2] Vol.%	σ	10085, 12-7	σ
Plagioclase	21.74	0.90	22.16	1.19	23.60	1.17	23.62	0.83	23.95	0.65	24.47	1.22	36.27	2.32	22.49	1.18	23.26	1.26	21.65	0.72	absent	—	—	—
Pyroxene	51.37	1.23	52.61	1.74	47.80	1.18	50.60	1.61	50.84	1.31	51.03	1.69	40.74	2.82	51.00	1.10	51.32	1.27	52.61	0.88	40.79	1.62	38.25	2.67
Ilmenite	16.41	0.77	16.45	0.71	14.77	0.87	15.17	0.81	15.47	0.83	14.12	1.05	6.31	0.94	13.17	1.19	16.62	0.83	14.08	0.77	13.81	1.23	12.91	1.12
Cristobalite	1.31	0.21	0.94	0.19	2.19	0.28	1.36	0.21	1.05	0.17	1.38	0.28	5.04	0.71	1.34	0.24	0.97	0.19	0.83	0.14	absent	—	—	—
Olivine	0.11	0.06	0.11	0.06	1.27	0.20	absent	—	<.04	—	absent	—	absent	—	0.41	0.14	.04	0.04	0.10	0.05	2.68	0.57	absent	—
Troilite	0.53	0.14	0.72	0.17	0.44	0.12	0.54	0.13	0.42	0.13	0.72	0.19	0.43	0.21	0.62	0.17	0.37	0.12	0.62	0.12	0.18	0.08	0.31	0.18
Phosphate	0.24	0.09	0.24	0.10	0.24	0.09	0.20	0.08	0.21	0.10	0.27	0.12	0.34	0.18	0.15	0.08	0.14	0.07	0.23	0.08	absent	—	0.01	0.01
Ulvöspinel	0.04	0.04	<.04	—	<.03	—	<.03	—	<.04	—	<.05	—	<.10	—	0.04	0.04	<.04	—	<.03	—	absent	—	<.05	—
Mesostasis	8.24	0.54	6.66	0.50	9.63	0.57	8.48	0.53	8.04	0.46	8.01	0.64	10.88	1.04	10.78	0.66	7.24	0.52	9.89	0.49	41.23	1.35	46.49	2.98
Fe-metal	0.01	0.01	0.08	0.06	0.02	0.02	0.04	0.04	0.04	0.04	<.05	—	<.10	—	<.04	—	0.03	0.03	<.03	—	absent	—	<.05	—
Armalcolite	absent	—	absent	—	0.03	—	absent	—	absent	—	absent	—	absent	—	<.04	—	absent	—	absent	—	1.31	0.51	absent	—
Pyroxene Zonation																								
% Pyx[3] = LoCa	10.1		10.6		7.8		6.4		6.5		3.3		0.7		6.6		8.3		6.6		1.3		1.0	
Augite	64.8		66.2		64.2		63.2		63.0		60.2		14.7		61.3		59.3		63.4		98.7		99.0	
MedFe	22.9		21.1		26.4		27.8		28.3		35.6		65.3		29.0		32.5		26.8		—		—	
HiFe	2.2		2.1		1.5		1.5		2.2		0.9		19.3		3.0		—		3.1		—		—	
Phase Chemistry																								
Ave. Plag (An)	78.1		77.1		76.7		78.0		79.0		79.2		76.0		76.0		78.8		77.8		absent		72.3	
Ave. Px Wo	25.0		24.6		24.4		25.1		24.7		26.0		23.3		25.3		23.0		25.3		39.4		28.5	
En	43.8		44.4		40.6		41.6		41.5		39.4		28.5		41.5		41.7		40.9		26.0		39.2	
Fs	24.4		23.7		25.3		25.8		26.6		27.7		43.1		26.1		29.8		26.0		19.1		19.2	
Other	6.8		7.2		9.7		7.5		7.2		6.9		5.1		7.1		5.5		7.8		15.5		13.1	
Ave. Oliv (Fo)	67.3		67.0		67.5		absent		69.1		absent		absent		66.4		68.4		66.6		69.8		70.1	
Ave. Ilm (Fe)	93.8		96.7		93.5		95.2		96.6		96.7		98.0		94.2		92.3		95.0		90.0		93.8	
% Meso = Glass	59		72		60		66		56		65		61		48		62		51		px. 21.9		px. 28.7	
Plag	20		17		23		72		26		17		19		37		17		43		53.8		58.7	
Crist	21		11		17		16		18		18		20		15		21		6		19.3		9.7	
ρ calc	3.38		3.40		3.33		3.36		3.37		3.35		3.14		3.31		3.40		3.34		3.33		3.37	

Notes:

All values were measured by computer-controlled microprobe point count. The quoted errors are the standard deviation of the mean (SDM), a statistical parameter which describes the uncertainty in an infinite population (lava flow) based on measurements of a finite subset (hand sample). The mode of each thin section considered alone is more precise than this (see Analytical Techniques).

[1]Iota is our designation for a cross-cutting igneous feature in thin section 10071,31 (see text).

[2]Clast δ is a large vitrophyre clast in soil breccia 10060,71.

[3]Pyroxenes were subdivided using K-values from the point count. For LoCaPx MgO/CaO >1.75; boundaries of the others are at approximately Fs_{30} and Fs_{60}.

Texture A continuous range in texture is present, formed in response to different cooling rates. Average grain size in the main textural sequence ranges from 30μm to 250μm in the following order: 10049<10069<10032 = 10057< 10017<10071<10072<10024. In these eight samples pyroxene, ilmenite and plagioclase are all roughly equant. Pyroxene and plagioclase are equigranular only in 10032 and 10049, however. In 10057, 10017, and locally in 10049, the plagioclase is much larger than, and completely encloses, pyroxene euhedra in an "antiophitic" texture. Ilmenite in all samples tends to be either the same size or somewhat smaller than the pyroxene. In the coarsest samples, 10072 and 10024, however, plagioclase is smaller than pyroxene and is segregated into interstitial clumps. Individual laths may project into the margins of pyroxene in a semblance of ophitic texture. The trend, therefore, with slower cooling is from fine-grained, equigranular, subhedral pyroxene surrounded by coarse poikilitic plagioclase, to coarse pyroxene with plagioclase segregated into interstitial areas and subophitically enclosed in the pyroxene margins. Pyroxene and ilmenite increase monotonically in size across this sequence; whereas, plagioclase first increases, then decreases. Sympathetically, the ilmenite morphology changes continuously from euhedral rectangular shapes to more equant, anhedral forms with lobate contacts against pyroxene, plagioclase and glass (Fig. 21). The mesostasis areas are similar in all samples. Cristobalite or a low-index colorless glass is typically intimately intergrown with plagioclase, accompanied by Ca-phosphate mineral(s), tranquillityite and ulvöspinel. Troilite very commonly occurs as spheres, indicating sulfide immiscibility. Vesicles are large (up to 3mm), abundant (up to 20 vol.%) and usually perfectly spherical. They commonly contain globules of troilite, but the rock-forming minerals do not project into cavities.

Textural variability is common even within individual samples. In 10069, for instance, there are grain size inhomogeneities on a scale of about 1 mm with the grain size varying by a factor of two. Typically, the coarser and finer-grained regions occur as smooth-sided, gradationally-bounded pods, with the same antiophitic texture as the "normal" portion of the sample. The minerals have the same compositions in all portions of the rock. In 10049,39, two contacts which separate a finer-grained zone from the rest of the sample can be traced continuously across the length of the thin section. This fine-grained band is about 800μm wide, has smoothly curving, gradational to sharp contacts, and exhibits a grain size contrast of about a factor of two when compared to the host. On a traverse away from this band, the plagioclase becomes noticeably coarser, and the antiophitic texture becomes better and better developed. Again, the mineral chemistries are independent of texture. In 10024,29, a similarly fine-grained area with a smooth, mappable contact has a suitable shape for point count analysis. This study indicated that the fine-grained portion is richer in ilmenite (21% vs. 16.4%) and proportionately poorer in all the other minerals except pyroxene, which is the same. Interestingly enough, the phase compositions are also different. Pyroxene and ilmenite are both distinctly more magnesian in the finer-grained portion (Fig. 22); whereas, plagioclase is more calcic. The average pyroxene and plagioclase in the fine grained portion (determined by a point count

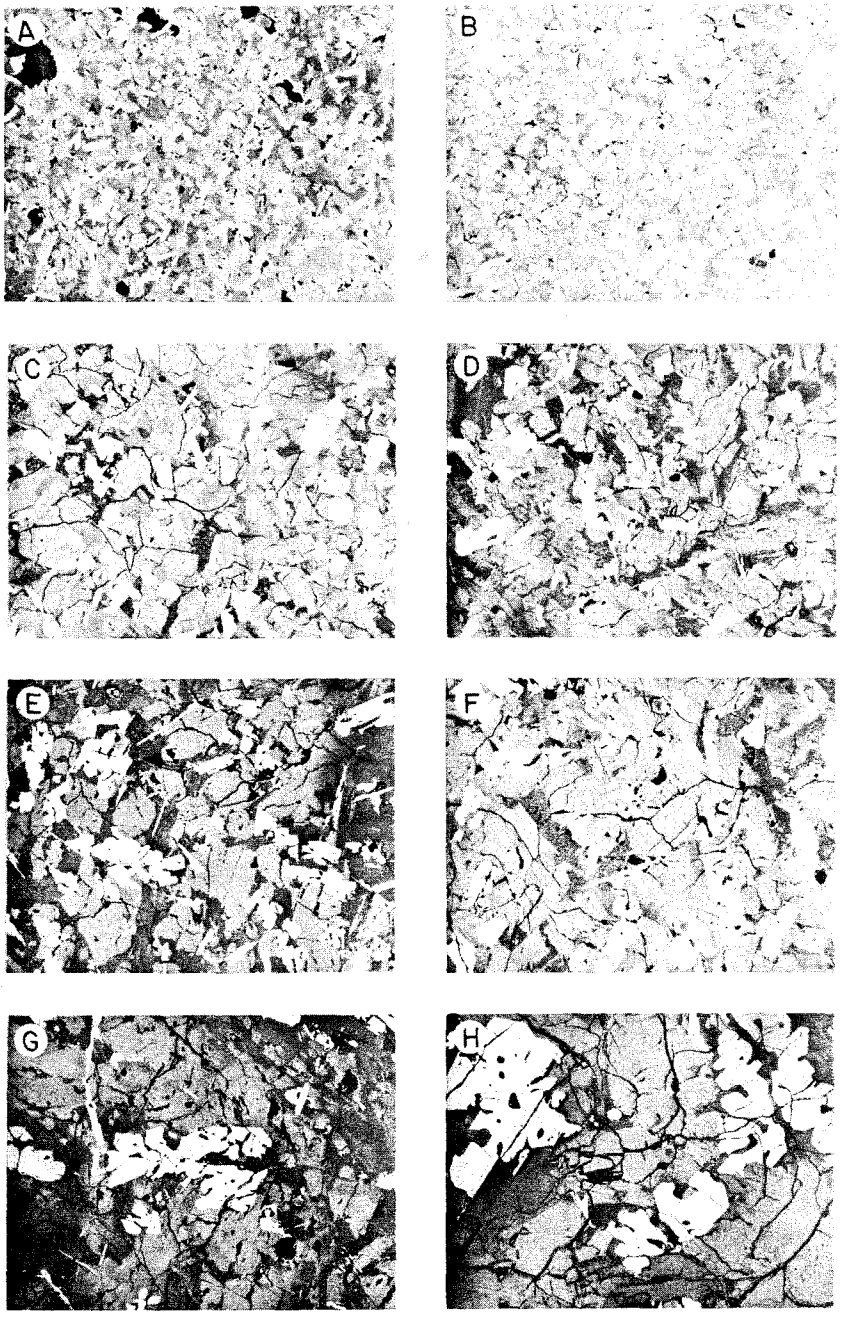

Fig. 21. Photomicrographs of non-porphyritic Apollo 11 high-K basalts. Field of view is 1.0 mm in all cases; reflected light. (A) 10049 (B) 10069 (C) 10032 (D) 10057 (E) 10071 (F) 10017 (G) 10072 (H) 10024. Three phases are visible: ilmenite (white), pyroxene (medium gray), plagioclase (dark gray).

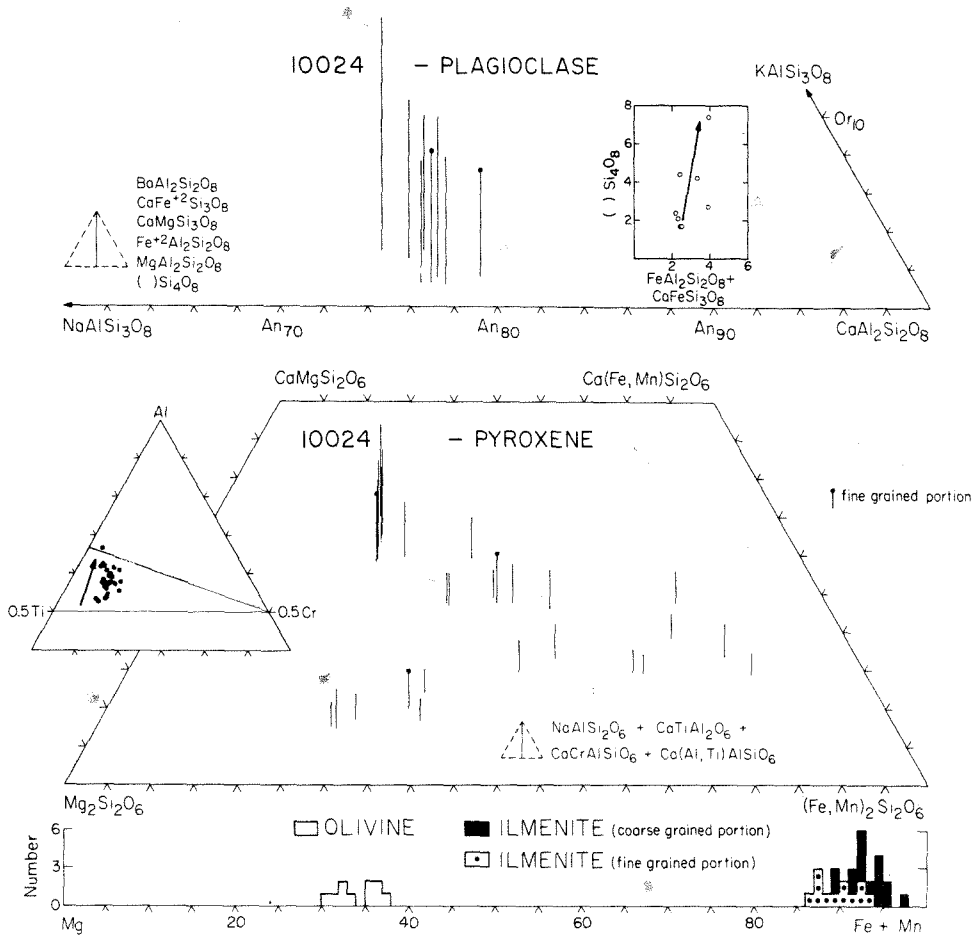

Fig. 22. Composition of pyroxene, plagioclase, olivine and ilmenite in 10024.

with 571 points) are $Wo_{29}En_{48}Fs_{23}$ and $An_{79.8}$ as compared to $Wo_{27}En_{47}Fs_{26}$ and $An_{78.1}$, in the "normal" portion. As can be seen by comparison with Table 4, these are large differences.

The finer-grained portion, therefore, has a more primitive composition than that of the rock as a whole. The contact between this finer-grained portion and the bulk sample is apparently sharp, but it is difficult to be certain because of the small textural contrast across the boundary. Although these textural and, in at least one case, compositional heterogeneities are difficult to interpret, they may be very important. Sample 10071 contains a similar, but larger, fine-grained area, first pointed out by Drake and Weill (1971). In this case the textural contrast is great enough and the contact sharp enough that it can unambiguously

be called a cross-cutting igneous contact of some sort. This feature is very significant and is described in a later section in more detail.

Mineral chemistry Olivine is present in five of the eight samples, invariably occurring as small, anhedral, rounded to embayed grains mantled by pyroxene. In all samples except 10032, the most magnesian olivine present is Fa_{30}, which gives $(Fe/Mg)_{Ol}$ $(Fe/Mg)_{Rock} \cong 0.30$ (Fig. 10). Although this is somewhat higher than the value calculated from the relation given by Longhi (1977), the constancy of this number suggests that it is the equilibrium value for this composition. This indicates that the earliest olivine grew from a liquid of the composition of the bulk sample, i.e., that these samples represent magmatic compositions. The most magnesian olivine measured in 10032 is Fa_{31} (Fig. 23), but the difference between this and the composition in the other samples is probably not significant. In those samples with the highest bulk Fe/(Fe + Mg) ratios (10017, 10057, 10069 and 10049), only one grain of olivine was sampled by the point count, and only in 10057 were traces of olivine seen optically. The presence or absence of olivine is therefore correlated with bulk composition, implying either olivine fractionation or fundamental compositional differences. Note that unlike the low-K samples, the amounts of olivine and cristobalite do not increase with cooling rate. This is a reflection of the fact that the high-K basalts are all highly quartz-normative (Fig. 1) and under no circumstance can much olivine form.

Inclusions in olivine are rather rare, consisting of only a few micron-sized ilmenite grains. Cr-spinel was neither observed optically nor sampled by any of the point counts. In all samples, zoning is restricted; most analyses fall between Fa_{30} and Fa_{35}, with scattered analyses as high as Fa_{45} (Figs. 22–29). Only about half the total range in zonation is spanned by any one crystal. Compositionally, the olivine is very close to stoichiometric; minor amounts of CaO (0.4 wt.%), Cr_2O_3 (0.10 wt.%) and TiO_2 (0.20 wt.%) are present.

Ilmenite in the Apollo 11 high-K basalts exhibits little zoning within individual ilmenite grains, but intergranular variation may be extensive. As the grain size increases, both the total range of zonation and the average Mg content increase. In 10049, the finest-grained sample, most analyses are Gi_3 with a range of only Gi_{1-4} (Fig. 27) and in 10069, also fine-grained, the average is Gi_7 and the range Gi_{5-9} (Fig. 28). In 10024, the coarsest sample, the average ilmenite has a composition of Gi_7, and the total range is Gi_{2-13} (Fig. 22). Isolated, much more magnesian grains (Gi_{16-23}) are present in 10032, 10017, and 10071 (Figs. 23–25). High-Mg grains occur in the cores of olivine in 10071 and in pyroxene cyrstals in 10032, which isolated them from the melt. As in the Apollo 11 low-K basalts, the high-Mg ilmenite is characterized by the presence of rutile and spinel lamellae. That the high-Mg ilmenite is resorbed armalcolite is doubtful because ilmenite which actually mantles armalcolite in 10071 has a constant composition of about Gi_{12}. The fact that the most magnesian ilmenite in many of both the low- and high-K Apollo 11 basalts is around Gi_{20-23} suggests that composition is the liquidus ilmenite composition for both groups of high-Ti basalts.

Cr_2O_3 is abundant in ilmenite and shows a positive correlation with MgO

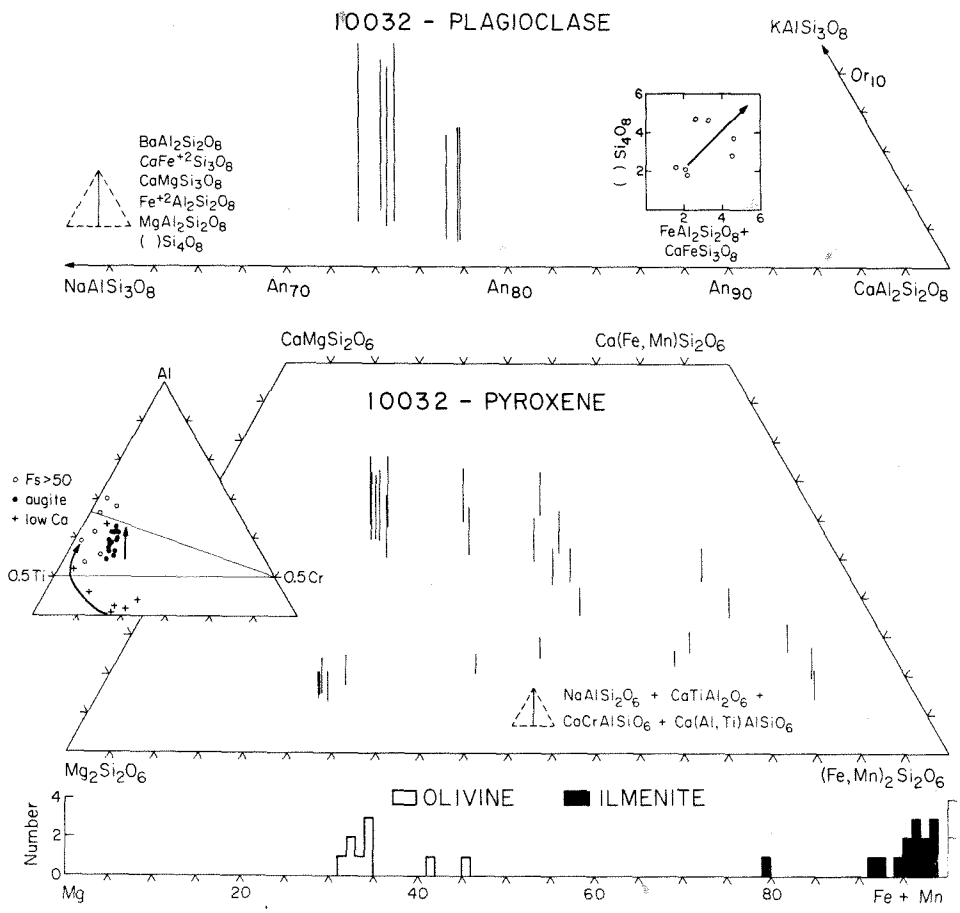

Fig. 23. Composition of pyroxene, plagioclase, olivine and ilmenite in 10032.

content. The high-Mg ilmenite grains have 1.40 wt.% Cr_2O_3, decreasing to 0.10 wt.% in the Gi_1 grains. SiO_2 and Al_2O_3 are usually close to the detection level; whereas, Nb_2O_5 and V_2O_3 are typically below it. ZrO_2, on the other hand, ranges up to about 0.40 wt.%, and a large number of analyses exceed 0.10 wt.%, particularly those representing the latter stages of crystallization. This reflects the high ZrO_2 abundances in the bulk samples.

Armalcolite is present in only two samples. In 10071, there are several large grains of armalcolite, all of which are mantled by ilmenite (Gi_{12}), but in 10072, only one small (40μ) grain was found. That grain poikilitically encloses a euhedral ilmenite blade, and the entire aggregate is armored by pyroxene. The armalcolite in 10071 is weakly zoned in Fe/(Fe + Mg) (0.52–0.59) (Fig. 24), the rims being more Fe-rich than the cores. Al_2O_3 is uniformly ~1.6 wt.%, or 3.3 mole% Al_2TiO_5, while Cr_2O_3 ranges from 2.2 to 1.8 wt.% or 3.2 to 2.6 mole%

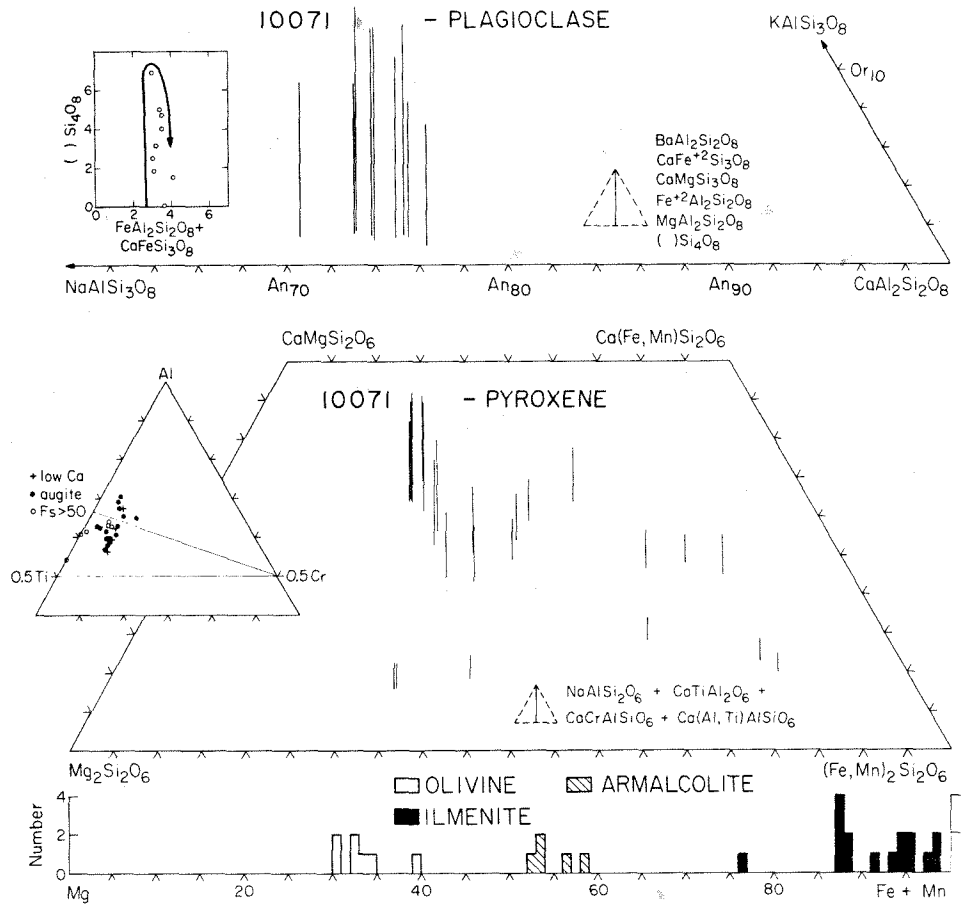

Fig. 24. Composition of pyroxene, plagioclase, olivine and ilmenite in 10071.

Cr_2TiO_5, decreasing towards the armalcolite rim. An excess of Ti is present, requiring the presence of either structural vacancies or $(Ti^{3+})_2\ Ti^{4+}O_5$. Assuming full occupancy, we have calculated the abundance of the $(Ti^{3+})_2\ Ti^{4+}O_5$ molecule. This component ranges from 6.8 to 5.3 mole percent from core to rim which translates to 4.8 to 3.7 weight percent Ti_2O_3 and a $Ti^{+3}/(Ti^{+4} + Ti^{+3})$ ratio of from 0.07 to 0.05. According to the experiments of Usselman and Lofgren (1976), this indicates that fO_2 during armalcolite crystallization was between the iron-wüstite buffer and half a log unit below it. Although Nb_2O_5 is <.05 weight percent (the detection level), both ZrO_2 and V_2O_3 range up to 0.18 weight percent.

Plagioclase is poorly twinned and shows the least zonation of any of the major minerals. The most calcic cores analysed range from An_{79} to An_{82} (Figs. 22–29), and this value is not correlated with either grain size (cooling rate) or bulk

composition. Likewise, the most sodic feldspar analyzed ranges from An_{75} to An_{78}, and again the differences between samples are apparently random. These results are in contrast to the Apollo 11 low-K basalts in which the composition of the earliest plagioclase is constant at An_{94}. The total range in zonation of any given sample is low, about 4–6 mole percent An. This is a reflection of the late appearance of feldspar on the liquidus and its crystallization through a narrow temperature interval close to the solidus.

Three important minor substitutions are present in plagioclase, $[\ ]Si_4O_8$, $Fe(Al_2Si_2O_8)$, and $Ca(FeSi_3O_8)$. As can be seen in Figs. 22 through 27, the total iron feldspar ranges from 2.6 to 4.3 mole percent, while the $[\ ]Si_4O_8$ ranges from 0 to 7 mole percent. For these samples, therefore, the minor component zoning is more extensive than that of the major components. In most cases, FeO content increases steadily with albite content of the feldspar. The increase is not as large,

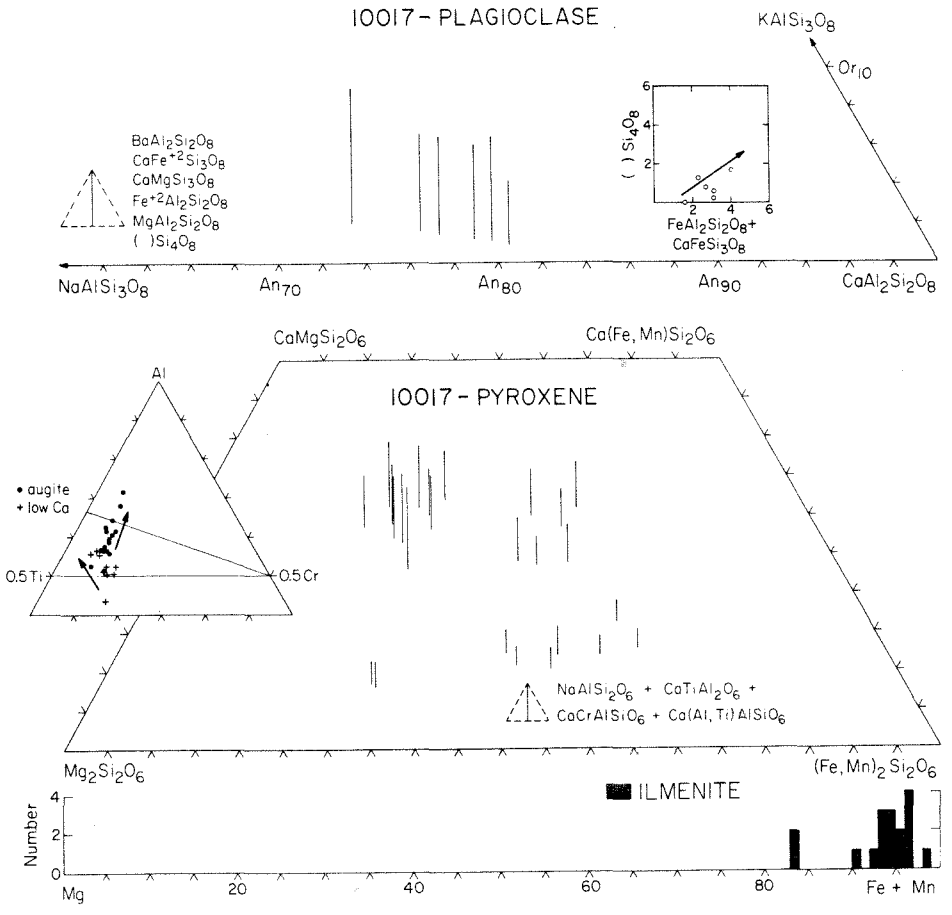

Fig. 25. Composition of pyroxene, plagioclase and ilmenite in 10017.

nor as consistent as that in the low-K basalts, however, possibly due to the restricted temperature interval of crystallization. The apparent distribution of iron between the two sites can be calculated by comparing the total contents of the distorted eight-coordinated site to the total aluminum and assuming that all the iron is ferrous iron. This procedure indicates that most of the iron is tetrahedral and that less than ten percent of the iron is in the 8-fold site. This ratio is apparently independent of both the bulk cooling rate and An content.

Excess silica in plagioclase either increases monotonically with sodium as in 10024, 10017 and 10032 (Figs. 22, 23, 25) or first increases then decreases as in 10049 and 10071 (Figs. 24, 27) and possibly in 10069, 10057 and 10072 (Figs. 26, 28, 29). This trend of silica enrichment followed by silica depletion may be explained by the experimental work of Longhi and Hays (1978) in the binary system anorthite-silica. At temperatures above the eutectic, appreciable

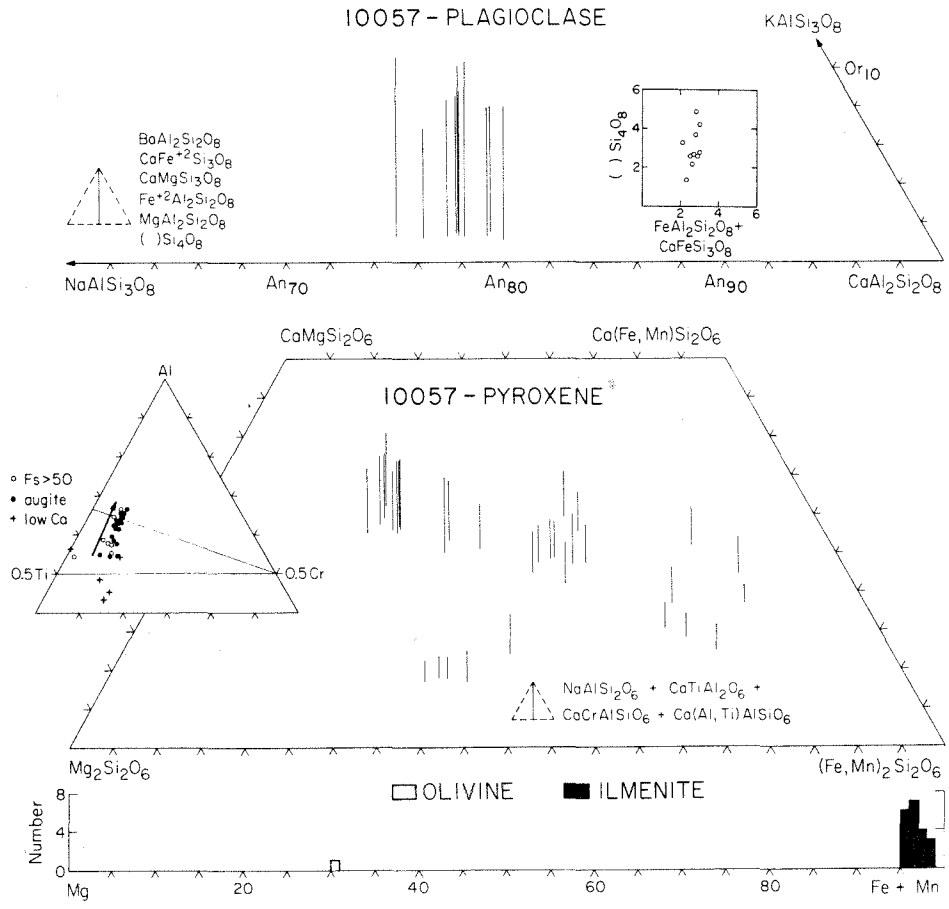

Fig. 26. Composition of pyroxene, plagioclase, olivine and ilmenite in 10057.

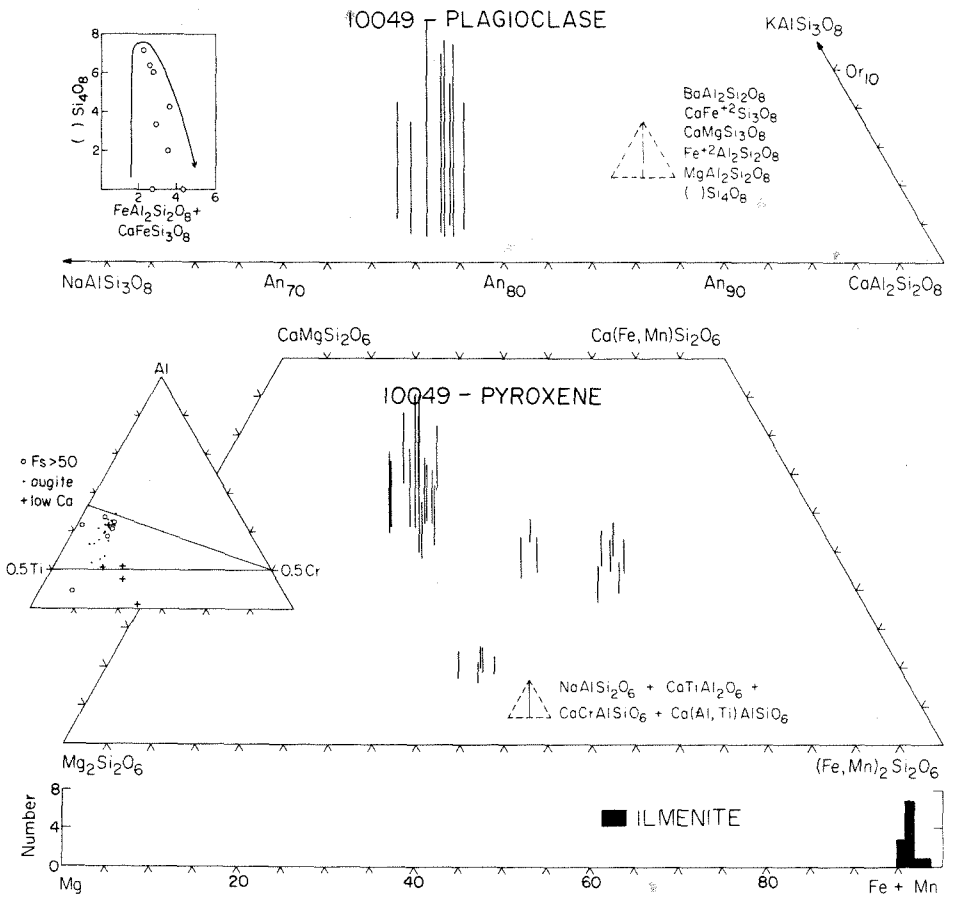

Fig. 27. Composition of pyroxene, plagioclase and ilmenite in 10049.

excess silica will dissolve in anorthite, and as temperature falls and X_{SiO_2} in the melt increases, the amount of excess silica in feldspar increases. Once the eutectic is reached, however, cristobalite begins to form, and with further cooling, the feldspar in equilibrium with cristobalite will lose more and more of its excess silica to cristobalite. From this we may conclude that in 10024, 10017 and 10032, which do not show this predicted [ ]Si_4O_8 depletion, the plagioclase was probably not in equilibrium with the cristobalite. These three samples, however, show no obvious textural dissimilarity when compared to the others concerning plagioclase and cristobalite, so their different excess silica zoning is unexplained.

Pyroxene ranges in habit from small subhedral to euhedral crystals enclosed by plagioclase in the finer-grained samples, to large anhedral grains intergrown with plagioclase and ilmenite on their margins in the coarser samples. In all samples, however, the zonation is the same: an augite to pyroxferroite trend combined

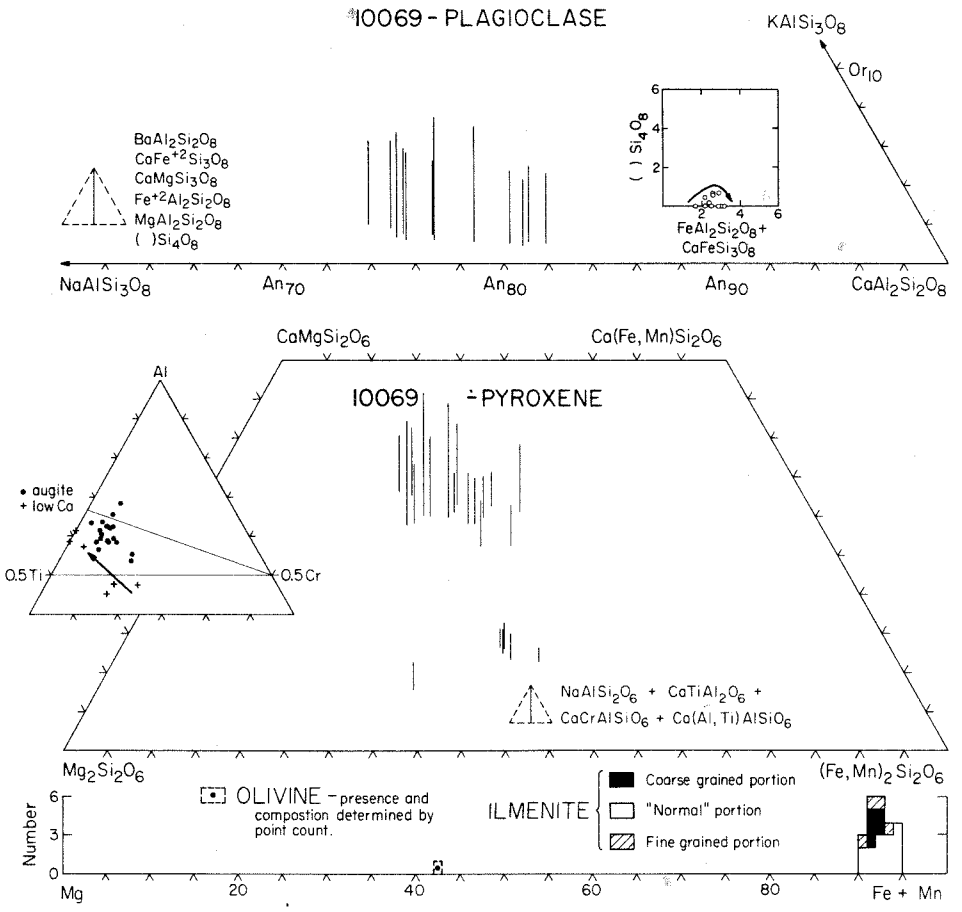

Fig. 28. Composition of pyroxene, plagioclase, olivine and ilmenite in 10069.

with a pigeonite to ferropigeonite to pyroxferroite trend (Figs. 22–29). In 10017, a ferrohedenbergite trend was initiated. As in the low-K basalts, there are no pyroxenes which fall in the two-pyroxene field. The low-Ca pyroxenes may be so intricately intergrown with the augites, however, that indiscriminate measurements with the microprobe will give compositions which apparently correspond to intermediate-Ca pyroxenes. In our experience, these analyses may always be eliminated through the careful use of electron beam scans.

The entire high-Ca trend may be found in single crystals, but the low-Ca trend must be defined by a number of individual slightly-zoned crystals. The low-Ca grains are usually enclosed by high-Ca pyroxene and are subhedral to irregular in shape. Several samples, such as 10032, have augite with optically visible pigeonite cores. Neither the pigeonite cores nor most of the irregular shapes could have formed by exsolution. Thus, although magmatic growth proceeded on

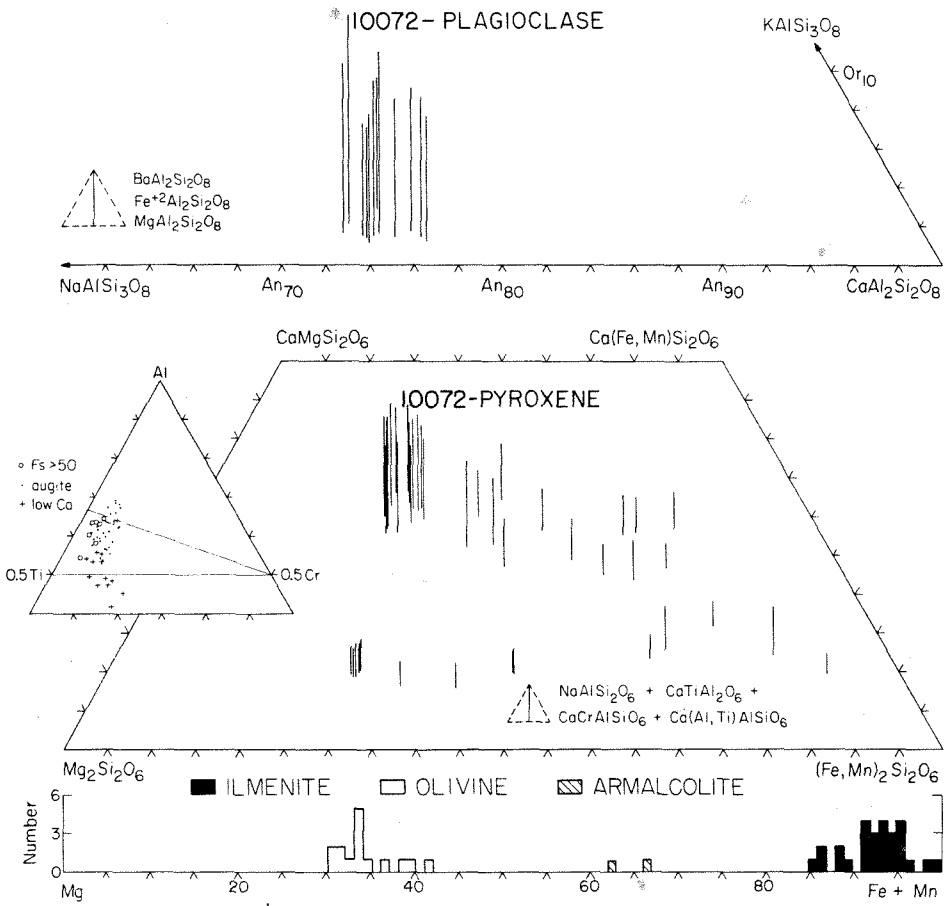

Fig. 29. Composition of pyroxene, plagioclase, olivine and ilmenite in 10072.

both branches of the pyroxene solvus, the low-Ca branch in some samples apparently commenced marginally before the high-Ca branch. Although the zoning trends in these samples are fundamentally the same, the amount of material in each zone is not. The proportion of pyroxene more iron-rich than Fs_{60} decreases steadily from 2.8% in 10024 to 0.9% in 10049 (Table 4). This indicates that fractional crystallization was more efficient in the more slowly cooled samples.

None of the high-K basalts contain optically-discontinuous pyroxferroite or even compositions suggestive of pyroxferroite. The most Fe-rich pyroxene compositions in 10024, 10032, 10071 and 10072 are about $Wo_{10}En_{10}Fs_{80}$ (Figs. 22–24, 29). Although not shown in Figs. 26 and 27, 10057 and 10049 also zone to near this point, as shown by data from the point count. In contrast, 10017 and 10069 do not. The most iron-rich pyroxene in 10017 is about $Wo_{15}En_{25}Fs_{60}$

(Fig. 25), while in 10069 it is only $Wo_{28}En_{35}Fs_{37}$ (Fig. 28). The early termination of the 10017 and 10069 pyroxene trends is unexpected and may in some way relate to their coarse antiophitic texture. The proportion of low-Ca pyroxene ranges from 3.3% to 10.6% in these samples (Table 4) with smaller amounts in the more chemically fractionated specimens. This may be related to the fact that when olivine is lost, the eventual average pyroxene will be more calcic, moving closer to the boundary of the two pyroxene field.

Most of the high-K basalts show identical trends on the Al-Ti-Cr plot for pyroxene (Figs. 22–29). There is a distinct separation of low-Ca pyroxene, augite, and high-Fe pyroxene. Low-Ca pyroxene analyses fall well below the 0.5 Ti-0.5 Cr join and are relatively much more Cr-rich than the coexisting augite. Pigeonite zoning trends to be directly away from the Cr apex, followed by an Al enrichment trend (Figs. 23, 25, 28). The points below the 0.5 Ti-0.5 Cr join demand an unusual substitution, such as $Cr^{2+}SiO_3$, $R^{2+}Ti^{4+}O_3$, [ ] $Ti^{4+}Si_2O_6$, or $R^{2+}Ti_2^{3+}SiO_6$. The extreme Cr enrichment of these low-Ca pyroxenes is suggestive of Cr^{2+}, but without spectroscopic data, it is not possible to evaluate these possibilities. Augite analyses fall in a fairly tight cluster in the lower triangle indicating the dominant substitutions are $R^{2+}Ti^{4+}Al_2O_6$, $R^{2+}Ti^{3+}AlSiO_6$, and $R^{2+}Cr^{3+}AlSiO_6$ (Figs. 22, 23, 26). Interestingly enough, the formula proportion of Al + Si averages about 1.97 in the augite (and pigeonite) and then increases systematically to greater than 2.00 in the more Fe-rich varieties. This suggests that some other ion occupies the tetrahedral site, such as Fe^{2+} or Ti^{+4}. A possibility might be either $Fe(TiO_3)$ or $Ti(FeO_3)$, which would be an "excess ilmenite" substitution. The high-Fe pyroxene analyses show scatter in the minor substitutions, due to the lower absolute abundances of Al, Ti and Cr, but fall away from Cr and towards Al compared to the augite (Figs. 23, 27, 29). The high-Ca pyroxenes, therefore, show an Al-enrichement and Cr-depletion trend with crystallization. The Cr-depletion trend is easily explained by the steadily decreasing amounts of Cr in the melt with crystallization. Al increases in the melt with crystallization until plagioclase saturation is reached, at which time it becomes "buffered". The fact that this point is not recorded in the pyroxene indicates that plagioclase was not appreciably undercooled; otherwise, there would be an Al-depletion after plagioclase nucleation.

In the latter stages of crystallization, cristobalite begins to form. Although discrete grains are present, much of it is intimately intergrown with plagioclase, a texture termed "myrmekitic" by James and Jackson (1970). Most of the residual high-K glass is also intimately associated with plagioclase, but the mesostasis intergrowths are always binary, either plagioclase-cristobalite or plagioclase-glass, but never all three. In each sample, the point-count data for the mesostasis shows two clusters on an Al vs. Si plot. One clump has 90–100% SiO_2 and <5% Al_2O_3, while the other falls between 50–70% SiO_2 and 5–15% Al_2O_3. These high silica points apparently correspond to the isolated grains of cristobalite, and they have been separated and reported in the mode (Table 4). The remaining mesostasis points were averaged and then normatively calculated to plagioclase, cristobalite, and glass, the three phases actually present. Thus, there is more

cristobalite present in these samples than that reported in our mode as cristobalite.

Other mesostasis phases include Ca-phosphates, which are either in euhedral crystals or in vermicular intergrowths with cristobalite, plagioclase, or glass. Ulvöspinel is present both as isolated anhedra and as vermicular intergrowths, usually with pyroxene. Tranquillityite has also been observed in the coarser samples. Troilite is commonly present in the mesostasis areas, and perfectly formed spheres are abundant—convincing evidence for sulfide immiscibility. Fe-metal is almost invariably associated with the troilite, but its mode of origin is uncertain. Gibson and Moore (1974) have shown that for Apollo 17 basalts; there is an inverse correlation between sulfur content and native iron, suggesting the iron was formed by sulfur volatilization. This correlation does not hold for Apollo 12, however (Gibson *et al.*, 1977). For Apollo 11, Skinner (1970) reported that the ratio of metal to sulfide is constant for 10072 and two of the low-K samples and concluded that Fe-metal formed by direct eutectic crystallization form immiscible iron-sulfide globules, whose composition was intermediate between Fe and FeS. Within the resolution of our data, these possibilities cannot be distinguished. Troilite ranges from 0.4 to 0.7 volume percent in the high-K basalts and 0.2 to 0.7 volume percent in the low-K basalts.

Sample 10071,31 Iota Thin section 10071,31 has two areas of sharply contrasting texture and grain size separated by a sharp, smoothly curving contact (Fig. 30). Both textures are clearly igneous in origin, a fact pointed out by Drake and Weill (1971). The fine grained portion is chemically more evolved than the coarse grained portion, leading Drake and Weill (1971, p. 68) to conclude that "the simplest explanation would involve autoinjection of the intermediate liquid into already solidified portions of a lava flow or crusted lava pond". Because we can now measure the mode, bulk composition and average phase compositions much more accurately than could Drake and Weill, we have named the finer grained portion Iota and studied it as an additional sample.

The sharp contact, combined with the contrasting textures, mineral chemistries and modes indicates that two liquid compositions are present, separated by an igneous contact. Only one contact is visible; so, we cannot distinguish between an injection of some sort and a xenolith. By comparison with the experimental work of Usselman *et al.* (1975), the two portions have experienced quite different cooling rates. The finer-grained portion cooled at between 86° and 18°C/hr; whereas, the main part of 10071 cooled at 7°C/hr or slower. This evidence indicates that the two portions did not crystallize together. Had Iota been injected while 10071 was still hot, the two would have cooled at the same rate. Either Iota is a xenolith, or it was emplaced after 10071 had cooled.

Iota is composed of 6% ilmenite, 41% pyroxene, 36% plagioclase, 5% cristobalite, and 11% mesostasis (Table 4). The other high-K basalts have 13–16% ilmenite and 22–24% plagioclase, so it can be seen at a glance that Iota has a radically different composition. The texture is dominated by extremely elongate morphologies which appear acicular in thin section (Fig. 30). Plagioclase and ilmenite are both about 500 μm long, but are typically less then 20 μm wide. The

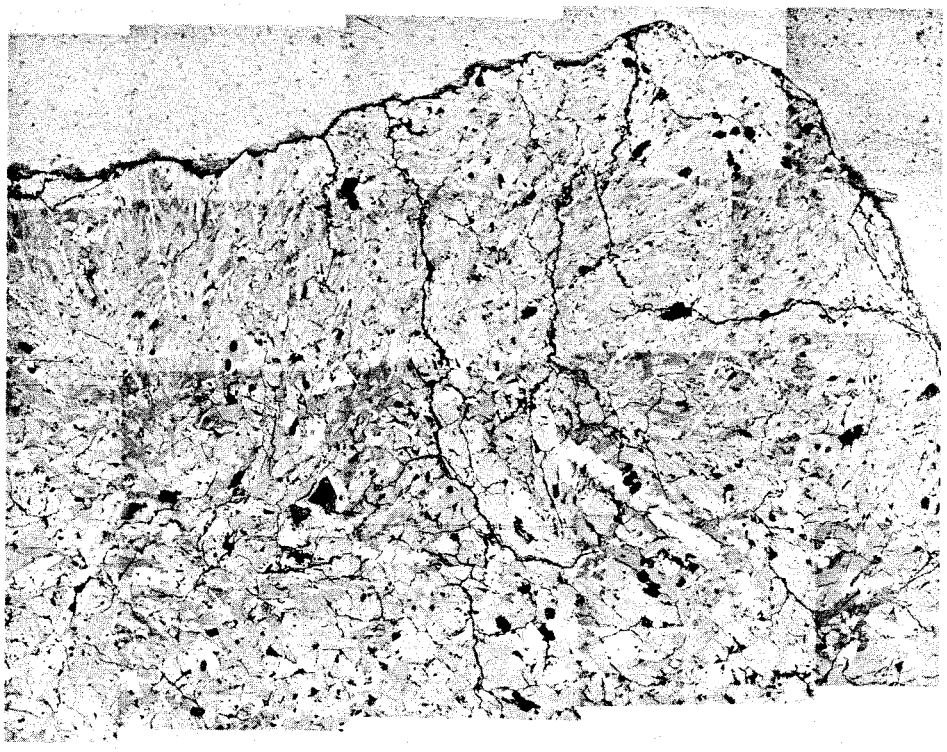

Fig. 30. 10071,31 reflected light. Width of field = 4 mm. Note the sharp contact which separates the normal portion (lower left) from the finer-grained portion. The different textures indicate different cooling rates, so this contact separates two liquid compositions. We have named the fine-grained portion Iota, and point counted it (see text).

plagioclase tends to occur in subparallel sheaves, and the individual plagioclase laths are separated by fine-grained granular to elongate pyroxene. The fact that none of these needle-like minerals are bent or broken indicates that the magma crystallized from an entirely molten state. There is no preferred orientation of the crystals with respect to the contact.

All of the minerals in Iota have unusual compositions when compared to those in 10081, all being closer to the low temperature ends of their solid solution series (Fig. 31). Ilmenite ranges from Gi_0–Gi_1, plagioclase ranges from An_{79} to An_{74}, and olivine is completely missing. The most magnesian pyroxene in Iota is $Wo_{35}En_{38}Fs_{27}$, while the most iron-rich is $Wo_{13}En_4Fs_{83}$, both of which are higher in iron than their counterparts in 10071. The more evolved nature of the pyroxene and plagioclase in Iota can be seen in Fig. 18, which shows how the average compositions of these two phases compare to those from the other Apollo 11 basalts. Since Iota and 10071 both apparently crystallized from a completely

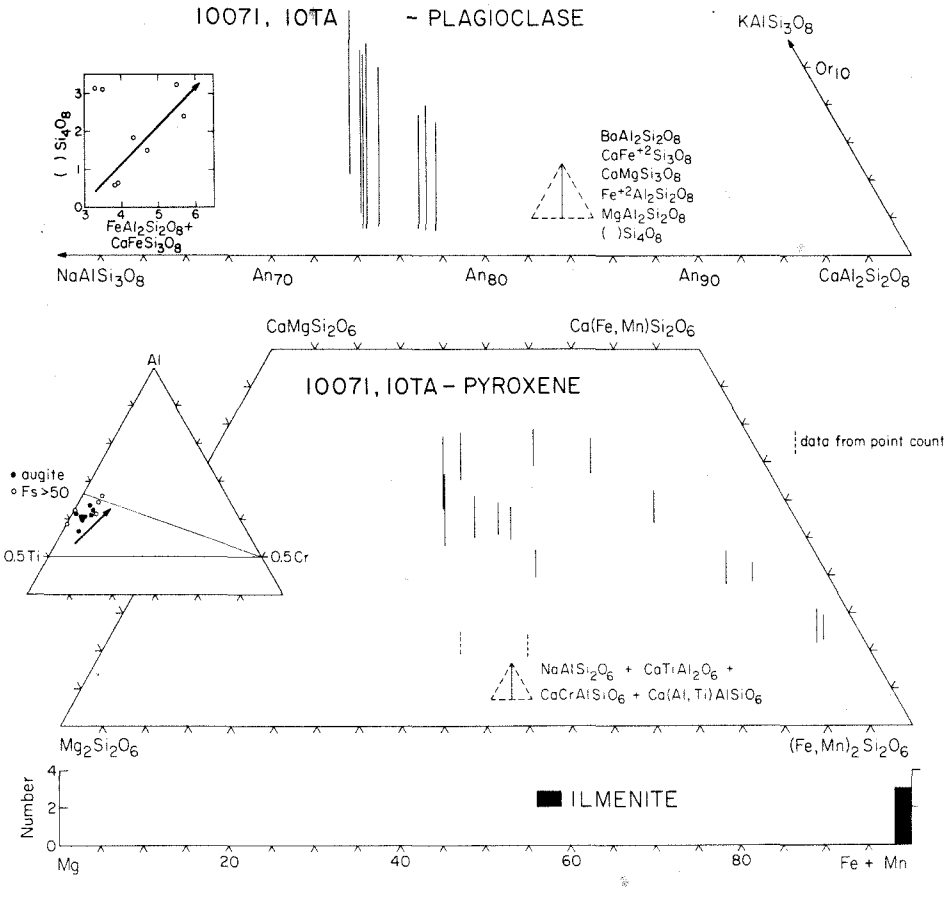

Fig. 31. Composition of pyroxene, plagioclase and ilmenite in 10071, 31-Iota.

molten state, they need not be genetically related. However, extending the work of Drake and Weill (1971), it can be shown the Iota may be simply related to the other high-K basalts through fractionation of about 40% of the early-crystallizing, dense phases.

B. Porphyritic samples

10022. 10022 is medium-grained (average grain size ≈150 μm) (Fig. 32a) relative to the main group of samples and contains numerous large (3 mm), perfectly-spherical, vesicles. The texture is microporphyritic, pyroxene phenocrysts being about twice the size of the groundmass minerals (Fig. 32c). Pyroxene phenocrysts are intergrown with coarse lobate ilmenite grains. The groundmass consists of euhedral plagioclase laths, much finer-grained pyroxene and acicular ilmenite. Olivine cores are present in some of the pyroxene phenocrysts.

Armalcolite is present in some thin sections (Anderson *et al.*, 1970) but not in others, including the ones used in this study. Modally, 10022 differs from the other high-K samples in that it has more pyroxene (52.6 volume percent) and more mesostasis (9.9 volume percent) (Table 4).

The pyroxene phenocrysts are subhedral (rectangular) grains which range in size up to about 400 μm (Fig. 32c). Sector zoning is commonly well developed, in contrast to the other high-K samples where it is rare even in the coarsest samples. The prophyritic natue of this sample was not recognized by previous workers (such as Weill *et al.*, 1970), probably because the grain size appears to range continuously down to groundmass size. However, one can see that the size, habit, and composition of the groundmass pyroxene and ilmenite are different than

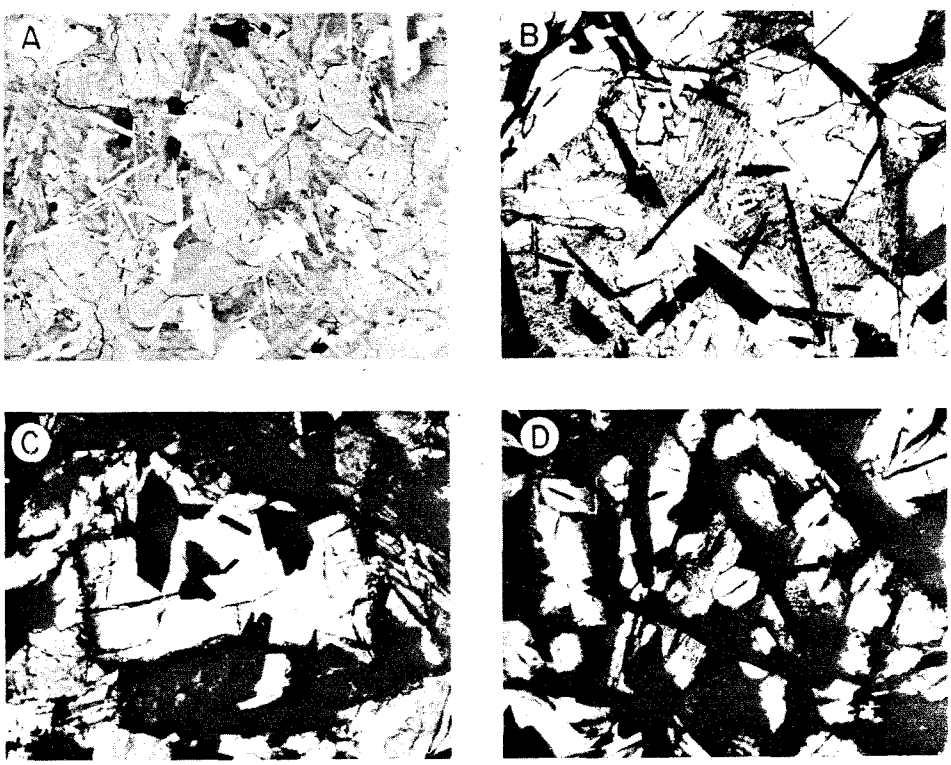

Fig. 32. Porphyritic high-K samples. (A) 10022 Field of view 1.0 mm; reflected light (same as Fig. 21 for comparison). Three phases are visible, ilmenite (white), pyroxene (medium gray), plagioclase (dark gray). (B) 10085,12-7 Field of view 500 μm; transmitted light. Pyroxene (light) and ilmenite (black) phenocrysts set in a finely crystalline groundmass. (C) 10022 crossed polars, 500 μm full scale. Subhedral pyroxene phenocryst enclosing ilmenite grains (opaque), set in a finer-grained groundmass of plagioclase and pyroxene (right and top). (D) 10060,71 clast δ Field of view 200 μm; transmitted light. Pyroxene euhedra (light) and ilmenite plates (black) set in basaltic glass (dark gray).

those of the phenocrysts. Pyroxene becomes much finer grained and anhedral (Fig. 32c), and ilmenite changes from equant to bladed (Fig. 32a). Plagioclase nucleation occurred at or about the time the groundmass started to grow.

The cores of the phenocrysts have compositions similar to early pyroxene in the other high-K basalts, being $Wo_{29}En_{44}Fs_{17}Other_{10}$ (Fig. 33) with typically 3.0 weight percent Al_2O_3 and 2.8 weight percent TiO_2. This pyroxene is intergrown with, and poikilitically encloses, the coarsest and most magnesian ilmenite analyzed in this study, Gi_8. Weill *et al.* (1970) reported some euhedral ilmenite poikilitically enclosed in pyroxene of composition about Gi_{15}—similar to some of the magnesian ilmenite of the non-prophritic samples. In some grains the earliest pyroxene zones outward to more calcic and more aluminous compositions, reaching 5.5 weight percent Al_2O_3, whicle other traverses show decreasing Al_2O_3

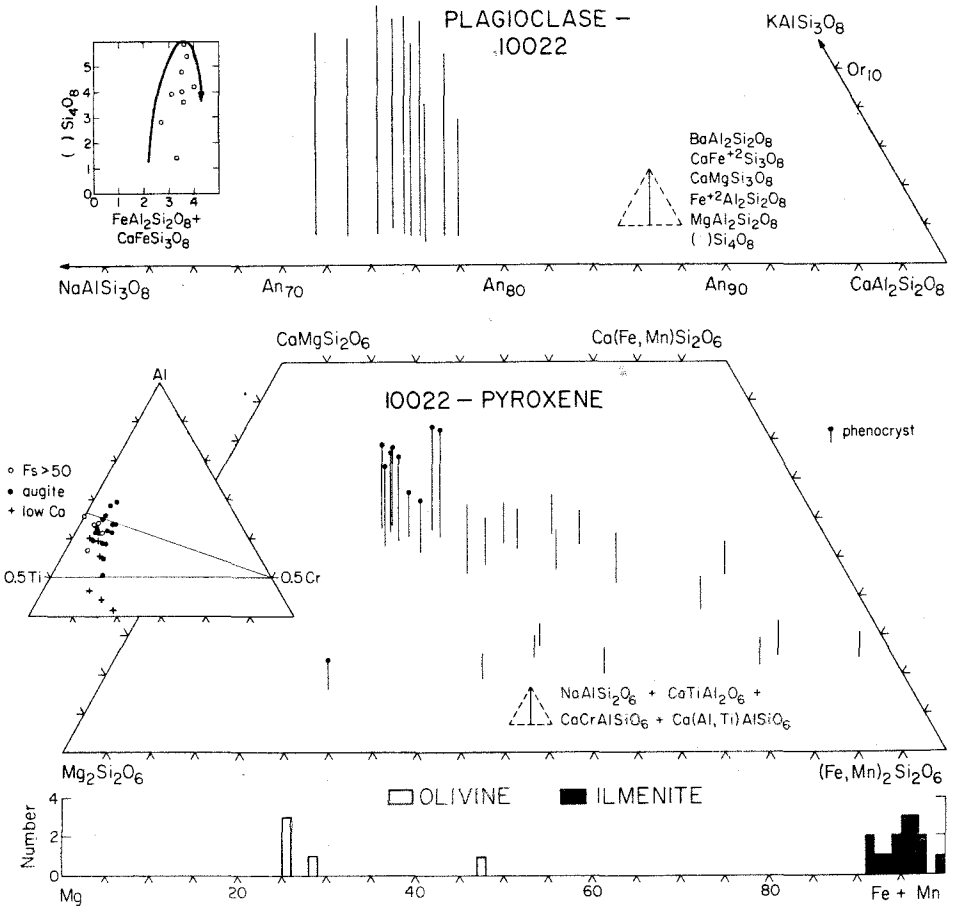

Fig. 33. Composition of pyroxene, plagioclase, olivine and ilmenite in 10022.

and constant CaO. These two trends might be related to different sectors of the growing pyroxene. In all cases, the phenocryst is separated from the groundmass by a thin, discontinuous rim of low-Ca pyroxene ($Wo_9En_{46}Fs_{45}$). This rim belongs to the groundmass due to its high iron content and may be caused by a combination of increased cooling rate and the onset of plagioclase crystallization.

Although we are using the term phenocryst purely in a descriptive manner, referring to larger crystals, the term has classically been equated with a two-stage cooling history. However, Walker *et al.* (1976) and Usselman *et al.* (1975) have both produced phenocrysts experimentally using only a single stage cooling history. While the interpretation of these phenocrysts is open to debate, 10022 is texturally distinct from the other high-K basalts.

10060,71 clast δ 10060,71 clast δ is a vitrophyre, and based entirely on petrology, James and Jackson (1970) concluded that it crystallized from a different magma than the other high-K samples. We have measured the bulk composition as well as the petrographic featues and can now evaluate this question more fully.

10060 is a soil breccia containing a variety of mineral and lithic clasts. In thin section ,71 is a clast of basaltic vitrophyre with a surface area of 1.0mm^2 that we have named clast δ. Clast δ contains subhedral to euhedral pyroxene phenocrysts (41%), subhedral to anhedral olivine phenocrysts (3%), bladed armalcolite mantled by ilmenite or pyroxene (1%), and bladed ilmenite (14%) set in a groundmass of basaltic glass with incipient feathery pyroxene (Fig. 32d). Troilite spheres are present in the glass, indicating that sulfide immiscibility had occurred by the time of quenching, but native Fe was not observed.

Ilmenite in clast δ is subhedral, acicular, and commonly skeletal with an average grain size of 40 μm × 4 μm. Rutile lamellae are almost completely lacking except in the ilmenite that mantles armalcolite, in which they are abundant. The total range in ilmenite zonation is from Gi_6 to Gi_{12} (Fig. 34), the most magnesian analyses coming from the armalcolite mantles and grains poikilitically included in olivine and pyroxene. Cr_2O_3 is the most abundant minor component, ranging up to 1.5 weight percent and is roughly correlated with MgO content. Al_2O_3 varies systematically with Cr_2O_3, and may be as high as 0.3 weight percent. ZrO_2 and Nb_2O_5 rarely exceed our detection level (0.05 weight percent), but V_2O_3 does not.

Armalcolite is the largest mineral present, up to 340 μm long, and is always in reaction relation with the melt. Euhedral grains may be found in the cores of pyroxene crystals without ilmenite mantles. Textural evidence, therefore, is conclusive that pyroxene nucleated before armalcolite became unstable. This is similar to the paragenetic sequence of 10072 and at variance with that of 10071, in which the earliest olivines and pyroxenes have ilmenite inclusions but never armalcolite. Fe/(Fe + Mg) of the armalcolite ranges from 0.50 in the cores to 0.61 in the rims (Fig. 34). Cr_2O_3 decreases from 2.4 weight percent to 1.8 weight percent, while Al_2O_3 decreases from 1.8 weight percent to 1.5 weight percent from core to rim. V_2O_3 averages about 0.3 weight percent, and ZrO_2 about 0.05

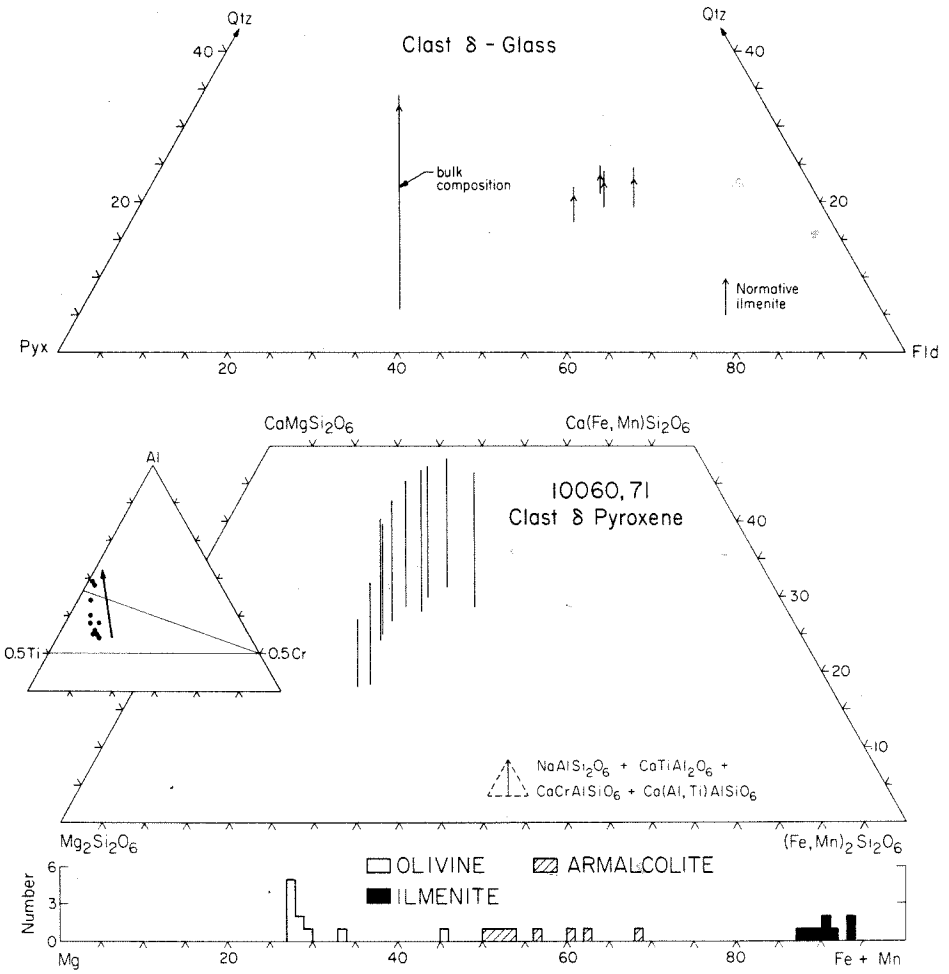

Fig. 34. Composition of pyroxene, glass, olivine and ilmenite in 10060,71 clast δ.

weight percent. The $Ti_2^{3+}Ti^{4+}O_5$ molecule ranges from 6.1 mole percent in the most magnesian grains to 2.8 mole percent in the most ferrous. $Ti^{3+}/(Ti^{+3}+Ti^{+4})$ in the melt, therefore, decreased with time, with fO_2 ranging from half a log unit below to half a log unit above the iron-wüstite buffer (Usselman and Lofgren, 1976).

Olivine is approximately the same size and shape as the pyroxene phenocrysts with the exception that the olivine grains are typically anhedral and have embayed margins filled with glass. Inclusions of ilmenite are frequently present, and some grains are mantled by pyroxene. Most olivine grains have a composition of Fa_{27} (Fig. 34), which is also the most magnesian olivine in the rock. The total

range in zoning is to Fa_{45}, this entire range being present in a single crystal. Fa_{27} is significantly different than the Fa_{30} displayed by all of the other high-K rocks, in spite of the fact that they have similar bulk Fe/(Fe + Mg) ratios. This suggest that there was either extensive ilmenite crystallization prior to olivine formation in clast δ, or $K_{D_{liq}}^{ol}$ is not a constant, but depends on oxygen fugacity, cooling rate or some other such variable. Prior crystallization of armalcolite would not have changed the bulk Fe/(Fe + Mg) and, hence, cannot explain the observed deviation.

Pyroxene phenocrysts are euhedral to subhedral, with a prismatic habit (Fig. 32d). Most grains are about 20 μm across, but some are as large as 120 μm. The color is a pale brown, and no pleochroism was detected. Many crystals show feathery overgrowths on their euhedral outlines, representing quench crystallization on the existing crystal faces. The pyroxene is optically as well as compositionally zoned but not extensively. The earliest pyroxene to crystallize was probably a low-Ca pyroxene, whose presence and composition were determined from point count data (Fig. 34). This is discontinuously separated from an intermediate-Ca pyroxene ($Wo_{18}En_{51}Fs_{22}Other_9$), which zones continuously to higher Ca and higher Fe. The most Fe-rich pyroxene anayzed was $Wo_{29}En_{28}Fs_{26}Other_{17}$. About 99% of the pyroxene in the rock falls in this intermediate- to high-Ca trend (Table 4). Along this trend both Al and Ti increase consistently in the pyroxene from 2.5 weight percent TiO_2 and 2.4 weight percent Al_2O_3 to 4.8 weight percent TiO_2 and 7.2 weight percent Al_2O_3. Cr_2O_3 increases from 0.7 weight percent in the intermediate-Ca pyroxene to 1.2 weight percent in the augite, then decreases to 0.25 weight percent in the Fe-rich compositions. This shows up on the normalized Al-Ti-Cr plot (Fig. 34) as a linear trend away from Cr and towards Al. This indicates that the later pyroxenes have an increasing amount of Ca-Tschermak's molecule substitution.

The groundmass consists of a brown to reddish brown glass that contains variable amounts of (feathery), dendritic pyroxene. The glass commonly contains about 30% of such pyroxene, along with minor amounts of tiny troilite spheres and ilmenite platelets. Defocussed beam analyses on the groundmass indicate that the normative composition is 17–21% quartz, 50–56% feldspar, 20–28% pyroxene, 3% ilmenite and 1% apatite. The variations in normative quartz, feldspar and pyroxene (Fig. 34) lie on a pyroxene control line, which indicates that the composition of the glass is controlled by the amount of pyroxene precipitated locally.

10085,12-7 10085,12-7 is a "vitrophyre" with a crystalline groundmass which was described by James and Jackson (1970). Euhedral to subhedral phenocrysts of olivine, pyroxene, and ilmenite (13%) are set in a very fine grained groundmass composed of plagioclase, pyroxene, glass, and minor ilmenite (Fig. 32b). Small troilite spheres and phosphate minerals are also present. Many phenocrysts are larger than 200 μm in diameter, while the surface area of 10085,12-7 is only 1.2 mm^2. The mode and bulk composition, therefore, have large uncertainties.

There are two olivine crystals in the rock, one of which is 160 μm across and euhedral. Several melt inclusions are trapped near the core (Fa_{28}) and ilmenite

needles are included in the margin (up to Fa_{45}) (Fig. 35.)

Pyroxene phenocrysts are subhedral to euhedral with a seriate size distribution averaging 250 μ × 80 μ and ranging up to 500 μ in length (Fig. 32b). Irregular and patchy extinction is common, while sector zoning is rare. Ilmenite grains are poikilitically enclosed in essentially every pyroxene phenocryst in the rock, including the cores of the largest grains. Compositionally, the pyroxene zones from $Wo_{25}En_{48}Fs_{16}Other_9$ to $Wo_{22}En_{29}Fs_{30}Other_{19}$ (Fig. 35). Also sampled during the point count, but not subsequently studied, was pigeonite (Fig. 35). These grains are probably in the cores of the phenocrysts. The normalized, Al, Ti and Cr abundances in pyroxene (Fig. 35) are very similar to those of clast δ: a strong Al-enrichment trend coupled with a depletion in Cr. Ca-Tschermak's molecule becomes increasingly important with differentiation.

Ilmenite is lath-shaped with an average size of about 100 μ × 5 μ (Fig. 32b).

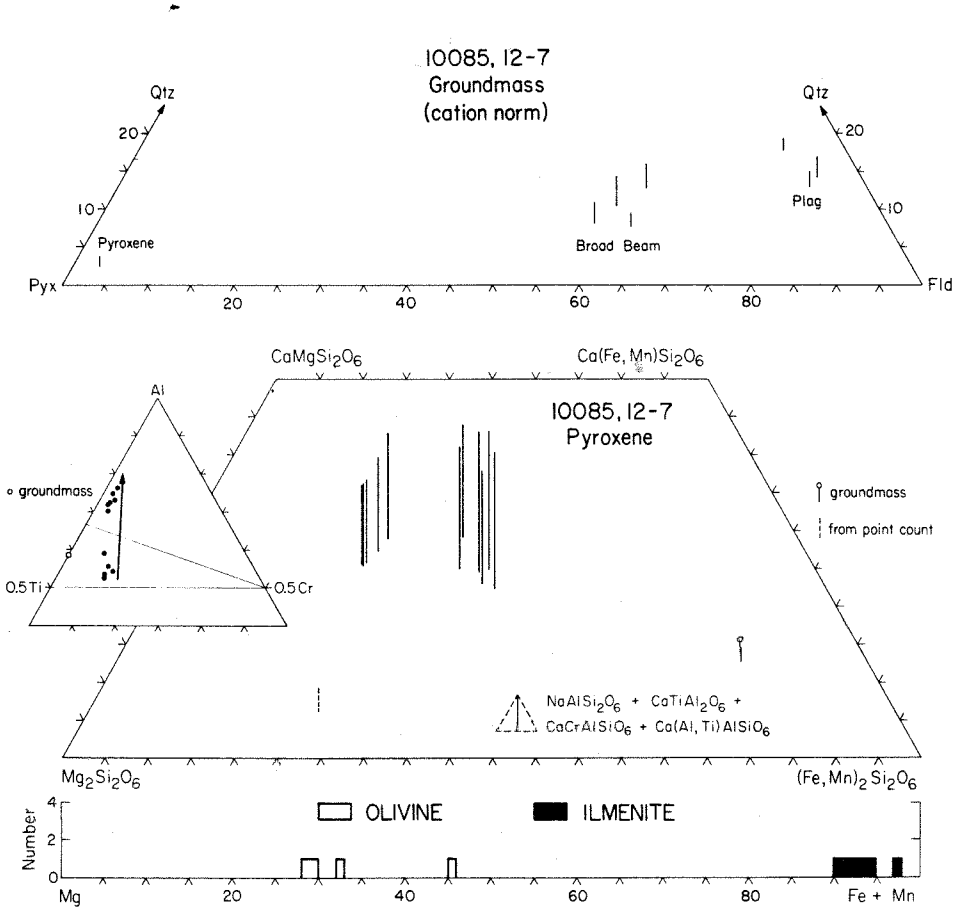

Fig. 35. Composition of pyroxene, groundmass, olivine and ilmenite in 10085,12-7.

The measured compositions span the range Gi_9–Gi_3 (Fig. 35), but only the largest grains could be analyzed. Cr_2O_3 ranges from 0.72 to 0.34 wt.%, and SiO_2, Al_2O_3 and ZrO_2 may be as abundant as 0.15 wt.%.

The groundmass consists of a fine grained (1–2μm) mixture of pyroxene, plagioclase and glass, with minor ilmenite. Plagioclase comprises about 65% of the groundmass and is present as sheaves of subparallel, acicular (80 μ × 1 μm) crystals (Fig. 32b). These are ophitically enclosed by apparently fine grained but optically continuous pyroxene up to 60 μm across. Disseminated residual glass, ilmenite and troilite spheres comprise the remainder. Four broad beam analyses of the groundmass as well as analyses of the plagioclase and groundmass pyroxene are shown in Fig. 35. The plagioclase has a composition of about An_{72} with 15 mole% excess silica, and the pyroxene has a composition of $Wo_{14}En_{14}Fs_{72}$. Both of these minerals, therefore, were greatly undercooled before crystallization. Using these mineral compositions and an assumed average glass composition (7 wt.% K_2O), it is possible to calculate a mineral composition from the broad beam analyses. This indicates that the groundmass is composed of 4% glass, 1% troilite, 2% ilmenite, 67% plagioclase, and 26% pyroxene.

Clast δ and 10085,12-7, the two Apollo 11 vitrophyres, are similar in many important respects. Except for the armalcolite in clast δ, they have virtually indistinguishable modes. In particular, the percentage of crystals at the time of quenching was the same (54–59% vol.%). Both the pyroxene and olivine zonation are similar and differ from all of the other high-K samples. They differ in that the glass in clast δ is more siliceous (20% normative quartz) than that in 10085,12-7 (10% normative quartz) (Figs. 34, 35).

C. Crystallization sequence of the high-K basalts

Although the vitrophyre 10060,71 clast δ has a different texture than the main body of samples, its bulk composition is very similar. Since it was quenched with about 60% crystals, studies of its residual glass give a key data point on the liquid line of descent, which is summarized in Fig. 36. 10085,12-7 was not used because of the uncertainties in its mode and composition. All of the relations shown in Fig. 36 near the liquidus are inferred from textural observations, and those near the solidus are obtained from studies of the mesostasis.

In some, if not all, of the samples, armalcolite was the liquidus phase. As opposed to the low-K basalts, there is no evidence of any early Cr-spinel. Armalcolite then began reacting to ilmenite, and high-Mg ilmenite started nucleating on its own in the magma. Olivine began precipitating when the melt had about 5% ilmenite and/or armalcolite crystals suspended in it, but by the time the melt was 10% crystalline, olivine was reacting to pyroxene. Low-Ca pyroxene preceeded augite in many samples. Ilmenite and first one, then two, pyroxenes co-crystallized, each becoming more iron-rich. When the magma was about 60% solid, plagioclase joined the sequence. Cristobalite saturation occurred at 80–85% solid, while ulvöspinel, phosphate, mineral(s), and tranquillityite precipitated after that. Sulfide immiscibility occurred shortly after the termina-

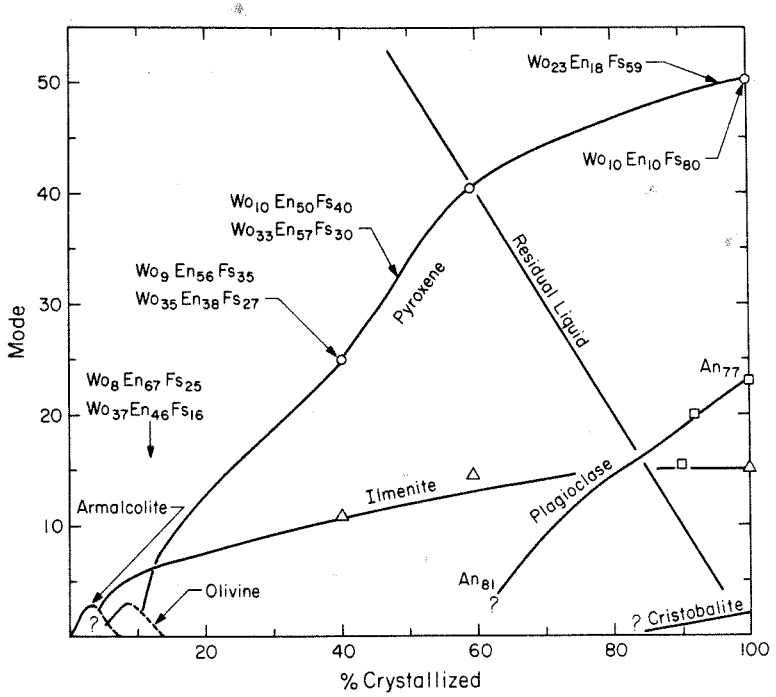

Fig. 36. Inferred crystallization history for high-K samples. Armalcolite and olivine may not have been present in all rocks, and are variably preserved.

tion of olivine crystallization, probably in the range 20–30% solid. Silicate liquid immiscibility occurred at about the point that cristobalite precipitated, or perhaps shortly afterwards, at about 80–90% crystalline.

Walker *et al.* (1975) have experimentally calibrated this sequence using rock powder from 10072 as a starting material. In their run at 1195°C, no crystals were present, but at 1159°C, olivine, armalcolite, and ilmenite were present. At 1149°C, armalcolite had reacted out, and at 1145°C, low-Ca pyroxene had formed. High-Ca pyroxene was present at 1130°C, while plagioclase was present only at 1122°C, their lowest temperature run. This sequence is exactly that observed in thin section.

It is also possible to see from Fig. 36 how the amount of any given mineral in the melt changed with time. Whether or not armalcolite was the liquidus phase, note that most of the ilmenite forms early. When the melt was only 20% crystalline, half of the total ilmenite in the sample had been crystallized. Likewise, most of the pyroxene growth takes place between 20% and 60% crystallized. Both pyroxene and especially ilmenite show only minor growth after 60%. From 60% to 100%, large amounts of plagioclase form, supplemented by cristobalite and the remaining pyroxene. The spherical vesicles which are characteristic of the high-K basalts must have formed early because of their

shape, and were probably present before crystallization started. Figure 36 also shows how the mineral compositions changed with crystallization. Note that the pyroxene shows extremely non-linear zoning: the composition changes from Fs_{16} to Fs_{30} over the first 50% of crystallization but changes from Fs_{60} to Fs_{80} over the last 4%. Ilmenite compositions have not been shown on Fig. 36 because the most Mg-rich and the most Fe-rich analyses do not seem to vary in a systematic way.

3. Genetic Relationships

As shown above, the textural and petrologic data are consistent with most of the Apollo 11 high-K basalts being derived from a single lava flow which underwent minor olivine fractionation. 10022, clast δ and 10085,12-7 have porphyritic textures and could represent a second flow with a different cooling history. To fully evaluate the possible genetic relations, however, two additional types of data are important. First, samples of the same igneous cooling unit must have the same age. Second, all comagmatic samples should have either the same bulk composition, or their bulk compositions should be relatable by crystal-liquid fractionation.

Isotopic data

Five of these ten high-K samples have been accurately dated by the ^{39}Ar-^{40}Ar method (Geiss *et al.*, 1977; Guggisberg *et al.*, 1977). Three of these, 10032, 10072 and 10022, have ages of about 3.60 b.y. The age of 10071 is 3.51 ± 0.06, which is the same within the errors, but 10049 is 3.45 ± 0.04, which is distinctly lower. The age for 10049, however, was obtained on an intermediate temperature plateau, and is considered less reliable (Geiss *et al.*, 1977). Rb-Sr ages have been obtained on six of these samples (Papanastassiou *et al.*, 1977), and an Sm-Nd age was measured on 10072 (Papanastassiou *et al.*, 1977). Within the limits of the errors, all of these specimens fall within the range of 3.60–3.65 b.y. In conclusion, although 10049 may be somewhat younger, these samples apparently have the same age, between 3.60 and 3.65 b.y. Therefore, the isotopic data are consistent with their being consanguinous.

Bulk compositional data

The bulk compositions of these samples are summarized in Table 5, and it can be seen that they are in a general way very similar. Two variation diagrams, CaO and TiO_2 vs. Fe/(Fe + Mg) are plotted in Fig. 37a,b. Six samples, 10024, 10032, 10071, 10017, 10057 and 10049, form a consistent trend on both of these plots and are enclosed by an envelope. These rocks show similar relations to each other on most variation diagrams involving bulk compositions, so they have been called the main compositional series. 10085,12-7 is included on Fig. 37 in spite of the fact that the uncertainty in its bulk composition is 2–3 times as large as that for

Table 5. Compositional summary: Apollo 11 high-K basalts.

	MAIN SERIES																		PORPHYRITIC SERIES					
	10024	σ	10032	σ	10071	σ	10017	σ	10057	σ	10049	σ	Iota[1]	σ	10072	σ	10069	σ	10022	σ	Clast δ[2]	σ	10085, 12-7	σ
P_2O_5	0.10	0.04	0.11	0.05	0.15	0.06	0.09	0.04	0.09	0.05	0.15	0.07	0.16	0.08	0.07	0.04	0.10	0.05	0.10	0.04	0.19	0.04	0.10	0.02
SiO_2	40.00	0.80	39.49	1.05	40.35	0.83	40.63	0.95	40.34	0.78	41.56	1.08	47.89	2.01	41.62	0.83	39.15	0.87	40.93	0.62	39.80	1.09	41.66	2.02
TiO_2	12.93	0.58	13.06	0.53	12.36	0.65	12.18	0.61	12.42	0.63	11.51	0.78	5.75	0.73	11.02	0.89	12.75	0.61	11.72	0.59	14.11	1.06	11.53	0.87
Al_2O_3	7.20	0.24	7.08	0.31	8.29	0.31	7.85	0.24	8.18	0.20	7.95	0.33	11.29	0.61	8.25	0.30	7.39	0.33	8.01	0.20	7.74	0.45	9.09	0.67
Cr_2O_3	0.41	0.03	0.38	0.03	0.42	0.03	0.35	0.03	0.36	0.03	0.34	0.03	0.07	0.02	0.40	0.03	0.40	0.03	0.40	0.03	0.52	0.08	0.45	0.04
MgO	8.74	0.25	8.81	0.32	8.14	0.23	8.16	0.29	7.93	0.24	7.54	0.28	4.69	0.34	8.06	0.21	8.34	0.24	8.29	0.20	8.17	0.36	7.26	0.57
CaO	10.10	0.25	10.21	0.32	10.44	0.27	10.60	0.28	10.54	0.25	10.93	0.33	10.87	0.50	11.04	0.25	9.80	0.27	11.01	0.22	9.59	0.34	10.51	0.59
FeO	19.09	0.54	19.37	0.54	18.55	0.59	19.10	0.60	19.24	0.59	19.21	0.74	17.56	1.09	18.53	0.79	20.57	0.59	18.66	0.53	18.75	0.80	19.15	1.06
MnO	0.23	0.02	0.27	0.02	0.15	0.02	0.23	0.02	0.22	0.02	0.24	0.02	0.22	0.03	0.17	0.02	0.31	0.02	0.23	0.02	0.26	0.02	0.25	0.03
Na_2O	0.43	0.02	0.45	0.03	0.53	0.03	0.49	0.02	0.48	0.02	0.47	0.03	0.80	0.06	0.55	0.03	0.48	0.03	0.48	0.02	0.24	0.07	0.67	0.13
K_2O	0.41	0.06	0.28	0.05	0.24	0.06	0.31	0.06	0.23	0.06	0.31	0.06	0.42	0.08	0.26	0.05	0.23	0.06	0.22	0.06	0.36	0.07	0.24	0.08
BaO	0.05	0.03	0.03	0.01	0.02	0.01	0.04	0.02	0.03	0.01	0.02	0.01	0.10	0.05	0.04	0.02	0.05	0.03	0.04	0.02	0.06	0.06	0.04	0.02
S	0.26	0.07	0.36	0.08	0.23	0.06	0.27	0.07	0.21	0.07	0.38	0.10	0.25	10.12	0.31	0.09	0.19	0.06	0.31	0.06	0.17	0.04	0.19	0.09
Total	99.95		99.96		99.90		100.32		100.29		100.66		100.11		100.38		99.77		100.30		99.97		101.18	
Barth-Niggli norm (cation%)																								
Qtz	2.61		2.20		3.05		2.60		2.86		3.70		7.18		2.58		1.39		2.60		5.83		3.08	
Oliv	—		—		—		—		—		—		—		—		—		—		—		—	
An	17.83		17.83		21.06		19.68		20.98		20.06		27.68		20.63		18.82		20.42		20.62		22.46	
Ab	4.17		4.37		5.13		4.73		4.64		4.53		7.65		5.28		4.68		4.62		2.34		6.40	
Or	2.62		1.79		1.53		1.97		1.46		1.97		2.64		1.64		1.47		1.39		2.31		1.51	
Di	28.54		29.01		27.00		29.04		27.79		29.74		23.08		30.06		26.68		29.99		23.87		25.95	
Hy	23.84		24.07		22.62		22.87		22.82		21.65		22.55		22.46		26.81		22.50		22.47		22.56	
Ilm	19.45		19.68		18.56		18.24		18.62		17.22		8.53		16.43		19.28		17.49		21.35		17.10	
Chr	0.49		0.45		0.50		0.41		0.43		0.40		0.08		0.47		0.48		0.47		0.62		0.53	
Py	0.24		0.34		0.22		0.25		0.20		0.35		0.23		0.29		0.18		0.29		0.16		0.18	
Ap	0.23		0.25		0.34		0.20		0.20		0.34		0.36		0.16		0.23		0.22		0.43		0.22	
Fe/ (Fe + Mg)	.551		.552		.561		.568		.575		.588		.677		.563		.580		.559		.563		.597	

Notes

All bulk compositions calculated from point count data. The quoted errors are the standard deviation of the mean (SDM), a statistical parameter which describes the uncertainty in an infinite population (lava flow) based on measurements of a finite subset (hand sample). The composition of each thin section considered alone is considerably more precise than this (see Analytical Techniques).

[1]Iota is our designation for a cross-cutting igneous feature in thin section 10071,31. Only one contact is present, preventing determination of shape and relative age of the two liquids.

[2]Clast δ is a large vitrophyre clast in soil breccia 10060,71.

the other samples. Note, however, that it is very similar chemically to 10049 (Table 5) and may be a seventh member of the main series. The main series is also shown in Fig. 38, which shows the variations in modal ilmenite and modal plagioclase. The similarity of the patterns of Figs. 37a,b and 38 is noteworthy, despite the fact that they are very different types of data. The linearity of the trend is also important because it shows that the differentiation process was very uniform. The other four samples (including both prophyritic samples) scatter about the main series on most plots. The main series is consistent enough that it is important to examine in each case why the other four samples fall off the common trend. In this way we can evaluate the possibility of anomalous rocks, which may have sampled separate igneous units. The main series will be discussed first, then the other four samples compared to it.

It can be seen graphically in Fig. 37 that removal of armalcolite or ilmenite combined with olivine or pyroxene will produce the observed trend. A least squares solution to this fractionation process suggests that 10049, the most differentiated sample, can be derived from 10024, the most primitive, by loss of

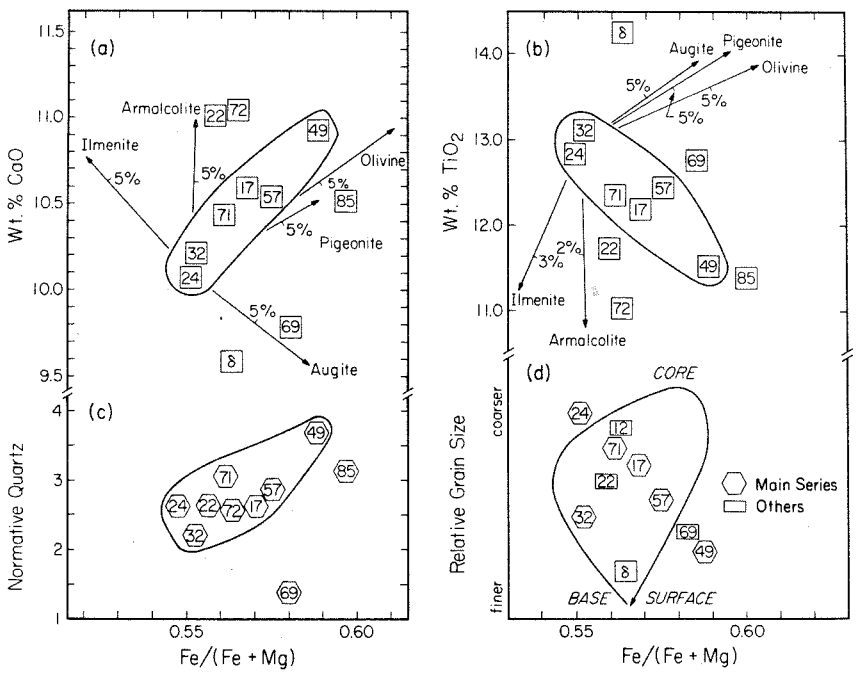

Fig. 37. a) CaO, b) TiO_2, c) normative quartz, and d) relative grain size as a function of bulk Fe/(Fe + Mg) for high-K basalts. Envelopes are drawn around the main series, which is controlled by olivine or pyroxene + ilmenite or armalcolite fractionation. The analysis of 10085,12-7 is far less precise than the others. d) the scatter on this plot indicates that differentiation took place prior to the final cooling of the high-K lava flow.

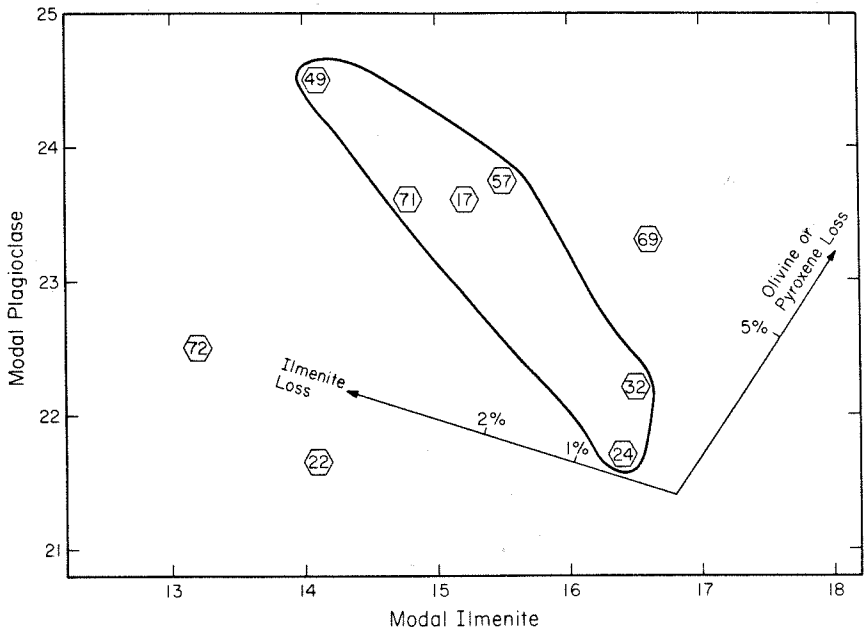

Fig. 38. Modal plagioclase and modal ilmenite in high-K basalts. Envelope drawn around main series defined in Fig 37. Note the similarity of this pattern to that in Fig. 37a,b.

3.2% armalcolite, 0.5% ilmenite, 3.1% olivine, 1.5% augite, and 1.4% pigeonite. In all, approximately 10% crystals must be removed. Note that the amount of olivine is confirmed by Fig. 37c, which shows that the amount of normative quartz increases with differentiation. The rest of the main series, of course, lies directly on a mixing line between 10024 and 10049.

On a La/Sm vs. La trace element plot, 10024 and 10049 are near the La abundance extremes of the field enclosing the high-K data points (Ma and Schmitt, pers. comm.). 10049 could be derived from 10024 through removal of about 25% of crystals of armalcolite, olivine, augite or pigeonite. Even though 25% is larger than the 10% inferred from major element considerations, these two percentage values are not inconsistent with the dispersions observed in single lava flows (Haskin *et al.*, 1977).

As can be seen in Table 4, several important petrologic properties change consistently across the main differentiation series. The amount of pigeonite decreases steadily from 11% of the total pyroxene to 3%, augite decreases from 66% to 60%, while the medium Fe pyroxene increases from 21% to 36%. The average pyroxene (shown on Fig. 18) becomes more iron-rich in a very systematic manner. The average ilmenite contains less Mg with differentiation, but the average plagioclase composition varies independently. Finally, the calculated density decreases in a general way across the main series.

A possible simple model to explain the main series of samples would be a vertical section through a simply-cooled differentiated lava flow. In this case, both cooling rate and differentiation index should vary in a predictable way through the flow. Figure 37 shows the schematic profile of a differentiated lava flow, constructed by assuming olivine and ilmenite or armalcolite depletion in the upper part of the flow, with complementary accumulation in the lower part (e.g., Grove and Walker, 1977, p. 1513), and by assuming that grain size is proportional to the cooling rate. Not only are the data for the samples scattered, but they show no relation to the schematic profile. The fact that the two parameters are independent indicates that the simple differentiated lava flow model is not valid. Therefore, there must have been differentiation prior to the lava's final emplacement. Two reasonable possibilities are flow differentiation and crystal-liquid fractionation in a magma chamber prior to or during eruption.

The physics of flow differentiation have been summarized by Komar (1972a,b). When a magma containing phenocrysts is emplaced as a dike or a sill, "the phenocrysts interact mechanically with one another and give rise to a grain dispersive pressure" (Komar 1972b, p. 3443). This causes them to migrate up the velocity gradient and to be concentrated in the more rapidly flowing core of the dike or sill. In a lava flow, the upper surface is no longer a sheared suspension, but the phenocrysts would still migrate towards the core of the flow. Thus, whether differentiation occurred during flow upward to the surface or during surficial flow away from the vent, the result is similar: Phenocrysts are concentrated in the core of the flow. The core would cool more slowly, and therefore, there should be a correlation between differentiation index and cooling rate, which is not observed. Furthermore, there are no phenocrysts in the main series and the absence of any planar flow fabric suggests that the lava(s) came to rest in an entirely molten state. Therefore, we conclude that the main series of high-K samples is the volcanic product of a magma chamber that was differentiating during eruption. Note that the main series might represent multiple lava flows, or it might represent a single flow that has lateral compositional gradients away from the vent. This conclusion can be strengthened considerably through evidence from Iota.

As can be seen on Fig. 39, Iota has a very different bulk composition than the other high-K basalts. However, on three of these plots, SiO_2, CaO and TiO_2 vs. Fe/(Fe + Mg), Iota can be seen to lie on the extension of the main series. This suggests that whatever the differentiation process which produced the main series, it also produced extremely fractionated compositions like Iota. Because the high-K samples are all quartz normative, we have assumed that a maximum of 2 weight percent olivine could form. With this assumption, it is possible to calculate the amounts of ilmenite, armalcolite and pyroxene that need to fractionate, as well as the average composition of the pyroxene. On each of the plots in Fig. 39, Iota may be derived from 10024 by loss of 2% olivine, 12% ilmenite, 3% armalcolite, and 23% pyroxene of an average composition $Wo_{31}En_{51}Fs_{18}$. The augite in 10071 is Wo_{40} and the pigeonite Wo_9, so the pyroxene which fractionated was probably 20–30% pigeonite. The fact that this

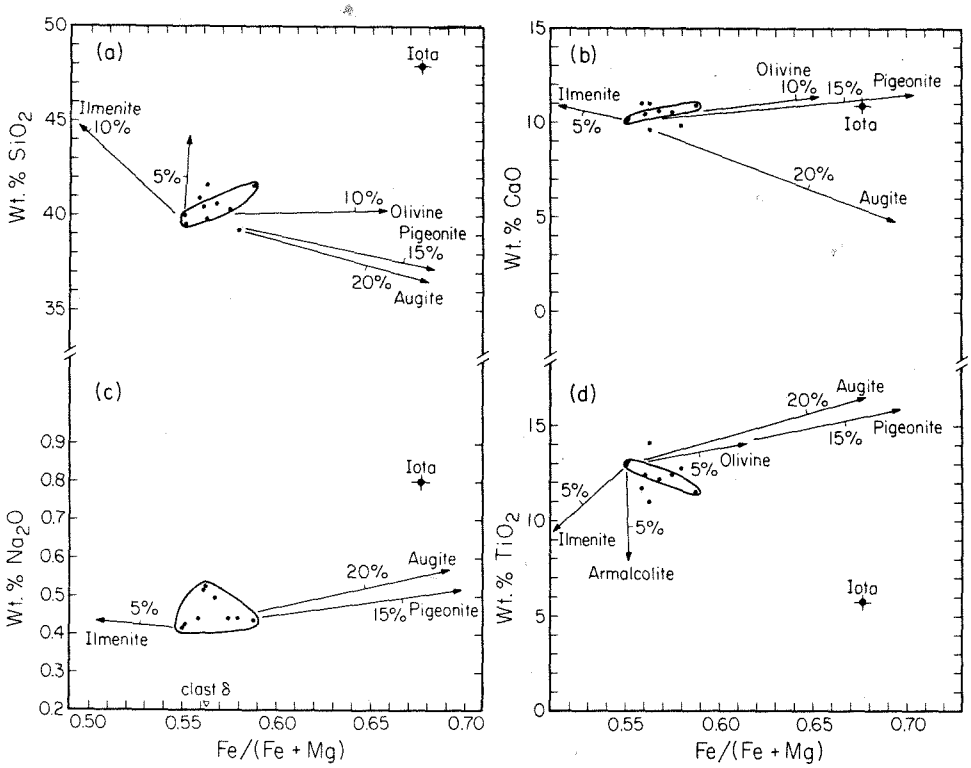

Fig. 39. SiO_2, CaO, Na_2O, and TiO_2 vs. bulk Fe/(Fe + Mg) diagram showing relation of Iota to other high-K samples. Envelope encloses the main series. In all but c), Iota lies on the extension of the main series, suggesting that the differentiation process which produced the main series also produced highly fractionated compositions like Iota.

assemblage of crystals is exactly what one infers from textural evidence in 10024 at 40% crystallized is another argument that Iota is genetically related to other high-K samples. Every indication, therefore, is that Iota is a late-stage differentiate of the same process which produced the main series. It must be remembered, however, that Iota discordantly cuts 10071 (Fig. 30), *requiring* two separate igneous events. This strongly suggests that the differentiating magma chamber produced multiple igneous events.

Next we need to address the problem of how the four high-K samples, which are not part of the main series, fit this model. In particular, are there any differences which suggest an origin other than in this postulated magma chamber?

The mode of 10069 is similar to those of the main series except that it contains more ilmenite and/or plagioclase (Fig. 38). Chemically, 10069 is lower in CaO

and Al_2O_3 and richer in TiO_2 and FeO than the main series (Fig. 37). Therefore, all of the data, both modal and chemical, are consistent with 10069 having been derived from a composition similar to that of 10071 through gain of about 2 weight percent ilmenite and loss of about 2 weight percent plagioclase. Two possible anomalies are the normative quartz (Fig. 37c) and the average pyroxene (Fig. 18). On both plots, 10069 falls away from the field of the other high-K samples.

10072 falls off the trend on Fig. 38 because of its higher modal mesostasis. Compositionally, 10072 is higher in CaO and Al_2O_3 and lower in TiO_2 than the main series. This can be explained by the separation of 2% ilmenite and the addition of 2% plagioclase to a composition similar to that of 10017.

Compositionally, 10022 is lower in TiO_2 and higher in CaO and Al_2O_3 than the main series. It may be reasonably related to a composition such as 10017 by fractionation of pyroxene alone. This is consistent with both the higher modal pyroxene in 10022 and its porphyritic nature. If 10022 crystallized from a pyroxene phenocryst charged lava, some degree of pyroxene fractionation would be natural.

Clast δ has higher Cr_2O_3 and TiO_2, lower Na_2O and CaO, and about the same K_2O, FeO, MgO, SiO_2 and Al_2O_3 as the main series. A major difference, however, is that clast δ has a 5.8% normative quartz, as compared to the range 2.2–3.7% in the main series. All of these differences, however, including the normative quartz, may be explained by clast δ having accumulated armalcolite from a main series composition similar to 10032 and 10024. One unexplained anomaly is the abnormally low Na_2O content of clast δ, 0.24 weight percent, as compared to 0.43–0.53 weight percent in the main series.

4. Discussion

It has been shown that the main series of samples can reasonably be related to a differentiating magma chamber which was fractionating armalcolite, olivine, ilmenite, and pyroxene. 10071, Iota is an extreme differentiate, but is still part of the main series. The four unusual samples can be related to this series through crystal-liquid fractionations of four different sets of crystals. 10069 and 10072 both require involvement of plagioclase to be related to the main series. Since plagioclase does not nucleate until the magma is 50–60% solid, magmatic plagioclase fractionation can only occur after extensive pyroxene and ilmenite fractionation, which is not observed. It would be reasonable, however, to have hand sample-sized inhomogeneities such that 10069 had more ilmenite and 10072 more mesostasis than would be expected. This requires only that the crystals in a crystal-liquid mush shift around slightly (e.g., the short-range unmixing of Lindstrom and Haskin, 1978). Primary magmatic inhomogeneities are another possibility, due perhaps to local assimilation of blocks of country rock. The remarkable consistency of the main series, however, argues that most of the magma chamber was very uniform, or possibly, uniformly stratified. In conclusion, considering the textural and general compositional similarities of

10069 and 10072 to the main series, one may reasonably assume they are from the same lava flow or magma series.

10022, 10085,12-7 and clast δ are all texturally dissimilar to the main series of samples: all are porphyritic. Although 10085,12-7 may be part of the main series and 10022 can be derived by addition of pyroxene and clast δ by addition of armalcolite, their textures indicate that they may have undergone a different cooling history. There are other mechanisms for creating porphyritic textures besides a two-stage cooling history, (e.g., Walker *et al.*, 1976, Usselman *et al.*, 1975), but in this case, it seems clear that the vitrophyres did cool in two stages. A reasonable hypothesis for the formation of these samples is that they represent a separate high-K lava flow produced by the common high-K igneous system, which underwent a different cooling history. Because the differentiation in the magma chamber had proceeded to about the same point at the eruption of both the porphyritic samples and the main series (for example 10085,12-7 is similar to 10049), perhaps the two flows came out of different vents at approximately the same time. If the magma in one of these conduits paused on its way to the surface, it could easily develop phenocrysts. This conclusion is supported isotopically: 10022 has an age indistinguishable from most of the other high-K basalts. Another possible model is that the main series lava flow was impacted by a meteorite at about 60% crystalline. The ejected bits of magma may then have crystallized to the two vitrophyres and the one porphyry.

In conclusion, the six samples of the main series form a well-defined differentiation trend involving separation of the early crystallizing phases. The fact that position in this fractionation series is independent of grain size indicates that the differentiation occurred prior to the final emplacement and cooling of the lava flow. A logical mechanism is the fractionation of a high-level magma chamber prior to or during eruption. 10071, Iota strengthens this hypothesis because it is highly fractionated, having lost about 40% crystals, yet chemically lies on the extension of, and physically cross-cuts the main series. 10069 and 10072 may be related to these samples through mineralogic inhomogeneities. The simplest model for these samples is that they represent a single flow which sampled lateral chemical variations away from the vent. Three other samples are porphyritic, yet chemically similar to the main series. This suggests that the fractionating magma chamber might have produced two eruptions at the same time and that the two batches of magma then underwent different cooling histories. Alternatively, they might have been derived by a meteorite impact on the partially crystalline main series flow.

PART III. SIGNIFICANCE OF THE APOLLO 11 BASALTS

Field relations

It is possible through consideration of the exposure histories along with the astronauts' observations and photo interpretations, to reach conclusions about the field relations at the Apollo landing site. In Fig. 40, modified from the work of

Geiss *et al.* (1977), is shown the Xe^{131}/Xe^{126} ratio as a function of exposure age. Since Xe^{131} is produced by slow neutrons as well as by cosmic ray induced spallation, Xe^{131}/Xe^{126} is a function of depth of irradiation. As pointed out by Eberhardt *et al.* (1970) and Geiss *et al.* (1977) the correlation of rock type and exposure history suggests that the high-K lava flow was the surficial flow at Tranquillity Base (having received some irradiation at depth) and that it shielded B1, B2 and B3, which underlay it, from cosmic irradiation prior to their excavation. These data also indicate that B1, B2 and B3 were exposed by the same cratering event and that 10050 is from a separate, earlier impact. Which single cratering event, then, is the most likely candidate for exposing the low-K suite?

At the time of the landing, it was recognized that at least two sets of rays passed near the landing site (Apollo 11 Preliminary Science Report, 1969). These

Geiss *et al.* (1977), is shown the Xe^{131}/Xe^{126} ratio as a function of exposure age. Since Xe^{131} is produced by slow neutrons as well as by cosmic ray induced spallation, Xe^{131}/Xe^{126} is a function of depth of irradiation. As pointed out by Eberhardt *et al.* (1970) and Geiss *et al.* (1977) the correlation of rock type and exposure history suggests that the high-K lava flow was the surficial flow at Tranquillity Base (having received some irradiation at depth) and that it shielded B1, B2 and B3, which underlay it, from cosmic irradiation prior to their excavation. These data also indicate that B1, B2 and B3 were exposed by the

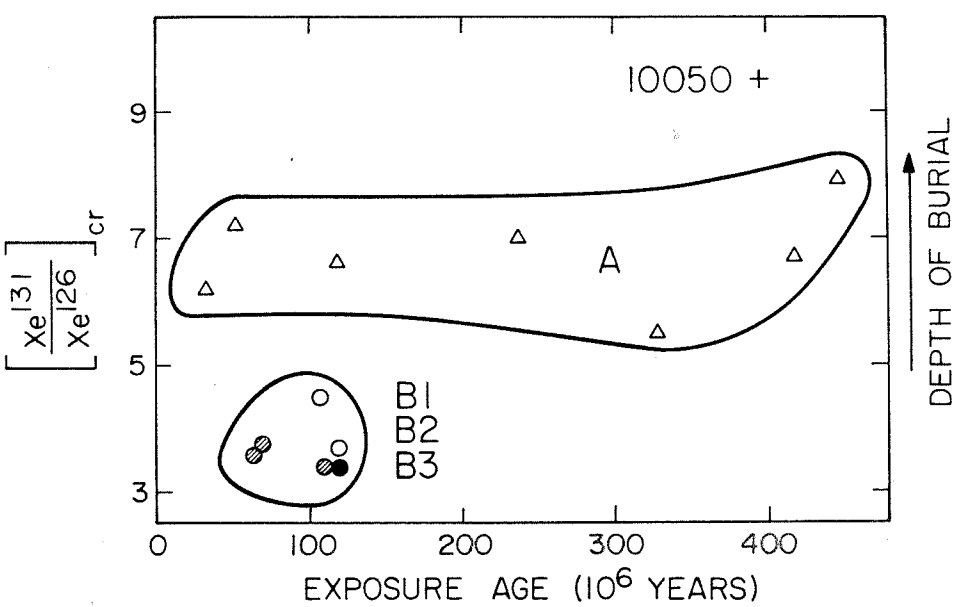

Fig. 40. Exposure histories of Apollo 11 samples (modified after Geiss *et al.*, 1977). Note the correlation of rock type and exposure history. Triangles, high-K. Shaded circles, B1. Filled circles, B2. Open circles, B3. Cross, 10050.

same cratering event and that 10050 is from a separate, earlier impact. Which single cratering event, then, is the most likely candidate for exposing the low-K suite?

At the time of the landing, it was recognized that at least two sets of rays passed near the landing site (Apollo 11 Preliminary Science Report, 1969). These were thought to be associated with Theophilus, Tycho or Alfraganus, all of which are in the highlands. It was also thought that the crater Moltke, which lies 40 km to the southeast in the mare, may have provided fragments lying near the module. Moltke has a dark mantle extending to a distance of 25 km which may be a continuous ejecta blanket (Apollo 11 PSR, 1969). A much more plausible source, however, is West Crater, located 400 meters east of the landing site. West Crater is a sharp-rimmed, rayed crater about 180 meters in diameter and 30 meters deep with a blocky-ejecta apron extending almost symmetrically outward to a distance of about 250 meters. Blocky rays extend several hundred meters beyond that, and according to astronaut observations, the landing vehicle was set down between two of these rays (Apollo 11 PSR, 1969, p. 35). One ray passes 50 m to the north of the lunar module and was described from the ground as a boulder field. Although no unique solution is possible, if six out of the seven samples measured were exposed in the same event (Fig. 40), it is most probable that the source was West Crater. 10050, the unique sample, either may have been derived locally at an earlier date, or it may have come from a distant event, such as Moltke.

The data presented above suggest that there were three low-K lava flows and one high-K flow sampled by West Crater, which exposed only 30m of stratigraphy. Whether or not the four flow interpretation stands the test of time, ~300 m.y. of volcanism are represented by these rocks and inferentially, also by the stratigraphy in the top 30 meters of West Crater. Two models are proposed to interpret this observation.

Most simply, if all samples are from outcrops in West Crater, then it took 300 m.y. to fill the last 30 meters of this portion of the Tranquillitatis Basin. The absence of craters like Archimedes, which impacted the already formed mare basin before the basalts filled it, argues for very rapid filling of the basin. Since DeHon (1975) has argued that Mare Tranquillitatis is about 500 m deep in this area, the early stages of volcanism must have been both voluminous and rapid, followed by much less frequent volcanism. Note that most of Tranquillitatis would have been filled before 3.9 b.y. (the age of B2), suggesting that mare basalt volcanism overlapped somewhat the mare basin forming events.

A second model involves the interlayering of flows and ejecta blankets. It is possible that all of the low-K basalts were part of a series of ejecta blankets which were then covered by the high-K flow at 3.60–3.65 b.y. ago. This would have shielded the low-K samples from cosmic irradiation until their excavation by West Crater. In this case, nothing at all can be said about the volcanic history at Mare Tranquillitatis except that volcanism and heavy cratering overlapped and the structure of the basin fill is likely to consist of interlayered basalts and ejecta blankets. This model requires the ejecta blanket or blankets to be covered up

shortly after their deposition because the exposure ages of B1, B2 and B3 are the same to within 50 m.y. (Fig. 40). Mixtures of the above two endmember models are possible: Any one of the low-K flows could have been in place in West Crater with the others being in ejecta layers. All that is required is that the low-K samples be shielded from cosmic rays by the mantling high-K flow.

Conclusions

Detailed petrographic and petrologic studies on the Apollo 11 low-K samples indicate that there are three petrologic groups, which have been named B1, B2 and B3 as subdivisions of LPSET's type B basalt. All of the textural and petrologic differences except one between these groups can be explained by fractionation of olivine and ilmenite and variations in cooling rate. That one difference is the tremendous range of olivine zonation in B2, from Fa_{35} to Fa_{97}, as compared with the more normal magnesian olivine followed discontinuously by crystallization of fayalite in B3. This difference is apparently related to a fundamental compositional difference between the groups, one reflection of which is the olivine normative character of B2 as compared to the quartz normative character of B3.

To determine how many lava flows are represented, two types of data are of paramount importance: a) the isotopic data and b) the bulk compositional data. The isotopic data tell us that B1 and B2 are from different cooling units because they have different ages. The bulk compositional data tell us that B3 is different from either B1 or B2 and that the differences cannot be produced by crystal-liquid fractionation. 10050 and 10062 cannot uniquely be classified, but each can be related to one of the above groups. Three igneous cooling units, therefore, adequately explain all of the data. This solution is not unique, of course, and there may have been more igneous bodies.

Detailed petrographic and petrologic studies on the Apollo 11 high-K samples indicate only one petrologic group. Eight of the samples form a textural sequence across which the grain size changes by an order of magnitude; whereas, three others may be distinguished on the basis of their porphyritic textures. Chemically, six of these samples lie on a mixing line which defines what has been termed the main series. This linear trend indicates fractionation of olivine or pyroxene along with ilmenite or armalcolite in very constant proportions. The fact that grain size is independent of position in the main series rules out the possibility of *in situ* lava differentiation, and indicates that fractionation took place before the lava's final emplacement. Flow differentiation would also produce a correlation between grain size and differentiation index, so the differentiation must have taken place in a magma chamber prior to or during eruption. If the main series is from a single flow (which is not necessary), then they represent a sampling of lateral compositional gradients away from the vent. The presence of a cross-cutting igneous feature in 10071 with a highly evolved composition, also on the trend of the main series, suggests that the differentiating magma chamber produced multiple eruptions. Three additional high-K samples are porphyritic,

yet chemically similar to the main series. This suggests that one of these multiple eruptions underwent a two-stage cooling history, and that the porphyritic samples are from a separate high-K flow. Alternatively, they might have been derived by meteorite impact on the partially-crystalline main series lava flow.

The field relations of these samples can be inferred from the exposure age data of Geiss *et al.* (1977), and the photographs and astronaut observations of the area around the landing site. The high-K samples have all received part of their irradiation at depth, suggesting that the high-K flow(s) is the surficial flow in this part of Mare Tranquillitatis.

Six of the seven low-K samples measured by Geiss *et al.* (1977) had been exposed to cosmic rays for 100 m.y. and at a level corresponding to the lunar surface, suggesting excavation in a single cratering event. The seventh sample was ejected in a separate impact. The most likely source of the six samples was West Crater, a sharp-rimmed, rayed crater 30 meters deep located 400 meters east of the landing point. From this data, two end-member structural models are suggested:

1) The high-K flow and all three low-K flows are in place in West Crater, and 300 m.y. of volcanic history are recorded in its stratigraphy.
2) The low-K samples are from ejecta blankets that were shielded from irradiation by the overlying high-K flow. West Crater then sampled these ejecta layers.

Acknowledgments—This study has been supported by NASA grant NGL-05-002-338. None of the analytic data reported here could have been obtained without the continuous and untiring work of Art Chodos, who helped collect some of the data, but more importantly, maintained the microprobe lab at a high level of efficiency. W. S. Baldridge and R. F. Dymek also assisted with the microprobe work. Lou Ann Cordell painstakingly typed all of the data tables. J. M. Rhodes and D. J. Lindstrom performed the monumental task of reviewing the manuscript. The point count program was developed in collaboration with Art Chodos and J. E. Quick. The microprobe laboratory has been developed with the support of the National Science Foundation, the Jet Propulsion Laboratory and the Union Pacific Foundation.

REFERENCES

Agrell S. O., Schoon J. H., Muir I. D., Long J. V. P., McConnell J. D. C. and Peckett A. (1970) Observations on the chemistry, mineralogy and petrology of some Apollo 11 lunar samples. *Proc. Apollo 11 Lunar Sci. Conf.*, p. 93–128.

Albee A. L., Beaty D. W., Chodos A. A. and Quick J. E. (1978) Quantitative analysis of petrographic properties and of mineral compositions with a computer-controlled energy-dispersive system. *Proc. Nat'l. Conf. on Electron Probe Anal. 12th.* In press.

Albee A. L. and Chodos A. A. (1970) Microprobe investigations on Apollo 11 samples. *Proc. Apollo 11 Lunar Sci. Conf.*, p. 135–157.

Anderson A. T., Boyd F. R., Bunch T. E., Cameron E. M., El Gorsey A., Finger L. W., Haggerty S. E., James O. B., Keil K., Prinz M. and Ramdohr P. (1970) Armalcolite: A new mineral from the Apollo 11 samples. *Proc. Apollo 11 Lunar Sci. Conf.*, p. 55–64.

Annell C. S. and Helz A. W. (1970) Emission spectrographic determination of trace elements in lunar samples from Apollo 11. *Proc. Apollo 11 Lunar Sci. Conf.*, p. 991–994.

Apollo 11 Preliminary Science Report (1969) NASA SP-214. 204 pp.

Bailey J. C., Champness P. E., Dunham A. C., Esson J., Fyfe W. S., MacKenzie W. S., Stumpfl E. F. and Zussman J. (1970) Mineralogy and petrology of Apollo 11 lunar samples. *Proc. Apollo 11 Lunar Sci. Conf.*, p. 169–194.

Beaty D. W., Dymek R. F. and Albee A. L. (1977) Petrographic investigation of sample 10003, the oldest mare basalt (abstract). In *Lunar Science VIII*, p. 79–81. The Lunar Science Institute, Houston.

Brown G. M., Emeleus C. H., Holland J. G. and Phillips R. (1970) Mineralogical, chemical and petrological features of Apollo 11 rocks and their relationship to igneous processes. *Proc. Apollo 11 Lunar Sci. Conf.*, p. 195–219.

Champion D. E., Albee A. L. and Chodos A. A. (1975) Reproducibility and operator bias in a computer-controlled system for quantitative electron microprobe analysis. *Proc. Nat'l. Conf. on Electron Probe Anal. 10th.* Microbeam Analysis Society, Las Vegas, Nevada.

Chao E. C. T., Minkin J. A., Frondel C., Klein C. Jr., Drake J. C., Fuchs L., Tani B., Smith J. V., Anderson A. T., Moore P. B., Zechman G. R. Jr, Traill R. J., Plant A. G., Douglas J. A. V. and Dence M. R. (1970) Pyroxferroite, a new calcium bearing iron silicate from Tranquillity Base. *Proc. Apollo 11 Lunar Sci. Conf.*, p. 65–79.

Compston W., Arriens P. A., Vernon M. J. and Chappell B. W. (1970a) Rubidium-strontium chronology and chemistry of lunar material. *Science* **167**, 474–476.

Compston W., Chappell B. W., Arriens P. A. and Vernon M. J. (1970b) The chemistry and age of Apollo 11 lunar material. *Proc. Apollo 11 Lunar Sci. Conf.*, p. 1007–1028.

DeHon R. A. (1975) An isopach map of the eastern mare basalts (abstract). In *Papers Presented to the Conference on the Origins of Mare Basalts and Their Implications for Planetary Evolution*, p. 29–31. The Lunar Science Institute, Houston.

Dence M. R. J., Douglas A. V., Plant A. G. and Traill R. J. (1970) Petrology, mineralogy and deformation of Apollo 11 samples. *Proc Apollo 11 Lunar Sci. Conf.*, p. 315–140.

Drake M. J. and Weill D. F. (1971) Petrology of Apollo 11 sample 10071. A differentiated mini-igneous complex. *Earth Planet. Sci. Lett.* **13**, 61–70.

Dymek R. F., Albee A. L. and Chodos A. A. (1975) Comparative mineralogy and petrology of Apollo 17 mare basalts: Samples 70215, 71055, 74225, and 75055. *Proc. Lunar Sci. Conf. 6th*, p. 49–77.

Eberhardt P., Geiss J., Graf H., Grögler N., Krähenbühl U., Schwaller H., Schwarzmüller J. and Stettler A. (1970) Correlation between rock type and irradiation history of Apollo 11 igneous rocks. *Earth Planet. Sci. Lett.* **10**, 67–72.

Engel A. E. J. and Engel C. G. (1970) Lunar rock compositions and some interpretations. *Proc. Apollo 11 Lunar Sci. Conf.*, p. 1081–1084.

Gamble R. P., Coish R. A. and Taylor L. A. (1978) The oldest mare basalts: Mineralogy and petrology (abstract). In *Lunar and Planetary Science IX*, p. 368–370. Lunar and Planetary Institute, Houston.

Gast P. W. and Hubbard N. J. (1970) Abundance of alkali metals, alkaline and rare earths, and strontium-87/strontium-86 ratios in lunar samples. *Science* **167**, 485–487.

Gast P. W., Hubbard N. J. and Wiesmann H. (1970) Chemical composition and petrogenesis of basalts from Tranquility Base. *Proc. Apollo 11 Lunar Sci. Conf.*, p. 1143–1163.

Gay P., Bancroft G. M. and Brown M. G. (1970) Diffraction and Mössbauer studies of minerals from lunar soils and rocks. *Proc. Apollo 11 Lunar Sci. Conf.*, p. 481–497.

Geiss J., Eberhardt P., Grögler N., Guggisbert S., Maurer P. and Stettler A. (1977) Absolute time scale of lunar mare formation and filling. *Phil. Trans. Roy. Soc. London* **A285**, 151–158.

Gibson E. K. Jr., Brett R. and Andrawes F. (1977) Sulfur in lunar mare basalts as a function of bulk composition. *Proc. Lunar Sci. Conf. 8th*, p. 1416–1428.

Gibson E. K. Jr. and Moore G. W. (1974) Total sulfur abundances and distribution in the valley of Taurus-Littrow: Evidence of mixing (abstract). In *Lunar Science V*, p. 267–269. The Lunar Science Institute, Houston.

Goles G. G., Randle K., Osawa M., Schmitt R. A., Wakita H., Ehmann W. D., Morgan J. W. (1970) Elemental abundances by instrumental activation analyses in chips from 27 lunar rocks. *Proc. Apollo 11 Lunar Sci. Conf.*, p. 1165–1176.

Grove T. L. (1977) Cooling histories of Apollo 15 quartz normative basalts (abstract). In *Lunar Science VIII*, p. 380–382. The Lunar Science Institute, Houston.

Grove T. L. (1978) Cooling histories of Luna 24 low-Ti ferrobasalts and ferrogabbros (abstract). In *Lunar and Planetary Science IX*, p. 424–426. Lunar and Planetary Institute, Houston.

Grove T. L. and Walker D. (1977) Cooling histories of Apollo 15 quartz-normative basalts. *Proc. Lunar Sci. Conf. 8th*, p. 1501–1520.

Guggisberg S., Eberhardt D., Geiss J., Grögler N. and Stettler A. (1977) Youngest and oldest mare basalts: The temporal extent of mare filling (abstract). In *Lunar Science VIII*, p. 386–388. The Lunar Science Institute, Houston.

Haskin L. A., Allen R. O., Helmke P. A., Paster T. P., Anderson M. R., Korotev R. L. and Zweifel K. A. (1970) Rare earths and other trace elements in Apollo 11 lunar samples. *Proc. Apollo 11 Lunar Sci. Conf.*, p. 1213–1231.

Haskin L. A., Jacobs J. W., Brannon J. C. and Haskin M. A. (1977) Compositional dispersions in lunar and terrestrial basalts. *Proc. Lunar Sci. Conf. 8th*, p. 1731–1750.

James O. B. and Jackson E. D. (1970) Petrology of the Apollo 11 ilmenite basalts. *J. Geophys. Res.* **75**, 5793–5824.

James O. B. and Wright T. L. (1972) Apollo 11 and 12 mare basalts and gabbros: Classification, compositional variations, and possible petrogenetic relations. *Bull. Geol. Soc. Amer.* **83**, 2357–2382.

Komar P. D. (1972a) Mechanical interactions of phenocrysts and flow differentiation of igneous dikes and sills. *Bull. Geol. Soc. Amer.* **83**, 973–988.

Komar P. D. (1972b) Flow differentiation in igneous dikes and sills: Profiles of velocity and phenocryst concentration. *Bull. Geol. Soc. Amer.* **83**, 3443–3448.

Kramer F. E., Twedell D. B. and Walton W. J. A. Jr. (1977) Apollo 11 lunar sample information catalogue (revised), February 1977. *JCS 12522*, Curator's Office, NASA Johnson Space Center, Houston. 471 pp.

Lindstrom M. M. and Haskin L. A. (1978) Causes of compositional variations within mare basalt suites. *Proc. Lunar Planet. Sci. Conf. 9th*, This volume.

Longhi J. (1977) Magma oceanography: 2. Chemical evolution (abstract). In *Lunar Science VIII*, p. 592–594. The Lunar Science Institute, Houston.

Longhi J. and Hays J. F. (1978) Phase equilibria and solid solution along the join $CaAl_2Si_2O_8$-SiO_2. *Amer. J. Sci.* In press.

Longhi J., Walker D. and Hays J. F. (1976) Fe, Mg and silica in lunar plagioclase (abstract). In *Lunar Science VII*, p. 501–503. The Lunar Science Institute, Houston.

Lovering J. F., Wark D. A., Gleadow A. J. W. and Britten R. (1974) Lunar monazite: A late-stage (mesostasis) phase in mare basalt. *Earth Planet. Sci. Lett.* **21**, 164–168.

LSPET (Lunar Sample Preliminary Examination Team) (1969) Preliminary examination of lunar samples from Apollo 11. *Science* **165**, 1211–1227.

Maxwell J. A., Peck L. C. and Wiik H. B. (1970) Chemical composition of Apollo 11 lunar samples 10017, 10020, 10072 and 10084. *Proc. Apollo 11 Lunar Sci. Conf.*, p. 1369–1374.

Neilson M. J. and Brockman G. F. (1977) The error associated with pointcounting. *Amer Mineral.* **62**, 1238–1244.

Nord G. L. Jr., Lally J. S., Heuer A. H. and Christie J. M. (1974) A mineralogic study of rock 70017, and ilmenite-rich basalt, by high voltage electron microscopy (abstract). In *Lunar Science V*, p. 556–558. The Lunar Science Institute, Houston.

O'Hara M. J., Biggar G. M., Hill P. G., Jeffries B. and Humphries D. J. (1974) Plagioclase saturation in lunar high-titanium basalt. *Earth Planet. Sci. Lett.* **21**, 253–268.

Papanastassiou D. A., DePaolo D. J. and Wasserburg G. J. (1977) Rb-Sr and Sm-Nd chronology and genealogy of mare basalts from the Sea of Tranquility. *Proc. Lunar Sci. Conf. 8th*, p. 1639–1672.

Papike J. J., Hodges F. M., Bence A. E., Cameron M. and Rhodes J. M. (1976) Mare basalts: Crystal chemistry, mineralogy and petrology. *Rev. Geophys. Space Phys.* **14**, 475–540.

Philpotts J. A. and Schnetzler C. C. (1970) Apollo 11 lunar samples: K, Rb, Sr, Ba and rare-earth concentrations in some rocks and separated phases. *Proc. Apollo 11 Lunar Sci. Conf.*, p. 1471–1486.

Roedder E. and Weiblen P. W. (1970) Lunar petrology of silicate melt inclusions, Apollo 11 rocks. *Proc. Apollo 11 Lunar Sci. Conf.*, p. 801–837.

Roedder E. and Weiblen P. W. (1977) Compositional variation in late-stage differentiates in mare lavas, as indicated by silicate melt inclusions. *Proc. Lunar Sci. Conf. 8th*, p. 1767–1783.

Rose H. J., Cuttitta F., Dwornik E. J., Carron M. K., Christian R. P., Lindsay J. R., Ligon D. T. and Larson R. R. (1970) Semimicro X-ray fluorescence analysis of lunar samples. *Proc. Apollo 11 Lunar Sci. Conf.*, p. 1493–1497.

Skinner B. J. (1970) High crystallization temperatures indicated for igneous rocks from Tranquility Base. *Proc. Apollo 11 Lunar Sci. Conf.*, p. 891–895.

Taylor L. A., McCallister R. H. and Sandi O. (1973) Cooling histories of lunar rocks based on opaque mineral geothermometers. *Proc. Lunar Sci. Conf. 4th*, p. 819–828.

Tera F., Eugster O., Burnett D. S. and Wasserburg G. J. (1970) Comparative study of Li, Na, K, Rb, Cs, Ca, Sr and Ba abundances in achondrites and in Apollo 11 lunar samples. *Proc. Apollo 11 Lunar Sci. Conf.*, p. 1637–1657.

Turekian K. K. and Kharkar D. P. (1970) Neutron activation analysis of milligram quantities of Apollo 11 lunar rocks and soil. *Proc. Apollo 11 Lunar Sci. Conf.*, p. 1659–1664.

Usselman T. M. and Lofgren G. E. (1976) The phase relations, textures, and mineral chemistries of high-titanium mare basalts as a function of oxygen fugacity and cooling rate. *Proc. Lunar Sci. Conf. 7th*, p. 1345–1363.

Usselman T. M., Lofgren G. E., Donaldson C. H. and Williams R. J. (1975) Experimentally reproduced textures and mineral chemistries of high-titanium mare basalts. *Proc. Lunar Sci. Conf. 6th*, p. 997–1202.

Wakita H., Schmitt R. A. and Rey P. (1970) Elemental abundances of major, minor and trace elements in Apollo 11 lunar rocks, soil and core samples. *Proc. Apollo 11 Lunar Sci. Conf.*, p. 1685–1717.

Walker D., Kirkpatrick R. J., Longhi J. and Hays J. F. (1976) Crystallization history of lunar picrite basalt sample 12002: Phase-equilibria and cooling-rate studies. *Bull. Geol. Soc. Amer.* **87**, 646–656.

Walker D., Longhi J., Stolper E. M., Grove T. L. and Hays J. F. (1975) Origin of titaniferous lunar basalts. *Geochim. Cosmochim. Acta* **39**, 1219–1236.

Walker D., Powell M. A. and Hays J. F. (1978) Dynamic crystallization of a eucritic basalt (abstract). In *Lunar and Planetary Science IX*, p. 1196–1198. Lunar and Planetary Institute, Houston.

Wänke H., Riedler R., Baddenhausen H., Spettel B., Teschke F., Quijano-Rico M. and Balacescu A. (1970) Major and minor trace elements in lunar material. *Proc. Apollo 11 Lunar Sci. Conf.*, p. 1719–1727.

Wark D. A., Reid A. F., Lovering J. F. and El Goresy A. (1973) Zirconolite (versus zirkelite) in lunar rocks (abstract). In *Lunar Science IV* (J. W. Chamberlain and C. Watkins, eds.), p. 764–766. The Lunar Science Institute, Houston.

Weill D. F., McCallum I. S., Bottinga Y., Drake M. J. and McKay G. A. (1970) Mineralogy and petrology of some Apollo 11 igneous rocks. *Proc. Apollo 11 Lunar Sci. Conf.*, p. 937–955.

APPENDIX

Table A1. 10003: Phase abundances, "average" phase compositions, and bulk composition

		Pyroxene					Olivine		
(3738 pts)	plag	LoFePx*	LoCaPx*	MedFePx**	HiFePx**	ferrohed	intermed	highFe	"SiO_2"
Vol. %	34.18	21.40	7.64	18.28	2.60	0.05	0.40	0.12	1.06
σ (SDM)	0.82	0.71	0.42	0.66	0.25	0.04	0.14	0.06	0.25
ρ	2.74	3.40	3.49	3.52	3.68	3.63	3.76	4.31	2.33
Wt. %	27.71	21.53	7.89	19.04	2.83	0.05	0.44	0.15	0.73
σ (SDM)	0.66	0.71	0.43	0.69	0.27	0.04	0.15	0.07	0.17
P_2O_5									
SiO_2	46.91	50.49	51.78	49.57	47.63	46.67	35.13	31.39	97.92
TiO_2	0.16	2.00	0.81	1.06	0.75	1.21	0.12	0.13	0.29
Cr_2O_3		0.33	0.22	0.22	0.18	0.17	0.11	<.01	
Al_2O_3	33.93	2.47	0.70	1.05	0.79	1.06	<.01	0.14	0.63
CaO	17.61	14.87	5.39	11.39	8.51	15.12	0.30	0.43	0.10
MgO	0.12	15.64	19.09	11.84	4.81	2.06	25.00	1.84	<.01
FeO	0.50	14.02	21.55	24.08	37.29	32.73	40.13	65.91	0.10
MnO		0.27	0.37	0.43	0.61	0.47	0.30	0.81	
BaO	0.07								<.01
Na_2O	1.41	0.06	0.03	0.07	0.05	0.08			0.05
K_2O	0.10								0.03
ZrO_2									
V_2O_3									
Nb_2O_5									
NiO							<.01	0.03	
S									
F									
TOTAL	100.81	100.15	99.94	99.71	100.62	99.56	101.09	100.69	99.10
	An 84.4	Wo 27.0	Wo 9.8	Wo 22.3	Wo 17.6	Wo 31.9	Fo 52.4	Fo 4.7	
	Ab 12.2	En 43.6	En 52.8	En 34.0	En 14.6	En 6.3	Fa 47.6	Fa 95.3	
	Or 0.6	Fs 22.4	Fs 34.0	Fs 39.5	Fs 64.6	Fs 56.9			
	Other 2.8	Other 7.0	Other 3.4	Other 4.2	Other 3.2	Other 4.9			

*Average of two analyses
**Average of three analyses
(1)Elemental abundances; converted to oxides for calculation of bulk composition

Table A1. 10003: (*Continued*)

(3738 pts)	ilmenite	troilite[1]	apatite	glass	Ulvöspinel	10003,37 area = 160 mm^2 10003,120 area = 83 mm^2 ρ calc = 3.38 Bulk composition[2]				
Vo. %	13.28	0.68	0.25	0.03	0.01					
σ (SDM)	0.53	0.13	0.08	0.03	0.01					
ρ	4.69	4.60	3.20	2.65	4.76					
Wt. %	18.43	0.93	0.24	0.02	0.01	10003,37	σ	10003,120	Rose	Compston
σ (SDM)	0.74	0.18	0.08	0.02	0.01	(3738 pts)	(SDM)	(1829 pts)	(1970)	(1970)
$P_2 9_5$			41.04	0.04		0.10	0.04	0.11	<.2	0.12
SiO_2	<.01	0.02	1.72	75.79	0.11	39.70	0.69	38.2	37.8	39.76
TiO_2	52.60	0.04		0.30	33.71	10.46	0.40	11.4	12.0	10.50
Cr_2O_3	0.50			0.22	1.00	0.23	0.03	0.25	0.26	
Ao_2O_3	0.03		<.01	10.55	1.43	10.23	0.27	10.2	11.0	10.43
CaO			51.32	1.99		11.06	0.21	10.9	11.0	11.13
MgO	1.05		<.01	0.07	0.23	7.60	0.18	7.25	7.20	6.69
FeO	45.56	61.02	1.34	0.81	63.03	19.92	0.44	20.7	19.8	19.80
MnO	0.37	<.01		<.01	0.37	0.26	0.02	0.25	0.29	0.30
BaO				2.67		0.02	0.01	0.02		
Na_2O			<0.1	0.78		0.42	0.03	0.35	0.85	0.40
K_2				5.34		0.03	0.02	0.03	0.05	0.06
ZrO_2	<.01			1.53	0.10				<.03	
V_2O_3	<.01				<.01					
Nb_2O_5	0.05				0.03					
NiO		<.01		0.09					<.001	
S		38.88		<.01		0.36	0.07	0.20		0.18
F			3.50							
Total	100.15	100.16	99.93	100.17	100.00	100.39		99.84	100.25	99.37
	Gi 3.9	Co <.01	Ce_2O_3 0.49	Fld 51.0	Ulv 95.3					
	Ilm 96.1	Cu .12	Cl 0.19	Qtz 43.6	Chr 1.5					
		Zn .07	Y_2O_3 1.06	Pyx 3.0	Her 3.2					
			La_2O_3 0.01	Other 2.4						
			Nd_2O_3 0.79							

[2]10003,37 was point counted with our EDS system, whereas ,120 was WDS. The average phase compositions and bulk composition are therefore more precise for ,37. Most of the differences in bulk composition are a reflection of different ilmenite abundances, 13.28% in ,37 and 14.3% in ,120.

Table A2. 10017: Phase abundances, average "phase" compositions, and bulk composition

		Pyroxene													
(3063 pts)	Plag	LoCaPx	Augite	MedFePx	HiFePx	Ilmenite	Glass	"SiO_2"	Meso[3]	Troilite[1]	Phosphate[2]	Metal[1]	10017,16 area = 188 mm^2 10017,82 area = 209 mm^2 ρ calc = 3.36			
Vol. %	23.62	3.24	31.98	14.72	0.66	15.17		1.36	8.48	0.54	0.20	0.04				
σ (SDM)	0.83	0.41	1.28	0.87	0.18	0.81		0.21	0.53	0.13	0.08	0.04				
ρ	2.73	3.47	3.38	3.50	3.65	4.69		2.33	2.40	4.60	3.20	8.00				
Wt. %	19.20	3.35	32.18	15.34	0.72	21.18		0.94	6.06	0.74	0.19	0.10	Bulk Comp.	σ (SDM)	Compston (1970)	Maxwell (1970)
σ (SDM)	0.67	0.42	1.29	0.91	0.20	1.13		0.15	0.38	0.18	0.08	0.10				
P_2O_5							0.25		0.17		43.15		0.09	0.04	0.18	0.16
SiO_2	49.53	51.16	50.36	49.52	49.50	0.03	71.46	96.50	71.52				40.63	0.95	40.69	40.78
TiO_2	0.14	0.89	2.06	1.20	0.58	52.99	0.94	0.36	0.68				12.18	0.61	11.92	11.77
Al_2O_3	31.35	0.83	2.50	1.29	0.54	<.01	10.88	1.10	12.99				7.85	0.24	7.78	8.02
Cr_2O_3		0.26	0.43	0.33	0.09	0.72	<.01		<.01				0.35	0.03		0.35
MgO	0.23	19.58	16.16	12.52	9.26	1.27	0.14	<.01	0.13				8.16	0.29	7.51	7.70
CaO	15.94	6.49	15.76	12.06	6.50		1.82	0.27	4.11		54.54		10.60	0.28	10.76	10.57
FeO	0.70	20.59	12.87	22.62	34.92	44.70	4.96	0.08	3.41	63.53		100.00	19.10	0.60	19.49	19.81
MnO		0.32	0.24	0.32	0.57	0.42	0.03		0.02				0.23	0.02	0.28	9.22
Na_2O	2.20	0.04	0.08	0.05	0.07		0.21	<.01	0.53				0.49	0.02	0.51	0.51
K_2O	0.24						6.48	0.02	4.32				0.31	0.06	0.30	0.30
BaO	0.04						0.74	0.10	0.51				0.04	0.02		0.02
ZrO_2						0.04	0.21		0.14				0.02	0.01		
V_2O_3						<.01										
Nb_2O_5						<.01										
NiO							0.02		0.01							
S							0.08		0.05	36.47			0.27	0.07	0.23	0.22
F											2.31					
Totals	100.37	100.16**	100.46**	99.92**	102.03	100.17	98.22	98.43	98.61	100.00	100.00	100.00	100.32		99.65	100.43
	An 74.0	Wo 11.6	Wo 28.1	Wo 23.0	Wo 13.0	Gi 4.8	Qtz 37.7									
	Ab 19.5	En 53.1	En 44.2	En 35.6	En 26.8	Ilm 95.2	Fld 52.5									
	Or 1.4	Fs 31.8	Fs 20.1	Fs 36.6	Fs 57.7		Pyx 7.2									
	Other 5.1	3.5	7.6	4.8	2.5		Other 2.6									

**Average of three analyses

[1]Theoretical elemental abundances; converted to oxides for bulk calculation

[2]Assumed 1:1 mix of fluoropatite and whitlockite

[3]Composition constructed from weighted average (66:18:16) of glass, plagioclase, and cristobalite

Table A3. 10020: Phase abundances, average "phase" compositions, and bulk composition.

(2194 pts)	Plag	Pyroxene LoFePx	Pyroxene LoCaPx	Pyroxene MedFePx	Pyroxene HiFePx	*Olivine*	*Ilmenite*	"SiO_2"	*Troilite*[1]	Glass	Cr-spinel	Ulvöspinel	10020,150 area = 70 mm^2, ρ calc = 3.33 Bulk Comp.	σ (SDM)	Maxwell (1970)	Maxwell (1970)
Vol. %	31.36	31.07	0.41	11.01	3.20	4.71	12.45	4.86	0.47	0.18	0.05	0.05				
σ (SDM)	1.13	1.35	0.16	0.81	0.43	0.73	0.84	0.54	0.15	0.09	0.05	0.05				
ρ	2.74	3.38	3.49	3.51	3.73	3.52	4.68	2.33	4.60	2.65	4.70	4.77				
Wt. %	25.82	31.56	0.43	11.61	3.59	4.98	17.51	3.40	0.65	0.14	0.07	0.07				
σ (SDM)	0.93	1.37	0.17	0.85	0.48	0.77	1.18	0.38	0.21	0.07	0.07	0.07				
P_2O_5										0.33			0.07	0.03	0.08	0.07
SiO_2	48.00	48.06	50.77	49.48	46.27	36.62	0.05	98.23		79.03	0.06	0.18	40.47	1.06	39.92	39.95
TiO_2	0.13	3.19	1.47	1.48	1.40	0.31	52.96	0.33		1.21	23.16	33.30	10.61	0.64	10.72	10.52
Al_2O_3	31.95	3.76	1.70	1.64	1.31	<.01	0.04	0.61		11.58	5.66	1.70	9.73	0.33	10.04	10.19
Cr_2O_3		0.67	0.31	0.27	0.09	0.20	0.63			0.09	23.45	<.01	0.38	0.03	0.40	0.38
MgO	0.13	13.95	18.80	10.69	2.65	35.79	1.86	<.01		0.14	5.80	<.01	7.97	0.36	7.81	7.87
CaO	17.32	17.66	5.10	13.23	8.98	0.32		0.22		2.08			12.04	0.34	11.24	11.31
FeO	1.12	12.83	22.19	23.67	39.19	27.65	43.94	0.55	63.53	2.48	41.52	64.21	18.29	0.66	19.35	19.14
MnO		0.25	0.35	0.41	0.64	0.38	0.43			0.33	0.33	0.52	0.25	0.02	0.24	0.27
Na_2O	1.40	0.01	<.01	0.03	0.03			<.01		0.01			0.37	0.03	0.37	0.39
K_2O	0.13							<.01		3.01			0.04	0.03	0.05	0.05
BaO	0.03							0.07		0.08			0.01			
ZrO_2							0.08			0.21	0.03	0.09	0.01			
V_2O_3							<.01				0.28	<.01				
Nb_2O_5							0.03				<.01	<.01				
NiO						0.06				<.01						
S									36.47	0.04			0.24	0.08	0.15	
F																
Total	100.21*	100.38*	100.69	100.90**	100.56**	101.33	100.02*	100.01	100.00	100.62	100.28	99.99	100.48		100.39	100.35
	An 82.2	Wo 30.4	Wo 8.1	Wo 25.3	Wo 18.2	Fa 30.5	Gi 6.3			data	Ulv 58.0	Ulv 96.2				
	Ab 12.0	En 38.5	En 52.0	En 30.7	En 8.1	Fo 69.5	Ilm 93.7			from	Her 11.1	Her 3.8				
	Or 0.7	Fs 20.2	Fs 35.0	Fs 38.7	Fs 68.7					10062	Chr 30.9	Chr 0.0				
Other	5.1	10.9	4.9	5.3	5.0											

*Average of two analyses.

**Average of three analyses.

[1]Theoretical elemental abundances; converted to oxides for bulk calculation.

Note: 10020 also contains 0.17 Vol. % unidentified Ca-phosphate minerals, assumed to be a 1:1 mix of fluorapatite and whitlockite.

Table A4. 10022: Phase abundances, average "phase" compositions, and bulk composition.

		Pyroxene												
(4076 pts)	Plag	LoCaPx	Augite	MedFePx	HiFePx	Ilmenite	Olivine	"SiO_2"	Meso[3]	Troilite[1]	Phosphate[2]	Glass	10022,28 area = 96.4 mm^2 10022,42 area = 66.8 mm^2 ρ calc = 3.34	
Vol. %	21.65	3.47	33.35	14.10	1.63	14.08	0.10	0.83	9.89	0.62	0.23			
σ (SDM)	0.72	0.23	0.70	0.46	0.15	0.77	0.05	0.14	0.49	0.12	0.08			
ρ	2.73	3.42	3.36	3.51	3.70	4.69	3.56	2.33	2.40	4.60	3.20			
Wt. %	17.68	3.55	33.53	14.81	1.80	19.76	0.11	0.58	7.10	0.85	0.22		Bulk	σ
σ (SDM)	0.59	0.24	0.70	0.48	0.17	1.08	0.05	0.10	0.35	0.16	0.08		comp.	(SDM)
P_2O_5									0.03		43.15	0.06	0.10	0.04
SiO_2	50.62	52.52	49.51	49.32	47.16	0.05	36.57	94.03	67.15			77.92	40.93	0.62
TiO_2	0.20	1.07	2.64	1.41	1.09	53.23	0.20	0.42	0.87			1.49	11.72	0.59
Al_2O_3	30.12	0.98	3.07	1.76	1.30	<.01	0.01	2.48	18.60			10.78	8.01	0.20
Cr_2O_3		0.31	0.65	0.17	0.09	0.66	0.11		<.01			<.01	0.40	0.03
MgO	0.23	21.79	15.95	11.72	4.91	1.33	33.94	0.01	0.10			<.01	8.29	0.20
CaO	15.57	6.20	16.57	11.62	7.68		0.35	0.69	7.00		54.54	0 51	11.36	0.22
FeO	0.70	17.43	11.87	23.76	37.37	44.95	29.97	0.95	1.95	63.53		3.13	18.66	0.53
MnO		0.25	0.20	0.37	0.51	0.45	0.36		0.05			0.09	0.23	0.02
Na_2O	2.18	0.03	0.07	0.02	0.03			0.12	0.99			0.08	0.48	0.02
K_2O	0.21							0.44	2.46			4.60	0.22	0.06
BaO	<.01							0.03	0.58			1.14	0.04	0.02
ZrO_2						0.07			0.08			0.16	0.02	0.01
V_2O_3						<.01								
Nb_2O_5						<.01								
NiO							0.07		0.02			0.04		
S									0.02	36.47		0.04	0.31	0.06
F											2.31			
Totals	99.83	100.58**	100.53*	100.15**	100.14**	100.74	101.76	99.17	99.90	100.00	100.00	100.04	100.30	
	An 72.3	Wo 10.8	Wo 28.7	Wo 22.1	Wo 15.4	Gi 5.0	Fo 66.6					Qtz 55.5		
	Ab 19.4	En 58.6	En 43.3	En 33.9	En 15.1	Ilm 95.0	Fa 33.4					Fld 34.1		
	Or 1.2	Fs 26.7	Fs 18.4	Fs 34.2	Fs 65.6							Pyx 3.0		
												Cor 4.8		
Other	7.1	3.9	9.6	4.8	3.9							Other 4.8		

*Average of two analyses.
**Average of three analyses.
[1]Theoretical elemental abundances; converted to oxides for bulk calculation.
[2]Assumed 1:1 mix of fluorapatite and whitlockite.
[3]Analysis constructed from weighted average (51:43:6) of glass, plagioclase and cristobalite.

Table A5. 10024: Phase abundances, average "phase" compositions, and bulk composition.

		Pyroxene													
(2830 pts)	Plag	LoCaPx	Augite	MedFePx	HiFePx	Ilmenite	"SiO_2"	Meso[2]	Olivine	Troilite[(1)]	Phosphate[(3)]	Ulvöspinel[(4)]			
Vol. %	21.74	5.42	33.68	11.18	1.09	16.41	1.31	8.24	0.11	0.53	0.24	0.04	10024,29 area = 104mm^2		
σ (SDM)	0.90	0.39	0.99	0.59	0.18	0.77	0.21	0.54	0.06	0.14	0.09	0.01	10024,25 area = 21mm^2		
ρ	2.73	3.44	3.37	3.49	3.69	4.68	2.33	2.4	3.55	4.60	3.20	4.78	ρ calc = 3.38		
Wt. %	17.54	5.51	33.56	11.53	1.19	22.70	0.90	5.92	0.12	0.72	0.23	0.06	Bulk	σ	Compston
σ (SDM)	0.73	0.40	0.99	0.61	0.20	1.07	0.14	0.39	0.07	0.19	0.09	0.06	comp.	(SDM)	(1970)
P_2O_5											43.15		0.10	0.04	0.20
SiO_2	50.01	51.99	50.31	49.58	47.72	0.02	96.39	72.20	37.28				40.00	0.80	40.25
TiO_2	0.15	1.25	2.38	0.96	0.82	52.31	0.24	0.31	0.10			35.73	12.93	0.58	11.90
Al_2O_3	30.55	1.26	2.44	1.15	1.03	0.04	1.29	13.35	<.01				7.20	0.24	8.09
Cr_2O_3		0.36	0.60	0.26	0.12	0.69		<.01	0.10				0.41	0.03	0.38
MgO	0.07	20.82	16.73	12.87	5.63	1.65	<.01	0.05	34.40				8.74	0.25	7.53
CaO	15.29	6.30	15.72	11.93	7.97		0.31	3.36	0.32		54.54		10.10	0.25	10.66
FeO	1.01	18.23	11.79	22.38	36.72	44.65	0.12	1.79	29.49	63.53		64.27	19.09	0.54	19.46
MnO		0.25	0.22	0.40	0.49	0.37		0.06	0.33				0.23	0.02	0.24
Na_2O	2.04	0.02	0.07	0.05	0.03		0.02	0.63					0.43	0.02	0.52
K_2O	0.49						0.01	5.43					0.41	0.06	0.30
BaO	0.11						0.11	0.60					0.05	0.03	0.03
ZrO_2						0.06		0.18							
V_2O_3						<.01									
Nb_2O_5						0.05									
NiO								0.05	0.01						
S								<.01		36.47			0.26	0.07	0.22
F											2.31				
Total	99.72	100.48**	100.26**	99.58**	100.53**	99.84	98.49	98.09	102.03	100.00	100.00	100.00	99.95		99.78
	An 72.2	Wo 10.7	Wo 27.7	Wo 24.4	Wo 16.1	Ilm 93.8			Fa 32.7						
	Ab 17.4	En 56.5	En 45.3	En 36.6	En 17.0	Gi 6.2			Fo 67.3						
	Or 2.8	Fs 28.2	Fs 18.2	Fs 36.5	Fs 63.7										
	Other 7.6	Other 4.6	Other 8.8	Other 2.5	Other 3.2										

	Rose (1970)
	39.00
	13.20
	9.50
	0.40
	8.11
	10.00
	18.50
	0.24
	0.46
	0.28
	99.69

**Average of three analyses.
(1)Theoretical elemental abundances; converted to oxides for bulk calculation.
(2)Analysis constructed from weighted average (65:15:20) of glass, cristobalite and plagioclase.
(3)Assumed 1:1 mix of fluorapatite and whitlockite.
(4)Theoretical end-member oxide abundances.
Note: 10024 also contains 0.01 Vol. % Fe-metal.

Table A6. 10029: Phase abundances, average "phase" compositions, and bulk composition.

		Pyroxene							
(3091 pts)	Plag	LoCaPx	Augite	MedFePx	HiFePx	Ilmenite	Mg-Oliv	Fe-Oliv	"SiO_2"
Vol. %	35.01	9.10	16.93	19.40	2.06	15.76	0.26	0.06	0.58
error	1.09	0.53	0.72	0.77	0.25	0.87	0.09	0.04	0.14
ρ	2.74	3.47	3.40	3.51	3.68	4.68	3.76	4.22	2.33
Wt. %	28.16	9.27	16.90	19.99	2.23	21.65	0.29	0.07	0.40
error	0.88	0.54	0.72	0.79	0.27	1.19	0.10	0.05	0.10
P_2O_5									
SiO_2	46.56	51.23	50.90	49.17	47.59	0.05	34.28	31.04	96.63
TiO_2	0.14	0.88	1.74	1.20	0.97	52.89	0.26	0.13	0.17
Al_2O_3	33.99	0.86	2.16	1.32	0.70	0.06	<.01	<.01	1.37
Cr_2O_3		0.25	0.39	0.21	0.16	0.57	0.02	0.02	
MgO	0.07	19.00	15.74	12.62	6.13	1.63	25.27	5.68	<.01
CaO	17.56	6.05	14.70	10.94	7.72		0.25	0.28	1.19
FeO	0.58	21.27	13.92	24.22	36.00	44.10	40.89	61.68	0.15
MnO		0.35	0.31	0.40	0.50	0.32	0.42	0.65	
Na_2O	1.31	0.02	0.07	0.04	0.03				0.29
K_2O	0.09								0.01
BaO	<.01								<.01
ZrO_2						0.01			
V_2O_3						<.01			
Nb_2O_5						0.02			
NiO							0.01	<.01	
S									
F									
Total	100.30	99.91**	99.93*	100.12**	99.80**	99.65	101.40	99.48	99.81
	An 84.0	Wo 10.9	We 27.0	Wo 20.7	Wo 15.9	Gi 6.2	Fa 47.8	Fa 86.0	
	Ab 11.3	En 52.4	En 44.1	En 35.8	En 18.6	Ilm 93.8	Fo 52.2	Fo 14.0	
	Or 0.5	Fs 33.4	Fs 22.4	Fs 39.2	Fs 62.1				
Other	4.2	3.3	6.5	4.3	3.4				

*Average of two analyses

**Average of three analyses

(1)Theoretical elemental abundances; converted to oxides for bulk calculation.

Table A6. 10029: (*Continued*).

(3091 pts)	Phosphate	Troilite[1]	Ulv&spinel	Metal[1]	K-glass	Cr-spinel	Fe-glass	10029,17 area = 93mm^2 ρ calc = 3.41	
Vol. %	0.25	0.47	0.03	0.03	0.03	0.03			
error	0.09	0.12	0.03	0.03	0.03	0.03	<.03		
ρ	3.20	4.60	4.81	8.00	2.65	4.70	—		
Wt. %	0.23	0.63	0.04	0.07	0.02	0.04			
error	0.08	0.16	0.04	0.07	0.02	0.04	<.04	bulk comp.	σ (SDM)
P_2O_3	38.95				0.08		1.33	0.09	0.03
SiO_2	0.95		<.01		76.37	<.01	35.32	37.89	0.76
TiO_2			34.91		0.48	24.45	4.43	12.15	0.64
Al_2O_3	<.01		0.95		11.31	6.93	1.48	10.32	0.32
Cr_2O_3			0.24		<.01	19.15	0.08	0.27	0.03
MgO	<.01		0.07		<.01	6.85	0.36	7.53	0.21
CaO	50.96				0.93		7.11	10.47	0.24
FeO	0.59	63.53	63.54	100.00	2.09	42.11	48.99	20.49	0.61
MnO			0.45		<.01	0.33	0.67	0.23	0.02
Na_2O	0.08				0.59		0.02	0.39	0.03
K_2O					7.76		0.17	0.03	0.03
BaO					0.49	<.01	<.01		
ZrO_2			<.01		0.21	0.41	0.61		
V_2O_3			<.01			<.01			
Nb_2O_5			0.14						
NiO					<.01		0.05		
S		36.47			0.02		1.46	0.23	0.06
F	4.15								
Total	96.13	100.00	100.30	100.00	100.33	100.23	102.08	100.09	
	Y_2O_3 0.56		Ulv 97.6		Qtz 34.2	data	Fld 5.4		
	La_2O_3 0.28		Chr 0.3		Fld 60.6	from	Pyx 49.3		
	Ce_2O_3 0.92		Her 2.1		Pyx 3.7	10062,39	Oliv 31.8		
	Nd_2O_3 0.27				Other 1.5		Ilm 7.2		
	Cl 0.21						Other 6.3		

Table A7. 10032: Phase abundances, average "phase" compositions, and bulk composition.

		Pyroxene													
(2636 pts)	Plag	Augite	LoCaPx	MedFePx	HiFePx	Ilmenite	Olivine	"SiO_2"	Meso[3]	Troilite[1]	Phosphate[2]	Metal[1]	Glass	10032,26 area = 16.9 mm^2 ρ calc = 3.40	
Vol.%	22.16	34.83	5.56	11.09	1.13	16.45	0.11	0.94	6.66	0.72	0.24	0.08			
σ (SDM)	1.19	1.42	0.57	0.80	0.25	0.71	0.06	0.19	0.50	0.17	0.10	0.06			
ρ	2.73	3.35	3.44	3.49	3.68	4.70	3.56	2.33	2.40	4.60	3.20	8.00			
Wt.%	17.81	34.34	5.63	11.39	.1.22	22.76	0.11	0.64	4.70	0.97	0.23	0.19		Bulk comp.	σ (SDM)
σ (SDM)	0.96	1.40	0.58	0.82	0.27	0.98	0.06	0.13	0.35	0.23	0.10	0.14			
P_2O_5									0.22		43.15		0.31	0.11	0.05
SiO_2	51.31	49.88	52.37	49.00	47.56	0.03	36.42	98.52	73.19				74.48	39.49	1.05
TiO_2	0.23	2.35	0.96	1.32	0.80	52.55	0.13	0.19	0.73				0.93	13.06	0.53
Al_2O_3	30.06	2.58	0.77	1.62	0.92	<.01	0.01	0.39	12.62				10.37	7.08	0.31
Cr_2O_3		0.60	0.25	0.35	0.14	0.52	0.13		0.06				*0.08*	*0.38*	*0.03*
MgO	0.17	17.10	20.83	12.44	6.67	0.86	34.73	0.01	0.10				0.10	8.81	0.32
CaO	14.85	16.02	5.99	11.81	6.71			0.10	3.65		54.54		1.55	10.21	0.32
FeO	0.86	11.14	18.73	23.03	37.16	45.37	30.30	0.69	2.35	63.53		100.00	2.95	19.37	0.54
MnO		0.21	0.33	0.41	0.54	0.38	0.23		0.04				0.05	0.27	0.02
Na_2O	2.19	0.08	0.01	0.05	0.03			0.01	0.58				0.29	0.45	0.03
K_2O	0.40							0.01	4.35				5.94	0.28	0.05
BaO	0.06							0.14	0.30				0.40	0.03	0.01
ZrO_2						0.23			0.12				0.17	0.06	0.04
V_2O_3						<.01									
Nb_2O_5						<.01									
NiO							<.01		<.01				<.01		
S									0.03	36.47			0.04	0.36	0.08
F											2.31				
Total	100.13	99.96*	100.24**	100.03**	100.53**	99.94	102.31	100.06	98.33	100.00	100.00	100.00	97.65	99.96	
	An 69.5	Wo 28.0	Wo 10.7	Wo 22.1	Wo 13.3	Gi 3.3	Fa 33.0								
	Ab 18.5	En 46.1	En 56.7	En 35.3	En 20.1	Ilm 96.7	Fo 67.0								
	Or 2.2	Fs 17.2	Fs 29.1	Fs 37.4	Fs 63.5										
Other	9.8	8.7	3.5	5.2	3.1										

*Average of two analyses.
**Average of three analyses.
[1]Theoretical elemental abundances; converted to oxides for bulk calculation.
[2]Assumed 1:1 mix of fluroapatite and whitlockite.
[3]Analysis constructed from weighted average (72:17:11) of glass, plag, and cristobalite.

Table A8. 10044: Phase abundances, average "phase" compositions, and bulk composition.

(2946 pts)	Plag	Pyroxene Augite	Pyroxene MedFePx	Pyroxene HiFePx	Ilmenite	Fayalite	"SiO_2"	Glass	Troilite[1]	Apatite	Ulvöspinel
Vol.%	35.06	26.76	13.85	4.21	12.56	0.13	6.71	0.10	0.43	0.10	0.08
σ (SDM)	1.29	1.10	0.79	0.44	1.20	0.07	0.78	0.06	0.12	0.06	0.05
ρ	2.74	3.37	3.51	3.74	4.71	4.37	2.33	2.65	4.60	3.20	4.76
Wt.%	29.21	27.42	14.78	4.79	17.99	0.17	4.75	0.08	0.60	0.10	0.12
σ (SDM)	1.07	1.13	0.84	0.50	1.72	0.09	0.55	0.05	0.17	0.06	0.08
P_2O_5								<.01		39.30	
SiO_2	47.66	50.77	49.51	47.05	0.08	29.73	98.32	76.76		1.20	0.06
TiO_2		1.90	1.33	0.70	52.48	0.10	0.35	0.19			31.51
Al_2O_3	32.19	2.22	1.55	0.83	0.06	<.01	0.91	11.90		<.01	2.59
Cr_2O_3		0.40	0.27	0.13	0.45	<.01		<.01			0.35
MgO	0.22	15.19	10.40	2.35	0.40	0.19	0.02	0.02		<.01	0.10
CaO	17.19	16.79	13.40	8.68		0.32	0.17	1.39		52.20	
FeO	0.52	12.54	23.55	39.67	45.66	68.45	0.04	1.03	63.53	1.90	65.23
MnO		0.28	0.45	0.73	0.48	0.73		<.01			0.38
Na_2O	1.67	.01	.02	0.04			0.14	0.23		<.01	
K_2O	0.09						0.03	7.50			
BaO	<.01							<.01			
ZrO_2					<.01			<.01			0.25
V_2O_3					<.01						<.01
Nb_2O_5											0.04
NiO						0.09		<.01			
S								<.01	36.47		
F										3.40	
Total	99.54	100.10**	100.48*	100.18**	99.59	99.60	99.98	99.02	100.00	97.21	100.50
	An 81.7	Wo 30.9	Wo 26.0	Wo 18.5	Gi 1.5	data				Cl = 0.10	data
	Ab 14.4	En 42.4	En 30.1	En 7.4	Ilm 98.5	from				Y_2O_3 = 1.30	from
	Or 0.5	Fs 20.1	Fs 39.0	Fs 71.1		10047				REE = 0.73	10047
Other	3.4	6.4	4.9	3.0							

10044,33 area = 150 mm^2
ρ calc = 3.29

Bulk comp.	σ (SDM)	Dymek (1975)	Agrell (1970)	Engel (1970)
0.04	0.02	0.07	0.04	0.08
42.21	1.07	41.61	42.46	42.01
10.25	0.91	10.05	9.18	8.81
10.35	0.38	11.10	10.21	11.67
0.24	0.02	0.23	0.21	N.A.
5.95	0.23	5.58	5.96	6.25
12.08	0.33	12.33	12.25	12.18
17.88	0.86	17.73	18.24	17.98
0.27	0.02	0.27	0.28	0.24
0.50	0.03	0.51	0.48	0.48
0.03	0.03	0.16	0.11	0.11
0.22	0.06	0.06	0.18	N.A.
100.02		99.71	99.81	99.81

*Average of two analyses.
**Average of three analyses.
[1]Theoretical elemental abundances; converted to oxides for bulk composition.

Table A9. 10045: Phase abundances, average "phase" compositions, and bulk composition.

		Pyroxene						
	Plag.	Augite	Low-Ca Pyx.	Med-Fe Pyx.	High-Fe Pyx.	Ilm.	Olivine	SiO_2	K-glass
Vol.%	33.32	25.33	1.94	14.64	3.09	13.49	3.50	3.13	0.68
σ (SDM)	1.24	0.95	0.26	0.72	0.33	0.64	0.48	0.46	0.16
ρ	2.74	3.39	3.47	3.51	3.73	4.68	4.61	2.33	2.65
Wt.%	26.98	25.38	1.99	15.19	3.41	18.66	4.77	2.15	0.53
σ (SDM)	1.00	0.95	0.27	0.75	0.36	0.88	0.65	0.32	0.12
P_2O_5									0.20
SiO_2	48.45	48.92	52.24	48.51	46.93	0.09	36.90	98.84	80.58
TiO_2	0.03	2.96	1.04	1.70	1.22	52.67	0.16	0.43	0.64
Al_2O_3	32.12	3.44	1.04	2.11	1.20	0.01	<.01	0.85	12.15
Cr_2O_3		0.65	0.18	0.29	0.16	0.61	0.17		<.01
MgO	0.18	14.22	18.86	10.79	2.47	1.57	33.60	0.02	0.02
CaO	16.89	16.37	5.77	12.73	8.93		0.36	0.23	0.56
FeO	0.93	13.20	20.59	23.19	38.92	44.68	29.92	0.18	2.52
MnO		0.31	0.34	0.50	0.59	0.40	0.36		0.08
Na_2O	1.55	0.08	0.01	0.04	<.01			<.01	0.04
K_2O	0.09							0.04	2.51
BaO	<.01								0.25
ZrO_2						0.09			0.16
V_2O_3						<.01			
Nb_2O_5						<.01			
NiO							0.02		0.07
S									0.02
F									
Total	100.23	100.15**	100.07**	99.86**	100.42**	100.12	101.50	100.59	99.80
	An 81.3	Wo 28.6	10.4	24.0	18.5	Gi 5.8	Fa 33.6		Qtz 66.8
	Ab 13.5	En 39.5	53.0	31.3	7.7	Ilm 94.2	Fo 66.4		Fld 18.2
	Or 0.5	Fs 21.1	33.0	38.6	69.4				Pyx 3.4
	Other 4.7	10.8	3.6	6.1	4.4				Cor 10.0
									Other 1.6

*Average of two analyses.
**Average of three analyses.
(1)Theoretical elemental abundances; converted to oxides for bulk calculation.
(2)Assumed 1:1 mix of fluorapatite and whitlockite.

Table A9. 10045: (*Continued*).

	Metal[1]	Ca-Phosphate[2]	Ulvö-spinel	Cr-spinel	Troilite[1]	Fe-glass	10045,16 area = 112 mm^2 ρ calc = 3.38 comp (2795 pts)	σ (SDM)	Agrell *et al.* (1970)	Compston *et al.* (1970)
Vol.%	0.04	0.07	0.05	0.22	0.30	<.04				
σ (SDM)	0.04	0.05	0.09	0.09	0.10					
ρ	8.00	3.20	4.77	4.71	4.60					
Wt.%	0.09	0.07	0.07	0.31	0.41					
σ (SDM)	0.09	0.05	0.06	0.13	0.14					
P_2O_5		43.15				0.45	0.03	0.02	0.04	0.10
SiO_2			0.16	0.05		37.59	39.83	0.91	39.60	39.04
TiO_2			34.11	21.38		9.74	11.02	0.48	11.10	11.32
Al_2O_3			1.69	7.59		2.04	10.03	0.36	9.51	9.51
Cr_2O_3			0.15	23.59		0.05	0.41	0.04	0.47	N.A.
MgO			0.07	4.72		2.66	7.67	0.29	8.10	7.73
CaO		54.54				9.46	11.13	0.28	11.07	11.28
FeO	100.00		63.04	42.47	63.40	36.73	19.27	0.52	19.12	19.40
MnO			0.39	0.39		0.53	0.28	0.02	0.28	0.27
Na_2O						0.08	0.44	0.03	0.36	0.36
K_2O						0.08	0.04	0.03	0.05	0.05
BaO						0.11				
ZrO_2			0.26	<.01		<.01	0.02	0.01	N.A.	N.A.
V_2O_3			<.01	0.39						
Nb_2O_5			0.09	<.01						
NiO						<.01				
S					36.60	1.04	0.15	0.05	0.14	0.15
F		2.31								
Total	100.00	100.00	99.94	100.59	100.00	100.57	100.32		100.25	99.60
			Ulv 96.1	Ulv 53.8		Ol 2.6				
			Her 3.7	Her 15.0		Px 72.0				
			Chr 0.2	Chr 31.2		Fld 7.1				
						Ilm 15.6				
						Other 2.7				

Table A10. 10047: Phase abundances, average "phase" compositions, and bulk composition.

		Pyroxene							
(1971 pts)	Plag	Augite	MedFePx	HiFePx	Ferrohed	Ilmenite	Fayalite	"SiO_2"	K-glass
Vol.%	34.91	21.30	16.37	8.66	0.21	11.20	0.10	6.22	0.10
σ (SDM)	1.58	1.43	1.26	0.91	0.14	1.25	0.07	0.78	0.07
ρ	2.74	3.37	3.51	3.75	3.72	4.70	4.37	2.33	2.65
Wt.%	28.97	21.74	17.40	9.84	0.24	15.94	0.13	4.39	0.08
σ (SDM)	1.31	1.46	1.34	1.03	0.16	1.78	0.09	0.55	0.06
P_2O_5									0.07
SiO_2	47.65	50.20	50.08	46.31	45.43	0.04	29.73	97.97	79.33
TiO_2	0.10	2.51	1.21	0.63	1.05	52.23	0.10	0.27	0.29
Al_2O_3	32.99	2.96	1.34	0.61	0.85	0.03	<.01	0.70	10.35
Cr_2O_3		0.56	0.23	0.06	0.04	0.38	<.01		0.06
MgO	0.17	15.06	10.77	2.24	0.75	0.70	0.19	0.06	<.01
CaO	16.93	16.70	12.97	8.21	12.01		0.32	0.13	0.87
FeO	0.54	11.78	23.83	41.38	39.05	46.07	68.45	0.08	0.49
MnO		0.24	0.46	0.64	0.46	0.41	0.73		<.01
Na_2O	1.57	0.08	0.03	0.01	<.01			0.14	0.30
K_2O	0.04							<.01	7.64
BaO	<.01							<.01	0.07
ZrO_2						0.05			0.31
V_2O_3						0.03			
Nb_2O_5						<.01			
NiO							0.09		0.03
S									<.01
F									
Total	99.99	100.09**	100.92**	100.09**	99.63	99.93	99.60	99.36	99.80
	An 82.7	Wo 29.9	Wo 25.2	Wo 17.5	Wo 25.6	Gi 2.6	Fa 99.5		Qtz 44.7
	Ab 13.9	En 42.0	En 31.0	En 7.0	En 2.3	Ilm 97.4	Fo 0.5		Fld 53.9
	Or 0.2	Fs 18.8	Fs 39.3	Fs 73.2	Fs 68.6				Pyx 0.3
Other	3.2	9.3	4.5	2.3	3.5				1.1

**Average of three analyses.

(1)Theoretical elemental abundances; converted to oxides for bulk calculations.

Table A10. 10047: (*Continued*).

(1971 pts)	Troilite[1]	Apatite	Ulvöspinel	Fe-metal	Fe-glass	K-spar	10047,47 area = 152 mm^2 10047,9 area = 84 mm^2 ρ calc = 3.30			
Vol.%	0.43	0.36	0.05	0.10	<.05	<.05				
σ (SDM)	0.15	0.14	0.05	0.07						
ρ	4.60	3.20	4.76	8.00						
Wt.%	0.60	0.35	0.07	0.24			bulk comp.	σ (SDM)	Rose (1970)	Compston (1970)
σ (SDM)	0.21	0.14	0.07	0.17						
P_2O_5		39.53			2.71		0.13	0.05	<.20	0.11
SiO_2		1.37	0.06		37.95	58.84	42.51	1.37	41.30	42.16
TiO_2			31.51		4.59	<.01	9.21	0.92	10.20	9.43
Al_2O_3		0.26	2.59		7.70	21.06	10.54	0.46	9.80	9.89
Cr_2O_3			0.35		<.01		0.23	0.03	0.22	N.A.
MgO		0.02	0.10		0.19	0.06	5.51	0.27	6.10	5.67
CaO		53.13			10.13	0.86	11.82	0.40	12.20	12.15
FeO	63.53	1.21	65.23	100.00	28.96	0.49	19.31	0.99	19.00	19.11
MnO			0.38		0.29		0.26	0.02	0.29	0.28
Na_2O		<.01			0.32	0.60	0.48	0.03	0.65	0.45
K_2O					1.14	11.37	0.02	0.02	0.11	0.11
BaO					<.01	6.71				
ArO_2			0.25		1.98					
V_2O_3			<.01							
Nb_2O_5			0.04							
NiO					0.02					
S	36.47				0.44		0.22	0.08		0.18
F		2.01								
Total	100.00	98.59	100.50	100.00	96.41	99.98	100.24		99.87	99.84
		Ce_2O_3 = .35	Ulv 93.4		Ol 2.4	An 4.7				
		Cl = <.01	Chr 0.6		Fld 30.4	Ab 5.9				
		Y_2O_3 = .94	Her 6.0		Pyx 50.2	Or 73.6				
		La_2O_3 = .04			Ilm 7.5	Cel 13.3				
					Ap 6.7	Other 2.5				

Table A11. 10049: Phase abundances, average "phase" compositions, and bulk composition.

		Pyroxene												
(1947 pts)	Plag	LoCaPx	Augite	MedFePx	HiFePx	Ilmenite	"SiO_2"	Meso[3]	Glass	Troilite[1]	Phosphate[2]			
Vol.%	24.47	1.68	30.72	18.17	0.46	14.12	1.38	8.01		0.72	0.27	10049,39 area = 43.8 mm^2		
σ (SDM)	1.22	0.31	1.31	1.01	0.16	1.05	0.28	0.64		0.19	0.12	ρ calc = 3.35		
ρ	2.73	3.49	3.38	3.51	3.65	4.69	2.33	2.40		4.60	3.20			
Wt.%	19.95	1.75	31.01	19.05	0.50	19.78	0.96	5.74		0.99	0.26	Bulk	σ	Rose
σ (SDM)	0.99	0.32	1.32	1.06	0.17	1.47	0.19	0.46		0.26	0.12	Comp.	(SDM)	(1970)
P_2O_5								0.60	0.92		43.15	0.15	0.07	
SiO_2	49.91	51.90	50.51	50.57	48.26	0.08	98.22	73.07	71.83			41.56	1.08	41.00
TiO_2	0.46	0.95	2.14	1.33	0.91	52.67	0.40	1.07	1.53			11.51	0.78	11.30
Al_2O_3	31.10	0.83	2.59	1.21	0.97	<.01	1.39	11.79	10.05			7.95	0.33	9.50
Cr_2O_3		0.30	0.55	0.31	0.09	0.52		<.01	<.01			0.34	0.03	0.32
MgO	0.17	17.37	15.31	11.70	8.03	0.88	0.06	0.06	0.03			7.54	0.28	7.03
CaO	16.06	6.26	15.97	11.85	5.91		0.39	4.05	2.07		54.54	10.93	0.33	11.00
FeO	0.91	22.01	13.00	23.51	34.78	45.03	0.25	4.25	6.18	63.53		19.21	0.74	18.70
MnO		0.27	0.15	0.33	0.44	0.59		0.10	0.16			0.24	0.02	0.25
Na_2O	2.00	0.01	0.09	0.01	<.01		<.01	0.65	0.39			0.47	0.03	0.51
K_2O	0.30						0.08	4.35	6.58			0.31	0.06	0.36
BaO	<.01						<.01	0.38	0.45			0.02	0.01	
ZrO_2						0.25		<.01	<.01			0.05	0.03	
V_2O_3						<.01								
Nb_2O_5						0.04								
NiO					(Data			<.01	<.01					
S					from			0.25	0.38	36.47		0.38	0.10	
F					10072)						2.31			
Totals	100.91	99.90**	100.31**	100.82**	99.99	100.04	100.80	100.62	100.58	100.00	100.00	100.66		99.97
	An 74.0	Wo 11.6	Wo 28.8	Wo 22.9	Wo 11.5	Gi 3.3			Qtz 37.2					
	Ab 17.7	En 49.2	En 42.5	En 33.7	En 26.0	Ilm 96.7			Fld 49.9					
	Or 1.7	Fs 35.4	Fs 20.5	Fe 38.5	Fs 59.4				Pyx 7.6					
Other	6.6	3.8	8.2	4.9	3.1				Cor 4.8					
									4.8					

**Average of two analyses.

[1]Theoretical elemental abundances; converted to oxides for bulk calculation.

[2]Assumed 1:1 mix of fluorapatite and whitlockite.

[3]Composition constructed from weighted average (65:17:18) of glass, plagioclase, and cristobalite.

Table A12. 10050: Phase abundances, average "phase" compositions, and bulk composition.

		Pyroxene														
(2151 pts)	Plag	Augite	LoCaPx	MedFePx	HiFePx	Ilmenite	"SiO_2"	Olivine	Glass	Troilite[1]	Phosphate[2]	Ulvöspinel	Cr-spinel	10050,31 area = 104 mm^2 ρ calc = 3.35		
Vol.%	33.65	29.60	5.51	12.29	1.41	14.21	2.31	0.73	0.07	0.23	0.05	<.05	<.05			
σ (DSM)	1.47	1.44	0.62	0.93	0.32	0.70	0.39	0.18	0.06	0.10	0.05	—	—			
ρ	2.74	3.38	3.45	3.46	3.73	4.69	2.33	3.62	2.65	4.60	3.20					
Wt.%	27.51	29.86	5.67	12.69	1.57	19.89	1.61	0.79	0.06	0.32	0.05			Bulk Comp.	σ (SDM)	Rose (1970)
σ (SDM)	1.20	1.45	0.64	0.96	0.36	0.98	0.27	0.19	0.05	0.14	0.05					
P_2O_5									0.09		43.15			0.02	0.02	<.20
SiO_2	46.55	51.15	52.53	48.95	46.81	0.61	98.60	36.53	77.40			0.10	0.07	40.05	1.14	40.90
TiO_2	0.09	1.23	0.70	1.77	0.92	52.49	0.51	0.09	0.51			33.74	21.52	11.12	0.54	12.60
Al_2O_3	33.76	2.81	1.42	1.99	1.05	<.01	0.66	<.01	11.21			1.71	7.65	10.49	0.43	8.90
Cr_2O_3		0.61	0.61	0.29	0.04	0.41		0.10	0.02			0.35	22.05	0.34	0.03	0.35
MgO	0.09	15.68	19.80	11.86	3.72	1.32	0.01	31.48	0.02			0.17	4.77	7.90	0.31	8.03
CaO	17.69	16.12	5.37	12.09	7.78		0.15	0.28	1.49		54.54			11.67	0.36	11.30
FeO	0.47	12.20	19.32	22.57	38.60	45.06	0.27	32.67	2.61	63.60		62.31	44.15	17.83	0.58	17.30
MnO		0.42	0.21	0.35	0.63	0.45		0.30	0.06			0.45	0.34	0.28	0.03	0.27
Na_2O	1.17	0.10	<.01	0.06	.01		<.01		0.20					0.36	0.03	0.66
K_2O	0.13						0.01		4.95					0.04	0.01	0.05
BaO	<.01						0.04		0.48							
ZrO_2						0.02			0.27			0.07	<.01			
V_2O_3						<.01						<.01	0.50			
Nb_2O_5						<.01						0.07	<.01			
NiO								0.05	0.09							
S									0.02	36.40				0.12	0.05	
F											2.31					
Total	99.94	100.32*	99.95	99.93**	99.56**	99.81	100.24	101.49	99.42	100.00	100.00	98.97	101.04	100.22		100.36
	An 86.5	Wo 29.0	Wo 8.9	Wo 22.6	Wo 16.2	Gi 4.9		Fa 37.0	Qtz 50.9			Ulv 95.7	Ulv 55.0			
	Ab 10.3	En 43.8	En 56.0	En 34.0	En 11.7	Ilm 95.1		Fo 63.0	Fld 41.0			Chr 0.5	Chr 29.6			
	Or 0.8	Fs 19.8	Fs 31.0	Fs 36.9	Fs 69.0				Pyx 3.6			Her 3.8	Her 15.3			
Other	2.4	7.4	4.1	6.5	3.1				4.5							

*Average of two analyses.
**Average of three analyses.
[1]Theoretical abundances; converted to oxides for calculating bulk compositions.
[2]Assumed 1:1 mixture of fluorapatite and whitlockite.

Table A13. 10057: Phase abundances, average "phase" compositions, and bulk composition.

		Pyroxene													
(2314 pts)	Plag	LoCaPx	Augite	MedFePx	HiFePx	Ilmenite	Olivine	"SiO_2"	Meso[3]	Troilite[1]	Phosphate[2]	Fe-metal[1]	Glass	10057,65 area = 90 mm^2 10057,67 area = 118 mm^2 ρ calc = 3.37		
														Bulk comp.	σ (SDM)	Engel (1970)
Vol.%	23.75	3.30	32.03	14.39	1.12	15.47	<.04	1.05	8.04	0.42	0.21	0.04	<.04			
σ (SDM)	0.65	0.33	1.04	0.70	0.19	0.83		0.17	0.46	0.13	0.10	0.04				
ρ	2.73	3.45	3.38	3.51	3.66	4.70		2.33	2.40	4.60	3.20	8.00				
Wt.%	19.40	3.38	32.12	14.99	1.22	21.57		0.73	5.73	0.57	0.20	0.09				
σ (SDM)	0.53	0.34	1.04	0.73	0.21	1.16		0.12	0.33	0.18	0.10	0.09				
P_2O_5									0.12		43.15		0.21	0.09	0.05	0.17
SiO_2	50.16	52.47	49.73	49.38	48.16	0.02	38.89	97.39	75.52				75.01	40.34	0.78	39.79
TiO_2	0.11	1.07	2.27	1.18	0.86	52.94	0.58	0.21	0.48				0.70	12.42	0.63	11.44
Al_2O_3	31.36	0.94	3.06	1.54	0.92	0.06	1.13	0.49	14.41				10.69	8.18	0.20	10.84
Cr_2O_3		0.15	0.58	0.30	0.15	0.56	0.11		0.03				0.05	0.36	0.03	
MgO	0.18	19.49	16.19	11.71	6.79	0.88	33.90	<.01	0.08				0.05	7.93	0.24	7.65
CaO	15.73	6.16	15.80	11.52	7.12		0.92	0.18	4.82		54.54		1.61	10.54	0.25	10.08
FeO	0.79	19.39	12.35	23.71	35.11	45.12	26.74	0.67	2.87	63.53		100.00	4.57	19.24	0.59	19.35
MnO		0.28	0.26	0.36	0.45	0.32	0.22		0.04				0.08	0.22	0.02	0.20
Na_2O	2.04	0.04	0.11	0.07	0.02			0.02	0.70				0.37	0.48	0.02	0.54
K_2O	0.26							0.02	32.9				5.76	0.23	0.06	0.32
BaO	<.01							0.03	0.41				0.72	0.03	0.01	
ZrO_2						0.09			0.04				0.08	0.02	0.01	
V_2O_3						0.15										
Nb_2O_5						<.01										
NiO							0.24		0.02				0.03			
S									0.02	36.47			0.04	0.21	0.07	
F											2.31					
Totals	100.63	99.99**	100.36**	99.78**	99.58**	100.14	102.72	99.01	99.85	100.00	100.00	100.00	99.97	100.29		100.38
	An 73.5	Wo 11.3	Wo 27.6	Wo 22.1	Wo 14.5	Gi 3.4	Fo 69.1						Qtz 42.9			
	Ab 18.0	En 54.3	En 44.3	En 33.9	En 20.9	Ilm 96.6	Fa 30.9						Fld 47.7			
	Or 1.5	Fs 30.7	Fs 19.4	Fs 39.1	Fs 61.3								Pyx 6.6			
Other	7.0	3.7	8.7	4.9	3.3								2.8			

**Average of three analyses.
[1]Theoretical elemental abundances; converted or oxides for bulk calculation.
[2]Assumed 1:1 mix of fluorapatite and whitlockite.
[3]Analysis constructed from weighted average (56:26:18) of glass, plagioclase, and cristobalite.

Table A14. 10058: Phase abundances, average "phase" compositions, and bulk composition.

		Pyroxene														
(2037 pts)	Plag	Augite	MedFePx	HiFePx	Ferrohed	Ilmenite	"SiO_2"	Troilite[1]	Phosphate[2]	Fayalite	Ulvöspinel	Glass	10058,46 area = 104mm^2 10058,33 area = 152mm^2 ρ calc = 3.33			
Vol.%	33.89	24.48	15.05	7.32	0.15	12.94	4.77	0.42	0.38	0.43	0.05	0.10	Bulk Composition			
σ (SDM)	1.82	1.46	1.14	0.80	0.12	1.59	0.58	0.14	0.14	0.14	0.05	0.07				
ρ	2.73	3.38	3.52	3.72	3.67	4.70	2.33	4.60	3.20	4.37	4.77	2.65				
Wt.%	27.74	24.81	15.89	8.17	0.16	18.24	3.33	0.58	0.37	0.56	0.07	0.08	10058,33	σ	10058,46[3]	Rose
σ (SDM)	1.49	1.48	1.20	0.89	0.13	2.24	0.40	0.19	0.14	0.18	0.07	0.06	(2037 pts)	(SDM)	(2380 pts)	(1970)
P_2O_5								—	43.15			0.07	0.16	0.06	0.09	<.20
SiO_2	46.38	49.39	48.57	46.97	47.49	0.02	97.90	—	—	29.73	0.04	79.01	40.24	1.33	39.76	41.40
TiO_2	0.08	2.53	1.46	0.79	0.85	52.70	0.38	—	—	0.10	31.75	0.52	10.60	1.19	10.52	11.10
Al_2O_3	33.60	2.78	1.44	0.68	0.84	<.01	0.84	—	—	<.01	2.73	10.70	10.34	0.51	10.54	10.70
Cr_2O_3		0.48	0.22	0.13	0.07	0.28		—	—	<.01	0.70	<.01	0.22	0.02	0.19	0.21
MgO	0.09	15.15	10.23	3.19	0.82	0.69	<.01	—	—	0.19	0.05	0.04	5.80	0.28	6.22	6.25
CaO	17.74	16.77	13.35	9.13	13.29		0.18	—	54.54	0.32		1.95	12.18	0.44	12.53	12.10
FeO	0.57	12.50	24.28	38.70	37.89	45.91	0.13	63.53	—	68.45	64.52	1.07	19.60	1.15	19.36	17.30
MnO		0.28	0.43	0.66	0.39	0.49		—	—	0.73	0.32	<.01	0.29	0.02	0.28	0.27
Na_2O	1.38	0.09	0.07	0.05	<.01		0.06	—	—			0.26	0.42	0.03	0.42	0.79
K_2O	0.21						<.01					4.57	0.06	0.04	0.02	0.07
BaO	0.10						<.01	—	—			<.01	0.03	0.02		
ZrO_2						0.08		—	—		0.18	0.40	0.01	0.01		
V_2O_3						<.01		—	—		<.01					
Nb_2O_5						<.01		—	—		0.06					
NiO								—	—	0.09		<.01				
S								36.47	—			0.06	0.20	0.07	0.22	N.A.
F								—	2.31							
Total	100.15	99.97**	100.05**	100.30**	101.64	100.17	99.49	100.00	100.00	99.60	100.34	98.64	100.15		100.27	100.19
	An 83.8	Wo 29.8	Wo 25.8	Wo 19.3	Wo 28.4	Ilm 97.4				Fa 99.5	Ulv 92.7	Qtz 54.4				
	Ab 12.1	En 41.5	En 29.3	En 9.8	En 2.5	Gi 2.6				Fo 0.5	Chr 1.1	Fld 40.9				
	Or 1.2	Fs 19.6	Fs 39.6	Fs 67.7	Fs 66.2						Her 6.2	Pyx 1.0				
Other	2.9	9.1	5.3	3.2	2.9							Cor 2.3				
												Other 1.4				

**Average of three analyses.

[1]Theoretical elemental abundances, converted to oxides for bulk calculation.

[2]Assumed 1:1 mix of fluorapatite and whitlockite.

[3]10058,33 and 10058,46 are similar except that ,33 has more cristobalite (4.77% vs. 1.92%). This may be due to plucking of ,46. 10058,46 also contains a single crystal of Mg-olivine (Fa_{32}). The mode given here is for 10058,33, and that bulk composition is considered more reliable.

Table A15. Lunar breccia 10060,71 clast δ: Phase abundances, "average" phase compositions, and bulk composition.

	Pyroxene								
(2473 pts)	LoCaPx[1]	HiCaPx**	Glass*	Olivine	Armalcolite	Ilmenite	Troilite[2]	Clast δ area = 1.0 mm², ρ calc = 3.33	
Vol.%	0.54	40.25	41.23	2.68	1.31	13.81	0.18		
σ (SDM)	0.26	1.60	1.35	0.57	0.51	1.23	0.08		
ρ	3.40	3.38	2.78	3.53	4.64	4.65	4.60		
Wt.%	0.55	40.84	34.41	2.84	1.82	19.28	0.25	Bulk Comp.	σ (SDM)
σ (SDM)	0.26	1.62	1.13	0.60	0.71	1.72	0.11		
P_2O_5			0.54				—	0.19	0.04
SiO_2	51.39	47.75	55.08	37.24	0.13	0.02	—	39.80	1.09
TiO_2	2.87	4.30	2.34	0.25	73.30	52.88	—	14.11	1.06
Al_2O_3	2.61	4.97	16.45	0.17	1.78	<.01	—	7.74	0.45
Cr_2O_3	0.69	0.91	0.04	0.03	2.32	0.44	—	0.52	0.08
MgO	21.32	14.08	1.76	36.73	7.44	2.70	—	8.17	0.36
CaO	6.60	16.08	8.66	0.40			—	9.59	0.34
FeO	14.36	11.89	12.34	28.15	15.32	42.97	63.60	18.75	0.80
MnO	0.34	0.31	0.05	0.24	0.05	0.57	—	0.26	0.02
Na_2O	0.01	0.09	0.59				—	0.24	0.07
K_2O			1.05				—	0.36	0.07
BaO			0.19				—	0.06	0.06
ZrO_2			<.01		0.14	<.01	—		
V_2O_3					0.32	<.01	—		
Nb_2O_5					0.06	0.07	—	0.01	0.01
NiO			0.02	<.01			—		
S			0.23				34.40	0.17	0.04
Total	100.19	100.38	99.34	103.21	100.87	99.66	100.00	99.97	
	En 58.0	En 39.2	Qtz 19.3	Fa 30.2	Fe 53.6	Ilm 90.0			
	Wo 9.6	Wo 26.2	Fld 53.8	Fo 69.8	Mg 46.4	Gi 10.0			
	Fs 22.4	Fs 19.1	Pyx 21.9						
	Other 10.0	Other 15.5	Ilm 3.5						
			Other 1.5						

*Average of two analyses.
**Average of three analyses.
[1]Composition constructed from average K-values.
[2]Theoretical elemental abundances; converted to oxides for bulk calculation.

Table A16. 10062: Phase abundances, average "phase" compositions, and bulk compositions.

		Pyroxene													
(2112 pts)	Plag	LoCaPx	Augite	MedFePx	HiFePx	Ferrohed	Mg-Oliv	"SiO_2"	Ilmenite	Glass	Ulvöspinel	Cr-spinel	Fe-oliv	10062,39 area = 95mm^2 10062,38 area = 28mm^2 ρ calc = 3.29		
Vol %	37.58	0.58	22.77	12.40	3.20	0.05	4.98	4.64	12.48	0.62	0.06	0.10	<.05			
error	1.58	0.20	0.95	0.73	0.45	0.05	0.62	0.85	1.09	0.17	0.05	0.07	–			
ρ	2.74	3.51	3.38	3.51	3.72	3.59	3.55	2.33	4.69	2.65	4.76	4.70				
Wt %	31.27	0.62	23.37	13.22	3.61	0.05	5.37	3.28	17.78	0.50	0.09	0.14		bulk comp.	σ (SDM)	Rose (1970)
error	1.31	0.21	0.98	0.78	0.51	0.05	0.67	0.60	1.55	0.14	0.08	0.10				
P_2O_5										0.33				0.10	0.04	<.20
SiO_2	47.95	50.42	47.97	47.89	47.16	47.29	37.66	98.52	0.06	79.03	0.16	<.01	31.90	40.23	1.13	38.80
TiO_2	0.10	1.40	3.27	2.09	1.13	1.37	0.10	0.24	52.65	1.21	34.11	24.45	0.24	10.57	0.83	10.30
Al_2O_3	31.63	1.66	3.65	2.39	1.04	1.66	<.01	0.86	0.04	11.58	1.69	6.93	0.44	11.21	0.44	12.10
Cr_2O_3		0.20	0.69	0.25	0.08	0.09	0.12		0.46	0.09	0.15	19.15	<.01	0.31	0.03	0.25
MgO	0.13	16.68	13.57	10.15	2.91	3.16	33.97	<.01	1.21	0.14	0.07	6.85	1.80	6.81	0.28	7.21
CaO	17.54	5.92	17.61	13.43	9.34	15.60	0.32	0.24		2.08			0.38	11.91	0.33	12.00
FeO	0.86	23.76	13.22	23.33	37.84	30.65	28.15	0.26	45.22	2.48	63.04	42.11	64.25	18.04	0.79	18.30
MnO		0.46	0.24	0.47	0.64	0.47	0.43		0.33	0.33	0.39	0.33	0.74	0.23	0.02	0.27
Na_2O	1.48	0.02	0.12	0.04	0.11	0.10		0.04		0.01				0.50	0.04	0.69
K_2O	0.13							0.01		3.01				0.06	0.02	0.07
BaO	0.10							0.21		0.08				0.03	0.02	
ZrO_2									0.22	0.21	0.26	<.01		0.04	0.03	
V_2O_3									<.01		<.01	0.41				
Nb_2O_5									<.01		0.09	<.01				
NiO							0.03			<.01			<.01			
S										0.04				0.17	0.06	
F																
Total	99.92*	100.52*	100.34	100.04**	100.25*	100.40	100.78	100.29	100.19*	100.62	99.94	100.23	99.75	100.21		99.99
	An 82.5	Wo 10.0	Wo 30.4	Wo 25.0	Wo 19.6	Wo 32.2	Fa 32.1		Gi 4.4	Qtz 60.5	Analysis	Ulv 61.2	Fa 95.3			
	Ab 12.6	En 47.0	En 37.1	En 29.3	En 9.0	En 9.6	Fo 67.9		Ilm 95.6	Fld 27.5	from	Chr 25.2	Fo 4.7			
	Or 0.7	Fs 38.3	Fs 20.6	Fs 38.5	Fs 66.7	Fs 53.0				Pyx 3.1	10045	Her 13.6				
Other	4.2	4.7	11.9	7.2	4.7	5.2				8.9						

* Average of two analyses.

** Average of three analyses.

Note: 10062 also contains 0.33 Vol. % troilite and 0.23 Vol. % unidentified Ca-phosphate minerals, assumed to be a 1:1 mix of fluorapatite and whitlockite.

Table A17. 10069: Phase abundances, average "phase" compositions, and bulk composition.

(2720 pts)	Plag	Pyroxene LoCaPx	Pyroxene Augite	Pyroxene MedFePx	Phosphate[1]	Ilmenite	Olivine	"SiO_2"	Meso[3]	Troilite[2]	Glass	Fe-metal[2]	10069,30 area = 88.1 mm^2 ρ calc = 3.40 Bulk comp.	σ (SDM)
Vol.%	23.26	4.26	30.43	16.63	0.14	16.62	0.04	0.97	7.24	0.37		0.03		
σ (SDM)	1.26	0.37	0.98	0.72	0.07	0.83	0.04	0.19	0.52	0.12		0.03		
ρ	2.73	3.49	3.39	3.52	3.20	4.67	3.54	2.33	2.40	4.60		8.00		
Wt.%	18.68	4.38	30.35	17.23	0.13	22.84	0.04	0.67	5.11	0.50		0.07		
σ (SDM)	1.01	0.38	0.98	0.75	0.07	1.14	0.04	0.13	0.37	0.16		0.07		
P_2O_5					43.15				0.77		1.25		0.10	0.05
SiO_2	48.95	49.86	49.16	49.47		6.08	36.88	95.45	72.46		70.81		39.15	0.87
TiO_2	0.11	0.78	1.87	0.87		52.06	0.12	0.17	1.57		2.42		12.75	0.61
Al_2O_3	31.54	0.74	2.17	0.95		0.06	0.04	1.30	12.23		10.74		7.39	0.33
Cr_2O_3		0.21	0.44	0.27		0.93	0.07		<.01		<.01		0.40	0.03
MgO	0.16	18.25	15.21	13.94		2.08	34.40	0.04	0.15		0.19		8.34	0.24
CaO	16.08	6.17	15.89	8.24	54.54		0.34	0.34	4.11		2.36		9.80	0.27
FeO	0.63	22.68	14.44	25.55		44.04	28.08	0.34	3.72	63.53	5.71	100.00	20.57	0.59
MnO		0.39	0.26	0.40		0.60	0.23		0.14		0.22		0.31	0.02
Na_2O	2.17	0.13	0.08	0.01				0.04	0.86		0.66		0.48	0.03
K_2O	0.18							<.01	3.82		6.06		0.23	0.06
BaO	0.06							0.70	0.67		0.77		0.05	0.03
ZrO_2						0.04			0.42		0.67			0.02
V_2O_3						<.01								
Vb_2O_5						0.04							0.01	0.01
NiO							<.01		<.01		<.01			
S									0.06	36.47	0.09		0.19	0.06
F					2.31									
Total	99.88*	99.21**	99.52**	99.70**	100.09	99.93	100.16	98.38	100.98	100.00	101.95	100.00	99.77	
	An 75.7	Wo 11.4	Wo 28.7	Wo 15.6		Gi 7.7	Fo 68.4				Qtz 36.6			
	Ab 19.3	En 49.7	En 41.7	En 39.6		Ilm 92.3	data				Fld 48.5			
	Or 1.1	Fs 35.3	Fs 22.6	Fs 41.4			from				Pyx 6.5			
	Other 3.9	Other 3.6	Other 7.0	Other 3.4			10032				Other 8.4			

*Average of two analyses.
**Average of three analyses.
[1]Assumed 1:1 mix of fluorapatite and whitlockite.
[2]Theoretical elemental abundances; converted to oxides for bulk calculation.
[3]Constructed from weighted average (62:17:21) of glass, plagioclase and cristobalite.

Table A18. 10071: Phase abundances, average "phase" compositions, and bulk composition.

		Pyroxene														
(2857 pgs)	Plag	LoCaPx	Augite	MedFePx	HiFePx	Ilmenite	Olivine	"SiO_2"	Meso[3]	Armalcolite	Troilite[1]	Phosphate[2]	Glass	Fe-Metal[1]	10071,31 area = 73.1mm^2 ρ calc = 3.33	
Vol.%	23.60	3.73	30.69	12.62	0.72	14.77	1.27	2.19	9.63	0.03	0.44	0.24		0.02		
σ (SDM)	1.17	0.33	0.95	0.61	0.14	0.87	0.20	0.28	0.57	0.03	0.12	0.09		0.02		
ρ	2.74	3.48	3.73	3.50	3.69	4.68	3.55	2.33	2.40	4.64	4.60	3.20		8.00		
Wt.%	19.43	3.90	31.08	13.27	0.80	20.77	1.36	1.53	6.94	0.04	0.61	0.23		0.05	Bulk comp.	σ (SDM)
σ (SDM)	0.96	0.34	0.96	0.64	0.16	1.22	0.21	0.20	0.41	0.04	0.17	0.09		0.09		
P_2O_5									0.67			43.15	1.11		0.15	0.06
SiO_2	50.15	51.02	47.70	49.13	47.48	0.07	36.18	97.11	70.56	0.11			70.08		40.35	0.83
TiO_2	0.16	1.14	3.38	1.44	0.83	52.56	0.11	0.47	1.14	73.15			1.71		12.36	0.65
Al_2O_3	30.64	1.60	3.74	1.54	1.01	0.03	<.01	1.21	12.59	1.57			9.63		8.29	0.31
Cr_2O_3		0.24	0.73	0.28	0.09	0.71	0.16		<.01	2.02			0.01		0.42	0.03
MgO	0.32	19.21	15.24	12.91	5.41	1.72	34.29	<.01	0.24	7.66			0.30		8.14	0.23
CaO	15.45	6.48	16.39	11.76	7.93		0.37	0.47	4.68			54.54	2.16		10.44	0.27
FeO	0.80	20.44	12.28	22.83	36.37	44.02	28.62	0.29	5.97	15.51	63.53		9.57	100.00	18.55	0.59
MnO		0.34	0.22	0.35	0.55	0.37	0.26		0.04	0.01			0.07		0.15	0.02
Na_2O	2.92	0.02	0.09	0.01	0.12			0.16	0.80				0.42		0.53	0.03
K_2O	0.22							0.02	2.86				4.65		0.24	0.06
BaO	<.01							0.49	0.16				0.13		0.02	0.01
ZrO_2						0.05			0.23	0.07			0.39		0.03	0.02
V_2O_3						<.01				0.07						
Nb_2O_5						<.01				<.01						
NiO							<.01		0.11				0.19			
S									0.06		36.47		0.10		0.23	0.06
F												2.31				
Totals	100.03	100.49**	99.79**	100.25**	99.79**	99.53	99.99	100.22	100.12	100.17	100.00	100.00	100.52	100.00	99.90	
	An 71.3	Wo 10.9	Wo 27.6	Wo 21.9	Wo 16.4	Ilm 93.5	Fa 32.5									
	Ab 20.4	En 52.9	En 41.4	En 36.4	En 16.5	Gi 6.5	Fo 67.5									
	Or 1.3	Fs 32.1	Fs 19.0	Fs 36.7	Fs 63.3											
Other	7.0	4.1	12.0	5.0	3.8											

**Average of three analyses.
[1]Theoretical elemental abundances; converted to oxides for bulk calculation.
[2]Assumed 1:1 mix of fluorapatite and whitlockite.
[3]Analysis constructed from weighted average (60:23:17) of glass, plagioclase, and cristobalite.

Table A19. 10071, Iota: Phase abundances, average "phase" compositions, and bulk composition.

(1007 pts)	Plag	Pyroxene LoCaPx	Pyroxene Augite	Pyroxene MedFePx	Pyroxene HiFePx	Ilmenite	"SiO_2"	Meso[3]	Troilite[1]	Phosphate[2]	Glass	10071,31 Iota sector[5] area = 3.8mm[2] ρ calc = 3.14 Bulk Comp.	σ (SDM)	10071 "normal"
Vol.%	36.27	0.29	5.99	26.60	7.86	6.31	5.04	10.88	0.43	0.34				
σ (SDM)	2.32	0.20	1.08	2.28	1.24	0.94	0.71	1.04	0.21	0.18				
ρ	2.73	3.54	3.43	3.52	3.72	4.71	2.33	2.40	4.60	3.20				
Wt.%	31.52	0.32	6.54	29.82	9.31	9.46	3.74	8.32	0.63	0.35				
σ (SDM)	2.02	0.22	1.18	2.55	1.47	1.41	0.53	0.80	0.31	0.81				
P_2O_5								0.15		43.15	0.25	0.16	0.08	0.15
SiO_2	50.08	49.28	48.69	49.03	47.63	0.27	96.88	72.81			71.83	47.89	2.01	40.35
TiO_2	0.29	0.93	2.63	1.35	1.01	51.64	0.32	1.04			1.53	5.75	0.73	12.36
Al_2O_3	30.08	1.20	3.51	1.39	0.92	0.03	1.49	12.18			10.05	11.29	0.61	8.29
Cr_2O_3		0.21	0.32	0.10	<.01	0.13		<.01			<.01	0.07	0.02	0.42
MgO	0.39	15.96	13.45	10.87	3.66	0.54	<.01	0.06			0.03	4.69	0.34	8.14
CaO	15.15	5.75	14.94	12.67	8.22		0.41	4.22		54.54	2.07	10.87	0.50	10.44
FeO	1.21	26.46	16.59	24.10	38.70	46.06	0.37	4.02	63.53		6.18	17.56	1.09	18.55
MnO		0.38	0.24	0.40	0.48	0.47		0.10			0.16	0.22	0.03	0.15
Na_2O	2.28	0.02	0.04	0.03	0.12		0.12	0.69			0.39	0.80	0.06	0.53
K_2O	0.24						0.09	4.08			6.58	0.42	0.08	0.24
BaO	0.22						0.19	0.33			0.45	0.10	0.05	0.02
ZrO_2						0.38		<.01			<.01	0.04	0.02	0.03
V_2O_3						<.01								
Nb_2O_5						0.02								
NiO								<.01			<.01			
S								0.23	36.47		0.38	0.25	0.12	0.23
F										2.31				
Totals	99.94	100.19[4]	100.41**	99.95**	100.74*	99.54	99.87	99.92	100.00	100.00	99.91	100.11		99.90
	An 68.9	Wo 10.1	Wo 26.3	Wo 24.6	Wo 17.2	Ilm 98.0					data			
	Ab 20.4	En 44.5	En 38.1	En 31.3	En 11.2	Gi 2.0					from			
	Or 1.4	Fs 42.0	Fs 26.8	Fs 39.6	Fs 67.5						10049			
Other	9.3	3.4	8.8	4.5	4.1									

*Average of two analyses.

**Average of three analyses.

[1]Theoretical elemental abundances; converted to oxides for bulk calculation.

[2]Assumed 1:1 mix of fluorapatite and whitlockite.

[3]Analysis constructed from weighted average (61:19:20) of glass, plagioclase and cristobalite.

[4]Analysis constructed from K-values collected during point-count.

[5]The Iota sector is an area of vastly different texture separated from the "normal" portion by a smooth, sharp contact. Both have igneous texture, so it is thought that two liquid compositions are present.

Table A20. 10072: Phase abundances, average "phase" compositions, and bulk composition.

		Pyroxene													
(2244 pts)	Plag	LoCaPx	Augite	MedFePx	HiFePx	Ilmenite	Olivine	"SiO_2"	Meso[1]	Armalcolite	Ulvöspinel[2]	Glass			
Vol.%	22.49	3.37	31.26	14.79	1.53	13.17	0.41	1.34	10.78	<.04	0.04		10072,43 area = 89.8mm^2		
σ (SDM)	1.18	0.28	0.86	0.59	0.19	1.19	0.14	0.24	0.66		0.04		ρ calc = 3.31		
ρ	2.73	3.46	3.73	3.49	3.70	4.68	3.56	2.35	2.40		4.78				
Wt.%	18.53	3.52	31.80	15.58	1.71	18.61	0.44	0.94	7.81		0.06		Bulk comp.	σ (SDM)	Compston (1970)	Maxwell (1970)
σ (SDM)	0.97	0.29	0.87	0.62	0.21	1.68	0.15	0.17	0.48		0.06					
P_2O_5									0.13			0.28	0.07	0.04	0.19	0.16
SiO_2	51.02	52.00	49.11	48.71	47.47	0.03	36.51	99.21	66.84	0.07		69.05	41.62	0.83	40.49	40.37
TiO_2	0.15	1.09	2.68	1.75	0.83	52.35	0.11	0.17	0.63	72.32	35.74	1.32	11.02	0.89	11.99	12.01
Al_2O_3	29.26	1.01	3.66	2.07	0.85	0.03	<.01	0.25	16.45	1.56		10.48	8.25	0.30	7.74	8.15
Cr_2O_5		0.35	0.73	0.32	0.09	0.54	0.13		<.01	1.40		<.01	0.40	0.03	0.33	0.36
MgO	0.45	19.55	15.32	12.09	4.80	1.58	33.29	<.01	0.14	5.54		0.11	8.06	0.21	7.45	7.87
CaO	15.54	6.30	16.59	12.17	8.30		0.35	0.05	7.04			3.09	11.04	0.25	10.56	10.35
FeO	1.15	19.98	11.91	22.58	37.36	45.09	29.78	0.69	4.26	19.40	64.26	8.19	18.53	0.79	19.38	19.77
MnO		0.21	0.18	0.26	0.53	0.21	0.26		0.14	0.05		0.30	0.17	0.02	0.24	0.23
Na_2O	2.26	0.02	0.11	0.03	0.01			<.01	1.15			0.40	0.55	0.03	0.50	0.53
K_2O	0.27							0.05	2.64			5.29	0.26	0.05	0.29	0.28
BaO	0.12							0.58	0.13			0.27	0.04	0.02	0.03	
ZrO_2						0.07			0.63	<.01		1.31	0.06	0.05		
V_2O_3						<.01				0.06						
Nb_2O_5						0.03				<.01						
NiO							<.01		<.01			<.01				
S									<.01			0.02	0.31	0.09	0.23	0.24
F																
Totals	100.24	100.52**	100.29**	99.96**	100.23**	99.92	100.42	100.99	100.20	100.40	100.00	100.00	100.38		99.42	100.32
	An 68.9	Wo 11.1	Wo 28.6	Wo 22.5	Wo 17.2	Gi 5.8	Fa 33.6			Fe 66.3						
	Ab 20.1	En 53.6	En 42.3	En 34.6	En 14.7	Ilm 94.2	Fo 66.4			Mg 33.7						
	Or 1.6	Fs 31.1	Fs 18.7	Fs 36.7	Fs 65.2											
Other	9.4	4.2	10.4	2.9												

**Average of two analyses.

[1]Analysis constructed from weighted average (48:37:15) of glass, plagioclase and cristobalite.

[2]Assumed end-member abundances.

Note: 10072 also contains 0.62 Vol. % troilite, and 0.15 Vol. % unidentified Ca-phosphate minerals, assumed to be a 1:1 mix of fluorapatite and whitlockite.

Table A21. 10085,12-7: Phase abundances, average "phase" compositions, and bulk composition.

(1928 pts)	Pyroxene LoCaPx[3]	Pyroxene HiCaPx	Ground mass	Olivine	Ilmenite	Troilite[1]	Phosphate[2]	Groundmass Pyx	Groundmass Plag	area = 1.2mm², ρ calc = 3.37 Bulk Comp.	σ (SDM)
Vol.%	0.37	37.88	46.49	2.03	12.91	0.31	0.01				
σ (SDM)	0.26	2.66	2.98	1.03	1.12	0.18	0.01				
ρ	3.41	3.37	3.00	3.52	4.68	4.60	3.20				
Wt.%	0.37	37.84	41.34	2.12	17.91	0.42	0.01				
σ (SDM)	0.26	2.66	2.65	1.08	1.55	0.24	0.01				
P_2O_5			0.23			43.15			0.10	0.02	
SiO_2	52.93	48.31	54.09	38.20	0.09			48.87	56.76	41.66	2.02
TiO_2	1.24	3.66	1.43	0.19	53.31			0.90	0.37	11.53	0.87
Al_2O_3	1.01	4.43	17.93	0.02	<.01			0.81	26.98	9.09	0.67
Cr_2O_3	0.42	0.77	0.05	0.24	0.75			<.01		0.45	0.05
MgO	23.19	14.03	1.93	36.50	1.66			4.24	0.26	7.26	0.57
CaO	6.32	16.70	10.06	0.35			54.54	6.07	11.86	10.51	0.59
FeO	15.23	11.83	13.88	27.32	44.40	63.53		39.88	2.15	19.15	1.06
MnO	0.22	0.28	0.20	0.46	0.31			0.62		0.25	0.03
Na_2O	0.04	0.06	1.56					<.01	2.01	0.67	0.13
K_2O			0.57						0.52	0.24	0.08
BaO			0.10						0.69	0.04	0.02
ZrO_2			0.01		0.15					0.03	0.02
V_2O_3					<.01						
Nb_2O_5					<.01						
NiO			0.02	0.23						0.01	0.01
S			0.24[4]			36.47				0.19	0.09
Total	100.60	100.07*	102.30**	103.51	100.67	100.00	100.00	101.39	101.60	101.18	
	Wo 10.8	Wo 28.5	Qtz 9.7	Fo 70.1	Gi 6.2		F = 2.31	Wo 12.7	An 53.5		
	En 61.5	En 39.2	Fld 58.7	Fa 29.9	Ilm 93.8			En 13.3	Ab 17.5		
	Fs 23.0	Fs 19.2	Pyx 28.7					Fs 71.2	Or 3.0		
	Other 4.7	Other 13.1	Other 2.9					Other 2.8	Si 15.1		
									Other 10.9		

*Average of three analyses.

**Average of four defocused beam analyses.

[1]Theoretical elemental abundances; converted to oxides for bulk calculation.

[2]Assumed 1:1 mix of fluorapatite and whitlockite.

[3]Constructed from K-values collected during point count.

[4]Reported as SO_3.

Table A22. 10092: Phase abundances, average "phase" compositions, and bulk composition.

		Pyroxene													
(2204 pts)	Plag	Augite	LoCaPx	MedFePx	HiFePx	Ferrohed	Olivine	"SiO_2"	Ilmenite	Ulvöspinel	Cr-spinel	Troilite[1]	K-glass	Fe-glass	10092,6 area = 11.3mm^2 ρ calc = 3.38
Vol.%	30.64	32.61	3.00	9.16	0.84	0.05	4.91	2.59	15.59	0.04	0.05	0.23	0.14	<.05	
σ (SDM)	1.55	1.74	0.53	0.92	0.28	0.05	0.72	0.33	1.26	0.04	0.05	0.10	0.08	—	
ρ	2.74	3.37	3.44	3.49	3.69	3.57	3.55	2.33	4.66	4.77	4.70	4.60	2.65	—	
Wt.%	24.82	32.49	3.05	9.45	0.92	0.05	5.15	1.78	21.48	0.06	0.07	0.31	0.11	—	Bulk Comp.
σ (SDM)	1.26	1.73	0.54	0.95	0.31	0.05	0.76	0.23	1.74	0.06	0.07	0.13	0.06	—	σ (SDM)
P_2O_5															
SiO_2	47.08	48.69	52.23	49.85	47.79	47.54	37.45	98.35	0.06				<.01	3.80	0.03 0.02
TiO_2	0.23	2.92	0.95	1.43	1.00	1.67	0.13	0.43	53.31	0.19	0.09		75.70	35.95	38.05 1.24
Al_2O_3	33.03	3.85	1.13	1.44	1.15	1.68	<.01	0.68	<.01	33.95	22.75		0.76	4.13	12.74 0.94
Cr_2O_3		0.66	0.33	0.26	0.14	<.01	0.13		0.76	1.71	7.38		10.02	2.42	9.66 0.44
MgO	0.09	14.79	19.48	11.54	4.06	3.39	35.03	<.01	2.52	0.08	22.41		<.01	<.01	0.44 0.04
CaO	17.79	16.76	6.30	12.44	9.34	17.01	0.30	0.22		0.41	6.47		0.02	0.49	8.90 0.42
FeO	0.52	12.10	19.72	22.52	36.36	28.12	29.05	0.36	43.12				2.04	11.90	11.38 0.40
MnO		0.26	0.34	0.43	0.52	0.61	0.26		0.36	62.96	40.64	63.53	3.71	37.83	18.38 0.85
Na_2O	1.22	0.06	0.02	0.06	0.04	0.02		0.01		0.47	0.34		<.01	0.68	0.23 0.02
K_2O	0.03							<.01					0.17	<.01	0.33 0.03
BaO	<.01							<.01					6.49	0.44	0.02 0.02
ZrO_2									0.05				0.22	0.14	
V_2O_3									0.01	0.30	0.09		0.05	0.04	0.01 0.01
Nb_2O_5									<.01	0.14	0.19				
NiO							<.01			<.01	<.01				
S												36.47	0.27	0.57	0.11 0.05
F															
Total	99.98	100.09**	100.50**	99.97**	100.40**	100.04	102.36	100.05	100.20	100.19	100.36	100.00	99.81	98.84	100.28
	An 86.2	Wo 28.9	Wo 11.1	Wo 24.1	Wo 19.4	Wo 35.3	Fo 68.0		Gi 9.4	Ulv 96.1	Ulv 56.4		Qtz 42.5	Ol 13.0	
	Ab 11.0	En 41.2	En 54.0	En 33.3	En 12.6	En 10.3	Fa 32.0		Ilm 90.6	Her 3.8	Her 14.3		Fld 49.7	Fld 9.6	
	Or 0.17	Fs 19.3	Fs 31.2	Fs 37.2	Fs 64.1	Fs 49.2				Chr 0.1	Chr 29.2		Pyx 5.9	Pyx 60.1	
Other	2.6	10.6	3.7	5.2	3.9	5.2							1.9	Ilm 6.7	
														Ap 9.3	
														1.3	

**Average of three individual analyses.

[1]Theoretical elemental abundances; converted to oxides for bulk calculation.

Note: 10092 also contains 0.05 Vol. % Fe-metal, 0.05 Vol. % rutile, and 0.06 Vol. % unidentified Ca-phosphate minerals, assumed to be a 1:1 mix of fluorapatite and whitlockite.

Proc. Lunar Planet. Sci. Conf. 10th (1979), p. 41–75.
Printed in the United States of America

The petrology and chemistry of basaltic fragments from the Apollo 11 soil, part I

D. W. Beaty, S. M. R. Hill, and A. L. Albee

Division of Geological and Planetary Sciences* California Institute of Technology, Pasadena, California 91125

M.-S. Ma and R. A. Schmitt

Department of Chemistry and the Radiation Center, Oregon State University, Corvallis, Oregon 97331

Abstract—Twenty-four peanut sized basaltic fragments obtained from the Apollo 11 bulk sample have been studied using INAA, the petrographic microscope, and the electron microprobe. Only two of these samples had previously been released to the scientific community. Twenty-one of the fragments fit the Apollo 11 classification system proposed by Beaty and Albee (1978). Included are 13 Group A (high-K) basalts, 3 Group B2 and 5 Group B3 basalts, but none of these samples are members of Group B1. These petrologic groups are unambiguously resolved on a plot of La vs. K.

Two of the Group A samples are vitrophyres with bulk compositions indistinguishable from those of the crystalline high-K rocks. Despite the compositional similarity, the constituent minerals of the two types have different sizes, morphologies and compositions. This indicates that the vitrophyres have crystallized under different physical conditions and represent a second high-K cooling unit. The B2 samples can be related to each other through ilmenite fractionation, whereas the B3 samples are related to one another through olivine fractionation. This contrast in differentiation is related to different sizes and morphologies, and consequently settling rates, of olivine and ilmenite in the two rock types.

The remaining three of the 24 samples are similar to each other, but are petrologically and chemically unlike any rock type yet described from the moon, and are here named Apollo 11 Group D. Most distinctively, they are rich in all of the incompatible trace elements except K, which is low. Because most igneous processes do not fractionate K from the REE, the Group D magmas were probably generated in a chemically distinct source region. The Apollo 11 B2 samples also have an anomalously high La/K ratio and they may have been generated in the same source region as the Group D basalts.

I. INTRODUCTION

Twenty-four small basaltic fragments from the Apollo 11 bulk sample have been studied in an effort to improve the sampling of basalts from this landing site. This continues a previous study on the comparative petrology based on the large samples from this site (Beaty and Albee, 1978).

* Contribution No. 3241.

Our objectives were threefold: 1) To characterize and classify these new samples. 2) To evaluate the significance of any unusual rock types discovered. 3) To use the additional sampling to help characterize the magma types present and to help understand the fractionation processes which have affected the Apollo 11 lava flows. This research is continuing with the study of a second group of 30 peanut-sized basalt fragments ("peanuts") during 1979 (Part II).

II. ANALYTICAL TECHNIQUES

Megascopic descriptions of all these samples can be found in Kramer *et al.* (1977). Prior to any cutting, the samples were sent to the Oregon State University Radiation Center for determination of 29 major, minor and trace element abundances by instrumental neutron activation analysis (INAA) (Tables 2, 5). Sample preparation and the detailed INAA procedures are essentially the same as reported by Wakita *et al.* (1970) and Laul and Schmitt (1973a).

Following INAA, the samples were returned to the Lunar Sample Curator, who prepared one thin section of each (Table 1). These thin sections were sent to Caltech for petrographic analysis and microprobe studies. For each sample, detailed textural and mineralogical observations were made. For about half of the samples, the mode, average mineral compositions, range and distribution of all mineral zonations, and the bulk rock composition were measured using microprobe point counts (Table 4). Single spot microprobe analyses were also obtained on these samples. The details of the point count program may be found in Albee *et al.* (1977) and a description of our microprobe technique, operating conditions and mineral normalizations may be found in Beaty and Albee (1978). Despite the small size of the samples and the small area of the thin sections, the results of the two techniques are in good agreement with the notable exception of 10085,918 (Table 5). It seems likely that the small thin section for this sample contained a nonrepresentative amount of ilmenite.

III. CLASSIFICATION

Twenty-one of the "peanuts" may be unambiguously classified using the classification system of Beaty and Albee (1978). There are 13 "peanuts" in Group A, none in Group B1, 3 in Group B2 and 5 in Group B3. The remaining three samples are of a new rock type, dissimilar to any of the other Apollo 11 rocks and here named Group D. Ma and Schmitt (1979), using trace element data alone, and Beaty *et al.* (1979a, b, c), using petrography and microprobe studies, done independently, arrived at exactly the same classification. The essence of the trace element classification is contained in Fig. 1, a plot of La vs. K_2O. Ma and Schmitt (1979) demonstrated that the different Apollo 11 rock types fall in different places on this diagram, which they in turn used to name the data clusters: low-K, low-La; low-K, intermediate-La; low-K, high-La; high-K, high-La. These groupings coincide with petrologic groupings established using the criteria of Beaty and Albee (1978) except that the low-K, low-La cluster can be further resolved into two groups (Fig. 1). The petrologic groups were named A, B1, B2, B3 and D, following the nomenclature originally established by LSPET (1969), and since that terminology is less cumbersome than the La-K system, it is used for the remainder of this report. Table 1 summarizes the classification of all Apollo 11

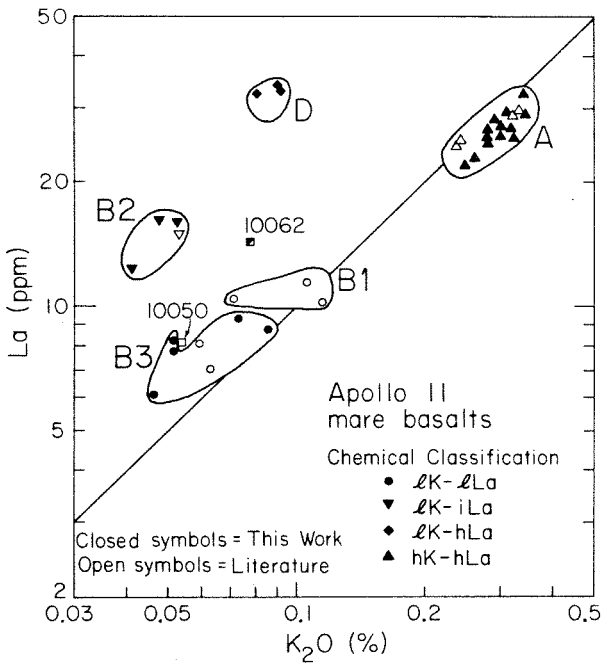

Fig. 1. La and K_2O abundances in the Apollo 11 basalts. This plot was used by Ma and Schmitt (1979) to define four chemical groups: low-K, low-La; low-K, intermediate-La; low-K, high-La; and high-K, high-La. These groups correspond to the petrologic groups of Beaty and Albee (1978), which are labelled A, B1, B2, B3 and D. Samples 10050 and 10062 are anomalous and are unclassified (Table 1).

basalt samples. Although the Group D (low-K, high-La) specimens constitute a new rock type, the addition of these 24 samples does not affect the basic conclusions of Beaty and Albee (1978). Apollo 11 Groups B1, B2 and B3 must come from separate igneous cooling units, and two types of high-K rocks are recognized—vitrophyres and crystalline. However, study of these samples does allow further evaluation of the relationships within the individual groups.

IV. GROUP A (HIGH-K, HIGH-LA)

General petrography

Fourteen of these 24 basalt fragments are both high in K and high in La (Fig. 1, Table 2). These samples all have a distinctive intersertal texture (with the exception of two vitrophyres) produced by the very late crystallization of plagioclase. Either the composition or the texture, therefore, allow unambiguous separation from the other Apollo 11 basalts. The texture of the 12 holocrystalline fragments is somewhat variable, consisting of either abundant pyroxene and ilmenite grains

Table 1. Classification of Apollo 11 basalt samples.

	A (high-K, high-La)		B1 (low-K, low-La)	B2 (low-K, int.-La)	B3 (low-K, low-La)	D (low-K, high-La)	Unclassified
	Crystalline	Vitrophyre					
This report	10002,114(119)*	10031,6(7)		10085,779	10002,113(118)†	10002,116(121)	
	10002,115(120)	10085,832		10085,829(921)	10085,775(914)	10085,808(918)	
	10002,117(122)				10085,839(924)	10085,836(923)	
	10085,782(915)				10085,844(925)		
	10085,789				10085,847(926)		
	10085,796						
	10085,803						
	10085,814(920)						
	10085,820						
	10085,824(919)						
Beaty and Albee, 1978	10017	10060,71	10044	10003	10020		10050
	10022†	10085,12–7	10047	10029	10045		10062
	10024		10058		10092		
	10032						
	10049						
	10057						
	10069						
	10071						
	10072						

* The subsample numbers in parentheses refer to the thin section prepared from the rock fragment used for INAA. Descriptions in the text are keyed to fragment numbers, but figures with photomicrographs or microprobe data are keyed to the thin section from which the data was obtained.

† porphyritic

Table 2. Apollo 11 high-K basaltic fragments: Compositional summary.

Wt. %	10085, 782	10085, 789	10085, 796	10085, 803	10085, 814	10085, 820	10085, 824	10002, 114	10002, 115	10002, 117	10032, 30	10085, 832	10031, 6	INAA errors (%)
TiO_2	10.2	11.6	10.2	10.1	9.3	10.3	12.1	11.1	11.5	10.2	10.3	11.1	11.4	<5
Al_2O_3	8.0	8.2	8.1	8.1	8.7	8.2	8.8	7.3	7.7	8.6	7.6	8.3	8.0	<5
FeO	20.0	21.5	20.2	20.4	20.0	20.6	20.4	20.5	20.1	20.2	19.1	19.5	20.7	<5
MgO	8	8	8	7	7	7	8	9	8	8	8	7	8	10–20
CaO	10.0	11.1	10.6	11.0	10.8	10.1	10.7	10.5	10.9	10.8	9.4	10.0	10.6	5–10
Na_2O	0.505	0.477	0.524	0.513	0.578	0.492	0.499	0.462	0.474	0.527	0.482	0.478	0.503	<5
K_2O	0.26	0.25	0.32	0.32	0.34	0.31	0.28	0.28	0.28	0.33	0.29	0.30	0.30	5–20
MnO	0.253	0.247	0.247	0.245	0.247	0.239	0.235	0.218	0.220	0.223	0.219	0.247	0.225	<5
Cr_2O_3	0.310	0.377	0.314	0.318	0.255	0.296	0.337	0.342	0.348	0.289	0.323	0.294	0.346	<5
ppm														
Sc	84	89	82	84	76	84	85	83	84	83	77	80	87	<5
V	66	84	63	66	52	56	79	74	72	59	70	59	65	10–15
Co	26	29	27	27	24	26	27	27	28	35	26	25	28	<5
Zr	520	360	430	440	400	500	—	500	320	490	370	470	370	30–40
Ba	230	240	330	320	380	330	290	250	330	330	270	400	330	10–35
La	23.0	22.3	27.2	26.9	33.0	28.7	25.2	27.0	25.6	29.9	27.7	25.7	27.3	<5
Ce	75	72	83	80	98	100	90	79	73	87	73	79	78	10–30
Nd	62	58	71	70	80	74	64	64	60	68	65	65	64	20–25
Sm	19.2	18.2	21.6	21.1	24.6	22.6	20.1	20.8	19.9	22.5	20.5	20.6	20.7	<5
Eu	2.11	2.06	2.25	2.26	2.55	2.55	2.19	2.31	2.29	2.61	2.17	2.18	2.23	5–10
Tb	4.4	4.2	4.7	4.6	5.2	5.0	4.6	4.5	4.4	4.7	4.5	4.5	4.3	10–15
Dy	31	29	32	31	37	33	30	29	29	32	30	30	30	10–20
Yb	15.5	15.1	17.3	17.2	19.6	18.2	16.3	16.6	15.1	18.2	16.9	16.8	17.2	<5
Lu	2.27	2.24	2.55	2.54	2.86	2.63	2.32	2.40	2.14	2.70	2.40	2.46	2.43	5–10
Hf	14.4	15.3	15.9	14.9	16.7	15.8	15.1	16.5	16.0	17.0	14.5	15.4	15.4	5–10
Ta	2.5	2.2	2.6	2.3	2.6	2.4	2.2	2.7	2.5	2.5	2.3	2.7	2.5	5–10
Th	1.8	1.6	2.1	1.9	2.8	2.3	2.0	3.6	3.5	3.8	3.3	2.1	2.8	10–15
Sample Wt. (Mg)	48	50	45	48	50	34	46	31	76	69	115	50	64	

All values determined by INAA on uncut basaltic fragments.

poikilitically enclosed by larger plagioclase, or larger pyroxene and ilmenite grains with interstitial plagioclase. Olivine is scarce, small, embayed and mantled by pyroxene, and ilmenite tends to be equant regardless of the grain size. Interstitial residual phases include cristobalite, apatite, ulvöspinel, tranquillityite and small (<1%) amounts of glass. The scattered occurrence of armalcolite and the absence of early Cr-spinel further serves to distinguish these specimens from the low-K suite. The average grain size of the twelve crystalline samples ranges from 10-1000 microns and the textural variations are the same as those reported by Beaty and Albee (1978) for the large high-K rocks. The chemical compositions (Table 2) are indistinguishable as well. In common with the larger rocks (Beaty and Albee, 1978) these fragments show a well-defined differentiation trend (e.g., Fig. 1) indicating fractionation of the early crystallizing mafic minerals. Integrating these new samples with the large rocks, the entire high-K suite may be ranked in order of increasing grain size: 10002,117<10049<10069≈10085,796≈10085,803≈10085,782<10085,824≈10002,115<10032≈10085,820≈10057<10017≈10002,114<10071<10085,814≈10072<10024<10085,789. Samples 10032 and 10024 most nearly approach the composition of the primitive melt.

Vitrophyres. Two of the fourteen high-K basaltic fragments (10031 and 10085,832) do not fall into this textural sequence, but are vitrophyres. Chemically (Table 2) they are indistinguishable from the crystalline high-K samples.

10031 contains about 60% crystals which consist of equant armalcolite mantled by rutile-bearing ilmenite, platy ilmenite (50 × 5 μm) with feathery edges, pyroxene (to 100 μm) and minute troilite spheres. These crystals are enclosed in a dark brown glass which contains numerous incipient crystallites of ilmenite and pyroxene. These textural relations are illustrated in Fig. 2a. A photomicrograph of one of the finer-grained high-K crystalline rocks is included for comparison (Fig. 2b). Armalcolite has Fe/(Fe + Mg) = 0.53, contains 2.3% Cr_2O_3, 1.3% Al_2O_3 and has 6.4 mole percent $Ti_2^{3+}Ti^{4+}O_5$. Ilmenite ranges in composition from Gi_{4-12} (Fig. 3) and contains about 0.8% Cr_2O_3. Pyroxene is only weakly zoned from $Wo_{28}En_{40}Fs_{17}Oth_{15}$ to $Wo_{33}En_{29}Fs_{21}Oth_{17}$, but Al_2O_3 and TiO_2 increased from 4.0% and 4.5% to 6.5% and 5.5%, respectively, from core to rim. The glass has a normative composition of about $Pyx_{26}Fld_{49}Qtz_{21}Oth_4$. Texturally and petrologically, 10031 is very similar to 10060,71, clast δ, a vitrophyre described by Beaty and Albee (1978). The principal difference between the two is that the phenocrysts in 10031 are about twice as large as those in clast δ.

10085,832 has 8.4% crystals including euhedral armalcolite grains up to 200 μm in length mantled by a thin rim of ilmenite, euhedral lath-shaped olivine (up to 290 μm in length) commonly with hollow glassy cores, euhedral ilmenite plates with an average size of 4 × 50 μm (Fig. 2c), minute troilite spheres in both the glass and some olivine, and small (10–20 μm) H-shaped pyroxene crystals, typically with curved limbs (Fig. 2d). The armalcolite (0.1 volume percent) is unzoned with Fe/(Fe + Mg) = 0.49, Cr_2O_3 = 2.2%, Al_2O_3 = 1.6% and Ti_3O_5 = 9.1 mole percent. The olivine (3.1 volume percent) ranges from Fo_{73} to Fo_{68} (Fig. 3), and there is no sign of reaction with the melt. Ilmenite (3.8 volume percent) compositions range from Gi_{10} to Gi_{14} (Fig. 3), and the Cr_2O_3 content ranges from 0.5% to 0.8%. Pyroxene (1.4 volume percent) has a slight range in composition, zoning from $Wo_{17}En_{52}Fs_{20}Oth_{11}$ to $Wo_{25}En_{46}Fs_{16}Oth_{13}$. Cr_2O_3 content is high (1.0%) while Al_2O_3 (2.2%) and TiO_2 (2.7%) are relatively low. The glass is dark brown and has a normative composition of $Fld_{28}Pyx_{50}Ilm_{16}Qtz_6$ (Table 3) with slight zoning around the phenocrysts. For example, the amount of normative quartz in one traverse increased from 5.8% to 7.3% up to the edge of an olivine crystal. The mode, average phase compositions, and calculated bulk composition of 10085,832 are listed in Table 3.

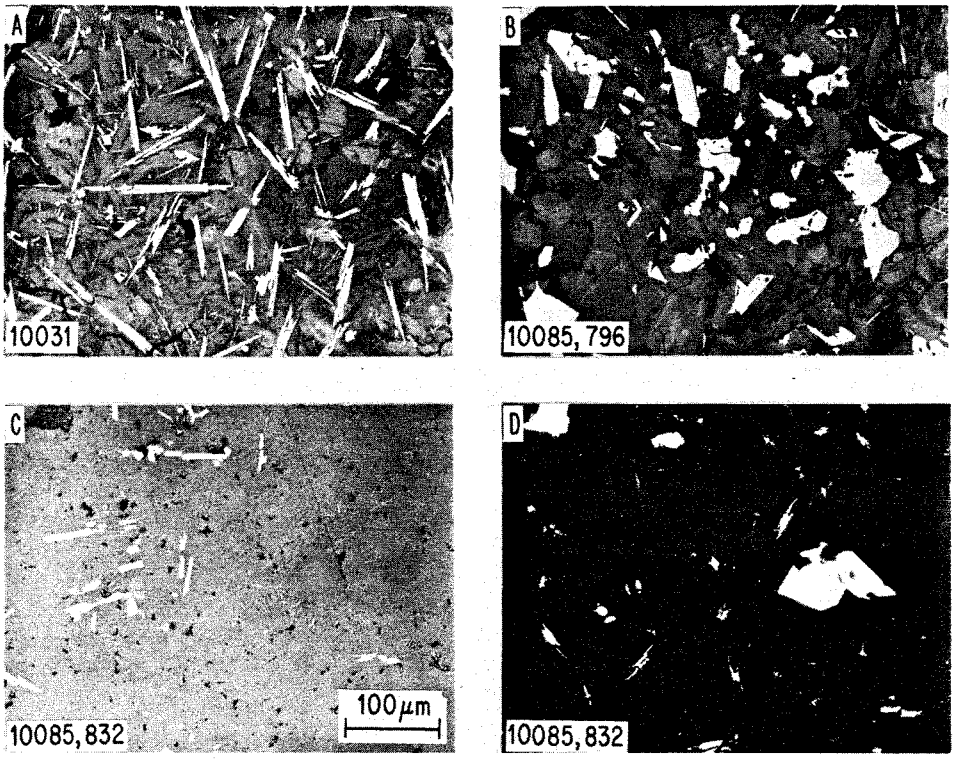

Fig. 2. Photomicrographs of Group A (high-K) samples. Scale is the same for comparison. (a) reflected light showing platy ilmenite (white), equant pyroxene (grey) and interstitial glass (dark) in vitrophyre 10031. (b) 10085,796 is shown for comparison, illustrating the textural differences between the crystalline and vitrophyric samples. (c) 10085,832 reflected light and (d) some view plane-polarized light. Ilmenite plates, euhedral olivine crystals, tiny filamental H-shaped pyroxenes (transmitted light) and a dark brown glass are present.

Discussion

A total of four vitrophyres from the Apollo 11 site have now been studied (James and Jackson, 1970; Beaty and Albee, 1978; this work). Three of them were quenched at about 60% crystalline and one at about 10% crystalline. These four rocks have the same bulk composition as the Apollo 11 high-K suite.

Other than the amount of glass, there are important differences in the sizes and morphologies of the constituent minerals between the two suites. In the vitrophyres, ilmenite occurs as thin plates with irregular edges and pointed terminations. In the crystalline rocks ilmenite tends to be subhedral and equant, regardless of the grain size (Fig. 2b). Olivine in the vitrophyres is typically euhedral, despite the fact that it is grossly out of equilibrium with the surrounding glass,

whereas in the crystalline rocks olivine is invariably small, embayed and mantled by pyroxene. The olivine and armalcolite crystals in the vitrophyres are much larger and the pyroxene crystals smaller than their counterparts in the crystalline rocks.

The major minerals also have different compositions in the two suites. The pyroxene in the crystalline rocks shows growth on both branches of the two pyroxene field (Fig. 4), along with limited growth of ferrohedenbergite. In the vitrophyres the pyroxene zones from Wo_{20} to Wo_{45} along a line of constant Fs content, then decreases to Wo_{35} with constant En-content (Fig. 4). There may also be a second low-Ca pyroxene (Beaty and Albee, 1978) in the vitrophyres,

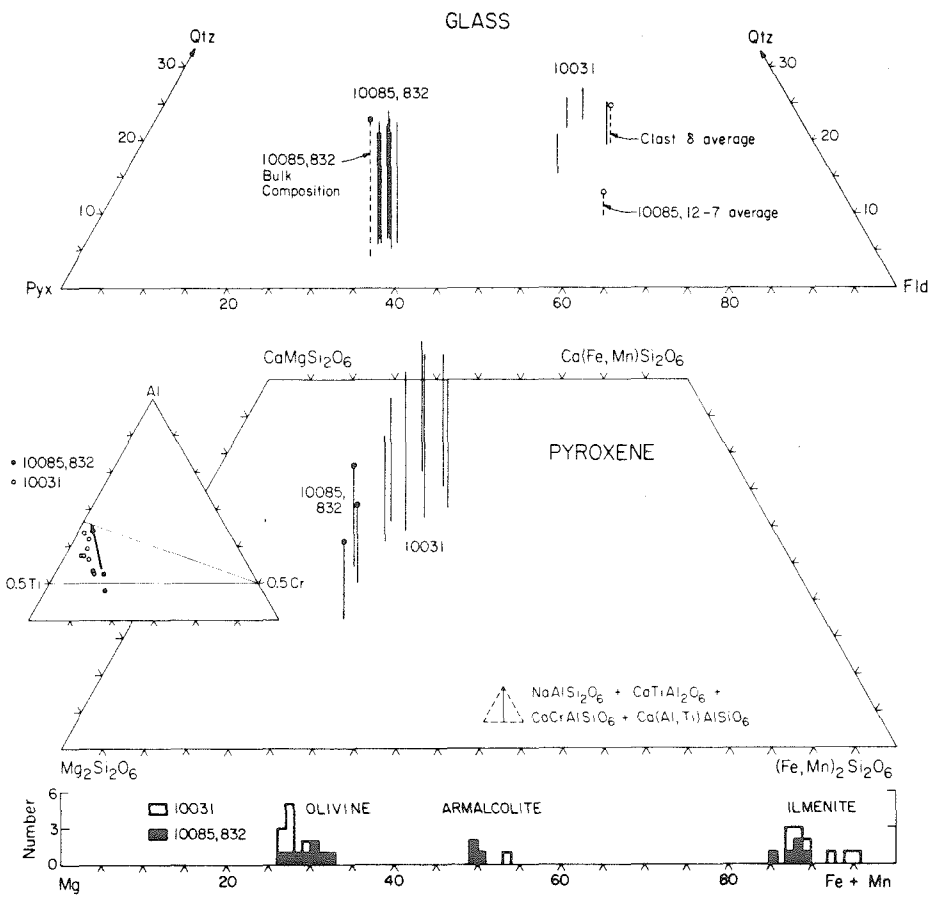

Fig. 3. Compositions of pyroxene, olivine, armalcolite, ilmenite and glass in high-K vitrophyres 10031 and 10085,832. Shown for comparison are the glass and quenched groundmass in clast δ and 10085,12–7, respectively (Beaty and Albee, 1978), and the bulk composition of 10085,832.

Table 3. 10085,832: Mode, average phase compositions and bulk composition.

2163 pts.	Mesostasis	Pyroxene	Olivine	Ilmenite	Armalcolite	
Vol. %	91.61	1.35	3.18	3.75	0.11	Area = 8.04 mm^2
σ (SDM)	2.00	0.74	0.35	0.77	0.08	ρ calc = 3.21
ρ	3.13	3.40	3.52	4.65	4.64	
Wt. %	89.33	1.43	3.39	5.43	0.16	Bulk
σ (SDM)	1.95	0.78	0.38	1.12	0.12	Comp.
P_2O_5	0.21					0.19
SiO_2	43.78	49.78	38.17	0.11	0.12	41.16
TiO_2	10.00	2.76	0.27	52.51	73.83	11.95
Al_2O_3	8.79	2.23	<.01	<.01	1.55	7.89
Cr_2O_3	0.24	1.00	0.16	0.76	2.18	0.28
MgO	6.68	19.78	35.74	2.83	7.85	7.64
CaO	11.57	10.60	0.30		<.01	10.50
FeO	17.76	12.76	26.73	42.44	13.57	19.35
MnO	0.23	0.70	0.21	0.30	.04	0.24
Na_2O	0.38	0.05				0.34
K_2O	0.30					0.27
BaO	0.12					0.11
ZrO_2	0.07			0.08	0.10	0.07
V_2O_5					0.15	
Nb_2O_5				<.01		
NiO	0.01		<.01			<.01
S	0.01					0.01
Σ	100.08	99.64	101.58	99.03	99.39	100.00
	Qtz 5.9	Wo 17.2	Fa 29.7		Gi 10.6	
	Fd 28.3	En 52.3	$Fo_{70.3}$		Ilm 89.4	
	Px 50.2	Fs 20.0				
	Oth 15.6	Oth 10.5				

but it is much less abundant (<1% vs. 10–20%). The vitrophyric pyroxene also shows well developed zoning towards Al on an Al, Ti, Cr plot (Fig. 4), whereas in the crystalline samples the low-Ca pyroxenes fall in a field below the 0.5 Ti–0.5 Cr join (Fig. 4), the high-Ca pyroxenes lie above that join, and zoning (away from Cr) is typically indefinite. The most magnesian olivine in the vitrophyres is Fo_{74-72} (Fig. 4), while in the crystalline rocks it is almost invariably Fo_{70}, despite indistinguishable bulk Fe/(Fe + Mg) ratios. Ilmenite ranges up to Gi_{14} in the vitrophyres (Fig. 4), but up to Gi_{20} in the crystalline rocks.

The fact that the parent magmas for the two suites have the same bulk chemistry and nevertheless crystallized minerals of different compositions indicates that the physical conditions of crystallization were different. The differences in mineral composition may indicate that the vitrophyres crystallized at higher temperatures than the crystalline rocks. Alternatively, the differences observed may have been caused by undercooling or other kinetic effects concerning crystal nucleation and growth. Whatever the cause, these two rock types contain signif-

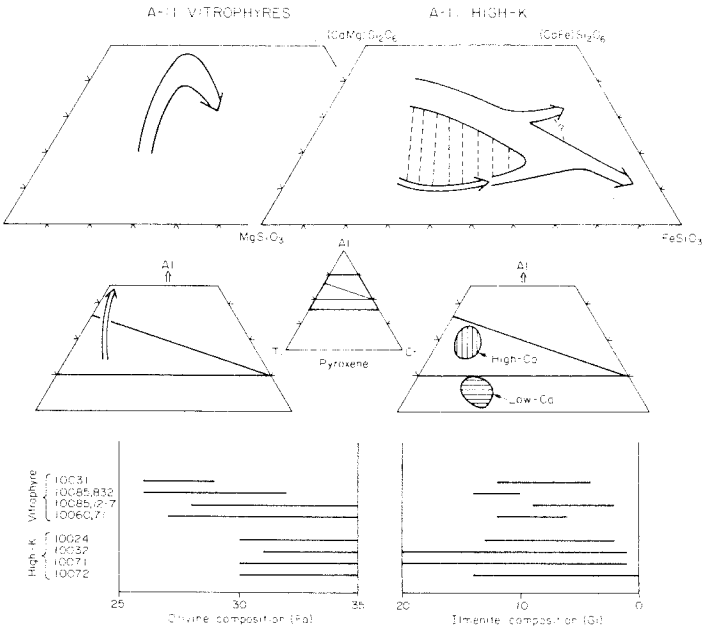

Fig. 4. Summary of the petrologic differences between the high-K crystalline samples and the high-K vitrophyres. Pyroxene, olivine and ilmenite all have different compositions in the two suites. Plagioclase is present in the crystalline samples, but is quenched in the glass in the vitrophyres.

icant petrologic differences which are not simply related to the difference in cooling rates.

Because of their chemical similarities, the parental magmas were probably produced in the same source region. Beaty and Albee (1978) suggested that the crystalline samples were produced by successive eruptions of a differentiating magma chamber. The vitrophyres could not have been produced from the crystal-rich cumulate portions of this chamber, because such a phenocryst-charged magma would no longer have the common bulk composition. It seems most plausible that the vitrophyres represent a second aliquot of magma generated by the high-K source region, which partially crystallized at depth, and was then rapidly erupted to the surface.

V. GROUP B2 (LOW-K, INTERMEDIATE-LA)

Three of the 24 basaltic fragments (10085,829), 10085,779 and 10029,31) are members of petrologic group B2 (Beaty and Albee, 1978). A detailed study of 10029 was included in Beaty and Albee (1978), so the following discussion deals principally with 779 and 829.

Both samples are medium-grained basalts with small lath-shaped plagioclase (34, 37%, respectively) and larger (to 600 μ), subhedral to euhedral, blocky ilmenite (12, 15%) which is either interstitial to or enclosed by granular, equant pyroxene (49, 45%) (Fig. 5d). The overall texture may therefore be classified intergranular-ophitic. Pyroxene typically shows complex patchy extinction and commonly encloses small, rounded olivine (2, 1%). Accessory mesostasis minerals are cristobalite (2, 1%), apatite, ulvöspinel, troilite and tranquillityite. Troilite typically contains ameoboid Fe-metal inclusions and, although usually interstitial, may be found as inclusions in early formed minerals. The modes and average mineral compositions of these samples determined by the electron microprobe point count are listed in Table 4.

Several features serve to distinguish these samples from the other low-K "peanuts" and to classify them with Group B2 of Beaty and Albee (1978). 829 and 779 have blocky ilmenite and small, mantled olivine (Table 4), instead of the platy to anhedral ilmenite and olivine phenocrysts of Group B3.

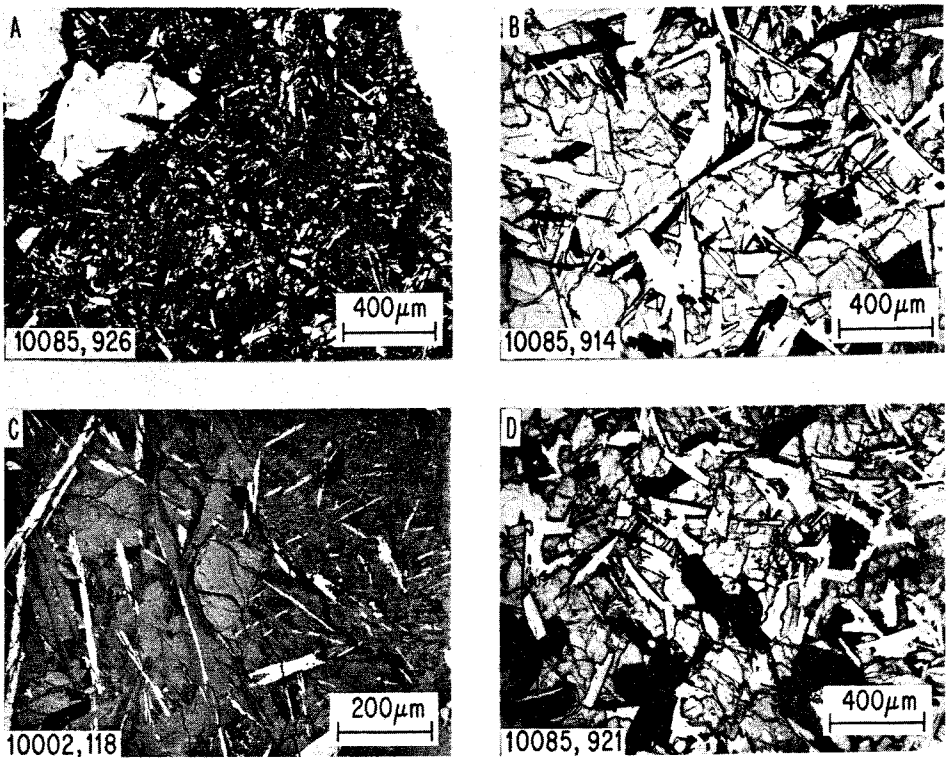

Fig. 5. Photomicrographs of Groups B2 and B3. (a), (b), (d) are in transmitted light at the same scale for comparison. 10085,847(926) and 10085,775(914) are the finest- and coarsest-grained B3 samples, respectively. The large white crystal in 926 is an olivine phenocryst. Other minerals visible in 926, 914 and 921 are ilmenite (black), pyroxene (grey, fractured) and plagioclase (white laths). 914 and 921 can be classified B3 and B2, respectively, on the basis of ilmenite morphology and olivine size, as well as mineral chemistry. (c) Reflected light view of 10002,113(118) illustrating the two textural domains. On the left are coarse, equant olivine and pyroxene (grey), large bladed ilmenites (white) and plagioclase laths (dark). On the right, pyroxene, plagioclase and ilmenite occur as a very fine-grained intergrowth.

Table 4. Apollo 11 low-K basaltic fragments: Petrologic summary.

	B3									
Rock number	10085,847		10002,113		10085,839		10085,844		10085,775	
Thin section	10085, 926	σ (SDM)	10002, 118	σ (SDM)	10085, 924	σ (SDM)	10085, 925	σ (SDM)	10085, 914	σ (SDM)
Plagioclase	33.47	1.87	31.51	1.52	32.71	2.06	34.04	3.15	29.68	1.34
Pyroxene	44.95	2.75	49.49	1.85	38.02	1.68	50.99	2.28	50.09	1.93
Ilmenite	12.43	1.08	12.52	1.29	13.68	1.26	11.56	1.56	12.20	1.43
Cristobalite	3.17	0.41	3.38	0.40	4.29	0.41	2.43	0.34	1.83	0.26
Mg-olivine	5.16	2.63	2.21	1.25	10.25	2.08	absent		4.64	0.88
Fayalite	<.03	—	<.02	—	<.02	—	0.01	0.01	<.02	—
Troilite	0.43	0.15	0.50	0.15	0.26	0.10	0.42	0.14	0.37	0.12
Phosphate	0.06	0.06	0.06	0.05	0.09	0.06	0.10	0.07	0.18	0.08
Ulvöspinel	<.03	—	<.02	—	0.05	0.04	<.02	—	<.02	—
Glass[1]	<.05	—	0.27	0.11	0.08	0.05	0.43	0.14	0.27	0.10
Cr-spinel	0.26	0.12	0.05	0.05	0.45	0.13	absent		0.72	0.16
Fe-metal	0.06	0.06	<.02	—	0.03	0.03	<.02	—	0.01	0.01
Others[3]	—				—		—		—	
Phase chemistries										
Ave. Plag (An)	83.9		81.1		85.2		85.4		87.2	
Ave. Px Wo	26.5		27.5		28.0		28.2		21.7	
En	35.4		35.7		35.7		35.1		40.7	
Fs	30.8		28.5		28.4		28.7		30.0	
Other	7.3		8.3		7.9		8.0		7.6	
Ave. Mg-ol (Fo)	72.0		70.3		69.0		absent		67.3	
Ave. Ilm (Fe)	92.4		92.4		91.5		96.8		92.8	
% Pyx[2] Lo Ca	2.4		0.9		1.9		0.8		10.2	
Augite	53.3		64.8		58.7		61.4		49.8	
MedFe	37.7		26.9		34.2		30.3		32.6	
HiFe	6.6		7.3		3.8		7.3		7.0	
Ferrohed	—		0.1		1.4		0.2		0.2	
Petrography										
Texture	porphyritic, intergranular						intergranular-ophitic			
Max plag ⊥ (010) (μm)	10		40		50		60		180	
Ilm morphology	platy		platy		platy-		platy		anhedral	
Olivine morphology	phenocryst		phenocryst		anhedral phenocryst		absent		phenocryst	

[1] We can detect only relatively coarse potassic glasses with this technique, so this value is unreliable. For example, by optical inspection 10085,926 has as much or more glass than 10085,925.

[2] Pyroxenes were subdivided along lines of constant Fa content: augite < Fs_{30}; MedFe < Fs_{60}; HiFe > Fs_{60}. LoCa Pyx is < Wo_{15}, and ferrohed is < En_{10} and > Wo_{33}.

[3] 10029,918,121, and 923 contain 0.10, 0.10,0; 0.25, 0.04,0; 0.17, 0.04, 0.01; and 0.18, 0.08, 0.02, respectively, of modal K-spar, tranquillityite and rutile.

Table 4. *(Continued)*

B2						D					
10085,779		10085,829		10029		10085, 808		10002,116		10085,836	
10085, 779	σ (SDM)	10085, 921	σ (SDM)	10029, 42	σ (SDM)	10085, 918	σ (SDM)	10002, 121	σ (SDM)	10085, 923	σ (SDM)
34.44	2.13	37.03	1.95	41.03	1.92	34.73	4.10	31.74	2.00	30.00	2.54
49.05	2.15	44.92	1.59	42.98	1.97	52.30	4.18	49.53	2.52	52.36	3.20
11.92	1.19	15.26	2.31	13.67	1.82	5.68	0.96	12.40	1.30	11.54	2.17
1.76	0.44	1.01	0.29	0.20	0.14	1.35	0.42	3.84	0.67	3.88	0.77
1.97	0.54	0.81	0.39	0.69	0.26	3.65	1.65	0.28	0.10	0.20	0.10
<.02	—	<.02	—	<.05	—	0.03	0.03	0.07	0.05	0.01	0.01
0.31	0.12	0.53	0.16	0.39	0.20	0.09	0.06	0.31	0.10	0.35	0.13
0.28	0.11	0.29	0.12	0.30	0.17	0.36	0.12	0.72	0.16	0.55	0.17
<.02	—	<.02	—	<.05	—	<.02	—	0.02	0.02	0.08	0.06
0.28	0.11	0.11	0.07	0.45	0.21	0.60	0.15	0.63	0.15	0.64	0.18
absent		absent		absent	—	0.90	0.19	0.09	0.05	0.10	0.07
<.02	—	0.05	0.05	<.05	—	0.04	0.04	0.07	0.05	<.05	—
				0.20		0.29		0.28		0.28	
88.0		87.7		88.9		88.6		87.1		87.1	
24.3		21.2		22		20.4		22.9		24.0	
39.8		39.7		39		43.1		39.6		38.8	
27.9		33.2		34		30.8		30.6		31.2	
8.0		5.9		5		5.7		6.9		6.0	
57.4		57.4		32		62.0		60.3		62.0	
90.7		88.0		97		97.2		97.2		97.9	
8.2		15.6		16.6		26.7		12.9		11.1	
60.3		27.7		30.1		38.0		47.9		49.8	
26.8		61.9		47.2		29.3		30.6		29.2	
4.6		1.8		6.7		5.8		8.6		10.0	
—		—		—		0.1		—		—	
intergranular-ophitic				ophitic		intersertal-ophitic					
60 blocky small, mantled		60 blocky small, mantled		100 blocky small, mantled		40 anhedral large, mantled		120 anhedral small, mantled		110 anhedral small, mantled	

All values (except petrography) were determined by automated eletron microprobe point count, using 2000–3000 points per sample. σ (SDM) is the standard deviation of the mean, a statistical parameter which describes the uncertainty in an infinite population (lava flow) based on measurements of a finite subset (thin section). The mode of each thin section alone is much more precise than σ (SDM).

Furthermore, the average plagioclase is more calcic (An_{88}), the average pyroxene is more magnesian (En_{40}) and less calcic (Wo_{21-24}), the average olivine is more Fe-rich (Fo_{57}), the average ilmenite (Gi_{10-12}) is more Mg-rich and early Cr-spinel is missing (Table 4). Chemically, the B2 samples have distinctly higher La/K (Fig. 1).

Discussion

The addition of 10085,779 and 10085,829 brings to four the number of samples in Group B2 (Table 1). Because of the close similarities of these rocks, they are assumed to come from the same lava flow. Thus examination of the detailed differences between these samples allows an evaluation of the physical processes which have operated during crystallization. Three factors have been identified which control the differences between samples: (1) different cooling rates, (2) crystal fractionation and, (3) sample inhomogeneity.

Several lines of evidence indicate that 779 and 921 have undergone similar cooling rates which were faster than those for 10003 and 10029. These samples coarsen in the order 779≈921<10003<10029. The amounts of Al, Ti, Na and Cr in the augite decrease in the same order, as do the modal abundances of the incompatible pair olivine and cristobalite. Each of these properties is known to correlate with cooling rate (Beaty and Albee, 1978). The pyroxenes show an increase in the extent of fractional crystallization with slower cooling, along with an increase in the amount of low-Ca pyroxene (Table 4). This is related to the kinetics of pyroxene formation and both effects are well known among experimental petrologists (Grove, pers. comm., 1979).

The principal modal difference between these four samples lies in the amount of ilmenite, which increases from 11.9% to 15.8% in the following order: 779< 10003<921<10029. Ilmenite is a dense, early crystallizing phase which, along with olivine and Cr-spinel, might be expected to sink. The amount of normative olivine, however, is similar in all four samples, and Cr-spinel is essentially absent. This apparent fractionation of ilmenite, but not olivine, can be related to the texture. Ilmenite is relatively large and equant (Fig. 5d), the most favorable shape for settling, whereas olivine is much smaller. Using the average mineral sizes present in 10029, Stokes law calculations indicate that 200 μm ilmenite will settle about 11 times as fast as 100 μm olivine. Point count data on two thin sections each of 10029 and 10003 (Table 4; Beaty and Albee, 1978, Tables A1, A6) indicate that some of the variation takes place on the scale of a hand sample. This may reflect sample inhomogeneity.

VI. GROUP B3 (LOW-K, LOW-LA)

Five "peanuts" (Table 1) belong to Group B3 of Beaty and Albee (1978). All contain olivine phenocrysts, platy ilmenite and have either intergranular or intergranular-ophitic textures (Table 4).

Group B3 basalts range from very fine-grained (maximum plagioclase width = 10 μm) to relatively coarse-grained (maximum plagioclase width = 180 μm) (Table 3) in the order: 10085,847<10002,113<10085,839≈10020≈10045≈10092<10085,844<10085,775. As grain size progressively coarsens, the general texture becomes more ophitic, ilmenite morphology becomes more equant and anhedral and olivine is increasingly resorbed (Fig. 5a, b).

With the exception of 10085,844, these samples contain high modal olivine (2–10%) and early Cr-spinel. Average olivine is magnesian (Fo_{67-72}), average plagioclase is relatively sodic (An_{81-87}) and the pyroxene (except for 10085,775) contains a low proportion of low-Ca pyroxene (0.8–2.4%) (Table 4). The B3 group contains much less La at similar K_2O than B2, but similar La/K to the high-K rocks (Fig. 1). The modes, average mineral compositions and key petrographic features of these rocks are tabulated in Table 4.

Two samples exhibit distinctive features. 10085,844 has a xenolith occupying about 20% of the thin section area (see Beaty *et al.*, 1979a). This has been partially digested by the melt and may account for an unusual feature of 10085,844—its absence of olivine.

Sample 10002,113 has a distinctive porphyritic texture and appears to have undergone a two-stage cooling history. Like the other B3 samples it has large, euhedral olivine phenocrysts, but it also has large ilmenite (20 × 400 μm) and plagioclase (30 × 300 μm) laths which form a loose network (Fig. 5c). Partially enclosing this network are coarse equant pyroxene (200 μm). The total abundance of phenocrysts is about 30–40%. Between these large crystals is a very fine-grained intergrowth of pyroxene (10–20 μm), anhedral poikilitic plagioclase (50 μm) and ilmenite (3 × 50 μm) (Fig. 5c). All three major minerals show a bimodality of grain size, as well as a textural change. Groundmass ilmenite platelets grow perpendicularly away from the olivine phenocrysts, a texture also found in the quench ilmenite of 10031, a vitrophyre. Petrologically the groundmass is easily distinguished from the phenocrysts (Fig. 6). Pyroxene phenocrysts zone from $Wo_{33}En_{48}Fs_{19}$ to $Wo_{39}En_{40}Fs_{21}$ from core to rim, while the groundmass pyroxenes are more Fe-rich. The groundmass pyroxene also contains less Cr relative to Al and Ti than the phenocrysts (Fig. 6, inset). Plagioclase phenocrysts zone from An_{87}–An_{83} while the groundmass zones from An_{83}–An_{81}. The compositions of olivine, Cr-spinel and ilmenite are also shown on Fig. 6 and are similar to those from the other B3 samples.

Discussion

The petrological variations among the B3 samples (Beaty and Albee, 1978; this work) formed in response to differences in both cooling rate and bulk composition (due to crystal-liquid fractionation). By evaluating each of these processes in detail, it is possible to reconstruct the hypothetical B3 lava flow.

A useful index of *cooling rate* is the sample grain size, a parameter which has been quantified in Table 4 by the maximum plagioclase size measured perpendicular to (010) (Grove and Walker, 1977; Walker *et al.*, 1978). With increasing plagioclase size, the average olivine becomes more Fe-rich, and the plagioclase more calcic (Table 4). This can be related to more extensive equilibration with the late-stage liquids and decreased undercooling, respectively. Furthermore, the amount of pigeonite increases with decreased cooling rate. This is a response to the increased resorption of olivine in the more slowly cooled samples, which causes their average pyroxene to be less calcic (Table 4; Beaty and Albee, 1978, Table 2). On the other hand, the average ilmenite and pyroxene compositions vary independently of grain size.

To evaluate the effects of *fractionation,* the petrology must be compared to the bulk compositions. Chemically, the eight Group B3 samples lie on a mixing line

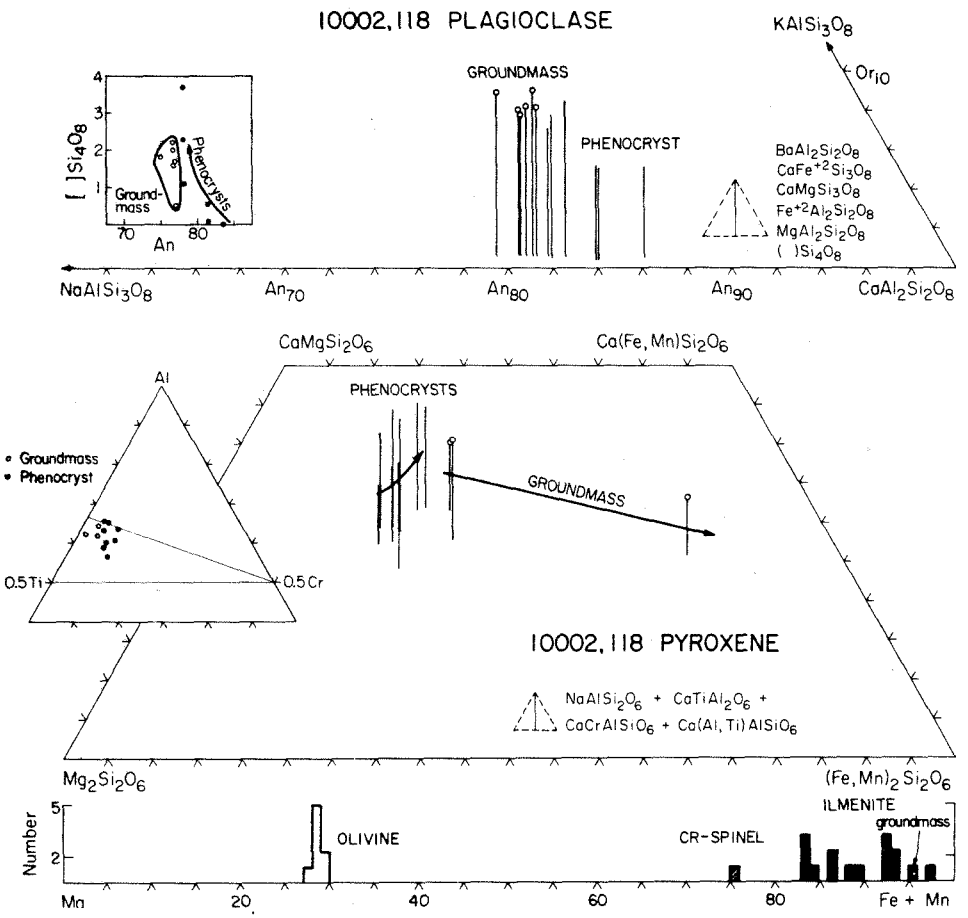

Fig. 6. Composition of pyroxene, olivine, plagioclase, spinel and ilmenite in Group B3 sample 10002,113(118). Note the differences in composition between the phenocrysts and groundmass.

between 10085,775 and 10085,844 (Table 5; Beaty and Albee, 1978, Table 3). 10085,775 is the most primitive of the suite, while 10085,844 is the most differentiated. Least squares analysis indicates that 844 can be derived from 775 through removal of 9 ± 1% olivine, 1 ± 1% Cr-spinel and 2 ± 1% ilmenite. This fractionation series has affected some aspects of the petrology. With increasing bulk Fe/(Fe + Mg) the average pyroxene and average ilmenite both become more Fe-rich, modal plagioclase increases and modal Cr-spinel decreases (Table 4). An important test of a fractionation model such as the above involves comparing the most magnesian olivines (as opposed to the average olivine discussed above).

The most magnesian olivine in each of the eight samples is Fo_{74-73}. This olivine

is in equilibrium with a bulk composition with Fe/(Fe + Mg) ≃ 0.56–0.57 (see Beaty and Albee, 1978, Fig. 10). The most primitive rocks (0.53), therefore, are too magnesian to be in equilibrium with their olivine phenocrysts. This, combined with the constant olivine composition, indicates olivine fractionation, in agreement with the bulk compositional data. Although Cr-spinel accompanies olivine, the amount of ilmenite fractionation is insignificant. As in Group B2, this style of differentiation can be related to the textures of the rocks. Using the average mineral sizes in 10020 (see also Figs. 5a, b, c), Stokes law calculations indicate that olivine (500 μm) will settle about five times as fast as ilmenite (500 × 10 μm). In contrast to B2, which is dominated by ilmenite fractionation, B3 is controlled by olivine fractionation. In summary, the textural, petrologic and chemical variations present are consistent with the hypothesis that the eight B3 samples were derived from a single lava flow.

Because of the range in composition and the relatively large number of B3 samples, it is possible to make a detailed reconstruction of the B3 flow (using the same arguments advanced by Walker *et al.* (1976) for the Apollo 12 olivine basalts). The coarsest samples are those with both low and high Mg values, whereas the samples with intermediate compositions are the finest-grained (Fig. 7). This suggests that the finest-grained sample, 10085,847, most closely approximates a liquid composition. This agrees with the olivine data: Fo_{73-74} phenocrysts are in equilibrium with the bulk composition of 10085,847 (Fe/(Fe + Mg) = 0.56). 847, therefore, is most likely a sample of the rapidly cooled surface or base of a lava flow. Samples with higher Fe/(Fe + Mg) represent the depleted upper portions of a differentiated magma body, while the rocks with lower Fe/(Fe + Mg) have sampled the complimentary basal cumulates, both of which have cooled more slowly.

VII. GROUP D (LOW-K, HIGH-LA)

The remaining three basaltic fragments do not fall into the subdivisions reported by Beaty and Albee (1978), nor do they correspond to the unclassified samples 10050 and 10062. In particular, they can be optically distinguished from the Apollo 11 high-K suite by the presence of early Cr-spinel, high modal olivine, low modal ilmenite, and lath-shaped plagioclase, and from the low-K suite by the intersertal texture and the late position of plagioclase in the paragenetic sequence. Chemically, they are low-K and high-La, a property they share with no other lunar samples. There are no significant differences between 10002,116 and 10085,836 either chemically, texturally, or in their mineral chemistry, so one description is sufficient for the two samples. 10085,808, however, is different in a number of ways. The modes and average mineral compositions of these three samples are summarized in Table 4.

10002,116(121): The sample is medium-grained (ave. size ≈500 μm), inequigranular, hypidiomorphic and essentially holocrystalline, with an intersertal to subophitic texture similar to that found

Table 5. Apollo 11 low-K basaltic fragments: Compositional summary.

	B3									
INAA chip	10085,847		10002,113		10085,839		10085,844		10085,775	
Section[1]	10085,926		10002,118		10085,924		10085,925		10085,914	
Wt. %	Pt. Ct	INAA	Pt. Ct	INAA	Pt. Ct	INAA	Pt. Ct	INAA	Pt. Ct	INAA
P_2O_5	.03		0.03		0.04		0.04		0.07	
SiO_2	40.40		40.97		39.14		41.07		39.98	
TiO_2	10.23	10.0	10.44	9.7	11.16	9.1	9.87	9.8	10.21	9.9
Al_2O_3	10.13	10.8	9.84	9.5	9.97	10.2	10.86	11.3	9.57	9.1
Cr_2O_3	0.41	0.300	0.40	0.266	0.45	0.384	0.32	0.228	0.63	0.494
MgO	8.19	7	7.70	7	9.06	9	6.69	7	9.46	9
CaO	11.21	11.5	11.92	11.1	10.53	11.0	12.94	12.5	10.46	10.9
FeO	18.74	19.4	17.81	19.5	19.07	20.2	17.53	18.5	19.31	18.0
MnO	0.24	0.276	0.24	0.248	0.25	0.278	0.24	0.273	0.29	0.255
Na_2O	0.47	0.351	0.52	0.396	0.42	0.373	0.45	0.440	0.33	0.326
K_2O	0.04	0.053	0.07	0.073	0.04	0.053	0.06	0.085	0.04	0.046
S	0.22		0.25		0.13		0.21		0.18	
	100.31		100.19		100.26		100.30		100.53	
Barth-Niggli norm (cation %)										
Qtz	0.03		1.35		—		1.37		—	
Oliv.	—		—		3.24		—		2.63	
Fe/(Fe+Mg)	.562		.565		.541		.595		.534	
ppm (INAA)										
Sc	86		103		88		99		80	
V	95		85		103		72		136	
Co	17		14		19		12		16	
Zr	—		—		210		420		—	
Ba	150		120		100		130		60	
La	7.9		9.3		8.3		8.8		6.1	
Ce	29		36		30		37		25	
Nd	28		36		29		39		23	
Sm	9.0		13.4		9.7		14.2		7.9	
Eu	1.63		2.31		1.68		2.62		1.30	
Tb	2.0		2.9		2.2		3.2		1.8	
Dy	14		20		15		20		12	
Yb	8.3		11.5		8.8		11.5		7.6	
Lu	1.25		1.64		1.31		1.58		1.18	
Hf	6.7		9.7		7.4		9.6		5.5	
Ta	1.4		2.0		1.7		2.3		1.3	
Th	—		—		—		—		—	
Wt. (mg)[2]	27		84		55		15		165	
Area (mm^2)[3]	4.1		8.1		5.7		2.7		16.3	

[1] Excepting 10029, the thin section used in the point count was prepared from the same chip used for INAA. 10029,17 was point counted by Beaty and Albee (1978).

[2] Weight of INAA chip.

[3] Surface area of thin section point counted.

Table 5. *(Continued)*

B2						D						
10085,779 10085,779		10085,829 10085,921		10029,31 10029,17		10085,808 10085,918		10002,116 10002,121		10085,836 10085,923		INAA
Pt. Ct	INAA	Pt. Ct	INAA	Pt. Ct	INAA	Pt. Ct	INAA	Pt. Ct.	INAA	Pt. Ct	INAA	Errors (%)
0.12		0.12		0.09		0.15		0.28		0.21		
40.40		38.14		37.89		44.04		41.19		40.73		
9.97	9.1	11.84	9.5	12.15	10.6	5.46	10.0	10.27	8.6	9.74	6.7	<5
11.03	11.7	11.07	11.1	10.32	10.9	10.91	10.8	9.92	11.8	9.57	11.6	<5
0.42	0.204	0.34	0.226	0.27	0.222	0.52	0.389	0.42	0.301	0.39	0.297	<5
8.22	7	7.39	6	7.53	7	9.99	7	7.58	8	7.71	7	10–20
11.99	12.1	10.67	11.2	10.47	9.9	11.50	11.2	11.44	11.5	11.59	11.9	5–10
17.19	19.4	19.37	20.7	20.49	20.1	16.52	20.6	18.22	19.0	19.67	18.0	<5
0.25	0.263	0.24	0.268	0.23	0.250	0.24	0.275	0.28	0.249	0.27	0.252	<5
0.38	0.394	0.40	0.404	0.39	0.382	0.36	0.370	0.38	0.367	0.34	0.398	<5
0.04	0.052	0.04	0.047	0.03	0.041	0.08	0.091	0.08	0.090	0.07	0.080	5–20
0.16		0.26		0.23		0.04		0.16		0.17		
100.20		99.88		100.09		99.84		100.25		100.47		
0.21		0.15		—		—		2.61		0.55		
—		—		1.09		3.11		—		—		
.540		.595		.604		.481		.574		.589		
80		84		79		77		76		81		
64		76		77		89		100		102		10–15
13		14		13		20		15		15		<5
320		280		300		630		320		500		30–40
130		130		90		220		160		230		10–35
16.2		16.4		12.3		32.8		32.5		34.1		<5
53		50		38		98		88		93		10–30
45		45		32		81		68		77		20–25
14.9		15.3		11.1		24.6		21.5		23.7		<5
1.83		1.85		1.81		2.02		1.91		1.85		5–10
3.4		3.3		2.5		4.9		4.6		4.7		10–15
23		22		17		32		31		32		10–20
11.6		12.0		9.3		17.0		16.0		17.3		<5
1.72		1.81		1.35		2.48		2.23		2.47		5–10
9.7		9.9		9.3		13.0		12.3		12.4		5–10
1.7		1.7		1.7		1.6		1.8		1.8		5–10
—		—		—		2.3		3.1		2.1		10–15
62		55		227		26		187		41		
7.0		8.1		93[1]		5.3		19.1		7.7		

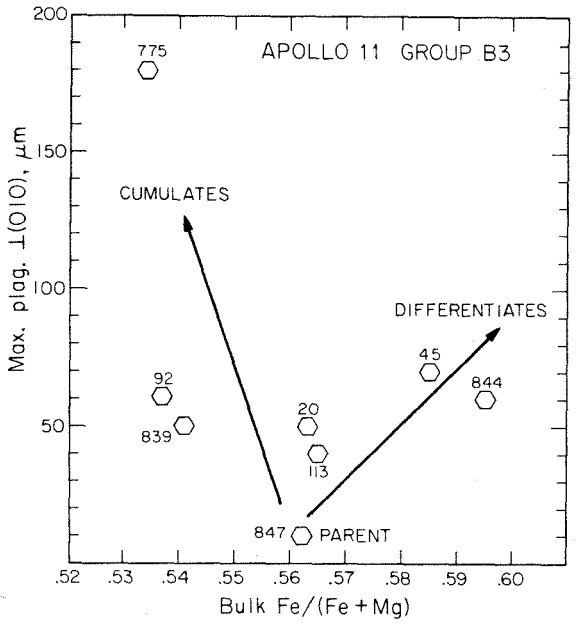

Fig. 7. Inferred cooling rate vs. bulk Fe/(Fe + Mg) for the eight B3 samples. The data are consistent with these samples having been derived from a single lava flow, with 10085,847(926) representing the original liquid composition, and the others having undergone minor gain or loss of olivine.

in the coarser-grained Apollo 11 high-K basalts. Smaller plagioclase laths (32%) are segregated and clumped interstitial to the much larger pyroxene grains (50%) (Figs. 8a, b). Ilmenite (12%) occurs as large, anhedral, equant grains which have lobate intergrowths with plagioclase and pyroxene (Figs. 8a, c). Olivine (0.3%) is present as embayed, partially resorbed grains mantled by pyroxene. Spinel (0.1%) is commonly also enclosed by pyroxene (and rarely by olivine), and where it contacts the mesostasis areas, a rim of ilmenite has developed. Cristobalite (4%) is confined to the plagioclase segregations, as are the minor phases—ulvöspinel, apatite, fayalite, troilite, Fe-metal, baddelyite, tranquillityite, K, Ba-feldspar and two immiscible glasses. One perfectly spherical and one subrounded vesicle are present in 10002,121 (Fig. 8a).

Pyroxene is pale brown and zones from augite ($Wo_{26}En_{41}Fs_{18}Oth_{15}$) and pigeonite ($Wo_{14}En_{60}Fs_{25}Oth_6$) along both branches of the two pyroxene field to pyroxferroite ($Wo_{14}En_1Fs_{83}Oth_2$) (Fig. 9). Some grains have optically distinct pigeonite cores, suggesting that initial growth of the low-Ca branch preceeded that of the high-Ca branch. The pyroxferroite is not optically discontinuous, and the breakdown reaction pyroxene → fayalite + SiO_2 + ferrohedenbergite can be observed. Al_2O_3 content ranges up to 3.6% and TiO_2 up to 2.9%, and the relative proportions of Al, Ti and Cr (Fig. 9) indicate zoning away from Cr.

Olivine zones from Fo_{70} to Fo_{54} (Fig. 9) with the measured average being Fo_{60}. Minor late-stage fayalite is also present. Cr, Ti, Ca and Mn are trace constituents (0.1–0.4%), whereas Al and Ni are typically low (<.05%).

Plagioclase is typically lath-shaped with an average grain size of 40 × 300 μm. Compositional zoning is from $An_{90}Ab_7Or_0Oth_3$ to $An_{68}Ab_{20}Or_5Oth_7$ (Fig. 9), with excess silica increasing sympathetically from 0 to 4% (Fig. 9). The presence of 0.2% K, Ba-feldspar ($Or_{78}Ab_4Cn_{12}Oth_6$) indicates late-stage entry into the two feldspar field.

Ilmenite is blocky and subhedral with an average grain size of about 700 μm. Individual grains are not zoned, but intergranular variation spans the range Gi_{10}–Gi_0 (Fig. 9). Early Cr-spinel (Fig. 9) has a composition of $Ulv_{57}Chr_{30}Her_{13}$ and zones to $Ulv_{63}Chr_{24}Her_{11}$. Late-stage ulvöspinel has a slight range in composition, but averages $Ulv_{94}Chr_2Her_4$. Analyses of each of these minerals along with the calculated bulk composition of 10002,116(121) are listed in Table 6.

10085,808(918): Our point count and petrographic data indicate that 10085,808 is different from 10002,116 and 10085,836. Texturally, 808 is finer-grained (average ≈300 μm, Fig. 8d), and has more olivine (3.7%), Cr-spinel (0.9%) and less cristobalite (1.4%). The pyroxene and plagioclase zoning trends are identical to those in 10002,116, but the olivine zones from Fo_{67}–Fo_{52}, (vs. 70–54), the ilmenite from Gi_{15}–Gi_0, (vs. 10–0), and the Cr-spinel is more Fe-rich. In addition, average plagioclase is measurably more calcic ($An_{88.6}$ vs. $An_{87.1}$), and the average pyroxene is more magnesian ($En_{43.1}$ vs. $En_{39.6}$, Table 4). 10085,808, therefore, is both more rapidly cooled and petrologically more primitive than 10021,121. A final difference is that all of our phosphate analyses from 808 are whitlockite, whereas those from 116 and 836 are fluorapatite.

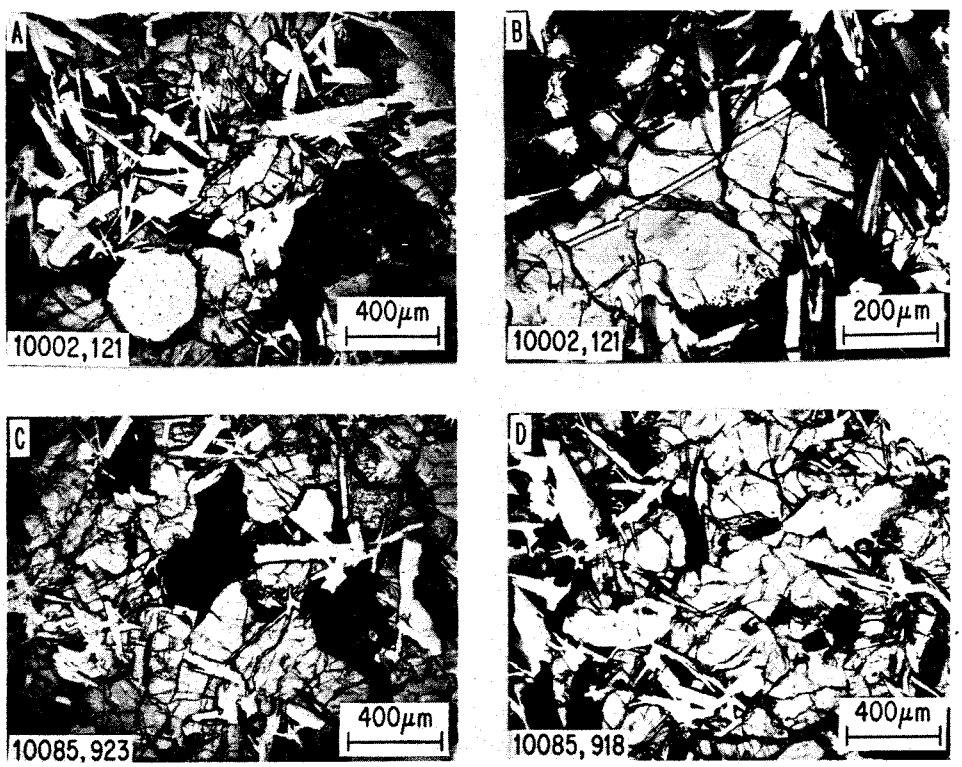

Fig. 8. Photomicrographs of the three Group D samples. (a), (c), (d) are in transmitted light at the same scale for comparison. Three minerals are visible: ilmenite (black), pyroxene (grey), plagioclase (white laths). Note the rounded vesicle in 10002,116(121). Large ilmenite size and plagioclase segregations (a, c) account for the inhomogeneity of these chips. (b) Segregation of plagioclase laths around a large, twinned pyroxene; crossed polars.

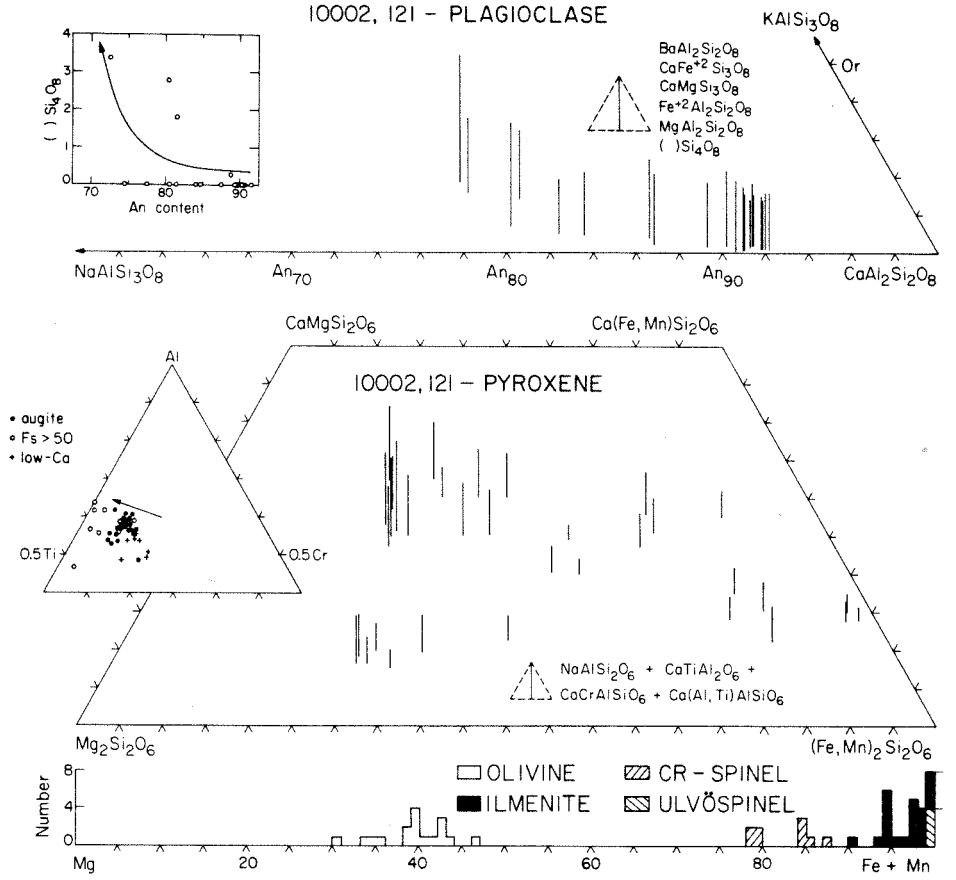

Fig. 9. Composition of pyroxene, olivine, plagioclase, spinel and ilmenite in Group D sample 10002,116(121).

Paragenetic sequence: The inferred crystallization history of these samples is as follows. Either olivine or Cr-spinel was the liquidus phase. In 116 and 836, olivine then reacted to form pyroxene. Pigeonite cores are present in some pyroxenes, so first one, then two pyroxenes and spinel co-precipitated. Ilmenite and plagioclase appear on the liquidus next (~15–20% crystalline) but their relative order is difficult to determine. Sulfide immiscibility occurred at about the time of ilmenite saturation. Cristobalite, the residual phases and immiscible silicate melts all appeared in the final stages of crystallization. In 808, the more rapidly cooled sample, ilmenite began to crystallize just prior to the incoming of pyroxene whereas the other minerals follow the same sequence as in 836 and 116. These interpretations are summarized in Fig. 10, which also shows how the crystallization sequence can be used to distinguish the Apollo 11 basalt types.

Discussion

The three type D samples can be distinguished from the Apollo 11 high-K suite by the presence of early Cr-spinel, high modal olivine, low modal ilmenite and lath-shaped plagioclase and from the low-K suite by the intersertal texture and the late position of plagioclase in the paragenetic sequence. In spite of these differences, our microprobe data indicate that the Group D samples are strikingly similar to the Apollo 11 low-K basalts in many respects. The plagioclase (An_{95}–An_{70}) and pyroxene (two branches to pyroxferroite) zoning trends are identical. The modes (except for ilmenite) and average plagioclase and pyroxene compositions all lie within the range spanned by the low-K samples. This is a reflection of the fact that the major element bulk compositions (except Ti) of the two suites are similar (Table 5). Nevertheless, there are distinctive petrologic differences. The Group D basalts contain from 0.17 to 0.25% K, Ba-feldspar, while the low-K basalts have essentially none. The plagioclase has a higher orthoclase component (up to five mole percent, see Fig. 9) than in low-K basalts. The Group D basalts have two to three times as much phosphate minerals and half as much troilite (Table 4). Finally, the most magnesian olivine and ilmenite are both more Fe-rich than their counterparts in the low-K basalts.

The relationship of the three Group D basalts to one another is less certain. Interpretation is made more difficult by observed sample inhomogeneities and the small sample size. Thin section-scale inhomogeneities can be observed in the distribution of plagioclase, which occurs in millimeter-sized segregations containing a mesostasis matrix, and also in ilmenite, which occurs as large, scattered crystals. For example, INAA gave bulk TiO_2 concentrations of 10.0%, 8.6% and 6.7% for the three samples, whereas the point counts yielded 5.4%, 9.5% and 10.2%, respectively. Both types of measurement are much more precise than the differences observed, indicating an uneven distribution of ilmenite. The point count measurements were made on a section through the samples used for INAA and thus the INAA bulk compositions represent a larger volume.

Considering the inhomogeneous nature and small size of these samples, 116 and 836 are remarkably similar to one another. It seems likely that they are fragments of a larger rock which was shattered by meteorite impact on the lunar surface. Calculations by Shoemaker *et al.* (1970), for example, indicate that the mean lifetime of a 10cm rock in Mare Tranquillitatis is only about 40 m.y. 808, on the other hand, is distinctively more primitive; for example its bulk (Fe/Fe + Mg) is 0.48, as compared with 0.57 and 0.59 for 116 and 836. This agrees with the petrology—808 has more olivine, more Cr-spinel, more calcic average plagioclase and more magnesian average pyroxene. However, 808 is also higher in most of the incompatible elements such as Zr and the REE (Table 5). These conflicting indices of differentiation suggest that 808 is not simply related to 836 and 116 by either crystal-liquid fractionation or by different degrees of partial melting of an identical source. However, the differences are within the bounds suggested by Haskin *et al.* (1977), and, considering the proven inhomogeneities, it is possible that these samples are from the same flow.

Table 6. Mode, average "phase" compositions and bulk composition of 10002,121.

		Pyroxene				Olivine			
(2876 pts)	Plag	LoCa	Augite	MedFe	HighFe	Mg-Ol	Fe-Ol	"SiO_2"	Ilmenite
Vol%	31.74	6.39	23.72	15.16	4.26	0.28	0.07	3.84	12.40
σ (SDM)	2.00	0.91	1.74	1.39	0.74	0.10	0.05	0.67	1.30
ρ	2.74	3.42	3.38	3.51	3.72	3.65	4.35	2.33	4.68
Wt %	26.12	6.56	24.08	15.98	4.76	0.31	0.09	2.69	17.43
σ (SDM)	1.65	0.94	1.76	1.47	0.83	0.11	0.07	0.47	1.83
P_2O_5									
SiO_2	46.70	53.17	49.47	49.71	48.91	36.58	31.23	99.92	0.05
TiO_2	0.10	0.88	2.37	1.27	0.96	0.06	0.08	0.35	53.36
Al_2O_3	33.76	1.02	2.79	1.41	0.58	<.01	<.01	0.80	<.01
Cr_2O_3		0.37	0.80	0.33	0.07	0.06	<.01		0.69
MgO	0.08	21.17	15.92	11.24	4.34	30.18	1.12	<.01	1.56
CaO	17.21	5.68	15.45	12.13	8.36	0.29	0.48	0.19	
FeO	0.69	17.74	12.49	23.13	36.27	35.02	67.19	0.12	44.66
MnO		0.36	0.28	0.56	0.50	0.41	0.88		0.45
Na_2O	1.30	0.02	0.08	0.10	<.01			0.05	
K_2O	0.12							0.02	
BaO	<.01							<.01	
ZrO_2									0.07
V_2O_3									<.01
Nb_2O_5									<.01
NiO						<.01	<.01		
S									
F									
Σ	99.97[2]	100.41	99.65*	99.88*	103.01	102.60	100.98[1]	101.44	100.83
	An 82.9	Wo 9.9.	Wo 27.0	Wo 23.5	Wo 17.2	Fo 60.3	Fo 2.8		Ilm 94.2
	Ab 11.5	En 58.4	En 43.8	En 32.5	En 13.0	Fa 39.7	Fa 97.2		Gi 5.8
	Or 0.7	Fs 28.0	Fs 19.7	Fs 38.5	Fs 66.7				
	Oth 4.9	Oth 3.7	Oth 9.5	Oth 5.5	Oth 3.1				

[1] Data from 10029

* Average of three analyses

[2] Weighted average of two analyses from 10047 and 10029

Also sampled by the point count were 0.01% rutile, 0.03% baddelyite, and 0.03% zircon?

VIII. CHEMISTRY OF THE APOLLO 11 MARE BASALTS

1. Chemical groups

Ma and Schmitt (1979) showed that the Apollo 11 mare basalts can be chemically classified into four groups on the basis of their La and K_2O abundances. The correspondence of these groups to the petrologic groupings is shown in Fig. 1 and Table 1. Petrologic groups A, B1, B2 and B3 were originally recognized by

Table 6. *(Continued)*

		Pyroxene				Olivine		
Cr-Spinel	Glass	K-Spar	Troilite	Apatite	Ulvöspinel	Tranq.		
0.09	0.63	0.17	0.31	0.72	0.02	0.04	Surface area =	
0.05	0.15	0.08	0.10	0.16	0.02	0.04	19.1 mm^2	
4.70	2.65	2.68	4.6	3.2	4.77	4.7	ρ calc = 3.33	
0.13	0.50	0.14	0.43	0.69	0.03	0.06	Bulk	σ
0.07	0.12	0.06	0.14	0.15	0.03	0.06	comp	(SDM)
	0.04			40.38			0.28	0.06
0.07	76.39	61.23		1.45	0.11	14.27	41.19	1.53
23.29	0.45	0.14			31.99	20.59	10.27	0.99
5.80	11.48	20.09		0.04	3.20	0.80	9.92	0.57
20.96	<.01				0.35	0.21	0.42	0.04
4.56	<.01	<.01		<.01	0.05	0.03	7.58	0.40
	1.51	0.18		53.82		0.89	11.44	0.45
45.10	2.31	0.36	63.53	0.96	63.56	44.12	18.22	0.92
0.33	<.01				0.45	0.30	0.28	0.02
	0.46	0.49		<.01		<.01	0.38	0.03
	7.13	12.94					0.08	0.02
	0.60	6.26					0.01	0.01
<.01	0.18				0.34	12.45	0.02	0.01
0.46					0.03			
<.01					<.01			
	<.01							
	0.01		36.47				0.16	0.05
				3.66				
100.57	100.56	101.68	100.00	100.75	100.06	96.98	100.25	
Ulv 59.5	Qtz 39.6	An 0.9		Ce_2O_3 0.70	Ulv 92.2	La_2O_3 <.01		
Chr 28.4	Fld 56.4	Ab 4.5		Cl 0.14	Chr 0.5	Nd_2O_3 0.30		
Her 11.7	Pyx 3.1	Or 77.8		Y_2O_3 0.63	Her 7.2	Ce_2O_3 <.01		
		Cel 11.5		La_2O_3 0.15		Nb_2O_5 0.45		
	Oth 0.9	Oth 4.3		Nd_2O_3 0.39		Y_2O_3 2.57		

Beaty and Albee (1978) in their study of the large Apollo 11 rocks. The fourth group, Group D (low-K, high-La) is a new rock type which was previously unrecognized in the lunar collection. Figure 11 shows that lunar basalts, with the exception of the new low-K high-La Group D and the low-K inter-La Group B2, have similar La to K_2O ratios over nearly two orders of magnitude of concentration. This suggests that the B2 and D magmas were derived from fundamentally different source materials or by fundamentally different processes.

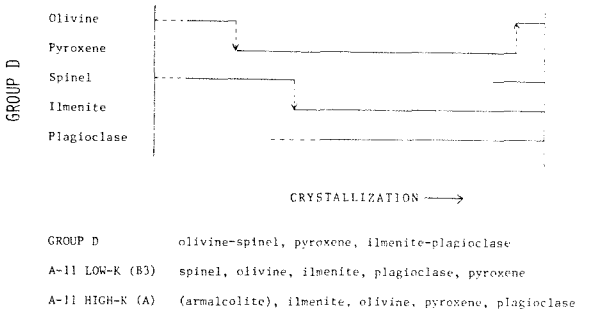

Fig. 10. Inferred crystallization history for the Group D basalts. Shown for comparison are the crystallization sequence for the Apollo 11 low-K (B3) and high-K (A) rocks.

Table 5 lists the bulk chemical compositions of individual samples obtained both by INAA and by microprobe point count. Table 7 shows average abundances of major and minor elements for all of the Apollo 11 basalt types. The composition of the new Group D basalt is closer to that of the other low-K basalts (B1, B2, B3) than to that of the high-K Group A basalts. The K_2O and Al_2O_3 abundances are particularly useful for making this distinction. However, the average TiO_2 content in Group D is lower and the average P_2O_5 is higher than those in any of the other Apollo 11 basalt types.

The Group A (high-K, high-La) basalts are characterized by higher contents of incompatible trace elements (including REE, Hf and Ta) than those in the B groups (Tables 2, 5). Cobalt, an element typically associated with olivine, is also higher in Group A. The variations in V and Cr_2O_3, two geochemically coherent elements, are shown in Fig. 12. A strong positive correlation is present, and the data indicate that the Group A samples have a distinctly lower V/Cr ratio than the B rocks. The high-K vitrophyres have compositions similar to those of the other Group A samples (Table 7), and they probably share a common source region.

Although the Group B1 basalts have higher contents of K_2O, La and P_2O_5 than the B3 basalts, they are generally similar in composition and have similar La/K_2O. The Group B2 samples have REE contents between those of A and B3 and a high La/K_2O. The K_2O, V and Cr_2O_3 contents, however, are among the lowest of any Apollo 11 basalts. The B3 samples have the lowest REE abundance of the Apollo 11 basalts, along with a depletion in the light REE compared to B2, and this depletion is reflected in the La abundance. Cr_2O_3 and V contents are directly correlated over a wide range (Fig. 12) and the differences are related to fractionation of Cr-spinel in the B3 lava flow. B2 and B3 have the same V/Cr ratio, but B3 contains less Al_2O_3, less FeO and more MgO, K_2O and Cr_2O_3 than the B2 samples.

In comparison with the B (low-K) basalts, the Group D samples are strongly enriched in all of the incompatible elements except K. The REE, Zr, Hf and Th

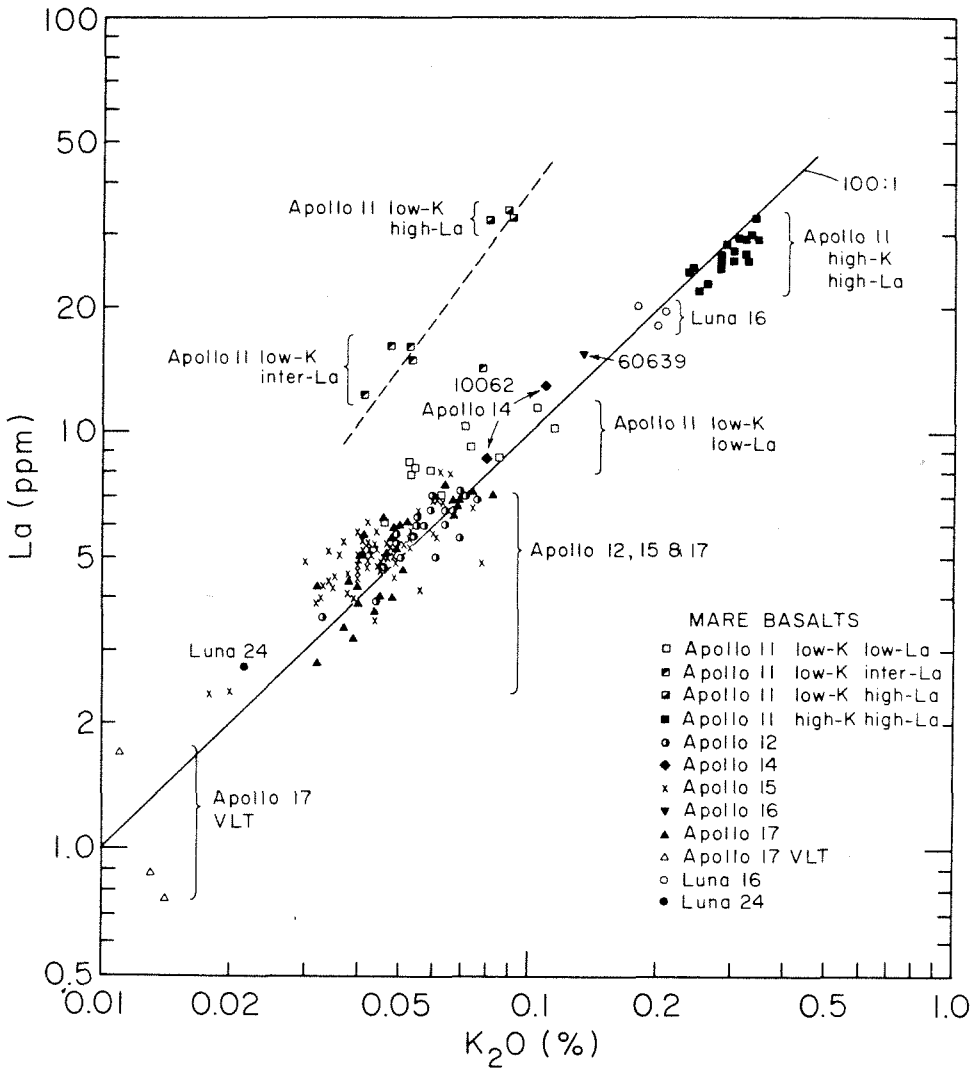

Fig. 11. La and K_2O abundances for all lunar basalt types thus far analyzed. Most lunar basalts have $K_2O/La = 100$ as first pointed out by Wänke *et al.* (1973). Apollo 11 Groups B2 and D, however, have $K_2O/La \approx 30$. Dashed line is the least squares fit to the B2 and D data. Literature data for Apollo 11 are obtained from Gast *et al.* (1970), Wakita *et al.* (1970), Wänke *et al.* (1970) and Ma and Schmitt (1979). Apollo 12 data are taken from Hubbard and Gast (1971), Wänke *et al.* (1971), Wakita and Schmitt (1971) and Nyquist *et al.* (1977). Apollo 14 data are taken from Hubbard *et al.* (1972) and Taylor *et al.* (1972), and Apollo 15 data are taken from Laul and Schmitt (1973b), Rhodes and Hubbard (1973), Helmke *et al.* (1973), Ma *et al.* (1976) and Ma *et al.* (1978). Data of Apollo 16, Apollo 17, Apollo 17 VLT basalts, Luna 16 and Luna 24 are taken from Murali *et al.* (1976), Ma *et al.* (1979b), Wentworth *et al.* (1979), Ma *et al.* (1979a) and Laul *et al.* (1978), respectively.

Table 7. Average and "most primitive" compositions of Apollo 11 basalt types.†

Basalt type	A (crystalline)			A (vitrophyre)		B1		B2		B3			D		
Wt. %	Ave (9)*	σ	10032†	Ave (3)	σ	Ave (3)	σ	Ave (4)	σ	Ave (8)	σ	10085,† 847	Ave (3)	σ	10085,† 808 5
SiO_2	40.45	0.84	39.49	40.87	0.96	41.65	1.23	38.80	1.17	39.99	1.00	40.04	41.98	1.79	44.04
TiO_2	12.21	0.68	13.06	12.53	1.38	10.02	0.72	11.31	1.02	10.78	0.90	10.23	8.49	2.64	5.46
Al_2O_3	7.80	0.46	7.08	8.24	0.74	10.41	0.11	10.59	0.42	9.97	0.40	10.13	10.13	0.69	10.91
Cr_2O_3	0.32	0.04	0.30	0.42	0.12	0.23	0.03	0.21	0.01	0.35	0.10	0.30	0.33	0.05	0.39
MgO	8.22	0.39	8.81	7.69	0.46	5.75	0.22	7.65	0.32	8.20	0.90	8.19	8.42	1.35	9.99
CaO	10.53	0.44	10.21	10.20	0.53	12.03	0.18	11.05	0.67	11.45	0.83	11.21	11.51	0.07	11.50
FeO	19.15	0.62	19.37	19.08	0.30	18.93	0.92	19.24	1.44	18.55	0.66	18.74	18.14	1.58	16.52
MnO	0.24	0.02	0.24	0.25	0.01	0.27	0.03	0.25	0.02	0.26	0.01	0.28	0.26	0.02	0.28
Na_2O	0.49	0.04	0.49	0.42	0.22	0.43	0.06	0.39	0.02	0.37	0.04	0.35	0.38	0.02	0.37
K_2O	0.30	0.03	0.31	0.29	0.06	0.097	0.023	0.049	0.006	0.062	0.013	0.05	0.087	0.006	0.09
P_2O_5	0.11	0.03	0.11	0.16	0.05	0.11	0.06	0.11	0.02	0.04	0.02	0.03	0.21	0.06	0.15
S	0.28	0.06	0.36	0.12	0.09	0.22	0.01	0.25	0.08	0.19	0.05	0.22	0.12	0.07	0.04
Total	100.10		99.93	100.25		100.15		99.90		100.21		100.13	100.06		99.74
La	26.9	2.6	27.7	26.5		10.7	0.7	15.0	1.9	7.9	1.1	7.9	33.1	0.9	32.8
La/Sm	1.27	0.06	1.35	1.28		0.6	0.06	1.08	0.02	0.77	0.1	0.87	1.43	0.09	1.33
Sm/Eu	9.4	0.6	9.45	9.36		6.8	0.3	7.6	1.0	5.9	0.5	5.52	12.0	0.7	12.18
Sm/Yb	1.22	0.05	1.21	1.21		1.1	0.09	1.28	0.20	1.08	0.1	1.08	1.39	0.06	0.12

* Number in brackets refers to number of analyses averaged.

† 10032 and 10085,808 represent the most primitive compositions from their respective groups. 10085,847 is believed to represent the liquid composition for Group B3. For Groups B1 and B2 the original liquid composition is indeterminate (see text).

References. Major elements (point count): this work, Beaty and Albee (1978).

Trace elements (INAA): this work, Gast *et al.* (1970), Wakita *et al.* (1970).

Minor elements (Mn, Cr, Na, K) (INAA): this work, Gast *et al.* (1970), Wakita *et al.* (1970), Wänke *et al.* (1970), Goles *et al.* (1970).

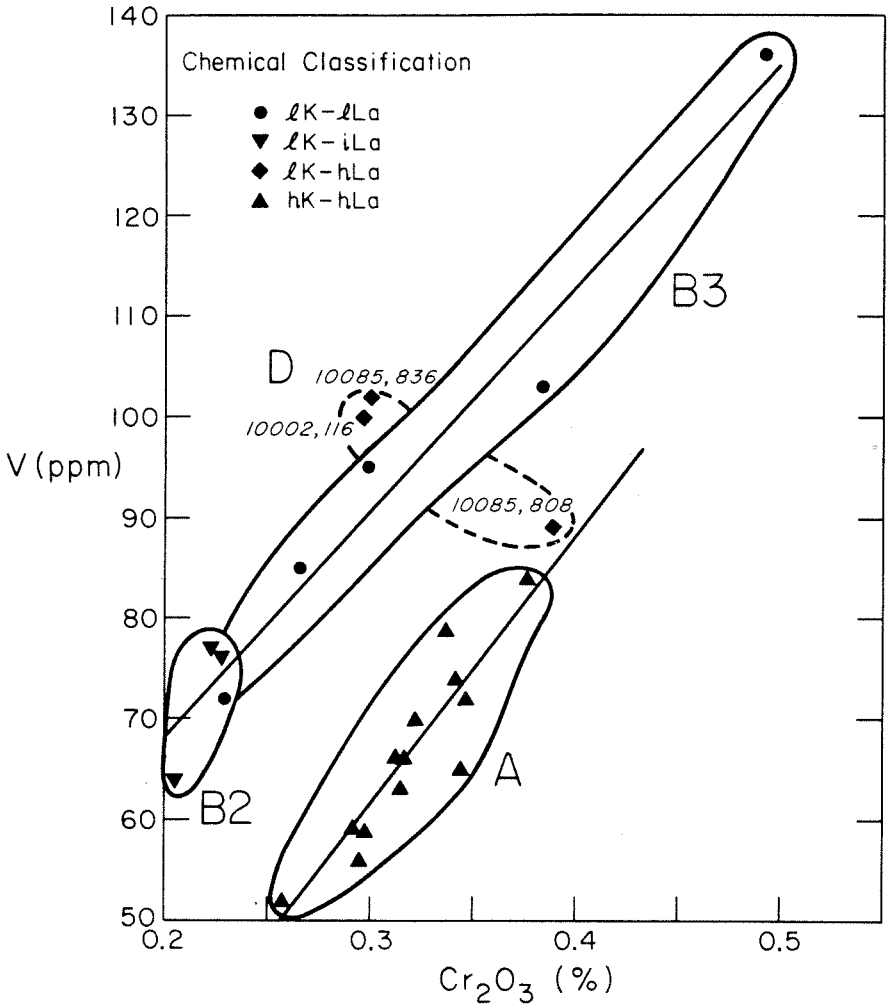

Fig. 12. V vs. Cr_2O_3 plot for the 24 basalt fragments examined in this study. The two trends indicate that Group A must come from a different source region than B2 and B3. Note that two Group D source regions are also suggested.

are all present in concentrations close to those of the Group A basalts. K_2O, however, is anomalously low (Fig. 1). On a Cr_2O_3-V diagram (Fig. 12) two of the Group D samples fall close to the trend defined by B2 and B3 while the third lies on a Group A trend. Group D samples have titanium concentrations intermediate to those of Apollos 11 and 17, and Apollos 12 and 15. The discovery of this new rock type therefore fulfills the prediction of medium-Ti lavas on the moon, based on spectral reflectance data (e.g., Pieters, 1978).

2. Source materials

Beaty and Albee (1978) and Beaty *et al.* (1979b) have shown that the various Apollo 11 basaltic groups represent different basaltic units and that these cannot be related by surface or near-surface crystal-liquid fractionation. We will now test whether or not these basaltic groups can be related by different degrees of partial melting from a chemically and mineralogically homogeneous source region. As discussed above and in Beaty and Albee (1978), the compositions of most of the Apollo 11 basalts have been modified by near-surface frationation. Only in Group B3 can the primitive liquid composition be deduced with any degree of certainty. In Groups A and D the most primitive samples can be identified (Table 7), but there is no assurance that those compositions are direct products of the lunar mantle. Finally, in B1, B2 and the A vitrophyres, it is not even possible to identify the most mafic sample. In spite of these uncertainities, certain constraints can be placed on the basalt source regions beneath Mare Tranquillitatis and it can be shown that several distinctly different sources are required.

First of all, the Rb/Sr systematics require that the Group A basalts come from a different source than any of the B basalts (e.g., Papanastassiou *et al.*, 1977) but such data is not available for Group D samples. The Group A source region is probably different from that of the Group D basalts as well, as indicated by the distinctly different K_2O/La. As shown in Fig. 11, Groups D and B2 have a different K_2O/La than all other analysed lunar basalt samples. Considering the evolution of the lunar interior (Taylor and Jakes, 1974), a constant K_2O/La is expected for most lunar samples. As olivine, ortho- and clinopyroxene, ilmenite, Cr-spinel and anorthite crystallize from the lunar magma ocean, K and La are enriched together in the residual liquid. Similarly, in partial melting, they are both partitioned into the melt at a low degree of melting. Thus it seems very likely that the Group D basalts had a distinctive source region, probably one richer in phosphate minerals.

Because the B2 basalts also fall off the normal K-La correlation (Fig. 11), having K_2O/La ratios of about 35, the B2 and D basalts could be related to each other by different degrees of partial melting of a homogeneous source material, provided that plagioclase was a residual phase in the source region to account for their Sm/Eu differences (Fig. 13). The higher K_2O, P_2O_5 and La abundances and the higher La/Sm and Sm/Eu ratios in Group D as compared to B2 are all consistent with the hypothesis that the Group D basalts were produced by a smaller degree of partial melting in a common source. There are several processes that could separate La and K which could occur as localized, late-stage, near-surface phenomena; these include silicate liquid immiscibility, separation of K-rich melt subsequent to crystallization of phosphate minerals, localized accumulation of phosphate crystals and K-volatilization. Petrologic, textural and chemical evidence neither proves nor disproves the occurrence of these processes and we will continue to make a more fundamental interpretation of the K_2O/La ratio.

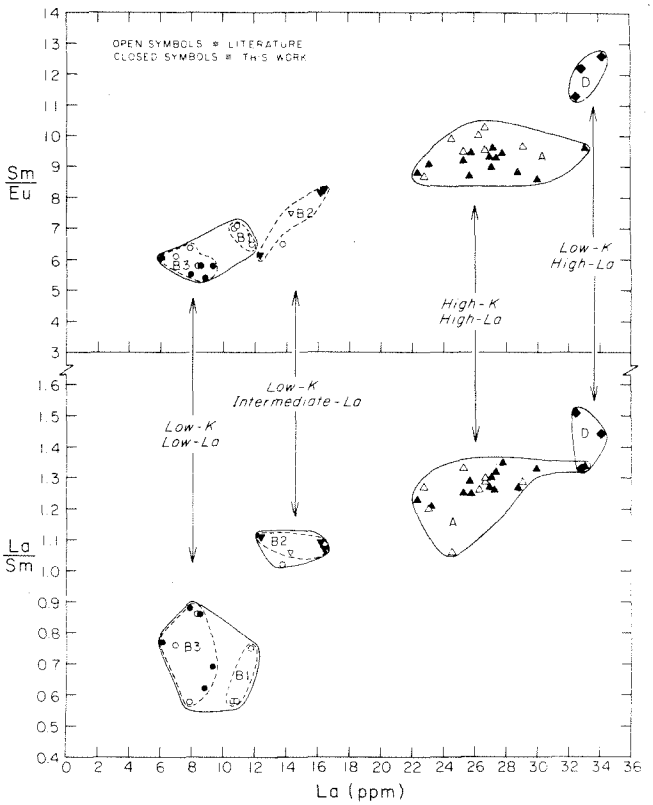

Fig. 13. Sm/Eu and La/Sm ratios as a function of La content for the Apollo 11 basalts. Data sources same as those in Fig. 11.

Even though Group D has a higher average La abundance than even the type A basalts, its average Hf and Ta abundances are lower (Fig. 14). This could be related to the lower ilmenite contents of the Group D basalts. Since ilmenite has higher crystal/liquid partition coefficients for Hf (Haskin and Korotev, 1977) and Ta (McCallum and Charette, 1978; first approximation to Nb) than those for REE's (McKay and Weill, 1976), it seems likely that the cumulate source for the Group D basalts crystallized from a magma which had experienced prior crystallization of ilmenite.

Two separate correlation trends for V vs. Cr_2O_3 are shown on Fig. 12. Group D basalt 10085,808 falls on the high-K basaltic trend while the other two Group D samples, 10085,836 and 10002,116 fall on the low-K basaltic trend. It is possible, therefore, that the three type D basalts were derived from two different sources containing different V/Cr_2O_3 ratios.

Beaty and Albee (1978) showed that Groups B1, B2 and B3 represent at least three cooling units and that B1 and B2 differed in age by 200 m.y. Although the source region of B2 is distinguished from that of B3 by its K_2O/La, we must

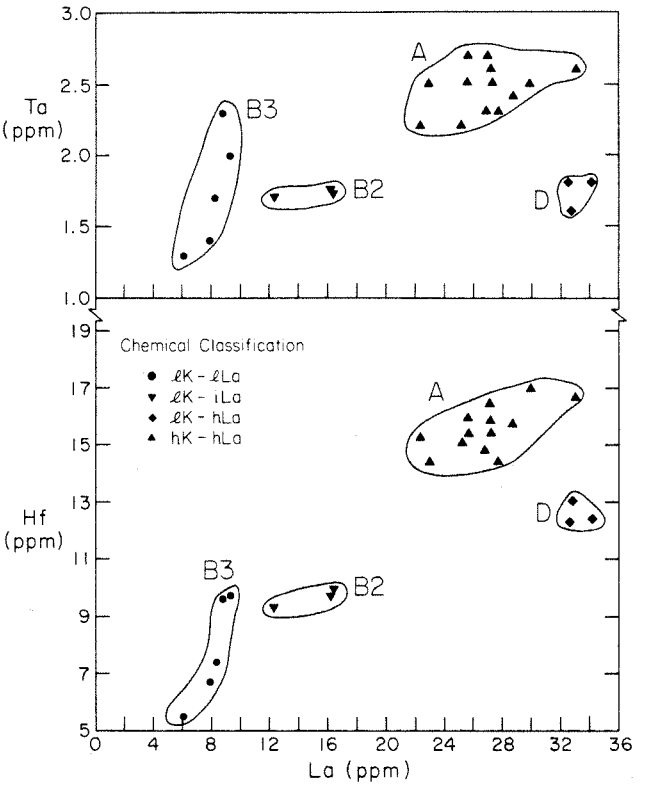

Fig. 14. Ta-La and Hf-La variations for the Apollo 11 mare basalts. The Group D samples have higher average La abundances but lower average Ta and Hf abundances than those of Group A.

consider the relationship of Groups B1 and B3. The higher K_2O, P_2O_5 and La abundances (Table 7) in B1 relative to those in B3 could indicate that the B1 group was produced by a smaller degree of partial melting. The differences in the Sm/Eu and La/Sm ratios (Table 7), however, present problems in relating B3 and B1 by a simple melting process. In addition, the factor of nearly three enrichment in P_2O_5 but only 40–60% enrichment in La and K_2O abundances in B1 relative to B3 is inconsistent with partial melting of a homogeneous source material. This suggests that the B1 and B3 basalts were not derived by different degrees of partial melting from a similar source material, regardless of their similar major and minor element chemistry.

The available information indicates that the Apollo 11 basalts were produced from at least three and probably five distinct source regions: Group A, Groups B1 and B3, Groups B2 and D.

IX. CONCLUSIONS

Petrologic and chemical investigations of these 24 peanuts confirm the Beaty and Albee (1978) subdivisions of the Apollo 11 basalts. There are three low-K groups (of which there are "peanuts" belonging to two) as well as two high-K groups. Each of these five groups probably represents a separate lava flow. Finally, we have discovered a new rock type, herein named Group D basalts. These may be distinguished from all other lunar basalt samples by their crystallization sequence, slight differences in olivine, ilmenite and plagioclase compositions, the abundance of trace phases and the trace element composition. In spite of the differences, these samples are petrologically and petrographically similar to the Apollo 11 low-K samples. Detailed comparison of the three Group D specimens indicates that they may have sampled two lava flows. Small sample size, however, precludes a more definite solution. The new chemical data unambiguously define Group D which has low K_2O abundances similar to that for Group B1 but higher REE abundances similar to those for the Group A basalt.

The fact that B2 and D basalts fall off the main La-K_2O lunar correlation line indicates that they could be derived from a source region which is distinct from those of the other lunar basalts. Two of the three Group D basalts can be derived by smaller degrees of partial melting from a source material similar to that for the B2 basalts with plagioclase in the residue; however, the other Group D basalt (10085,808) may be derived from a source material having a lower V/Cr_2O_3 ratio. Chemically distinct parent reservoirs, which are not reflected in their La-K_2O correlations, are required for generation of the basaltic types B1, B3 and A.

In summary, the Apollo 11 basalt samples represent at least six cooling units that were derived from at least three and probably five mineralogically and chemically-distinct source regions. Chemistries of these source materials cannot be simply related to that of cumulate layers which crystallized at different stratigraphic levels. The diversity of the chemistries observed in the Apollo 11 mare basalts reveals the complex nature of the Apollo 11 basaltic source materials which cannot be satisfactorily explained by simplified geochemical models.

Acknowledgments—Art Chodos was responsible for maintaining the Caltech microprobe at its usual level of excellence. We thank T. V. Anderson, W. T. Carpenter and S. L. Bennett at the Oregon State University TRIGA reactor for neutron activation. Lou Ann Cordell, our long-suffering but esteemed secretary performed her usual miracles on our illegible writing. Constructive criticism from L. E. Nyquist, R. D. Warner and an anonymous reviewer is appreciated. The support of NASA grants NGL-05-002-338 and NGL-38-002-039 are gratefully acknowledged.

REFERENCES

Albee A. L., Beaty D. W., Chodos A. A., and Quick J. E. (1977) Quantitative analysis of petrographic properties and of mineral compositions with a computer-controlled energy-dispersive system. *Proc. 12th Nat. Conf. Electron Probe Anal.* In press.

Beaty D. W. and Albee A. L. (1978) Comparative petrology and possible genetic relations among the Apollo 11 basalts. *Proc. Lunar Planet. Sci. Conf. 9th*, p. 359–463.

Beaty D. W., Hill S. M. R., and Albee A. L. (1979a) Low-K basaltic fragments from Apollo 11 soils (abstract). In *Lunar and Planetary Science X*, p. 86–88. Lunar and Planetary Institute, Houston.

Beaty D. W., Hill S. M. R., and Albee A. L. (1979b) Petrology of a new rock type from Apollo 11: Group D Basalts (abstract). In *Lunar and Planetary Science X*, p. 89–91. Lunar and Planetary Institute, Houston.

Beaty D. W., Hill S. M. R., and Albee A. L. (1979c) Comparative petrology and significance of the Apollo 11 high-K vitrophyres (abstract). In *Lunar and Planetary Science X*, p. 83–85. Lunar and Planetary Institute, Houston.

Gast P. W., Hubbard N. J., and Wiesmann H. (1970) Chemical composition and petrogenesis of basalts from Tranquillity Base. *Proc. Apollo 11 Lunar Sci. Conf.*, p. 1143–1163.

Goles G. G., Randle K., Owasa M., Schmitt R. A., Wakita H., Ehmann W. D., and Morgan J. W. (1970) Elemental abundances by instrumental activation analyses in chips from 27 lunar rocks. *Proc. Apollo 11 Lunar Sci. Conf.*, p. 1165–1176.

Grove T. L. and Walker D. (1977) Cooling histories of Apollo 15 quartz normative basalts. *Proc. Lunar Sci. Conf. 8th*, p. 1501–1520.

Haskin L. A., Jacobs J. W., Brannon J. C., and Haskin M. A. (1977) Compositional dispersions in lunar and terrestrial basalts. *Proc. Lunar Sci. Conf. 8th*, p. 1731–1750.

Haskin L. A. and Korotev R. L. (1977) Test of model for trace element partition during closed-system solidification of a silicate liquid. *Geochim. Cosmochim. Acta* **41**, 921–939.

Helmke P. A., Blanchard D. P., Haskin L. A., Telander K., Weiss C., and Jacob J. W. (1973) Major and trace elements in igneous rocks from Apollo 15. *The Moon* **8**, 129–148.

Hubbard N. J. and Gast P. W. (1971) Chemical composition and origin of nonmare lunar basalts. *Proc. Lunar Sci. Conf. 2nd*, p. 999–1020.

Hubbard N. J., Gast P. W., Rhodes J. M., Bansal B. M., Wiesmann H., and Church S. E. (1972) Nonmare basalts: Part II. *Proc. Lunar Sci. Conf. 3rd*, p. 1161–1179.

James O. B. and Jackson E. D. (1970) Petrology of the Apollo 11 ilmenite basalts. *J. Geophys. Res.* **75**, 5793–5824.

Kramer F. E., Twedell D. B., and Walton W. J. A. Jr. (1977) *Apollo 11 Lunar Sample Information Catalogue*. MSC 12522, NASA Johnson Space Center, Houston. 471 pp.

Laul J. C. and Schmitt R. A. (1973a) Chemical composition of Luna 20 rocks and soil and Apollo 16 soils. *Geochim. Cosmochim. Acta* **37**, p. 927–942.

Laul J. C. and Schmitt R. A. (1973b) Chemical composition of Apollo 15, 16, and 17 samples. *Proc. Lunar Sci. Conf. 4th*, p. 1349–1367.

Laul J. C., Vaniman D. T., and Papike J. J. (1978) Chemistry, mineralogy and petrology of seven > 1 mm fragments from Mare Crisium. In *Mare Crisium: The View from Luna 24* (R. B. Merrill and J. J. Papike, eds.), p. 537–568. Pergamon, N.Y.

LSPET (Lunar Sample Preliminary Examination Team) (1969) Preliminary examination of lunar samples from Apollo 11. *Science* **165**, 1211.

Ma M.-S., Murali A. V., and Schmitt R. A. (1976) Chemical constraints for mare basalt genesis. *Proc. Lunar Sci. Conf. 7th*, p. 1673–1695.

Ma M.-S. and Schmitt R. A. (1979) Chemistry of a new type of Apollo 11 low-K mare basalt (abstract). In *Lunar and Planetary Science X*, p. 759–761. Lunar and Planetary Institute, Houston.

Ma M.-S., Schmitt R. A., Nielsen R. L., Warner R. D., Taylor G. J., and Keil K. (1979a) Luna 16 basalts and breccias: New chemical and petrological data (abstract). In *Lunar and Planetary Science X*, p. 762–764. Lunar and Planetary Institute, Houston.

Ma M.-S., Schmitt R. A., Warner R. D., Taylor G. J., and Keil K., (1978) Genesis of Apollo 15 olivine normative mare basalts: Trace element correlation. *Proc. Lunar Planet. Sci. Conf. 9th*, p. 523–533.

Ma M.-S., Schmitt R. A., Warner R. D., Taylor G. J., and Keil K. (1979b) Composition, petrography, and genesis of Apollo 17 high-Ti mare basalts (abstract). In *Lunar and Planetary Science X*, 765–767. Lunar and Planetary Institute, Houston.

McCallum I. S. and Charette M. P. (1978) Partition coefficients for Nb and Zr among armalcolite, ilmenite, clinopyroxene and silicate melt. *Geochim. Cosmochim. Acta* **42,** 859–869.

McKay G. A. and Weill D. F. (1976) KREEP petrogenesis revisited. *Proc. Lunar Sci. Conf. 7th,* p. 2427–2447.

Murali A. V., Ma M.-S., and Schmitt R. A. (1976) Mare basalt 60639, another eastern lunar basalt (abstract). In *Lunar Science VII,* p. 636–638. The Lunar Science Institute, Houston.

Nyquist L. E., Bansal B. M., Wooden J. L., and Wiesmann H. (1977) Sr-isotopic constraints on the petrogenesis of Apollo 12 mare basalts. *Proc. Lunar Sci. Conf. 8th,* p. 1383–1415.

Papanastassiou D. A., DePaolo D. J., and Wasserburg G. J. (1977) Rb-Sr and Sm-Nd chronology and genealogy of mare basalts from the Sea of Tranquillity. *Proc. Lunar Sci. Conf. 8th,* p. 1639–1672.

Pieters C. M. (1978) Mare basalt types on the front side of the moon: A summary of spectral reflectance data. *Proc. Lunar Planet. Sci. Conf. 9th,* p. 2825–2849.

Rhodes J. M. and Hubbard N. J. (1973) Chemistry, classification, and petrogenesis of Apollo 15 mare basalts. *Proc. Lunar Sci. Conf. 4th,* p. 1127–1148.

Shoemaker E. M., Hait M. H., Swann G. A., Schleicher D. L., Schaber G. G., Sutton R. L., Dahlem D. H., Goddard E. N., and Water A. C. (1970) Origin of the lunar regolith at Tranquillity Base. *Proc. Apollo 11 Lunar Sci. Conf.,* p. 2399–2412.

Taylor S. R. and Jakeš P. (1974) The geochemical evolution of the moon. *Proc. Lunar Sci. Conf. 5th,* p. 1287–1305.

Taylor S. R., Kaye M., Muir P., Nance W., Rudowski R., and Ware N. (1972) Composition of the lunar upland: Chemistry of Apollo 14 samples from Fra Mauro. *Proc. Lunar Sci. Conf. 3rd,* p. 1231–1249.

Wakita H. and Schmitt R. A. (1971) Abundances of the 14 rare-earth elements and 12 other trace elements in Apollo 12 samples: Five igneous and one breccia rocks and four soils. *Proc. Lunar Sci. Conf. 2nd,* p. 1319–1329.

Wakita H., Schmitt R. A., and Rey P., (1970) Elemental abundances of major, minor and trace elements in Apollo 11 lunar rocks, soil and core samples. *Proc. Apollo 11 Lunar Sci. Conf.,* p. 1685–1717.

Walker D., Longhi J., Kirkpatrick R. J., and Hays J. R., (1976) Differentiation of an Apollo 12 picrite magma. *Proc. Lunar Sci. Conf. 7th,* p. 1365–1389.

Walker D., Powell M. A., and Hays J. R. (1978) Dynamic crystallization of a eucritic basalt (abstract). In *Lunar and Planetary Science IX,* p. 1196–1198. Lunar and Planetary Institute, Houston.

Wänke H., Baddenhausen H., Dreibus G., Jagoutz E., Kruse H., Palme H., Spettel B., and Teschke F. (1973) Multielement analyses of Apollo 15, 16, and 17 samples and the bulk composition of the moon. *Proc. Lunar Sci. Conf. 4th,* p. 1461–1481.

Wänke H., Rieder R., Baddenhausen H., Spettel B., Teschke F., Quijano-Rico M., and Balacescu A. (1970) Major and trace elements in lunar material. *Proc. Apollo 11 Lunar Sci. Conf.,* p. 1719–1727.

Wänke H., Wlotzka F., Baddenhausen H., Balacescu A., Spettel B., Teschke F., Jagoutz E., Druse H., Quijano-Rico M., and Rieder R. (1971) Apollo 12 samples: Chemical composition and its relation to sample locations and exposure ages, and two component origin of the various soil samples and studies on lunar metallic particles. *Proc. Lunar Sci. Conf. 2nd,* p. 1187–1208.

Wentworth S., Taylor G. J., Warner R. D., Keil K., Ma M.-S., and Schmitt R. A. (1979) The unique nature of Apollo 17 VLT mare basalts (abstract). In *Lunar and Planetary Science X,* 1332–1334. Lunar and Planetary Institute, Houston.

THE PETROGRAPHY OF BASALTIC FRAGMENTS IN APOLLO 11 DRIVE TUBES 10004 AND 10005. D.W. Beaty and A.L. Albee, Division of Geological and Planetary Sciences, California Institute of Technology, Pasadena, CA. 91125

Introduction. Thirty small basaltic fragments (1-19 mg) have recently been separated from the two Apollo 11 drive tube soil samples, 10004 and 10005. To characterize these specimens a combined INAA and petrographic study was undertaken. This report contains the petrographic analysis of these samples, while the INAA chemical data are contained in Ma and Schmitt (1980). Core tube 1 (10005) contained 10 cm of material, and core tube 2 (10004) contained 13.5 cm (LSPET, 1969), so the 30 fragments were originally present in the uppermost portion of the lunar regolith.

General Petrography. Twenty-nine of the 30 fragments are basalts of various types. The remaining sample, 10004,225, is a brecciated basalt which has been cemented by glass. The samples are all hypidimorphic, hyalocrystalline and ilmenite-rich, with an overall texture ranging from ophitic to intergranular to intersertal, and an average grain size from 40 to 600 microns (Table 1). All of these specimens are petrographically similar to the previously described Apollo 11 basalts: No new rocks types are present. This conclusion is identical to that reached independently by Ma and Schmitt (1980) by interpreting the chemical data.

Classification. Beaty and Albee (1978) and Beaty et al. (1979) established petrographic and mineral-chemical criteria for subdividing the Apollo 11 basalts into six petrologic groups: A (crystalline), A (vitrophyre), B1, B2, B3 and D. The petrographic criteria (Table 1) classify the present group of 30 samples as follows: 10 Group A (crystalline), 0 A (vitrophyre), 0 B1, 6 B2, 9 B3, 0 D, four which are from one of the B groups, and one that could not be classified at all. Although microprobe studies would certainly improve these assignments, they are not warranted because of the small sample

TABLE 1. PETROGRAPHY OF APOLLO 11 BASALTIC FRAGMENTS

Sample	Sample Size (μm)	Ave. Grain Size (μm)	Texture	Ilmenite Habit	Olivine Habit [1]	Max. Plag. ⊥(010) (μm)	Modal Oliv. (Est.)	Modal Crist. (Est.)	Petrographic Group [2]	Chemical Group [3]
10004,204	1400	200	ophitic	blocky	absent	65	0	1	B2	B2
205	800	150	intersertal	anhedral	absent	35	0	4	A	A
206	1100	150	intersertal	bladed,anhedral	absent	50	0	4	A	A
207	1000	200	ophitic	blocky	absent	60	0	1	B2	B2
208	2100	200	coarse ophitic	blocky	small,mantled	90	tr.	1	B2	B2
210	1400	80	poikilitic-intersertal	equant	absent	300	0	4	A	A
211	1000	60	poikilitic-intersertal	bladed	absent	140	0	4	A	A
212	1000	150	intergranular	blocky,anhedral	absent	25	0	3	B3	B3
213	1000	300	ophitic	blocky,anhedral	absent	110	0	1	B2	B3
214	1200	150	ophitic	blocky	small,mantled	135	1	2	B2	B2
215	200	50?	intersertal?	bladed?	absent	20?	0	4?	?	B3
217	200	200?	?	?	absent	100?	0	1?	B3?	?
218	1600	300	ophitic	platy,anhedral	absent	30	0	1	B3	B3
220	1600	500	ophitic	blocky,anhedral	absent	220	0	5	B	B3
221	1200	100	ophitic	blocky	small,mantled	60	3	3	B	B3
224	1400	50	intersertal	variable	small,mantled	40	2	4	A	A
225	1000	50	glass-cemented breccia	equant	absent	40	0	?	A	A
226	700	40	intersertal,equigr.	blocky	absent	20	0	4	A	A
227	1700	600	subophitic	ext. skeletal	small,mantled	80	tr.	5	B	B2
10005,200	900	50	intergranular	platy	large,resorbed	20	2	3	B3	B3
202	1200	300	ophitic	bladed, anhedral	absent	110	0	1	B	B3
203	500	200?	ophitic	blocky	small,mantled	70	3	2	B2?	B2
204	900	150	intersertal-ophitic	anhedral	large,resorbed	65	10	2	B3?	B3
205	1200	100	intergranular-ophitic	anhedral	microphenos	35	5	2	B3	B3
206	1100	50	intersertal-porph.	bladed	anh. phenos.	5	2	5	A	A
207	1400	300	subophitic	equant,anhedral	small,resorbed	120	1	5	A	A
208	1000	100	intergranular	platy,anhedral	phenocryst	40	4	6	B3	B3
209	1500	100	intergranular-ophitic	platy	absent	60	0	2	B3	B3
210	900	80	intergranular	anhedral	absent	30	0	4	B3?	B3
211	1000	200	intersertal-granular	equant,anhedral	small,resorbed	40	1	4	A	A

[1]Mantled olivines are enclosed by clinopyroxene. [2]Plagioclase shape was also used to help distinguish B2 and B3 (Beaty and Albee, 1978). [3]From Ma and Schmitt (1980).

BASALTS IN APOLLO 11 DRIVE TUBES

D.W. Beaty

size and the lack of new rock types. Beaty et al. (1979) also demonstrated that chemical data alone are sufficient to distinguish five of the six petrologic groups (the two A groups have similar compositions). Using those criteria, Ma and Schmitt (1980) have classified these 30 samples as follows: 10 A, 0 B1, 6 B2, 13 B3, 0 D, and one which could not be classified. The correspondence between the chemical and petrographic classifications is close, but not exact (Table 1), and the reasons for the differences are discussed in detail.

Group A (High-K) Basalts. The two sets of criteria coincide for each of the ten type A (high-K) samples. This reflects the presence of certain distinctive petrographic features, such as intersertal texture, mesostasis intergrowths of glass, plagioclase and cristobalite, low (20%) modal plagioclase, high (15%) modal ilmenite, and a high degree of silica saturation (about 4% more cristobalite than olivine)(Table 1). Although a microprobe study of the plagioclase would confirm the identification, the above observations leave little room for doubt. Like the petrography, the chemistry of this group of samples is unmistakable. None of the ten high-K samples are true vitrophyres. 10005,206, however, contains subhedral pyroxene, olivine and ilmenite phenocrysts (total=60-70%) set in a finely crystalline groundmass. Texturally, therefore, it resembles the high-K vitrophyres, particularly 10085,12-7.

Group B1. The absence of B1 samples is a consequence of the fact that the average grain size in B1 is about 800 microns (Beaty and Albee, 1978) whereas those 30 fragments range in size from 200 to 2100 microns with an average of about 1100 microns (Table 1). If a B1 rock were crushed to this size it would consist of mineral fragments and aggregates of several grains, neither of which would have been separated from the soil sample as a basaltic fragment.

Groups B2 and B3. With the exception of 10004,217, the chemical data are sufficiently clear-cut that all of the low-K samples can be unambiguously assigned to either B2 or B3 (Ma and Schmitt, 1980). The petrographic data, however, were unable to distinguish 3 B3 and 1 B2 samples (classifying them only as B), identified 10004,213 as B2 when it is chemically B3, and failed to classify 10004,215 at all. 10004,217 could not be classified chemically, but petrographically appears to be B3. These problems are obviously related to small sample size. In all but one of the discrepancies listed above, the rock is less than four times as large as the average grain size (Table 1). The number of crystals is so small that not only is the overall texture poorly defined, it is likely to be unrepresentative of its parental igneous body. For example, study of 1000μm-sized areas in 10045,16 (a B3 basalt with a surface area of 116 mm^2) indicates that on this scale there are olivine-rich and olivine-free regions, plagioclase clots and random plagioclase laths, platy and anhedral ilmenite, and an overal texture ranging from ophitic to subophitic to intergranular. The thin section is dominantly intergranular and olivine-phyric with platy ilmenite (a typical B3 texture), but by reducing the scale of observation, almost any texture can be found, including that characteristic of Group B2. Minimal significance, therefore, is attached to the discrepancies between the chemical and petrographic classification of these 30 small fragments. Although the mineral compositions are more independent of sample size than the texture, the four major minerals present (olivine, pyroxene, plagioclase and ilmenite) are typically strongly zoned, and may also be unrepresentative of the parental igneous body. Elemental abundances are subject to the same problem, and the chemical analyses of these small samples must be treated with caution. Certain elemental ratios, however are more reliable. For example, La and K are both concentrated in the mesostasis areas, so that whether there are two patches of mesostasis in a sample or three, La/K should

BASALTS IN APOLLO 11 DRIVE TUBES

Beaty, D.W.

be similar. For this reason, the minor element chemical classification is preferrable for minute samples.

Size-Frequency Distribution. The size-frequency distribution of the various Apollo 11 basalt types are listed in Table 2. Two principal conclusions may be drawn. First, the six described rock types probably represent all of the basalt types close to the landing site. Shoemaker et al. (1970) calculate that in each lunar cratering event, about 25% of the ejected material is transported more than 10 km. The type D basalts (4% of sample) may be derived from a younger, medium-Ti unit which crops out about 30 km east of the landing site (Pieters, 1978). Other than that there is no evidence for any rock type other than the low- and high-K basalts (96% of sample) in the southern part of Mare Tranquillitatis.

Table 2. Size-Frequency Distribution

Apollo 11 Basalt type	Fragment size: >1 gm[1]	25 mg-1 gm[2]	<25 mg[3]	Total
A (cryst.)	9 (50%)	10 (48)	10 (31)	29 (41)
A (vitro.)	1 (6)	2 (10)	1 (3)	4 (6)
B1	3 (17)	0 (0)	0 (0)	3 (4)
B2	2 (11)	2 (10)	6 (19)	10 (14)
B3	3 (17)	4 (19)	14 (44)	21 (30)
D	0 (0)	3 (14)	0 (0)	3 (4)
unclass.	2	0	1	3
Total	20	21	32	73

[1]Beaty and Albee (1978); [2]Beaty et al. (1979); [3]This work.

Second, it can be argued that most of the coarse surficial debris at the Apollo 11 landing site was ejected from West Crater, a young, sharp-rimmed, rayed crater 180 m. in diameter and 30 m. deep located 400 m. east of the LM (Beaty and Albee, 1978). Assuming a simple, stratified structure, the size-frequency distribution of the coarse-grained fraction can be used to estimate formation thicknesses in that 30 m. section. Using a parabolic crater shape and five meters of regolith (Shoemaker et al., 1970), from top to bottom West Crater contains 9 m. of high-K (A) basalts, 2 m. of B1, 6 m. of B3, and 8 m. of B2. This admittedly speculative calculation suggests that the 2 m. layer containing B1 is an ejecta blanket, because the very slow cooling rates in B1 could not have been achieved in a 2 m. lava flow. The medium size fraction (mostly collected with the scoop) is distributed similar to the coarse fraction (Table 2), consistent with derivation of both from West Crater. The fine fraction (drive tubes), however, is different and probably has a larger component of the pre-West Crater regolith. This is consistent with the greater depth of sampling in the drive tubes. The greater abundance of B3 and reduced abundance of A in the fine fraction (Table 2) suggests a greater contribution of deep craters (consistent with an increased B2 abundance), or a thickening of B3 relative to A away from West Crater.

References. Beaty and Albee (1978, PLPSC 9th, p. 359-463; Beaty et al. (1979), PLPSC 10th; LSPET (1969), Science 165, p. 1211-1227; Ma and Schmitt (1980), this volume; Pieters (1978), PLPSC 9th, p. 2825-2849; Shoemaker et al. (1970), PLSC 1st, p. 2399-2412.

American Mineralogist, Volume 65, pages 63-74, 1980

Silica solid solution and zoning in natural plagioclase

DAVID W. BEATY AND ARDEN L. ALBEE

Division of Geological and Planetary Sciences[1]
California Institute of Technology
Pasadena, California 91125

Abstract

Microprobe analyses of plagioclase from some lunar basalts have anomalous stoichiometry as compared to terrestrial feldspars. The anomaly indicates the presence of the "excess silica" substitution, [ ]Si_4O_8. This coupled substitution leaves a vacancy in the feldspar lattice and is effectively SiO_2 dissolved in the feldspar. Detailed study indicates that core–rim [ ]Si_4O_8 zoning is a common phenomenon in plagioclase from lunar basalts. Anorthite–albite zoning is also typically present, so plots of [ ]Si_4O_8 as a function of anorthite content provide a convenient measure of the [ ]Si_4O_8 variations present. Most lunar basaltic plagioclase shows a monotonic increase in [ ]Si_4O_8 with albite content, typically ranging from 0 mole percent [ ]Si_4O_8 in the cores to 5–7 percent in the rims. This zoning is produced by two cooperating processes: a falling temperature of formation, and growth from a progressively siliceous liquid. In addition, rapid growth and delayed nucleation of plagioclase and silica phase appear to be important to the disequilibrium incorporation of [ ]Si_4O_8.

By contrast, plagioclase from a wide variety of terrestrial occurrences lacks [ ]Si_4O_8. The absence of [ ]Si_4O_8 in many terrestrial igneous plagioclases is primarily related to the presence of H_2O, which decreases the liquidus temperatures relative to those in lunar rocks. Terrestrial basalts which have comparable crystallization temperatures to their lunar counterparts lack [ ]Si_4O_8 in part because of an absence of strong *in situ* differentiation. In addition, plagioclase typically crystallizes prior to pyroxene (the reverse of the mare basalts), so kinetic effects have a reduced role. If a melt is in equilibrium with cristobalite (or tridymite or quartz), the silica activity is buffered, and the [ ]Si_4O_8 content of the plagioclase is directly related to the temperature. [ ]Si_4O_8 incorporation, however, is typically not an equilibrium process, so there is little hope of using it directly as a geothermometer.

Introduction

This paper is concerned with the extent and significance of silica solid solution in natural plagioclase, a subject which has had a long history in the geological literature. Myrmekite was thought by Schwantke (1909) and Phillips (1964) to have formed by the subsolidus unmixing of feldspar and a dissolved silica-rich component. The first discoveries of excess silica in natural feldspars were those of Chayes and Zies (1962) and Carmen and Tuttle (1963, 1967), in sanidine from rhyolites. Luth and Tuttle (1966), however, found no evidence for excess silica in alkali feldspars (mostly microcline and orthoclase) from a wide variety of geologic environments. Wyart and Sabatier (1965), Kim and Burley (1971), Orville (1972), Bruno and Facchinelli (1974), Ito (1976), and Longhi and Hays (1979) all succeeded in producing excess-silica-bearing feldspars in the laboratory, including both anorthite and albite. The Longhi and Hays study presented the $CaAl_2Si_2O_8$–SiO_2 phase diagram, laying the foundation for the interpretation of excess silica in natural feldspars. Consistent with the idea of silica solid solution is the fact that feldspar has a structure polytypic to that of coesite (Megaw, 1970; Thompson and Hovis, 1979), a condition favoring mutual solubility.

The first demonstration of excess silica in natural plagioclase came from studies of the lunar samples (*e.g.*, Weill *et al.*, 1970). Many workers noted that some lunar plagioclase analyses differed in stoichiometry from their terrestrial counterparts. The "anomalous" analyses had too much Si, too little Al, and a deficiency of the singly- and doubly-charged

[1] Contribution No. 3260.

0003-004X/80/0102-0063$02.00

cations which fill the larger site (Table 1). Wenk and Wilde (1973) and Longhi *et al.* (1976a) demonstrated that the feldspar substitution [ ]Si_4O_8 is necessary to balance these anomalous analyses. This coupled substitution,

$$[\ ] \text{ (vacancy)} + Si = Na + Al, \text{ or}$$

$$[\ ] + 2Si = Ca + 2Al$$

is hereafter referred to as the excess silica substitution. By routinely calculating the amount of [ ]Si_4O_8 in plagioclase analyses from the Apollo 11 basalts, Beaty and Albee (1978) discovered well-defined core–rim excess silica zoning in single crystals. Subsequent studies of other groups of lunar basalts (Beaty and Albee, 1979; Beaty *et al.*, 1979a, b, c; Baldridge *et al.*, 1979) showed that [ ]Si_4O_8 zoning is a common phenomenon in lunar plagioclase. Our purpose is to synthesize these data, supplement them with new analyses from other rock types and other geologic environments, and develop a meaningful picture of the extent, causes, and significance of silica solid solution and zoning in plagioclase.

Table 1. Representative plagioclase analyses

	(1)	(2)	(3)	(4)	(5)	(6)	(7)	(8)
SiO_2	50.98	52.75	50.46	51.76	50.48	49.89	50.67	52.26
TiO_2	0.12	0.09	0.12	0.01	0.11	0.08	0.21	0.25
Al_2O_3	31.29	29.72	30.88	30.51	31.06	32.07	29.37	29.05
MgO	0.03	0.10	0.20	0.14	0.14	0.10	0.30	0.42
CaO	14.54	13.07	14.27	13.72	14.91	16.07	16.56	15.35
FeO	0.45	0.64	0.50	0.54	0.86	0.85	1.63	1.51
Na_2O	3.24	3.96	3.81	4.12	2.18	1.90	1.39	1.71
K_2O	0.16	0.22	0.18	0.18	0.24	0.08	0.09	0.08
BaO	0.02	0.04	<.01	<.01	<.01	<.01	<.01	0.13
Σ	100.83	100.59	100.42	100.98	99.98	101.04	100.22	100.76
Number of cations normalized to 8 oxygens								
Si	2.310	2.388	2.302	2.340	2.307	2.262	2.326	2.376
Ti	0.004	0.003	0.004	0.000	0.004	0.003	0.007	0.009
Al	1.672	1.586	1.661	1.626	1.674	1.714	1.590	1.557
Mg	0.002	0.007	0.014	0.009	0.010	0.007	0.021	0.028
Ca	0.706	0.634	0.698	0.665	0.730	0.781	0.815	0.748
Fe	0.017	0.024	0.019	0.020	0.033	0.032	0.063	0.057
Na	0.285	0.348	0.337	0.361	0.193	0.167	0.124	0.151
K	0.009	0.013	0.010	0.010	0.014	0.005	0.005	0.005
Ba	0.000	0.001	0.000	0.000	0.000	0.000	0.000	0.002
End-member abundances								
$KFe^{3+}Si_3O_8$	0.0	0.0	0.0	0.0	0.0	0.0	0.0	0.0
$KAlSi_3O_8$	0.9	1.3	1.0	1.0	1.4	0.5	0.5	0.5
$NaAlSi_3O_8$	28.4	34.8	32.3	34.9	19.3	16.7	12.4	15.1
$BaAl_2Si_2O_8$	0.0	0.1	0.0	0.0	0.0	0.0	0.0	0.2
$CaAl_2Si_2O_8$	68.7	60.8	63.6	61.3	71.0	75.6	73.2	68.0
$FmAl_2Si_2O_8$	0.1	0.5	0.0	0.0	2.3	1.5	0.0	1.8
$CaFmSi_3O_8$	1.8	2.6	3.1	2.9	2.0	2.4	8.3	6.8
[ ]Si_4O_8	0.0	0.0	0.0	0.0	4.0	3.3	5.6	7.6

(1)-(2) Skaergaard intrusion (unpub. data from R. Gregory); (3)-(4) New Mexico basalt (unpub. data from W. S. Baldridge); (5)-(6) 10047 (Beaty and Albee, 1978); (7)-(8) 70215 (Dymek et al., 1975).

Analytical techniques

Small variations in the amount of any of the major cations can drastically effect the amount of excess silica which is subsequently calculated. Systematic differences, such as those introduced by using different analytical methods or even the same method but different instruments, may affect the excess silica values. For this reason, we have used only data collected on the Caltech microprobe. Analyses for all elements were performed consecutively on a single spot with a MAC-5-SA3 electron microprobe interfaced to a PDP-8/L computer for on-line control and data processing. Operating conditions were uniformly 15 kV accelerating voltage and either 0.05 or 0.005 μA sample current (on brass) with beam current integration and pulse height selection. Elements with peak to background ratios greater than five (about 1 weight percent of the oxide) are counted to a precision of 1% or better. Minor elements (<1 percent abundances) are usually counted for 90 seconds, which yields counting statistics of better than 10% for elements present in amounts greater than ~0.1 weight percent. Reproducibility (1σ) on two "known unknowns" over a 13-month period ranged from 1.5 (for elements with abundances >1 percent) to 3 percent of the amount present (for elements with abundances >0.1 percent) (Champion *et al.*, 1975).

All plagioclase analyses were normalized to 16 positive charges (assuming ferrous iron), and then the formulae calculated in the following manner. First, the tetrahedral site was filled by making $Ca(Fe,Mg)Si_3O_8 = 4 - (Si + Al)$. Next, we set $KAlSi_3O_8 = K$, $NaAlSi_3O_8 = Na$, $BaAl_2Si_2O_8 = Ba$, $CaAl_2Si_2O_8 = Ca - Ca(Fm,Mg)Si_3O_8$, $(Fe,Mg)Al_2Si_2O_8 = Mg+Fe - Ca(Fe,Mg)Si_3O_8$, and finally [ ]$Si_4O_8 = 1 - [Na+Mg+K+Ca+Fe+Ba - Ca(Fe,Mg)Si_3O_8]$. Ti was measured but ignored; in basaltic plagioclase it is typically 0.05–0.10 weight percent (Table 1), which would decrease the calculated excess silica by 0.2–0.3 mole percent. The calculated uncertainties (1σ, using Bernoulli counting statistics) for this algorithm are ±0.2 mole percent for the An content, and ±1.5 mole percent for the excess silica.

The tetrahedral Fe calculation $[Ca(FeSi_3)O_8]$ is based on spectroscopic experiments. Mössbauer studies by Hafner *et al.* (1971) and Appleman *et al.* (1971) suggest that, in Apollo 11 and 12 plagioclase at room temperature, 20–60% of the Fe^{2+} is in tet-

rahedral coordination. Although these results were not confirmed in a near-infrared spectral study (using Luna 20 material) by Bell and Mao (1973), Sclar and Kastelik (1979) were able to synthesize a complete isostructural series ranging in composition from $CaAl_2Si_2O_8$ to $CaFeSi_3O_8$. Furthermore, Wenk and Wilde (1973), Longhi *et al.* (1976a,b), and our studies all indicate that both [ ]Si_4O_8 and $Ca(Mg,Fe)Si_3O_8$ are necessary to balance lunar plagioclase analyses. Note, however, that the [ ]Si_4O_8 calculation is independent of site-occupancy assumptions, depending only on the total number of cations. If ferric iron were present in a plagioclase crystal, the amount of excess silica calculated using the above method would be about 0.1 mole percent less than that actually present for every 0.5 weight percent Fe_2O_3.

Our analytical technique was cross-checked by analyzing in a single microprobe run a variety of plagioclase samples that had been previously analyzed at different times. By relocating old analysis points we were able to determine our total reproducibility, as well as to directly compare different feldspar analyses. This experiment showed better reproducibility in excess silica determination than the calculated 1.5 mole percent (σ = 0.58 based on 26 measurements). In addition, our analyses of well-characterized terrestrial plagioclase standards indicated no excess silica, even when analyzed alternately with high-[ ]Si_4O_8 lunar feldspars.

One of our major conclusions is that detectable excess silica is not present in most terrestrial plagioclase. This means that the crystallographic sites are fully occupied. It is equally valid, therefore, that instead of normalizing to a total positive charge of 16, terrestrial feldspar analyses be normalized to 5 total cations. The ferric/ferrous ratio, however, typically cannot be determined from the total positive charge because the uncertainties are too large (see above).

Silica solid solution in natural plagioclase

Apollo 11 low-K basalts

Figure 1 illustrates the compositional dependence of excess silica in plagioclase from three Apollo 11 low-K basalts. In each rock, [ ]Si_4O_8 shows a strong inverse correlation with anorthite content. Plagioclase (An_{91}) is on the liquidus in 10047, and continues to crystallize to the solidus (An_{69}). The first plagioclase to form has no excess silica, but as the rock crystallizes, more and more excess silica is incorporated, reaching a maximum of 4.6 mole percent in the mesostasis areas (Fig. 1). The entire zoning

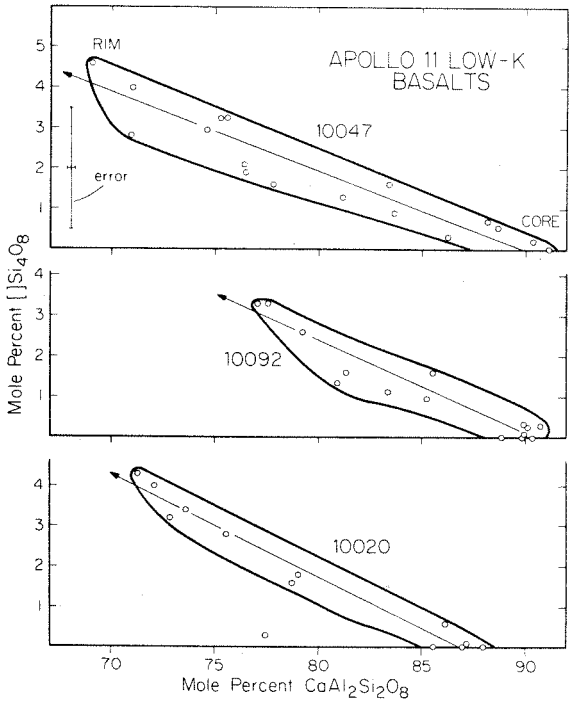

Fig. 1. Variations in [ ]Si_4O_8 as a function of $CaAl_2Si_2O_8$ for plagioclase in Apollo 11 low-K basalts 10047, 10092, and 10020. In each case excess silica increases in a regular way from core to rim of the plagioclase, and the three samples show the same zoning trend. This trend is produced by both falling temperature and *in situ* differentiation. The error bar is the calculated absolute uncertainty, but the reproducibility (width of the data envelopes) is somewhat less.

trend can be found in core–rim profiles of single crystals, and each grain shows the same profile.

10092 and 10020 are much finer-grained than 10047, and in both rocks plagioclase is the third phase to appear on the liquidus (after olivine and spinel). Nevertheless, both samples have excess silica zoning profiles very similar to that of 10047. The principal difference lies in the extent of the zoning; *in situ* differentiation was not as efficient in 10092. The remainder of the Apollo 11 low-K basalts have zoning patterns similar to those in 10047, 10092, and 10020 (Beaty and Albee, 1978; Beaty *et al.*, 1979b).

The simple excess-silica zoning profiles in plagioclase from the low-K basalts can easily be understood in terms of the phase diagram plagioclase–SiO_2. The An–SiO_2 join of this diagram has been experimentally determined at low pressure by Longhi and Hays (1979) and is reproduced in simplified form in Figure 2. The excess silica substitution is equivalent to SiO_2 dissolved in anorthite and is therefore governed by the univariant curves bounding the anorthite field. At temperatures close to its melting

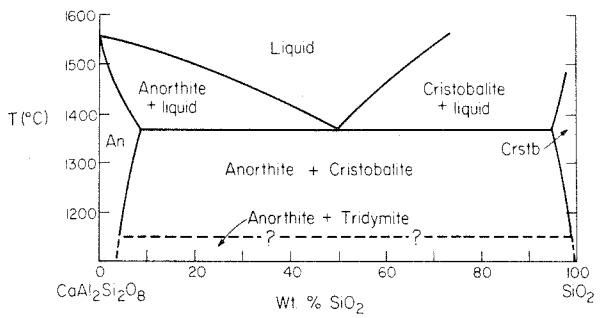

Fig. 2. Experimentally-determined phase diagram for the binary system $CaAl_2Si_2O_8$–SiO_2 (after Longhi and Hays, in press). The width of the An field determines the maximum solubility of [ ]Si_4O_8 at any given temperature. Additional details involving the silica polymorphs on the right side of the diagram have been omitted for simplicity.

point, anorthite can contain very little dissolved silica. As the temperature falls, the solubility of silica in anorthite steadily increases, reaching a maximum of 9 mole percent [ ]Si_4O_8 (8 weight percent) at 1370°C, the temperature of the anorthite–cristobalite eutectic. With further cooling, the anorthite will progressively lose its [ ]Si_4O_8 to cristobalite, tridymite, and then quartz.

In the Apollo 11 low-K basalts, the first plagioclase crystallized at high temperature from a melt that was marginally quartz-normative. As predicted by the phase diagram, it contains negligible amounts of [ ]Si_4O_8. As the magma cooled it differentiated, and the residual liquid was enriched in SiO_2. The monotonic increase in [ ]Si_4O_8 from core to rim of the plagioclase crystals is therefore caused by two factors: increasing silica solubility in plagioclase at lower temperatures, and an increasingly siliceous parental melt. Because both temperature and composition determine the amount of [ ]Si_4O_8 incorporated in the feldspar, excess-silica zoning profiles must depend strongly on the liquid line of descent. The fact that all of the Apollo 11 low-K basalts have similar zoning trends therefore indicates that they followed similar liquid lines of descent. This is consistent with the bulk chemical and petrologic similarities present within the suite (Beaty and Albee, 1978).

Apollo 12 pigeonite basalts

Like the low-K basalts, the Apollo 12 pigeonite basalts also show an inverse correlation between [ ]Si_4O_8 and anorthite content (Fig. 3). In each rock, plagioclase rims contain more excess silica than the cores. In contrast to the low-K basalts, however, the several pigeonite basalts do not have similar profiles. 12011 ranges from 3–6 percent [ ]Si_4O_8, 12043 has from 0–4 percent, and 12007 zones from 0–2 percent (Baldridge *et al.*, 1979). When these excess silica contents are compared to the anorthite contents (Fig. 3), the plagioclase analyses from all three samples fall along a common trend. For the reasons discussed above, the inverse relation between [ ]Si_4O_8 and An content suggests that the three samples crystallized from the same parental liquid along the same liquid line of descent. The different positions along the common trend suggest different positions of plagioclase saturation.

Petrologic evidence indicates that the cooling rate decreases in the order 12011 > 12043 > 12007 (Baldridge *et al.*, 1979), the same order in which [ ]Si_4O_8 decreases. This correlation is also found in the Apollo 12 feldspathic basalts (Beaty *et al.*, 1979c). Plagioclase saturation occurs after olivine, pigeonite, and augite in these rocks. With increased cooling rate all the saturation temperatures are depressed, but the temperature of plagioclase appearance is depressed most (Walker *et al.*, 1978; Grove and Raudsepp, 1978; Grove and Bence, 1979). Therefore, in the more rapidly cooled samples more of the early ferromagnesian phenocrysts form. This enriches the residual melt in silica, and depletes it in Ca and Al through the incorporation of $CaAl_2SiO_6$ in pyroxene. The excess-silica data can therefore be understood in terms of a simple undercooling series. In 12011 plagioclase began crystallizing at a lower temper-

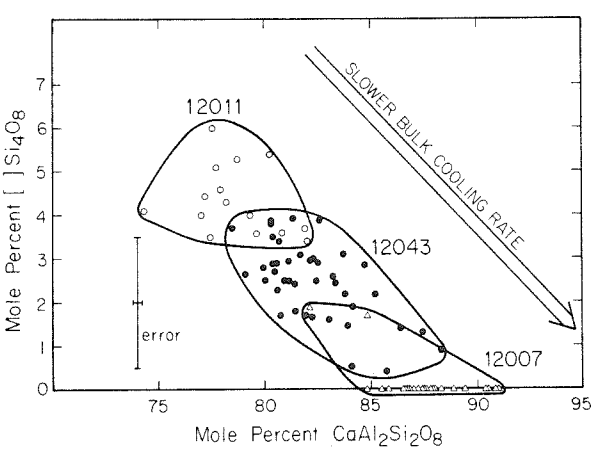

Fig. 3. Excess silica in plagioclase from the Apollo 12 pigeonite basalts. In each sample, single crystals are zoned from calcic [ ]Si_4O_8-poor cores to sodic [ ]Si_4O_8-rich rims. Superimposed on this is a cooling rate effect: the slower the rock cooled, the less overall excess silica its feldspar contains. This indicates that kinetic factors are also responsible for the incorporation of excess silica in plagioclase.

ature and from a more siliceous melt than the plagioclase in 12007.

When plagioclase and one of the silica polymorphs are in equilibrium, their compositions are determined by the solvus portion of Figure 2. The position of the solvus is relatively insensitive to the liquid composition (for a more detailed discussion, see below). Therefore, since all the pigeonite basalts are in equilibrium with either cristobalite or tridymite at their solidi, it is theoretically possible to compare solidus temperatures by examining the excess silica contents of the last plagioclase to crystallize. This suggests that 12011, which has more [ ]Si_4O_8, had a higher solidus temperature than 12007. Figure 2, however, indicates that this temperature difference would have to be several hundred degrees, which is petrologically unreasonable. This evidence argues that the high [ ]Si_4O_8 contents of the more rapidly cooled samples, such as 12011 and 12043, are produced by disequilibrium kinetic factors.

Experimental studies (*e.g.* Grove and Bence, 1979) show that with increased cooling rates the abundances of the minor constituents increase in each mineral. This is thought to be related to kinetic factors: if the material in the magma at the mineral–melt interface does not have time to diffuse away from the growing crystal, it is incorporated (Albarede and Bottinga, 1972). The high [ ]Si_4O_8 contents of 12011 and 12043 may in part be related to this process. Also important is the delayed nucleation of the silica phase (Longhi, personal communication, 1979), which could cause the metastable incorporation of [ ]Si_4O_8 in plagioclase in large amounts. The significance of kinetic effects is confirmed by the observation that most lunar basalts have solidi about 1050°C, and at that temperature plagioclase in equilibrium (using Longhi and Hays' Fig. 1) with tridymite contains about 3 mole percent [ ]Si_4O_8. The high [ ]Si_4O_8 contents of mesostasis plagioclase, therefore, appear to be kinetically controlled.

Apollo 17 basalts

The positive correlation between overall excess silica content and cooling rate is also present in a suite of Apollo 17 basalts (Fig. 4). 70215 contains from 2–7.5 percent [ ]Si_4O_8, 74255 has 0–6 percent, 71055 has 1–4 percent, and 75055 ranges from 0–2 percent. According to the petrographic observations of Dymek *et al.* (1975), the cooling rate decreased in the same order (70215 > 74255 > 71055 > 75055). In contrast to the Apollo 12 pigeonite basalt suite, these data do not define a common trend. Unlike the pigeonite basalts, however, there is little assurance that these four samples came from the same lava flow. The excess silica data suggests that 70215 and 71055 followed the same liquid line of descent (Fig. 4), but that 74255 crystallized along a different path. Note that each sample considered alone shows the anticipated inverse correlation between [ ]Si_4O_8 and anorthite content.

Apollo 15 basalts

We have analyzed plagioclase from three Apollo 15 basalts. In both 15555 and 15682, olivine-normative and quartz-normative samples respectively, the excess silica increases from 0 percent at An_{86} to 4 percent at An_{76}. In common with the Apollo 12 pigeonite basalts, plagioclase was the last major phase to crystallize. The trends suggest similar liquid lines of descent for the two magmas. However, 15976, another quartz-normative basalt, has a maximum of only about 1 mole percent excess silica.

Apollo 11 high-K basalts

Most of the Apollo 11 high-K basalts have plagioclase containing large amounts of excess silica (Beaty and Albee, 1978). In some samples [ ]Si_4O_8 is correlated with anorthite content (Fig. 5, 10024, 10017), but in others it is not (*e.g.* 10072). 10024, the coarsest-grained rock of the suite, ranges from 2–7 percent [ ]Si_4O_8 (Fig. 5). In order of decreasing grain size 10072, 10071, 10017, 10069, and 10049 contain 1–4, 0–7, 0–2, 0–1, and 0–7 percent excess silica, respectively. Unlike the Apollo 12 and 17 suites, the overall amount of excess silica is not correlated with the in-

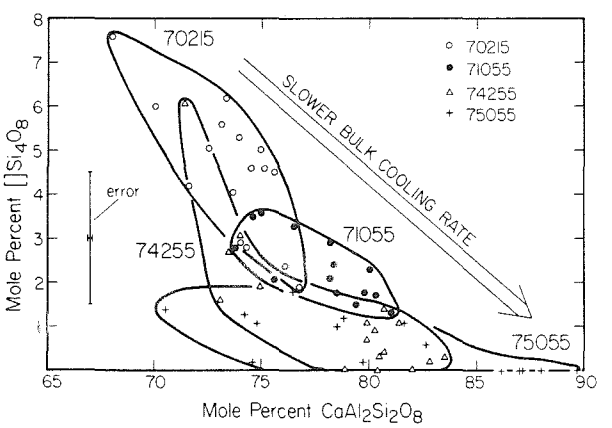

Fig. 4. Excess silica zoning in Apollo 17 basalts. In each sample excess silica increases from core to rim of the plagioclase. As in Apollo 12 basalts (Fig. 3), the bulk cooling rate also affects the amount of excess silica.

ferred cooling rate. Neither does it depend on the bulk composition. In short, the excess silica contents of these samples vary in a way not easily understood in terms of any of the arguments advanced above.

As discussed in the section on Apollo 11 low-K basalts, a natural consequence of the anorthite–SiO_2 phase diagram (Fig. 2) is that the amount of excess silica in plagioclase will steadily increase with crystallization until cristobalite saturation occurs (at the eutectic), where crystallization is completed. In multicomponent systems cristobalite saturation will occur at a cotectic and plagioclase and cristobalite will cocrystallize down the cotectic. As long as the liquid is in equilibrium with both cristobalite and plagioclase, the amount of [ ]Si_4O_8 in the plagioclase will decrease with falling temperature. Thus, [ ]Si_4O_8 reversals ought to be present in the rims of feldspars from cristobalite-bearing lavas. Such reversals were reported for six of the ten Apollo 11 high-K samples (Beaty and Albee, 1978). Reexamination, however, indicates that the data are only suggestive, not conclusive.

Luna 24 and Apollo 14 basalts

In contrast to the above data, several lunar basalts contain little or no excess silica in their plagioclase. Ferrobasalt 24170, for example, has excess silica values close to zero. The data range from 0–2 percent [ ]Si_4O_8, and are scattered with no detectable zoning. Since the data spread is somewhat shifted off zero, there is probably a small (~0.5 percent) amount of [ ]Si_4O_8 actually present in the plagioclase. Grove and Bence (1979), however, report that in their dynamic crystallization experiments on a Luna 24 composition, [ ]Si_4O_8 in plagioclase increases from rock to rock with both cooling rate and falling temperature. Like 24170, Apollo 14 basalts 14310 and 14053 also contain very little excess silica.

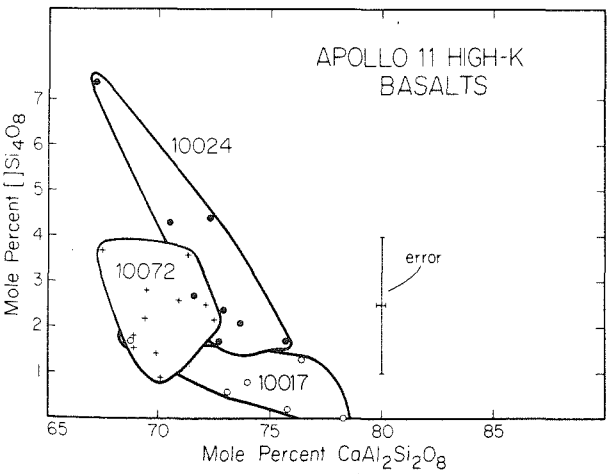

Fig. 5. [ ]Si_4O_8 in plagioclase from the Apollo 11 high-K basalts 10024, 10072, and 10017. Unlike Figs. 3 and 4, there is no correlation with bulk cooling rate; the variations within the suite cannot be related to any known parameter. 10024 and 10017 show the negative correlation between [ ]Si_4O_8 and $CaAl_2Si_2O_8$ found in plagioclase from most lunar basalts (Figs. 1, 3, and 4).

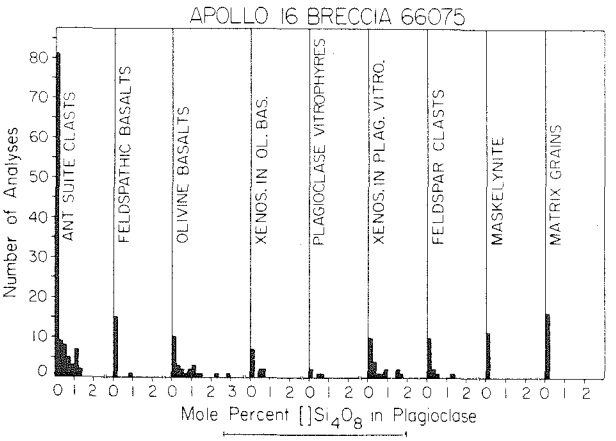

Fig. 6. Excess silica in plagioclase from lunar highlands breccia 66075. Unlike those in the mare basalts, these feldspars are virtually devoid of [ ]Si_4O_8. In all but the olivine basalt clasts the data lie within analytical uncertainty (1.5 mole percent) of zero. These plagioclases are also essentially unzoned (An_{97-93}). In the olivine basalts, however, the plagioclase is zoned from An_{94-83} and from 0–3 percent [ ]Si_4O_8. This illustrates the importance of *in situ* differentiation to the formation of [ ]Si_4O_8.

It is difficult to understand why the plagioclase in these samples contains no excess silica. The pyroxene zoning trends indicate *in situ* differentiation (Gancarz *et al.*, 1971; Wasserburg *et al.*, 1978), and the liquids all became siliceous enough near their solidi to precipitate cristobalite. Furthermore, the parental liquids are thought to have crystallized through temperature intervals (Grove and Vaniman, 1978; Walker *et al.*, 1975) similar to the previously discussed mare basalts. One possible explanation lies in the observation (Longhi, personal communication 1979) that most lunar basalts crystallized pyroxene before plagioclase, whereas in Luna 24 and Apollo 14 plagioclase precedes or is simultaneous with pyroxene. Perhaps the delayed nucleation of plagioclase followed by supersaturation and rapid growth is necessary for the incorporation of large amounts of excess silica.

The lunar highlands (Apollo 16)

There is negligible excess silica in plagioclase from the anorthositic lunar highlands. Quick *et al.* (1978) divided the plagioclase in highlands soil breccia

66075 into nine populations: anorthosite–norite–troctolite (ANT) clasts, feldspathic basalts, olivine basalts, xenoliths in the olivine basalts, plagioclase vitrophyres, xenoliths in the plagioclase vitrophyres, feldspar clasts, maskelynite clasts, and matrix grains. All plagioclases except those from the olivine basalts have compositions in the range An_{93}–An_{97} and excess silica contents of between 0 and 1.3 mole percent (Fig. 6). About 80 percent of these analyses indicate less than 0.2 percent [ ]Si_4O_8, and the data spread reflects analytic uncertainty about a true value of zero. In the olivine basalt clasts, however, the plagioclase is zoned from An_{94} to An_{83} and the excess silica increases sympathetically from 0–3 mole percent (Fig. 6). Because the olivine basalts are extremely rare, it is possible to conclude from this that there is no measurable excess silica in the large anorthosite–gabbro masses that make up the lunar highlands.

Both the plagioclase vitrophyres and the olivine basalts are interpreted to be impact melt-rocks (Quick *et al.*, 1978), and as such have undergone similar cooling histories. Both melts were highly olivine-normative and were rapidly cooled from a high temperature under similar conditions. The olivine basalts, however, underwent fractional crystallization to a greater degree than did the plagioclase vitrophyres, as indicated by the more sodic feldspars. Greater differentiation can also explain the differences in [ ]Si_4O_8 contents—the more evolved residual liquids in the olivine basalts were probably more siliceous than those in the plagioclase vitrophyres. Consequently, they were able to crystallize more [ ]Si_4O_8-rich plagioclase. Study of these melt-rocks, therefore, underlines the importance of *in situ* differentiation to increase [ ]Si_4O_8; it is a common means of producing the necessarily siliceous parental melts.

Terrestrial plagioclase

In contrast to the lunar samples discussed above, none of the terrestrial rocks studied contain [ ]Si_4O_8-bearing plagioclase. Figure 7 shows a set of plagioclase analyses from a basalt flow in the Jemez Mountains, New Mexico. Most data indicate a complete absence of [ ]Si_4O_8, and all analyses are within the analytical uncertainly of zero. Similar results were obtained from four other basalt flows in the area as well as from tholeiites (Longhi and Hays, 1979).

The differences between these samples and most of the mare basalts are profound. Figure 7 also shows data for the Skaergaard intrusion, probably the best-understood igneous body in world. Like the New Mexican basalts, none of its plagioclase contains measurable amounts of [ ]Si_4O_8. Although they are not illustrated, excess silica is also absent in plagio-

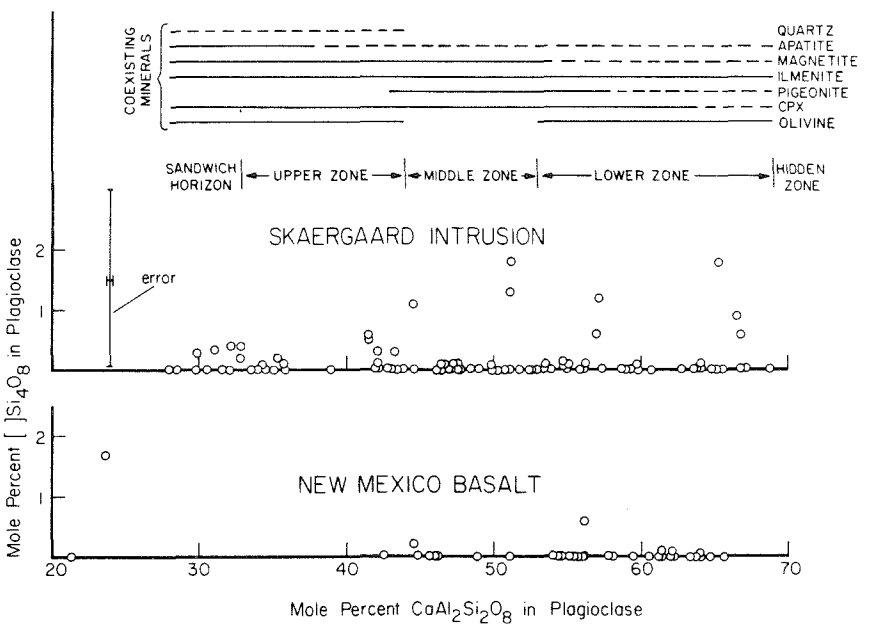

Fig. 7. Excess silica content of plagioclase as a function of anorthite content for the Skaergaard intrusion and a basalt from the Jemez Mountains, New Mexico. Shown for reference are the coexisting minerals of the Skaergaard (solid = cumulus phase, dashed = intercumulus or indeterminate) (Wager and Brown, 1967, p. 26–27). The data represent analytic uncertainty about a value of zero, indicating an absence of [ ]Si_4O_8 in the plagioclase. This pattern is typical of that found in all terrestrial rocks examined in this study.

clase analyses from amphibolites from Vermont, granulites from Greenland, lherzolite from California, andesite from Paricutin, peridotite xenoliths in New Mexico basalt flows, a granodiorite from Australia, a tonalite from the Baja California batholith, pelitic schists from Death Valley, and arkosic sandstones from California.

Note that if Na and K are lost by volatilization from the volume being analyzed, there will be deficiency in the larger site, and depending on how the end-members are calculated, the resulting composition may have fictitious excess silica. This alkali loss can occur when the electron beam has too small a diameter. Although such analyses need to be eliminated, it is difficult to distinguish genuine excess silica from alkali loss or otherwise bad analyses. Zoning patterns like that in Figure 7, however, lead us to conclude that for the terrestrial samples we have studied, the presence of large amounts (>2 percent) of excess silica is a good criterion for discarding the analysis. Furthermore, none of the high-[ ]Si_4O_8 analyses could be reproduced when analyzed a second time.

Discussion of terrestrial data

There are several possible explanations for the absence of [ ]Si_4O_8 in terrestrial plagioclase. First of all, terrestrial basalts typically do not show extensive *in situ* fractional crystallization. As discussed above in connection with Apollo 16, fractional crystallization is essential to the production of [ ]Si_4O_8 in basaltic plagioclase. In addition, terrestrial basalts, like Luna 24 and Apollo 14, crystallize plagioclase before pyroxene, so there is less opportunity for delayed nucleation effects to generate [ ]Si_4O_8.

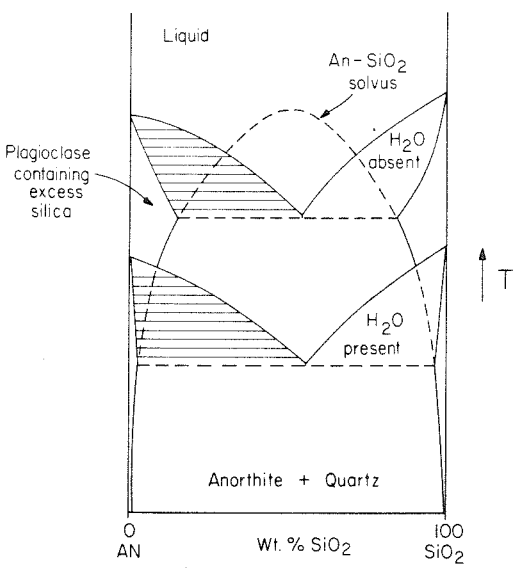

Fig. 8. Schematic phase diagram anorthite–SiO_2 illustrating the effect of adding H_2O. The liquidus is significantly depressed, but the solvus is not affected. This in turn dramatically decreases the amount of [ ]Si_4O_8 in the plagioclase (shown by the tie lines). This is one reason why (wet) terrestrial magmas such as the Skaergaard (Fig. 7) have no [ ]Si_4O_8, but in equally differentiated (dry) lunar basalts (Figs. 1, 3, 4, and 5) it abounds.

The liquid line of descent followed by the Skaergaard as it crystallized, however, was similar to that followed by the lunar mare basalts. The degree of silica saturation increased steadily with fractional crystallization, culminating in quartz precipitation in the Upper Zone and Sandwich Horizon (Fig. 7). Although the liquid paths of the Skaergaard and the lunar basalts were similar chemically, they were different thermally. The lunar basalts were dry, whereas the Skaergaard magma, like all terrestrial magmas, contained a small amount of water, appreciably depressing its liquidus temperature. The plagioclase therefore crystallized at lower temperature, a condition sufficient to cause the plagioclase to incorporate much less [ ]Si_4O_8.

This effect is schematically illustrated in Figure 8. As other components, such as albite, orthoclase, pyroxene, olivine, and particularly volatiles, are added to the binary system anorthite–SiO_2 (Figure 2) to make a rock, the liquidus will be depressed to lower temperatures. The effect on the plagioclase–SiO_2 solvus is more difficult to predict. The presence of a component which is insoluble in either anorthite or the SiO_2 polymorphs at all temperatures will not affect the equilibrium between them. The addition of phases like pyroxene, ilmenite and water to the simple binary system, therefore, will closely approximate the behavior shown in Figure 8. The melting loop will be lowered, whereas the solvus will have a nearly constant position independent of the bulk composition.

Varying the albite content of the plagioclase, however, could either increase or decrease the solvus temperature. According to Kim and Burley (1971), albite may contain up to 5 mole percent silica in solid solution at 5.15 kbar and 670°C. From size and charge considerations, albite might be expected to contain more [ ]Si_4O_8 than anorthite at any given temperature (J. B. Thompson, personal communication, 1979). Although both albite and anorthite are therefore known to contain excess silica, the detailed shape of the "SiO_2"–plagioclase solvus as a function of plagioclase composition is uncertain. Note that this problem can be avoided by comparing feldspars

of constant albite content. With these limitations in mind, a great deal of insight can be gained from Figure 8.

Figure 8 shows in a schematic way one reason why measurable amounts of [ ]Si_4O_8 are not present in the Skaergaard plagioclases. The solubility of silica in plagioclase decreases with temperature, and the temperature interval over which the Skaergaard crystallized was too low for measurable amounts of [ ]Si_4O_8. The effect is more important for magmas such as granites and tonalites which have high water contents and even lower crystallization temperatures. A low temperature of formation can also explain why excess silica was not found in any of the metamorphic plagioclase studied. In addition to the temperature effect, terrestrial plutonic feldspar is less subject to the disequilibrium kinetic factors which are important in producing [ ]Si_4O_8 in lunar basaltic plagioclase.

Meteorites

We have analyzed plagioclase from the St. Severin chondrite (LL6) and found that it contains no excess silica. The anorthite in the white inclusions in Allende also contain no excess silica (Lee *et al.*, 1977; Bradley *et al.*, 1978). Colomera, an unusual iron meteorite with silicate globules, has both plagioclase and K-feldspar which are [ ]Si_4O_8-free. Using data from other laboratories, Bence and Burnett (1969) reported that crypto-antiperthite from Kodaikanal ranged from 0–4 percent high in SiO_2. Partial (6-element) analyses of the plagioclase in enstatite chondrites (Keil, 1968) also suggest small amounts of excess silica. The enstatite chondrites are an extremely reduced group containing Si dissolved in the metal (Ringwood, 1961; Keil, 1968). The excess silica in the plagioclase may be related to the presence of elemental silicon. Additional work is necessary to more fully evaluate the [ ]Si_4O_8 variations among meteorites.

Excess silica preservation

Most of the preceding discussion has treated the variable incorporation of [ ]Si_4O_8 in plagioclase crystals at high temperature. [ ]Si_4O_8 may or may not have been preserved as the crystal cooled to room temperature, however. Two mechanisms are available by which the excess silica could be lost: exsolution and diffusion. If the [ ]Si_4O_8 were lost by exsolution, a distinctive myrmekite consisting of ~5 percent quartz and 95 percent plagioclase (as opposed to a 50–50 mixture) would be formed. The authors have neither seen such an intergrowth nor are aware of any reported in the literature. Observation is made more difficult by the uncertainty in distinguishing magmatic from exsolved quartz inclusions (*e.g.*, Walker *et al.*, 1973, p. 1018). Submicroscopic exsolutions may be present, but if so they are in low abundance, otherwise they would show up in the microprobe analyses.

Likewise there is little evidence that [ ]Si_4O_8 is lost by diffusion. The excess silica gradients in the Apollo 11 low-K basalts (Fig. 1) show no evidence of being flattened, even in the most slowly cooled samples. Although less [ ]Si_4O_8 is contained in the more slowly cooled Apollo 12 and Apollo 17 basalts, this is probably related to the physical conditions of growth rather than diffusive loss (see above). The apparent low diffusion coefficient of [ ]Si_4O_8 is related to the fact that it is an integral part of the feldspar structure. In order for [ ]Si_4O_8 to be lost, a crystal must both lose Si and gain either Ca and Al or Na and Al, a complicated coupled diffusion process. If such processes were operating the anorthite–albite zoning of the crystals would also be affected. Therefore, any plagioclase grain which has preserved its anorthite–albite zoning might also be expected to preserve its excess silica zoning.

Thus far, excess silica has been confirmed in plagioclase from relatively rapidly cooled lunar volcanic rocks. In the much more slowly cooled plutonic rocks from both the moon and the earth, [ ]Si_4O_8 is absent. Plutonic plagioclase is also typically unzoned, hence it is not possible to be certain whether or not [ ]Si_4O_8 was originally present.

Summary

Most of the variations in the [ ]Si_4O_8 content of natural plagioclase can be understood in terms of a few simple factors. Most importantly, a high temperature of formation and a siliceous parental melt are essential. Excess silica typically increases monotonically from core to rim of the plagioclase in lunar basalts. This trend is caused by two cooperative effects—falling temperature increases the solubility of [ ]Si_4O_8 in plagioclase, and fractional crystallization of the melt causes the plagioclase to grow from an increasingly siliceous residual liquid. In addition to these equilibrium processes, delayed nucleation of plagioclase and a silica phase followed by rapid feldspar growth can cause metastable incorporation of [ ]Si_4O_8 in large amounts.

These effects are schematically illustrated in Figure 9. Lunar basalts, which crystallize at high temperatures with large degrees of fractional crystalliza-

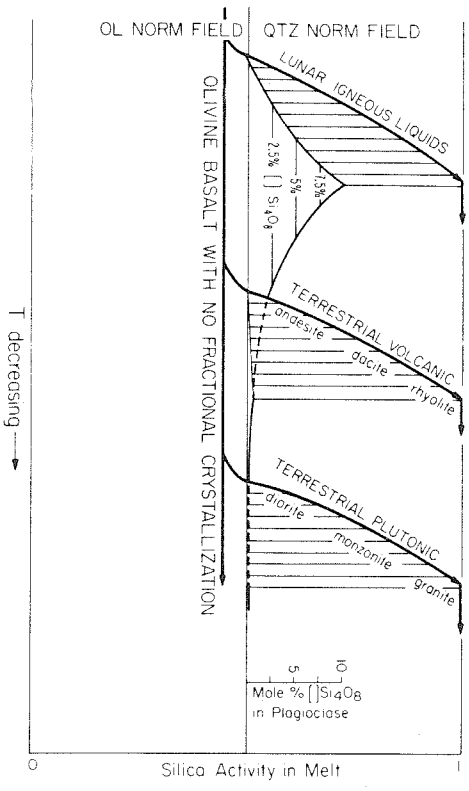

Fig. 9. Schematic diagram showing the relationship between the field of excess silica and natural igneous rocks. By projecting different liquid lines of descent onto this diagram it is possible to illustrate the major factors responsible for the incorporation of [ ]Si_4O_8 in plagioclase. If an olivine-normative basalt undergoes no fractional crystallization, it will follow the arrow so labeled and never enter the [ ]Si_4O_8 stability field. With differentiation at high temperature (*e.g.* lunar igneous liquids), much [ ]Si_4O_8 will be present. At lower temperatures, the terrestrial volcanic spectrum is expected to have only minor amounts of [ ]Si_4O_8. At even lower temperatures, plagioclase in terrestrial plutonic rocks should have even less [ ]Si_4O_8. In addition, the delayed nucleation and rapid growth of plagioclase can cause the disequilibrium incorporation of large amounts of [ ]Si_4O_8.

tion, contain large amounts of [ ]Si_4O_8. The fact that the observed [ ]Si_4O_8 concentrations (up to 8%) exceed those predicted by Figure 2 (3%) can be attributed to kinetic effects. In contrast to the lunar basalts, terrestrial basalts have no [ ]Si_4O_8 in their plagioclase. This is related to two reasons. First, terrestrial basalts do not show the strong *in situ* differentiation of the lunar basalts—the residual liquids do not have high silica activities. As shown on Figure 9, an olivine basalt which undergoes no fractional crystallization will not enter the [ ]Si_4O_8 stability field. In addition, plagioclase crystallizes before pyroxene in most terrestrial basalts, reducing the possibility of metastable [ ]Si_4O_8. Secondly, terrestrial lavas contain water, which significantly depresses their liquidi compared to their lunar counterparts. Even if a terrestrial lava were to differentiate to a siliceous residual liquid, the temperature would be so low that [ ]Si_4O_8 would be below the detection limit (Fig. 9). The most siliceous terrestrial volcanic rocks (most favorable compositionally for [ ]Si_4O_8) also have the lowest liquidus temperatures (least favorable thermally for [ ]Si_4O_8) and *vice versa*. Plagioclases in terrestrial plutonic rocks should contain even less [ ]Si_4O_8 than those in the volcanic rocks, because they crystallize at even lower temperatures (Fig. 9). Applying these results to actual rocks, the detailed differences in [ ]Si_4O_8 zoning between samples can be used to compare the temperatures, nucleation histories, and liquid lines of descent of different magmas.

Because of the kinetic complications, care is needed when applying equilibrium phase diagrams to rapidly cooled samples. Once [ ]Si_4O_8 has been incorporated in a plagioclase crystal at high temperature, however, it is preserved. There is no evidence that the excess silica is lost, either through exsolution or diffusion, as the crystal cools to room temperature. For all but the most rapidly cooled samples, therefore, the amount of [ ]Si_4O_8 in the plagioclase as we measure it today is directly related to the condition of its formation.

If a magma is in equilibrium with cristobalite (or tridymite or quartz), the silica activity of the melt is buffered, and [ ]Si_4O_8 can be directly used as a geothermometer. This technique appears to be most promising as a means of comparing the solidus temperatures of lunar basalts. Measurement of the effect of albite substitution (determination of the An–Ab–Qtz ternary solvus) should enable this geothermometer to be quantified. Alternatively, for magmas with the same solidus temperatures, [ ]Si_4O_8 should allow measurement of the departure from equilibrium crystallization.

Acknowledgments

Discussions with John Longhi, Bob Dymek, and George Rossman stimulated the authors' interest in this study. The data were collected by several Caltech graduate students between 1975 and 1978 as parts of their theses and research projects. Bob Gregory and Scott Baldridge were particularly generous with their unpublished data. The manuscript was typed by Lou Ann Cordell and Betty Robinson. Early comments by Bob Gregory and George Rossman and thorough reviews by Tim Grove and John Longhi have significantly improved the manuscript. The support of NASA grant NGL-05-002-338 is gratefully acknowledged.

References

Albarede, F. and Y. Bottinga (1972) Kinetic disequilibrium in trace element partitioning between phenocrysts and host lava. *Geochim. Cosmochim. Acta, 36*, 141–156.

Appleman, D. E., H.-U. Nissen, D. B. Stewart, J. R. Clark, E. Dowty and J. S. Huebner (1971) Studies of lunar plagioclases, tridymite, and cristobalite. *Proc. Lunar Sci. Conf. 2nd*, 117–133.

Baldridge, W. S., D. W. Beaty, S. M. R. Hill and A. L. Albee (1979) The petrology of the Apollo 12 pigeonite basalt suite. *Proc. Lunar Sci. Conf. 10th*, in press.

Beaty, D. W. and A. L. Albee (1978) Comparative petrology and possible genetic relations among the Apollo 11 basalts. *Proc. Lunar Sci. Conf. 9th*, 359–463.

——— and ——— (1979) Silica solid solution in natural plagioclase (abstr.). *EOS, 60*, 415.

———, S. M. R. Hill and A. L. Albee (1979a) Petrology of a new rock type from Apollo 11: Group D basalts (abstr.). *Lunar and Planetary Science, X*, 89–91.

———, ———, ———, M.-S. Ma and R. A. Schmitt (1979b) The petrology and chemistry of basaltic fragments from the Apollo 11 soil, Part I. *Proc. Lunar Sci. Conf. 10th*, in press.

———, ——— and ——— (1979c) Apollo 12 feldspathic basalts 12031, 12038 and 12072; petrology, comparison and interpretations. *Proc. Lunar Sci. Conf. 10th*, in press.

Bell, P. M. and H. K. Mao (1973) Optical and chemical analysis of iron in Luna 20 plagioclase. *Geochim. Cosmochim. Acta, 37*, 755–759.

Bence, A. E. and D. S. Burnett (1969) Chemistry and mineralogy of the Kodaikanal meteorite. *Geochim. Cosmochim. Acta, 33*, 387–407.

Bradley, J. G., J. C. Huneke and G. J. Wasserburg (1978) Ion microprobe evidence for the presence of excess ^{26}Mg in an Allende anorthite crystal. *J. Geophys. Res., 83*, 244–254.

Bruno, E. and A. Facchinelli (1974) Experimental studies on anorthite crystallization along the join $CaAl_2Si_2O_8$–SiO_2. *Bull. Soc. fr. Mineral. Cristallogr., 97*, 422–432. (not seen, *fide* Longhi and Hays, 1979).

Carmen, J. H. and O. F. Tuttle (1963) Experimental study bearing on the origin of myrmekite (abstr.) *Geol. Soc. Am. Spec. Pap., 76*, 29.

——— and ——— (1967) Experimental verification of solid solution of excess silica in sanidine from rhyolites (abstr.) *Geol. Soc. Am. Spec. Pap., 115*, 33–34.

Champion, D. E., A. L. Albee and A. A. Chodos (1975) Reproducibility and operator bias in a computer-controlled system for quantitative electron microprobe analysis. *Proc. Natl. Conf. on Electron Probe Anal., 10th*, Microbeam Analysis Society, Las Vegas, Nevada.

Chayes, F. and E. G. Zies (1962) Sanidine phenocrysts in some peralkaline volcanic rocks. *Carnegie Inst. Wash. Year Book, 61*, 112–118.

Dymek, R. F., A. L. Albee and A. A. Chodos (1975) Comparative mineralogy and petrology of Apollo 17 mare basalts: samples 70215, 71055, 74255 and 75055. *Proc. Lunar Sci. Conf. 6th*, 49–77.

Gancarz, A. J., A. L. Albee and A. A. Chodos (1971) Petrologic and mineralogic investigation of some crystalline rocks returned by the Apollo 14 mission. *Earth Planet. Sci. Lett., 12*, 1–18.

Grove, T. L. and A. E. Bence (1979) Crystallization kinetics in a multiply saturated basalt magma: an experimental study of Luna 24 ferrobasalt. *Proc. Lunar Sci. Conf. 10th*, in press.

——— and M. Raudsepp (1978) Effects of kinetics on the crystallization of quartz normative basalt 15597: an experimental study. *Proc. Lunar Sci. Conf. 9th*, 585–599.

——— and D. T. Vaniman (1978) Experimental petrology of very low Ti (VLT) basalts. *Mare Crisium: The View from Luna 24*, p. 445–471. Pergamon Press, New York.

Hafner, S. S., D. Virgo and D. Warburton (1971) Oxidation state of iron in plagioclase from lunar basalts. *Earth Planet. Sci. Lett., 12*, 159–166.

Ito, J. (1976) High temperature solvent growth of anorthite on the join $CaAl_2Si_2O_8$–SiO_2. *Contrib. Mineral. Petrol., 59*, 187–194.

Keil, K. (1968) Mineralogical and chemical relationships among enstatite chondrites. *J. Geophys. Res., 73*, 6945–6976.

Kim, K.-T. and B. J. Burley (1971) Phase equilibria in the system $NaAlSi_3O_8$–$NaAlSiO_4$–H_2O with special emphasis on the stability of analcite. *Can. J. Earth Sci., 8*, 311–337.

Lee, T., D. A. Papanastassiou and G. J. Wasserburg (1977) Mg and Ca isotopic study of individual microscopic crystals from the Allende meteorite by the direct loading technique. *Geochim. Cosmochim. Acta, 41*, 1473–1485.

Longhi, J. and J. F. Hays (1979) Phase equilibria and solid solution along the join $CaAl_2Si_2O_8$–SiO_2. *Am J. Sci., 279*, 876–890.

———, D. Walker and J. F. Hays (1976a) Fe, Mg and silica in lunar plagioclase (abstr.). *Lunar Science, VII*, 501–503. The Lunar Science Institute, Houston.

———, ——— and ——— (1976b) Fe and Mg in plagioclase. *Proc. Lunar Sci. Conf. 7th*, 1281–1300.

Luth, W. C. and O. F. Tuttle (1966) The alkali feldspar solvus in the system Na_2O–K_2O–Al_2O_3–SiO_2–H_2O. *Am. Mineral., 51*, 1359–1375.

Megaw, H. (1970) Structural relationship between coesite and feldspar. *Acta Crystallogr., B26*, 261–265.

Orville, P. M. (1972) Plagioclase cation exchange equilibria with aqueous chloride solution: results at 700°C and 2000 bars in the presence of quartz. *Am. J. Sci., 272*, 234–272.

Phillips, E. R. (1964) Myrmekite and albite in some granites of the New England batholith, New South Wales. *J. Geol. Soc. Aust., 11*, 49–60.

Quick, J. E., B. S. Brock and A. L. Albee (1978) Petrology of Apollo 16 breccia 66075. *Proc. Lunar Sci. Conf. 9th*, 921–939.

Ringwood, A. E. (1961) Silicon in the metal phase of enstatite chondrites and some geochemical implications. *Geochim. Cosmochim. Acta, 25*, 1–13.

Schwantke, A. (1909) Die Beimischung von Ca im Kalifeldspat und die Myrmekitbildung. *Centralbl. Mineral.*, 311–316. (not seen, *fide* Longhi and Hays, 1979).

Sclar, C. B. and R. L. Kastelic (1979) Iron in anorthite: synthesis and characterization of the $CaAl_2Si_2O_8$–$CaFeSi_3O_8$ series (abstr.) *EOS, 60*, 421.

Spencer, E. (1945) Myrmekite in graphic granite and in vein perthite. *Mineral. Mag., 27*, 79–98.

Thompson, J. B. and G. L. Hovis (1979) Structural-thermodynamic relations of the alkali feldspars. *Am. Crystallogr. Assoc. Programs with Abstracts, 6*, No. 2, 49.

Wager, L. R. and G. M. Brown (1967) *Layered Igneous Rocks.* Freeman, San Francisco.

Walker, D., M. A. Powell and J. F. Hays (1978) Dynamic crystallization of a eucritic basalt (abstr.). *Lunar and Planetary Science, IX*, 1196–1198.

———, J. Longhi, T. L. Grove, E. Stolper and J. F. Hays (1973) Experimental petrology and origin of rocks from the Descartes Highlands. *Proc. Lunar Sci. Conf. 4th*, 1013–1032.

———, ———, E. M. Stolper, T. L. Grove and J. F. Hays (1975)

Origin of titaniferous lunar basalts. *Geochim. Cosmochim. Acta, 39*, 1219–1235.

Wasserburg, G. J. and The Lunatic Asylum (1978) Petrology, chemistry, age and irradiation history of Luna 24 samples. *Mare Crisium: The View from Luna 24*, p. 657–678. Pergamon Press, New York.

Weill, D. F., I. S. McCallum, Y. Bottinga, M. J. Drake and G. A. McKay (1970) Mineralogy and petrology of some Apollo 11 igneous rocks. *Proc. Apollo 11 Lunar Sci. Conf.*, 937–956.

Wenk, H. R. and W. R. Wilde (1973) Chemical anomalies of lunar plagioclase, described by substitution vectors and their relation to optical and structural properties. *Contrib. Mineral. Petrol., 41*, 89–104.

Wyart, J. and G. Sabatier (1965) Reactions of alkalic feldspars with hydrothermal CaCl solutions. *C. R. Acad. Sci., 260*, 1681–1685.

Manuscript received, May 21, 1979;
accepted for publication, October 1, 1979.

Proc. Lunar Planet. Sci. Conf. 10th (1979), p. 115–139.
Printed in the United States of America

Apollo 12 feldspathic basalts 12031, 12038 and 12072: Petrology, comparison and interpretations

D. W. Beaty, S. M. R. Hill, A. L. Albee and W. S. Baldridge†

Division of Geological and Planetary Sciences*, California Institute of Technology, Pasadena, California 91125
†Present address: Los Alamos Scientific Laboratory (Geological Research Group), Los Alamos, New Mexico 87545

Abstract—Modal and chemical data indicate that 12072, 12038, and 12031, the Apollo 12 feldspathic basalts, form a well-defined group which cannot be related to the other Apollo 12 rock types. 12072 contains phenocrysts of olivine and pigeonite and microphenocrysts of Cr-spinel set in a fine-grained, variolitic groundmass. 12038 is a medium-grained, equigranular basalt with a texture indicating it was multiply saturated. 12031 is a coarse-grained rock with granular to graphic intergrowths of pyroxene and plagioclase; it was also multiply saturated.

Petrologic observations, as well as the bulk chemistry, are consistent with the interpretation that 12031 could be derived from 12072 through fractionation of Cr-spinel, olivine, and pigeonite, the observed phenocryst assemblage. 12038, however, contains more pigeonite, less olivine, three times as much Ca-phosphate minerals, one-fifth as much troilite, and a much more sodic plagioclase than 12072. These differences indicate that 12038 must have come from a separate igneous body. Consideration of the bulk compositions indicates that neither 12072 and 12031 nor 12038 could have been derived from the Apollo 12 olivine, pigeonite, or ilmenite basalts by crystal-liquid fractionation. This extends to five the number of magma types represented in the Apollo 12 collection. The general petrologic similarities between 12072, 12031 and the other Apollo 12 basalts suggest that they were produced in either the same or similar source regions. 12038, however, is petrologically and chemically unique, and is probably exotic to the Apollo 12 landing site.

I. INTRODUCTION

12038 was among the first group of Apollo 12 basalts to be analyzed (LSPET, 1970), and it was immediately singled out as being different. In particular, LSPET noted that 12038 had a composition similar to that of the eucrites (basaltic achondrites). The uniqueness of 12038 was confirmed in the studies of Haskin *et al.* (1971), Compston *et al.* (1971), Cuttita *et al.* (1971), Biggar *et al.* (1971), and Schnetzler and Philpotts (1971). All of these workers except Biggar *et al.* (1971) concluded that it would be either difficult or impossible to derive 12038 from the other Apollo 12 basalts. In addition to the chemical differences, 12038 has a distinctly higher plagioclase content than most of the Apollo 12 basalts. This led James and Wright (1972) to classify 12038, along with 12006, as feldspathic ba-

*Contribution No. 3242

salts. Rhodes *et al.* (1977), using chemical data not available to James and Wright, showed that 12006 should be classed as an olivine basalt. In addition, their analyses suggested that 12031, originally classed as an ilmenite basalt (James and Wright, 1972), is also a feldspathic basalt. There are important differences between 12031 and 12038, however, so the grouping was only tentative (Rhodes *et al.*, 1977). 12072 was originally classified as an olivine basalt (Baldridge *et al.*, 1978) on the basis of its superficial resemblance to the finer-grained members of that suite. Measurement of its mode and bulk composition (this work), however, indicates that it is similar to 12031, and dissimilar to the olivine, pigeonite and ilmenite basalts. Accordingly, it is also termed a feldspathic basalt.

In spite of the past problems with classification, the feldspathic basalts constitute a well-defined group. Each sample fits the defining criteria originally established by James and Wright (TiO_2<4%, Al_2O_3>11.5%, FeO<18%). They are all relatively feldspar-rich, and none can be related to the other Apollo 12 rock types by crystal-liquid fractionation (see below). To further evaluate the significance of these three samples, we have undertaken a comparative petrologic study. First, we seek to answer the question, how are these feldspathic basalts related to one another? With this background, the evidence against their being related to the olivine, pigeonite or ilmenite basalts is summarized. Finally, the problem of petrogenesis is considered.

II. ANALYTICAL TECHNIQUES

Microprobe analyses were made using a MAC-5-SA3 electron microprobe interfaced to a PDP-8/L computer for control and on-line data processing. Each analysis was obtained by measuring on a single spot 9–15 elements in groups of three. The data were reduced using the Bence-Albee technique. Standard operating conditions were 15 kv accelerating voltage and 0.05 μA sample current (on brass) with beam current integration and pulse height selection. Reproducibility (1σ) on two "known unknown" secondary standards over a 13-month period ranged from 1½% (for elements with abundances >1%) to 3% of the amount present (for elements with abundances 0.1–1.0%) Champion *et al.* (1975).

Microprobe point counts were performed using a 161 Ev Si(Li) detector interfaced to a NS-880 multichannel analyzer with dual floppy disks. For each sample we have measured the abundance, average composition and range of composition of each mineral and calculated the bulk composition from the mass balance equations. The mathematics, software and hardware behind the point count technique are detailed in Albee *et al.* (1977), and the data reduction follows the same methods as Beaty and Albee (1978). All mineral formulae and normalizations follow the algorithms given by Beaty and Albee (1978).

The data in Fig. 7 are the five-second analyses collected during the point counts. The plagioclase histograms are more subject to error than the pyroxene quadrilaterals. Their abscissas are the Ca K-value divided by the Ca K-value in anorthite. Instrument drift during the course of a run can therefore cause the entire data spread to shift. The average plagioclase composition (Table 2) is calculated using Ca/Si, thereby sidestepping the problem. Note for example, that the average composition for 12072 is An_{90} (Table 2), but on the histogram only a small fraction of the points are more calcic than this. Also, because the data are only five second counts, the apparent spread is much larger than that actually present in the sample. All of the analyses less than An_{70} in 12031, for example, are probably spurious. With these problems in mind, the histograms are useful for two comparisons; the general position of the peak and the width of the data spread. The pyroxene quadrilaterals are plotted in terms of K-values, not atomic proportions, unduly emphasizing the iron-rich analyses.

III. PETROLOGY

i) General petrography

12038 has been partially described by both Keil *et al.* (1971) and Simpson and Bowie (1971). Prior to this work, however, no petrologic studies had been undertaken on 12031 and 12072. To provide internal consistency as well as a basis for comparison, detailed petrographic observations, microprobe analyses of the major minerals, and a microprobe point count have been performed on each sample.

Texturally, 12072, 12038 and 12031 are drastically different from one another. 12072 is porphyritic, with olivine and pyroxene phenocrysts set in a fine-grained, variolitic, groundmass (Fig. 1a). 12038 is medium-grained and equigranular, with

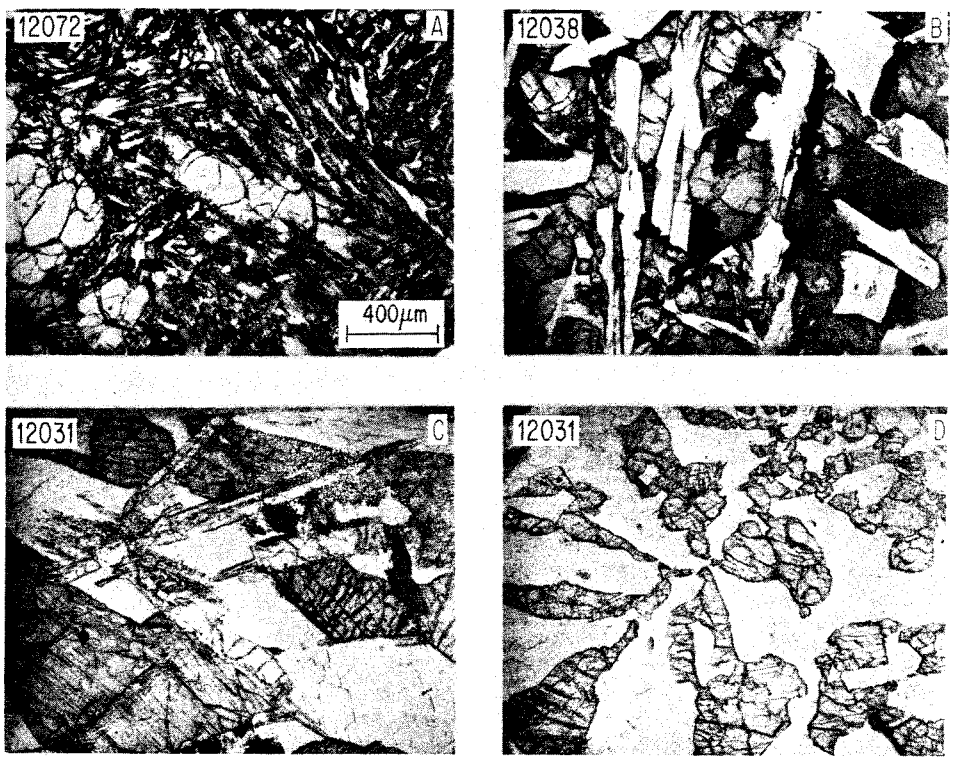

Fig. 1. Photomicrographs of Apollo 12 feldspathic basalts. All photographs are in transmitted light at the same scale for comparison. (A). In 12072 olivine and pigeonite, phenocrysts are set in a fine-grained variolitic groundmass of pyroxene, plagioclase and a variety of minor phases. (B). Lath-shaped plagioclase and equant to elongated pyroxene form an intergranular to subophitic texture in 12038. (C). Portions of 12031 show a granular, gabbroic texture. Note in particular the large tridymite laths (pale grey, high relief) which emanate from plagioclase (white) and cross-cut the dark gray pyroxene. (D). Graphic intergrowths of pyroxene (dark grey, high relief) occur with plagioclase (white, low relief) in 12031.

a subophitic to intergranular texture (Fig. 1b). 12031 is coarse-grained, and varies from a granular, gabbroic texture (Fig. 1c) to graphic intergrowths of pyroxene and plagioclase (Fig. 1d). This textural sequence might be expected in a section from either the top or the base to the core of a lava flow. On the other hand, the three samples may be totally unrelated. To test these hypotheses, it is necessary to compare the rocks in detail.

ii) 12072

Rock 12072 consists of 6 percent subhedral, partially resorbed phenocrysts of olivine (Fig. 2b), rare (0.2%) microphenocrysts of Cr-spinel rimmed by ulvöspinel (Fig. 2c) and about 5 percent lath-shaped phenocrysts of pyroxene (Fig. 2a) in a variolitic-textured groundmass of pyroxene, plagioclase and ilmenite (Fig.

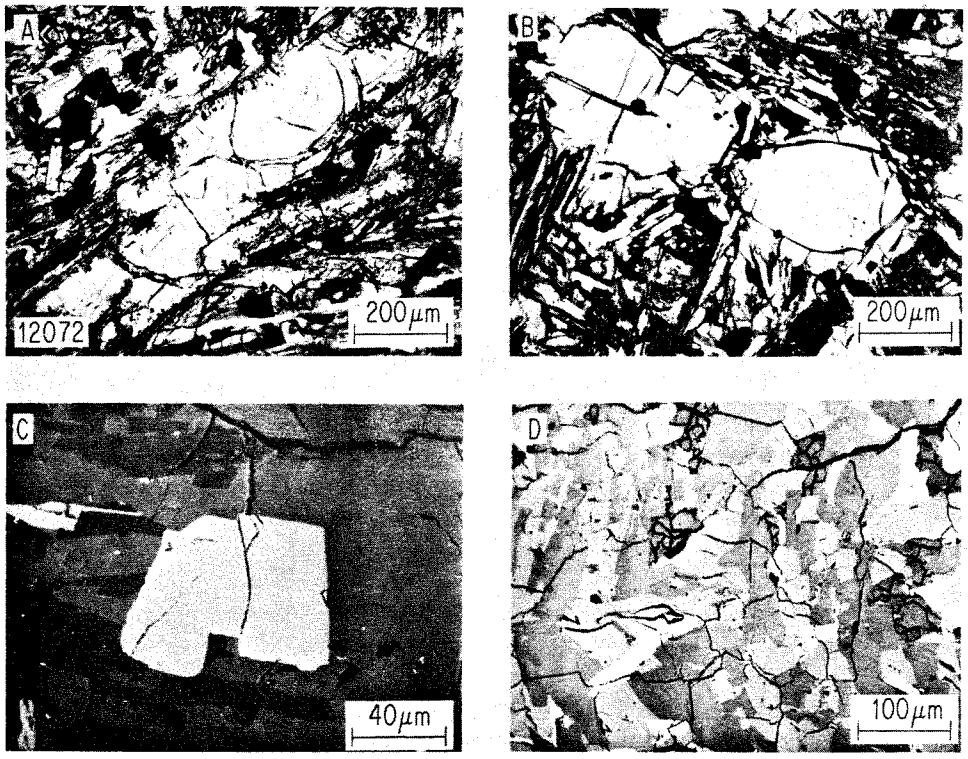

Fig. 2. Photomicrographs of 12072. (A). Lath-shaped pyroxene phenocryst with pigeonite core and augite rim. (B). Olivine phenocrysts are subhedral, sometimes embayed and set in a fine-grained, variolitic groundmasss. (C). Spinel microphenocryst. The central darker core of Cr-spinel has a pale rim of ulvöspinel. (D). Groundmass textures in reflected light showing acicular ilmenite (whitish-grey) anhedral pyroxene (pale grey), subhedral to acicular plagioclase (dark grey) and very dark grey interstitial cristobalite (irregular features).

2a,b,d) with minor amounts of spinel, troilite, cristobalite, Fe-metal, apatite, fayalite and two immiscible glasses. The mode, average mineral compositions and bulk composition of 12072 are listed in Table 1.

Olivine phenocrysts range from Fo_{76} to Fo_{62} (Fig. 3), and are partially to completely surrounded by irregular rims of pyroxene. Euhedral Cr-spinel inclusions are common in the margins of the olivine as well as in the pyroxene phenocrysts. Except where mantled by pyroxene or olivine, spinel is surrounded by a thin rim of ulvöspinel. The spinel cores are slightly zoned from $Chr_{65}Her_{24}Ulv_{11}$ with Fe/(Fe + Mg) = 0.68 to $Chr_{61}Her_{26}Ulv_{13}$ with Fe/(Fe + Mg) = 0.83 (Fig. 3), but the rims are too small to analyze.

Pyroxene phenocrysts consist of pinkish augite rims ($Wo_{37}En_{39}Fs_{24}$) mantling colorless to very pale buff-colored pigeonite cores ($Wo_{10}En_{56}Fs_{34}$) (Fig. 3). The augite rims grade continuously into the groundmass pyroxene. Chemically, the groundmass pyroxenes define a trend extending from iron-rich pigeonite ($Wo_{13}En_{42}Fs_{45}$) to iron-rich augite ($Wo_{25}En_{18}Fs_{57}$), and then toward pyroxferroite (Fig. 3). The pyroxferroite is not optically discontinuous, and no evidence of its subsolidus breakdown was observed. The relative abundances of Al, Ti, and Cr in the pyroxene (Fig. 3, inset) indicate that in the pigeonite phenocrysts the dominant substitutions are $R^{2+}Al_2SiO_6$, $R^{2+}TiAl_2O_6$, and $R^{2+}Cr^{3+}AlSiO_6$. During crystallization first the amount of Cr decreases, then Al/Ti drops. The sudden drop in Al/Ti may be related to the onset of plagioclase crystallization and subsequent pyroxenes apparently contain substantial $R^{2+}Ti^{3+}AlSiO_6$ (Fig. 3).

Plagioclase is present as anhedral, acicular grains averaging 0.4–0.6 mm in length intergrown with pyroxene in the groundmass (Fig. 2). Locally adjacent plagioclase grains are intergrown in optical continuity, giving rise to a poikilitic texture. Slight zoning is present, from $An_{85}Ab_8Or_{.2}Oth_{6.8}$ to $An_{96}Ab_{11}Or_{.2}Oth_{12.8}$. The amount of [ ]$Si_4O_8$ in the plagioclase shows a general increase from 0 to about 3 mole percent with decreasing anorthite content.

Ilmenite (Gi_{0-1}, Fig. 3) occurs mainly as acicular grains <0.3 mm (Fig. 2), but some occurs as more irregular, wedge-shaped, or blocky grains. Native iron typically occurs as 25 μm spheres, most of which are interstitial. More rarely, they are found included within spinel and pyroxene grains, but never within olivine. Troilite is present as spheroidal interstitial masses (10 μm) with rare ameoboid inclusions of Fe-metal, but is never found in the early-formed minerals. Cristobalite occurs as interstitial, anhedral grains generally <55 μm in size. Ulvöspinel is present not only as rims on the Cr-spinel phenocrysts, but also as small interstitial anhedral to vermicular grains, and in intergrowths with ilmenite. Fayalite is present as relatively large, equant crystals (up to 130 μm) which apparently crystallized directly from the melt, and traces of phosphate minerals are present. In addition, two immiscible glasses are present.

The crystallization history of 12072 can be inferred with considerable detail because of the widespread preservation of the early-formed minerals. Either olivine or Cr-spinel was the liquidus phase. The presence of metal inclusions in spinel but not olivine suggests that olivine preceded spinel, but alternatively, spinel may have preferentially nucleated on the metal grains. As pigeonite began to crystallize, olivine began to dissolve in the melt, and an immiscible metal phase

Table 1. 12072: Phase abundances, average "phase" compositions, and bulk composition.

		Pyroxene							
(2585 pts)	Plag	LoCaPx	Augite	MedFePx	HiFePx	Ferrohed	Olivine	"SiO_2"	Ilmenite
Vol %	38.94	8.51	8.83	23.24	8.24	0.22	5.71	3.07	1.15
σ (SDM)	1.07	0.76	0.78	1.26	0.75	0.12	0.47	0.34	0.21
ρ	2.74	3.49	3.40	3.51	3.72	3.57	3.53	2.33	4.72
Wt. %	33.36	9.29	9.38	25.51	9.59	0.25	6.31	2.24	1.70
σ (SDM)	0.92	0.83	0.83	1.38	0.87	0.14	0.52	0.25	0.31
P_2O_5									
SiO_2	48.91	51.10	48.57	48.65	48.18	48.65	37.43	100.45	0.06
TiO_2	0.29	1.01	1.56	1.53	1.16	1.25	0.01	0.40	51.88
Al_2O_3	30.39	1.91	4.04	2.55	1.06	1.14	0.02	0.60	0.08
Cr_2O_3		0.60	1.06	0.33	0.06	0.12	0.55		0.06
MgO	0.52	17.07	15.46	10.45	3.91	4.53	36.12	0.00	0.07
CaO	17.75	5.70	13.99	10.02	9.11	14.44	0.30	0.18	
FeO	1.12	22.53	14.18	26.28	36.83	31.03	26.85	0.29	47.16
MnO		0.36	0.26	0.47	0.48	0.33	0.26		0.30
Na_2O	0.98	0.01	0.21	0.03	0.08	0.01		0.12	
K_2O	0.04							0.07	
BaO	0.15							0.00	
ZrO_2									0.02
V_2O_3									0.00
Nb_2O_5									0.07
NiO							0.05		
S									
F									
Total	100.15**	100.29**	99.33**	100.31**	100.87**	101.50**	101.59**	102.11	99.70**
	An 79.9	Wo 9.1	Wo 23.1	Wo 18.1	Wo 19.0	Wo 29.6	Fo 70.4		Gi 0.3
	Ab 8.8	En 48.8	En 43.1	En 30.9	En 12.0	En 13.5	Fa 29.6		Ilm 99.7
	Or 0.2	Fs 36.8	Fs 22.6	Fs 44.4	Fs 64.5	Fs 52.6			
	Other 11.1	Other 5.3	Other 11.2	Other 6.6	Other 4.5	Other 4.3			

Table 1. (*Continued*)

	Troilite[1]	Phosphate[2]	Cr–spinel	Ulvöspinel[4]	Fe–metal[1]	Fayalite	Meso[3]	K–Glass	12072,2 area = 11.0 mm² ρ calc = 3.20	
Vol %	0.31	0.12	0.17	0.12	0.07	0.20	1.03	0.08		
σ (SDM)	0.11	0.07	0.08	0.07	0.05	0.09	0.20	0.06		
ρ	4.60	3.20	4.68	4.78	8.00	4.39	2.65	2.65		
Wt. %	0.45	0.12	0.25	0.18	0.18	0.28	0.85	0.07	Bulk comp.	σ (SDM)
σ (SDM)	0.16	0.07	0.12	0.11	0.13	0.13	0.17	0.05		
P_2O_5		43.15					0.33	0.64	0.06	0.03
SiO_2			0.08			35.06	70.41	79.75	48.14	1.14
TiO_2			4.71	35.73		0.18	0.45	0.58	1.81	0.18
Al_2O_3			12.67			0.34	15.65	8.07	11.64	0.34
Cr_2O_3			47.88			0.03	0.00	0.00	0.40	0.07
MgO			6.64			1.98	0.20	0.00	8.57	0.33
CaO		54.54				0.69	7.36	1.29	11.38	0.32
FeO	63.53		28.73	64.27	100.00	63.87	1.89	2.79	17.46	0.61
MnO			0.18			0.61	0.36	0.70	0.25	0.02
Na_2O							0.51	0.25	0.37	0.04
K_2O							2.86	5.51	0.04	0.02
BaO							0.33	0.54	0.05	0.02
ZrO_2			0.03				0.00	0.00	<0.01	
V_2O_3			1.03						<0.01	
Nb_2O_5			0.01						<0.01	
NiO						0.00	0.00	0.00	<0.01	
S	36.47						0.00	0.00	0.16	0.06
F		2.31							<0.01	
Total	100.00	100.00	101.94*	100.00	100.00	102.76*	100.35	100.12	100.33	
			Ulv 11.8			Fo 5.2		Qtz 52.1		
			Chr 63.3			Fa 94.8		Fld 40.1		
			Her 24.9					Pyx 4.9		
								Other 2.9		

* Average of two analyses.

** Average of three analyses.

[1] Theoretical elemental abundances; converted to oxides for bulk calculation.

[2] Assumed 1:1 mixture of fluorapatite and whitlockite.

[3] Composition constructed from weighted average (51:38:11) of K–glass, plagioclase, and "SiO_2".

[4] Theoretical end-member oxide abundances.

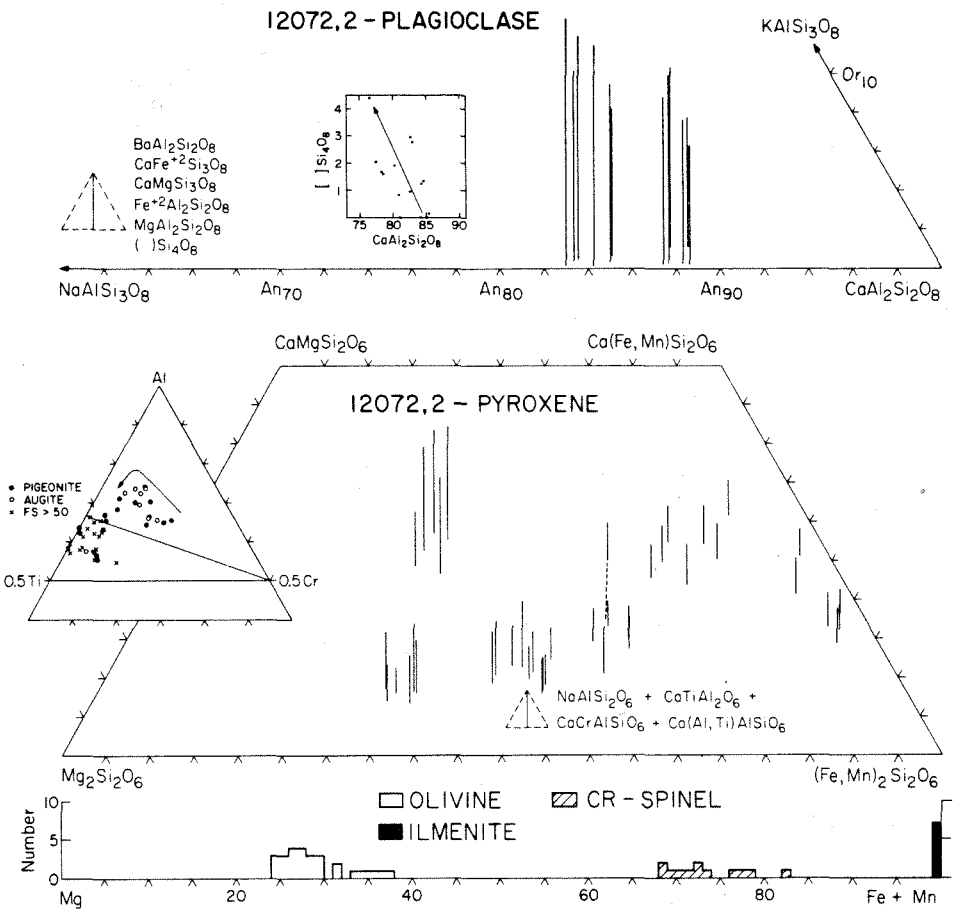

Fig. 3. Composition of pyroxene, olivine, plagioclase, spinel and ilmenite in 12072. Dashed line joins two adjacent pyroxene analyses.

appeared. While pigeonite and spinel precipitated, the liquid became progressively depleted in Cr and enriched in Ca. This led to the discontinuous rims of ulvöspinel on Cr-spinel and augite on pigeonite, but the exact sequence could not be determined. At this point the melt contained growing phenocrysts of pyroxene and spinel and dissolving phenocrysts of olivine. Then plagioclase, ilmenite, and cristobalite saturations occurred in rapid succession, probably over a narrow temperature interval, and the fine-grained groundmass was produced. By analogy with the experiments of Walker *et al.* (1976), the porphyritic texture could have been produced by a simple, single-stage cooling history. Sulfide saturation occurred well after plagioclase began to form. Small amounts of fayalite and phosphates are present, but the interstitial glass solidified before any Zr-minerals formed.

iii) 12038

This rock is hypidiomorphic and dominantly equigranular with a very homogeneous texture. Plagioclase laths (44%) form a loose, randomly oriented network in which pyroxene (49%) is either interstitial or partially enclosed (Fig. 1b). Also present are acicular ilmenite (35%, Fig. 4), interstitial cristobalite (3%, Fig. 4) and trace amounts of Ca-phosphate, fayalite, ulvöspinel, K-feldspar, troilite, K-glass, and Fe-metal. In addition, a solitary grain of Cr-spinel rimmed by ulvöspinel was observed in this study, and minor olivine was found by Keil *et al.* (1971). 12038 is medium-grained in comparison with 12072 and 12031, with an average-grain size of about 600 microns (Fig. 1).

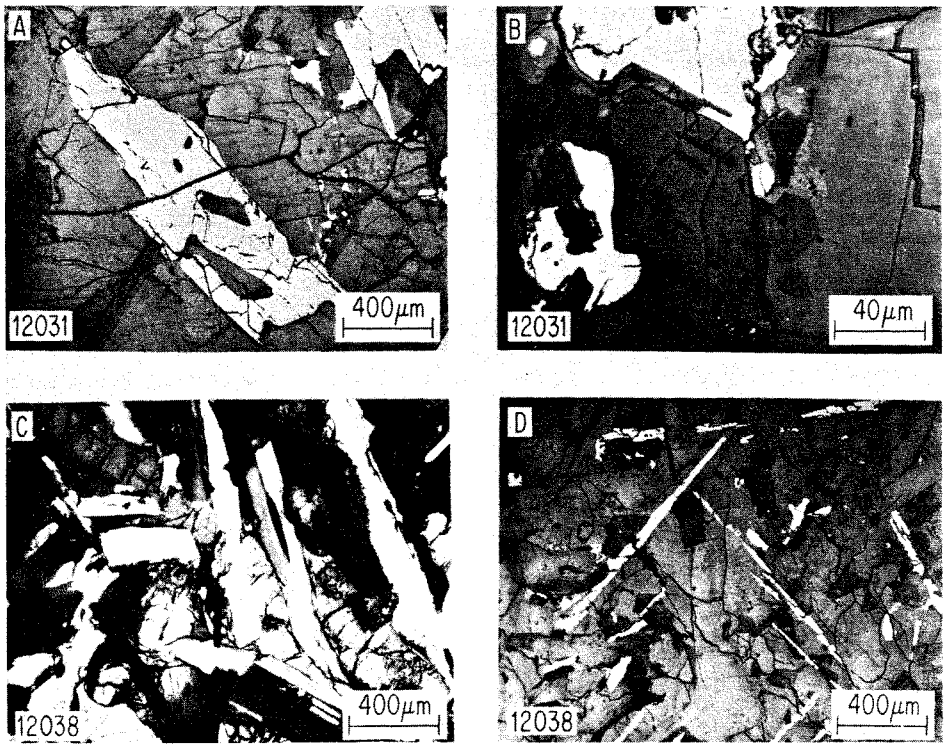

Fig. 4. Photomicrographs of 12031 (A,B) and 12038 (C,D). (A). Ilmenite (whitish-grey) typically has an externally skeletal, blocky habit. (B). Mesostasis phases are remarkably coarse-grained in 12031 as this reflected light photomicrograph shows. Troilite (white) is associated with apatite (mid-grey, imperfect hexagonal sections, criss-cross surface markings) at the junction between a pyroxene and a pyroxferroite grain (paler-grey). Some anhedral plagioclase (dark grey) is also present. At the pyroxferroite rim, where it meets the troilite, subsolidus breakdown to fayalite, cristobalite and iron-rich pyroxene has occurred (wormy intergrowths). (C). This view of 12038 in crossed nicols shows twinned, lath-shaped plagioclase cross-cutting a pigeonite lath. (D). Ilmenite (white) in 12038 is acicular and commonly externally skeletal. Subhedral blocky to anhedral plagioclase (dary grey) and anhedral pyroxene (paler grey) are also present.

Although most of the pyroxene is roughly equant, several large (2.8 × 2.0 mm), lath-shaped grains of pigeonite ($Wo_{11}En_{59}Fs_{30}$) are present (Fig. 4c). Strictly speaking, these grains are microphenocrysts. Pigeonite is surrounded by discontinuous rims of augite (Fig. 5; see also Keil *et al.*, 1971) which zones to pyroxferroite ($Wo_{17}En_3Fs_{80}$). An iron-rich pigeonite is also present (Keil *et al.*, 1971) which is compositionally distinct from the pigeonite cores. The zoning in Al, Ti, and Cr (Fig. 5, inset) is similar to that for the pyroxenes in 12072.

Plagioclase is typically lath-shaped, twinned and zones from about $An_{82}Ab_{14}Or_{.3}Oth_{3.7}$ to $An_{73}Ab_{20}Or_2Oth_5$ (Fig. 5) with steadily increasing amounts of Fe and [ ]Si_4O_8 (Fig. 5, inset). The last plagioclase to crystallize is anhedral and poikilitically surrounds the earlier formed minerals. The presence of small amounts of K-feldspar (0.19%) indicates late-stage entry into the two feldspar field.

Ilmenite is invariably acicular and typically externally skeletal as well (Fig. 4d.) Compositional zoning is essentially absent (Gi_{0-1}, Fig. 5) although small amounts of Al_2O_3 (0.45 weight percent) and Cr_2O_3 (0.12 weight percent) are present (Keil *et al.*, 1971).

Ulvöspinel ($Ulv_{81}Her_8Chr_{11}$; Simpson and Bowie, 1971) occurs as small anhedra included in the margins of pyroxene crystals and as interstitial intergrowths with ilmenite. In addition, one large (200 micron) grain is present, which may represent a completely reacted Cr-spinel microphenocryst. Fayalite typically occurs as spongy anhedral masses with rounded inclusions—evidence for direct precipitation from an immiscible high-Fe melt. Fayalite is also present as one of the subsolidus breakdown products of pyroxferroite, and as rims on some of the opaque grains. Cristobalite occurs as irregular, interstitial masses. Fe-metal is present as anhedral, subrounded grains with a very narrow size distribution centered around 10 microns. Most grains occur in the cores of plagioclase laths, where they may have acted as nucleation sites, but metal also occurs in the margins of pyroxene grains and interstitially. Much more rarely, metal is present as amoeboid inclusions within troilite. Chemically, the metal contains 1–4 weight percent Ni, and 1–2 weight percent Co (Simpson and Bowie, 1971). Troilite occurs as anhedral interstitial masses, 20–30 μm. Other interstitial phases include tranquillityite and baddelyite (for analyses see Simpson and Bowie, 1971), apatite and/or whitlockite, and traces of glass.

The paragenetic sequence of 12038 is more ambiguous than that of 12072. Olivine and Cr-spinel were apparently the liquidus phases, but they are present in such small amounts that their textural relations are unclear. Although pigeonite phenocrysts are present, they are transected by plagioclase laths (Fig. 4c) in such a way that either could have been the next mineral to crystallize. With falling temperature metal saturation occurred, then augite rims on the pigeonite and immiscible troilite spheres formed. Ilmenite was the next phase to appear, to be joined ultimately by cristobalite and the mesostasis assemblage. The textures of the fayalite and the glass in the mesostasis suggest that the melt underwent late-stage silicate liquid immiscibility.

These textural observations are consistent with the experimental work on 12038

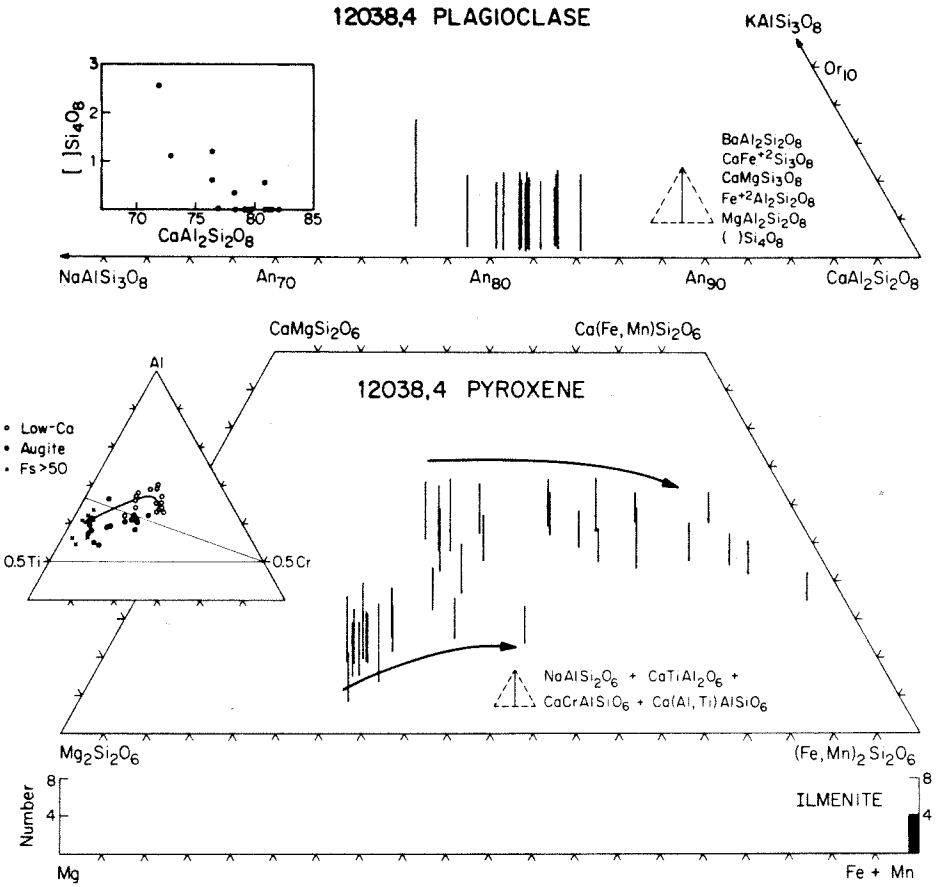

Fig. 5. Composition of pyroxene, plagioclase and ilmenite in 12038.

of Biggar *et al.* (1971). They found that olivine was the liquidus phase (1160°C) at one atmosphere pressure followed by pigeonite and plagioclase. The temperature difference between the liquidus and entry of the third phase was only 5°, however, indicating that 12038 is multiply saturated at low pressure. Crystallization of spinel also began near 1160°. The augite rims formed at about 1140°, ilmenite at about 1090°, troilite at 1080°, and by 1065° crystallization was complete.

iv)12031

12031 is a coarse-grained (average grain size = 2 mm), equigranular rock with a variable texture. Graphic intergrowths of pyroxene (49%) and plagioclase (40%) on one side of the thin section (Fig. 1d) give way to a more granular, gabbroic texture on the other side (Fig. 1c). Elongated and externally skeletal ilmenite

(3.8%, Figure 4) along with tridymite laths (Fig. 1) and interstitial cristobalite constitute most of the rest of the rock. Magnesian olivine and Cr-spinel are both absent, and in contrast to both 12072 and 12038, the pyroxenes are neither lath-shaped nor porphyritic.

Plagioclase occurs as large, anhedral, poikilitic grains with prominent and complicated twinning. The largest crystal is 3.5 mm across, and is bounded by the edges of the thin section. According to the work of Walker *et al.* (1978) and Grove and Walker (1977), this indicates that 12031 has undergone a very slow cooling rate. Compositional zoning is from $An_{91}Ab_5Or_{0.5}Oth_{2.5}$ to $An_{76}Ab_{12}Or_4Oth_8$ (Fig. 6) with $[\ ]Si_4O_8$ increasing from 0 to 2 mole % (Fig. 6, inset). Minor amounts (0.4%) of K-feldspar are also present.

Because of the intimate way in which it is intergrown with the plagioclase, pyroxene in 12031 is optically very complex, and core-rim relationships are difficult to decipher. Both pigeonite ($Wo_{12}En_{56}Fs_{32}$) and augite ($Wo_{30}En_{47}Fs_{23}$) are present (Fig. 6), and both apparently zone towards more iron-rich compositions. Optically and compositionally discontinuous grains of pyroxferroite ($Wo_{14}En_3Fs_{80}Oth_3$) are also present, ranging in size up to 3 mm. As the iron content in pyroxene increases, Ti is enriched at the expense of Al and Cr (Fig. 6, inset).

Ilmenite (Gi_{0-1}, Fig. 6) has a bladed, externally skeletal habit (Fig. 4a) and contains small amounts of Cr_2O_3 (0.13%), ZrO_2 (0.23%) and MnO (0.25%). Fayalite is present both as discrete interstitial grains, and as one of the subsolidus breakdown products of pyroxferroite. Tridymite laths range to more than 1 mm in length and cristobalite is present interstitially. Ulvöspinel, apatite or whitlockite, tranquillityite, and baddelyite are all present in the mesostasis areas, commonly as large, well-formed crystals (Fig. 4b). Fe-metal (2–5 μm) is virtually absent, but may be found contained in plagioclase, tridymite, and the margins of pyroxenes. Troilite forms anhedral interstitial masses ranging up to 500 μm.

The crystallization history of 12031 is as follows. Plagioclase and pyroxene appeared on the liquidus together, forming graphic intergrowths as well as discrete crystals. Metal saturation occurred next. The very low amount and small size of the metal grains may indicate that much of the dense, immiscible metal liquid was able to settle out of the melt. Tridymite and ilmenite were the next phases to begin crystallizing, but their relative order is indeterminate. Tridymite laths crosscut pyroxene and plagioclase (Fig. 1c) suggesting that it preceded cristobalite, which is interstitial. Although this sounds anomalous, textures suggesting early tridymite and late cristobalite are also present in 12021 (Dollase *et al.*, 1971) and 12064 (Klein *et al.*, 1971). Troilite saturation, silicate liquid immiscibility, and the mesostasis minerals all appeared in the late stages of crystallization.

IV. DISCUSSION

By detailed comparison of these three samples, it is possible to evaluate the hypothesis that they came from the same lava flow. If true, the modes, mineral

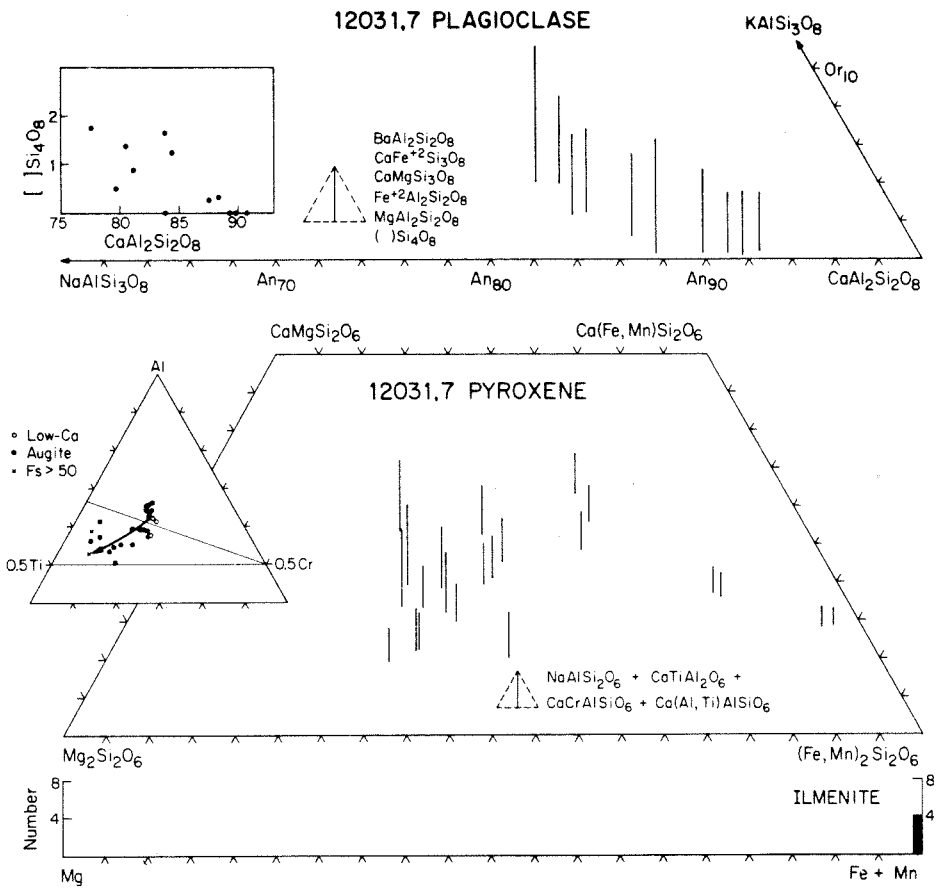

Fig. 6. Composition of pyroxene, plagioclase and ilmenite in 12031.

compositions, and textures would all vary in a predictable way. In addition, each sample would have the same paragenetic sequence; and the differences in bulk composition would be consistent with a realistic fractionation model. To test this hypothesis, therefore, the abundances and compositions of the minerals, the crystallization sequences, and the bulk compositions will be compared.

A. Petrology and mineralogy

Olivine and *Cr-spinel* are both relatively abundant in 12072 but essentially absent from 12038 and 12031. This, in conjunction with the grain sizes, is consistent with 12072 having been derived from the rapidly cooled base or top of a flow, and 12038 and 12031 from a more slowly cooled flow interior. The most Mg-rich olivine in 12072 is Fo_{76}, which gives an apparent K_D ol-liq of 0.28. Although this

is a little lower than K_D for the compositionally similar Apollo 12 pigeonite basalts (0.30–0.33, Baldridge *et al.*, 1979), it is close enough to be predicted value (Longhi, 1977) that 12072 probably crystallized from a liquid of the composition of the sample as it is now constituted. It is also possible that some of the olivine crystals in 12072 are magnesian xenocrysts which never equilibrated with the melt. By contrast, the earliest olivine in 12038 has not been preserved (Fo_{60}; Keil *et al.*, 1971), and in 12031 it is completely absent.

The *pyroxene* crystallization trends in 12072, 12038, and 12031 are generally similar (Fig. 7). Early pigeonite is followed by augite, and then zoning proceeds to pyroxferroite and ferrohedenbergite. The compositions of the earliest pigeonite and the earliest augite are variable, however. In 12072 and 12031 pigeonite has roughly the same Fe/(Fe + Mg) ratio as the augite (Fig. 7). In 12038 the first augite is much more Fe-rich (Fig. 7). This can be related to more extensive crystallization of pigeonite in 12038 (28% of total pyroxene) as compared to 12072 (17%) and 12031 (12%) (Table 2). This difference is at odds with the one-flow hypothesis—it is difficult to imagine a situation in which pigeonite phenocrysts would accumulate and olivine phenocrysts be lost (the melt densities are distinctly less than either mineral). The average pyroxene composition of 12038 is also somewhat unusual. 12072 and 12031 define a "normal" igneous differentiation trend from $Wo_{15}En_{37}Fs_{48}$ to $Wo_{22}En_{30}Fs_{48}$ (Table 2), reflecting the fractionation of pigeonite. 12038, however, has both higher Ca and higher Mg/(Mg + Fe) $Wo_{21}En_{37}Fs_{42}$) when compared to 12072, a difference which would require the fractionation of augite but not pigeonite. These data suggest that 12072 and 12031 may be related by crystal-liquid fractionation, but that 12038 is different.

The *plagioclase* in 12072 zones from An_{82}–An_{87}, in 12038 from An_{85}–An_{78}, and in 12031 from An_{94}–An_{86}. The average plagioclase compositions for 12072, 12038 and 12031 are $An_{90.1}$, $An_{83.1}$, and $An_{90.6}$, respectively (Table 2). In each sample the amount of [ ]Si_4O_8 increases steadily with albite content (Figs. 3,5,6), a common feature in lunar basalts (Beaty and Albee, 1977). Once again, if we assume that 12038 and 12031 are derived from 12072, we can test the single flow hypothesis. Fractionation of Cr-spinel, pigeonite, and olivine will enrich the residual melt in plagioclase, without changing its average composition. Because of the more rapid cooling rate of 12072, however, its augite would contain more $CaAl_2SiO_6$ than the more slowly cooled derivatives, and its average plagioclase composition should be slightly less calcic. Furthermore, plagioclase may have been slightly undercooled with respect to augite in 12072 (by analogy with the pigeonite basalts; Baldridge *et al.*, 1979) so its first plagioclase may be slightly more sodic than in its fractionated products.

The plagioclase compositions in 12072 and 12031 are in accord with the above model. The higher orthoclase contents of plagioclase in 12031 (Fig. 6) reflect a reduced amount of K-glass (Table 2). 12038, however, is clearly a discordant sample. Both its average and its initial plagioclase compositions are anomalously sodic in comparison with 12072 and 12031. To relate them would require massive plagioclase fractionation, a process inadmissable considering the textures present.

The abundance of *troilite* and *apatite* or *whitlockite* reflect a final important

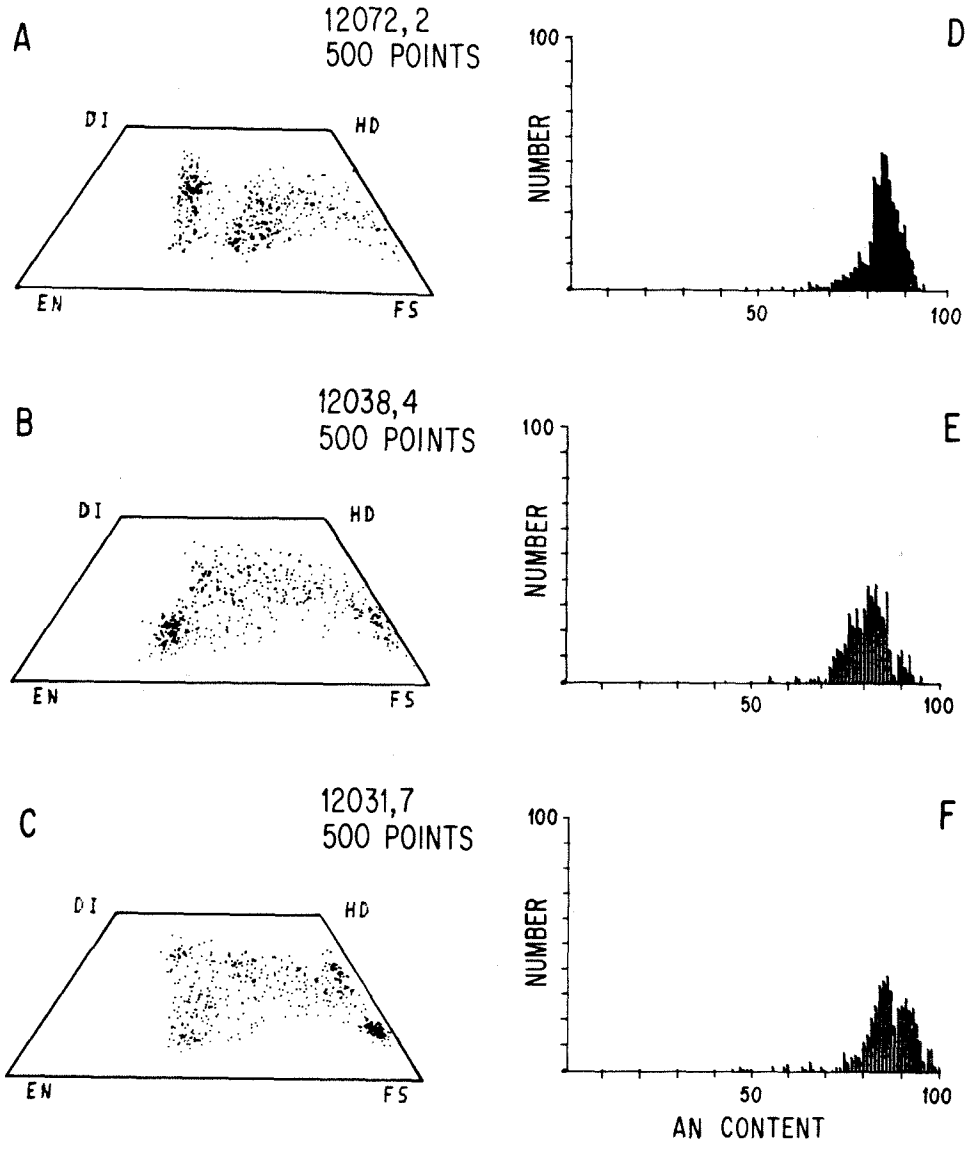

Fig. 7. Pyroxene quadrilaterals and plagioclase histograms for 12072, 12038 and 12031. The data was collected automatically on a pre-set grid using the electron microprobe, and is a random sampling of the pyroxene and feldspar in each sample. There are 500 points on each of the histograms as well as each of the quadrilaterals. Each analysis was counted for only five seconds, so although there are sizeable errors associated with individual points, the general patterns are meaningful. In 12072 there are large amounts of augite and ferropigeonite, along with small amounts of pyroxferroite. 12038 has much Mg-pigeonite, and little augite. 12031 is dominated by lots of ferrohedenbergite and discontinuous pyroxferroite. By having the computer count the number of points in selected areas of the pyroxene quadrilateral, it is also possible to quantitatively report (Table 2) the amounts of augite, pigeonite, med-Fe pyroxene, high-Fe pyroxene and ferrohedenbergite. For additional details, see Analytical Techniques.

Table 2. Feldspathic basalts—Apollo 12 petrologic summary.

	12072	12038	12031
Plagioclase	38.94	44.03	40.22
Pyroxene	49.04	48.85	49.18
Ilmenite	1.15	3.46	3.77
"SiO_2"	3.07	2.67	4.94
Mg–olivine	5.71	<.04	absent
Fayalite	<.04	0.18	0.14
Troilite	0.31	0.06	0.71
Phosphate	0.12	0.31	0.18
Ulvöspinel	0.12	0.14	0.05
Mesostasis[1]	1.11	0.05	0.36
Cr–spinel	0.17	<.04	absent
Fe–metal	0.07	<.04	0.03
K–spar	<.04	0.19	0.41
Ave. Plag (An)	90.1	83.1	90.6
Ave. Pyx Wo	15.2	20.6	21.7
En	37.0	36.8	30.4
Fs	47.8	42.5	47.8
Ave. MgOl (Fo)	70.4	—	—
Ave. Il (Fe)	99.7	99.6	99.4
% Pyx[2] Low Ca	17.4	28.4	11.8
Augite	18.0	10.2	42.7
Med Fe	47.4	40.5	15.1
Hi Fe	16.8	20.2	29.4
Ferrohed	0.4	0.7	1.1

[1] Mesostasis in 12072 is fine-grained mixtures of K–glass, silica and plagioclase. In 12031 and 12038 it is modal K–glass.

[2] Pyroxenes were subdivided along lines of constant Fs content: Augite < Fs_{30}, Med Fe < Fs_{60}, Hi Fe > Fs_{60}. LoCaPyx is < Wo_{15}, and Ferrohed is < En_{10} and > Wo_{33}.

difference between these samples. Troilite and the phosphate minerals are late-crystallizing, interstitial phases which should be fractionated together. 12072 contains 0.31% and 0.12% of troilite and phosphates, respectively (Table 2). 12031 has about double that amount: 0.71% and 0.18%, respectively. 12038, on the other hand, contains only 0.06% troilite, but 0.31% phosphate minerals. This difference cannot be accounted for by fractionation processes, but must represent a difference in the initial bulk compositions.

B. Paragenetic sequences

The paragenetic sequences of the three samples are consistent with their being consanguinous. 12031 and 12038 are multiply saturated with pyroxene and plagioclase, as would be expected if 12072 had lost its olivine, Cr-spinel, and pigeonite phenocrysts. Metal saturation occurs early and sulfide saturation late in each sample.

C. Bulk chemistry

The bulk compositions of 12072, 12038 and 12031 are listed in Table 3. Although slight differences exist, the three rocks are on the whole very similar to one another. In comparison with the rest of the Apollo 12 collection (Figs. 8 and 9), the three feldspathic basalts are not only similar to one another, they are unlike the other rock types. In particular, they may be distinguished on the basis of higher Al_2O_3, SiO_2 and CaO, and lower FeO and TiO_2.

Although the differences within the olivine, pigeonite, and ilmenite basalt suits are clearly produced by fractionation of olivine, Cr-spinel, and pigeonite (Fig. 8; Rhodes *et al.*, 1977), the feldspathic basalts are not differentiates of any of them. Plotting MgO (a fractionating element) versus Al_2O_3 (a non-fractionating element) (Fig. 8), it can be seen that the pigeonite, olivine, and ilmenite basalts lie on a common trend indicating olivine control. The feldspathic basalts follow a parallel trend which is displaced by about 2 weight percent Al_2O_3 (Fig. 8). The feldspathic basalts contain distinctly less FeO (16.8–17.7%) than the other rock types (Fig. 9). Fractionation of olivine and pigeonite, however, produces a late-stage iron enrichment trend. The multiply saturated residual liquids of both the olivine-pigeonite series (12039) and the ilmenite series (12047) contain about 20.5% FeO (Rhodes *et al.*, 1977). The multiply saturated character of 12038 and 12031 indicates that they are also residual liquids, but because of their low iron contents, they were not derived from the olivine, pigeonite or ilmenite basalts. In addition, fractionation of olivine, Cr-spinel and pigeonite will either enrich or deplete the residual liquid in plagioclase and ilmenite together. Although plagioclase is, in fact, higher in the feldspathic basalts, ilmenite is depleted. In summary, the Apollo 12 feldspathic basalts form a distinct, well-defined group which cannot be related to the other Apollo 12 rock types.

In comparision to each other, 12031 and 12038 have very similar major element compositions (Table 3), a fact noted by Rhodes *et al.* (1977). This reflects the fact that they were apparently both cotectic liquids in equilibrium with plagioclase and pyroxene. 12038, however, has roughly twice the concentrations of incompatible trace elements as 12031. For example, Na_2O, Ba, Ce, Eu and Zr are enriched in 12038 by factors of 2.0, 2.0, 1.9, 2.2 and 1.8 respectively (Table 3). Similar abundances were measured by Nyquist *et al.* (1979). P_2O_5, however, is concentrated by a factor of 2.8 and K_2O by a factor of only 1.4. Although late-stage mesostasis mobility (Lindstrom and Haskin, 1978; Haskin *et al.*, 1978) may

Table 3. Bulk compositions of the Apollo 12 feldspathic basalts.

		12038					
	12072[1]	(2)	(3)	(4)	(5)	(ave)*	12031[6]
SiO_2	48.14	47.1	46.56	47.13	46.61	46.85	46.97
TiO_2	1.81	3.17	3.31	3.28	3.25	3.25	2.88
Al_2O_3	11.64	12.8	12.53	13.03	12.45	12.70	12.63
FeO	17.46	17.4	17.99	17.73	17.75	17.72	16.78
MnO	0.25	0.24	0.27	0.25	0.251	0.25	0.26
MgO	8.57	6.80	6.71	6.60	6.83	6.74	7.13
CaO	11.38	11.4	11.62	11.43	11.48	11.48	12.25
Na_2O	0.37	0.64	0.66	0.69	0.67	0.67	0.33
K_2O	0.04	0.07	0.073	0.06	0.067	0.07	0.05
P_2O_5	0.06	0.17	0.14	0.14	0.12	0.14	0.05
S	0.16		0.06		0.07	0.07	0.05
Cr_2O_3	0.40	0.31	0.27		0.32	0.30	0.35
Σ	100.33	100.10	100.16	100.34	99.87	100.24	99.73
Mg/(Mg+Fe)	.467	.411	.399	.399	.407	.404	.431
Norm. Qtz	1.3	1.8	0.8	1.4	1.0	1.3	2.1
Sr		158	185.8		185	173	136
Ba		142	120		107	119	60
Ce			25			30	15.6
Sm						80	4.23
Eu						2.20	1.00
Tb						1.9	1.19
Yb		6.3				6.05	3.7
Lu						0.75	0.55
Y		71	46		50.5	59	35
Zr		186	160		182	182	100
Nb		12	7		9.3	9.0	7.0
Hf						6.5	3.3
Sc		50				48.2	48.9
Cr		2210	1840			2050	2460
Co		34	25			29.1	26
La		20	10			12.47	

[1] This work.
[2] Cuttita *et al.* (1971).
[3] Compston *et al.* (1971).
[4] Biggar *et al.* (1971).
[5] Willis *et al.* (1971).
[6] Rhodes *et al.* (1977).
* Average trace elements of 12038 include data by Taylor *et al.* (1971), Schnetzler and Philpotts (1971), Brunfelt *et al.* (1971) and Haskin *et al.* (1971).

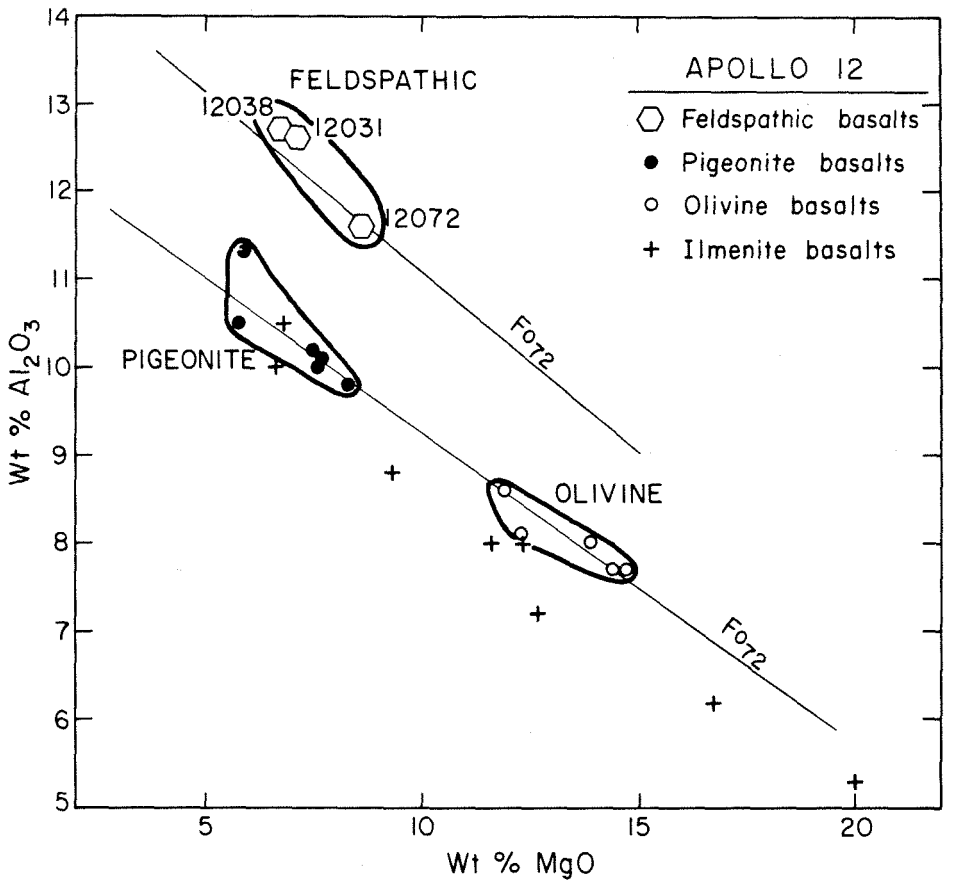

Fig. 8. Variation of Al_2O_3 with MgO for Apollo 12 basalts. The Apollo 12 ilmenite, pigeonite and olivine basalts are spread out along a common trend indicating olivine control whereas the feldspathic basalts lie distinctly off this trend. Feldspathic basalt data from Table 3; all others from Rhodes *et al.* (1977).

in part be responsible for these differences, the fractionation of the KREEP elements from one another suggests that 12038 and 12031 are not related by near surface fractionation. Furthermore, the liquidus plagioclase in 12038 is much more sodic than that in 12031 (see Section A), indicating that two magmas with different Na contents were involved.

12072 is chemically more primitive than 12038 and 12031, for example it has higher MgO and Cr_2O_3 and lower TiO_2, Al_2O_3 and CaO (Fig. 9). Except for Na_2O, all of the major element data are consistent with either 12031 or 12038 having been derived from 12072 through the loss of its ferromagnesian phenocrysts. 12031 has a similar sodium content as 12072, but 12038 contains about twice as much Na_2O (Table 3). These values are reflected in the plagioclase

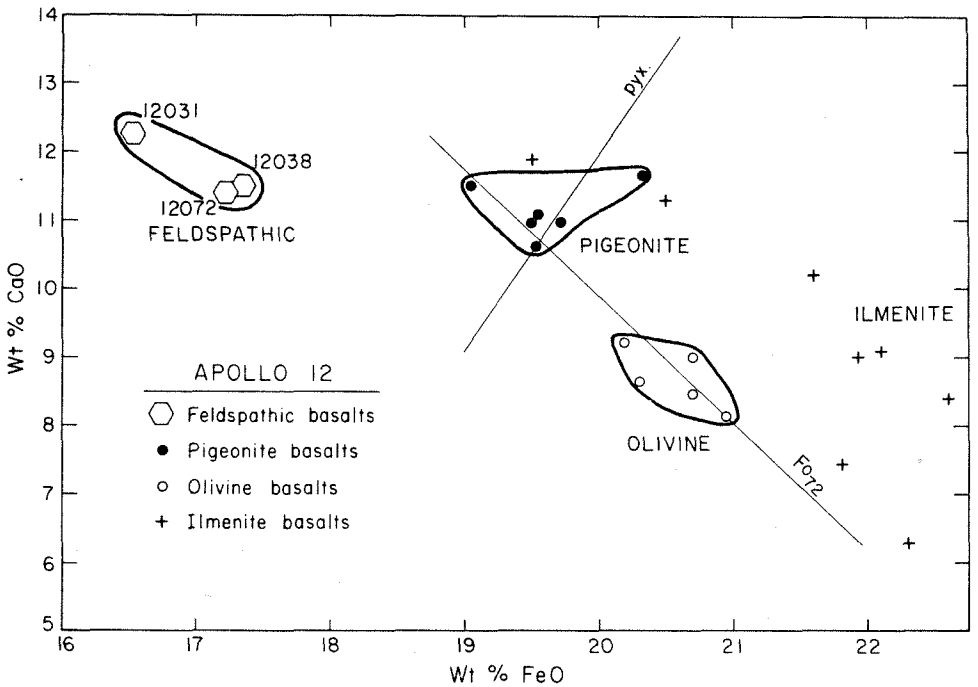

Fig. 9. Variation of CaO with FeO for the Apollo 12 basalts. The feldspathic basalts form a distinct cluster with lower FeO contents than the other rock types. Data sources same as Fig. 8.

compositions (Table 2), and suggest that 12072 is related to 12031, but not 12038. Again, this agrees with the petrology.

D. Isotopic data

12038 has been dated at 3.28 ± 0.21 b.y. (Compston *et al.*, 1971) and 3.11 + 0.05 b.y. (G. Turner, pers. comm.). 12031 has an age of 3.23 ± 0.07 b.y. (Nyquist *et al.*, 1979). The initial Sr ratio of 12038 is 0.69938 ± 8 (Compston *et al.*, 1971) or 0.69922 ± 5 (Nyquist *et al.*, 1979) and that of 12031 0.69957 ± 6 (Nyquist *et al.*, 1979). Although the ages of these two samples are similar, the initial Sr ratios indicate that they were produced in different source regions. The initial Nd ratios of the two samples are comparable (12038 = 0.50763 ± 26, 12031 = 0.50788 ± 9; Nyquist *et al.*, 1979).

Although 12038 is isotopically as well as chemically unique, 12031 is isotopically indistinguishable from the pigeonite basalts. This, in conjunction with similar rare earth patterns, led Nyquist *et al.* (1979) to conclude that 12031 is, in fact, a plagioclase enriched variant of the pigeonite basalts, as originally suggested by Rhodes *et al.* (1977). Plagioclase fractionation is certainly a possibility in

12031, considering its very slow cooling rate and large crystal size. The fine groundmass of 12072, however, precludes plagioclase fractionation, so it must represent a separate magma type. The proposed association of 12072 and 12031 is therefore based on the fact that 12031 can be derived from 12072—not from the pigeonite basalts, but by phenocryst fractionation. The absence of isotopic data on 12072 precludes a more definitive classification.

In summary, all of the petrologic, textural, chemical and isotopic data are consistent with 12072 and 12031 having been derived from the same magma body, but having undergone different cooling rates and degrees of differentiation. 12038 is a unique sample, unrelated to either 12072 and 12031. Neither of these two proposed magma bodies is related to the other Apollo 12 rock types, so there are five magma types represented in the Apollo 12 collection: 12038, 12031 and 12072, and the olivine, pigeonite and ilmenite basalt suites.

E. Petrogenesis

Lunar petrologists have tended to group all lunar feldspathic basalts together (e.g., Papike *et al.*, 1976; Reid and Jakes, 1974). Included are basaltic samples from Luna 16, Apollo 14 and Apollo 12. This miscellaneous collection has been variously interpreted as non-mare basalts (Hubbard and Gast, 1971; Hubbard *et al.*, 1972), high-Al mare basalts (Ridley, 1975), and in some cases as impact melts (James, 1973). Furthermore, in the soils at each mare landing site, glasses with the composition of the dominant rock types are rare, whereas glasses with the composition of feldspathic basalts are common (Reid and Jakes, 1974). This, in conjunction with the orbital measurements of Al/Si, would suggest that feldspathic basalts are widespread (Mare Fecunditatis, Oceanus Procellarum, Mare Crisium and Mare Nubium; Reid and Jakes, 1974). On the other hand, the abundance of high-Al glasses could reflect the large contribution to the mare soils of feldspathic material from the lunar highlands. Because the various feldspathic basalts may have formed in different ways, it is necessary to treat the different rock types separately.

The lunar feldspathic basalts may be divided into four broad groups, one of which contains 12031, 12038 and 12072. A second group consists of highly feldspar-rich (60–80%) basalts such as 68415, 14276, 14310 (Gancarz *et al.*, 1971, 1972), and many of the Apollo 16 melt rocks (Powell *et al.*, 1975). These samples are widely interpreted as impact melts of the feldspathic lunar crust. Third, Apollo 14 samples 14053 and 14072 are chemically similar (Hubbard *et al.*, 1972) and have plagioclase abundances (40%) comparable to those of the Apollo 12 feldspathic basalts (Longhi *et al.*, 1972; Gancarz *et al.*, 1971). Although 14053 is much older (Papanastassiou and Wasserburg, 1971; Turner *et al.*, 1973) than 12038 and 12031, it is chemically rather similar. Finally, the Luna 16 basalts differ from the Apollo 12 feldspathic basalts in having more Al_2O_3 and TiO_2 (Vinogradov, 1971; Albee *et al.*, 1972) and only one pyroxene (Albee *et al.*, 1972).

There is no evidence that 12072, 12038, and 12031 were produced as impact

melts. None of the three contain xenoliths, a common feature in impact melts in highlands breccias (e.g., Quick *et al.*, 1978). The parental liquids were not saturated in metallic iron, a condition which has been interpreted as indicating meteoritic contamination for 14310 (James, 1973). The Fe-metal gloubles are small, homogeneous, and in 12038 have compositions indistinguishable from the metal in the olivine basalts (Simpson and Bowie, 1971). The siderophile element (Au, Ag, Ir, Re) abundances in 12038 (Anders *et al.*, 1971; Baedecker *et al.*, 1971) are somewhat higher than in the other Apollo 12 mare basalts, but they are an order of magnitude less than the concentrations found in 14310 and the lunar soils (Morgan *et al.*, 1972; Baedecker *et al.*, 1972; Ridley, 1975). All of this data suggests an absence of meteoritic contamination.

The many similarities between 12072, 12031 and the other Apollo 12 basalts suggests that, like them, these two feldspathic basalts were derived from magmas produced by partial melting of the deep lunar interior. 12072 is marginally quartz normative, has olivine, Cr-spinel rimmed by ulvöspinel, and pigeonite rimmed by augite phenocrysts set in a fine-grained, variolitic groundmass—all of which characteristics it shares with 12011, a fine-grained pigeonite basalt (Baldridge *et al.*, 1979). 12011 and 12072 have identical pyroxene zoning profiles; early pigeonite is rimmed by augite, and then ferropigeonite zones to pyroxferroite. The Cr-spinel microphenocrysts in 12072 zone from $Chr_{65}Her_{24}Ulv_{11}$ to $Chr_{61}Her_{26}Ulv_{13}$, those in 12011 from $Chr_{65}Her_{25}Ulv_{10}$ to $Chr_{58}Her_{28}Ulv_{14}$. This similarity is noteworthy considering the wide variety of spinels returned from the moon (Haggerty, 1972; Frondel, 1975; Papike *et al.*, 1976). Finally, the plagioclase in 12072 zones from An_{92-87} whereas that in 12011 is An_{92-88}.

The petrology therefore indicates that the bulk compositions and conditions of crystallization of 12072 and 12011 were similar, and that the similarities may extend back to their source regions. Rhodes *et al.* (1977) report that the trace element abundances in 12031 are similar to those of the other Apollo 12 basalts, an observation consistent with the above interpretation. Nyquist *et al.* (1979) report that the isotopic characteristics of 12031 are indistinguishable from those of the olivine and pigeonite basalts, again suggesting similar source regions.

The magma parental to 12038 cannot be related to either 12031 and 12072 or any of the other Apollo 12 basalts. It has an unusual trace element character (Haskin *et al.*, 1971; Schnetzler and Philpotts, 1971; Cuttita *et al.*, 1971), along with a lower initial Sr ratio (Compston *et al.*, 1971; Nyquist *et al.*, 1977, 1979). The general chemical similarity between 12038, 12072 and 12031, however, suggests that by analogy, the magma parental to 12038 was derived by partial melting of the luanr interior. The detailed differences, along with the fact that 12038 is unique among the lunar collection, suggest that it is exotic to the Apollo 12 landing site.

Acknowledgments—Betty Robinson did a masterful job of typing the manuscript. Constructive criticism was provided by David Walker, Richard Warner, Larry Nyquist and an anonymous reviewer. Dr. Pat Butler, the lunar sample curator, deserves special thanks for providing us with the necessary thin sections on short notice. This research was supported by NASA grant NGL-05-002-338.

REFERENCES

Albee A. L., Beaty D. W., Chodos A. A., and Quick J. E. (1977) Quantitative analysis of petrographic properties and mineral compositions with a computer-controlled energy-dispersive system. *Proc. Nat'l. Conf. on Electron Probe Analysis 12th*. In Press.

Albee A. L., Chodos A. A., Gancarz A. J., Haines E. L., Papanastassiou D. A., Ray L., Tera F., Wasserburg G. J., and Wen T. (1972) Mineralogy, petrology and chemistry of Luna 16 basaltic fragment B-1. *Earth Planet. Sci. Lett.* **13**, 353–367.

Anders E., Ganapathy R., Keays R. R., Laul J. C., and Morgan J. W. (1971) Volatile and siderophile elements in lunar rocks: Comparison with terrestrial and meteoritic basalts. *Proc. Lunar Sci. Conf. 2nd*, p. 1021–1036.

Baedecker P. A., Chou C.-L., and Wasson J. T. (1972) The extralunar component in lunar soils and breccias. *Proc. Lunar Sci. Conf. 3rd*, p. 1343–1359.

Baedecker P. A., Schandy R., Elzie J. L., Kimberlin J., and Wasson J. T. (1971) Trace element studies of rocks and soils from Oceanus Procellarum and Mare Tranquillitatis. *Proc. Lunar Sci. Conf. 2nd*, p. 1037–1061.

Baldridge W. S., Albee A. L., and Chodos A. A. (1978) Petrology of Apollo 12 olivine-pigeonite mare basalts 12007, 12015, 12043 and 12072 (abstract). In *Lunar and Planetary Science IX*, p. 41–43. Lunar and Planetary Institute, Houston.

Baldridge W. S., Beaty D. W., Hill S. M. R., and Albee A. L. (1979) The petrology of the Apollo 12 pigeonite basalt suite. *Proc. Lunar Planet. Sci. Conf. 10th*. This volume.

Beaty D. W. and Albee A. L. (1978) Comparative petrology and possible genetic relations among the Apollo 11 basalts. *Proc. Lunar Planet. Sci. Conf. 9th*, p. 359–463.

Beaty D. W. and Albee A. L. (1979) Silica solid solution and zoning in natural plagioclase. *Amer. Mineral.* In press.

Biggar G. M., O'Hara M. J., Peckett A., and Humphries D. J. (1971) Lunar lavas and the achondrites: Petrogenesis of protohypersthene basalts in the maria lava lakes. *Proc. Lunar Sci. Conf. 2nd*, p. 617–643.

Brunfelt A. O., Heier K. S., and Steinnes E. (1971) Determination of 40 elements in Apollo 12 minerals by neutron activation analysis. *Proc. Lunar Sci. Conf. 2nd*, p. 1281–1290.

Champion D. E., Albee A. L., and Chodos A. A. (1975) Reproducibility and operator bias in a computer-controlled system for quantitative electron microprobe analysis. *Proc. 10th Ann. Microbeam Anal. Soc. Conf.*, p. 55A–55F.

Compston W., Berry H., Vernon M. G., Chappell B. W., and Kaye M. (1971) Rubidium-strontium chronology and chemistry of lunar material from the Ocean of Storms. *Proc. Lunar Sci. Conf. 2nd*, p. 1471–1485.

Cuttitta F., Rose H. J., Annell C. S., Carron M. K., Christian R. P., Dwornik E. G., Greenland L. P., Helz A. W., and Ligon D. T. (1971) Elemental composition of some Apollo 12 lunar rocks and soil. *Proc. Lunar Sci. Conf. 2nd*, p. 1217–1229.

Dollase W. A., Cliff R. A., and Wetherill G. W. (1971) Note on tridymite in rock 12021. *Proc. Lunar Sci. Conf. 2nd*, p. 141–142.

Frondel J. W. (1975) *Lunar Mineralogy*. Wiley, N.Y. 323 pp.

Gancarz A. J., Albee A. L., and Chodos A. A. (1971) Petrologic and mineralogic investigation of some crystalline rocks returned by the Apollo 14 mission. *Earth Planet. Sci. Lett.* **12**, 1–18.

Gancarz A. J., Albee A. L., and Chodos A. A. (1972) Comparative petrology of Apollo 16 sample 68415 and Apollo 14 samples 14276 and 14310. *Earth Planet. Sci. Lett.* **16**, 307–330.

Grove T. L. and Walker D. (1977) Cooling histories of Apollo 15 quartz-normative basalts. *Proc. Lunar Sci. Conf. 8th*, p. 1501–1520.

Haggerty S. E. (1972). Luna 16: An opaque mineral study and a systematic examination of compositional variations of spinels from Mare Fecunditatis. *Earth Planet. Sci. Lett.* **13** 328–352.

Haskin L. A., Helmke P. A., Allen R. O., Anderson M. R., Korotev R. L., and Zweifel K. A. (1971) Rare-earth elements in Apollo 12 lunar materials. *Proc. Lunar Sci. Conf. 2nd*, p. 1307–1317.

Haskin L. A., Lindstrom M. M., and Dungan M. A. (1978) Trace element fractionation during crystallization of thin tholeiitic lava flows (abstract). In *Lunar and Planetary Science IX*, p. 468–470. Lunar and Planetary Institute, Houston.

Hubbard N. J. and Gast P. W. (1971) Chemical composition and origin of nonmare lunar basalts. *Proc. Lunar Sci. Conf. 2nd*, p. 999–1020.

Hubbard N. J., Gast P. W., Rhodes J. M., Bansal B. M., Weismann H., and Church S. E. (1972) Nonmare basalts: Part II. *Proc. Lunar Sci. Conf. 3rd*, p. 1161–1179.

James O. B. (1973) Crystallization history of lunar feldspathic basalt 14310. *U.S. Geol. Survey Prof. Paper 841*, 29 pp.

James O. B. and Wright T. L. (1972) Apollo 11 and 12 mare basalts and gabbros: Classification, compositional variations and possible petrogenetic relations. *Bull. Geol. Soc. Amer.* **83**, 2357–2382.

Keil K., Prinz M., and Bunch T. E. (1971) Mineralogy, petrology and chemistry of some Apollo 12 samples. *Proc. Lunar Sci. Conf. 2nd*, p. 319–341.

Klein C. Jr., Drake J. C., and Frondel C. (1971) Mineralogical, petrological and chemical features of four Apollo 12 lunar microgabbros. *Proc. Lunar Sci. Conf. 2nd*, p. 265–284.

Lindstrom M. M. and Haskin L. A. (1978) Causes of compositional variations within mare basalt suites. *Proc. Lunar Planet. Sci. Conf. 9th*, p. 465–486.

Longhi J. (1977) Magma oceanography 2: Chemical evolution and crustal formation. *Proc. Lunar Sci. Conf. 8th*, p. 601–621.

Longhi J., Walker D., and Hays J. F. (1972) Petrography and crystallization history of basalts 14310 and 14072. *Proc. Lunar Sci. Conf. 3rd*, p. 131–139.

LSPET (Lunar Science Preliminary Examination Team) (1970) Preliminary examination of lunar samples from Apollo 12. *Science* **167**, 1325–1339.

Morgan J. W., Laul J. C., Krahenbuhl U., Ganapathy R., and Anders E. (1972) Major impacts on the moon: Characterization from trace elements in Apollo 12 and 14 samples. *Proc. Lunar Sci. Conf. 3rd*, p. 1377–1395.

Nyquist L. E., Bansal B. M., Wooden J. L., and Weismann H. (1977) Sr isotopic constraints on the petrogenesis of Apollo 12 mare basalts. *Proc. Lunar Sci. Conf. 8th*, p. 1383–1415.

Nyquist L. E., Shih C.-Y., Wooden J. L., Bansal B. M., and Weismann H. (1979) The Sr and Nd isotopic record of Apollo 12 basalts. *Proc. Lunar Planet. Conf. 10th*. This volume.

Papanastassiou D. A. and Wasserburg G. J. (1971) Rb-Sr ages of igneous rocks from Apollo 14 mission and the age of the Fra Mauro formation. *Earth Planet. Sci. Lett.* **12**, 36–48.

Papike J. J., Hodges F. J., Bence A. E., Cameron M., and Rhodes J. M. (1976) Mare basalts: Crystal chemistry, mineralogy and petrology. *Rev. Geophys. Space Phys.* **14**, 475–540.

Powell B. M., Dungan M. A., and Weiblen P. W. (1975) Apollo 16 feldspathic melt rocks: Clues to the magnetic history of the lunar crust. *Proc. Lunar Sci. Conf. 6th*, p. 415–433.

Quick J. E., Brock B. S., and Albee A. L. (1978) Petrology of Apollo 16 breccia 66075. *Proc. Lunar Planet. Sci. Conf. 9th*, p. 921–939.

Reid A. M. and Jakeš P. (1974) Luna 16 revisited: The case for aluminous mare basalts (abstract). In *Lunar Science V*, p. 627–629. The Lunar Science Institute, Houston.

Rhodes J. M., Blanchard D. P., Dungan M. A., Brannon J. C., and Rodgers K. V. (1977) Chemistry of Apollo 12 mare basalts: Magma types and fractionation processes. *Proc. Lunar Sci. Conf. 8th*, p. 1305–1339.

Ridley W. I. (1975) On high-alumina mare basalts. *Proc. Lunar Sci. Conf. 6th*, p. 131–145.

Schnetzler C. C. and Philpotts J. A. (1971) Alkali, alkaline earth, and rare-earth element concentrations in some Apollo 12 soils, rocks, and separated phases. *Proc. Lunar Sci. Conf. 2nd*, p. 1101–1122.

Simpson P. R. and Bowie S. H. U. (1971) Opaque phases in Apollo 12 samples. *Proc. Lunar Sci. Conf. 2nd*, p. 207–218.

Taylor S. R., Rudowski R., Muir P., Graham A., and Kaye M. (1971) Trace element chemistry of lunar samples from the Ocean of Storms. *Proc. Lunar Sci. Conf. 2nd*, p. 1083–1099.

Turner G., Cadogan P. H., and Yonge C. J. (1973) Argon selenschronology. *Proc. Lunar Sci. Conf. 4th*, p. 1889–1914.

Vinogradov A. P. (1971) Preliminary data on lunar ground brought to earth by automatic probe Luna 16. *Proc. Lunar Sci. Conf. 2nd*, p. 1–16.

Walker D., Kirkpatrick R. J., Longhi J., and Hays J. F. (1976) Crystallization history of lunar picritic basalt sample 12002: Phase-equilibria and cooling-rate studies. *Bull. Geol. Soc. Amer.* **87**, 646–656.

Walker D., Powell M. A., Lofgren G. E., and Hays J. F. (1978) Dynamic crystallization of a eucrite basalt. *Proc. Lunar Sci. Conf. 9th*, p. 1369–1391.

Willis J. P., Ahrens L. H., Danchin R. V., Erlank A. J., Gurney J. J., Hofmeyr P. K., McCarthy T. S., and Orren M. J. (1971) Some interelement relationships between lunar rocks and fines, and stony meteroites. *Proc. Lunar Sci. Conf. 2nd*, p. 1123–1138.

THE PETROLOGY OF A PYROXENITE XENOLITH IN MARE BASALT 10050. D.W. Beaty and A.L. Albee, Division of Geological and Planetary Sciences, California Institute of Technology, Pasadena, CA 91125

Most of the xenoliths in lunar igneous rocks (e.g., 1,2,3,4,5,6) are contained in the rocks returned from Apollos 14 and 16. These xenoliths consist, among other materials, of breccias, shocked and partially annealed feldspars, and glasses, evidence for incorporation through impact melting processes. Xenoliths in mare basalts, however, are rare; only three have been identified to date. Since mare basalts are thought to have been derived by partial melting of the lunar mantle, these xenoliths may be critically important direct samples of the lunar interior. This report describes one of those xenoliths, an unusual pyroxenite in low-K, high-Ti mare basalt 10050.

General Texture. Thin section 10050,31 (7) contains an irregular, very fine-grained, polycrystalline aggregate 170μm x 80μm, consisting of 17 plagioclase grains, 4 orthopyroxene grains and 2 augite grains set in a matrix of high-Al clinopyroxene (Fig. 1). Although the extinction is difficult to observe, the high-Al clinopyroxene appears to consist of only one crystal. The xenolith has three different textural regions, Areas 1, 2 and 3 (Fig. 1). All of the plagioclase crystals are contained in the central region (Area 2), which also contains one orthopyroxene grain. Area 1 consists of a large high-Al clinopyroxene grain which encloses three orthopyroxene crystals and one grain of optically discontinuous low-Al clinopyroxene ("augite"). Area 3 is an irregular, fine-grained complex zone consisting only of clinopyroxene (including one discontinuous grain of augite). The xenolith was point counted in reflected light with the following results: 80% total clinopyroxene (of which

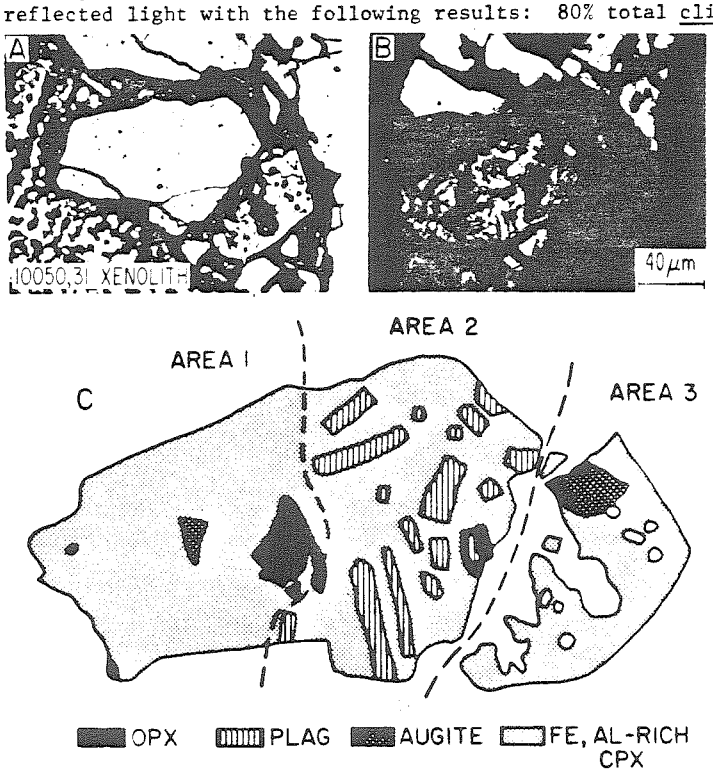

Figure 1. Xenolith in thin section 10050,31. A) Reflected light showing the optically discontinuous pyroxenes, and the gap surrounding the xenolith. B) Same view, transmitted light. Note the complexity of the right side (Area 3). C) Diagram drawn from high-resolution electron beam scans. Although some of the clinopyroxene is not Al-rich (e.g. Table 1), the only low-Al pyroxenes with sharp, mappable boundaries are the two augite grains.

PYROXENITE XENOLITH IN MARE BASALT 10050

D.W. Beaty

Figure 2

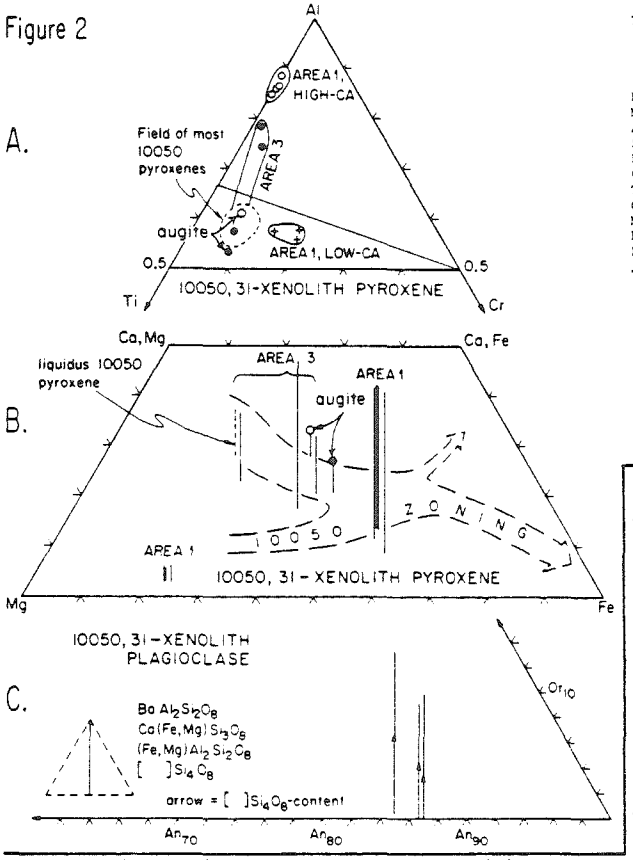

Table 1. Representative Microprobe Analyses

	Plagioclase	Pyroxene (1)	Pyroxene (2)	Pyroxene (3)
Na_2O	1.03	0.02	0.23	0.11
MgO	0.48	27.15	5.55	16.06
Al_2O_3	34.11	1.04	10.40	5.85
SiO_2	46.35	54.18	47.77	49.58
K_2O	<.01	n.a.	n.a.	n.a.
CaO	17.67	2.16	11.13	14.81
TiO_2	0.42	0.66	2.57	2.68
Cr_2O_3	n.a.	0.50	0.10	0.45
MnO	n.a.	0.18	0.25	0.26
FeO	0.55	13.80	21.27	11.84
BaO	<.01	n.a.	n.a.	n.a.
Total	100.59	99.68	99.26	101.64
An	82.0	Wo 2.8	13.3	22.9
Ab	8.7	En 72.8	18.4	44.4
Or	0.0	Fs 21.1	40.0	18.8
Si	4.3	Oth 3.3	28.3	13.9
Oth	5.0			

(1) Orthopyroxene from Area 1.
(2) Homogeneous high-Al clinopyroxene, Area 1.
(3) Resorbed clinopyroxene, Area 3.

1% is the discontinuous low-Al variety), 6% orthopyroxene, and 14% plagioclase. This leads to the rock name of pyroxenite. The xenolith is completely surrounded by a gap in the section (Fig. 1), and its contact relations against the host basalt are not visible.

Mineral Chemistry. High-Al clinopyroxene is both the most abundant and most complex mineral in the xenolith. On one end of the xenolith (Area 1) it is homogeneous, with a composition of $En_{23}Wo_{30}Fs_{47}$ containing 10.4 wt. % Al_2O_3, 2.2 wt. % TiO_2, and 0.1 wt. % Cr_2O_3 (Fig. 2). At the other end (Area 3) the pyroxene is more variable in composition and is more magnesian and less aluminos, e.g. $En_{48}Wo_{32}Fs_{20}$ with 5.9 wt. % Al_2O_3, 2.7 wt. % TiO_2 and 0.45 wt. % Cr_2O_3 (Fig. 2). Electron beam scans indicate that the pyroxene which surrounds the plagioclase in Area 2 has more Mg and less Fe than the high-Al clinopyroxene, but similar Ca, Al and Ti. The clinopyroxene matrix of the xenolith, therefore, shows wide compositional variability over a relatively short distance. In Area 3 the pyroxene compositions approach those in the main part of 10050 in three important respects: Proportions of Fe, Mg and Ca (Fig. 2B); proportions of Al, Ti and Cr (Fig. 2A); and abundances of Al, Ti and Cr (Fig. 2B). This, along with the textural and optical complexity of Area 3 (Fig. 1), suggests partial resorption by the surrounding melt.

Plagioclase is present as locally subparallel, subhedral to euhedral laths ranging in size up to 6μm x 30μm (Fig. 1). All 17 plagioclase crystals are located in the center third of the xenolith (Area 2). Three microprobe analyses show only slight variation, from $An_{82}Ab_8Or_0Oth_{10}$ with 3.4% [ ]Si_4O_8 to $An_{78}Ab_8Or_0Oth_{14}$ with 6.3% [ ]Si_4O_8. It was not possible to determine whether single crystals are compositionally zoned. The plagioclase contains an unusually high amount of MgO (0.5-0.7 wt. %), along with modest amounts of FeO (0.5-0.8%), TiO_2 (0.2-0.4%) and BaO (0.0-0.2%) (Table 1.).

PYROXENITE XENOLITH IN MARE BASALT 10050

D.W. Beaty

The orthopyroxene grains are anhedral, equant, and range in size up to 21 μm. One crystal has a minute plagioclase lath poikilitically enclosed in it, but apart from that, all grain contacts are against clinopyroxene and are irregular (Fig. 1). Like plagioclase, most of the orthopyroxene is located in the central part of the xenolith (Fig. 1C). Because of the small grain size, it was not possible to observe the extinction, so the identification of orthopyroxene is based on the composition, which is $En_{74}Wo_4Fs_{22}$ (Fig. 2). Small amounts of Al_2O_3 (1.0 wt. %), TiO_2 (0.66 wt. %), Cr_2O_3 (0.50 wt. %) and Na_2O (0.02 wt. %) are present (Table 1), and the ratio $Cr/(Cr+Al+Ti)=0.19$ is among the largest ever reported for lunar pyroxene.

Two optically distinct as well as chemically discontinuous low-Al, high-Ca pyroxene crystals are enclosed in the high-Al clinopyroxene (Fig. 1). One grain is located in Area 1 and the other in Area 3 (Fig. 1), but the two compositions are similar to one another ($Wo_{25}En_{35}Fs_{35}Oth_5$, with 1.6 wt. % Al_2O_3, 1.4 wt. % TiO_2, 0.3 wt. % Cr_2O_3, and 0.04 wt. % Na_2O). This composition is indistinguishable from some of the pyroxenes found in the main part of 10050 (Fig. 2A,B). These augite grains are difficult to interpret: It is possible that they formed by reaction with the surrounding melt, but this explains neither the discontinuous zoning, nor their presence in the cores of high-Al clinopyroxene.

Interpretation. The xenolith is obviously not in internal equilibrium. Not only does the clinopyroxene have a wide range of compositions, most of it is probably not in equilibrium with the orthopyroxene which is present. Data from natural assemblages as well as experimental data indicate that the clinopyroxene-orthopyroxene tie lines on a pyroxene quadrilateral radiate from near wollastonite. In the xenolith, however, no such relationship is observed. Furthermore, the plagioclase is very magnesian, with $Fe/(Fe+Mg)=0.32-0.41$. Such a feldspar is too Mg-rich to be in equilibrium with the high-Al clinopyroxene, which has $Fe/(Fe+Mg)=0.70$ (8). It is possible that the feldspar- and orthopyroxene-rich central portion (Area 2) originated through the breakdown of a preexisting mineral such as garnet. This might explain not only its unusual texture, but its different mineral compositions. In any case, two conclusions are warranted: Partial digestion of the xenolith by the melt has taken place, and the original mineralogy and composition of the xenolith is now obscure. The most likely candidate for an unaffected relic mineral is the high-Al clinopyroxene, because of its presence as a single, relatively large, unzoned crystal.

Origin. Two possibilities for the origin of this xenolith are as a sample of the lunar interior which was carried to the surface by an ascending basaltic magma, and as a high pressure crystallization product from such a magma (cognate xenolith). It is not possible to speculate about the depth of origin because of the problems with disequilibrium and the uncertainties regarding the original mineral assemblage.

References. (1) Dence, M.R. and A.G. Plant (1972), PLSC 3rd, p. 379-399. (2) Helz, R.T. and D.E. Appleman (1973) PLSC 4th, p. 643-659. (3) Chao, E.C.T. (1973) PLSC 4th, p. 719-732. (4) Walker, D. et al. (1973), PLSC 4th, p. 1013-1032. (5) Chao et al. (1975), PLSC 6th, p. 493-515. (6) Ryder, G. and J.F. Bower (1976) PLSC 7th, p. 1925-1948. (7) Beaty, D.W. and A.L. Albee (1978), PLPSC 9th, p. 359-463. (8) Longhi, J. et al. (1976), PLSC 7th, p. 1281-1300.

PART II. THE OXYGEN ISOTOPE GEOCHEMISTRY OF THE ABITIBI GREENSTONE BELT

CHAPTER 1

INTRODUCTION

CHAPTER 1A. BACKGROUND AND PURPOSE

The purpose of this part of the thesis is to answer the question: What are the origins and effects of the various hydrothermal fluids that have interacted with Archean greenstone belts, and what is their relationship to massive sulfide ore deposits? The importance of this question is outlined in the following paragraphs. In the first portion of this thesis the author has described work on remarkably fresh, unaltered lunar basalts with ages greater than 3.3 b.y. In this chapter terrestrial analogs of those lunar basalts are examined, with the significant difference that the ancient terrestrial basalts have interacted on a large scale with the hydrosphere. Both these sets of basalts started out with practically identical $\delta^{18}O$ values of about $+5.7 \pm 0.5$, but many of the basalts in the greenstone belts have subsequently undergone marked ^{18}O shifts due to hydrothermal alteration.

A variety of petrologic, geochemical and geophysical evidence indicates that the modern oceanic crust interacts on a massive scale with seawater (summarized in Gregory and Taylor, 1980). Most of this interaction takes place at mid-ocean spreading centers via the mechanism of very large hydrothermal convection cells. Cold seawater enters the oceanic crust, is heated by the mid-ocean ridge magmatism, and rises, ultimately to be discharged back into the ocean. Two aspects of this process are important to the present discussion: 1. The hydrothermal activity extensively alters the oceanic crust, producing $\delta^{18}O$ shifts in the rocks. By studying the oxygen isotopic distribution in these altered rocks, it is

possible to calculate the oxygen isotopic composition of seawater (Gregory and Taylor, 1980). 2. Where the hydrothermal effluent enters the ocean, sulfides are commonly precipitated, occasionally resulting in stratiform massive sulfide ore deposits (Corliss et al. 1979, Edmond et al. 1979a, 1979b). Beneath these submarine fumaroles a chimney or stockwork of intensely altered rock typically forms. Once again, by studying this alteration chimney, the oxygen isotopic composition of the fluid can be calculated (Heaton and Sheppard, 1976).

In the modern oceanic crust these two processes are related. Hydrothermal alteration in both cases is accomplished either by seawater or by slightly modified seawater. But what was happening in the Archean? The geologic record of the Archean differs in a number of respects from that of the Phanerozoic. In contrast to the presence of materials closely related to plate tectonics such as ophiolites, sheeted dike swarms, and island arcs, the Archean is characterized by the classical greenstone belt-granite association and the complete absence of true ophiolites. Like ophiolites, greenstone belts apparently formed in a marine environment, so in that sense they represent portions of some type of Archean oceanic crust. However, there is controversy concerning the type of basement rocks upon which the greenstone belts formed. Were they poured out upon an ancient gneissic basement complex or do they represent true ancient oceanic crust? Also, did the greenstone belts interact with Archean seawater as did the Phanerozoic oceanic crust? Like the modern basaltic crust, greenstone belts also contain massive sulfide ore deposits associated with great chimneys of alteration. Were the ore-forming hydrothermal processes similar? Was the hydrothermal solution recirculated seawater in each case?

If the above questions can be answered in the affirmative, then it may be possible to calculate $\delta^{18}O$ of Archean seawater from the $^{18}O/^{16}O$ distribution in the altered rocks. The validity of performing this calculation depends on the entire oxygen isotopic and hydrothermal history of the greenstone belt. In this connection, it is impossible to overemphasize the basic problem that besets all isotopic investigations of Archean rocks; namely, to what degree have the isotopic compositions been preserved? It is possible that any original seawater alteration effects may have only partially (or not at all) survived subsequent geologic events. Understanding the nature of the water/rock interactions in the Archean, however, should yield important information on the physical processes active in the Archean, the evolution of the crust, and the nature of the ore-forming process (which may have implications for exploration). Most importantly, however, an oxygen isotopic study of greenstone belts might provide important constraints on the oxygen isotopic composition of Archean seawater.

The isotopic evolution of seawater throughout geologic history is perhaps the largest unsolved problem of stable isotope geochemistry. Its importance lies in the fact that all of the major crustal processes (plate tectonics, sedimentation, weathering, plutonism, volcanism, metamorphism) interact in one way or another with the hydrosphere. If the relative rates of these processes were variable in the past, an effect of some sort should have been produced in the hydrosphere. Knowledge of the $^{18}O/^{16}O$ history of seawater, therefore, provides important constraints on the overall crustal evolution of the earth, particularly the evolution of meteoric waters and of marine sedimentary and volcanic rocks.

Essentially the same arguments can be advanced for studying the

hydrogen isotopic distribution in greenstone belts. Water/rock interactions typivslly produce extensive hydration of the rocks due to the growth of secondary hydrous minerals, and even more so than for $\delta^{18}O$, this will produce a clear-cut δD "signature" in the rocks. Although the mantle is the major reservoir of oxygen on earth, the ocean is the major reservoir of hydrogen. Consequently the evolutionary paths of δD and $\delta^{18}O$ in seawater might be governed by different geologic processes. By considering the hydrogen as well as the oxygen isotopic distribution in greenstone belts, a more complete knowledge of the early history of the earth would almost certainly emerge.

Unfortunately, the scope of this thesis was limited by the tenure of the author's stay at Caltech, and no hydrogen isotope measurements were made. The major reason for this absence of D/H data is that the principal problem connected with all D/H studies of rocks and minerals (to a much greater degree than in the case of $^{18}O/^{16}O$) lies in demonstrating that the δD values have been preserved subsequent to the formation of the rocks. Hydrogen isotope exchange in silicate minerals is known to proceed at a much faster rate than oxygen isotope exchange (O'Neil and Kharaka, 1976; Graham et al. 1980). Such difficulties become increasingly more important the older the rocks. Thus, any definitive proof concerning the preservation of the D/H record in Archean rocks and minerals will require a very lengthy and carefully planned scientific study.

CHAPTER 1B. METHOD OF STUDY

The effect of water/rock interactions on the isotopic compositions of rocks has been the subject of detailed investigation by Taylor and his co-workers over the past decade (Sheppard et al. 1971; Wenner and Taylor, 1971; Taylor, 1971; Forester and Taylor, 1972; Wenner and Taylor, 1973; Taylor, 1973; Sheppard and Taylor, 1974; Taylor, 1974; Heaton and Sheppard, 1976; Magaritz and Taylor, 1974; 1976 a, b; Taylor, 1977; Taylor, 1978; Taylor and Magaritz, 1978; Norton and Taylor, 1979; Taylor and Forester, 1979; Beaty and Taylor, 1979; Gregory and Taylor, 1980; Criss and Taylor, in prep.). Most of this work concerns the interaction of water with igneous and metamorphic rocks, and the present research is an extension of that broad-based research effort.

When water and rocks interact, several changes take place which can be used to study the process. An obvious change is that, in the appropriate temperature range, the originally anhydrous igneous rocks will recrystallize to form hydrous secondary minerals. The identity of these secondary minerals depends on the physicochemical conditions of recrystallization (T, P, f_{H_2O}, f_{CO_2}, f_{O_2}, etc.). A second important change is that the water and the rocks may exchange oxygen isotopes. Most rocks are about 50 wt. % oxygen, water is 89 wt. % oxygen, and the $^{18}O/^{16}O$ ratios of the two are typically different. When these two oxygen reservoirs interact, they commonly exchange, and the degree of change is dependent mainly on the temperature and the water/rock ratio. Thus, oxygen isotopic analysis is ideally suited to studying problems of water/rock interaction. Both of the above approaches (mineralogical and isotopic) are used in the present study.

Whole rock samples were crushed to a fine powder for oxygen isotopic

analysis. Where possible, mineral separates were obtained by hand-picking and by magnetic techniques. In some of the fine-grained rhyolites the groundmass quartz was separated by partially dissolving the rock in HF. Oxygen was liberated from silicates using the flourine technique described by Taylor and Epstein (1962). The results are reported in δ-notation in parts per thousand or per mil (‰) where:

$$\delta^{18}O_{SAMPLE} = \left[\frac{^{18}O/^{16}O_{SAMPLE}}{^{18}O/^{16}O_{STANDARD}} - 1 \right] X 1000$$

Precision is better than 0.2 per mil and raw $\delta^{18}O$ values are corrected to the SMOW scale using Caltech rose quartz ($\delta^{18}O = 8.45$). NBS-28 has $\delta^{18}O = +9.60$ on this scale.

The study of ancient water/rock interactions in the geological record faces the problem that only half of the reactants are preserved; the original aqueous fluid is no longer present, except perhaps in trapped fluid inclusions. Inasmuch as there are many difficulties associated with studies of the latter, even in Cenozoic rocks, in ancient Archean rocks we are forced to calculate the $\delta^{18}O$ of the fluid utilizing $^{18}O/^{16}O$ measurements of the rocks and minerals. From these data, the identity or source of the fluid can commonly be inferred. Such calculations are based on the conservation of mass: ^{18}O and ^{16}O are both stable, so the pre-reaction abundances are identical to the post-reaction abundances. This constraint defines an equation which relates the initial $\delta^{18}O$ of the rock (δ^{i}_{rock}), the final $\delta^{18}O$ of the rock (δ^{f}_{rock}), the initial $\delta^{18}O$ of the fluid (δ^{i}_{fluid}), the oxygen isotopic fractionation factor Δ between water and rock ($\Delta = \delta^{f}_{rock} - \delta^{f}_{fluid}$), and the water/rock ratio (W/R). In the case of a closed system, where given amounts of

water and rock are allowed to equilibrate, and expressing W/R in terms of mass of oxygen in each reservoir, the equation is:

$$W/R = \frac{\delta^{f}\text{Rock} - \delta^{i}\text{Rock}}{\delta^{i}_{H_2O} - (\delta^{f}\text{Rock} - \Delta)} \qquad \text{(eq. 1)}$$

In most water/rock interactions involving igneous rocks, the fluid is heated by a hot, crystalline igneous mass or magma, which causes the H_2O to convect through both the pluton and the surrounding country rocks. The closed system assumption in this case requires that the hydrothermal fluid is continuously recirculated through the rocks and none of the water escapes to the surface. If the system is redefined so that the water makes only one pass through the rock, and then undergoes no further reaction, the equation becomes (Taylor, 1977):

$$W/R = \log_e \left\{ \frac{\delta^{i}H_2O + \Delta - \delta^{i}\text{Rock}}{\delta^{i}H_2O - (\delta^{f}\text{Rock} - \Delta)} \right\} \qquad \text{(eq. 2)}$$

In contrast to the closed system case, the open system requires that oxygen isotopically fresh water enters the rock at all times. Natural hydrothermal systems lie between these two extremes: They will probably be more closely modelled by Eq. 1 if the systems are sealed by an impermeable cap rock and have a continuing input of new magma; they will lie closer to Eq. 2 if the H_2O is free to convect to the surface and if they represent injection and crystallization of only a single body of magma.

In the case of greenstone belts, most of the water/rock interaction has probably taken place in a submarine environment, and large amounts of water have apparently locally discharged from the rock into the sea (as

evidenced by the massive sulfide deposits). This suggests that the hydrothermal circulation systems were recharged with fresh seawater on the flanks of the convection cells. For this reason the open system equation is used in all of the following calculations. In any case, this equation gives a minimum value for the water/rock ratio. If recirculation were taking place, then the water/rock ratios would be higher than those calculated by this method, but the differences become important only at large W/R ratios (i.e. >10). Note that both equations also only give minimum W/R ratios in the sense that appreciable H_2O conceivably could move through fractures in the rock without exchanging (Taylor, 1977).

In applying equation 2 to a greenstone belt, five variables must be evaluated, W/R, $\delta^i_{H_2O}$, δ^i_{rock}, δ^f_{rock}, and Δ. δ^f_{rock} can be directly measured as long as subsequent geologic processes have not changed the $^{18}O/^{16}O$ ratio. δ^i_{rock} can either be calculated from analyses of relic primary igneous minerals such as pyroxene and quartz, or is assumed. This assumption for rocks of basaltic composition is very well documented, because fresh basalts are extremely uniform at $\delta^{18}O \approx 5.5$ to 6.5. For more silicic volcanic rocks the initial $\delta^{18}O$ values are known to cover a broader range. If we assume isotopic equilibrium, Δ is proportional to $1/T^2$, and is also dependent on the mineralogy. To calculate an equilibrium Δ between a rock and water, all of the constituent mineral-rock fractionations need to be added. Unfortunately, for many minerals this information is not known. Also, we know that many minerals in the rocks do not totally equilibrate with the fluid (e.g. quartz and pyroxene), while others seem to equilibrate very readily (plagioclase). An alternative approach is to approximate the oxygen isotopic properties of a fine-grained

rock such as a basalt with a single, "average" mineral, such as a somewhat more An-rich plagioclase than that actually present in the rock (Taylor and Forester, 1971). This technique has been successfully used, for example, in modelling the water/rock interactions in the Samail ophiolite (Gregory and Taylor, 1980). In the present study, An_{40} has been selected to model the basalts, basaltic andesites and andesites present in greenstone belts. This approximation introduces an uncertainty into equation 2, which is greatest at low temperature. The magnitude of this uncertainty is difficult to estimate, but in any case, as will be discussed in connection with the data, the temperature is generally more uncertain than any problems connected with this "feldspar" approximation.

Two variables in equation 2 then remain, W/R and δ_{H_2O}. Throughout most of the discussion these are both treated as unknowns, so the solutions to Equation 2 will plot on curves that cross each graph of W/R vs. δ_{H_2O}. In certain circumstances W/R can be estimated, or at least constrained within certain broad limits, for example beneath the massive sulfide deposits; in such cases δ_{H_2O} can be calculated directly. In general, however, only relatively broad limits can be placed on the combined parameters W/R and δ_{H_2O}.

CHAPTER 2

GEOLOGIC SETTING OF THE ABITIBI GREENSTONE BELT

To answer the question posed in Chapter 1, the Abitibi greenstone belt was selected for a reconnaissance oxygen isotope study. This selection was based primarily on the excellent state of preservation of this particular belt. This work was supplemented with a smaller-scale study of the Dubois greenstone belt in Colorado. These two data sets were then compared to each other and to the few oxygen isotope analyses in the literature from other greenstone belts.

In Figure 2-1 is shown a structural map of the Canadian shield. The Archean is represented by three structural provinces: Slave, Superior and Nutak. These areas consist predominantly of elongated greenstone belts surrounded by seas of granite. This geologic style is duplicated both in terms of rock types and in terms of scale in the shield areas of all of the major continental blocks (see e.g. Talbot, 1973; Fig. 1). The Superior province of Canada, therefore, is a typical portion of the Archean geologic record.

The generalized geology of greenstone belts world-wide has been summarized by Talbot (1973, p. 414-415): "The rocks in a characteristic greenstone belt are largely metavolcanic at the base and pass gradually to sediments at the top. The metavolcanic lavas, pillow lavas and pyroclastics are almost invariably calc-alkaline in overall chemistry and tend to be ultramafic at the base of the full characteristic sequence and pass upwards through tholeiite basaltic to andesitic, and less voluminous dacitic and rhyolitic rock types. Minor cycles of basic to acid eruptives are often present within this general succession . . . The sediments,

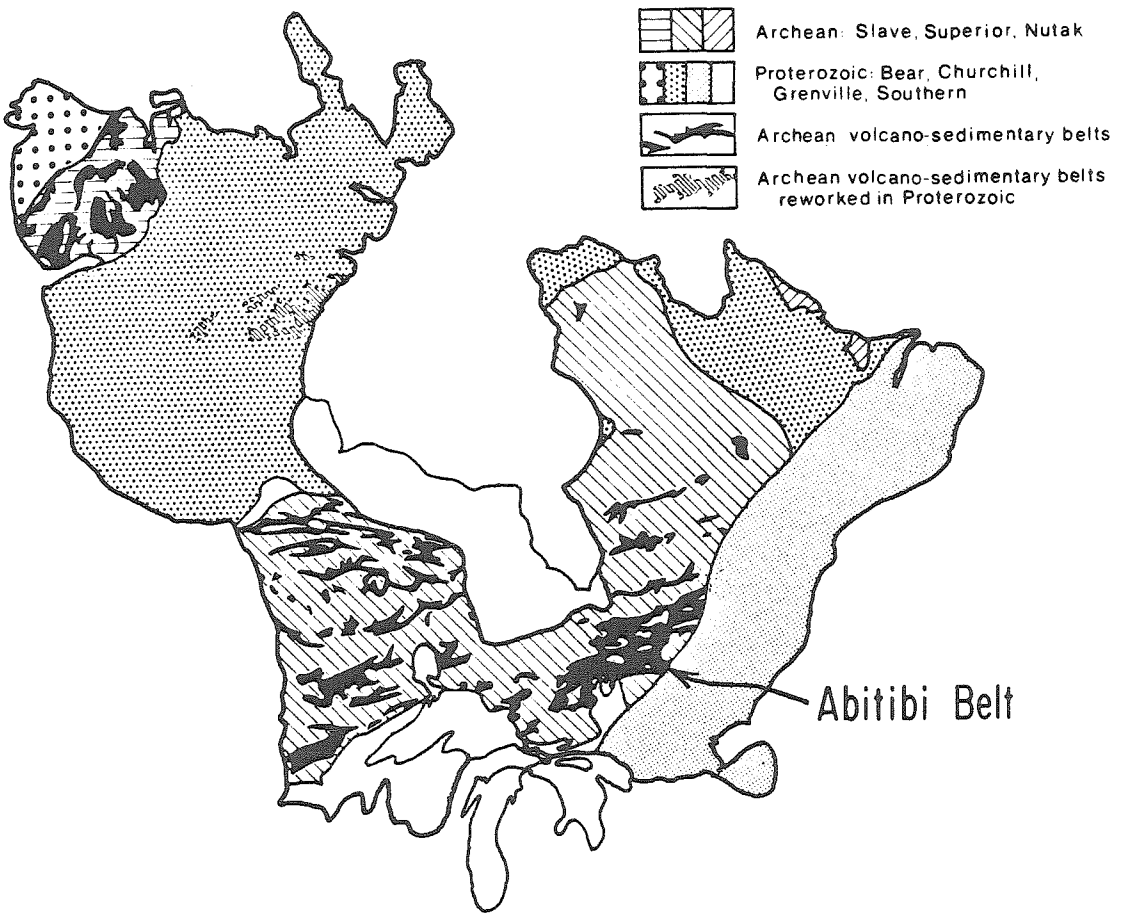

Figure 2-1. Map of the major structural provinces of Canada illustrating the major greenstone belts (after Baragar and McGlynn, 1976). The pattern of alternating granite-greenstone is typical of that found in all of the world's Archean cratons. The Abitibi greenstone belt is a typical Archean greenstone belt in all respects except two; it is the largest, and (probably because of this) it has the lowest metamorphic grade and highest state of structural and textural preservation.

which increase in volume and importance towards the top of the characteristic greenstone belt succession, are largely undifferentiated immature clastic sediments with pyroclastic additions important near the base. Subsidiary developments of chemical precipitates are thought to be locally represented by banded ironstone, cherts and jaspilites."

A very similar description has been published for the Abitibi greenstone belt (Goodwin and Ridler, 1970): "Basalt flows and associated gabbroic intrusions are common in the lower parts of the volcanic assemblages. Andesitic flows and pyroclastics are intercalated with basalt and characteristically increase in proportion upwards. Felsic rocks of dacite to rhyolite composition are generally present in the upper stratigraphic parts . . . Sediments characteristically occupy higher stratigraphic positions . . . Sediments of the 'poured-in' turbidite association predominate." Both in terms of its lithologies and its stratigraphic succession, therefore, Abitibi is typical of greenstone belts throughout the Archean.

In terms of style of deformation, the Abitibi greenstone belt is also very similar to other greenstone belts. In fact, Abitibi is a typical greenstone belt in all respects except two: It is the largest continuous Archean greenstone belt in the world (475 miles long by 125 miles wide; Goodwin and Ridler, 1970), and perhaps because of this, it is the least metamorphosed. The low metamorphic grade (prehnite-pumpellyite facies in many places) has contributed to the excellent textural preservation of the volcanic rocks. The low-grade portions of the Abitibi greenstone belt have suffered the least disturbance since their formation of any known Archean volcanic rocks, and for this reason are the most likely to have preserved their original oxygen isotopic character.

A geologic map of the entire Abitibi greenstone belt is presented in Figure 2-2. The metavolcanic and metasedimentary rocks have been intruded by diapiric granitic bodies which range in size up to batholiths. The greenstones, therefore, typically have the form of synclinal keels, with the intervening anticlines occupied by the granites. The greenstone belt is characterized by two major episodes of metamorphism (see below). An early prehnite-pumpellyite facies burial metamorphism was overprinted by a greenschist to amphibolite facies event associated with the intrusion of the granitic batholiths (Kenoran orogeny). Subsequent younger events include numerous younger Precambrian dikes, mostly of the Matachewan swarm (Goodwin and Ridler, 1970). Considering this geologic history, only two principal events are expected to have had an appreciable effect on the oxygen isotope distribution, namely, the prehnite-pumpellyite and greenschist metamorphic episodes.

The metamorphic petrology of the Abitibi greenstone belt is summarized in Jolly (1974), Jolly (1980), and Dimroth and Lichtblau (1979). Well developed metamorphic zonation is present. The lowest grade rocks are in the prehnite facies, with relic clinopyroxene and plagioclase (and in the rhyolites, biotite). With increasing grade the rocks pass into the pumpellyite zone, the actinolite (with relic pumpellyite) zone, the actinolite zone proper, and finally the hornblende zone. The hornblende zone is present only around post-orogenic intrusives, such as the Otto stock. Against the large granitic masses, the relatively low temperature actinolite zone is present, suggesting that the granitic bodies were emplaced by solid flow. This is consistent with the observation that the margins of these batholiths are typically gneissic, with concentric foliation. Use of overprinting relations indicates the following metamorphic history

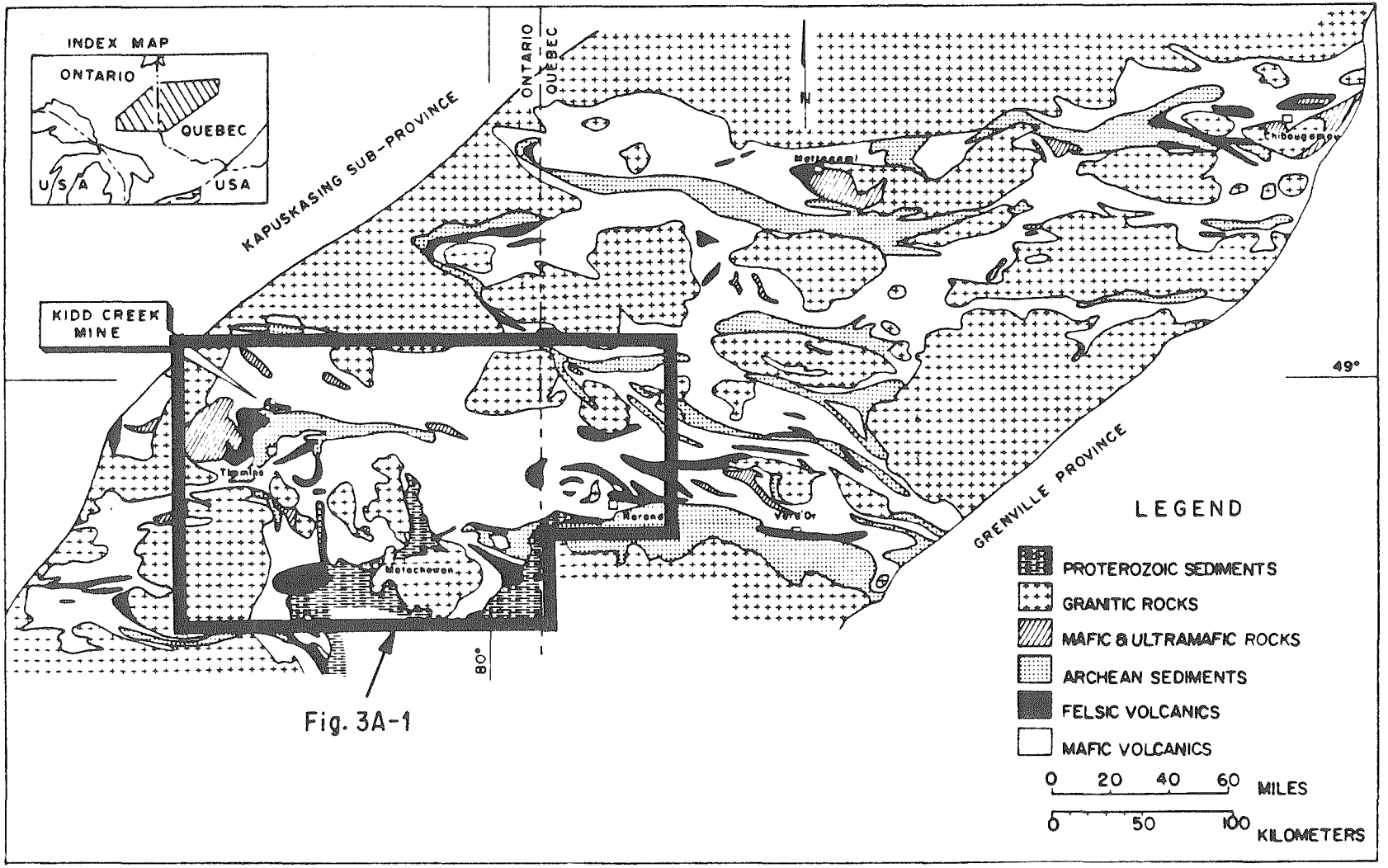

Figure 2-2. Generalized geologic map of the Abitibi greenstone belt (after Goodwin and Ridler, 1970). The rock types present are predominantly volcanics and associated subvolcanic intrusions, immature clastic sedimentary rocks, and granitic batholiths associated with the Kenoran orogeny. The area studied in this report is outlined at the western end of the belt.

(Jolly, 1974): The volcanic rocks underwent regional burial metamorphism, reaching a maximum grade of pumpellyite-epidote at the base. Three major subsequent episodes of plutonism have locally recrystallized the volcanic pile.

The prehnite-pumpellyite metamorphism took place either during or soon after eruption (Jolly, 1980), and Dimroth and Lichtblau (1979) specifically refer to it as sea-floor metamorphism. In their detailed petrographic comparison of Cenozoic and Archean sea-floor metamorphism, Dimroth and Lichtblau (1979) conclude, "the evidence indicates that Archean and Cenozoic sea-floor metamorphism took place at identical conditions." An important question that needs to be answered, however, is whether or not the oxygen isotopic effects which may have been introduced by seawater alteration have survived the later contact metamorphism associated with the granites.

To investigate the possibililty of lateral variations in the hydrothermal activity or in the source of the fluids, eight different areas were studied, leading to eight more-or-less independent calculations of the effects of the water/rock interactions. These eight areas are the Timmins area, Munro Township, western, central and eastern Blake River Group, the Skead Volcanics, and two massive sulfide deposits, the Kidd Creek and Amulet "A" mines. The detailed geological, petrological and oxygen isotopic relations of each of these areas is discussed in the sections that follow.

CHAPTER 3

$^{18}O/^{16}O$ RATIOS IN VOLCANIC ROCKS

CHAPTER 3A. GENERAL STATEMENT

The Abitibi greenstone belt consists of a small number of accumlations of volcanic rocks which are separated by less abundant volcanic rocks, faults and granitic plutons. These concentrations of volcanic rocks may represent individual volcanic edifices (Goodwin and Ridler, 1970), and at least three such volcanic piles were examined in the present study.

A large suite of samples was collected from the Blake River Group in the central part of Figure 3A-1. Not only has this area been studied extensively by other workers, it shows the best development of the prehnite-pumpellyite facies of any locality in the Abitibi greenstone belt (Jolly, pers. comm.). A large expanse in the core of the Blake River syncline is in the prehnite-pumpellyite facies, and only on the margins does the grade reach greenschist facies. The Blake River rocks are among the least metamorphosed Archean rocks known to science.

The thick sequence of volcanic rocks to the east of the Round Lake Batholith are termed the Skead Volcanics (Fig. 3A-1). This succession is most interesting because of its conformable contact with the granitic batholith at its base, and its structural simplicity.

The volcanic rocks around Timmins are structurally very complex, and furthermore are poorly exposed. For this reason it is not possible to interpret the Timmins data in as much detail as the data from Skead and Blake River. Regional geologic studies by Jensen (1979b) suggest that the Timmins and Skead terranes both stratigraphically underlie the

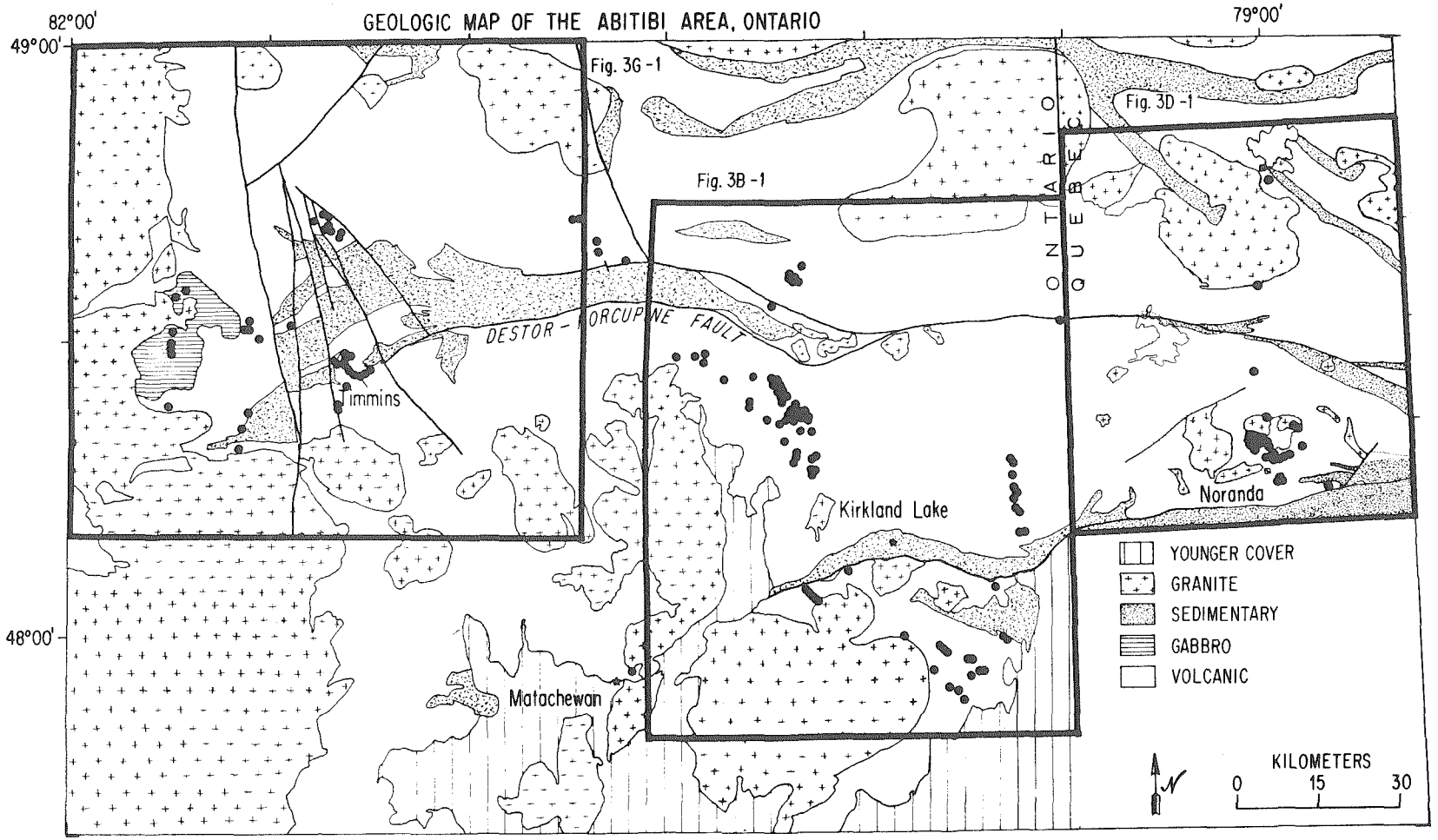

Figure 3A-1. Geologic map of the studied portion of the Abitibi greenstone belt.

Blake River Group.

A single komatiite flow from Munro Township was studied in detail in the present work because of the great petrologic interest in this rock type. The volcanic rocks in Munro Township are thought to be stratigraphically equivalent to the rocks in the Timmins area.

The whole-rock $\delta^{18}O$ data from these six areas are compared in Figure 3A-2, which contains most of the data on the metavolcanic rocks collected in this study, delineated according to primary igneous rock type. The samples from the Kidd Creek and Amulet "A" mines are not shown because the hydrothermal processes were clearly more intense and of a different type at those two localities. Each of the six localities in Figure 3A-2 are discussed in detail in the following sections, and are compared and summarized in Chapter 7.

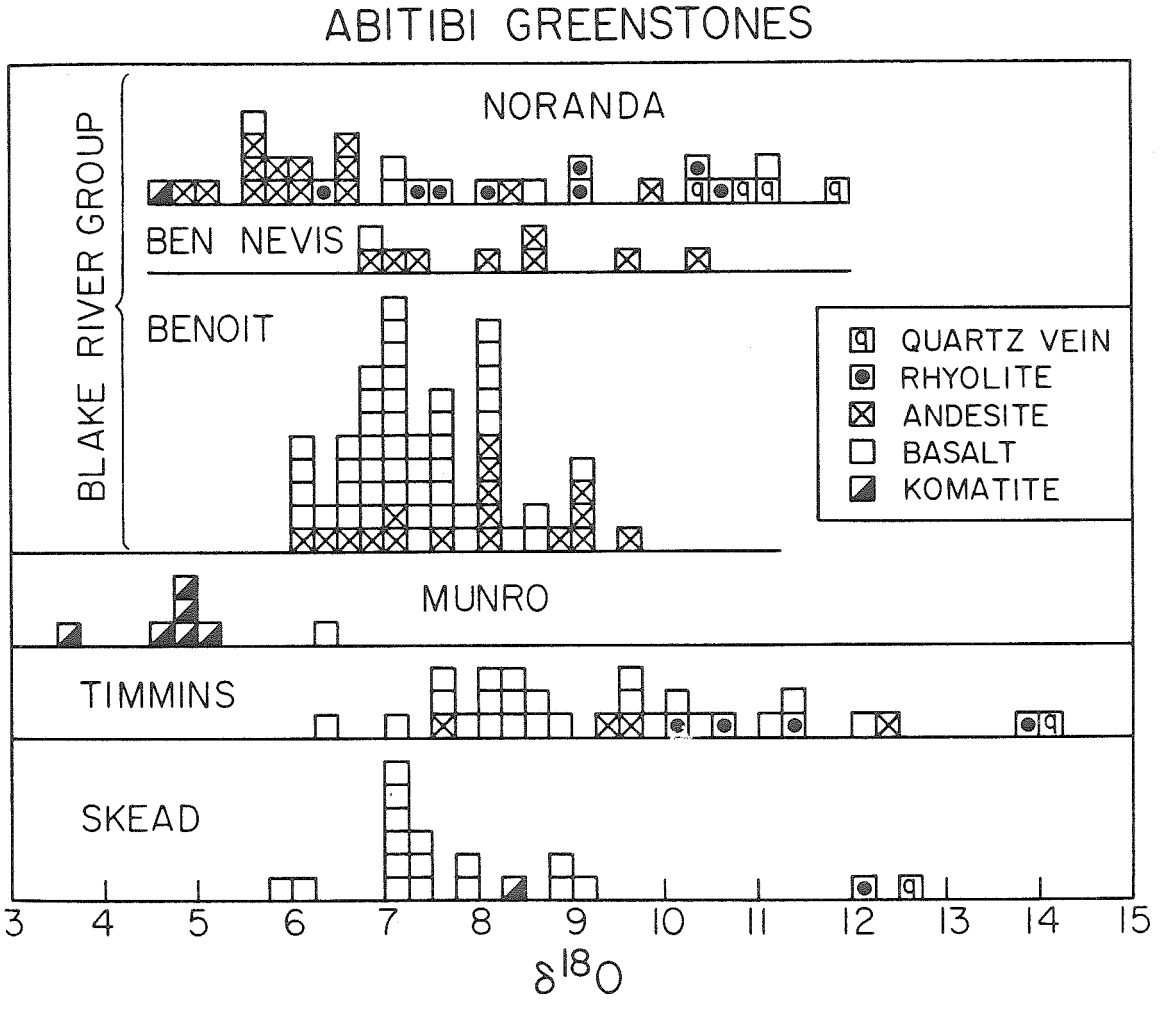

Figure 3A-2. Histogram of $\delta^{18}O$-values for the volcanic rocks and associated quartz veins from the Abitibi greenstone belt. The data are grouped according to geographic location, and four main rock types are distinguished. The detailed oxygen isotopic, petrologic and structural relationships within each of these six areas are discussed in detail in the following sections.

CHAPTER 3B. BEN NEVIS TRAVERSE

A suite of ten samples were collected and analyzed from a traverse beginning near Crosby Lake (McVittie Twp.) and ending about 15 km. north in the SE portion of Ben Nevis Twp. (Fig. 3B-1). This traverse is the same as that reported in Jolly (1974), and extended by Jolly (1980).

I. GEOLOGY

The main mass of mafic to felsic volcanic rocks which extends from Noranda, Quebec in the east to as far west as Timmins, Ontario is known as the Blake River Group (Fig. 3B-1). This group of rocks occupies an east-trending, east-plunging synclinorium (Fig. 3B-1), so its lower (predominantly basic) portion is exposed at its western extension (in English Township, Ontario), and the upper (predominently felsic) portion crops out at its eastern end (around Noranda, Quebec). The total stratigraphic thickness of this volcanic pile has been estimated to be 50,000 feet (Goodwin and Ridler, 1970). Because of its synclinal shape, the Blake River Group is well-suited for collecting suites of samples across the stratigraphy. Two such traverses were made, one near the (E-W) center of pile, around Ben Nevis Township, and one near the western end of the pile, through Cook and Benoit Townships. Finally, a set of samples were collected from the Noranda area, at the eastern end of the pile.

The Ben Nevis traverse begins near the southern edge of the Blake River synclinorium and extends across strike almost to the axis (Fig. 3B-1). In a broad sense, therefore, the traverse samples a large part of the stratigraphic section of the central Blake River Group. The detailed structure is actually somewhat more complicated than this, involving several faults of low displacement and secondary folds (Hogg, 1964; Jensen, 1975).

Table 3B-1. OXYGEN ISOTOPIC AND PETROGRAPHIC DATA FROM THE BEN NEVIS SYNCLINE

Sample	Field Description	$\delta^{18}O$ WR	$\delta^{18}O$ Min.	Microscopic Description: Texture	Ave. gr. size	Secondary Mineralogy	% Rec.	Location: Lat.	Location: Long.
Br-1	Variolitic pillow basalt	6.9		Variolitic, veined	10	qtz,chl,pu	100	48°31.4'	79°31.6'
Br-12	Massive andesite, Ben Nevis Twp.	8.7		Porphyritic (feld)	10	qtz,chl,ep,pr,pu	100	48°17.7'	79°40.5'
Br-13	Amygdular massive andesite, Ben Nevis Twp.	8.0		Amygdaloidal (qtz)	20	qtz,chl,pr,musc	100	48°17.6'	79°40.4'
Br-15	Fragmental andesite. Sample from altered matrix	10.3						48°17.4'	79°40.3'
Br-16	Fragmental andesite	6.8		Fragmental	50	qtz,chl,pr,pu,ep,cc	100	48°15.2'	79°40.1'
Br-18	Highly altered andesite, Katrine Twp	9.5		Equigr.,veined	10	qtz,chl,cc,pr,ep,musc	95	48°13.9'	79°39.6'
Br-19	Pillowed andesite	8.5		Porph. (feld),amyg.	50	qtz,chl,cc,pr	80	48°13.5'	79°39.9'
Br-20	Pillowed andesite	7.3		Equigr.,felted	100	qtz,chl,act,ep,musc	100	48°12.4'	79°39.3'
Br-21	Massive andesite w. vesicles	7.2		Amygdaloidal,Felted	10	qtz,ep,act,cc	100	48°12.2'	79°39.2'
Br-23	Coarse hbd gabbro, Crosby Lake sill	5.7	8.1(f)	Granophyric	2000	qtz,chl,ep,act,cc	40	48°10.0'	79°39.6'
Br-24	Plag-cpx gabbro, Crosby Lake sill	5.4	6.0(f) 4.6(px)	Ophitic	200	chl,act,musc.	50	48°9.8'	79°40.1'

WR	= Whole rock	(cc)	= calcite	biot	= biotite	per	= perthite
Min.	= Mineral	(ch)	= chlorite	cc	= calcite	pr	= prehnite
% Rec.	= percent recrystallized or modal secondary minerals	(f)	= feldspar	chl	= chlorite	pu	= pumpellyite
Lat.	= Latitude	(h)	= hornblende	ep	= epidote	qtz	= quartz
Long.	= Longitude	(nm)	= non-magnetic separate	hem	= hematite	serp	= serpentine
(a)	= amphibole	(pl)	= plagioclase	hbd	= hornblende	trem	= tremolite
(b)	= biotite	(px)	= pyroxene	mgt	= magnetite		
(c)	= calculated	(q)	= quartz	mic	= microcline		
		act	= actinolite	musc	= muscovite		

All of the rocks also contain opaques, and all of the volcanics except Qe-1 and Br-44 (komatiites) are presumed to contain albite (which is commonly difficult to distinguish optically from quartz because of its extremely fine grain size). Hematite, sphene and white mica are very common accessories (see Jolly, 1980). The order in which the minerals are listed in the tables has no significance.

Average grain size is in microns.

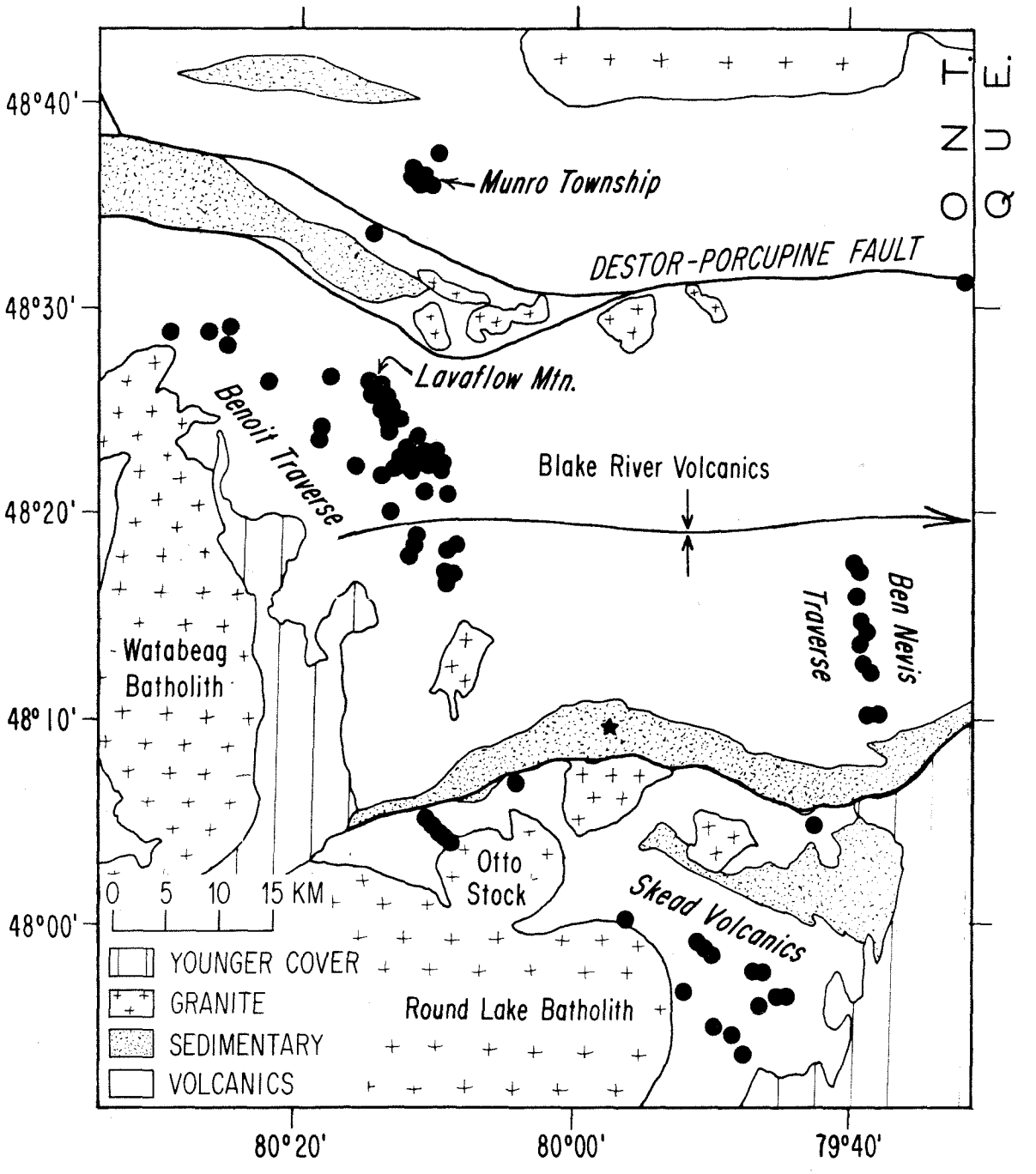

Figure 3B-1. Geologic map of the Blake River area, showing the locations of the analyzed samples. The Ben Nevis and Benoit traverses both sample the stratigraphic section of the Blake River Group. The Skead volcanics were also sampled from base to top. The Larder-Cadillac fault is the large unlabelled fault between the Ben Nevis and Skead areas.

A wide variety of volcanic rocks is present, including: basalt: massive, pillowed, flow-breccia, tuff-breccia; andesite and dacite: massive, pillowed, flow-breccia, tuff, argillite; and rhyodacite and rhyolite: massive, flow-breccia, tuff-breccia, tuff, and lapilli-tuff (Jensen, 1975). There is a general progression across this traverse from predominantly mafic units at the south (base of the pile) to predominantly felsic units at the north (top of the pile). In addition, the lowermost units have a tholeiitic affinity, whereas the upper units are calc-alkaline. The tholeiite-calc-alkaline boundary can be mapped for at least 40 miles across eastern Ontario, and intersects the sampled Ben Nevis traverse in the southern part of Katrine Twp. (Ont. Div. Mines Map 2205).

The volcanic group of rocks has been invaded by several generations of dikes and irregularly shaped masses of rhyolite, granodiorite, quartz-diorite, syenite, syenite porphyry, diorite, gabbro and diabase (Jensen, 1975; Hogg, 1964). Of particular interest to this study are the several diorite bodies and a solitary syenite body which cropout close to the sampled area. The diorite bodies have a tendency to follow the strike of the lava flows, but in most instances they transgress these flows. Many of the intrusive rocks are thought to have been sub-volcanic in nature (e.g. Jensen, 1975), and are hydrothermally altered along with the volcanic rocks.

II. PETROLOGY

The general petrology of the Ben Nevis samples is summarized in Table 3B-1. The original igneous textures and structures are typically well preserved, and there has been no development of schistosity (Fig. 3B-2). The only microscopic indication of deformation is the presence of veins, the overwhelming majority of which contain quartz (Fig. 3B-2c); these are

Figure 3B-2. Photomicrographs from the Ben Nevis area.

a.) Br-14, crossed polars. Prehnite filling an amygdule. Although prehnite is typically a vein or amygdular mineral, it also is present in the groundmass.

b.) Br-14, crossed polars. A relatively fresh portion of the thin section. Recrystallization is quite variable, on the scale of both outcrops and thin sections, and probably relates to the permeability of the rocks (see e.g. Jolly, 1970). Porphyritic rocks such as Br-14 are typically calc-alkaline, and are rare in the Archean.

c.) Br-16, transmitted light. Pumpellyite rods projecting into a small quartz vein (upper edge of vein).

d.) Br-20, crossed polars. Actinolite in the groundmass. This sample is in the greenschist facies, whereas the above samples are in the prehnite-pumpellyite facies.

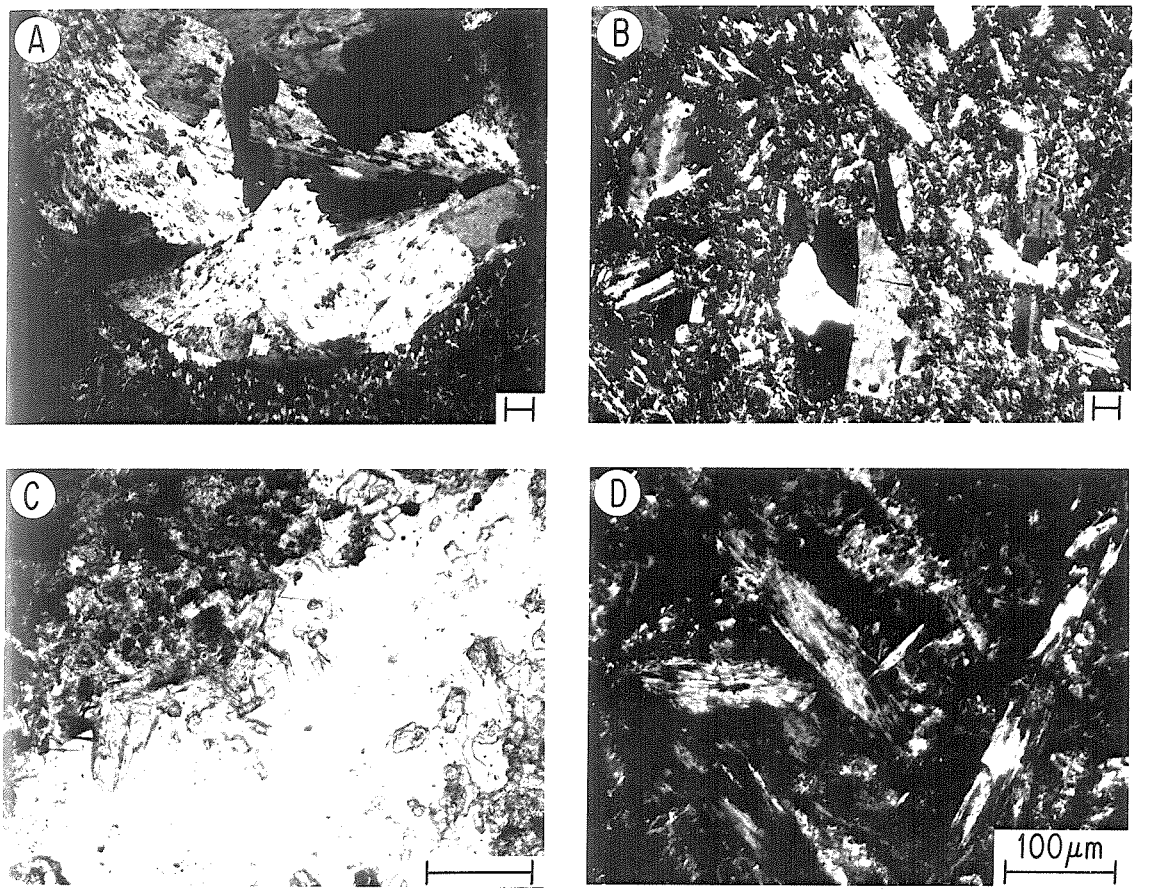
A
B
C
D
100μm

locally quite abundant. Quartz is also common, along with calcite, prehnite and chlorite, in amygdules (Fig. 3B-2a, Fig. 3B-7). The amount of recrystallization in this part of the greenstone belt is high; only rarely can relic igneous minerals be found (Fig. 3B-2b). Only one of the analyzed samples (Br-19), in fact, contained an appreciable amount of relic material, in this case twinned calcic plagioclase laths.

The secondary assemblages in Ben Nevis Twp. are those characteristic of the prehnite-pumpellyite facies. The rocks are recrystallized to an aggregate of quartz-chlorite-albite-prehnite-pumpellyite-muscovite, possibly also with epidote. Along the southern part of this traverse, pumpellyite is absent and actinolite is present. This reaction defines an isograd which has been mapped in some detail by Jolly (1980).

III. OXYGEN ISOTOPIC DATA

Whole-rock $\delta^{18}O$-values for the Ben Nevis traverse range from +5.4 to +10.3 (Table 3B-1). There is a broad, general increase in $\delta^{18}O$ to the north. This corresponds to increasing structural height, increasing distance from the Larder-Cadillac fault (Fig. 3B-1), increasing distance from the granitic batholith to the SE of Larder Lake, and an increasing proportion of siliceous lavas such as rhyolites. Which of these relationships are generic and which are coincidental is not easy to evaluate, and complete discussion is deferred to Chapter 3C. Several arguments can be advanced, however, which suggest that $\delta^{18}O$ is related to the stratigraphic height.

It is well known that more silica-rich igneous rocks tend to have higher primary $\delta^{18}O$-values (Taylor, 1968). It is possible, therefore, that the increase in $\delta^{18}O$ towards the center of the syncline is related to the higher proportion of acid volcanic rocks. Normal andesites, however,

have $\delta^{18}O$ in the range +6 to +7 (Taylor, 1968), which is considerably less than the +10 andesites in Ben Nevis Twp. Because of the later alterations there is no way to be absolutely certain that the Ben Nevis andesites were originally erupted with 'normal' $\delta^{18}O$-values, as there are a variety of mechanisms for producing both high- and low-^{18}O magmas (Taylor, 1977). However, all of the data collected on mineral separates (see below) indicates that 'normal'-^{18}O magmas were predominantly, if not exclusively, present, and there is no evidence that high-^{18}O andesitic magmas were ever produced during the Abitibi volcanism.

Figure 3B-3 illustrates the relationship of $\delta^{18}O$ and structural height for the Ben Nevis traverse samples. The structural height can only be approximately measured because of the minor structural complications mentioned above. For the purpose of this discussion, the synclinorium is treated as a simple syncline with vertically dipping flanks. All of the samples which contain prehnite and pumpellyite occupy the center of the syncline (stratigraphically higher) and have higher $\delta^{18}O$ (6.8 to 10.3). All of the samples which contain actinolite are on the margins of the syncline (stratigraphically lower) and have lower $\delta^{18}O$ (5.4 to 7.3). The relationship among these three variables; height, $\delta^{18}O$, and metamorphic grade, has great significance for the metamorphic fluid and is discussed in detail below.

IV. FLUID COMPOSITION

Generalizing the shape of the data spread in Figure 3B-3, and inferring a temperature from the metamorphic mineral assemblages, it is possible to calculate the $\delta^{18}O$ of the aqueous fluid which exchanged with the rocks. The uncertain nature of the oxygen isotopic fractionation between rocks and water detracts a little from the calculation, but the results

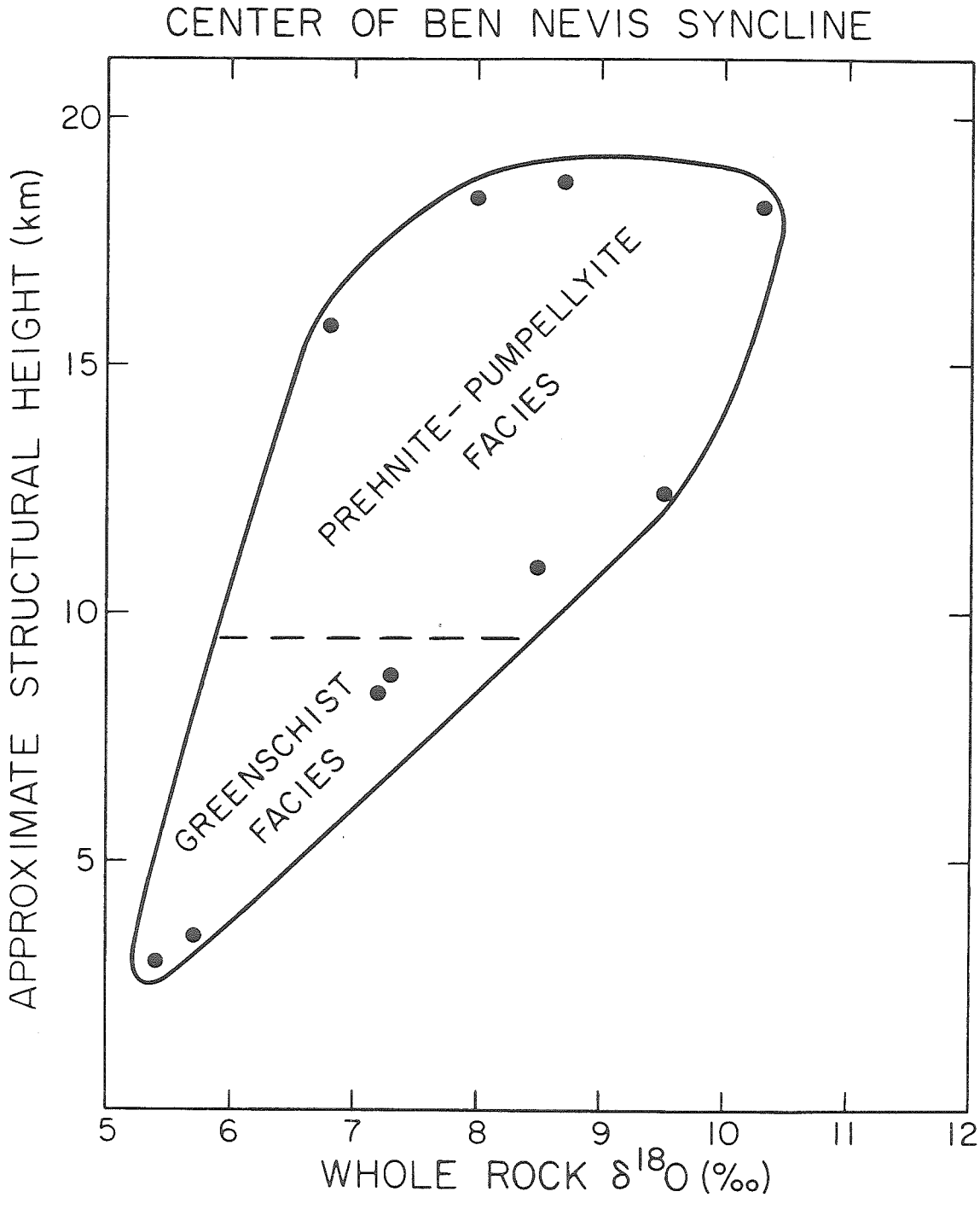

Figure 3B-3. Variation of $\delta^{18}O$ with stratigraphic height (and metamorphic grade) in igneous rocks of the Ben Nevis area.

cannot be far from the truth. The calculated final fluid at three points in the volcanic pile is shown in Figure 3B-4. The importance of the diagram is that at all three points the calculated $\delta^{18}O$ of the fluid is practically identical at +1.5. This suggests that a single, oxygen isotopically homogeneous fluid was in communication with, and in equilibrium with, the entire volcanic section.

Furthermore, the shape of Figure 3B-4 suggests that the water/rock ratio during hydrothermal alteration was high. Suppose that the volcanic pile were originally oxygen isotopically homogeneous, for instance at $\delta^{18}O = +6$. If a small amount of fluid were allowed to equilibrate with this oxygen reservoir under a temperature gradient, the rock (being the bulk of the oxygen) would show only a small $\delta^{18}O$ shift, whereas the fluid would have a large ^{18}O gradient from top to bottom. Alternatively, with large amounts of fluid, the fluid would maintain its initial $\delta^{18}O$, and the rock (now a small fraction of the total oxygen) would display the ^{18}O-shifts. The general shape of Figure 3B-4, therefore, suggests that the volcanic pile has undergone oxygen isotopic exchange with a large reservoir of fluid, and that the high-^{18}O rocks exchanged at a lower temperature than the low-^{18}O rocks (compatible with the stratigraphic relationships).

The isotopic composition of the final fluid is an interesting quantity, but more interesting still is the initial $\delta^{18}O$ value of the fluid. Because the hydrothermally altered rocks are presumed to have undergone a positive ^{18}O-shift (becoming richer in ^{18}O), the water must have undergone a complementary negative ^{18}O-shift to conserve mass (becoming poorer in ^{18}O). Just as the final fluid composition can be calculated (using the equilibrium fractionations) at any point in

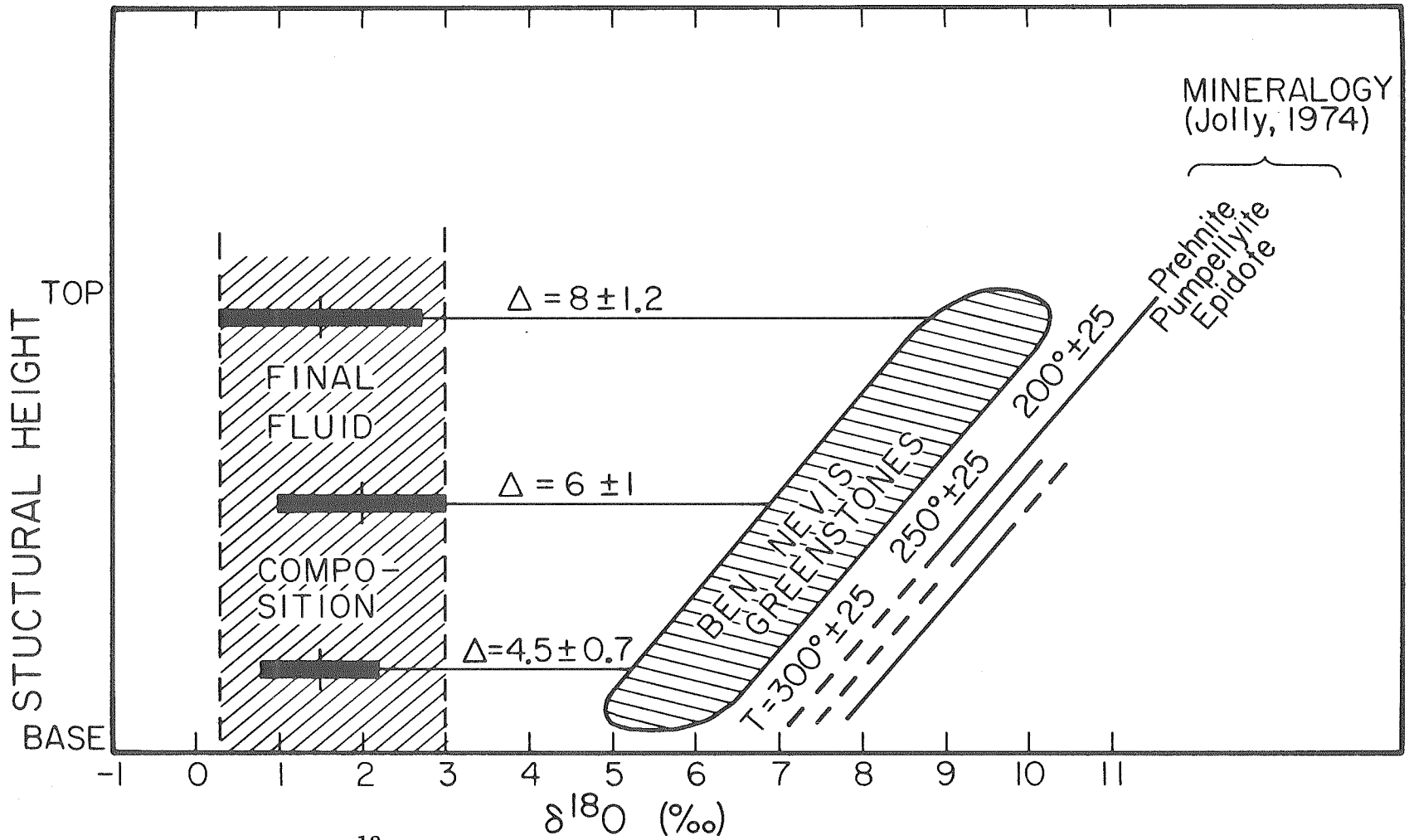

Figure 3B-4. Calculated $\delta^{18}O$ of the H_2O in equilibrium with the Ben Nevis volcanic section at three localities. Using the temperatures estimated from the metamorphic assemblages and the feldspar geothermometer the final fluid was apparently the same throughout the pile. Thus, the volcanic pile appears to have been close to internal oxygen isotopic equilibrium during metamorphism.

the volcanic pile, so can the initial fluid (using Eq. 2). This calculation has been performed for each of the three cases illustrated on Figure 3B-4; the top of the pile, the middle of the pile, and the bottom of the pile. The three unknowns in Equation 2 ($\delta^{18}O$ initial fluid, W/R, and T) are portrayed in two dimensions by plotting $\delta^{18}O$ against W/R, and contouring T. In each case (Fig. 3B-5 a,b,c) the assumptions used in constructing the diagram are listed in the upper right hand corner. These include the boundary conditions of the system (assumed to be open), and the $\delta^{18}O$ change produced in the rock.

Figures 3B-5 a,b,c indicate that at low water/rock ratios the initial hydrothermal fluid must have been extremely ^{18}O-rich. In order to add ^{18}O to a large mass of rock, a small mass of fluid would have to be very concentrated in ^{18}O. The lower limit on the water/rock ratio, of course, is the amount of water presently contained in the rock's hydrous minerals, such as chlorite. At high water/rock ratios, however, the exchange process is controlled by the initial fluid composition and is essentially independent of W/R. As long as W/R > 2, the water is the major reservoir of oxygen, and the $\delta^{18}O$ changes in the rock will have little effect on it.

Note that in addition to the dependence on W/R, the initial fluid calculation differs from the final fluid calculation in a second very important respect: The temperature is indeterminate. Although the final temperature experienced by any given rock can be estimated using the metamorphic assemblage, the temperature at which the water flux took place cannot be determined at all. This problem is illustrated in Figure 3B-6, and is inherent in this type of analysis. Consequently in each of Figures 3B-5 a,b,c, three possible temperatures are shown; the metamorphic

Figure 3B-5. Calculated possible $\delta^{18}O$-values for the hydrothermal fluid responsible for the alteration effects along the Ben Nevis traverse. Like Figure 3B-4, the calculation is performed independently for three different positions in the volcanic pile; a) lower, b) middle and c) top. In each case, the three variables $\delta^{18}O_{fluid}$, water/rock ratio and temperature are displayed in two dimensions as $\delta^{18}O$ vs. water/rock ratio, with contours of temperature. The assumptions behind each calculation are listed in the upper right.

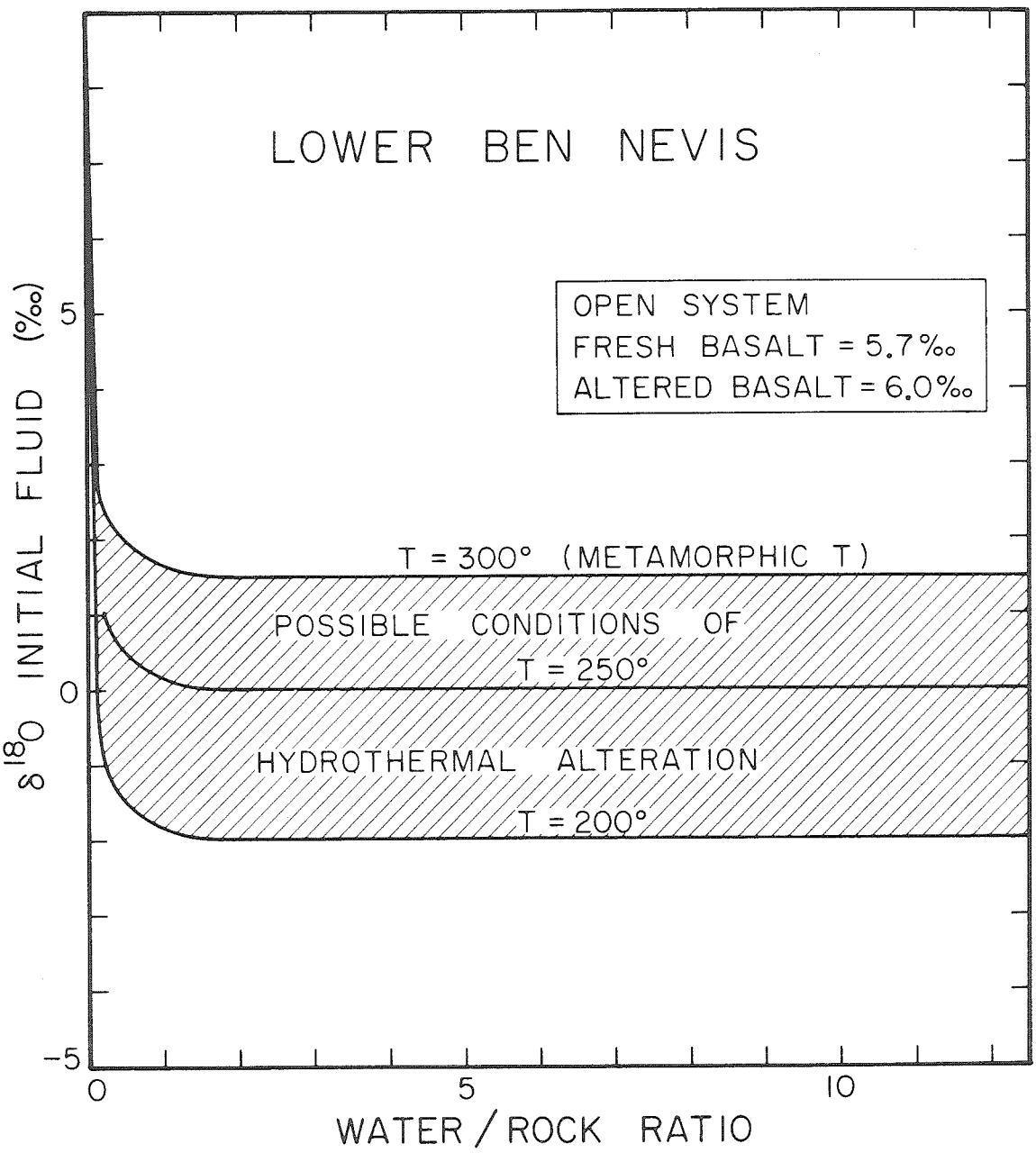
LOWER BEN NEVIS
OPEN SYSTEM
FRESH BASALT = 5.7‰
ALTERED BASALT = 6.0‰
T = 300° (METAMORPHIC T)
POSSIBLE CONDITIONS OF
T = 250°
HYDROTHERMAL ALTERATION
T = 200°
δ18O INITIAL FLUID (‰)
5
0
-5
0
5
10
WATER / ROCK RATIO

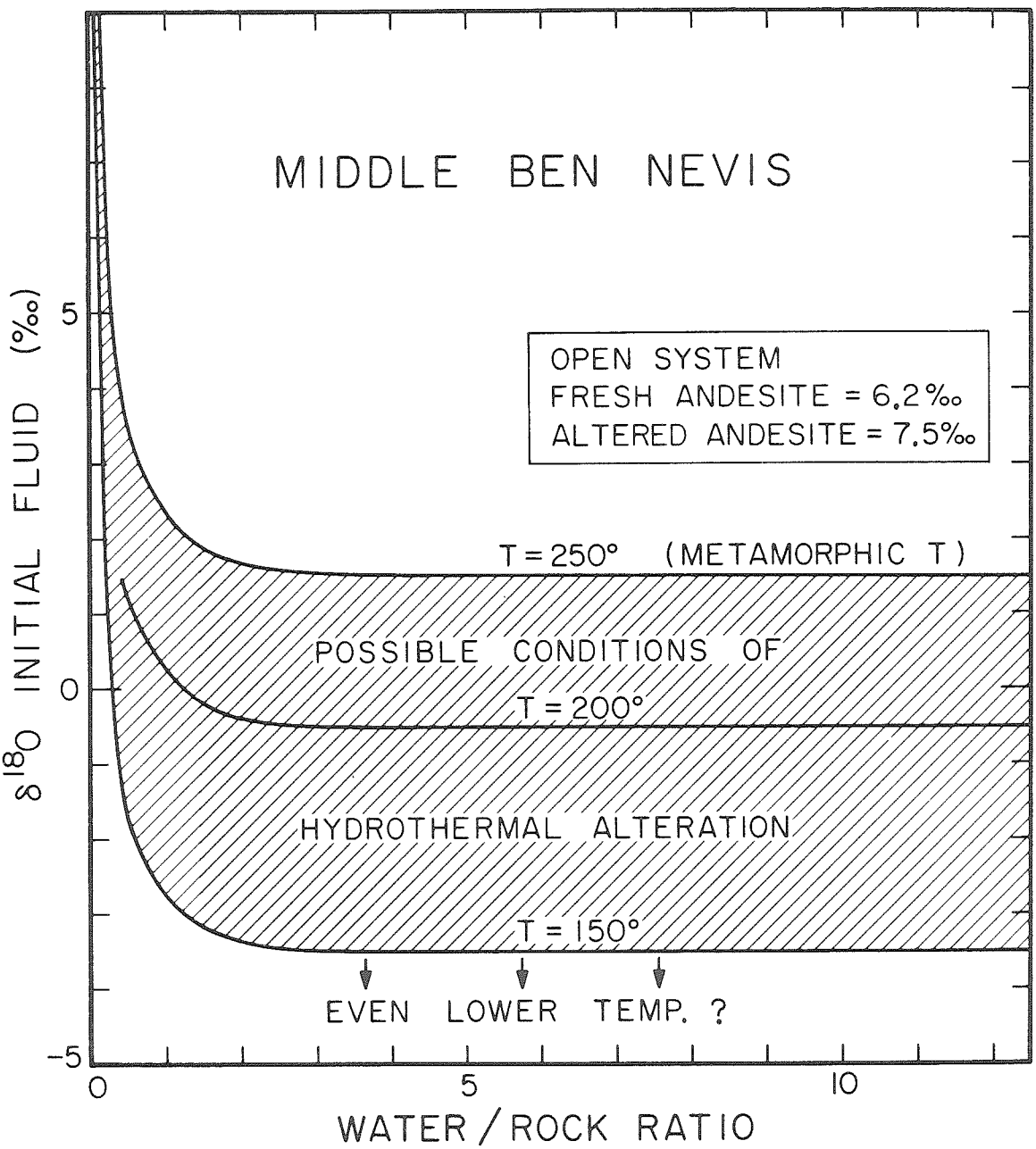
MIDDLE BEN NEVIS
OPEN SYSTEM
FRESH ANDESITE = 6.2‰
ALTERED ANDESITE = 7.5‰
T = 250° (METAMORPHIC T)
POSSIBLE CONDITIONS OF
T = 200°
HYDROTHERMAL ALTERATION
T = 150°
EVEN LOWER TEMP. ?
δ18O INITIAL FLUID (‰)
5
0
-5
0
5
10
WATER / ROCK RATIO

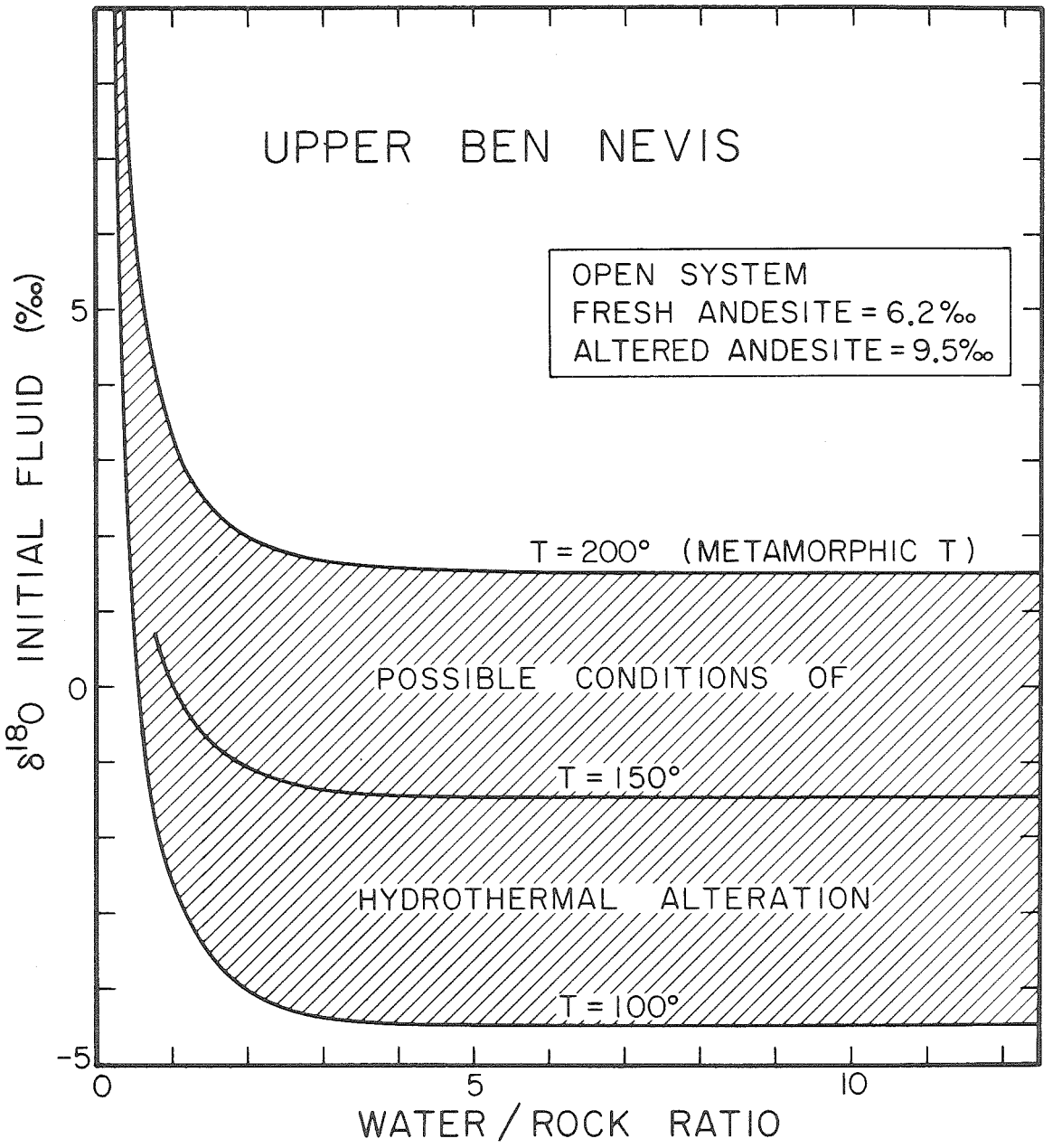
UPPER BEN NEVIS
OPEN SYSTEM
FRESH ANDESITE = 6.2‰
ALTERED ANDESITE = 9.5‰
T = 200° (METAMORPHIC T)
POSSIBLE CONDITIONS OF
T = 150°
HYDROTHERMAL ALTERATION
T = 100°
δ18O INITIAL FLUID (‰)
5
0
-5
0
5
10
WATER / ROCK RATIO

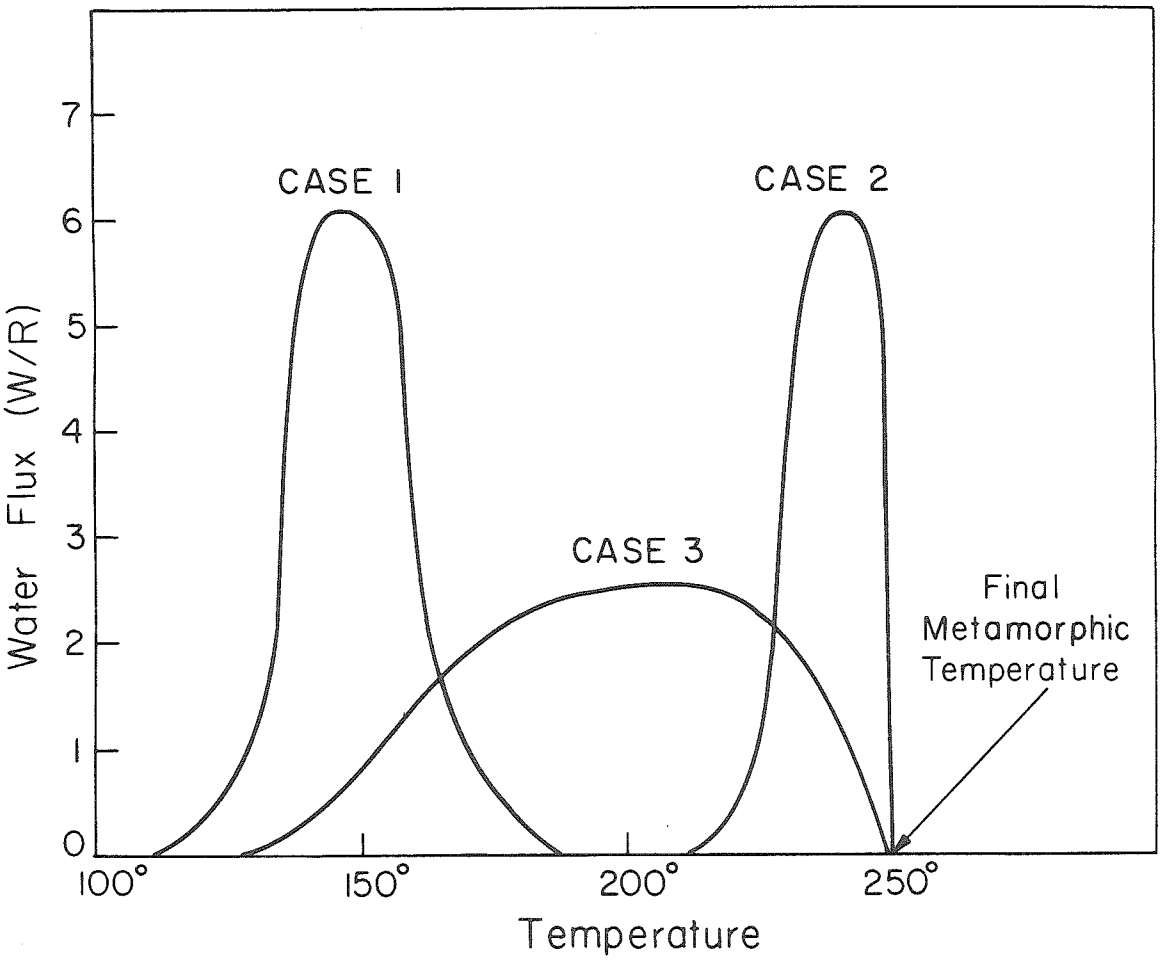

Figure 3B-6. Diagrammatic indication of 3 possible histories of the water flux in a greenstone belt as a function of temperature. One cannot assume that all of the water/rock interactions took place at a constant metamorphic temperature, nor is such a situation geologically plausible.

(maximum) temperature, and 50° and 100° less than that. It is possible that the temperatures were even less that this (e.g. K. Muehlenbachs, pers. comm. 1979), in which case the fluids could have been even lighter than those depicted on Figures 3B-5 a,b,c. This is considered unlikely for two reasons. First, studies of ophiolites (Gregory and Taylor, 1980) indicate that modern oceanic crustal sections are altered at high temperatures. Second, the hydrothermal fluid in the Abitibi belt was probably derived from seawater, and it is very doubtful that seawater ever had $\delta^{18}O$ much lower than -3 (see Chapter 7 for a detailed discussion of this).

Comparison of the calculated initial fluids for the upper, middle and lower portions of the Ben Nevis section indicates that they are rather similar. At low water/rock ratios all would require ^{18}O-rich fluids. At high water/rock ratios all would require a fluid with $\delta^{18}O \approx +1.5$ if the water flux took place at the metamorphic temperature, and with $\delta^{18}O = -2$ to -4 if the temperature were 100° less than that. There is a suggestion that the fluids may be lighter in the upper portions of the pile. This would be consistent with vertical streamlines during alteration and an ^{18}O-shifted fluid. The fluid which altered the lower parts of the pile may have been lowered in ^{18}O because of that interaction, and then been transmitted to the upper parts of the pile. Such an effect has been clearly demonstrated in the case of the Samail ophiolite (Gregory and Taylor, 1980). In any case, the data are consistent with all of the rock in the Ben Nevis area having been altered by hydrothermal solutions having an initial $\delta^{18}O$ in the range of 0 ± 2.

To return to the discussion of Figure 3B-3, it seems likely that the spread among the samples is caused by local variations in the water/rock ratio. On the outcrop the metamorphic style is characterized by the

development of enclaves, particularly in the fragmental rocks. It is common to find large, massive blocks of relatively unaltered andesite set in a thoroughly recrystallized matrix of tuffaceous andesite (Fig. 3B-7). This has been interpreted (Jolly, pers. comm., 1978) as indicating greatest access to the metamorphic fluid in the matrix areas, and least access in the massive blocks. In support of this line of reasoning, the two most ^{18}O-rich samples, Br-15 and Br-18, are from the matrix of an andesite breccia and a basic to intermediate agglomerate, respectively. Another suggestion of variable water/rock ratio is the variable degree of recrystallization. Sample Br-19 contains relic calcic plagioclase, and Br-23 and Br-24 contain both pyroxene and plagioclase relics, whereas in most of the other samples there are no relic igneous minerals whatsoever.

Figure 3B-7. Outcrop photographs from the Ben Nevis area. a.) Relatively fresh blocks of massive andesite (light) are set in a matrix of thoroughly recrystallized fragmental andesite (dark). Sample Br-15 is from the matrix of this outcrop. b.) Amygdaloidal andesite (sample Br-13).

FRAGMENTAL ANDESITE

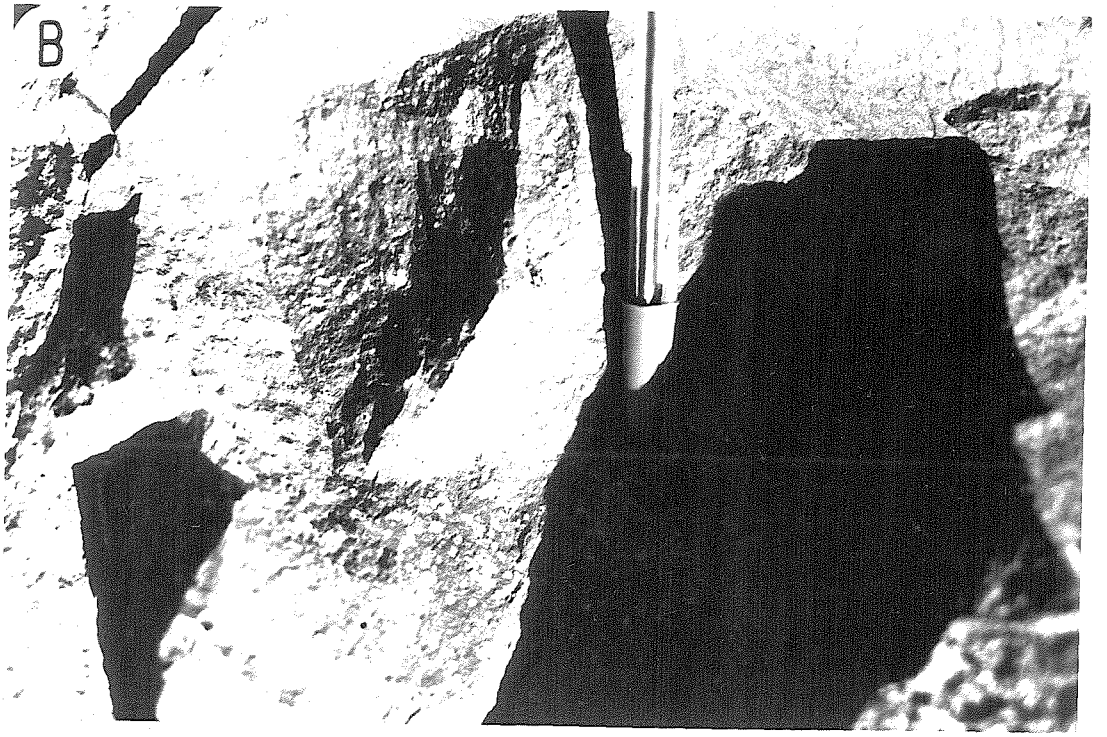

AMYGDULES

CHAPTER 3C. BENOIT SYNCLINE

I. GEOLOGY

The Benoit area lies near the western end of the Blake River Group near the town of Ramore. The Blake River synclinorium extends at least as far west as Benoit Twp., and the sample localities extend in a broad traverse north from the core of this syncline to the margins of the fold (Fig. 3B-1). Like the Ben Nevis traverse, therefore, the Benoit traverse samples a large portion of the volcanic stratigraphy. The Blake River Group is bounded in this area by a large batholith, the Watabeag batholith (Fig. 3B-1), which is apparently intrusive into the volcanics. The sampled traverse runs roughly parallel to the margin of this batholith, but separated by a distance of 5-10 miles.

The detailed geology of the Benoit area is not as well known as that of the Ben Nevis and Noranda areas. The area is part of the "great clay belt," and is covered by the glacial deposits of Pleistocene Lake Ojibway. Examination of the monadnocks and other outcrops indicates that the volcanic rocks in this area are characterized by a monotonous succession of pillowed or massive mafic lavas with pillowed or brecciated flow tops, and a lack of pyroclastic rocks, intercalated sediments and intermediate to felsic rocks (Jackson, 1980). There are several mafic intrusions, particularly in western Benoit Twp. and NE Black Twp., and several small granitic intrusions.

II. PETROLOGY

Like the Ben Nevis area, recrystallization in the Benoit area is characterized by both prehnite-pumpellyite and greenschist facies assemblages. As usual, tectonic deformation is minimal, and a variety of relic igneous textures are preserved. Spatially, the prehnite-

TABLE 3C-1. OXYGEN ISOTOPIC AND PETROGRAPHIC DATA FROM THE BENOIT AREA

Sample	$\delta^{18}O$ WR	$\delta^{18}O$ Min.	Microscopic Description: Texture	Ave. gr. size	Secondary Mineralogy	% Amyg.	% Veins	% Rec.	Location: Lat.	Location: Long.	Rock Type[1]	Struct. Height (km.)	Wt.% SiO_2[2]
ROCKS COLLECTED BY IAN SMITH													
S-2	6.9		equigr.	300	ep,act,chl,cc,qtz	0	0	60	43°21.0'	80°8.7'	basalt	9.9	50.4
S-9	9.2		equigr.	40	pr,qtz,chl,cc,ep	3	3	85	43°25.1'	80°14.2'	andesite	3.7	53.7
S-10	7.1		equigr.	700	act,chl,cc,ep,qtz	0	0	60	43°22.0'	80°12.5'	basalt	8.3	51.3
S-12	6.7		subophitic	300	qtz,serp,chl,musc	0	tr.	85	43°22.2'	80°12.5'	basalt	7.9	50.4
S-14	7.0		equigr.	20	pr,pu,qtz,cc,chl	tr.	0	40	43°22.3'	80°12.3'	basalt	7.9	49.9
S-15	7.5		equigr.	20	qtz,cc,pr?,chl	tr.	0	30	43°21.9'	80°11.2'	basalt	8.6	51.7
S-16	7.3		felted	100	qtz,cc,chl,pr	1	1	40	43°21.9'	80°11.1'	basalt	8.4	51.5
S-21	6.8		equigr.	20	pr,pu,cc,ep,chl,qtz	0	1	60	43°22.2'	80°11.0'	basalt	8.0	51.5
S-22	6.2		equigr.	50	qtz,cc,chl,pr	5	0	20	43°22.3'	80°11.1'	andesite	7.9	52.3
S-23	6.4		equigr.	300	qtz,ep,chl,cc	0	0	70	43°22.5'	80°11.2'	basalt	7.5	50.3
S-24	6.1		equ.-suboph.	200	chl,pu,pr,ep,cc,qtz	3	0	40	43°22.6'	80°11.3'	basalt	7.3	46.0
S-25	7.5		glomeroporph	10	chl,pu,pr,ep,cc,qtz	3	1	40	43°22.8'	80°11.1'	basalt	7.0	47.5
S-28	7.5		variolitic	80	pr,pu,ep,cc,qtz,chl	0	0	30	43°24.8'	80°14.0'	basalt	4.1	48.7
S-29	7.2		equigr.	100	qtz,chl,pr,pu,cc	tr.	tr.	60	43°24.6'	80°14.0'	basalt	4.3	48.2
S-33	8.1		micrographic	1000	qtz,chl,cc,pr,pu	0	3	20	43°23.2'	80°11.0'	basalt	6.4	51.5
S-35	7.2		porphyr.(qtz)	10	qtz,chl,ep,cc	0	3	50	43°23.6'	80°11.0'	basalt	5.8	47.0
S-37	6.6		equigr.	150	qtz,chl,pr,ep,cc	0	0	80	43°22.9'	80°10.6'	basalt	6.9	45.4
S-38	7.3		felted plag	10	qtz,cc,ep,chl	1	tr.	90	43°22.8'	80°10.8'	basalt	7.1	46.5
S-43	7.0								43°20.1'	80°12.5'		11.4	
S-47	8.2		equigr.	20	chl,cc,ep,qtz	0	0	85	43°25.2'	80°14.2'	basalt	3.4	51.3
S-55	8.2		equigr.	80	chl,cc,ep,qtz	1	tr.	70	43°25.9'	80°14.2'	basalt	2.3	50.3
S-56	8.2		equigr.	80	qtz,chl,pu,ep	0	1	70	43°25.8'	80°14.8'	andesite	2.0	55.4
S-58	8.2		equigr.	40	qtz,chl,cc,pu	0	tr.	80	43°25.4'	80°14.5'	basalt	2.8	51.5
S-59	8.5		equigr.	50	qtz,chl,cc,pr,ep	0	1	70	43°24.7'	80°13.3'	basalt	4.5	51.6
S-63	7.9		felted plag.	40	chl,cc,pr,pu,qtz	0	1	90	43°24.4'	80°13.1'	basalt	4.7	50.3
S-64	7.9		felted plag.	100	qtz,chl,cc,ep,pr	3	tr.	30	43°24.4'	80°13.1'	basalt	5.2	50.9
S-67	6.7		equigr.	200	qtz,chl,pr,ep	0	0	20	43°24.0'	80°13.0'	andesite	5.7	53.8
S-68	6.8		variolitic	40	qtz,chl,ep	1	0	50	43°23.8'	80°13.0'	basalt	5.9	49.7
S-69	6.8								43°23.8'	80°13.1'	andesite	6.0	54.5
S-70	7.1		equigr.	100	qtz,chl,cc,ep	0	tr.	40	43°23.7'	80°13.1'	andesite	6.1	52.0
S-78	7.7		equigr.	20	qtz,chl,cc,ep	1	tr.	50	43°22.0'	80°10.1'	andesite	8.3	55.4
S-79	7.0		variolitic	100	qtz,cc,ep,chl	0	5	40	43°22.2'	80°10.1'	basalt	8.0	50.4
S-81	7.1		equigr.	20	qtz,chl,ep,musc	0	1	70	43°22.4'	80°9.8'	basalt	7.8	49.3
S-83	9.0		equigr.	300	chl,cc,pr,qtz,ep	3	0		43°22.5'	80°9.7'	andesite	7.7	55.5
S-86	6.9		equigr.	40	qtz,chl,ep,pr?	1	tr.	30	43°22.1'	80°8.7'	basalt	8.1	51.6
S-87	6.8		equigr.	40	chl,qtz,act?	tr.	1	60	43°21.9'	80°8.9'	basalt	8.5	51.7
S-89	7.2		frag.	50	qtz,chl,cc,ep	0	4	95	43°18.4'	80°11.7'	basalt	8.9	50.3
S-90	6.4		felted	40	qtz,chl,cc,pr,ep	tr.	tr.	95	43°18.4'	80°11.7'	andesite	9.0	53.0
S-92	8.2		equigr.	10	qtz,chl,cc,ep,pr?	tr.	1	100	43°18.6'	80°11.7'	andesite	9.4	53.6
S-95	8.8		felted-porph.	40	qtz,cc,ep,musc				43°19.2'	80°11.8'	andesite	10.2	53.1
S-96		8.6(f)	porphy.(feld)						43°19.5'	80°10.9'		11.0	
S-99	9.0		equigr.	200	chl,cc,pr,pu,qtz	0	tr.	85	43°20.0'	80°11.1'	andesite	11.4	61.5
S-101	9.7		felted	40	chl,cc,pu,ep,act,qtz	tr.	tr.	95	43°20.5'	80°11.3'	andesite	11.4	63.7
S-102	8.2		glom.-porph.	20	qtz,cc,ep,pr,chl	0	5	50	43°20.9'	80°11.5'	andesite	10.2	56.1
S-104	8.2		felted	50	qtz,chl,ep	tr.	tr.	60	43°21.8'	80°14.6'	andesite	9.5	56.3
S-106	7.2		felted,porph.	10	qtz,cc,ep,chl	1		60	43°18.2'	80°8.9'	andesite	9.3	55.4
S-107	8.1		felted	20	qtz,cc,chl,ep	tr.	0	60	43°18.1'	80°8.9'	andesite	9.1	53.7
S-108	7.7		equigr.	30	qtz,chl,cc,ep	10	tr.	70	43°17.2'	80°8.1'	basalt	7.8	51.3
S-109	7.4		felted	80	qtz,chl,cc,ep	tr.	5	30	43°17.1'	80°8.4'	basalt	7.6	48.1
S-110	7.6		equigr.	40	qtz,chl,cc,ep	tr.	1	70	43°17.2'	80°8.5'	basalt	7.8	50.9
S-120	6.7		equigr.	300	qtz,chl,ep	0	1	70	43°26.6'	80°18.1'	(basalt)	3.9	
S-121	7.7								43°24.3'	80°18.8'		7.7	
S-122	8.5		variolitic	80	qtz,cc,ep,act,chl	0	tr.	100	43°22.8'	80°16.4'	(basalt)	9.0	
S-124	6.8		suborph.	500	chl,ep,act,musc,qtz	0	0	75	43°23.8'	80°18.7'	(basalt)	8.8	
S-125	6.1		felted	200	ep,act,qtz,chl	0	0	85	43°26.3'	80°22.0'	(basalt)	6.4	
S-126	6.8								43°28.4'	80°25.3'		4.0	
S-127	6.2		porphyr.	10	qtz,chl,ep,act	0	2	100	43°28.8'	80°26.5'	(basalt)	3.1	
S-128	6.2		frag.	200	qtz,ep,act,chl	0	0	100	43°28.4'	80°28.4'	(basalt)	3.9	
S-129	7.7		felted	20	qtz,chl,cc,ep,act	tr.	tr.	100	43°29.1'	80°25.2'	(basalt)	2.6	
LAVA FLOW MTN. (SAMPLED BY MICHAEL JACKSON)													
A2-4	7.3	5.9(p) 9.4(nm)	Equigr.	200	qtz,chl,ep,musc	tr.	0	60	43°25.5'	80°14'	(basalt)	~2.5	
A2-6	7.4		Ophitic	200	qtz,chl,ep,musc	3	1	60	43°25.5'	80°14'	(basalt)	~2.5	
A2-9	8.2	6.5(p) 9.8(nm)	Variolitic	150	qtz,chl,ep,pu,musc	0	0	60	43°25.5'	80°14'	(andesite)	~2.5	
B1-7	7.2	5.3(p) 9.8(nm)	Equigr.	600	qtz,chl,cc,ep,musc	0	tr.	60	43°25.5'	80°14'	(basalt)	~2.5	
D-5	9.1	10.2(nm)	Porphyr.	300	qtz,chl,cc,ep,musc	2	0	60	43°25.5'	80°14'	(basalt)	~2.5	

Abbreviations as in Table 3B-1.

[1]Defined from bulk chemistry (Williams et al. 1954). Basalt = 45-52 wt. % SiO_2, Andesite = 52-66%, Rhyolite = > 66%. Estimates from thin sections are in parentheses.

[2]Unpublished data from I.E.M. Smith.

pumpellyite facies samples tend to be located on the eastern side of the traverse (away from the Watabeag batholith) and towards the core of the syncline (see also Jolly, 1980). There also appears to be a large area with mixed assemblages, perhaps a reflection of variable P_{H_2O} or X_{CO_2}. In the lower portions of the volcanic pile (West of Lavaflow Mountain; Fig. 3B-1) greenschist facies rocks are exclusively present.

In thin section most of the analyzed rocks are fresher than those collected from the Ben Nevis area. The amount of recrystallization (Table 3C-1) is typically only 30-70%, whereas in Ben Nevis (Table 3B-1) recrystallization is in the range 80-100%. This difference probably reflects the more careful sampling procedure, and little significance is attached. The Benoit rocks were collected by Ian Smith and Michael Jackson as part of their trace element geochemical studies, and they were careful to collect only the freshest samples available. The author, on the other hand, tried to collect representative samples as well as examples of both the freshest and most altered rocks available. This bias in the sample must be considered when comparing these results to those from other areas.

Petrographically, most of the rocks show evidence that the plagioclase was much more unstable than the pyroxene in the alteration environment. Typically the plagioclase has been replaced by a fine-grained mat of secondary minerals, but the pyroxene shows only minor recrystallization to chlorite. The most abundant secondary minerals are chlorite, quartz and albite, which along with the other minerals listed in Table 3C-1 replace large portions of the groundmass. In addition, many of these rocks are amygdaloidal, and small veinlets are numerous; both features are typically occupied by quartz, chlorite and calcite. Commonly, the

mineral assemblage in the veins is different from that in the groundmass. For example, S-90 has prehnite in the groundmass and epidote in the veins. Because the abundance of amygdules may affect the whole-rock $\delta^{18}O$, and because the abundance of veins is clearly related to hydrothermal activity of some sort, both of these parameters are also listed in Table 3C-1.

III. OXYGEN ISOTOPIC DATA

The overall range of $\delta^{18}O$-values from the Benoit area is +6.1 to +9.7. This compares quite well with the total range of +5.4 to +10.3 in the Ben Nevis area to the east. The distribution of $\delta^{18}O$-values is somewhat different, however. Figure 3C-1 illustrates the variation of $\delta^{18}O$ with stratigraphic height in the Benoit area. Unlike Ben Nevis, there is not a simple, systematic upward increase in $\delta^{18}O$. To be sure, there is a suggestion of such a trend. From 5 to 7 km., $\delta^{18}O$ is typically in the range +6 to +7, from 7 to 9 km., $\delta^{18}O$ is typically +7 to +8, and above 9 km., $\delta^{18}O$ is typically +8 to +9 (Fig. 3C-1). Below 5 km., however, the $^{18}O/^{16}O$ distribution is less systematic. The samples from the western extension of the traverse (3 to 4 km. height) have low $\delta^{18}O$-values which are consistent with the above trend (+6 to +7). Lavaflow Mountain, however (2 to 3 km. height), has $\delta^{18}O$ ranging from +7.2 to +9.2 (Fig. 3C-1).

The oxygen isotopic gradient at the top of the pile, which can be seen on both limbs of the syncline, is similar to that described above for the Ben Nevis area. This suggests recrystallization under conditions of high water/rock ratio, with a temperature gradient imposed on the volcanic pile (see Chapter 3B).

In interpreting Figure 3C-1 (and the similar plots in other chapters), an extremely important question is posed: Were the oxygen isotopic

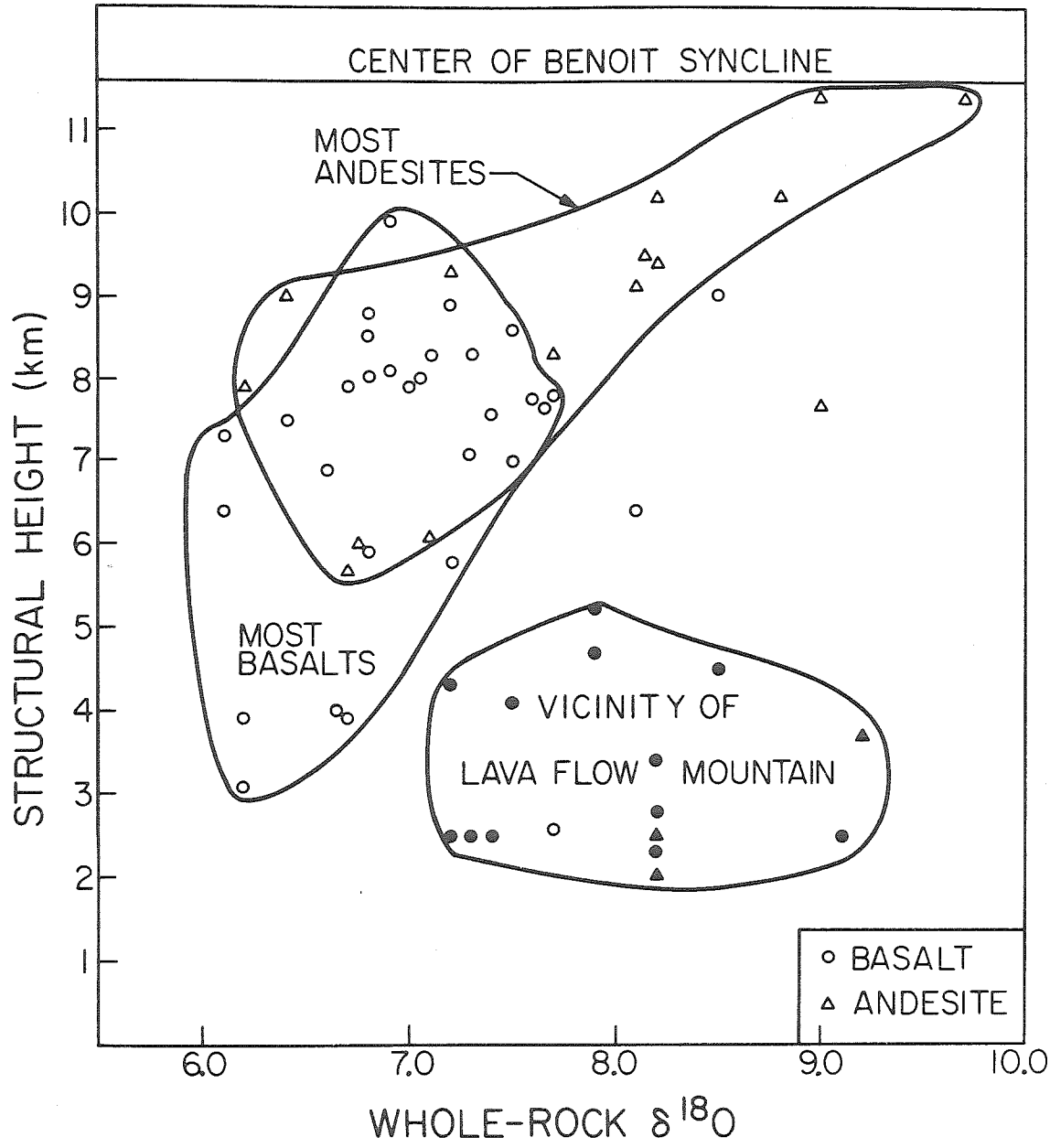

Figure 3C-1. Variation of $\delta^{18}O$ as a function of stratigraphic height for rocks in the Benoit syncline. Note that the fields delineated only indicate the positions of "most" basalts and "most" andesites (i.e. three basalts and one andesite are shown on the diagram but not included in the fields). Filled symbols are from near Lavaflow Mountain.

variations introduced during hydrothermal alteration, or was there an intrinsic $^{18}O/^{16}O$ variability in the igneous rocks? The Benoit samples provide an excellent framework for addressing this question for three reasons: 1. The availability of bulk chemical analyses (provided by I.E.M. Smith), 2. The variable and incomplete nature of the recrystallization, and 3. The presence of three different metamorphic assemblages. Thus, any given sample can be characterized by five parameters: $\delta^{18}O$, structural height, metamorphic assemblage, degree of alteration, and bulk composition. By studying the relationships among these five variables, it is possible to understand to some degree the physical processes which have affected the volcanic pile.

Figures 3C-1 and 3C-2 suggest that silica content, $\delta^{18}O$ and structural height are all positively correlated. Andesites (>52 wt. % SiO_2) are concentrated in the upper portions of the volcanic pile and tend to be richer in ^{18}O than the basalts. This could reflect original igneous oxygen isotopic zoning, because andesites are commonly richer in ^{18}O than basalts (Taylor, 1968). Note, however, that the andesites low in the section are lower-^{18}O, the andesites high in the section are higher-^{18}O, and likewise for the basalts. Thus the stratigraphic correlations in Figures 3C-1 and 3C-2 are not due to a simple upward change in primary igneous character. Although SiO_2-content and $\delta^{18}O$ are broadly correlated, at any given SiO_2 content the volcanic rocks display a broad variation in $\delta^{18}O$.

One of the effects of hydrothermal alteration can be silicification. Quartz amygdules, quartz veins and possible secondary quartz in the groundmass are all common features in these rocks. At the nearby Kidd Creek mine, hydrothermal alteration has enriched some of the rhyolites

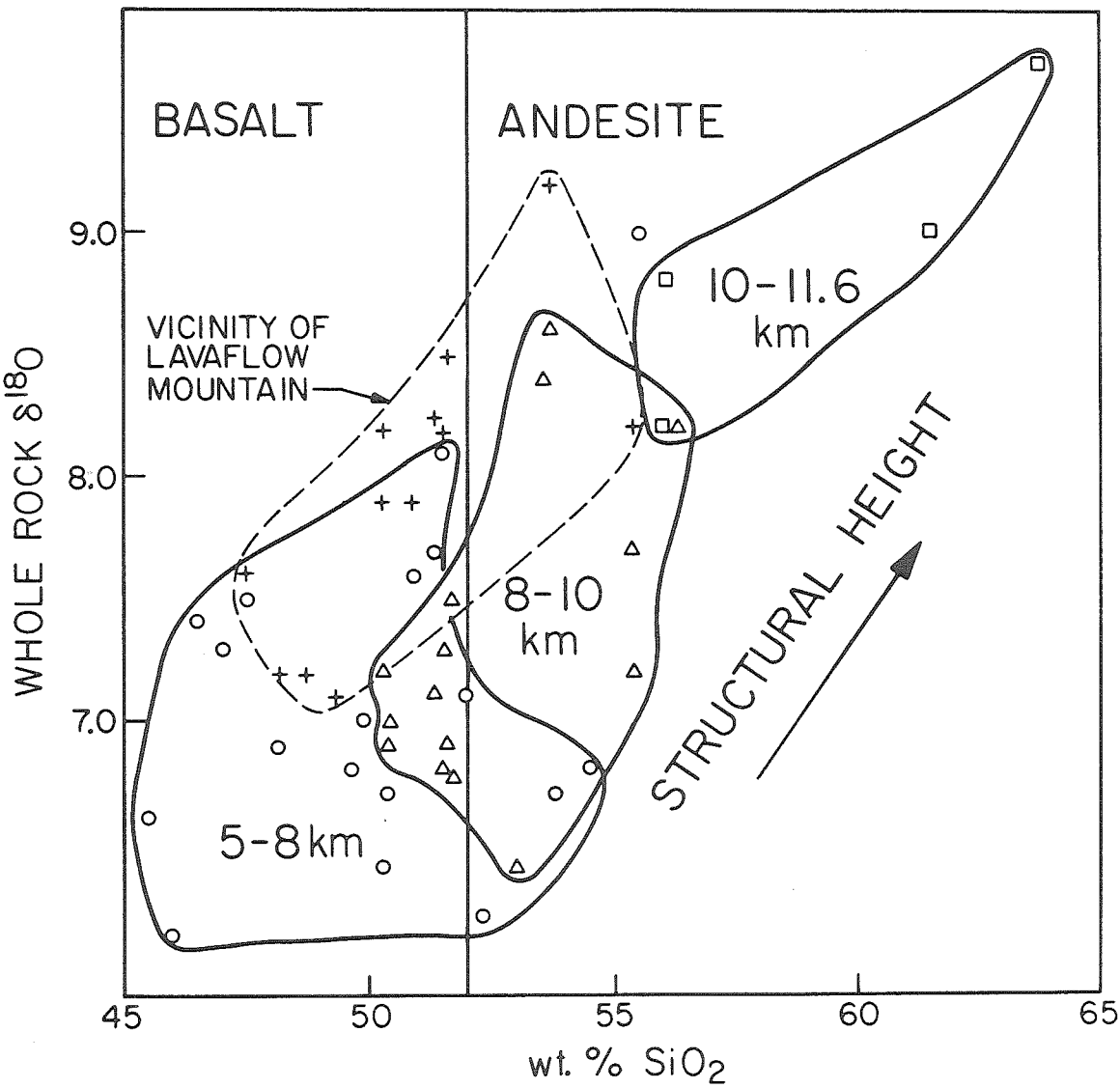

Figure 3C-2. Variation between whole-rock $\delta^{18}O$ and silica content. These two variables and structural height (shown with envelopes) are all positively correlated. The unpublished SiO_2 data are courtesy of Dr. I.E.M. Smith. The boundary between basalt and andesite (52% SiO_2) is taken from Williams et al. 1954, p. 27.

there to as much as 97 wt. % SiO_2 (Walker and Mannard, 1974). It is possible that the correlation of Figure 3C-2 is caused by this effect; possible increasing intensity of alteration in the upper parts of the pile may have produced higher degrees of silicification and a larger ^{18}O-shift. Figure 3C-3, however, suggests that this is not the case. The andesites (SiO_2-rich) are present both as petrographically fresh and as petrographically altered rocks, and likewise for the basalts (SiO_2-poor). The absence of a correlation on this diagram indicates that the SiO_2-contents of these rocks were not markedly affected by hydrothermal recrystallization. The SiO_2-content appears to be a relic igneous feature, and is therefore useful in distinguishing the basalts from the andesites.

By exchanging wt. % SiO_2 on Figure 3C-3 with $\delta^{18}O$ (Fig. 3C-4), the hydrothermal effects can be evaluated. Although SiO_2-content is not dependent of the degree of recrystallization (suggesting it is an igneous property), $\delta^{18}O$ definitely is (suggesting it is a hydrothermal property). On Figure 3C-4 fresh basalts plot at $\delta^{18}O = 5.7 \pm 0.2$, and 0% recrystallized. As such a fresh basalt sample is altered it will traverse across the figure with steadily increasing degree of recrystallization, either increasing or decreasing in $\delta^{18}O$, depending on the temperature. In general the trajectory will not be perfectly linear, because the minerals in the rock do not react at the same rates, and the growth of the secondary minerals (which have different $\delta^{18}O$) consequently also does not proceed at the same rate. To first approximation, however, at any given temperature the various stages of hydrothermal alteration of such a basalt lie on a mixing line between the completely altered and completely fresh endmembers. With a constant fluid composition, the

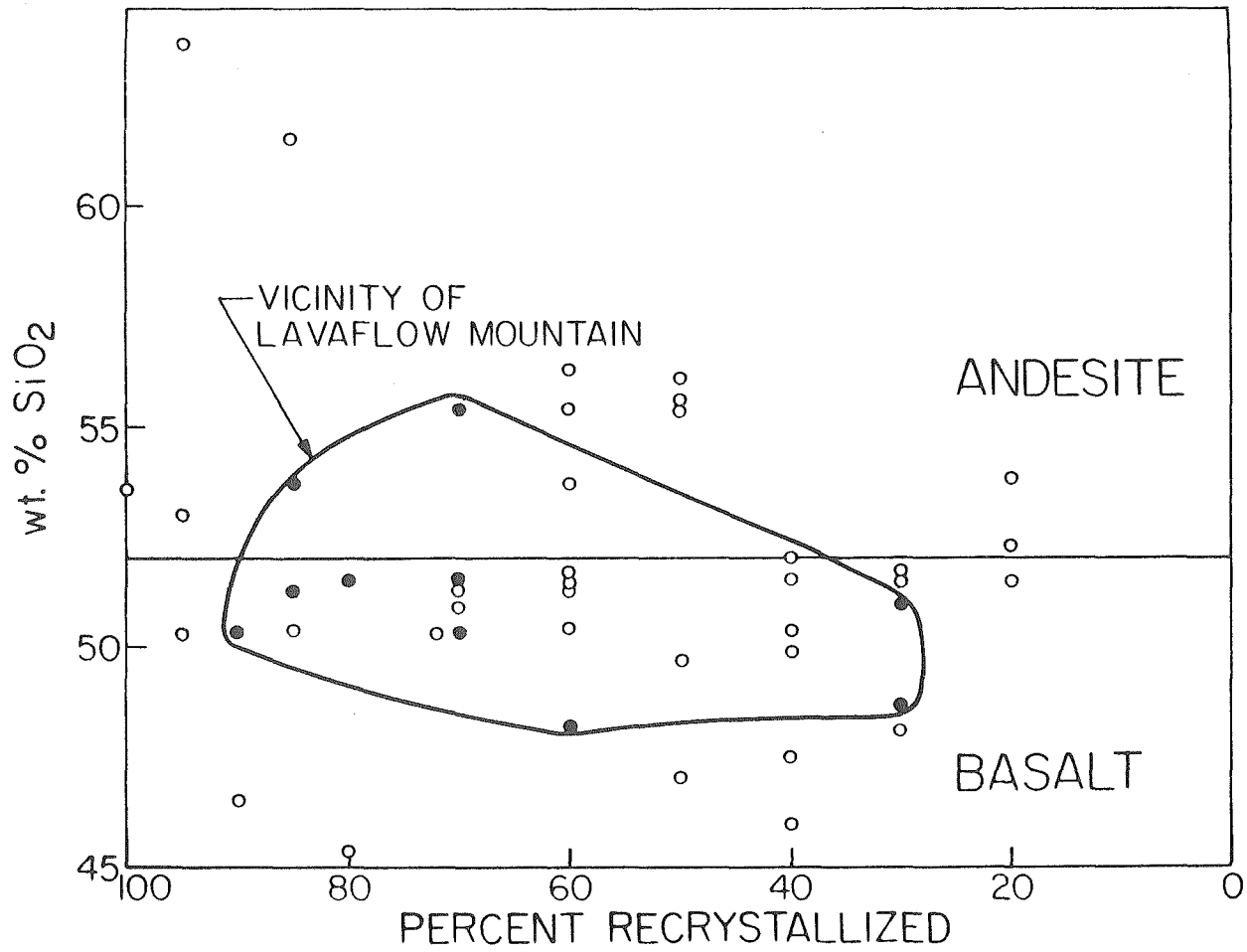

Figure 3C-3. Variation between silica content and the degree of recrystallization in the Benoit area. Both fresh and altered basalts are present, and likewise for the andesites. The lack of a correlation indicates that the high-SiO_2 rocks did not aquire that property through alteration, i.e. the silica content is an igneous feature.

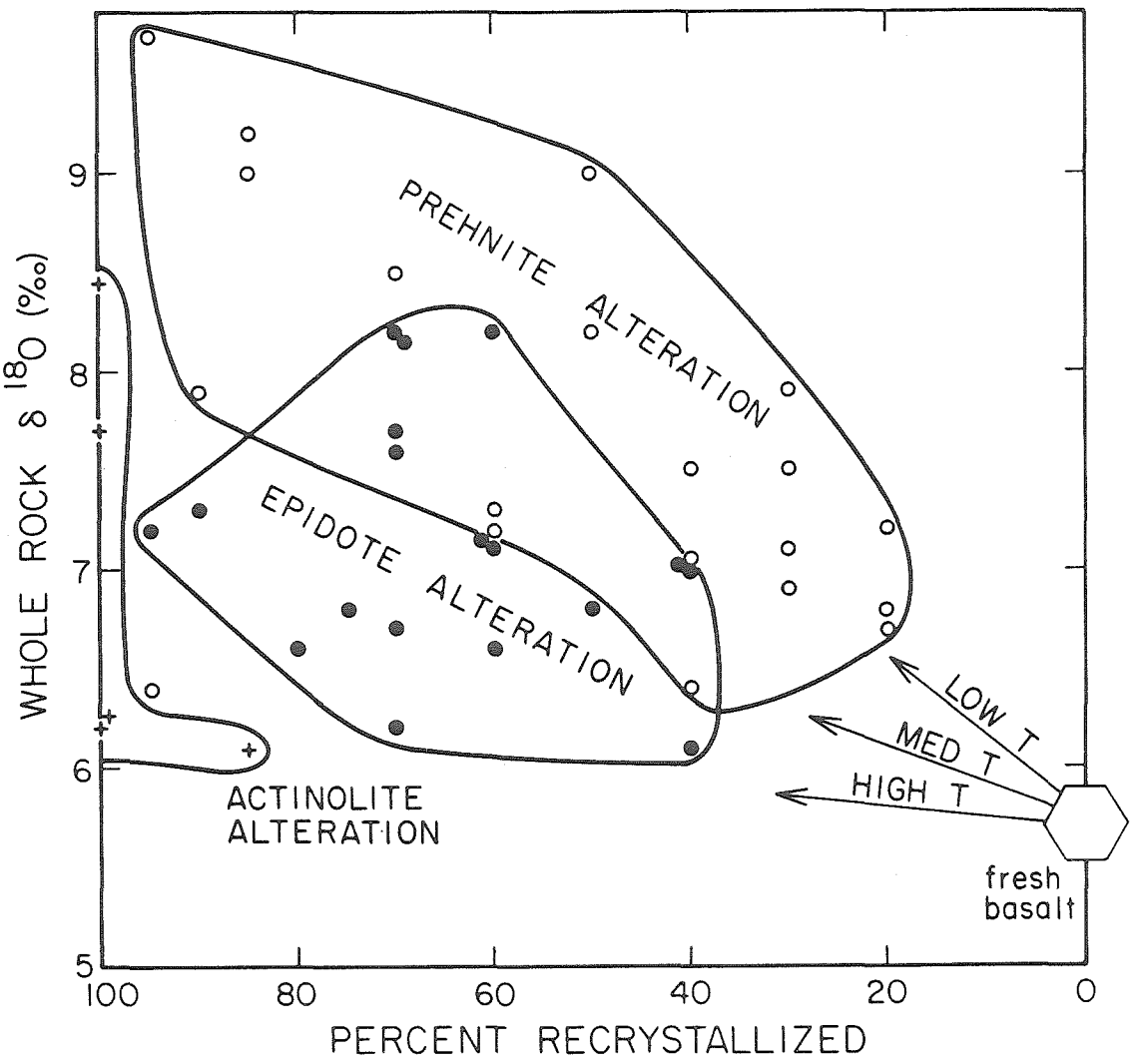

Figure 3C-4. Whole rock $\delta^{18}O$ as a function of the degree of recrystallization in the Benoit area. The three metamorphic assemblages each form an array which lies on a mixing line between fresh basalt and various hypothetical metabasalts. This indicates that the high $\delta^{18}O$ values were introduced during alteration.

lower the temperature, the higher the $\delta^{18}O$ of the altered endmember.

The Ben Nevis data form an array which follows the above theoretical considerations. The samples which contain prehnite (± pumpellyite) are the lowest-grade rocks in the area, and they lie on a mixing line between fresh basalt and a metabasalt with $\delta^{18}O = +10$ (Fig. 3C-4). The samples which contain epidote (± pumpellyite) but no prehnite lie on a mixing line which intersects the altered endmember at about +8 (Fig. 3C-4). The actinolite-bearing samples (i.e.the highest-grade rocks) locally indicate an endmember as low as +6 (Fig. 3C-4). Using these hypothetical 100% altered endmembers, the Benoit traverse compares quite favorably with the Ben Nevis area, where the analyzed samples are more altered. In each case the low-grade rocks occupy the highest structural position and have $\delta^{18}O \approx +10$, and the high-grade rocks in the lower levels have $\delta^{18}O \approx +6$.

It must be remembered that Figure 3C-4 was made possible by the sampling bias: The Benoit rocks were specifically selected by Smith and Jackson on the basis of their freshness. In none of the other areas studied is such a treatment possible. The variable degree of recrystallization also accounts for the horizontal spread on Figure 3C-1.

Figure 3C-4 indicates that the prehnite-bearing samples range to as low as 20% recrystallized, the epidote-grade samples to as low as 40% recrystallized, and the actinolite-bearing samples to as low as 80%. Thus with increasing grade, as might a priori be expected, the recrystallization becomes more severe. Note, however, that the data fields overlap one another, particularly the actinolite field. This may be related to progressive metamorphism but non-progressive water flux. It is possible that the high-^{18}O actinolite-bearing samples were originally altered

at a lower grade, producing the oxygen isotopic shifts, and then isochemically heated and recrystallized. Most of Lavaflow Mountain is in the epidote group on Figure 3C-4, but some of the rocks appear to contain prehnite. The Lavaflow Mountain samples are somewhat anomalous (see below) and are responsible for the high-^{18}O bump on the epidote field of Figure 3C-4.

The above arguments strongly indicate that the high-^{18}O characteristics of these rocks were introduced during hydrothermal alteration. There was apparently a general pre-alteration upward increase in SiO_2 in the volcanic pile, and probably a small increase in $\delta^{18}O$ (up to perhaps +7; Taylor, 1968), but most of the oxygen isotopic distribution is apparently a result of hydrothermal alteration. As a test of this hypothesis, four of the coarsest grained samples from Lavaflow Mountain (Fig. 3B-1) were selected for mineral separation. In each case the pyroxene is petrographically fresh, whereas the plagioclase is mineralogically completely altered. Using a magnetic separator it was possible to isolate the pyroxene in three of these rocks, and it was possible to separate what used to be plagioclase (but is now predominantly a mixture of quartz, albite and muscovite) in all of them. The pyroxene separates have $\delta^{18}O$-values of +5.3, +5.9 and +6.5, and the non-magnetic separates (formerly plagioclase) have $\delta^{18}O$ = +9.4, +9.8, +9.8 and +10.2 (Table 3C-1).

There is an inverse correlation between pyroxene grain size and $\delta^{18}O$. In B1-7 (pyx = +5.3) the pyroxene is present as very large (1000 microns), equant crystals, in A2-4 (pyx = +5.9) they are smaller (300 microns), and in A2-9 (pyx = +6.5) they are narrow prisms averaging only 80 microns wide. This observation suggests that the original pyroxene in these rocks in fact had $\delta^{18}O$ not far from +5.5, the value found in modern fresh basalts. The finer-grained pyroxenes have apparently undergone

subsolidus hydrothermal exchange, becoming richer in ^{18}O. A critical conclusion to be drawn from this discussion is that these rocks were not erupted as high-^{18}O lavas; the relic igneous pyroxenes have 'normal' igneous $\delta^{18}O$-values.

Using the relic pyroxene data, the plagioclase in these rocks must have had $\delta^{18}O$ close to +6.0 prior to alteration (Anderson et al. 1971). The pseudomorphs after plagioclase presently have $\delta^{18}O$ of about +10. This ^{18}O-enrichment is much too large to be explained by mineralogic effects. Quartz and albite, two of the secondary minerals, do have a slightly greater tendency to concentrate ^{18}O than calcic plagioclase. Muscovite, however, has a reduced affinity for ^{18}O, and in chlorite it is much reduced. The plagioclase pseudomorph has been about 4 per mil enriched in ^{18}O relative to its original magmatic value. Although, the plagioclase has gained ^{18}O through subsolidus hydrothermal recrystallization, the pyroxene, in general, has not. The pyroxene data, thus, clearly indicate that these rocks were not originally high in ^{18}O; the high $\delta^{18}O$-values at Lavaflow Mountain (and thus presumably those elsewhere in the volcanic pile as well) must have been caused by hydrothermal alteration.

The relatively ^{18}O-rich rocks at Lavaflow Mountain (Fig. 3C-1) are difficult to interpret. Three of the parameters that govern the isotopic exchange could have been different here: 1. Higher water/rock ratio, 2. Lower temperature, 3. Higher-^{18}O fluid. The possibility that the water/rock ratio was higher seems unlikely in light of the fact that W/R in the rest of the pile was apparently high; this could be a factor only if the water/ rock ratios at the other localities were very low (<1). The possibility that the temperature was lower also seems

difficult to reconcile with the fact that Lavaflow Mountain occupies the lowermost stratigraphic levels (Fig. 3B-1). Nevertheless, it is conceivable that this area was altered either before or after the rest of the volcanic section, but at a lower temperature. The final possibility, that the fluid was more ^{18}O-rich, is difficult to evaluate but cannot be eliminated. There is a variety of mechanisms whereby a fluid can be enriched in ^{18}O (see Chapter 4B for a complete discussion), any of which could have been operative in this area. The pattern on Figure 3C-1, therefore, is taken to indicate that the hydrothermal processes in the Lavaflow Mountain area were complex in some unidentified way. It is possible, for example, that Lavaflow Mountain was at one time altered at relatively low temperatures at the top of the underlying volcanic pile during a quiescent period in the volcanism. Alternatively, it may have been affected by subsequent geologic processes, such as the emplacement of the nearby Watabeag batholith.

Additional evidence that the Benoit rocks are hydrothermally altered comes from the strontium isotopic data (unpub. data courtesy of J.L. Wooden). Pyroxene and plagioclase separates have been analyzed for $^{87}Sr/^{86}Sr$ in six of the Benoit samples, and using the measured Rb and Sr concentrations and an assumed age of 2.7 b.y., the initial $^{87}Sr/^{86}Sr$ ratios have been calculated (J.L. Wooden, written comm., 1979). Three observations suggest hydrothermal exchange: 1. The initial $^{87}Sr/^{86}Sr$ ratios in pyroxene range from 0.70109 to 0.70202. If these lavas were all produced in the same source region then they should have been erupted with the same initial Sr isotope ratios. Furthermore, plagioclase averages 0.0007 less than the coexisting pyroxene (Fig. 3C-5). These $^{87}Sr/^{86}Sr$ ratios cannot all be primary; they must have been spread out by an event subsequent to the

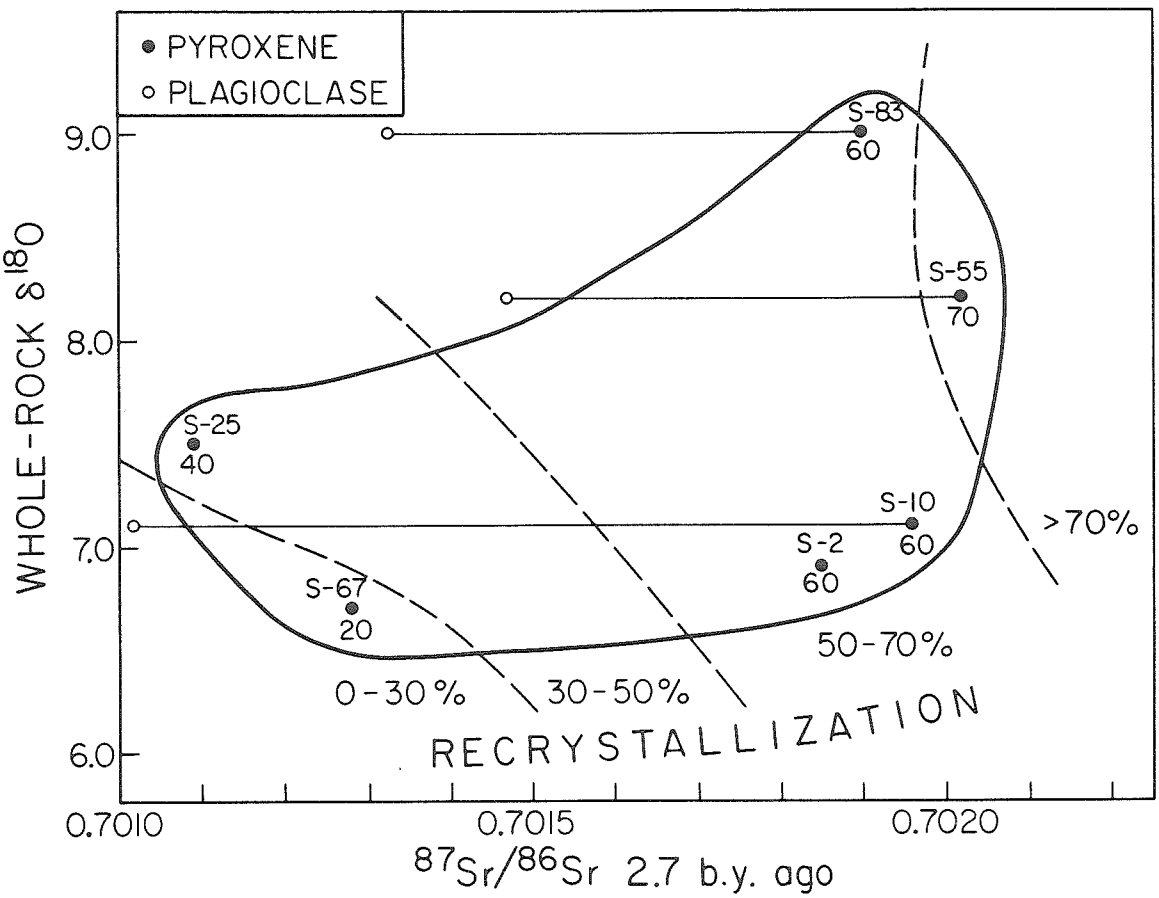

Figure 3C-5. Variation of initial $^{87}Sr/^{86}Sr$ and $\delta^{18}O$ in the Benoit area. The sample numbers and the percentage of recrystallization are shown for each point. The unpublished Sr data are courtesy of J.L. Wooden.

igneous history. 2. The initial $^{87}Sr/^{86}Sr$ ratios show a broad, positive correlation with $\delta^{18}O$ for both pyroxene and plagioclase (Fig. 3C-5). 3. The degree of petrographic recrystallization steadily increases with increasing $^{87}Sr/^{86}Sr$ (Fig. 3C-5). These three observations indicate that the high-$^{87}Sr/^{86}Sr$ rocks are the most altered, and the low-$^{87}Sr/^{86}Sr$ rocks are the least altered. Pyroxene may be most affected because it contains much less Sr than the coexisting plagioclase.

Similar results have been reported for the subseafloor hydrothermal alteration of the Samail ophiolite (McCulloch et al. 1980). Cretaceous seawater ($^{87}Sr/^{86}Sr$ = 0.7076) reacted with the oceanic crust ($^{87}Sr/^{86}Sr$ = 0.7030) to produce hydrothermally altered rocks with $^{87}Sr/^{86}Sr$ as high as 0.7053. Modelling the same process in the Archean is fraught with uncertainties, but assuming the lavas (160 ppm Sr) were erupted with $^{87}Sr/^{86}Sr$ = 0.7010 (the lowest observed value) and that Archan seawater (8 ppm Sr) had $^{87}Sr/^{86}Sr$ of 0.7025 (see Faure, 1977; p. 128-132), then the water/rock ratio during hydrothermal exchange (McCulloch et al. 1980; Eq. 1) must have been about 40. Many of the above values are, of course, subject to extensive revision, but the principal conclusions are the same as for the oxygen isotopic data; the volcanic pile has been thoroughly altered under conditions of high water/rock ratio, and Archean seawater is a viable source for the hydrothermal fluid.

IV. FLUID COMPOSITION

As discussed above, the hydrothermal processes in the Benoit area were not simple, so the hydrothermal fluid cannot adequately be modelled with a single calculation. However, to first approximation, Figure 3C-4 indicates that the oxygen isotope distribution closely resembles that of the Ben Nevis area. For the purpose of calculating $\delta^{18}O$ of the fluid,

therefore, Figures 3B-5 a,b,c also apply to the Benoit area. The initial fluid which entered the volcanic pile apparently had $\delta^{18}O = 0 \pm 2$, assuming a relatively high water/rock ratio.

CHAPTER 3D. NORANDA AREA

The Noranda area first achieved prominence in 1920, when Ed Horne discovered ore on the shores of Lake Osisko. Since then, the Noranda mining camp has proved to be one of the world's largest ore districts, and consequently has stimulated a considerable amount of interest in the local geology. Numerous researchers have published geological information, but the following discussion is drawn from three recent summary papers: Goodwin (1977), Spence and de Rosen-Spence (1975) and Gelinas et al. (1977).

I. GEOLOGY

The area shown on Figure 3D-1 encompasses two major geological provinces, bounded by the Destor-Porcupine fault zone. South of that fault lies the Blake River Group. The town of Noranda lies at the eastern end of the east-trending Blake River synclinorium, and hence occupies the highest stratigraphic position within that pile. Smaller scale structural features include a major, broad, easterly plunging anticlinorium a few kilometers north of Noranda flanked by tighter synclines to the north and south. Relatively flat dips prevail in the anticlinorium. Two major granitic bodies intrude the volcanic rocks and lie along the axis of the anticlinorium. The Flavrian Lake granite, and its faulted extension, the Powell granite, conform on their eastern contacts to the lavas. The Lake Dufault granodiorite (Fig. 3D-1) is a composite crosscutting body, and on the western end a contact aureole characterized by the presence of biotite extends about one mile into the county rocks. Dioritic dikes cut and commonly offset the volcanic rocks, and are in turn cut by the Lake Dufault granodiorite. Numerous other intrusions, some of which are synvolcanic, of basic, intermediate or acid composition, are widespread.

TABLE 3D-1. OXYGEN ISOTOPIC AND PETROGRAPHIC DATA FROM THE NORANDA, QUE. AREA

Sample	Field Description	$\delta^{18}O$ WR	$\delta^{18}O$ Min	Microscopic Description: Texture	Ave. gr. size	Secondary Mineralogy	% Rec.	Location: Lat.	Long.
Qe-1	Spinifex-textured komatiite, La Motte Twp.	4.5			80	Serp, chl, trem, mgt	100	48°21.7'	78°7.7'
Qe-3	Variolitic tholeiitic pillow basalt	11.0		Equigranular	20	chl, cc, qtz, ep, act	100	48°12.0'	78°57.3'
Qe-8	Qtz. pods in msv. pyrite, MacDonald mine		10.0(q)					48°18.8'	78°57.7'
Qe-16	Feldspar porphyritic rhyolite	6.3		Porphyritic	10	act, qtz, ep, chl, musc	100	48°18.8'	78°57.7'
Qe-20	Qtz. vein in Lake Dufault granodiorite		10.8(q)					48°18.9'	78°57.2'
Qe-22	Metaandesite near Lake Dufault	6.1		Equigr.-granophyric	300	chl, ep, cc, qtz, musc	90	48°16.6'	78°58.3'
Qe-23	Metadacite near Lake Dufault	9.8		Foliated-inhomogeneous	40	musc, cc, qtz, chl	100	48°16.5'	78°58.8'
Qe-24	Metarhyolite near Lake Dufault	9.2		Porphyritic (qtz)	10	musc, qtz, chl, cc	90	48°16.4'	79°59.3'
Qe-41	Qtz. vein from Rouyn ski hill		10.4(q)					48°14.0'	79°0.3'
Qe-46	Matrix of mill breccia, Rouyn ski hill	9.0						48°14.0'	79°0.3'
Qe-48	Fine gr. rhy. tuff, Rouyn ski hill	10.3		Foliated, fragmental	20	chl, ep, cc, act, qtz	100	48°14.0'	79°0.4'
Qe-49	Qtz. vein, Rouyn ski hill		11.9(q)					48°14.0'	79°0.4'
Qe-51	Qtz. vein, Rouyn ski hill		11.1(q)					48°14.0'	79°0.4'
Qe-52	Pillowed andesite near Amulet "A"	6.6		Poikiloblastic	100	hbd, qtz, biot, musc	100	48°18.6'	79°2.8'
Qe-53	Massive andesite near Amulet "A"	5.2	7.9(q)					48°18.6'	79°3.3'
			5.2(a)						
Qe-54	Massive, brittle andesite, near Amulet "A"	6.7						48°18.5'	79°3.6'
Qe-56	Massive andesite, near Amulet "A"	5.5		Variolitic	50	qtz, chl, ep, cc, act	100	48°18.4'	79°4.2'
Qe-57	Massive andesite, near Amulet "A"	5.6		Felted, porph.	100	chl, ep, act, qtz, musc	80	48°18.3'	79°4.5'
Qe-58	Massive brittle andesite	6.5		Felted	80	ep, chl, qt, act, cc	100	48°18.1'	79°3.8'
Qe-59	Massive andesite, near Millenbach	5.9		Felted	40	qtz, act, chl, ep	95	48°17.9'	79°3.5'
Qe-62	Massive brittle andesite, near Millenbach	5.9		Equigranular	50	chl, act, qtz, ep	100	48°17.9'	79°3.5'
Qe-65	Massive andesite, near Lake Dufault	4.9		Equigranular	200	hbd, qtz, chl, ep, biot	100	48°18.0'	79°2.7'
Qe-68	Massive andesite, shore of Lake Dufault	6.1		Equigr.-granophyric	400	chl, ep, act, cc, qtz	90	48°18.3'	79°2.7'
Qe-70	Massive andesite, Highway 101	8.3		Foliated	100	chl, cc, qtz, act, musc	70	48°17.4'	79°2.3'
Qe-75	Fragmental rhyolite, shore of Lake Dufault	10.5		Equigranular	10	chl, act, cc, musc	100	48°17.1'	79°0.7'
Qe-77	Massive brittle andesite	5.6		Equigranular	50	chl, act, qtz, musc, cc	100	48°16.3'	79°2.6'
Qe-78	Qtz. porph. rhyolite, N. of smelter	8.0	9.6(q)	Porphyritic	50	chl, qtz, cc, musc, ep	90	48°16.0'	79°1.2'
Qe-81	Aphanitic rhyolite, N. of smelter	7.6		Equigranular	10	chl, qtz, musc, cc	100	48°16.0'	79°0.1'
Qe-82	Lake Dufault granodiorite	6.4						48°20.4'	79°1.7'
Qe-84	Metabasalt, 10' from granodiorite contact	7.1		Porphyroblastic (biot.)	100	biot, act, qtz, ep, cc	100	48°20.4'	79°1.7'
Qe-88	Metabasalt near Renault	8.6		Equigranular	50	chl, cc, qtz, act	100	48°25.2'	79°4.0'
Qe-95	Porphyritic andesite, 20' from gran. contact	4.8		Equigranular	120	chl, act, ep, qtz	100	48°33.4'	79°2.3'
Qe-97	Metabasalt near Macamic	5.5		Equigranular	100	act, chl, qtz, ep, cc	100	48°43.8'	79°0.1'
#7598	QFP unit (rhyolite), Millenbach mine	7.4	7.6(q)					48°18.1'	79°3.2'

Abbreviations as in table 3B-1.

Figure 3D-1. Geologic map of the Noranda, Quebec area. Superimposed on the geology are the sample localities, the isograd boundary between prehnite-pumpellyite and greenschist facies rocks, and contours of the whole-rock $\delta^{18}O$ data. Much of the sampling is in the vicinity of the Amulet mine, which was investigated in detail (Chapter 4C).

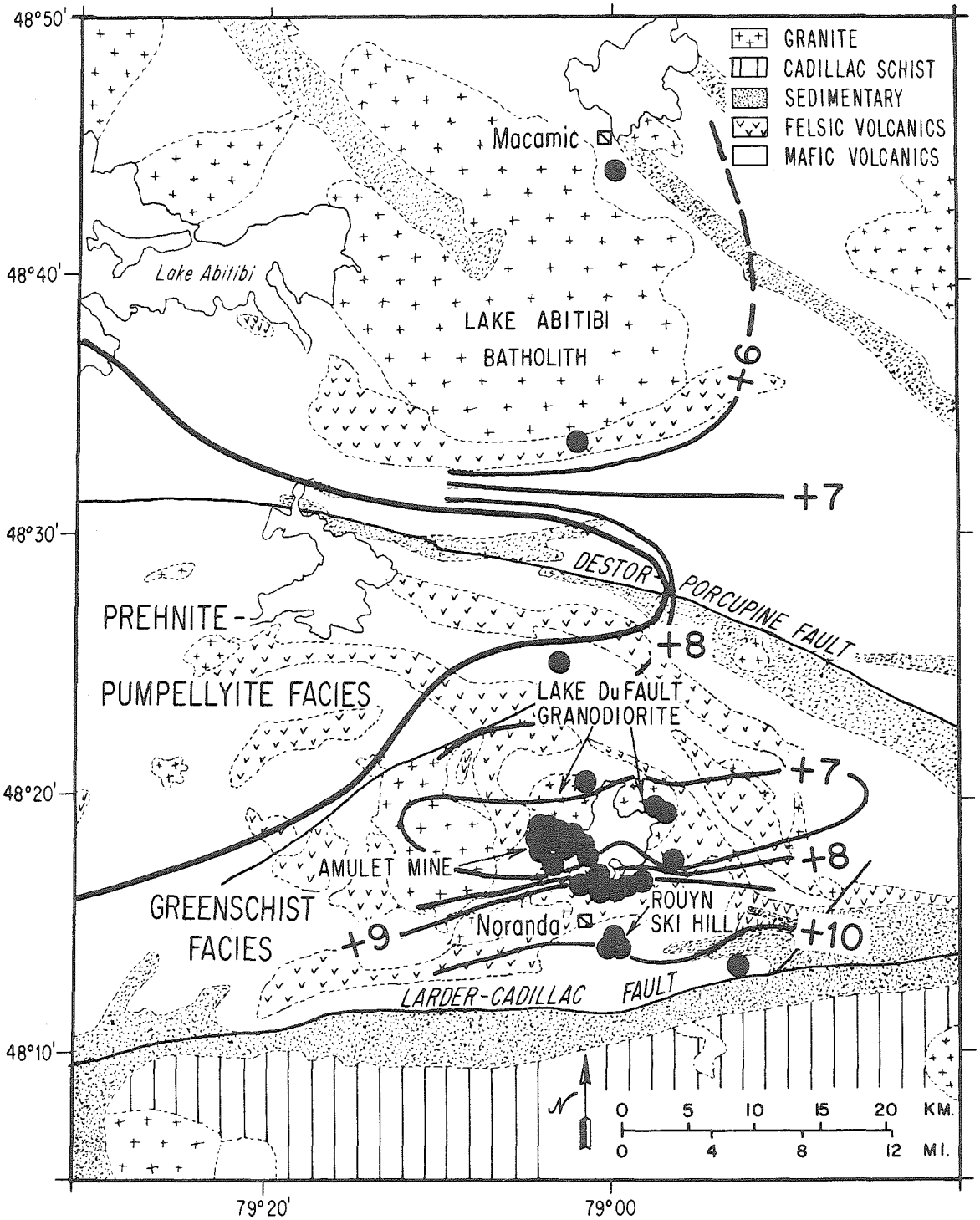
48°50'
48°40'
48°30'
48°20'
48°10'
79°20'
79°00
GRANITE
CADILLAC SCHIST
SEDIMENTARY
FELSIC VOLCANICS
MAFIC VOLCANICS
Macamic
Lake Abitibi
LAKE ABITIBI
BATHOLITH
+6
+7
DESTOR
PORCUPINE FAULT
PREHNITE-
PUMPELLYITE FACIES
+8
LAKE Du FAULT
GRANODIORITE
+7
+8
AMULET MINE
GREENSCHIST
FACIES
+9
Noranda
ROUYN
SKI HILL
+10
LARDER-CADILLAC FAULT
N
0 5 10 15 20 KM.
0 4 8 12 MI.

North of the Destor-Porcupine fault the geology is less well understood, due in large part to the poor outcrop. The granitic rocks in the NW portion of Figure 3D-1 are part of the Lake Abitibi batholith, one of the large Kenoran granitic bodies. The volcanic rocks which it intrudes are generally eastward-striking, vertically dipping and predominantly mafic, and are thought (Jensen, 1979b) to be the stratigraphic equivalent of the lower parts of the Blake River Group.

II. PETROLOGY

As in the Ben Nevis and Benoit areas, the Noranda area is characterized by both prehnite-pumpellyite and greenschist facies assemblages. The prehnite-pumpellyite rocks were first described by Gelinas and Brooks (1974), and the isograd boundary then was mapped by Jolly (1980). This boundary is shown on Figure 3D-1, which shows that none of the rocks examined in this study from this area are from the prehnite-pumpellyite zone. With the exception of a few amphibolite facies samples from near the Lake Dufault granodiorite, the analyzed samples from the Noranda area are all in the greenschist facies. Recrystallization is rather thorough within this area, ranging from 70-100% (Table 3D-1), and in a majority of the rocks no relic igneous minerals remain. The most common relic igneous mineral is the quartz (phenocrysts) in some of the rhyolites. Original igneous textures in the volcanic rocks are very well preserved, however, both on the outcrop (Fig. 3D-2) and in thin section.

III. OXYGEN ISOTOPIC DATA

Whole-rock $\delta^{18}O$-values from the Noranda area range from +4.9 to +11.0 (Table 3D-1). Not included within this spread are the analyses of the dalmatianite pipe at the Amulet "A" mine (discussed in Chapter 4C) and a spinifex-textured komatiite from LaMotte Township (discussed in

Figure 3D-2. Outcrop photographs from the Noranda area.

a.) Well developed pillow lavas SE of Noranda (Qe-3).

b.) Coarse rhyolite breccia from the Rouyn ski hill. Sample Qe-46 is from the matrix of this outcrop.

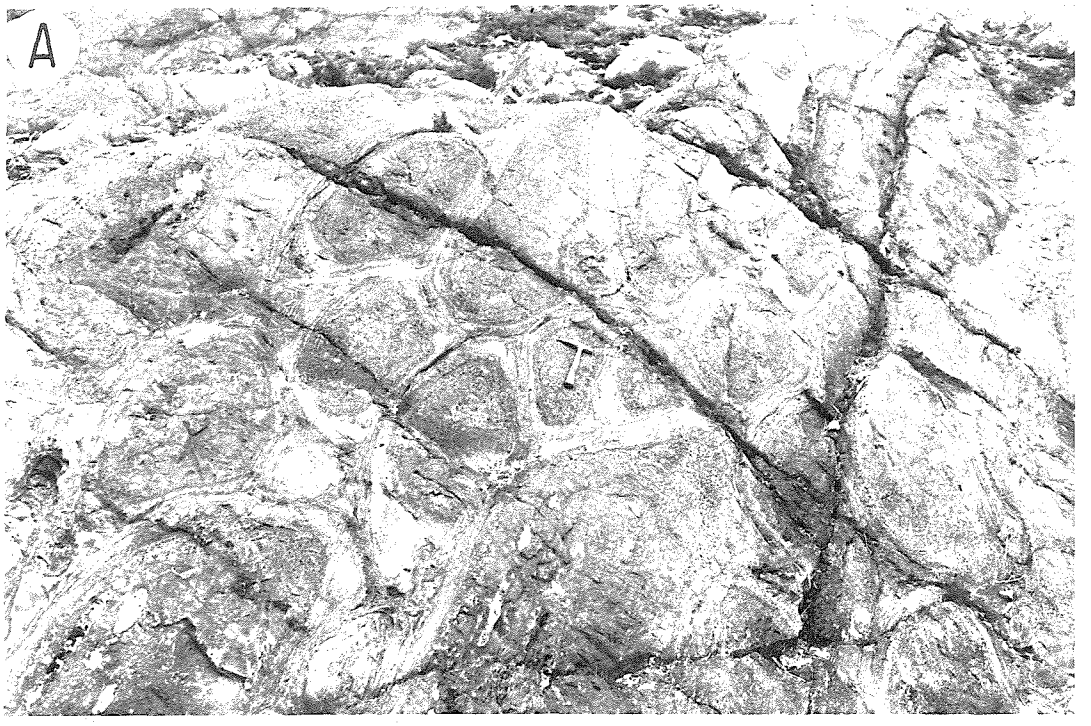

PILLOW BASALT

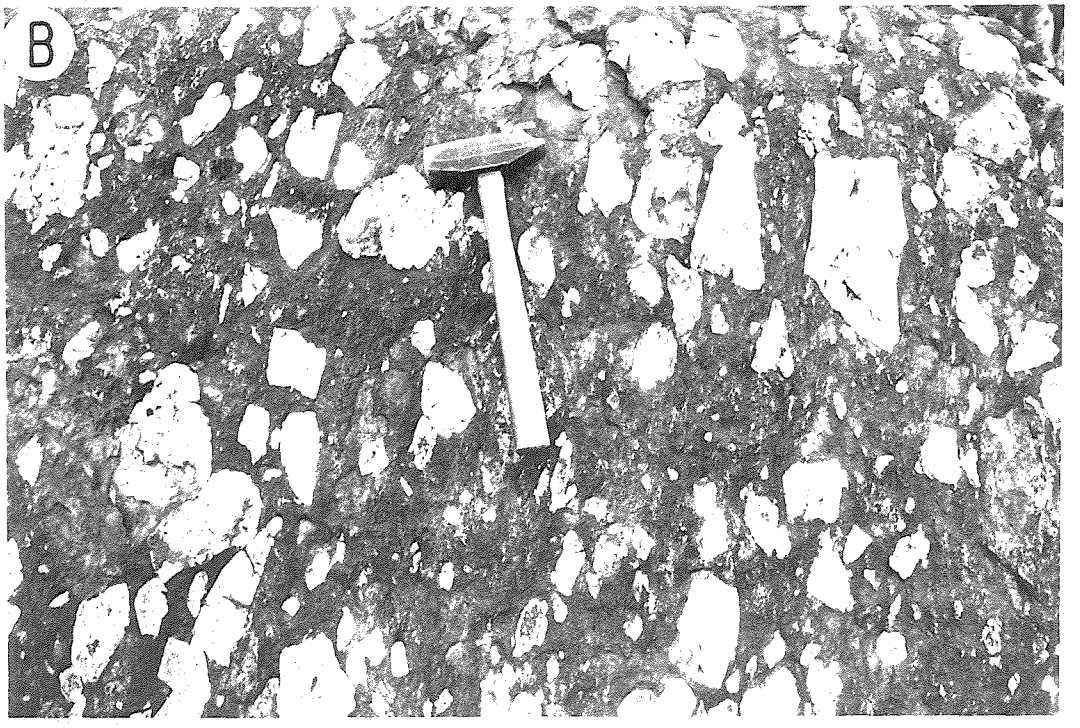

RHYOLITE BRECCIA

Chapter 3F). A variety of lithologies are present within the analyzed samples, ranging from basalt to rhyolite, so care must be exercised in comparing the data.

The general spatial distribution of $\delta^{18}O$ is shown in Figure 3D-1 by the use of contours. There is a low-^{18}O region around the Lake Dufault granodiorite, and particularly between the Lake Dufault and Powell plutons. Within this area, typical $\delta^{18}O$-values are +5 to +6 for the andesites and basalts, and +7 for the rhyolites. To the south $\delta^{18}O$ steadily increases towards the Larder-Cadillac fault, reaching values as high as +11 in the pillow basalt shown in Figure 3D-2. North of the Lake Dufault granodiorite $\delta^{18}O$ also increases, reaching a maximum of +9 near the axis of the Blake River synclinorium. North of that, $\delta^{18}O$ decreases towards the margin of the Lake Abitibi batholith, where values of 4.8 and 5.5 were measured (Fig. 3D-1).

The analyzed samples lie along a long, N-S trending traverse, which samples the stratigraphic section in three different places. From the Lake Dufault granodiorite, which occupies the core of an anticline, structural height increases both to the north and south into the flanking synclines. The syncline to the north is in turn bounded on the north by the domal Lake Abitibi batholith, and the stratigraphic section is again exposed between them (along with the Destor-Porcupine fault). In each of these three stratigraphic sections there is a gradient in $\delta^{18}O$, and in each case there is a positive correlation between $\delta^{18}O$ and structural height. $\delta^{18}O$ in the lower parts of the pile are +5 to +6, and are +9 to +11 in the upper parts. Thus, the oxygen isotopic structure of the Noranda area is essentially indistinguishable from that of the Ben Nevis and Benoit areas. Because of the structural complexities it is not

possible to plot $\delta^{18}O$ against stratigraphic height as in the Ben Nevis area, but all of the available data indicate that the oxygen isotopic profile is similar.

In contrast to the Benoit area, some of the rocks in the Noranda area have apparently been depleted in ^{18}O. In particular, some of the rocks adjacent to both the Lake Abitibi batholith and the Lake Dufault granodioite have $\delta^{18}O$-values as low as 4.8. This indicates that some of the water/rock interactions in this area took place at higher temperatures than in the Ben Nevis and Benoit areas. Whether these high temperature interactions accompanied the intrusion of the granitic bodies they are presently adjacent to or represent a high-temperature portion of the prehnitepumpellyite burial event is difficult to evaluate. The low-$\delta^{18}O$ values do not have an obvious systematic relationship to the granites. For example, Qe-65 ($\delta^{18}O$ = +4.9) is separated from the Lake Dufault granodiorite by Qe-68 ($\delta^{18}O$ = +6.1), although both rocks are andesitic. Clearly, additional sampling and field work are necessary to understand the origin and significance of these ^{18}O-depletions.

IV. FLUID COMPOSITION

The oxygen isotopic structure of the Noranda area is so similar to that of the Ben Nevis area that the exchange process is assumed to be similar. Thus the calculated hydrothermal fluids are given by Figures 3B-4 and 3B-5 a,b,c, and the initial fluid was apparently in the range $\delta^{18}O = 0 \pm 2$. Using this value, $\delta^{18}O$ of the groundmass quartz in Qe-78 (+9.6), indicates an alteration temperature for that sample of 210-300°C (Friedman and O'Neil, 1977). Likewise, if the quartz veins (+10 to +12, Table 3D-1) formed from the same fluid, the temperature of deposition would have been in the range 180-280°C. These temperatures

are within the general range of temperatures believed to be applicable during prehnite-pumpellyite facies metamorphism. Detailed study of the alteration zone at the Amulet "A" mine indicates that those rocks were also altered by the same or a similar fluid with $\delta^{18}O = 0.5 \pm 1.0$ (Chapter 4C).

Mineral separates were obtained from Qe-53, an amphibolite from the metamorphic aureole of the Lake Dufault granodiorite. Hornblende has $\delta^{18}O = +5.2$ and quartz (separated magnetically and then purified with HF) has $\delta^{18}O = +7.9$ (Table 3D-1). Using the fractionation factors given by Friedman and O'Neil (1977), these two values indicate a temperature in excess of 800°C, hence they are not in equilibrium. Using a more realistic temperature of 500°C, the amphibole would be in equilibrium with a fluid of $\delta^{18}O = +7.4$. This is consistent with either magmatic water or (more likely) with a metamorphic fluid that could have evolved from seawater through high-temperature, low-water/rock ratio, oxygen isotope exchange with the rocks.

CHAPTER 3E. SKEAD VOLCANICS

I. GEOLOGY

The Skead volcanics are an accumulation of volcanic rocks on the eastern margin of the Round Lake batholith (Fig. 3B-1), about 20 km. SE of Kirkland Lake, Ont. The structure of the volcanic pile is that of a steep anticline which plunges slightly to the east (Grant, 1963). The Round Lake batholith appears at the core of this major fold, but "unfortunately, the considerable cataclasis evident in the marginal augen gneiss does not permit the observer to be certain of the relation between the intrusion and the development of the fold" (Grant, 1963; p. 8-9). Although the contact between the granitic rocks and the volcanic rocks is typically conformable, the granites are locally intrusive.

Detailed mapping and stratigraphic work has shown that the volcanic pile consists of three major formations which consistently show tops to the east. These are sucessively (from base to top) called the Pacaud tuffs, the Catharine basalts, and the Skead pyroclastics (Ridler, 1970). The present erosional surface, therefore, exposes a cross section through these formations, and allows good stratigraphic control on the sampling. Regionally, the Skead volcanics are thought to stratigraphically underlie the Blake River volcanics to the north, placing them among the oldest volcanic rocks present in the Abitibi greenstone belt (Goodwin and Ridler, 1970; Jensen, 1979b).

II. PETROLOGY

In the Skead volcanics the evidence for the two metamorphic events which have affected most of the greenstone belt is well developed. In the upper part of the volcanic pile the assemblage has been described as "actinolite zone with prehnite and pumpellyite relics" (Jolly, 1974;

TABLE 3E-1. OXYGEN ISOTOPIC AND PETROGRAPHIC DATA FROM THE SKEAD AREA

Sample	Field Description	$\delta^{18}O$ WR	$\delta^{18}O$ Min.	Microscopic Description: Texture	Ave. gr. size	Secondary Mineralogy	% Rec.	Location: Lat.	Location: Long.
SKEAD VOLCANICS									
S-230	Sample collected by Ian Smith	5.8						47°58.3'	79°52.7'
S-236	Sample collected by Ian Smith	7.8						48°0.2'	79°51.3'
S-237	Sample collected by Ian Smith	7.4						48°0.3'	79°51.5'
S-238	Sample collected by Ian Smith	7.4						48°0.4'	79°51.6'
S-243	Sample collected by Ian Smith	9.0						47°58.1'	79°47.0'
S-246	Sample collected by Ian Smith	8.9						47°58.2'	79°46.5'
S-251	Sample collected by Ian Smith	7.2							~79°50'
S-252	Sample collected by Ian Smith	7.0							~79°50'
S-253	Sample collected by Ian Smith	7.1							~79°50'
S-255	Sample collected by Ian Smith	7.0						47°56.1'	79°47.5'
S-257	Sample collected by Ian Smith	7.4						47°56.7'	79°45.5'
S-258	Sample collected by Ian Smith	7.9						47°56.6'	79°45.7'
Br-40	Pacaud tuff near Boston Creek 20' from batholith	7.2		schistose	50	hbd,ep,qtz,cc	100	48°0.4'	79°56.8'
Br-43	Rhyolite volcaniclastic near Larder Lake	12.2	13.7(q)	fragmental,porph.	40	qtz,cc,musc,chl	70	48°0.3'	79°41.9'
Br-44	Komatiite flow, 5 m below upper contact	8.4		equigranular	50	trem,chl,hem,ep	100	48°0.3'	79°41.9'
Sk-33	qtz. vein cutting komatiite near Larder Lake		12.5(q)					~48°5'	~79.44'
OTTO STOCK AUREOLE									
Br-27	slightly altered pillow basalt	8.8		equigranular	10	act,ep,chl,cc, qtz	100	48°5.3'	80°11.0'
Br-38	coarse mafic hornfels in roof pendant	7.1		poikilitic	2000	hbd,bi,pl,qtz, pyx	100	48°3.8'	80°9.0'
OTHER									
Sk-32	Basalt from highway 66, E. of Matachewan	6.1						47°57.6'	80°17.7'

Abbreviations as in table 3B-1.

p. 504). Within this area isolated patches of pumpellyite-epidote bearing rocks are present within a broad band of greenschist-facies actinolite-bearing rocks. Pumpellyite is commonly embayed by later minerals, especially epidote and quartz. The lower part of the volcanic pile is adjacent to the Round Lake batholith, and it contains neither prehnite nor pumpellyite relics. The assemblages generally include actinolite (Jolly, 1974) and are typical of the greenschist facies. These rocks also display penetrative deformation with actinolite needles growing across grain boundaries; the prehnite-pumpellyite rocks lack such features. The actinolite zone forms a band 10-15 km. wide adjacent to the Round Lake batholith. These spatial, textural and mineralogic observations suggest that the Skead volcanics first underwent burial metamorphism in the prehnite-pumpellyite facies, and then were overprinted by the contact metamorphism associated with the emplacement of the Round Lake batholith.

III. OXYGEN ISOTOPE DATA

Whole-rock $\delta^{18}O$-values have been measured on 15 samples of the Skead volcanics, and range from +6.0 to +12.2 (Table 3E-1). The only mineral separate obtained from this set of rocks was an HF quartz separate from a rhyolite (+13.7). The spatial distribution of $\delta^{18}O$ is such that $^{18}O/^{16}O$ progressively increases to the east, which is stratigraphically up-section. If the data are contoured, the contours trend parallel to both the margin of the Round Lake batholith and to the intraformational contacts listed above. This variation can be graphically illustrated in a plot of whole rock $\delta^{18}O$ vs. structural height (Fig. 3E-1).

Figure 3E-1 shows that $\delta^{18}O$ systematically increases upward in the Skead stratigraphic section. The same correlation is present in the Ben Nevis area (Fig. 3A-4), the Benoit area (Fig. 3C-1) and the Noranda

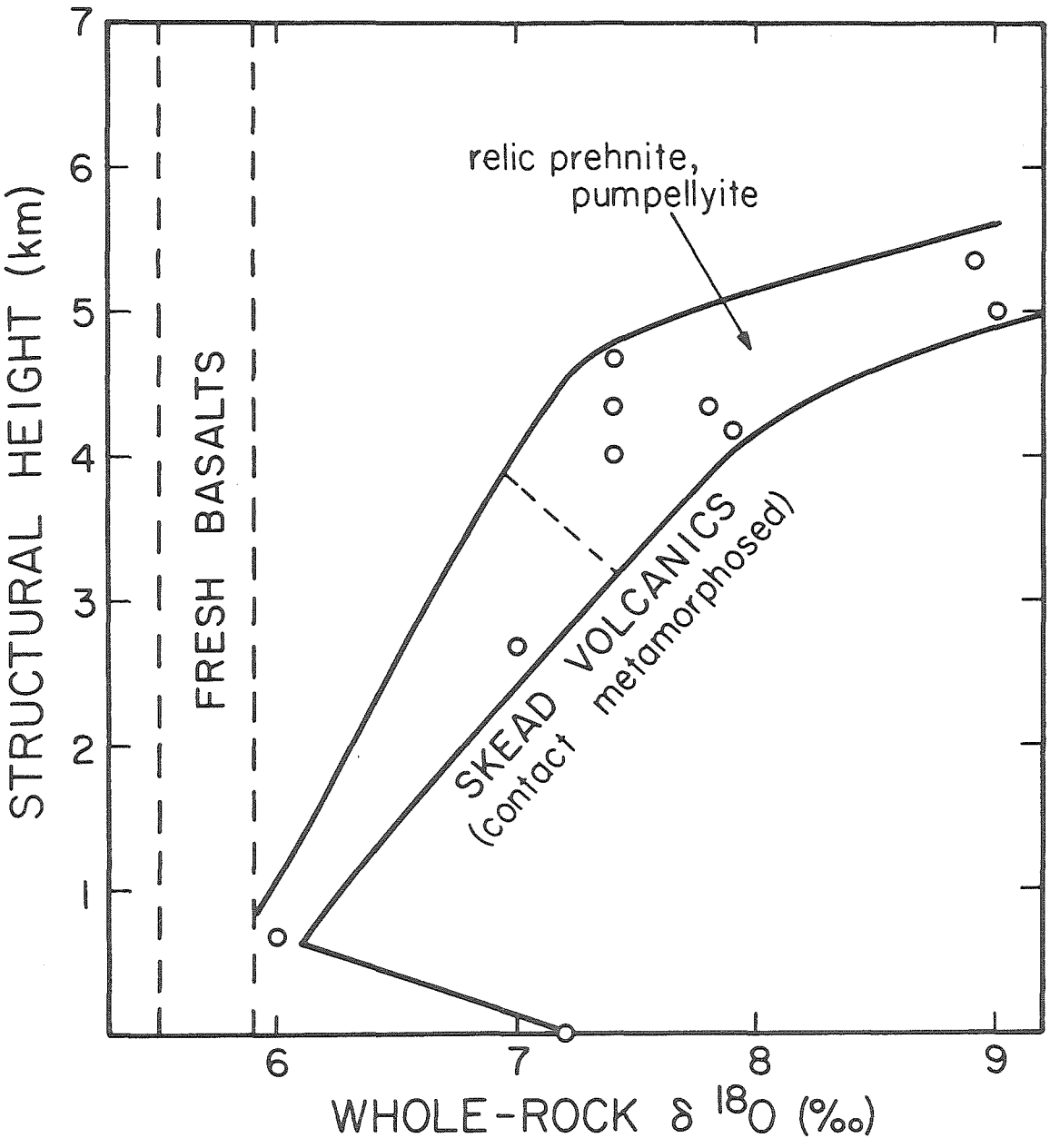

Figure 3E-1. Variation of whole-rock $\delta^{18}O$ with structural height for the Skead area. Not only is the pattern the same as found in the Ben Nevis, Benoit and Noranda areas, the magnitude of the values is similar.

area (Fig. 3D-1). The absolute $\delta^{18}O$-values are remarkably similar as well. At the base of the Skead volcanic pile, $\delta^{18}O = +6$, indistinguishable from the lower portions of the above mentioned piles. $\delta^{18}O$ of the upper part of the Skead section is poorly constrained because of inadequate sampling, but a continuous increase up to at least 9 per mil is present (Fig. 3E-1). The upper portions of the Ben Nevis, Benoit and Noranda sections also have $\delta^{18}O = +9$ to $+10$. It is reasonable to assume, therefore, that the same physical process was operative in all four areas.

The discussion in Chapter 3C suggests that the whole-rock oxygen isotopic compositions were produced through water/rock interactions during prehnite-pumpellyite facies metamorphism. In view of the relic pumpellyite in the Skead area, this mechanism seems equally valid there. An additional important feature is that the metamorphic overprinting associated with the Round Lake batholith has apparently not significantly affected the whole-rock $\delta^{18}O$ distribution. The $\delta^{18}O$ stratigraphic profile in the Skead area is indistinguishable from those in the other sampled sections, yet the second metamorphic event has had a different effect in each case. The common denominator in these areas is the early prehnite-pumpellyite facies metamorphism, and its accompanying widespread recrystallization and hydration, with $\delta^{18}O$ increasing as temperature decreases toward the top of the volcanic pile.

Further evidence that the contact metamorphism was essentially an isochemical dehydration comes from a traverse up to the margin of the Otto Stock (Fig. 3B-1). Along this traverse the metamorphic grade steadily increases from albite-epidote-actnolite rocks (greenschist facies) to pyroxene hornfels facies rocks over a horizontal distance of about 4 km.

$\delta^{18}O$ was measured at the two endpoints of this traverse, and a slight decrease towards the pluton is observed, +8.8 to +7.1 (Table 3E-1). Because this is also stratigraphically down-section, however, all of this variation could have preceeded the intrusion of the Otto Stock.

It is possible that sample Br-40 ($\delta^{18}O$ = +7.2), which was collected only 20 feet from the contact with the Round Lake batholith, has had its whole-rock $\delta^{18}O$ affected by the plutonism. Figure 3E-1 suggests that Br-40 is about 1 per mil richer in ^{18}O than one might predict. With this possible exception, however, the contact metamorphism of the Skead volcanics appears to have been essentially isochemical in $\delta^{18}O$.

Two other samples are reported in Table 3E-1, although they are not part of the Skead volcanics. Sk-32 is from Matachewan, an area with a large number of granitic intrusions (including the NW boundary of the Round Lake batholith) and has $\delta^{18}O$ = +6.1. It may be stratigraphically as well as oxygen isotopically equivalent to the lower parts of the Skead section. Sample Sk-33 is a quartz vein cutting a thoroughly altered komatiite immediately west of the town of Larder Lake, and has $\delta^{18}O$ = +12.5. The quartz vein contains abundant visible free gold, and is thought (Lowe, pers. comm., 1978) to be similar to the veins in the nearby Kerr Addison mine.

IV. FLUID COMPOSITION

Because of the similarities in metamorphic style and oxygen isotopic distribution, the calculations performed for the Ben Nevis area are equally valid in the Skead area. Thus the final fluid in the prehnite-pumpellyite facies event was apparently about +1.5 (± 1.5) (Fig. 3B-4) and the initial fluid apparently had $\delta^{18}O$ = 0 ± 2 (Fig. 3B-5 a,b,c). The small amount of fluid lost during dehydration in the second metamor-

phism would have been a few per mil richer in ^{18}O than this, because of the higher temperatures and presumed low water/rock ratios.

The relationship of these fluids to Sk-33, the gold-bearing quartz vein, is not clear from this study. The temperature of formation of the quartz is not known, but if it is assumed to be 300-400°C, then the hydrothermal fluid would have had $\delta^{18}O$ = +5.1 to +7.9. There are a number of ways to interpret this calculation. High-^{18}O fluids could have evolved from low-^{18}O water through evaporation of seawater in a closed basin, exchange with high-^{18}O country rocks, or boiling in the ore fluid. Alternatively, the solution could have been a magmatic or metamorphic dehydration water. These possibilities are discussed in detail in Chapter 4B.

The association of gold mineralization with komatiites has been well documented in the Timmins mining camp, 30 km. to the west (Pyke, 1975). Detailed oxygen isotopic study of the Dome mine (Kerrich and Fryer, 1979), in fact, indicates that it is rather similar to Sk-33 (quartz = +14 to +15 at Dome, +12.5 at Sk-33). Whatever the origin of the Dome vein system, it is plausible that Sk-33 had a similar origin.

CHAPTER 3F. MUNRO TOWNSHIP KOMATIITES

I. INTRODUCTION

In the first decade since the recognition of the significance of komatiites (Viljoen and Viljoen, 1969a,b), considerable effort has been expended to characterize both the igneous petrology and the chemistry of this unusual suite. With the possible exception of the Gorgona Island examples, however, all komatiites are presently metamorphic rocks, with varying amounts of relic igneous minerals. The purpose of this chapter is to evaluate the nature of the metamorphic event which has affected this rock type.

The most common occurrence of komatiites is as portions of Archean greenstone belts. Among these Archean komatiites, the sample locality with the highest degree of preservation is in Munro Township, Ontario (Fig. 3B-1). There, although structural and textural preservation is essentially perfect, the primary igneous minerals have been largely pseudomorphed by secondary, hydrous minerals such as serpentine, tremolite and brucite. By analyzing the oxygen isotopic compositions of these rocks it is possible to gain a measure of understanding into the nature of this hydrothermal event. The excellent preservation of the Munro komatiites is in part related to the fact that the surrounding greenstone belt has been subjected to only two principal metamorphic events, both of which are well understood. In addition, the metamorphic grade is relatively low (prehnite-pumpellyite facies). These two conditions, which greatly simplify the interpretation of the isotopic data, make Munro Township an ideal place for studying water/komatiite interactions. The degree of preservation in Munro Township also enables calculation of $\delta^{18}O$ of the initial komatiite magma, allowing certain constraints to be placed

Table 3F-1. Data from single komatiite flow, Pyke Hill, Ont.

	Br-2	Br-3	Br-4	Br-5	Br-6	Br-7
Height above base (meters)	2.9	2.1	2.6	1.1	0.05	0.2
$\delta^{18}O$ (%)	4.6	4.9	4.9	3.5 3.8	4.9	5.4 5.1
O_2 yield (umoles/mg)[1]	14.66	13.72	14.81	14.34 14.43	13.93	12.53 12.36
Mode[2]						
Olivine	(1)	13	7	6	27	32
Secondary after olivine	(43)	28	37	74	22	17
Groundmass (pyx+plag+chlorite +opaque)	(56)	59	56	20	51	51
Total Secondary	(45)	31	38	75	24	19
Antigorite	(23)	(13)	(20)	(64)	(13)	(7)
Magnetite	(3)	(2)	(3)	(8)	(1)	(1)
Tremolite	(15)	(11)	(12)	(2)	8	9
Brucite	(2)	(2)	(2)	(<1)	<1	<1
Chlorite	(2)	(3)	(1)	(1)	(2)	(2)
Talc	0	(tr.?)	0	(tr.?)	0	0

Notes [1] low oxygen yields are probably due to incomplete fluorination of olivine.

[2] values in parentheses are visual estimates, others determined by point counting in transmitted light.

on models of komatiite genesis.

II. SAMPLING

A set of six samples was collected across a single komatiite flow that crops out on Pyke Hill, the prominent monadnock in Munro Township (Arndt et al. 1977). This particular flow ranges from 2.5 to 3.0 m. thick, and has a well-developed upper chilled and fractured flow top. Beneath the flow top, textural changes progress through fine-grained spinifex, coarse-grained spinifex, a foliated zone, fine- to medium-grained peridotites, and finally a basal chilled zone (Fig. 3F-1). The six samples were selected to span most of the textural variations present, hence they are not evenly spaced through the flow (Fig. 3F-1). In addition, single samples of two other komatiite flows in the Abitibi greenstone belt (Lamotte Twp., Que. and Skead Twp., Ont.) were collected for comparison with the Munro Township samples and with other published komatiite analyses.

III. METAMORPHIC PETROLOGY

Megascopically there is little sign of hydrothermal activity at Pyke Hill. There are rare chrysotile veins, but the megascopic textures and structures of the komatiites are perfectly preserved. Similarly, although quartz veins are common, deformation is absent in the basalts of the surrounding volcanic pile. In thin section the relic igneous textures of the komatiites are also well preserved, even though largely pseudomorphed by secondary hydrous minerals.

The komatiites originally consisted of relatively large olivine crystals set in matrix ranging from devitrified glass to fine-grained intergrowths of pyroxene and plagioclase. The principal alteration effect is the replacement of olivine by fine-grained metamorphic minerals.

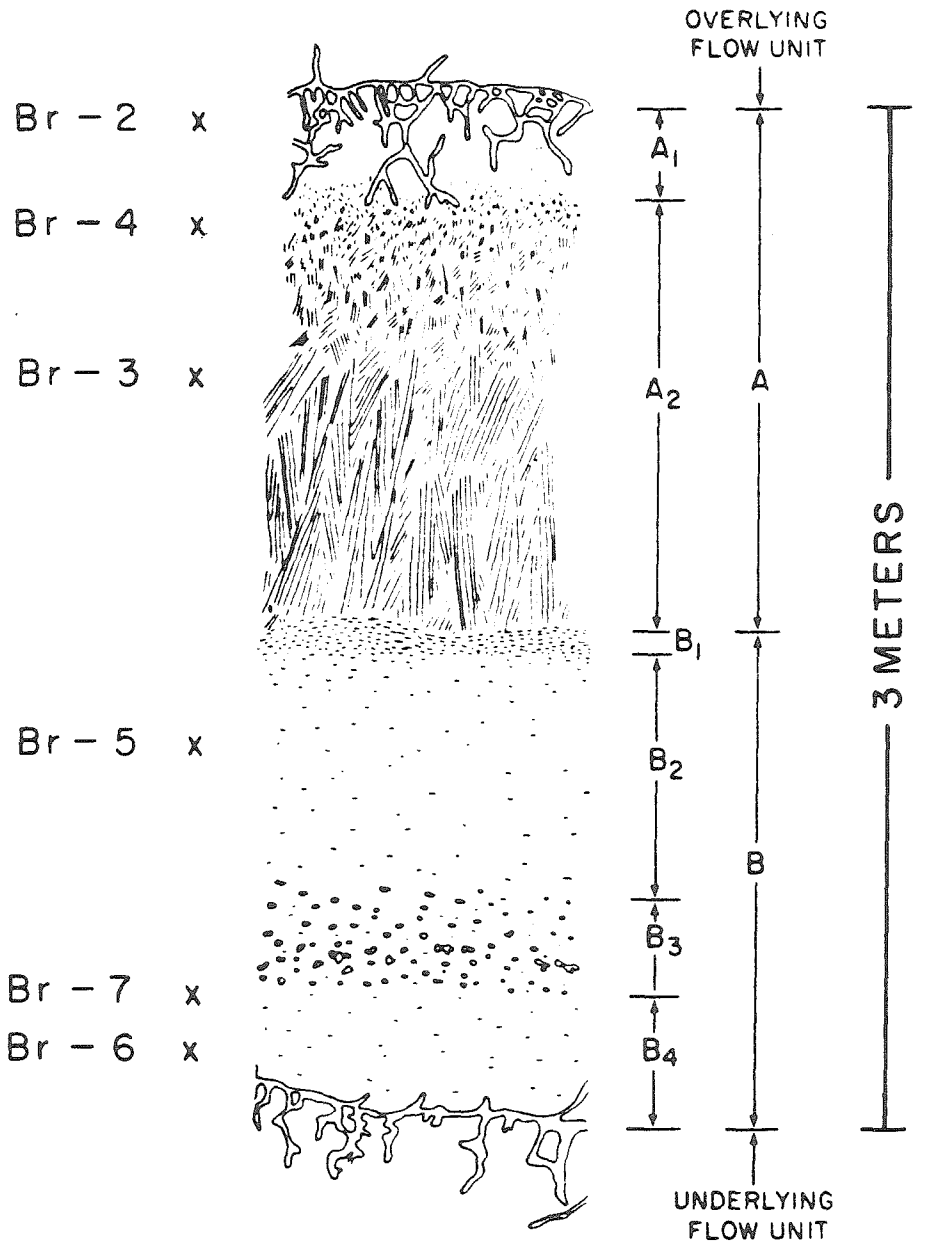

Figure 3F-1. Cross section of the komatiite flow studied in this work (taken from Fig. 7 of Arndt et al. 1977). The flow ranges in thickness from 2.5-3.0 m., and the sample localities are shown on the left.

The alteration assemblage, however, varies from grain to grain in response to the differential reactivities of the three main igneous minerals. About half of the olivine is partially replaced by the assemblage antigorite + brucite + magnetite (Fig. 3F-2c). Adjacent to these pseudomorphs the groundmass pyroxene and plagioclase are completely fresh. The other olivine pseudormorphs contain variable amounts of tremolite, (ranging up to 100%), antigorite, magnetite, and an absence of brucite (Fig. 3F-2a,b). Adjacent to these pseudomorphs the pyroxene and plagioclase have been variably replaced by chlorite (Fig. 3F-2a,b), the intensity of chloritization decreasing away from the olivine pseudomorph. The local abundance of chlorite is proportional to the local abundance of tremolite, and the chloritization of plagioclase is more extensive than that of pyroxene. The largest concentrations of tremolite and chlorite are along veins and fractures (Fig. 3F-2d), and the tremolitic alteration appears to crosscut the antigorite-brucite alteration. Talc is possibly also present along the veins. The tholeiitic basaltic lavas (greenstones) associated with the komatiites at Pyke Hill are recrystallized to an assemblage which includes prehnite, pumpellyite and chlorite (Arndt *et al.* 1977, p. 347).

These textural observations suggest that the relative susceptibility to recrystallization in the komatiites increases in the order pyroxene, plagioclase, olivine. Wherever plagioclase broke down, the Ca and Al released appear to have stabilized tremolite and chlorite, respectively, at the expense of olivine and pyroxene. The reaction describing this process is:

Figure 3F-2. Photomicrographs from Munro Township.

a.) Br-3, transmitted light. b.) Same view, crossed polars. An intensely altered portion of a komatiite in which the olivine has been replaced by tremolite, and the groundmass has been largely replaced by chlorite. In spite of the wholesale recrystallization, note the excellent state of textural preservation.

c.) Br-5, transmitted light. An equant olivine crystal which has been partially replaced by antigorite and magnetite. The rounded grains with high relief are relic olivine.

d.) Br-3, crossed polars. Close up view of the tremolite (prismatic) and chlorite (black).

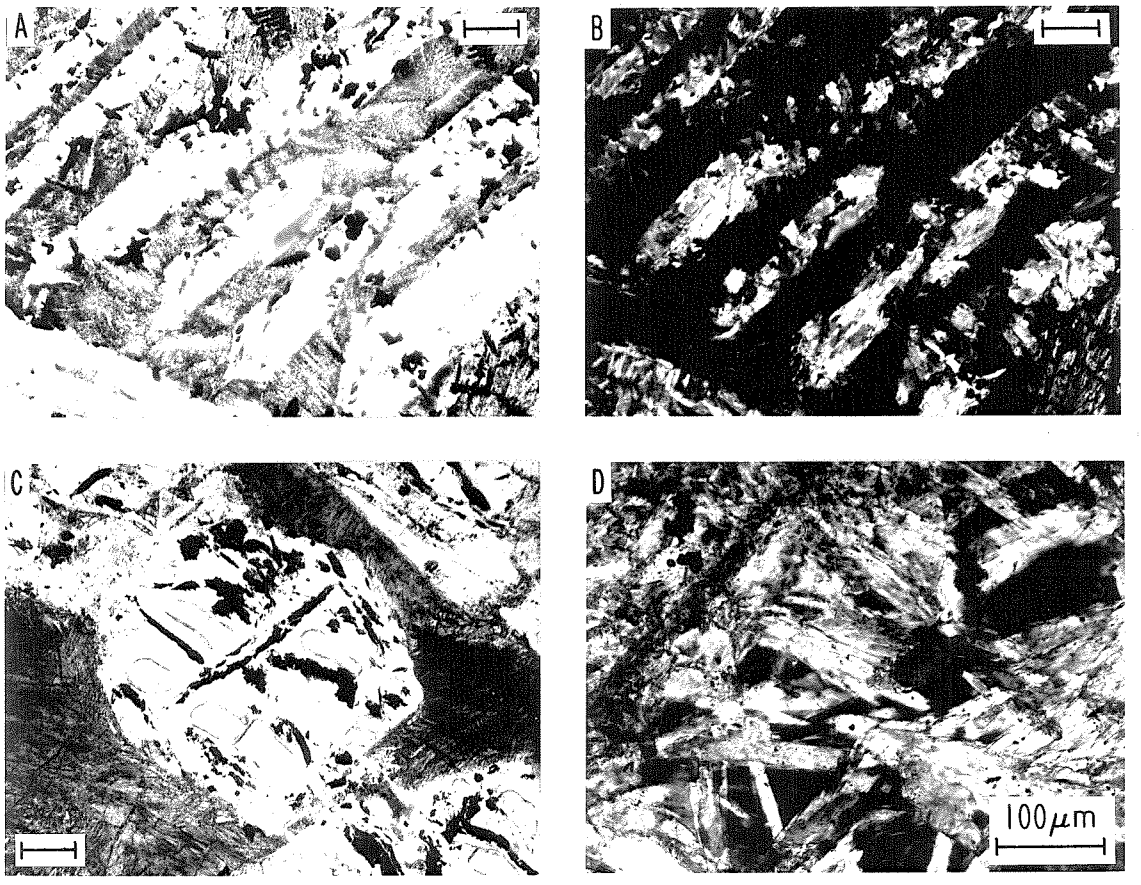
A
B
C
D
100μm

$$2\ CaAl_2Si_2O_8 + 9\ Mg_2SiO_4 + 2\ MgCaSi_2O_6 + 10\ H_2O + 5\ SiO_2 \rightarrow$$

(anorthite) (olivine) (pyroxene)

$$2\ Mg_5Al_2Si_3O_{10}(OH)_8 + 2\ Ca_2Mg_5Si_8O_{22}(OH)_2$$

(chlorite) (tremolite)

This requires addition of silica to the rock, and is consistent with the predominance of chlorite and tremolite (and possibly also talc) along veinlets and the ubiquitous presence of quartz veinlets in the nearby basalts. As would be expected, hydrothermal alteration of the Abitibi volcanic pile surrounding Pyke Hill has produced silica-bearing solutions, and these fluids evidently have reacted chemically as well as isotopically with the komatiites.

An additional complexity is the fact that brucite and tremolite are not stable together under any conditions (Evans and Trommsdorff, 1970) perhaps suggesting two metamorphic events. As long as pyroxene and plagioclase are not participating in the reactions, however, antigorite and brucite are the stable breakdown products of olivine. Although polymetamorphism is a possibility, the data are adequately explained by a single, progressive metamorphism involving a low-T olivine destructive stage, and a later high-T olivine, pyroxene and plagioclase destructive stage. In the basalts associated with the komatiites, no evidence for polymetamorphism was observed.

These observations are consistent with all of the volcanic rocks near Pyke Hill being recrystallized in a single hydrothermal metamorphic event. The metamorphic style is typical of that of the Abitibi greenstone belt as a whole, which is thought to have been subjected to subseafloor burial metamorphism (Dimroth and Lichtblau, 1979; Beaty and

Taylor, 1979; Jolly, 1980). Subsequent to this hydrothermal event, the Abitibi rocks were locally subjected to dehydration contact metamorphism associated with the intrusion of the Kenoran granitic batholiths (Jolly, 1974; Jolly, 1980). The nearest of these batholiths to Pyke Hill crops out about 15 km. to the NE (Fig. 3B-1), but this later metamorphic episode did not produce any obvious dehydration at Pyke Hill. Mineral-chemical data in conjunction with Abukuma-type assemblages in the metamorphic aureoles surrounding the granitic batholiths (Jolly, 1980) indicate a high geothermal gradient during metamorphism. This suggests (Figure 3F-3) that the maximum possible temperature experienced during hydrothermal alteration at Pyke Hill was about 300-330°C.

IV. OXYGEN ISOTOPIC DATA

1. Isotopic structure of the flow

The oxygen isotopic composition of the Pyke Hill komatiite flow ranges from $\delta^{18}O$ = +3.65 to +5.25 (Table 3F-1). The variation as a function of depth is shown in Figure 3F-4. The lowest-^{18}O values occur in the center and at the top of the flow, with higher-^{18}O values in between and at the base. Also shown on Figure 3F-4 are the amounts of modal secondary minerals. The two curves are obviously correlated, indicating that $\delta^{18}O$ depends on the degree of recrystalliztion and the amounts of new metamorphic minerals produced. By plotting these two variables against one another (Figure 3F-5), it is possible to extrapolate to the compositions of both the original fresh komatiite and the total secondary assemblage. The significance of these two values is discussed in detail below.

It seems likely that the komatiites, like the associated tholeiitic basalt flows, were erupted into the ocean and crystallized on the seafloor.

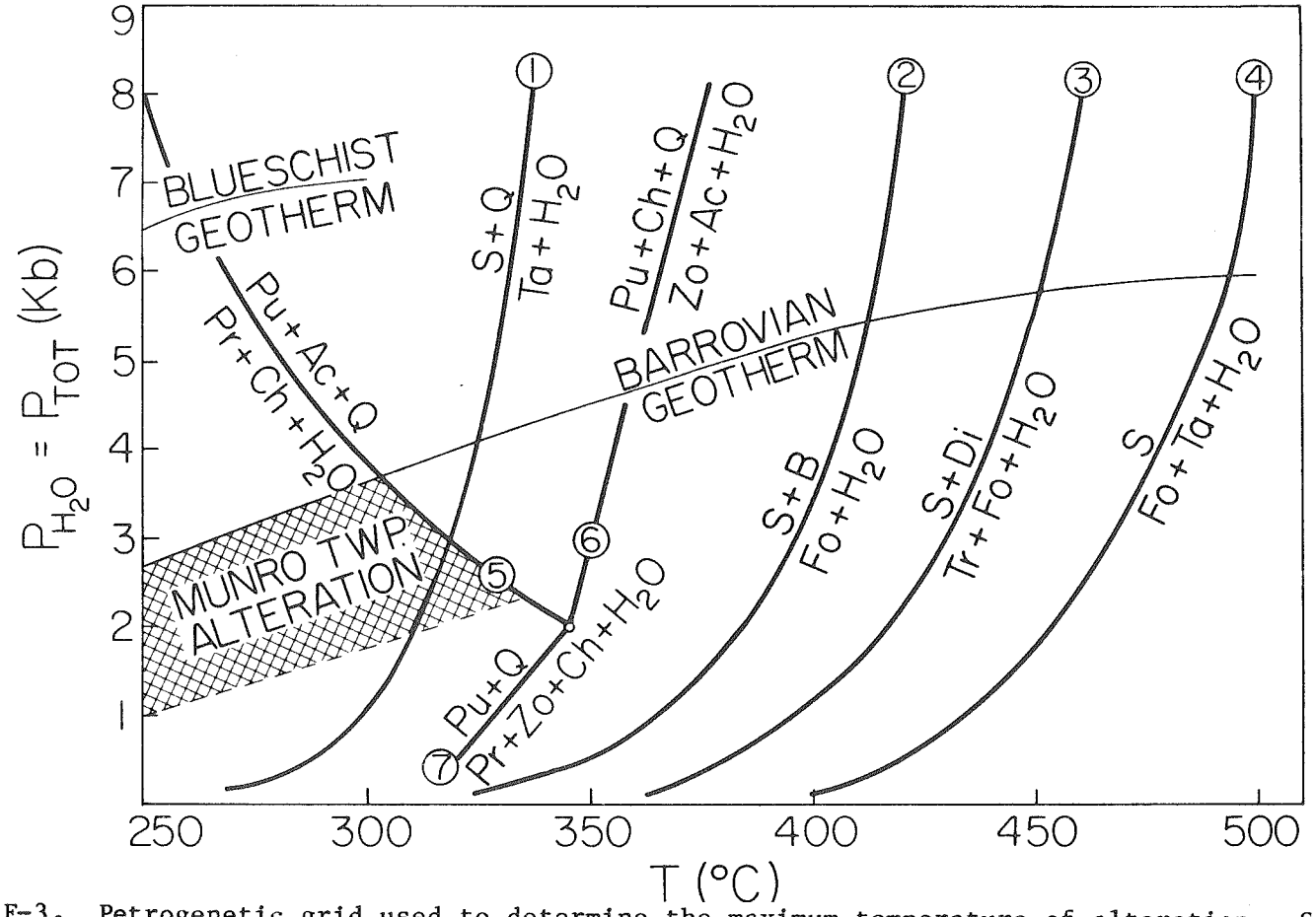

Figure 3F-3. Petrogenetic grid used to determine the maximum temperature of alteration. Sources of data are (1)-(4) Evans and Trommsdorff (1970); (5)-(7) Nitsch (1971). The location of the invariant point in the iron-free system is thought to be about 2 kb. and 345° ± 20°C (Winkler, 1979). The komatiites have no diagnositic assemblage, but the assemblage prehnite + pumpellyite + chlorite in the associated basalts places an upper limit of 300-330°C on the temperature. Because of the probable progressive nature of the alteration, no lower temperature limit is drawn.

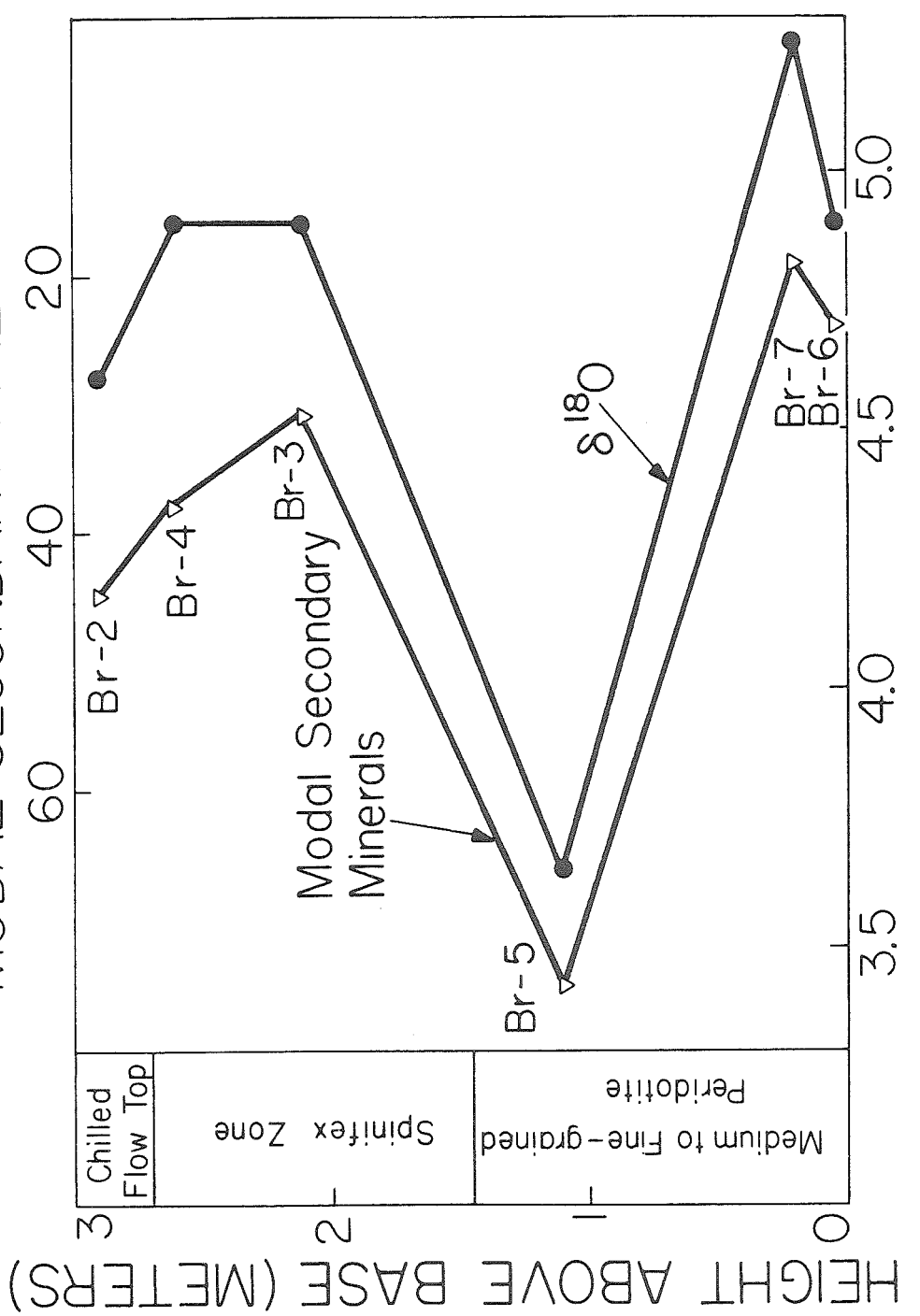

Figure 3F-4. Oxygen isotopic structure of the Pyke Hill komatiite flow. Shown for comparison is the total abundance of secondary minerals in each sample.

This is based not only on the widespread occurrence of pillow lavas and sedimentary rocks within greenstone belts (e.g. Goodwin and Ridler, 1970), but also on the proposed globe encircling seas deduced from calculations of the lunar tidal force (Hargraves, 1976). This suggests that the ubiquitous chilled and polyhedrally jointed flow tops (Arndt et al. 1977, p. 328) in the komatiites formed by the rapid loss of heat to the overlying water. As soon as such a fractured flow top formed, seawater would have entered the rock, and if the temperature were high enough (because of conduction from the center of the hot flow) serpentinization would immediately have begun to take place. One might anticipate, therefore, somewhat larger oxygen isotopic (and alteration) effects in the fractured flow tops than in the unfractured central and basal zones of the flow. However, although the chilled flow top is indeed lower in ^{18}O than the rocks immediately below it, it is not the most altered rock in the sampled section. This indicates that the serpentinizing process, whatever it was, had access to all parts of the flow. The fact that $\delta^{18}O$ is lowest in the core of the flow merely reflects the fact that this zone was originally richer in olivine (through accumulation) and consequently has produced more serpentine.

2. $\delta^{18}O$ of fresh komatiite

Figure 3F-5 indicates that the oxygen isotopic composition of the original komatiitic liquid was in the range +5.7 ± 0.3%. This is indistinguishable from $\delta^{18}O$ of basalts presently being erupted from mid-ocean spreading centers (+5.7 ± 0.2). The coincidence of these values may at first appear rather surprising; simple calculations suggest that komatiites should have less ^{18}O. In fresh basalt with $\delta^{18}O$ = +5.7 containing 50% plagioclase, 40% pyroxene and 10% olivine, the $\delta^{18}O$

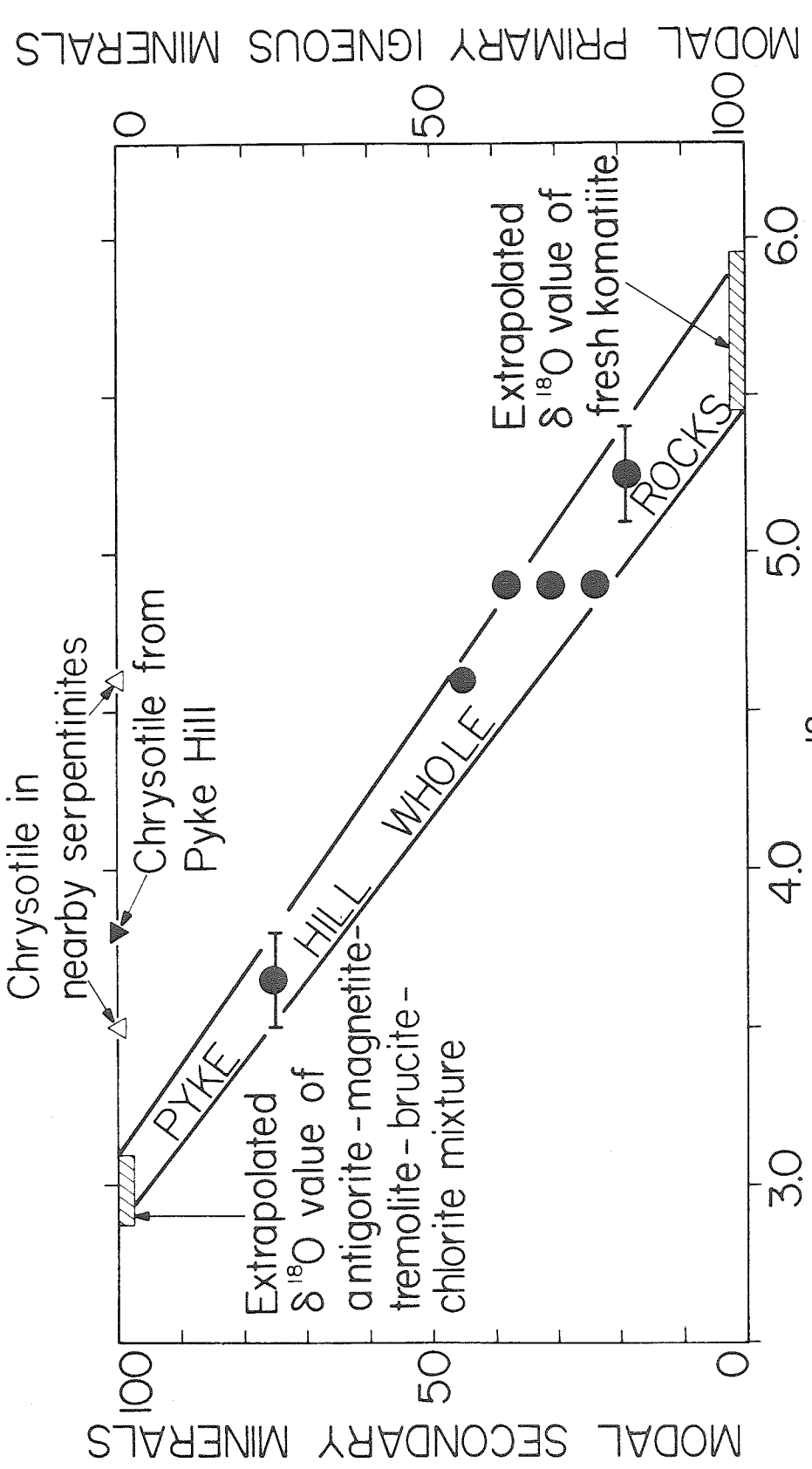

Figure 3F-5. Plot of $\delta^{18}O$ against total modal secondary minerals. The correlation allows extrapolation to $\delta^{18}O$ of fresh komatiite (5.7 ± 0.3) and to $\delta^{18}O$ of the antigorite-magnetite-tremolite-brucite-chlorite mixture (3.0 ± 0.1). Nearby chrysotile samples are shown for comparison.

values of these minerals are about +6.0, +5.5 and +5.1%, respectively (Taylor, 1968; Taylor and Epstein, 1970; Onuma et al. 1970; Anderson et al. 1971). If similar mineral compositions were present in komatiites but the respective proportions were 20, 30 and 50%, (Arndt et al. 1977, Table 7), the whole-rock $\delta^{18}O$ would be +5.4. This is, in fact, marginally within the projected Pyke Hill value of +5.7 ± 0.3. This calculation also indicates that igneous fractionations can be responsible for only a small part of the observed $\delta^{18}O$ spread on Figure 3F-4: The loss of 40% olivine would change the komatiite's whole rock $\delta^{18}O$ by only 0.3.

Komatiites, however, have considerably higher liquidus temperatures than basalts. The data of Arndt (1976) on the Pyke Hill komatiites, for example, indicate a liquidus (olivine saturation) temperature of about 1500°C, followed by the appearances of spinel (1350°), pyroxene (1200°) and plagioclase (1200°), and a solidus of about 1150°. Because the isotopic fractionation factor Δ between two phases is typically proportional to $1/T^2$ (e.g. Javoy, 1977), the olivine in komatiites may be richer in ^{18}O than basaltic olivine. Preliminary work by Kyser and O'Neil (1978) and Kyser (1979) suggests that the olivine-pyroxene fractionation may even reverse at high temperature. This effect might account for the high extrapolated Pyke Hill whole-rock value. In contrast to this, Hoefs and Binns (1978) reported olivine with $\delta^{18}O$ = +4.5 and pyroxene with $\delta^{18}O$ = +5.6 to +5.9 in the Australian komatiites. Further resolution of this problen must await the preparation and analysis of more mineral separates.

3. Source region

Because oxygen isotopic fractionations are independent of pressure, the assumptions of equilibrium partial melting and adiabatic rise to the

surface permit estimation of the composition of the mantle through analysis of the magmas produced there. In this regard $\delta^{18}O$ of the Pyke Hill komatiites (+5.7 ± 0.3) is remarkably similar to $\delta^{18}O$ of a variety of ultramafic rocks, including nodules in Hawaiian basalts: +5.8 per mil (Kyser and O'Neil, 1978); Beni Bousera, Lherz, Cassou and Lanzo: +5.56 ± 0.05 per mil (Javoy, 1978); and assorted peridotites, pyroxenites and dunites (including the SE Alaskan ultramafics): +5.6 ± 0.2 per mil (Taylor, 1968). Whether or not these materials could be in equilibrium with +5.7 tholeiitic basalt depends on the nature of the olivine-pyroxene-liquid fractionation at high-T which is poorly known. In any case, the komatiite data (see also Hoefs and Binns, 1978) suggest that mantle-derived magmas in the Archean had oxygen isotopic compositions similar to those derived during more recent episodes in the Earth's history.

4. $\delta^{18}O$ of secondary minerals

The extrapolated $\delta^{18}O$ of all the secondary minerals in the komatiite taken together (Fig. 3F-5) is about +3.0. None of the five main secondary minerals (antigorite, magnetite, tremolite, brucite, chlorite) could be separated from these rocks because of their fine grain size (typically 1-50 μm.) and textural complexity. Assuming final equilibration at 300°C and the presence of antigorite, magnetite, tremolite and chlorite in the proportions 60:5:30:5, these minerals probably have $\delta^{18}O$ of about +3.2, -3.7,+3.8, and +3.2, respectively (Friedman and O'Neil, 1977; Javoy, 1977). This calculation is admittedly speculative bacause of the uncertainty in the temperature and the somewhat variable proportions of the secondary minerals (Table 3F-1). However, the calculated antigorite value is similar to $\delta^{18}O$ of a 1-2 mm. wide chysotile vein which cuts Pyke Hill (+3.8), and to chrysotile from two nearby asbestos

mines (+3.5, +4.6) (Fig. 3F-5).

5. Fluid composition and water/rock ratio

In the case of the Munro komatiites, the initial and final rocks are known (Fig. 3F-5). Δ for the serpentinization reaction has been estimated by Wenner and Taylor (1973) as a function of temperature, so three unknowns describe the hydrothermal alteration: T, W/R and $\delta^{i}H_2O$. The most convenient way to represent these three variables is using a plot of $\delta^{i}H_2O$ vs. W/R on which the isotherms are contoured (Fig. 3F-6). Although the mineral assemblages suggest a metamorphic temperature of about 300°, there is little assurance that all or even most of the water flux took place at that temperature. It is perfectly possible that the rocks were altered at a lower temperature, such as 200°, and then isochemically heated to 300°. Most probably the water/rock interaction took place over a range of temperatures.

Because the rocks have lost ^{18}O during alteration, if the water/rock ratio were very small the fluid would have had to be very ^{18}O-depleted to have produced such a shift. On the other hand, if the water/rock ratio were greater than about two, the fluid would have had a $\delta^{18}O$ value in the vicinity of 0 per mil and the isotopic shifts would be essentially independent of W/R. Note that in spite of the uncertainty in temperature, once either W/R or $\delta^{i}H_2O$ is known, the other is reasonably determined.

Several lines of evidence indicate that this alteration took place under conditions of high water/rock ratio, indicating $\delta^{i}H_2O$ close to 0. The basaltic rocks associated with the komatiites (e.g. Theo's flow, Blake River Volcanics) are also extensively hydrothermally altered, but show ^{18}O enrichments (Chapters 3B, 3C, 3D, 3E). Similar water/rock calculations on those samples indicate possible hydrothermal fluids in

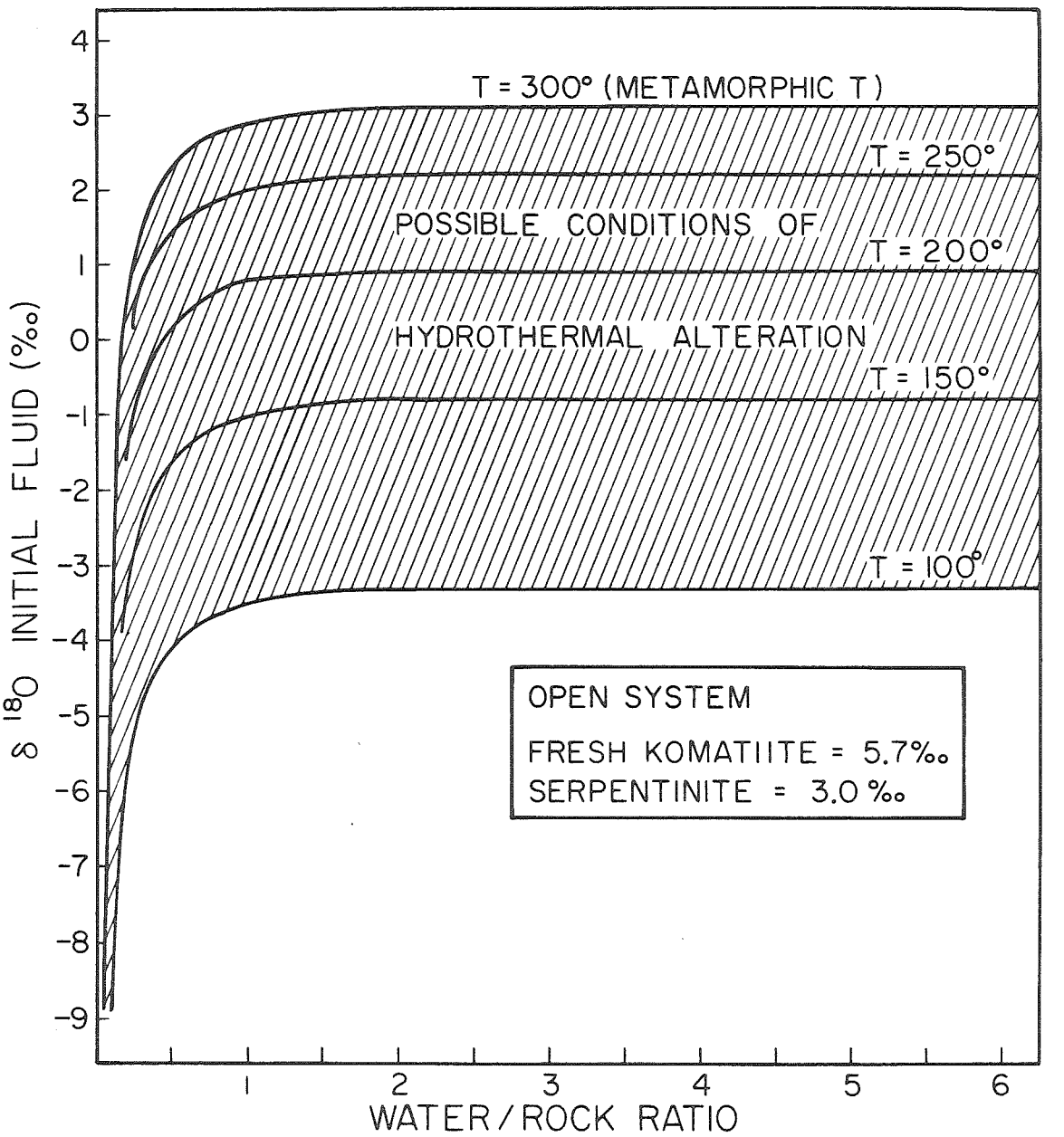

Figure 3F-6. Calculated possible water/rock ratios (by weight), initial fluid $\delta^{18}O$, and temperatures for the open system transformation of fresh komatiite (+5.7) to serpentinite (+3.0). For the details of construction and further explanation, see text.

the range -2 to +2 at high W/R, increasing to >8 at low W/R (Fig. 3B-5 a,b,c). Inasmuch as the two rock types were altered together, the Abitibi hydrothermal fluid must lie within the field of coincidence, which spans $\delta^{i}H_2O$ = -2 to +2, and W/R >1 (Fig. 3F-7). High water/rock ratios have also been calculated by White (1968) on the metamorphically similar Keweenawan basalts, and by McCulloch et al. (1980) for the subseafloor alteration of the Samail ophiolite. Independently, Taylor (1977), in his study of granitic batholiths, found evidence that $\delta^{18}O$ of ocean water has remained relatively constant (close to 0) over the last 2.5 b.y. Thus the data in this paper are consistent with the interpretation that the komatiites were hydrothermally altered by seawater, and that seawater has not changed in $\delta^{18}O$ since the Archean. In this regard it is interesting to note that modern oceanic serpentine (Wenner and Taylor, 1973) is similar in $\delta^{18}O$ to the komatiitic serpentine (Fig. 3F-7).

6. Komatiites from other areas

Two samples of komatiites from elsewhere in the Abitibi greenstone belt have been studied. A sample of coarse spinifex-textured komatiite from Spinifex ridge in Lamotte Twp., Que. (Lajoie and Gelinas, 1978) has $\delta^{18}O$ = +4.5 (Fig. 3F-8). This rock is completely recrystallized to an assemblage of tremolite + chlorite + serpentine + magnetite, and is thus mineralogically and isotopically similar to the Munro Twp. komatiites. The degree of alteration is greater, but as in Munro, the assemblage suggests an addition of silica to the rock.

By contrast, a komatiite (identified by Jensen, 1979a on the basis of texture and composition) from Skead Twp., Ont. has $\delta^{18}O$ = +8.4 (Fig. 3F-8). The metamorphic assemblage of this rock, however, is tremolite +

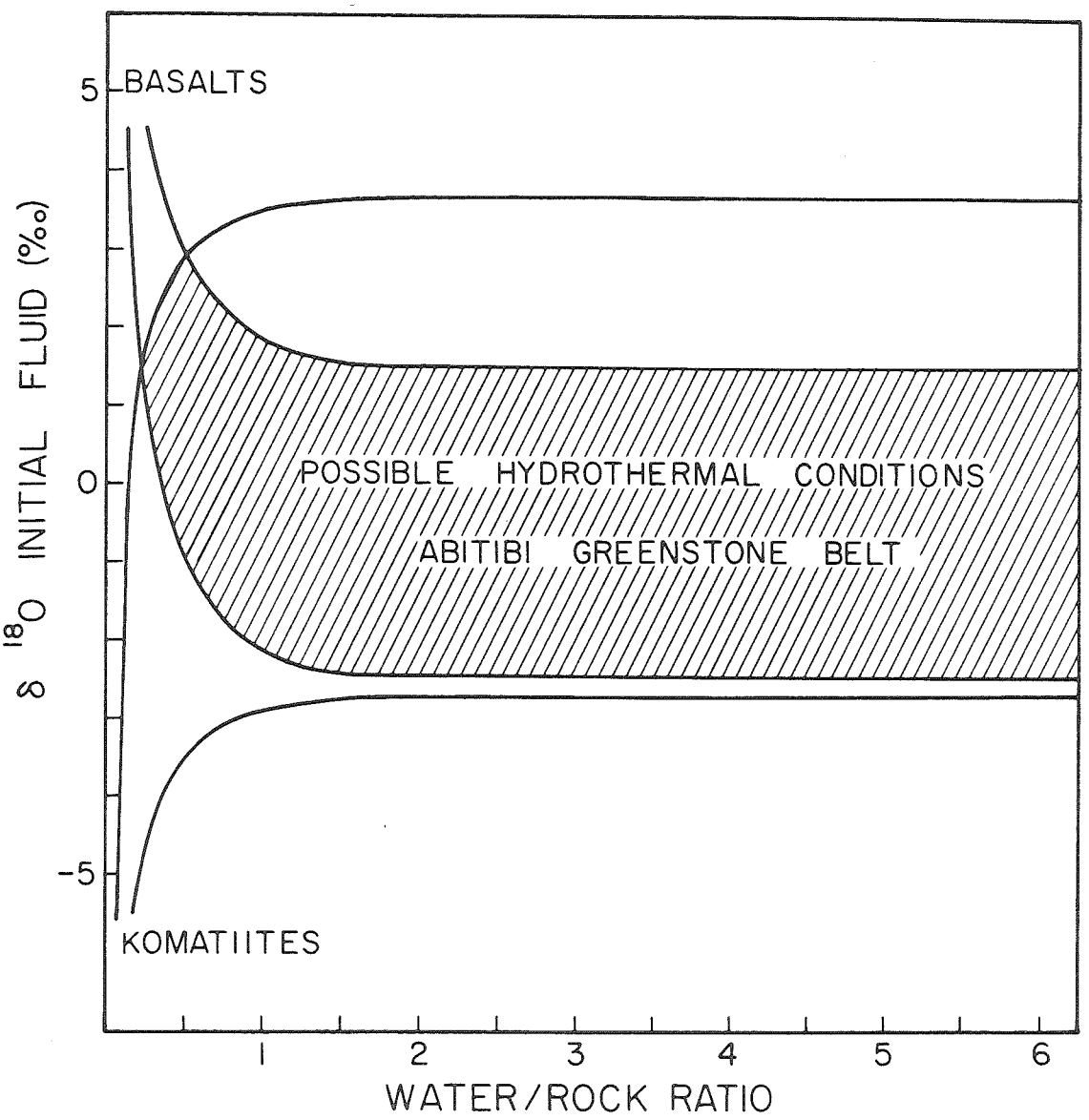

Figure 3F-7. If the komatiites and basalts were altered together, the hydrothermal conditions must lie within the field of coincidence. The basalt curve is from Fig. 3B-5 a,b,c, and the komatiite curve is from Fig. 3F-6.

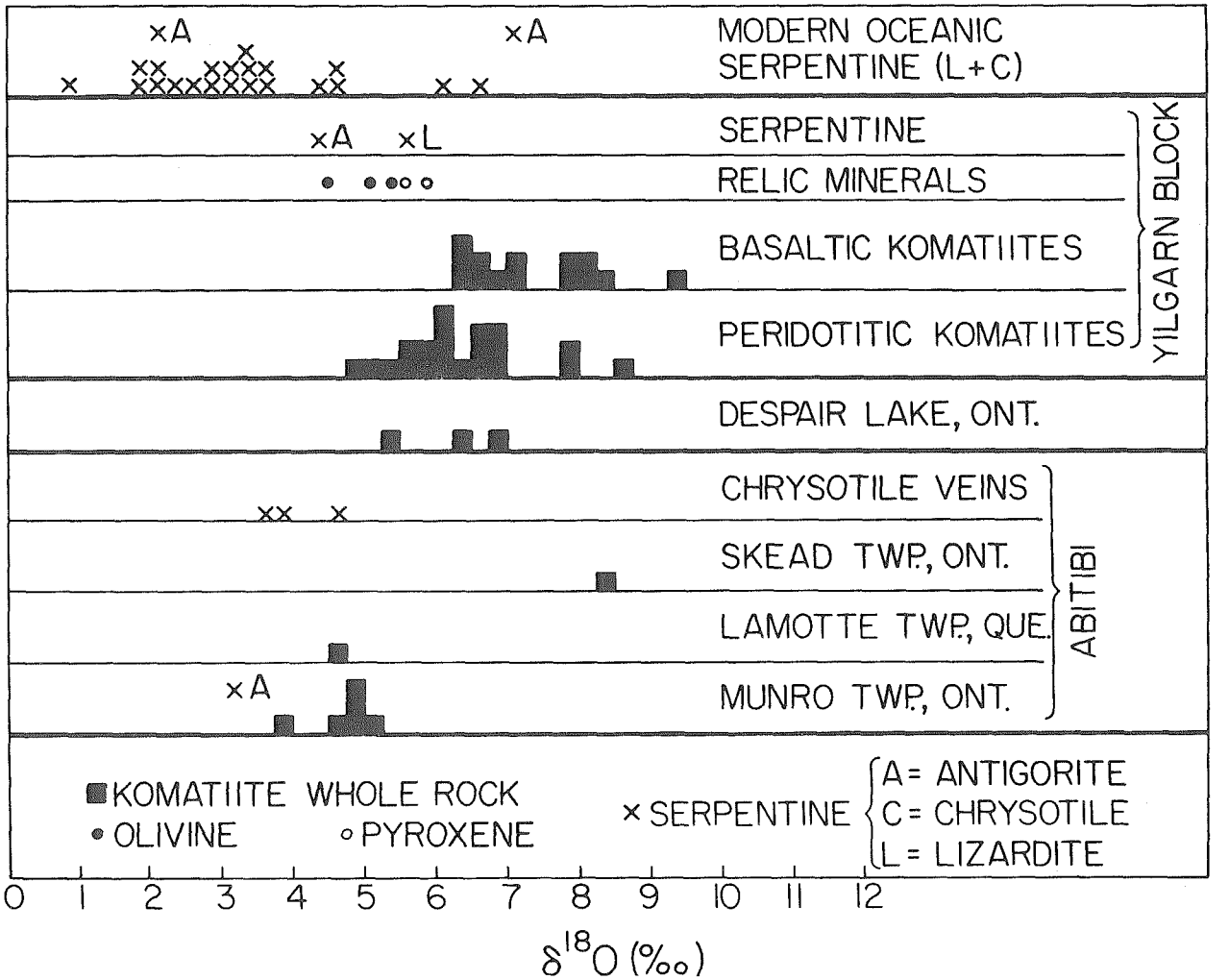

Figure 3F-8. Histogram of $\delta^{18}O$-values for all analyzed komatiites. Yilgarn Block data are from Hoefs and Binns (1978), Despair Lake data are from Longstaffe et al. (1977), and the Abitibi data are this work. Shown for comparison are modern oceanic serpentines from Wenner and Taylor (1973), along with one antigorite analysis (+7) from Magaritz and Taylor (1974).

chlorite + hematite + edidote + sphene. This komatiite is also chemically different from those in Munro and Lamotte Townships, containing only 14% MgO (vs. 20-35%), 15% CaO (vs. 3-9%) and 1.8% K_2O (vs. 0.01-0.10%). The K_2O concentration, the presence of hematite + epidote instead of magnetite, and the absence of serpentine suggest that this rock has been subjected to more complex hydrothermal processes than the Munro komatiites. This makes interpretation of the isotopic data very difficult. It is possible that the high-^{18}O character is related to the mineralogy: Tremolite and epidote (?) have a greater tendency to concentrate ^{18}O than serpentine and magnetite (O'Neil, 1977). A more likely possibility is that the Skead Twp. komatiites were altered at a lower temperature.

Some $\delta^{18}O$ data have also been collected for Australian komatiites by Hoefs and Binns (1978). In those samples the komatiites range from $\delta^{18}O = +5.0$ to $+9.4$ (Fig. 3F-8). If fresh komatiites started out at $\delta^{18}O = +5.7 \pm 0.3$, then these rocks show both increases and decreases in $\delta^{18}O$, similar to the Canadian results. The significance of these values is not clear, however, because of the incomplete petrographic data. The same conclusion applies to three analyses of ultramafic rocks ($\delta^{18}O = +5.3$ to $+6.8$) from the greenstone belts around Despair Lake, Ont. (Longstaffe et al. 1977).

V. CONCLUSIONS

Oxygen isotopic investigation of the Munro Township komatiites has led to the following conclusions. First, in spite of the excellent state of textural preservation, all of the komatiites analyzed have undergone oxygen isotopic exchange with very large quantities of hydrothermal fluid. This exchange manifests itself principally in the serpentinization of

olivine. Second, the hydrothermal fluid was apparently seawater or marine-derived pore fluids with $\delta^{18}O \approx 0 \pm 2$. Although the komatiite flows may have interacted directly with the ocean water they flowed into, probably most of the alteration was accomplished by seawater circulating deeply into the volcanic pile as the komatiites were buried and heated. Third, the $\delta^{18}O$ of the original komatiite magma was apparently +5.7 ± 0.3%. This value is indistinguishable from $\delta^{18}O$ of a wide variety of modern ultramafic rocks, including nodules in basalts, high-temperature peridotites, and the SE Alaskan intrusives. This suggests that $\delta^{18}O$ of the earth's mantle has not changed appreciably throughout geologic history.

CHAPTER 3G. TIMMINS AREA

Sixteen samples of volcanic rocks close to the town of Timmins, Ontario have been analyzed for $\delta^{18}O$. In addition, four samples from the Mt. Jameson area (15 km. west of Timmins), five samples from the Porquis Junction area (50 km. NE of Timmins) and a variety of rocks from the vicinity of the Kidd Creek mine (25 km. N of Timmins) were analyzed to improve the regional sampling of the volcanic rocks (Fig. 3G-1). The large Kamiskotia gabbro (30 km. W of Timmins) was also briefly studied (six analyses, see Chapter 5). Previous oxygen isotopic work within this area includes a detailed study of the Dome mine, a hydrothermal gold-quartz deposit 5 km. SE of Timmins (Kerrich and Fryer, 1979). Included in the Dome study are $\delta^{18}O$ analyses of several of the country rocks surrounding the mine.

I. GEOLOGY

The Timmins area lies at the western end of the Abitibi greenstone belt (Goodwin and Rider, 1970). The local geology has been described in many publications, but this summary is drawn from the recent reviews of Davies (1977) and Fryer et al. (1979). The Archean rocks around Timmins have been assigned to two supergroups, Keewatin and Timiskaming. The Keewatin consists of two groups, the Deloro and overlying Tisdale volcanics, which consist predominantly of subaqueous mafic volcanic flows, ranging from 70 to 150 m. thick, with interflow carbonate-sulfide facies chemical sediments including chert. Felsic schists (quartz-feldspar porphyries) overlie the mafic volcanics, and may include both subvolcanic and extrusive phases. Overlying these igneous rocks are carbonaceous schists, cherts, volcaniclastic greywackes, volcaniclastic conglomerates, slates and banded iron formations. Local unconformities are present,

TABLE 3G-1. OXYGEN ISOTOPIC AND PETROGRAPHIC DATA FROM THE TIMMINS, ONT. AREA

Sample	Field Description	$\delta^{18}O$ WR	$\delta^{18}O$ Min	Microscopic Description: Texture	Ave. gr. size	Secondary Mineralogy	% Rec.	Location: Lat.	Long.
Ti-1	8" wide qtz. vein cutting volcanics		14.0(q) 9.1(ch)					48°28.8'	81°18.8'
Ti-2	Sheared basalt, 2" from Ti-1	7.7		Equigr., veined	20	act, ep,chl	100	48°28.8'	81°18.8'
Ti-4	Core of pillow basalt, 20' from Ti-1	9.6		Equigranular	40	qtz, chl, cc, ep, act	100	48°28.8'	81°18.8'
Ti-5	Massive basalt, 200' from Ti-1	9.9						48°28.8'	81°18.8'
Ti-6	Well-foliated metadacite	12.3		Foliated, porph	200	qtz, musc, cc, chl	90	48°29.3'	81°18.7'
Ti-9	Fine-grained chlorite schist	10.2		Equigranular	50	qtz, chl, cc	100	48°29.2'	81°18.8'
Ti-10	Foliated felsic volcanic rock (dacite?)	9.4		Qtz porphyry	50	qtz, cc, musc	95	48°28.7'	81°18.8'
Ti-12	Metabasalt beneath Senator Hotel, Timmins	8.8		Equigr. foliated	50	qtz, act, chl, musc	90	48°28.6'	81°20.3'
Ti-15	Pillow basalt S of Timmins	11.1		Equigr. w. cc. veins	20	qtz, cc, chl, ep.	100	48°27.8'	81°18.3'
Ti-16	Well-foliated metabasalt S of Timmins	12.1						48°27.1'	81°17.5'
Ti-18	Hard, brittle, massive metabasite. Near Andesite mine	10.3		Qtz porphyry	50	qtz, chl, cc	90	48°26.7'	81°16.0'
Ti-19	Pillowed metabasalt	11.4		Equigr., heavily veined	20	qtz, chl, cc, musc	100	48°27.1'	81°15.8'
Ti-21	Metadacite near Dome mine	9.5		Qtz porphyry	20	qtz, cc, musc, act.	98	48°28.1'	81°14.1'
Ti-50	Metaandesite, shores of Skynner Lake	13.8		Qtz porph., veined	10	qtz, cc, chl, musc, act	95	48°26.0'	81°18.8'
Ti-51	Foliated metaandesite, Deloro Twp.	7.5		Felted, trachytic	40	qtz, chl, cc, ep, musc, act	70	48°24.3'	81°20.1'
Ti-52	Med. gr. metabasalt, Deloro Twp.	7.0	6.9(a) 8.0(nm)	Equigranular	300	qtz, act, ep, cc, chl	100	48°23.8'	81°19.9'
MT. JAMESON AREA									
Ti-47	Massive rhyolite w. local foliation	10.0		Equigranular	80	qtz, cc, musc, chl	90	48°31.4'	81°30.6'
Ti-48	Massive rhyolite with black, healed fractures	11.4	12.7(q)	Equigranular	80	qtz, chl, cc, musc	85	48°31.6'	81°30.8'
Ti-49	Massive rhyolite from base of Mt. Jameson	10.5		Equigr., foliated	80	qtz, chl, musc, act, ep	90	48°31.9'	81°30.6'
Go-2	Foliated, fractured metabasalt, Bristol Twp.	7.9		Equigr., veined	10	qtz, act, chl, ep, cc	100	48°20.8'	81°34.3'
KAMISKOTIA GABBRO									
Ti-32	Med. gr. gabbro. No layering, veining or structure.	5.6(c)	5.3(px) 5.9(pl)	Equigr., subophitic	500	qtz,chl,act,ep,musc	20	48°30.3'	81°44.8'
Ti-41	Recrystallized gabbro. Complex veining relations.	5.6(c)	5.5(a) 6.4(nm)	Equigr., foliated	300	qtz,act,ep,chl,musc	100	48°34.2'	81°44.3'
Ti-42	1" qtz vein cutting Ti-41		9.0(q)					48°34.2'	81°44.3'
Ti-36	1/2" qtz vein in gabbro		9.9(q)					48°31.5'	81°45.0'
PORQUIS JUNCTION AREA									
RG-23	near Porquis Junction	8.3						~48°42'	~80°46'
RG-36	near Porquis Junction	7.6						~48°42'	~80°46'
Ti-23	Course gr. metabasalt, 3 km N. of Monteith	6.4		Equigranular	1500	qtz, chl, ep, musc	60	48°39.9'	80°40.9'
Ti-24	Chloritc basalt, 1 km N. of Monteith	8.3		Equig., foliated	40	qtz, chl, act, ep	100	48°39.0'	80°40.9'
Ti-25	Fine gr. basalt, 5 km E. of Monteith	8.2						48°38.0'	80°36.7'

Abbreviations as in table 3B-1.

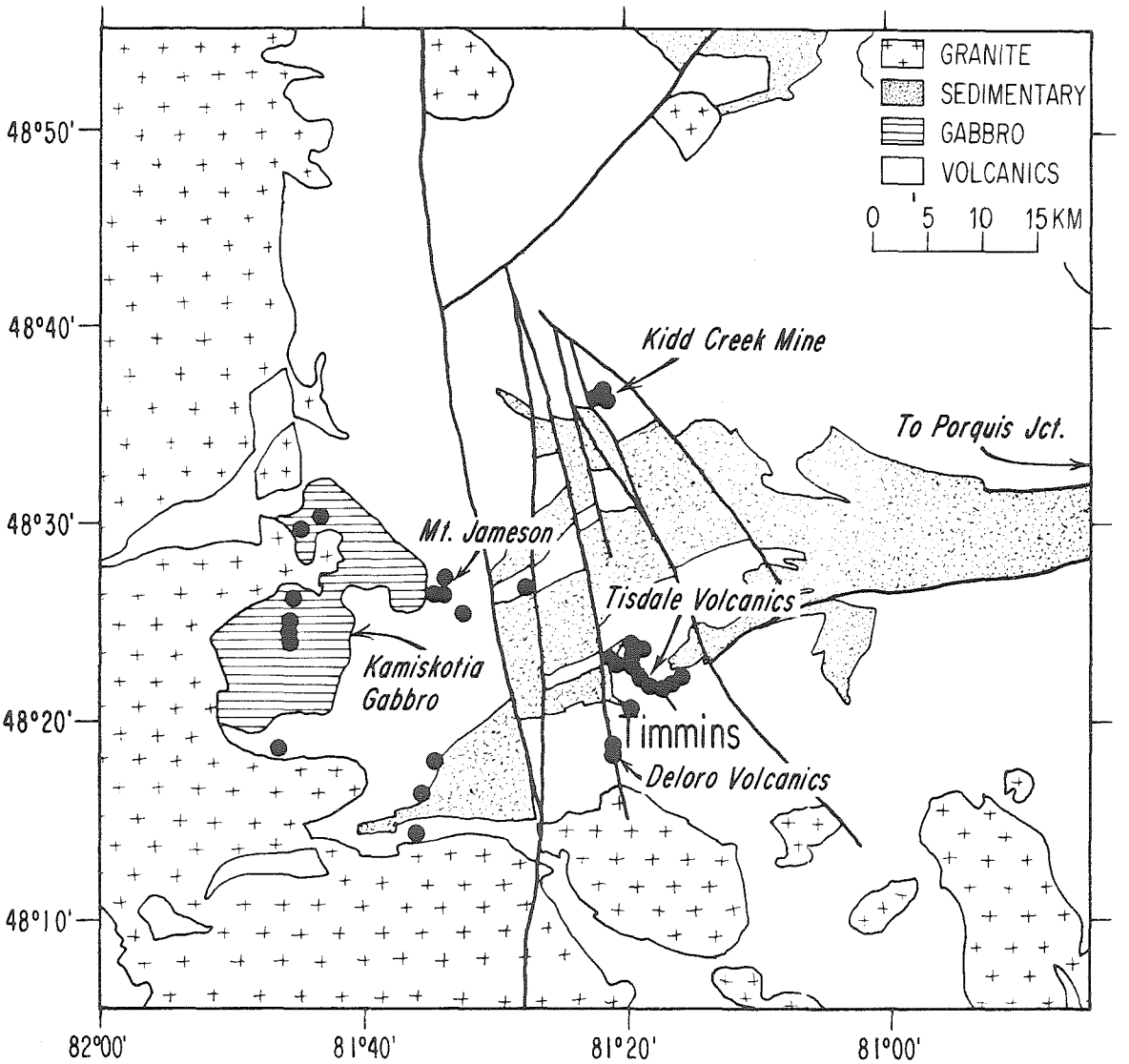

Figure 3G-1. Geologic map of the Timmins, Ont. area showing the sampled localities.

but the sedimentary section appears to be mainly coeval with the underlying volcanic rocks. Pyke (1975) has reported that the Deloro volcanics are predominantly calc-alkaline, whereas the Tisdale volcanics are predominantly tholeiitic. Using this, Jensen (1979b) has interpreted the volcanic rocks in the Kidd Creek - Porquis Junction area as being equivalent to the Deloro and Tisdale volcanics. The calc-alkaline rhyolites represent the uppermost Deloro group, and the mafic rocks represent the lowermost Tisdale.

The structure of the Timmins area is complex, characterized by two generations of folding and large-scale fracture systems developed during the Kenoran orogeny. For further discussion of these problems, see Davies (1977) and Roberts et al. (1978).

II. METAMORPHIC PETROLOGY

The volcanic rocks in the Timmins area are all recrystallized to the greenschist facies. Neither pumpellyite nor prehnite were observed (Table 3G-1), and this absence may be related to the presence of calcite, which is more abundant in this area than it is to the east (Fig. 3G-2c). The metabasalts are present both as foliated chlorite schists (Fig. 3G-2a) and as non-foliated rocks in which actinolite pseudormorphs the pyroxene (Fig. 3G-2d). For the rhyolites the secondary assemblage typically consists of quartz, muscovite, chlorite and calcite, and the rocks are generally fine-grained and equigranular (Fig. 3G-2b). The degree of petrographic recrystallization in the Timmins area is high, typically 90-100% (Table 3G-1).

III. OXYGEN ISOTOPE DATA

With the exception of one strongly sheared sample (Ti-2), whole-rock $\delta^{18}O$ values of 12 rocks in the immediate Timmins area range

Figure 3G-2. Photomicrographs from the Timmins area.

a.) Ti-9, transmitted light: foliated chlorite schist. Large diagonally-oriented light patch in the center is chlorite. Most of the volcanic rocks from this and other areas of the greenstone belt look like the lower left corner of this photograph - fine-grained, epnigranular and difficult to photograph.

b.) Ti-49, transmitted light. Fine-grained featureless intergrowth of quartz and feldspar in rhyolite. Cutting the rock is a quartz + epidote (high relief) veinlet.

c.) Ti-10, crossed polars. Large crystal of calcite filling a fracture in a fine-grained basalt. Calcite is more abundant in the Timmins area than elsewhere in the greenstone belt.

d.) Ti-52, crossed polars. Coarse-grained basalt recrystallized to qtz, chl, act, ep, cc. The field of view shows a large actinolite grain (white) surrounded by chlorite (dark). Although coarse-grained samples like this are unusual, they are the only ones which provide mineral separates.

e.) Ti-32, crossed polars. Gabbro consisting of plagioclase (twinned), opaque (lower left) and pyroxene (lower edge). The plagioclase is partially altered to fine-grained secondary minerals (upper right).

f.) Ti-41, transmitted light. Thoroughly recrystallized gabbro, now consisting of an amphibole schist.

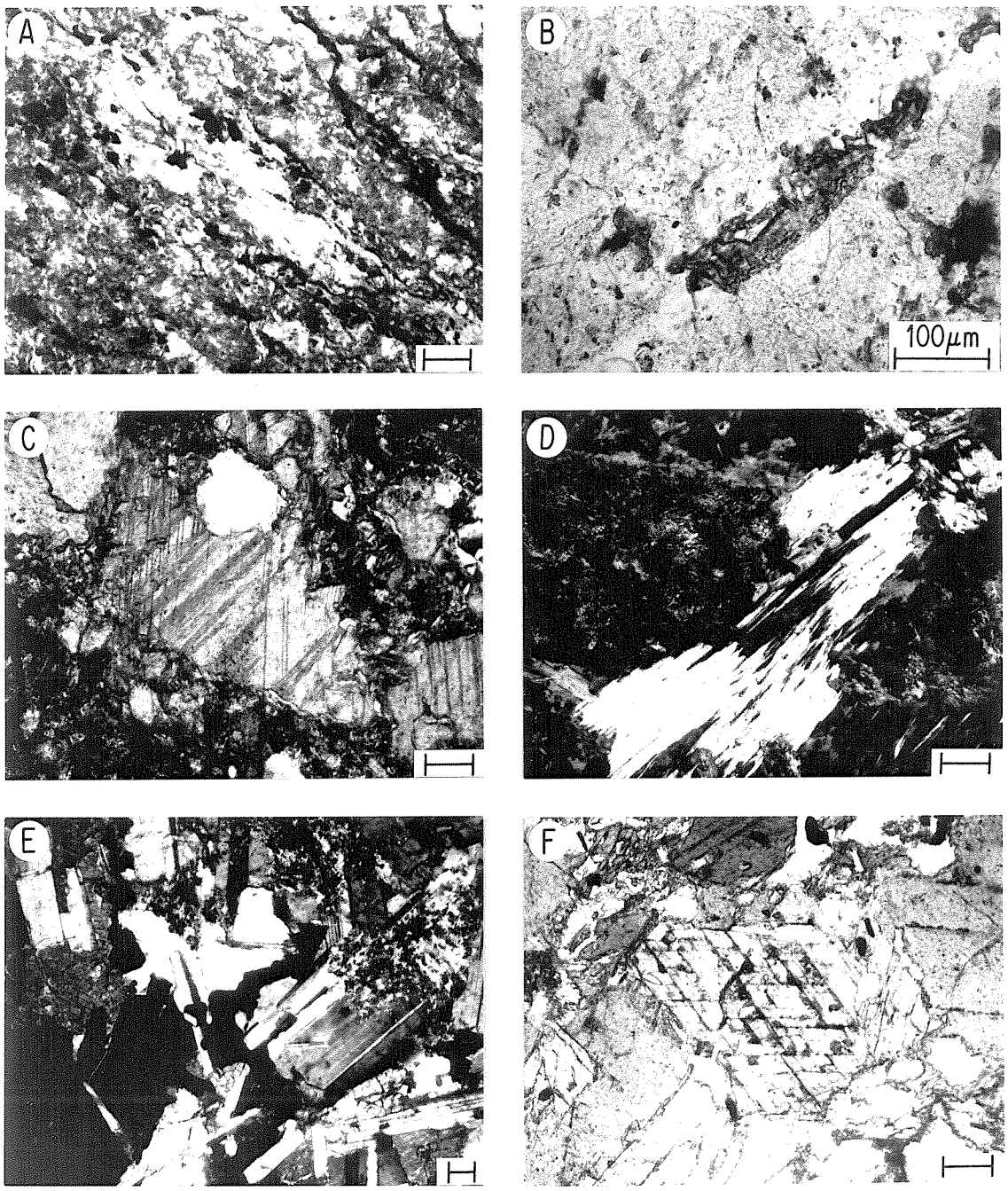
A
B
100μm
C
D
E
F

from +8.8 to +13.8. A quartz vein cutting basalt north of Timmins has $\delta^{18}O$ = +14.0 (Table 3G-1), and the quartz veins at the Dome mine have $\delta^{18}O$ = +14 to +15 (Kerrich and Fryer, 1979). Similar values are found in the vicinity of Mt. Jameson to the west of Timmins (+10.0 to +11.4; 3 samples), and high-^{18}O values are also present around the Kidd Creek mine N of Timmins (see Chapter 4B). Unmineralized andesite from the Dome mine ranges from +8 to +10, weakly mineralized andesite +11 to +14, and quartz-feldspar porphyry +9 to +10 (Kerrich and Fryer, 1979). The quartz-feldspar porphyry, incidentally, has reversed quartz-feldspar fractionation (qtz = +9.2, feld = +11.5), definite evidence for hydrothermal alteration (Kerrich and Fryer, 1979).

The entire Timmins area thus appears to be unusually enriched in $\delta^{18}O$ for some reason. Elsewhere, the Abitibi greenstone belt typically has $\delta^{18}O$ in the range +6 to +10; the Timmins area averages at least 3 per mil higher than that (Fig. 3G-3). The only low-^{18}O sample is the sheared basalt (Ti-2) alluded to above ($\delta^{18}O$ = +7.7). This sample may have undergone a more complex geologic history than its neighbors.

To the south of Timmins, $\delta^{18}O$ is lower and more similar to the rest of the Abitibi belt. Two samples from the Deloro Volcanics south of Timmins (Fig. 3G-1) have $\delta^{18}O$ = +7.5 and +7.0. Sample Go-2 from southern Bristol Twp (17 km. S of Mt. Jameson) has $\delta^{18}O$ = +7.9. Stratigraphically, both of these areas (Pyke, 1975; Jensen, 1979b) underlie the Tisdale volcanics. The total stratigraphic thickness present in the Deloro and Tisdale volcanics in this area is about 6 km (Pyke, 1975), but because of the intense structural complexities, no attempt was made to accurately measure the structural height of each analyzed sample. By plotting the approximate positions of these two sequences, however (Fig.

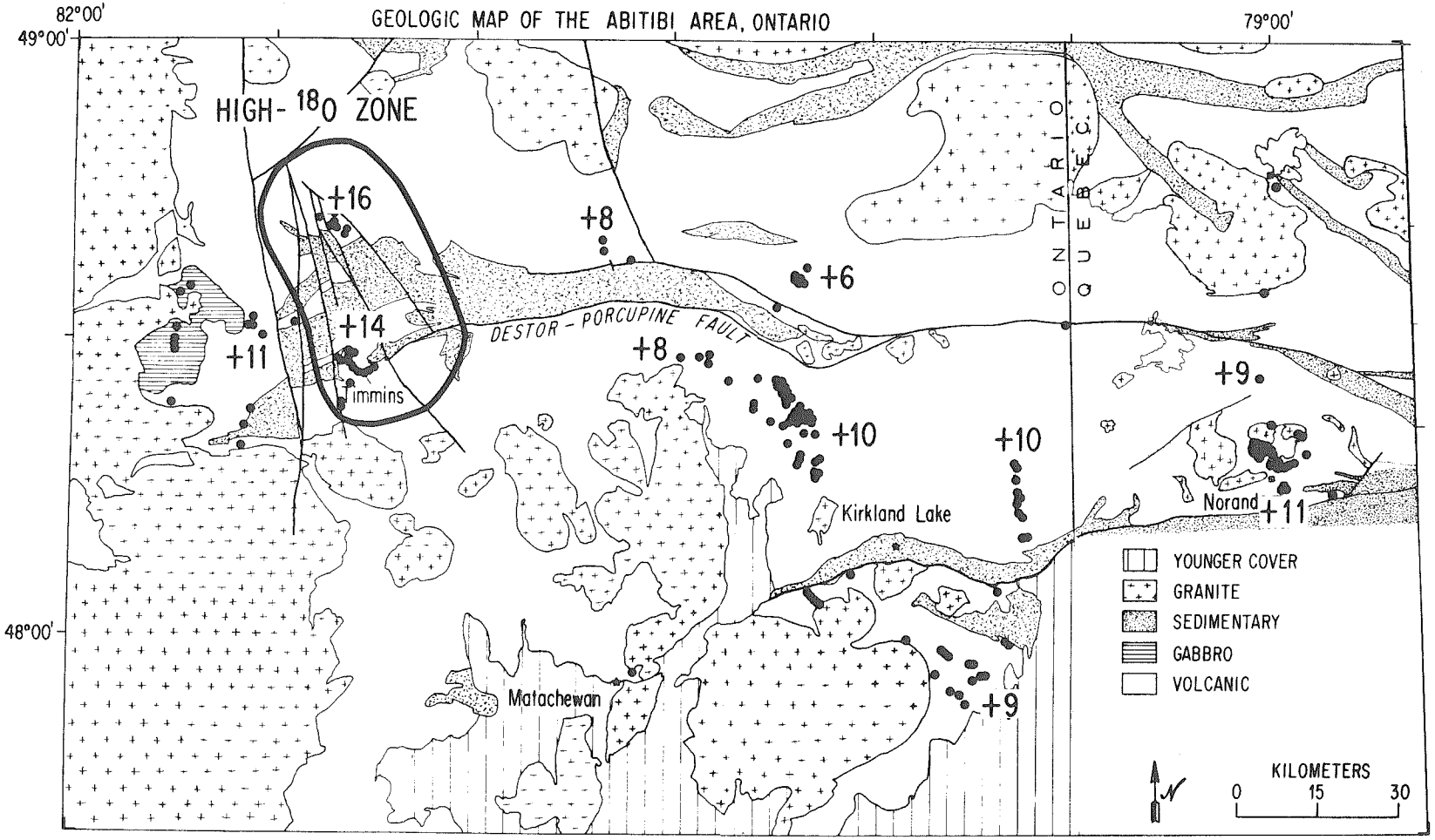

Figure 3G-3. Geologic map of the western part of the Abitibi greenstone belt, showing the sample localities. In each group of samples, the highest $\delta^{18}O$-value has been indicated. This emphasizes the high-^{18}O character of the Timmins area, which appears to extend north at least as far as the Kidd Creek mine.

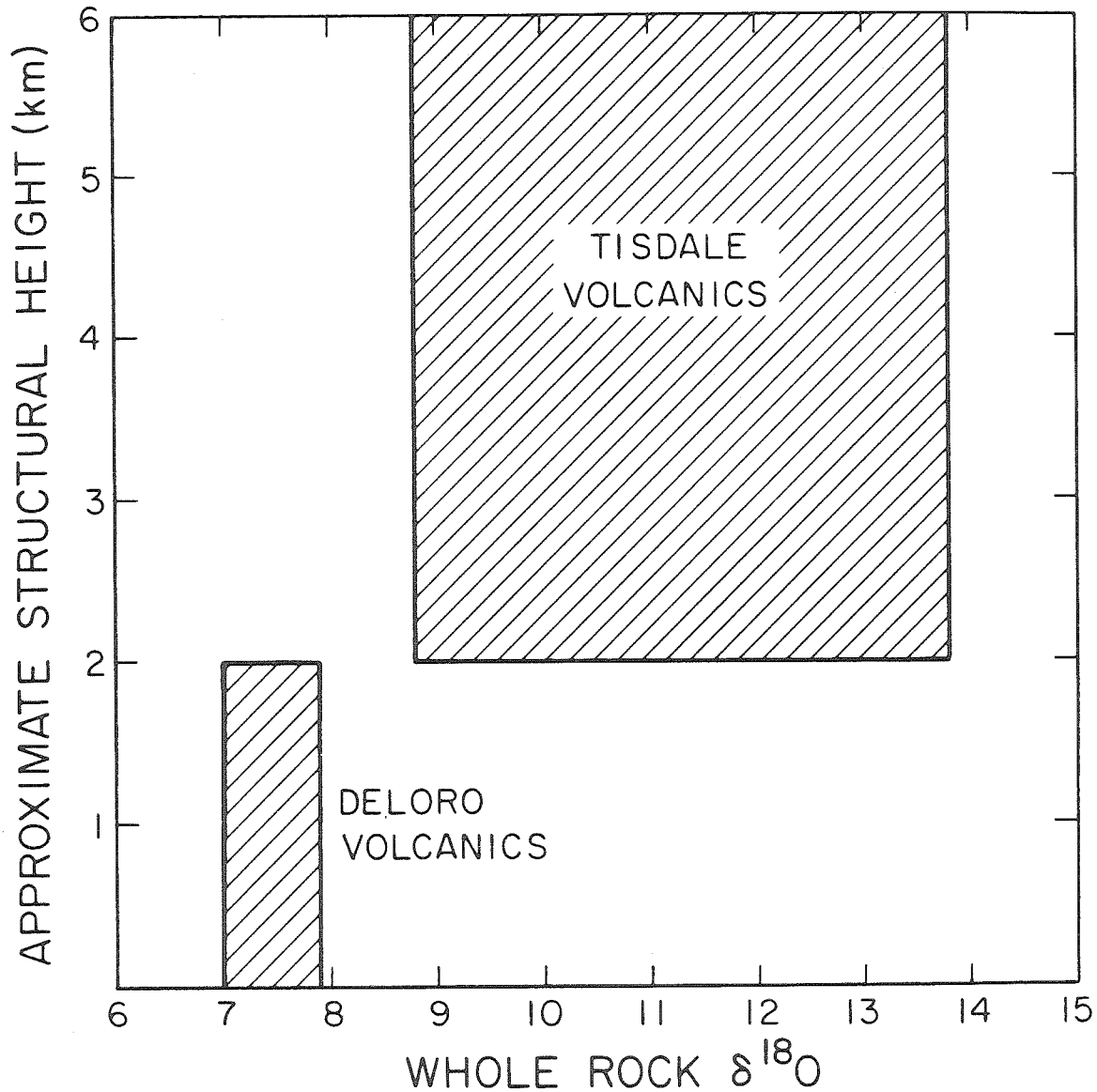

Figure 3G-4. Generalized relationship between whole-rock $\delta^{18}O$ and stratigraphic height in the Timmins area. The positive correlation is similar to that found in other portions of the greenstone belt.

3G-4), it is possible to illustrate the general variation of $\delta^{18}O$ with structural height. In common with the Benoit, Ben Nevis, Noranda, and Skead areas, there is a general $\delta^{18}O$ increase with stratigraphic height.

The rocks in the vicinity of Porquis Junction ($\delta^{18}O$ = +6.4 to +8.3) are thought to be stratigraphically equivalent to those of the Tisdale Group (Jensen, 1979b). The two areas are also similar mineralogically, the metabasalts being recrystallized in the greenschist facies. The Timmins area, however is 3-5 per mil richer in ^{18}O. It appears that the regionally high $\delta^{18}O$-values in the Timmins area do not extend as far east as Porquis Junction (a distance of 50 km.). The process responsible for producing the strong ^{18}O-enrichments around Timmins was apparently operative only locally.

The detailed variations in $\delta^{18}O$ around Porquis Junction can be ascribed to mineralogy. Ti-23 ($\delta^{18}O$ = +6.4) contains 40% large, relic pyroxene crystals, whereas Ti-24 (+8.3) is completely recrystallized (Table 3G-1). The more extensive recrystalliztion in Ti-24 has led to more extensive oxygen isotopic exchange.

III. FLUID COMPOSITION

In calculating $\delta^{18}O$ of the fluid responsible for the alteration effects, the inherent uncertainty in the temperature distribution precludes any firm answer to the question, "Why is the Timmins area higher in ^{18}O than the rest of the Abitibi greenstone belt?" By using different working hypotheses it is possible to place constraints on the problem, but it is not possible to find a unique solution. Consideration of the water/rock exchange equation (Eq. 2) indicates that there are four ways in which the high $\delta^{18}O$ values in the Timmins area could have arisen:

1. Initial $\delta^{18}O$ of the rocks was higher; 2. Water/rock ratio was different; 3. Temperature was lower; and 4. Initial $\delta^{18}O$ of the fluid was higher. The manner in which these variables relate to one another is illustrated in Figure 3G-5.

Initial high-^{18}O rocks. The possibility that the volcanic rocks in the Timmins area were initially higher in $\delta^{18}O$ than the rest of the greenstone belt is very unlikely. Although complex volcanic processes are known to produce high-^{18}O magmas under certain circumstances (e.g. Taylor et al. 1979) the relic igneous minerals in the Timmins area are all normal-^{18}O. Quartz phenocrysts in the quartz-feldspar porphyry near the Dome mine have $\delta^{18}O = +9.2$, along with reversed quartz-feldspar fractionations (Kerrich and Fryer, 1979), and the nearby Kamiskotia gabbro (which may be a subvolcanic feeder chamber) has normal $\delta^{18}O$ values of whole-rock = +5.6, plagioclase = +5.9, and pyroxene = +5.3.

Different water/rock ratio. Varying the water/rock ratio can change the post-isotopic exchange compositions of both materials. However, as seen in Figure 3G-5, the isotopic shifts are essentially indistinguishable as long as the water/rock ratio is greater than 2. Because the Timmins area rocks are richer in ^{18}O, W/R would have to be higher to account for it. However, the rest of the greenstone belt has also apparently been altered under high water/rock ratios (>2); hence increasing W/R at Timmins would have no effect.

Low temperature alteration. The rocks around Timmins could have been altered by unmodified seawater with $\delta^{18}O = 0$ if we assume that the temperature was relatively low, in the range 100°-180°C. Similarly, the isotopic data on the Deloro volcanics would imply alteration temperatures of 200-230°C. This possibility is a legitimate contender which cannot

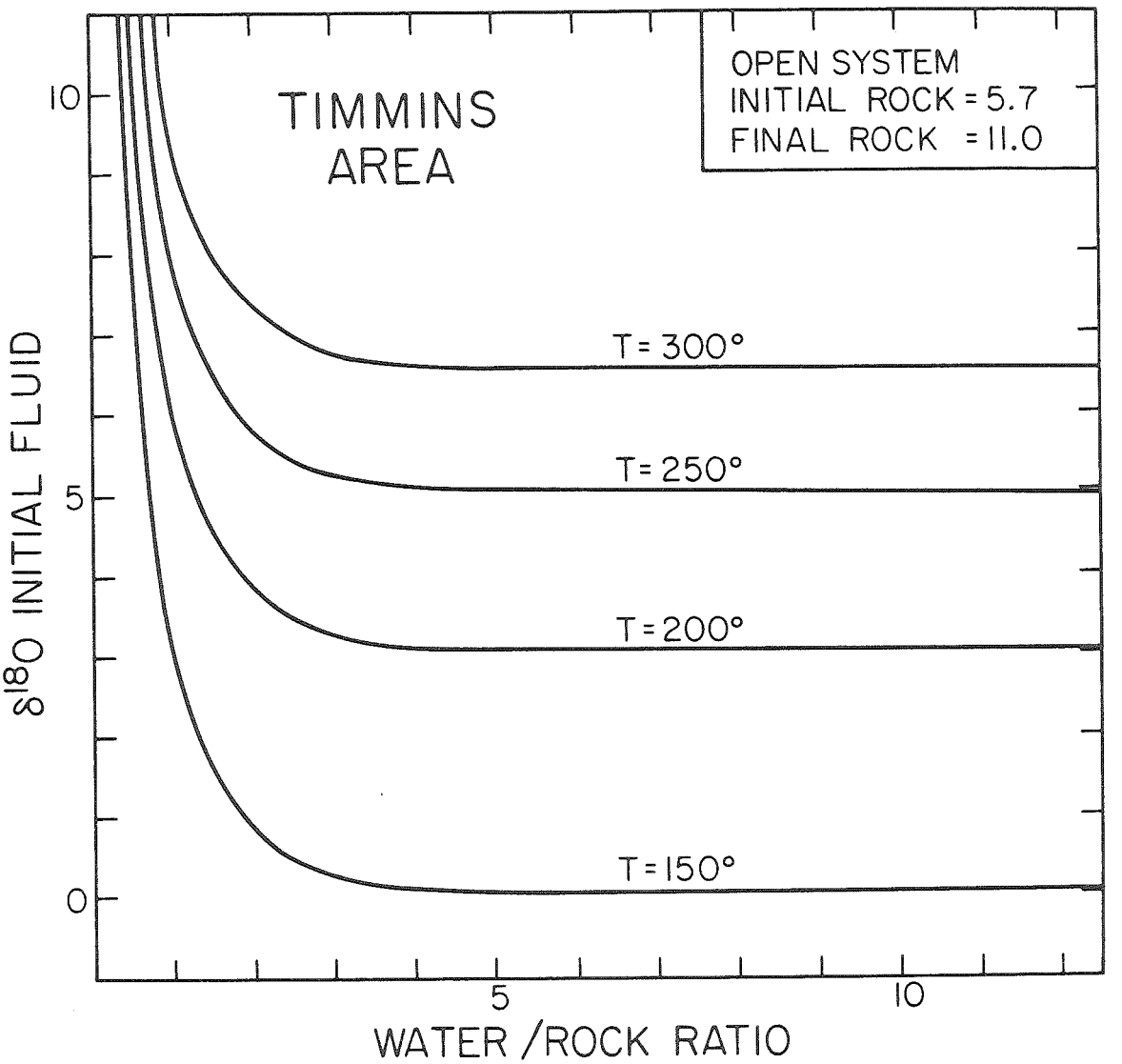

Figure 3G-5. Relationship between fluid composition, water/rock ratio and temperature for the water/rock interactions in the Timmins area.

be eliminated. However, it poses another question: "Why is the temperature of alteration apparently very systematic and similar elsewhere in the greenstone belt, but much lower around Timmins?"

High-^{18}O fluid. The final possibility is that the hydrothermal fluid was higher in ^{18}O than elsewhere in the greenstone belt. If the alteration temperature were 200-300°C, then the initial fluid composition as a function of water/rock ratio is displayed in Figure 3G-5. As long as the water/rock ratio is greater than about two, the initial fluid composition would have to been at least as high as +4. At lower water/rock ratios, the fluid would be even richer in ^{18}O, and the data are in fact compatible with a $\delta^{18}O$ as high as +10 for this fluid.

A high-^{18}O fluid is also suggested by the quartz vein data. Ti-1, a vein in central Tisdale Twp. has quartz with $\delta^{18}O$ = +14.0, and chlorite = +9.1. This is the highest-^{18}O vein measured in this study: Quartz veins from the Noranda area average +11 (Table 3D-1). These results are consistent with the extensive vein system at the Dome mine in southern Tisdale Twp., where the $\delta^{18}O$ of quartz veins ranges from +14 to +15. At the nearby Kidd Creek mine there are +11 quartz veins, but also highly altered rhyolites containing quartz with $\delta^{18}O$ = +15 in their groundmasses (Chapter 4B). The quartz veins in the Timmins area, therefore, like the whole-rock data, tend to be at least about 3 per mil richer than elsewhere in the greenstone belt. Thus, either all the quartz veins in the Timmins area formed at much lower temperatures than these elsewhere in the Abitibi belt, or the hydrothermal fluid was at least 3 per mil richer in ^{18}O.

There are several possible explanations for why the hydrothermal fluids were much higher in the vicinity of Timmins. A complete discussion

of these possibilities is deferred to Chapter 4B. Two of the most plausible, however, are that ocean water (initially $\delta^{18}O \approx 0$) either underwent extensive evaporation in a closed lagoonal basin, on the margins of the greenstone belt, or there was extensive oxygen isotopic exchange with the high-^{18}O sedimentary rocks that are particularly abundant around Timmins (Fig. 3G-1).

CHAPTER 4

$^{18}O/^{16}O$ RATIOS IN MASSIVE SULFIDE ORE DEPOSITS

CHAPTER 4A. GENERAL STATEMENT

One of the recurring uncertainties in the above discussion is the value of the water/rock ratio. In most of the calculations based on whole-rock data, the oxygen isotopic composition of the fluid and the water/rock ratio are determined together, but neither can be determined independently. In volcanogenic massive sulfide ore deposits, however, a stockwork zone of intense alteration is typically present in the footwall. It is through this stockwork that the ore-bearing solution is thought to have ascended. Because the ore-forming solution is likely to have been heated, recirculated seawater, studies of the alteration zones beneath massive sulfide bodies may provide the most compelling evidence concerning the oxygen isotopic composition of Archean seawater. Simple calculations relating the ore solubility to the masses of ore and altered rock indicate that water/rock ratios in the stockwork zones are commonly greater than 100. With this independent estimate of the water/rock ratio, the initial fluid composition can be calculated with more confidence.

To test these ideas, two massive sulfide bodies were selected for study. The Kidd Creek deposit near Timmins, Ont. (Fig. 3G-1) is one of the largest deposits of its kind known to man, hence the water/rock ratios beneath it should have been enormous. The mine is presently active, so excellent access to the stockwork zone was available. The Amulet "A" mine (near Noranda, Que.) is much smaller, and was selected because of its well-defined, concentrically zoned alteration pipe which

crops out at the surface. In the following discussion, these two deposits are analyzed separately, and then compared to geologically similar Phanerozoic massive sulfide bodies.

CHAPTER 4B. THE KIDD CREEK MINE

The Kidd Creek mine is located in the NE corner of Kidd Township, 27 km. north of the town of Timmins, Ont. (Fig. 3G-1). The ore deposit was discovered in 1963 and since has proved to be one of the world's greatest ore bodies. Reserves to the 2,800 ft. level are 95 million tons, but the deposit is known to extend down to at least 4,100 feet and the lower limit has not yet been discovered. The mine has been described as the world's largest single producer of zinc, cadmium and silver (Walker et al. 1975).

I. GEOLOGY

The Kidd Creek mine is located within a volcanic complex about 50 km. in diameter which contains a high proportion of felsic volcanic rocks. This is an area of great structural complexity and little outcrop. This led Berry (1941) to state "it was impossible to work out the age relations of the various rock types found in the area," and his words are almost as applicable today as they were four decades ago (Walker et al. 1975).

The Kidd Creek massive sulfide deposit is a stratabound body occurring within a sequence of steeply dipping, overturned felsic and mafic volcanic rocks. Intercalated with, and less commonly, cross-cutting these strata are bodies of serpentinite and peridotite (Walker et al. 1975). Stratigraphically underlying the massive ore is a volcanic sequence composed of rhyolite volcaniclastics and conformable to irregular bodies of massive rhyolite (Fig. 4B-1, 4B-2). On the East Outcrop these massive rhyolites appear to be intrusive, but elsewhere flows or welded tuffs may exist (Walker et al. 1975). It is within this rhyolite pile that the stockwork alteration zone is developed, so a great number of

TABLE 4B-1. OXYGEN ISOTOPIC AND PETROGRAPHIC DATA FROM THE KIDD CREEK MINE

Sample	Field Description	$\delta^{18}O$ WR	$\delta^{18}O$ Min	Microscopic Description: Texture	Ave. Gr. Size	Secondary Mineralogy	Musc.	Chl.	Cc.
DIAMOND DRILL HOLE J-628									
620.6'	rhyolite tuff	11.9		Porph (qtz)	5	qtz,musc,chl	20	15	0
640'	massive rhyolite	11.0		Porph (qtz)	5	qtz,musc,cc,chl	40	1	3
659.6'	brecciated rhyolite	12.9		Porph foliated	20	qtz,musc,cc,chl	15	5	1
679'	brecciated rhyolite	12.5		Porph. (qtz)	20	qtz,musc,chl	20	5	0
699'	flowy rhyolite	12.8		Equig., foliated	10	qtz,musc,chl	30	10	0
719.8'	flowy rhyolite	13.0	13.6(q')	Porph., foliated	10	qtz,musc,cc,chl	15	5	tr.
739'	rhy., more msv., less fract.	12.5		Equig., foliated	5	qtz,musc,cc,chl	30	10	3
759'	rhy., more msv., yellow ser. alt.	13.9		Porph., foliated	5	qtz,musc,cc	30	0	6
779.6'	msv. rhy., less altered	13.9		Porph., foliated	10	qtz,musc,cc,dolo	20	0	3
803'	black rhyolite, unaltered	14.6		Porph. (qtz)	10	qtz,musc,cc	15	0	8
824.2'	sl. altered massive rhyolite	13.0		Porph., veined	5	qtz,musc,cc,dolo	30	0	5
844'	mod. altered, massive rhyolite	14.9		Porph., foliated	5	qtz,musc,cc,ep?	20	0	3
864.5'	mod. altered massive rhyolite	14.0		Porph. foliated	10	qtz,musc,cc	20	0	1
944.5'	altered, flowy-textured rhyolite	13.9		Porph., veined	10	qtz,musc,cc,chl,ep	15	15	8
980'	msv. black rhy., slight fract.	13.6		Equigr.	5	qtz,chl,musc	15	30	0
999'	flowy rhyolite	12.9		Porph, veined	10	qtz,musc,ep,chl	15	10	0
1014'	tuffaceous rhyolite	13.3		Porph., foliated	10	qtz,chl,musc,ep?	20	20	0
1033.5'	tuffaceous rhyolite	14.4		Equig., veined	10	qtz,musc,chl	30	30	0
1044.5'	fractured, flowy rhyolite	14.6	15.5(q')	Porph., veined	5	qtz,musc,ep,cc,chl	20	15	3
1064'	rhyolite tuff	13.5		Porph., foliated	20	qtz,musc,chl	20	15	0
1124'	Well-foliated rhyolite	12.7		Porph., foliated	10	qtz,musc,cc,ep,chl	50	2	8
1144.2'	rhy. tuff, w. coarse blocks	13.7		Porph., foliated	5	qtz,musc,cc,chl,ep?	40	5	10
1160'	msv. rhy. w. plag. plenos.	14.1		Porph., veined	5	qtz,musc,cc,chl,ep?	30	20	2
1174.2'	msv. rhy. w. plag. plenos.	13.6		Porph., foliated	5	qtz,musc,chl,cc,ep?	10	30	5
1217.6'	black rhy. w. flow banding, no alt.	13.6	14.2(q')	Porph., veined	10	qtz,musc,cc,chl,ep?	30	20	2
1600 LEVEL, NORTH ORE BODY									
KC-1 matrix	1621 crosscut, #6 drawpoint, frag. rhy.	12.5		Equigr., veined	10	qtz,musc,cc,chl	15	2	2
KC-1 clast	1621 xc, #6 d.p., frag. rhy.	10.8							
KC-5	1621 xc, #7 d.p., rhyolite	12.7							
KC-7	1" wide, E-W qtz vein		11.9(q)						
KC-8	1621 xc, #4 d.p., rhyolite	10.4							
KC-10	2' wide qtz vein w. chloritic margin		11.8(c)						
KC-12	1621 xc, #1 d.p., qtz. vein in stockwork		11.9(q)						
KC-14	1621 xc, #1 d.p., frag. rhy.	10.0							
KC-15	1625 xc, #2 d.p., andesite/diorite	8.1							
KC-17	1631 xc, qtz porphyry	11.4		Porph. (qtz)	20	qtz,musc,biot,cc			
KC-18	#1 shaft, pillowed dacite	8.3		Equigr. veined	20	qtz,act,ep,cc,chl			
EAST OUTCROP									
KC-19	msv. black rhy. w. flow banding	14.5		Porph. (qtz,pl)	10	qtz,musc,cc,chl	5	30	tr.
KC-20	frag. rhy. from between blocks	14.5		Porph. (qtz,pl)	10	qtz,musc,cc,chl	10	20	tr.
KC-21	1' massive rhy. block	13.5		Equigr., veined	20	qtz,musc,cc,chl	5	10	1
KC-22	tuffaceous rhy., 1' from KC-21	10.9		Porph. foliated	5	qtz,musc,cc,chl	50	5	1
KC-24	core of msv. rhy. unit 15' thick	12.0		Porph., veined	10	qtz,musc,cc,chl	15	15	tr.
KC-25	lapilli-sized rhyolite breccia	11.7		Porph., veined	5	qtz,musc,cc,chl	30	5	1
KC-26	brecciated rhyolite	14.9		Porph. veined	5	qtz,musc,cc	50	0	2
KC-27	margin of 2' massive rhy. block	15.7							
KC-28	core of same block as KC-27	15.8		Porph.	10	qtz,musc,cc,chl	5	10	tr.
KC-30	rhyolite breccia S. of E. outcrop	10.8		Porph., foliated	10	qtz,musc,cc,chl	30	10	1
KC-31	diabase dike S. of E. outcrop	8.8		Equigranular	150	qtz,act,ep,chl,cc			
MARTIN'S OUTCROP									
KC-33	dacite	8.2		Equigr. veined	80	qtz,act,ep,cc			
KC-34	dacite	8.2		Equigr. veined	30	qtz,act,ep,chl,cc			
KC-35	dacite	8.5		Equigr. foliated	30	qtz,act,ep,chl			
KC-36	coarse dacite	8.3		Porphyroblastic	600	qtz,act,ep,chl,musc			
KC-37	andesite/diorite or dacite	9.7		Equigranular	200	qtz,act,ep,chl,cc			
RHYOLITES NEAR KIDD CREEK (collected by P. Coad)									
7589	feld-qtz porph. 7400' E of Kidd Creek	10.2		Seriate porph.	100	qtz,act,ep,musc,chl	15	5	0
7590	feld-qtz porph. 7400' E of K.C.	10.6		Seriate porph.	150	qtz,musc,cc,chl	15	5	1
7591	qtz. porph., S. Orebody, K.C. Mine	12.1		Porph., foliated	5	qtz,musc,chl	20	10	0
7592	alb. porph. rhy. 2400' E of K.C.	12.2		Porph., veined	10	qtz,musc,biot.	5	0	0
7593	msv. rhy., 4800' N. of K.C.	13.0		Equig., veined	10	qtz,chl,musc	5	30	0
7594	rhyolite, 4800' N. of K.C.	11.5		Equigranular	20	qtz,cc,musc	30	0	15
7595	alb. porph. rhy. 5000' of K.C.	11.3		Seriate porph.	100	qtz,musc,cc,chl	20	2	5
7596	alb. porph. rhy. 5000' of K.C.	11.0		Seriate porph.	100	qtz,musc,cc,chl	20	tr.	3
7597	msv. rhy. 3400' E of K.C.	11.8		Porph. veined	20	qtz,cc	0	0	5
7599	rhyolite from Kam-Kotia Mine	10.7		Porph., foliated	10	qtz,musc,cc,biot.	15	0	2
7601	qtz, alb. porph rhy. 1500' W. of K.C.	12.7		Porph., foliated	10	qtz,chl,musc	20	20	0
7602	qtz, alb. porph rhy. 1500' W. of K.C.	14.1		Porph., foliated	10	qtz,chl,musc,cc	20	20	1
7603	msv. rhy. 3600' E of K.C.	11.8		Porph., foliated	10	qtz,musc,biot,cc	5	0	1

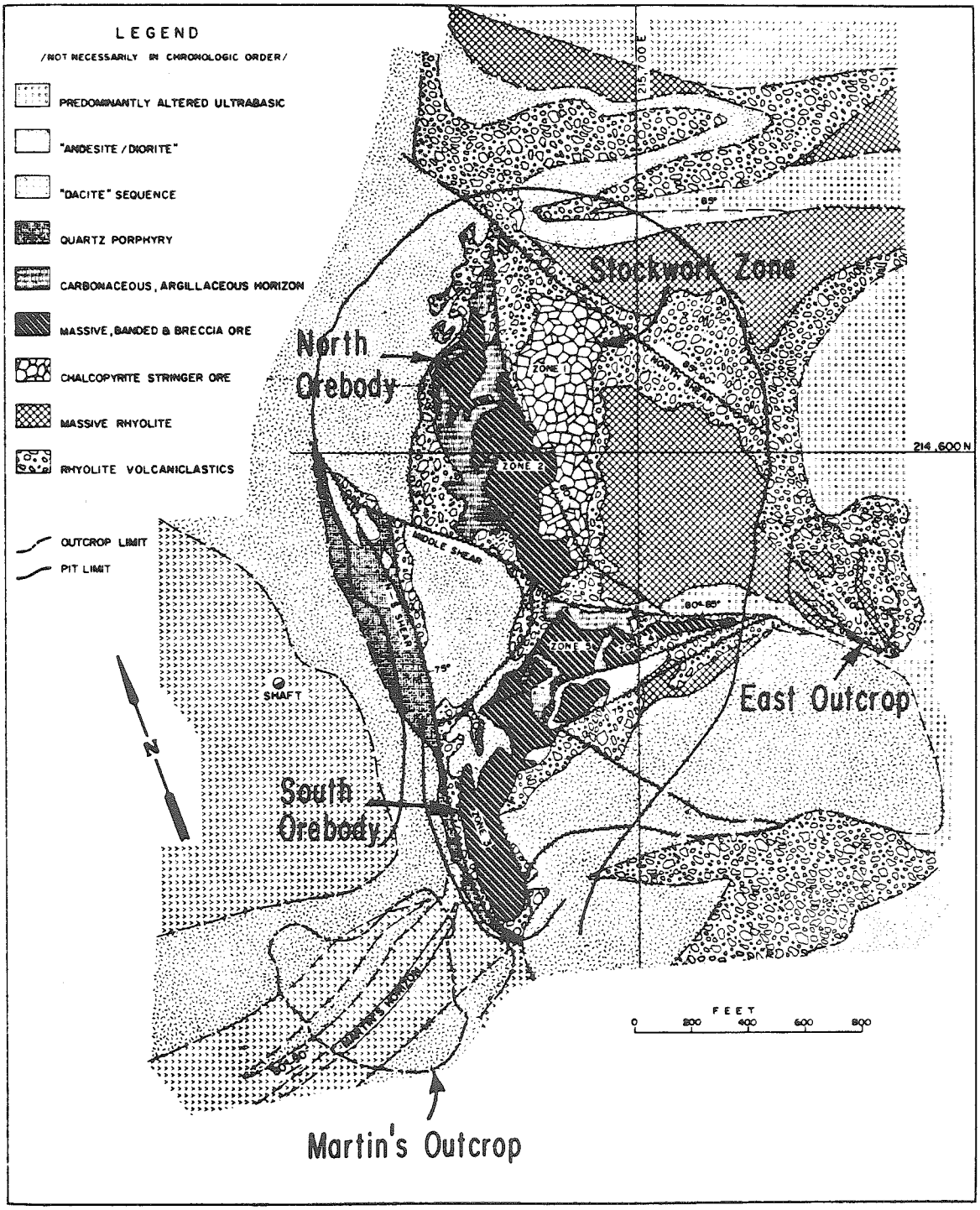

Figure 4B-1. Geologic map of the Kidd Creek mine (modified from Walker et al. 1975) showing the general sample localities.

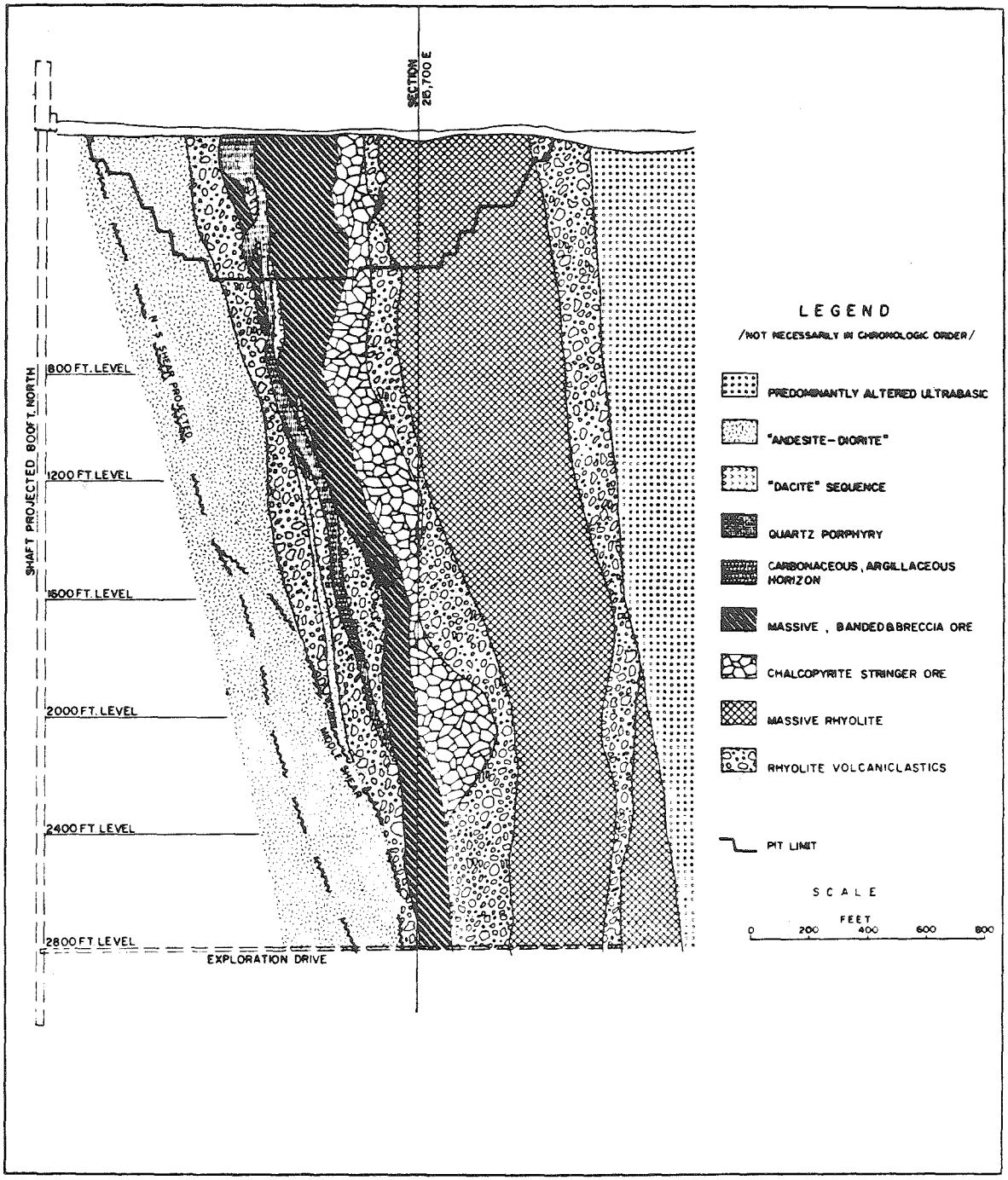

Figure 4B-2. Cross section of the Kidd Creek mine (from Walker et al. 1975). Hole J-628 was drilled horizontally to the right from the 2400 level.

samples were collected from this unit. Associated with the massive, banded ore is a sedimentary carbonaceous horizon (Fig. 4B-1, 4B-2) which consists of carbonaceous argillites, slates and cherts, along with heterogeneous volcaniclastics. Overlying the massive ore is a porphyritic rhyolite (Fig. 4B-1) containing quartz and feldspar phenocrysts which locally shows a coarse, tuffaceous texture. Overlying that is a sequence of basaltic to andesitic volcanic rocks (Fig. 4B-1) commonly pillowed, with numerous thin, intercalated interflow sedimentary horizons.

Two other rock types locally intrude this stratigraphic section, and may represent subvolcanic intrusions. In the pit area, the andesite/diorite occurs as three large masses which are thought to be intrusive (Fig. 4B-1), but beyond the pit the unit may also be extrusive. A large area east of the pit is underlain by serpentinite and talc-carbonate rocks (Fig. 4B-1) which locally exhibit spinifex textures: These rocks are thought to represent either extrustions or subvolcanic intrusions (Walker et al. 1975).

II. PETROLOGY

Petrographic study indicates that all of the rocks in the Kidd Creek area have been thoroughly recrystallized and are now full of secondary, hydrous minerals. Thus they have all clearly interacted with hydrothermal fluids of some sort. It is possible that several different fluids were involved in these hydration reactions. For example, hydrothermal alteration associated with the formation of the sulfide deposit may have affected the underlying rocks, and fluids associated with burial metamorphism may have subsequently affected the entire volcanic pile. To fully evaluate the water/rock interactions, the petrology and oxygen isotopic data of each of the geologic units at the mine are considered

separately.

III. OXYGEN ISOTOPE DATA

The oxygen isotope data are presented unit by unit in descending stratigraphic order, because that is the order of increasing complexity. All of the data are shown together on Figure 4B-3 for comparison.

1. Andesite/diorite (post-ore)

Within the limits of the Kidd Creek open pit, the post-ore andesite/diorite is thought to be intrusive into the hanging-wall volcanic section, but outside the pit, the unit includes both intrusive and extrusive phases (Matulich et al. 1974; Walker and Mannard, 1974; Walker et al. 1975). The unit was sampled in three widely separated places: KC-15 is from the 1625 crosscut (N. Orebody), KC-31 is from the south margin of the East Outcrop, and KC-37 is from the south end of Martin's Outcrop (Fig. 4B-1). Isotopically, these samples range from $\delta^{18}O$ = +8.1 to +9.7 (Figure 4B-3). These values are similar to those from the pillowed dacite sequence and mafic volcanic rocks from elsewhere in the Abitibi greenstone belt (Fig. 3A-2).

2. Dacite sequence (post-ore)

Five samples of the post-ore dacites were analyzed (four from Martin's Outcrop and one from the shaft) and the $\delta^{18}O$ values range from +8.2 to +8.5 (Figure 4B-3). Isotopically, these rocks are compositionally similar to the andesite/diorite and to mafic volcanic rocks from elsewhere in the Abitibi belt. Large suites of samples from the Blake River and Skead sections, for example, give $\delta^{18}O$ values in the range +6 to +10 with an average of about +7.5. Both of these volcanic piles are interpreted to be slightly enriched in ^{18}O from their primitive values of +5.7 ± 0.2 through interaction with Archean marine pore fluids (Beaty

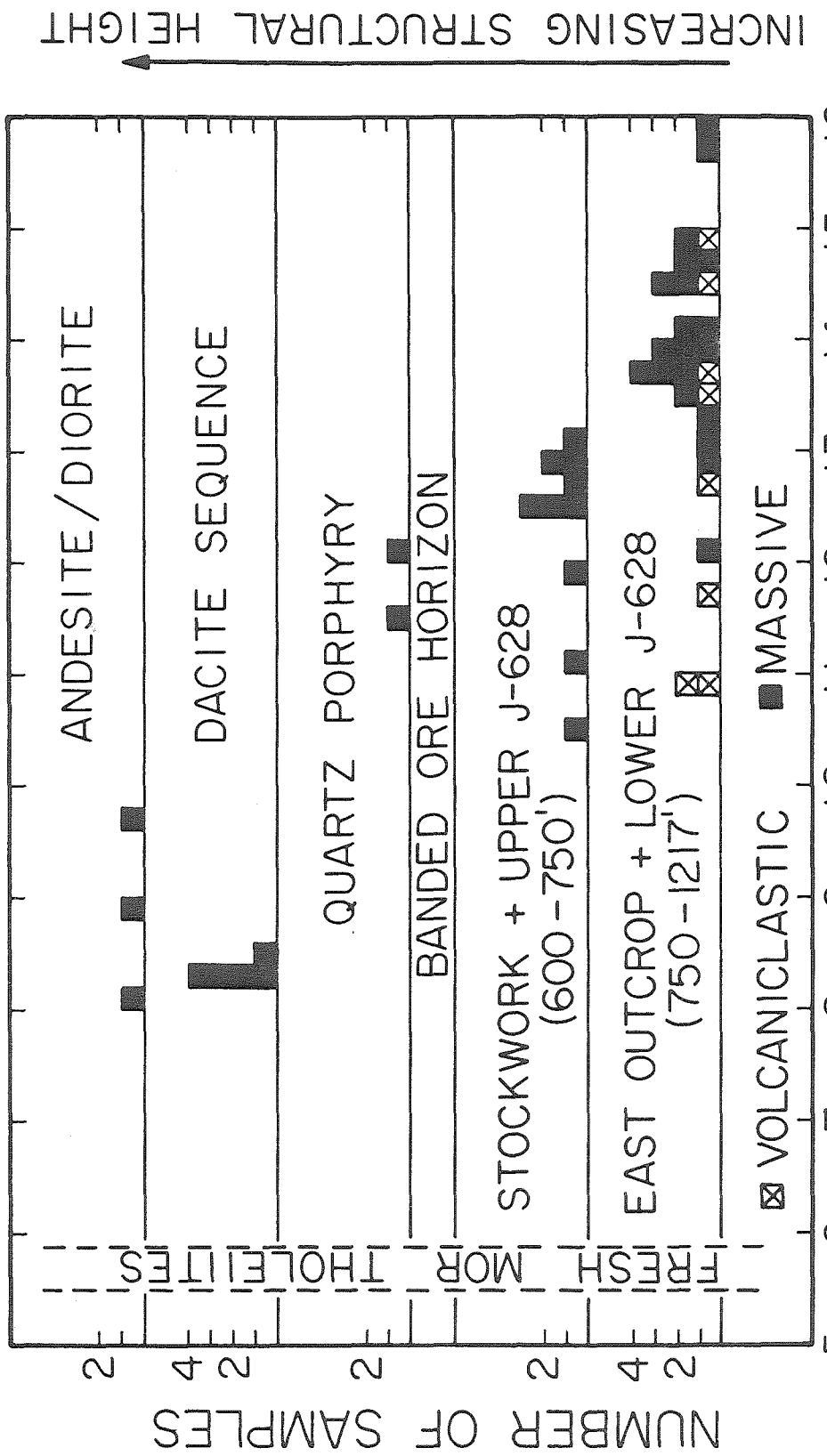

Figure 4B-3. Comparison of $\delta^{18}O$ of the various geologic units present at the Kidd Creek mine. All of the rocks are much richer in ^{18}O than mid-ocean ridge tholeiites, particularly the rocks which underlie the massive, banded ore.

and Taylor, 1979). These enrichments were apparently caused by hydrothermal exchange during burial metamorphism, and similar effects are found in greenstone belts throughout the world (See Chapter 6). The data from the Kidd Creek dacite and andesite/diorite suggest that after ore deposition, both of these volcanic rock units underwent the same type of low-temperture metamorphism and hydrothermal alteration that is observed throughout the Abitibi belt.

3. Quartz Porphyry

Two samples of the quartz porphyry have been analyzed. KC-17 is from the 1631 crosscut 200' west of the footwall drive, N. orebody, and has $\delta^{18}O = +11.4$. Sample 7591 is from an unknown location on the 1200 level, South orebody, and has $\delta^{18}O = +12.1$. The quartz porphyry ranges from 250 to 500 ft. thick (Walker and Mannard, 1974), and although it is generally massive, highly altered, and schistose, locally a coarse tuffaceous character can be recognized (Walker et al. 1975, p. 82).

Fresh rhyolites associated with Phanerozoic calc-alkaline (andesitic) volcanic terranes typically have $\delta^{18}O \approx +7$ to $+8$ (Taylor, 1968). The fact that the quartz porphyry now has $\delta^{18}O \approx +12$ indicates that it is either (1) hydrothermally altered; or (2) its parental magma was formed by some unusual process. High-^{18}O magmas could have been produced, for example, by partial melting of subducted oceanic crust that had previously been hydrothermally altered, or by various other mechanisms involving the melting of a high-^{18}O source region. The different possible origins probably could be unambiguously distinguished by analyzing the quartz phenocrysts (which are extremely resistant to hydrothermal exchange and often preserve their original magamatic values), but all efforts at separating the phenocrysts from the groundmass of this rock

have proved fruitless.

With the above-noted reservation, it is tentatively assumed that the distinctive isotopic character of the quartz porphyry (and other ^{18}O-enriched rocks at Kidd Creek) was produced by hydrothermal alteration. This is consistent with the observations of Walker et al. (1975) who found the quartz porphyry to be highly altered. It is also consistent with the reversed quartz-feldspar oxygen isotope fractionations found by Kerrich and Fryer (1979) in the ^{18}O-enriched quartz-feldspar porphyries at the nearby Dome mine (located about 30 km. from the Kidd Creek deposit).

4. Carbonaceous Horizon

No samples were analyzed.

5. Massive Banded Ore

No samples were analyzed due to the low abundance of silicates.

6. Rhyolites

The rhyolites stratigraphically underlying the massive, banded ore were sampled in three places; the East Outcrop, diamond drill hole J-628, and in the chalcopyrite stringer zone underground (1600 L, N. Orebody, Zone 1 on Fig. 4B-1). The rhyolites can be separated into two units, massive and volcaniclastic, and this distinction must be considered along with the locations in interpreting the data.

DDH J-628 drill hole. Drill hole J-628 (N 45 E, flat, 2400 L, N) intersects the base of the massive banded ore at 606', and then penetrates a series of alternating massive and tuffaceous rhyolites, reaching a total depth of 1217' (Fig. 4B-4). The cores of the massive rhyolite units are typically black and undeformed. Both the upper and lower margins of these massive units have a distinctive streaked texture which has been termed "flowy" texture (P. Coad, per. comm., 1978). The fragmental

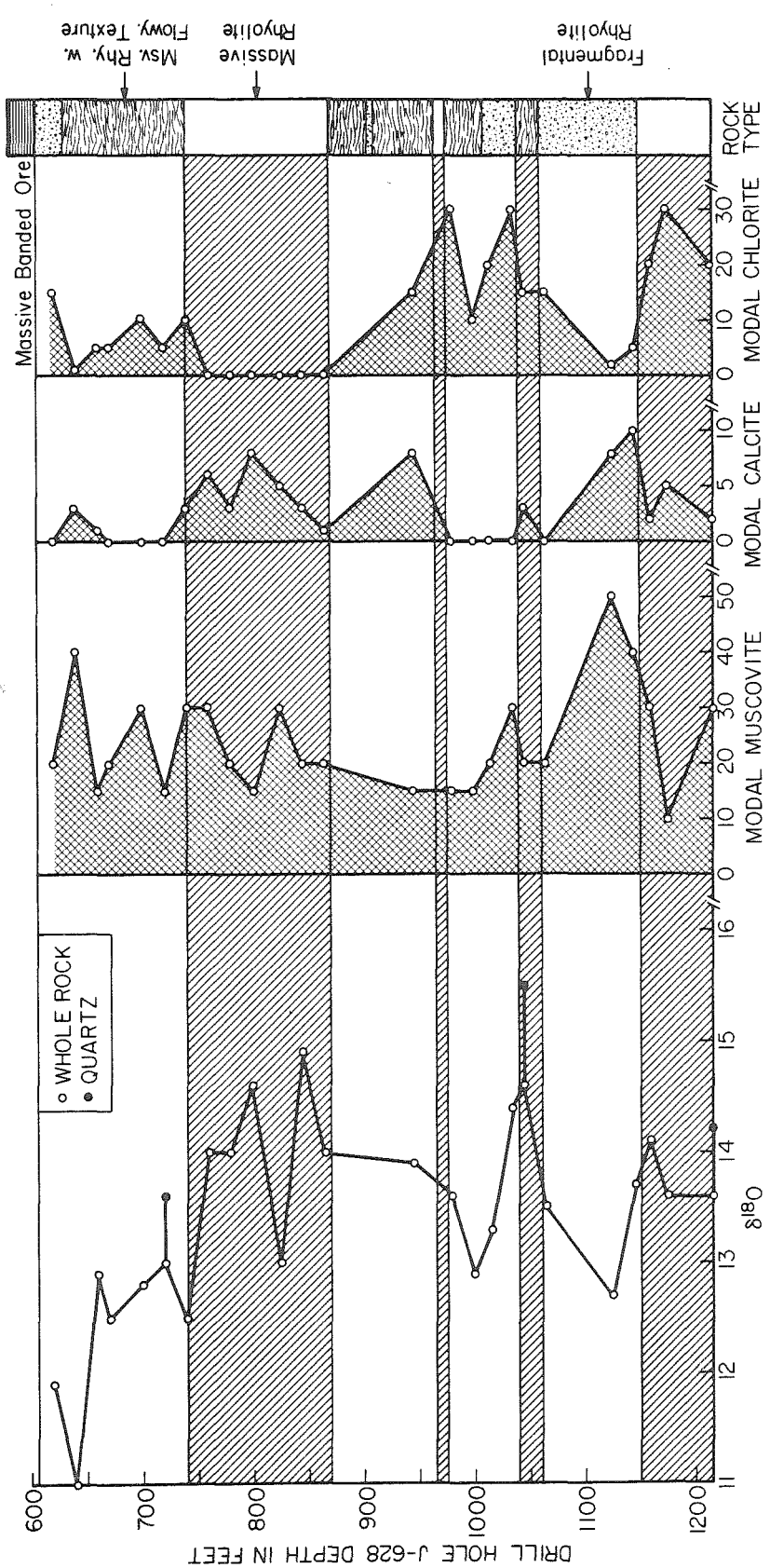

Figure 4B-4. Oxygen isotopic and petrographic data from diamond drill hole J-628. Shown for reference at the right is the distribution of the three rock types present; massive rhyolite, massive rhyolite with a 'flowy' texture, and fragmental rhyolite.

rhyolites show an excellent state of textural preservation, and are typically white. This sequence has tentatively been interpreted as alternating rhyolite flows and intercalated tuff horizons (P. Coad, pers. comm., 1978). The flowy texture is thought to be relic igneous foliation which formed in both the upper and lower portions of the (inferred) rhyolite flows.

In thin section, all of the rocks in J-628 are found to be extensively altered. There are four principal secondary minerals, quartz, muscovite, chlorite and calcite (Fig. 4B-5). These minerals typically have completely replaced the groundmasses of the rhyolites, leaving quartz phenocrysts as the only relic igneous mineral. Albite may also be present in the groundmass, but because of the extremely fine grain size (5-20 microns) it could not be distinguished from quartz. Tourmaline is a common accessory, and epidote may be present in some of the samples (Table 4B-1), but the identification could not be confirmed optically.

Because mineralogic recrystallization typically accompanies hydrothermal oxygen isotopic exchange, the abundances of three of these secondary minerals (chlorite, muscovite and calcite) were estimated (Table 4B-1). Although quartz is also very important, fine-grained secondary quartz in the groundmass cannot be distinguished from primary groundmass quartz. In general, the massive rhyolites are chlorite-rich, whereas the fragmental rhyolites are typically muscovite-rich. This explains why these rock types are black and white, respectively. The detailed relationships between $\delta^{18}O$ and the abundances of these secondary minerals are discussed in detail below.

The $\delta 180$ data from J-628 (Fig. 4B-4) indicate that all of the

Figure 4B-5. Photomicrographs from the Kidd Creek mine.

a.) KC-1, crossed polars. Intense silification in the chalcopyrite stockwork zone. Quartz and opaques are the only minerals present in the field of view.

b.) J-628, 1174.2', crossed polars. Two calcite rhombs are set in a fine-grained matrix of quartz, muscovite and albite.

c.) J-628, 1124', crossed polars. Altered rhyolite showing the development of muscovite. The diagonal streaking is predominantly muscovite; to the left is a quartz phenocryst; to the right is a quartz-filled pod.

d.) J-628, 620.6', crossed polars. Muscovite veinlets cutting through the footwall rhyolite.

e.) J-628, 1217.6', partially crossed polars. A fine-grained intergrowth of quartz (grey to white) and chlorite (darker, with high relief).

f.) KC-37, crossed polars. Metabasite from Martin's Outcrop, which stratigraphically overlies the ore deposit. Pyroxene has been pseudomorphed by actinolite, and plagioclase has been replaced by a fine-grained aggregate of secondary minerals.

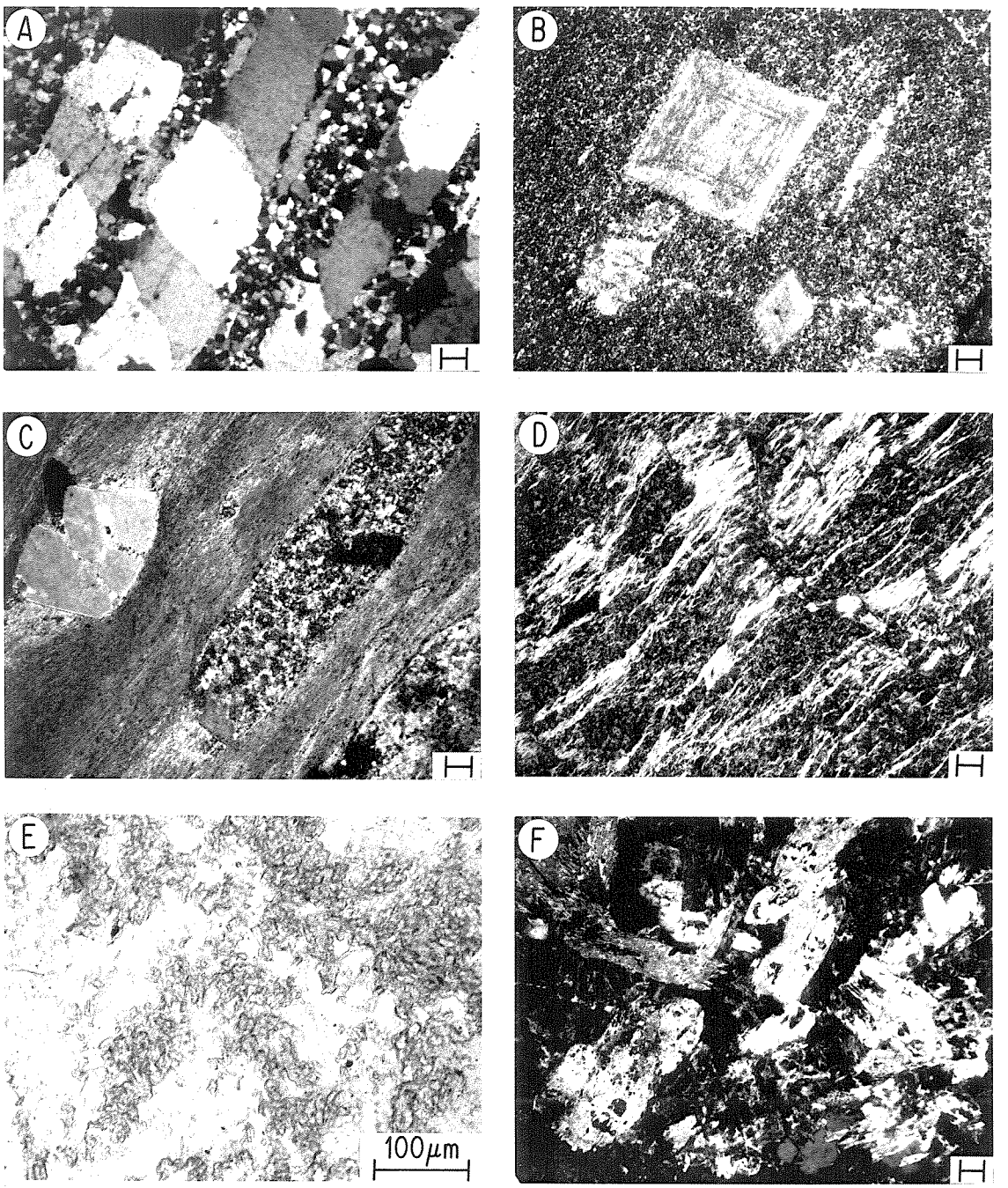
A
H
B
H
C
H
D
H
E
100μm
F
H

rhyolites have undergone isotopic enrichments to varying degrees, relative to the assumed primary value of +7 to +8. From 1200' up to about 800' the $\delta^{18}O$ gradually increases from about +13.5 to about +14.5 (Fig. 4B-4). From 800' to the massive ore horizon (606'), the $\delta^{18}O$ values decrease sharply (Fig. 4B-4), to about +11. Essentially the same trend can be found in the compositions of the groundmass quartz. At 1217.6' quartz has $\delta^{18}O$ = +14.2. This increases up the hole to +15.5 at 1044.5', then decreases to +13.6 at 719.8'.

As discussed in connection with the quartz porphyry, it is not possible to rule out the possibility that these high-^{18}O rocks were originally formed as high-^{18}O magmas. However, the present $\delta^{18}O$ values correlate with the type of mineralogic alteration, so it is reasonable to assume that these rocks have all been enriched in ^{18}O by hydrothermal alteration.

The general gradient in $\delta^{18}O$ in the lower portion of the drill hole is consistent with a vertical temperature gradient at the time of alteration. The lower $\delta^{18}O$ value at 1200' suggests that these rocks underwent hydrothermal oxygen isotope exchange at a higher temperature than the rocks at 800'. Detailed calculations (see below) indicate that alteration in this interval could have been accomplished by a single hydrothermal fluid. The decrease in $\delta^{18}O$ from 800' to 600', however, indicates additional complications. This entire interval is contained in the upper part of a single large massive flow unit and a small amount of overlying tuff (Fig. 4B-4), which must have been subjected to one or more of the following processes:

1. An upward increase in temperature of alteration
2. An upward decrease in water/rock ratio

3. Alteration by an isotopically lighter fluid

The first possibility requires that the geothermal gradient be reversed for a short distance beneath the ore deposit. This condition certainly holds in certain specialized geologic situations, for example, beneath a crystallizing sill. In this case, however, it seems extremely unlikely. The hot ore-forming solution would have been driven vertically by buoyant forces, and unless the flow was diverted somehow, the temperature should remain approximately uniform or decrease steadily upwards. There are no impermeable horizons in the geologic section which are capable of producing such a diversion, and besides, the mineralogic hydrothermal alteration affects extend right through to the massive, banded ore.

For the same reason, possibility #2 is also considered unlikely. If the water/rock ratios were high from 1200' to 800' and then low from 800' to 600', then the fluid must have been diverted laterally at the 800' level. The 800' level corresponds to the core of a thick, massive rhyolite unit which is similar in most respects to the rhyolites which underlie it. There seems to be no reason why this particular flow should be impermeable and the massive rhyolites below it should not. Furthermore, the degree of mineralogic alteration is as intense above that level as it is below it. It is more logical to assume that the buoyant fluids passed vertically through the volcanic section upward to the ocean floor.

The third possibility (multiple hydrothermal fluids) is indicated not only by the process of elimination, but by the detailed oxygen isotopic and mineralogic relationships. The stratigraphic $\delta^{18}O$ zonation in J-628 is far from smooth; there is a plethora of fine structure superimposed on the overall trend. This fine structure reflects in a general way the

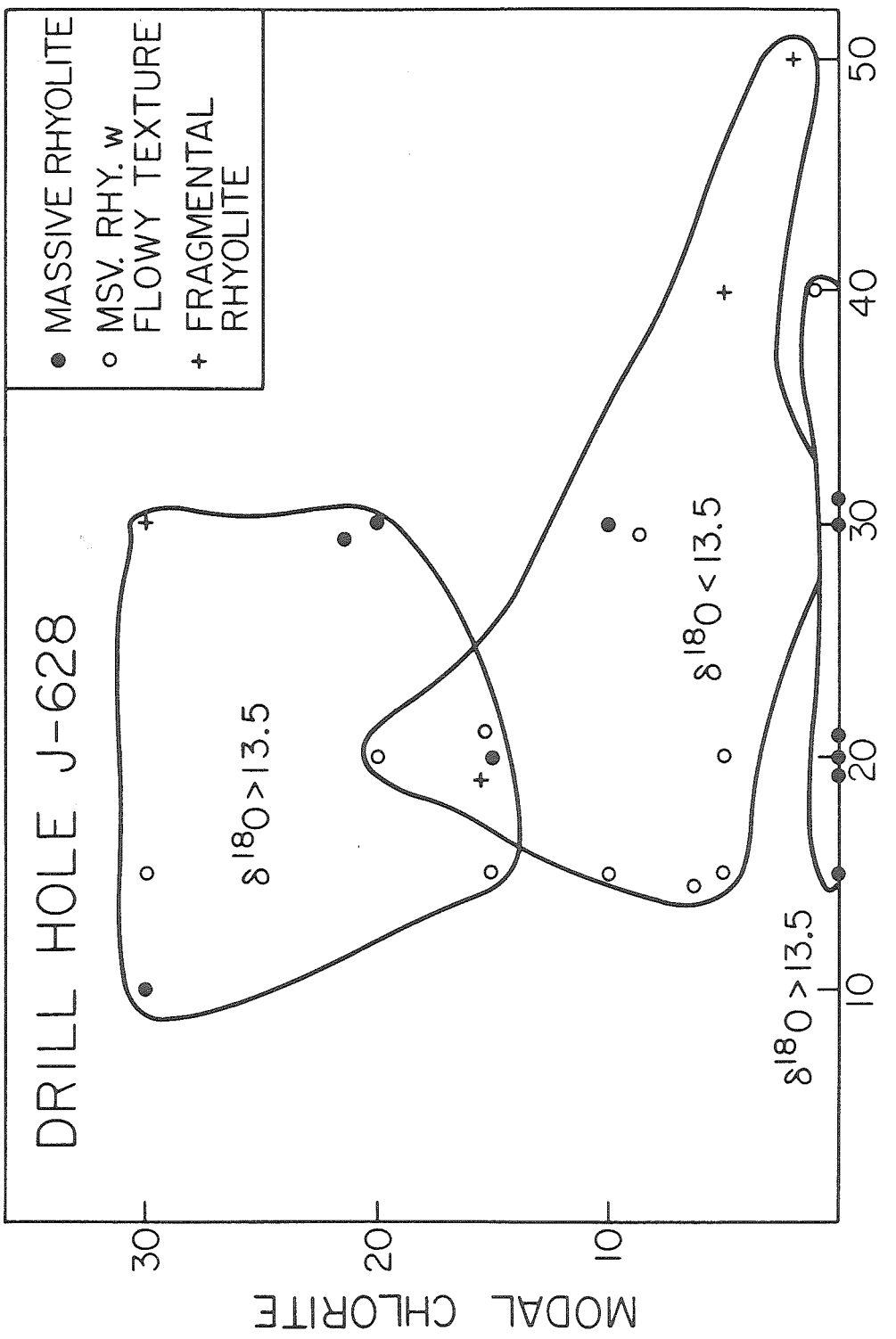

Figure 4B-6. Relationship between modal muscovite, modal chlorite, $\delta^{18}O$, and rock type for drill hole J-628. The massive rhyolites tend to be ^{18}O-rich, and are both richer and poorer in chlorite than the fragmental rhyolites.

geology (Fig. 4B-4). The massive rhyolites tend to be richer in $\delta^{18}O$ by about 1 per mil than the adjacent fragmental rhyolites. In addition, the massive rhyolites tend to be chlorite-rich, and muscovite- and calcite-poor (Fig. 4B-4, 4B-6). The opposite is true of the fragmental rhyolites, which are muscovite- and calcite-rich, and chlorite-poor. Because muscovite has a much greater tendency to concentrate ^{18}O than chlorite (Garlick and Epstein, 1962), the fragmental rhyolites should be richer in $\delta^{18}O$ than the massive rhyolites, the reverse of the observed situation. This indicates that the two rock types were not in oxygen isotopic exchange equilibrium with the same fluid, thus suggesting two different episodes of hydrothermal alteration or mixing between two different fluids. The same conclusion can be reached entirely on mineralogical grounds. All of the rhyolites in J-628 were probably initially isochemical, so a single hydrothermal fluid would be expected to produce a single characteristic alteration assemblage which would have depended on the composition of the fluid. The presence of two different alteration styles suggests two different fluids.

Although three of the four inferred rhyolite flows are rich in chlorite, the fourth is not. No chlorite at all was observed in the core of the upper flow, from 760' to 860' (Fig. 4B-4, 4B-6). The explanation for this is not obvious at this point, but it may be related to the mixing of the two fluids discussed above.

East Outcrop. Two general rock rypes are present on the East Outcrop (Fig. 4B-1); massive rhyolites of various form, and rhyolite volcaniclastics. The massive rhyolites are present as tabular, concordant bodies, large irregular masses, and as blocks within the rhyolite volcaniclastics. Matulich et al. (1974) and Walker et al. (1975) report

that "the massive rhyolite appears to be intrusive", at least on the East Outcrop, but allow the possibility that elsewhere flows and welded tuffs may exist. All of the rhyolite material has recrystallized to "siliceous, microcrystalline mosaics in which minor quartz and sodic plagioclase phenocrysts and occasional spherules have survived." (Walker and Mannard, 1974, p. 4).

Isotopically, the massive rhyolites, including blocks and larger bodies, range in $\delta^{18}O$ from +12.0 to +15.8, with an average of +14.3. The enclosing rhyolite volcaniclastics range from +10.8 to +14.9, and average +12.6 (Fig. 4B-3). The difference between the two is well illustrated by adjacent analyses of a massive rhyolite block and its enclosing fragmental rhyolite. KC-21 (+13.5) is from a one-foot diameter block, whereas KC-22 (+10.9) is located only a foot away in the volcaniclastics. Single blocks are apparently not zoned, as shown by KC-27 (+15.7) and KC-28 (+15.8), the rim and core, respectively, of a 3' diameter block.

Two aspects of the oxygen isotope distribution on the East Outcrop are of paramount importance. First, like the rhyolites in J-628, <u>all</u> of the rhyolites present have anomalously heavy oxygen. The most likely explanation for this is that all of the rocks have undergone extensive hydrothermal alteration, producing the recrystallized textures found by Walker and Mannard (1974). If the rhyolites initially had primary $\delta^{18}O$ = +7 to +8, they must have been thoroughly altered. This implies that there was a tremendous flow of water through the rock, which produced essentially complete recrystallization and a large ^{18}O shift, but which faithfully preserved the detailed textures and structures. Note that the oxygen isotopic compositions from the East Outcrop, which is

located 600-800' stratigraphically beneath the ore horizon (Walker et al. 1975, p. 3), are similar to the values from a comparable stratigraphic level in J-628.

The second important observation is that the massive rhyolites are isotopically heavier than the surrounding fragmental rhyolites. This is the same relationship found in J-628. The mineralogic relations in J-628 are also present on the East Outcrop. Figure 4B-7 shows that the massive rhyolites are chlorite-rich and muscovite-poor, and vice versa for the fragmental rhyolites. Two possible hydrothermal histories could account for these data. Either the massive, chlorite-rich rhyolites achieved their high-^{18}O characteristics prior to their incorporation in the volcaniclastics, or the more permeable fragmental rhyolite has undergone a second, much less thorough, hydrothermal event which slightly lightened its oxygen. These possibilities and their significance are discussed in detail below.

By comparing only the massive rhyolites with one another and the samples of rhyolite volcaniclastics to each other, it can be shown that there is a tendency for the higher $\delta^{18}O$ values to be towards the center and east side of the outcrop. This suggests either lower alteration temperatures, higher water/rock ratios, or both to the east.

1600 Level, N. Orebody. The suite of samples from the 1621 crosscut in the copper stringer zone (Zone 1 on Fig. 4B-1) range in $\delta^{18}O$ from +10.4 to +12.7 (Fig. 4B-3), and become lighter towards the massive, banded ore. These data are in complete agreement with those obtained from J-628. Not only does ^{18}O decrease toward the banded ore in both cases, the compositions are indistinguishable for comparable stratigraphic levels. In common with the isotopically and stratigraphically similar

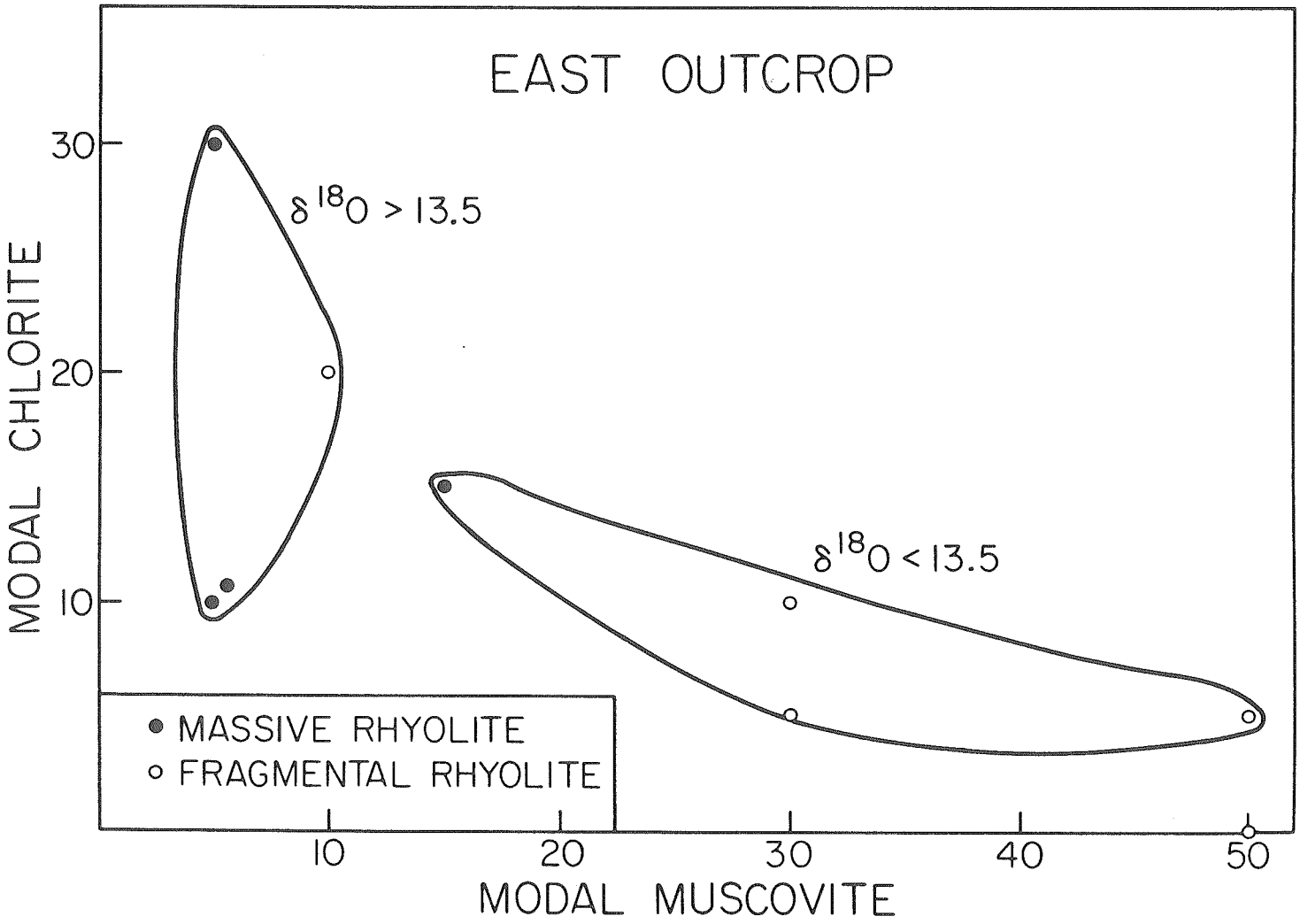

Figure 4B-7. Variation in modal chlorite, modal muscovite, $\delta^{18}O$ and rock type for the East Outcrop. The massive rhyolites are ^{18}O-rich, chlorite-rich, and muscovite-poor and vice versa for the franmental rhyolites.

upper part of J-628, the copper stringer zone is intensely altered. Walker and Mannard (1974) report that the host rhyolite "contains occasional phenocrysts of quartz in a recrystallized groundmass composed largely of microcrystalline quartz and minor sericite. Feldspar phenocrysts can only rarely be recognized as sericitic pseudomorphs. The silica content of the stringer ore host is generally between 75 and 90%, with occasional analyses as high as 97%. Primary texture has been largely obscured by silicification and recrystallization . . ." (p. 10). The water/rock ratio in this area was almost certainly very high.

These altered rhyolites are cut not only by chalcopyrite veins, but also by quartz veins, of which three were analyzed. The $\delta^{18}O$ of these samples is uniform at +11.9 per mil (Table 4B-1) which is slightly less than that of the rhyolites they cut. The position of these quartz veins in the geologic history of the area is not clear. Most of the veins are associated with the ore-forming event, but at least some quartz veins crosscut both the ore zones and the wall rocks (Walker and Mannard, 1974). It is not known into which of these categories the analyzed veins should be classified.

7. Nearby Rhyolites

A set of 13 samples of rhyolites collected within 2 km. of Kidd Creek were found to have $\delta^{18}O$ in the range +10.2 to +14.1 (Table 4B-1). Petrographically most of these rhyolites are also thoroughly altered (just like the Kidd Creek rhyolites), and the secondary minerals chlorite, muscovite, quartz and calcite are present in great quantity. In common with both the East Outcrop and J-628, the most chlorite-rich samples are the highest in $\delta^{18}O$. The nine samples which contain less than 5% chlorite have $\delta 180$ between +10 and +12, whereas the

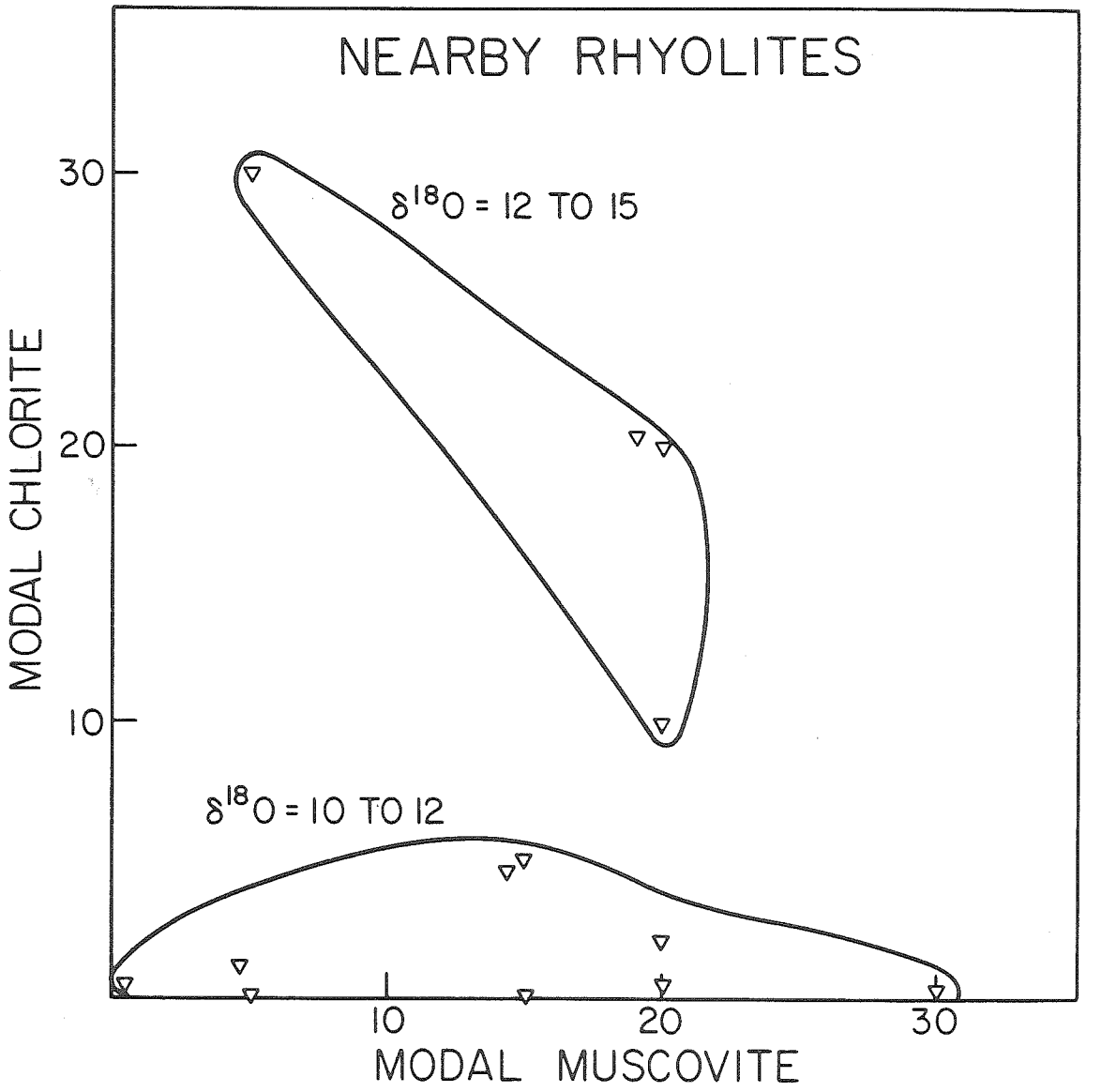

Figure 4B-8. Relationship between modal chlorite, modal muscovite and $\delta^{18}O$ for the rhyolites surrounding the Kidd Creek mine. The same oxygen isotopic and mineralogic alteration style found at the mine is present within these rhyolites.

four samples with more than 10% chlorite have $\delta^{18}O$ between +12 and +15 (Fig. 4B-8). This suggests that the hydrothermal processes responsible for the formation of the Kidd Creek orebody were not confined to the mine itself. The same alteration patterns, both in terms of mineralogy and $\delta^{18}O$, can be found away from the minesite.

IV. SUMMARY OF THE OXYGEN ISOTOPE DISTRIBUTION

Kidd Creek is a large, complicated ore deposit, and like the structure, the oxygen isotope relations are complex. In spite of this, the data can be summarized with a few simple generalizations. There is a definite stratigraphic control on the oxygen isotope distribution. The overlying, post-ore wall rocks are modestly enriched in ^{18}O (dacite and andesite/diorite = +8 to +10), and are similar to other samples of the Abitibi greenstone belt. The quartz porphyry has $\delta^{18}O$ = +11 to +12. The rhyolites are moderately to strongly enriched in ^{18}O (+10.5 to +16) as compared to primitive magmatic values of +6 to +8. Distinctive isotopic zoning is present within the rhyolite pile. The rocks immediately underlying the massive banded ore (in J-628 and underground) have $\delta^{18}O$ values of about +10.5 to +11.0, and $\delta^{18}O$ increases stratigraphically downward, away from the banded ore horizon. At 200-300' below the banded ore, $\delta^{18}O$ has reached its maximum of +15 to +16 (J-628 and East Outcrop) and below that it decreases slightly. The oxygen isotopic composition of the rhyolites away from the mineralized area is probably in the range +10 to +12, based on analyses of rhyolites up to 2 km. away from from near Kidd Creek. These relationships are schematically illustrated in Figure 4B-9.

V. HYDROTHERMAL HISTORY

Several observations suggest that at least two types of water were

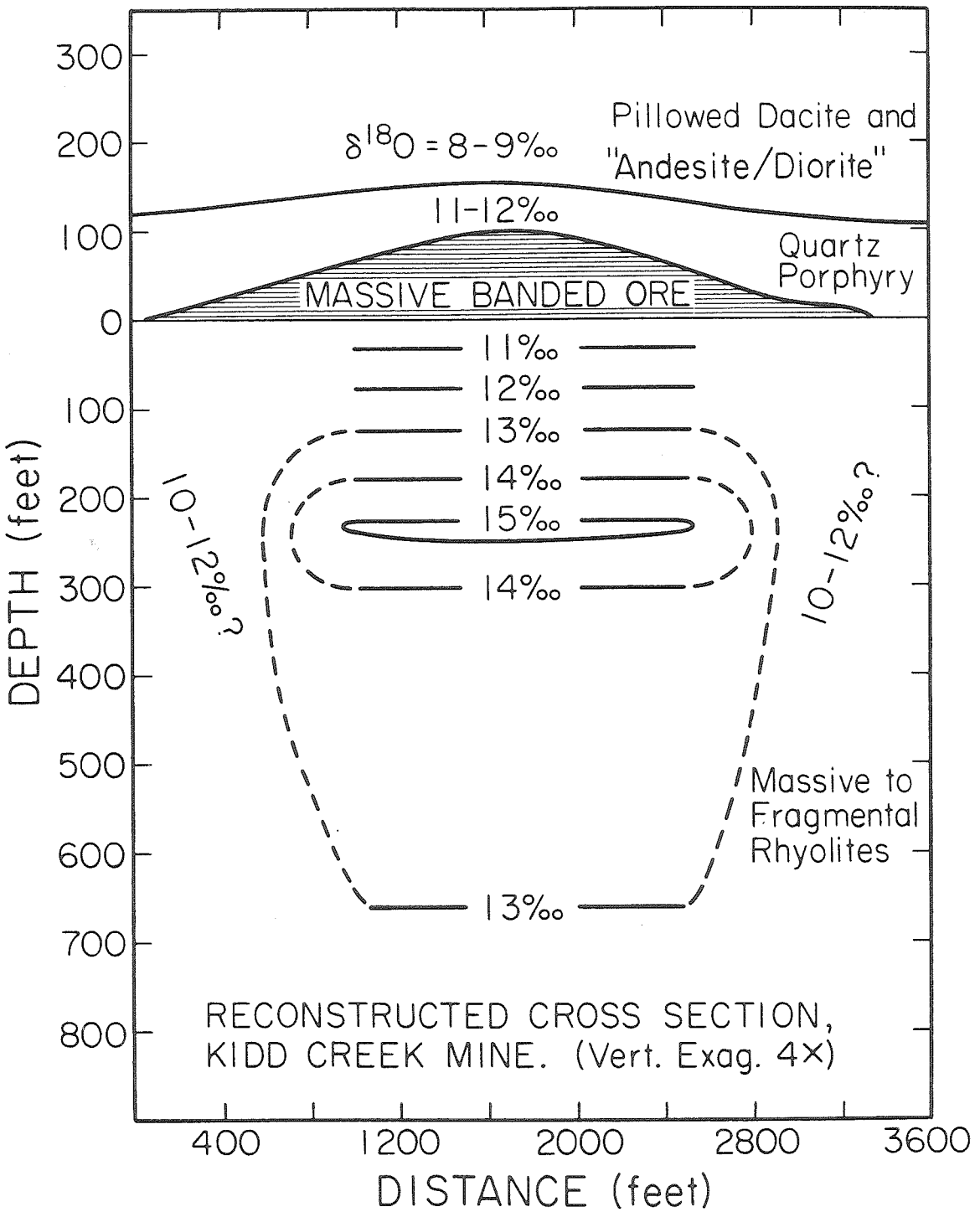

Figure 4B-9. Schematic diagram showing the distribution of $\delta^{18}O$ around the Kidd Creek mine. The deposit was rotated back to its original horizontal orientation, and the cross section then constructed.

responsible for the hydrothermal alteration at Kidd Creek. First of all, the quartz veins in the copper stringer zone are somewhat lighter than the rocks they cut. Given only one type of fluid with uniform $\delta^{18}O$ value, the quartz veins would have to be richer in ^{18}O than the altered host rocks which they cut. This effect would be even more enhanced if the quartz veining was the last process to affect the rocks, as it might then be expected to have occurred at a lower temperature than most of the earlier stages of hydrothermal alteration.

More importantly, the quartz veins are 3 to 4 per mil lighter than the groundmass quartz in the deeper portions of J-628. Once again, the deep alteration in J-628 probably took place at a temperature higher than that present during the formation of the late-stage quartz veins higher in the section. This would require that the quartz veins have formed from an isotopically lighter fluid than the one which altered lower J-628 and the East Outcrop.

Third, the rhyolite blocks on the East Outcrop are isotopically heavier than the rhyolite volcaniclastics enclosing them. Also, the massive rhyolites in J-628 are more ^{18}O-rich than the intercalated rhyolite tuffs. Although the possibility that the blocks were highly altered prior to their incorporation in the fragmental rhyolite can be suggested for the East Outcrop, it is unreasonable for the thick rhyolite flows in J-628. A more plausible situation is early high-^{18}O alteration of all of the footwall rhyolites followed by partial lower-^{18}O retrogression of the more permeable fragmental rhyolites. In any case, a two-stage alteration history of some sort is required by the fact that the massive and fragmental rhyolites are drastically out of oxygen isotopic equilibrium.

Fourth, in addition to having different oxygen isotopic ratios, the

massive and fragmental rhyolites have different alteration styles. The massive rhyolites have undergone a chloritic alteration, and the fragmental rhyolites have experienced a sericitic alteration. This suggests two fluids of different chemical composition and two different regimes of hydrothermal alteration.

Fifth, the lower isotopic ratios in the upper part of J-628 and in the copper stringer zone strongly suggest alteration by an isotopically lighter fluid. The alternative hypothesis that the water/rock ratio was lower is untenable on the grounds that texturally, the copper stringer zone is the most intensely hydrothermally altered area at the mine. The alternative possibility that alteration took place at a much higher temperature right at the ore horizon cannot be reconciled with vertical transport of the hot hydrothermal fluid. Rather than being deflected laterally away from the stockwork zone, it appears from textural and chemical evidence that the stockwork zone exerienced one of the highest water fluxes in the mine area.

Finally, the rocks overlying the ore deposit are also altered. Although hydrothermal alteration above the Kuroko massive sulfide deposits is apparently related to continued hydrothermal activity after the main episode of ore deposition (Lambert and Sato, 1974), there is little evidence that a similar process occurred at Kidd Creek. The hydrothermal alteration of the dacite sequence and the andesite/diorite is indistinguishable from the regional alteration of the Blake River volcanic pile, the Skead volcanics, and mafic rocks from elsewhere in the Abitibi area (Chapter 3). All of the volcanic rocks in the Abitibi greenstone belt have been slightly enriched in ^{18}O and the mafic rocks at Kidd Creek are entirely typical. The metamorphic event responsible for the hydro-

thermal alteration of the volcanic pile as a whole took place either during or soon after eruption (Jolly, 1980; Dimroth and Lichtblau, 1979) and is interpreted to be sea-floor burial metamorphism; the altering fluid is thought to be circulating marine pore fluids derived from seawater (see Chapter 7).

These lines of evidence indicate that two sources of fluid were responsible for the hydrothermal alteration at Kidd Creek. A deep-seated, isotopically heavy fluid seems to have been responsible for the bulk of the alteration, producing the strong ^{18}O enrichments in the rhyolite pile. A second, more ^{18}O-depleted fluid, almost certainly originally seawater, produced the isotopic depletions in the upper part of the rhyolite pile, retrograded the permeable rhyolite volcaniclastics, and formed the late-stage quartz veins. Through continued activity during deposition of the entire greenstone belt, a similar low-^{18}O fluid altered the volcanic rocks overlying the ore deposit.

The ^{18}O depletions in the upper part of the rhyolite pile (upper J-628 and stockwork zone) suggest that the two fluids were active more-or-less simultaneously during ore deposition and were undergoing mixing. On the basis of the $\delta^{18}O$ data, the depth of mixing, at least in J-628, appears to have been about 200 feet. Such mixing would have changed the temperature and compositional characteristics of the two fluids, perhaps in such a way as to precipitate sulfides. This is consistent with the 100-250 ft. stratigraphic thickness of the chalcopyrite stringer ore (Walter and Mannard, 1974). These relationships suggest the following hydrothermal model.

First of all, there must have been a massive upward flow of a deep-seated, isotopically heavy water beneath the ore deposit. As it neared

the seafloor it began to mix with the isotopically lighter seawater. The mixing changed the thermal and compositional properites of the fluid such that it began to precipitate sulfides: chalcopyrite at high temperature in the rocks themselves, and sphalerite and pyrite at lower temperature on the ocean floor. With time the deep-seated hydrothermal system lost energy and flow began to taper off. As this happened, the seawater hydrothermal system collapsed on the deep-seated system, altering for a second time the rhyolites beneath the ore deposit. The rather highly altered state of the quartz porphyry ($\delta^{18}O$ = +11 to +12), which overlies the massive, banded ore, may indicate that the deep-seated flow persisted after the formation of the ore deposit, affecting some of the overlying rocks. Eventually the deep flow ceased, and the rocks were buried beneath subsequent volcanic eruptions -- all the while interacting continuously with circulating marine pore fluids during burial metamorphism. After the formation of the ore deposit, the region underwent a complex geologic history, involving a minimum of two episodes of folding and polymetamorphism (Walker and Mannard, 1974; Walker et al. 1975). Regional metamorphism elsewhere in the Abitibi greenstone belt, however, appears to have been essentially isochemical, at least as far as the oxygen isotopes are concerned (Beaty and Taylor, 1979). Likewise at Kidd Creek, there is no evidence that the post-seafloor burial metamorphism history has appreciably affected the oxygen isotope distribution. For example, the sharp $\delta^{18}O$ gradient in J-628 has not been homogenized.

VI. $\delta^{18}O$ OF THE HYDROTHERMAL FLUIDS

The composition of the deep-seated ore-forming fluid can be calculated from $\delta^{18}O$ measurements of the groundmass quartz and assumed temperatures of alteration. By analogy with active geothermal systems around

the world (Salton Sea: McDowell and McCurry, 1977, Muffler and White, 1967; Wairaikei: Steiner, 1968) the temperature of alteration in J-628 is assumed to have been about 300°-350°C. These temperatures are consistent with the results obtained from other massive sulfide deposits. Heaton and Sheppard (1976) for example, estimated that the stockwork mineralization in the Cyprus copper deposits was 250-350°, and that the temperature of alteration inside the stockwork was much higher than that of the surrounding rocks. The temperature of formation of the stockwork ores of the Kuroko deposits has been estimated to be 300° (Ohmoto and Rye, 1974; Hattori et al. 1979). Furthermore, comparable temperatures have now been measured in submarine hot springs, for example 350°C water is currently flowing out of a spring in the Gulf of California at 21°N (Edmond et al. 1979a).

The groundmass quartz at 1200' has $\delta^{18}O \simeq +14$ and at 900' it is about +15. Using the fractionation factors of Clayton et al. (1972), and assuming a high water/rock ratio, these values indicate the following fluid compositions:

Depth	T	$\delta^{18}O$(qtz)	qtz-Δ water	$\delta^{18}O$(water)
900'	300°	15	7.4	7.6
	350°	15	5.8	9.2
1200'	300°	14	7.4	6.8
	350°	14	5.8	8.2

Similar fluid compositions are calculated from the whole-rock data, using the feldspar geothermometer. Thus, it can be fairly safely concluded that the rhyolites beneath the ore deposit have undergone oxygen isotopic

exchange with a fluid having $\delta^{18}O \approx +6$ to $+9$. This is clearly the fluid that produced the massive chloritization of the footwall rhyolites and that was responsible for indtroducing the metals that made the Kidd Creek ore deposit.

The second fluid was low in $\delta^{18}O$, and is thought to have been seawater. It is not possible to calculate precisely the oxygen isotopic composition of that fluid, but an estimate can be made using the quartz veins. As discussed above, the geologic age of the quartz veins is problematical, as there are a great many crosscutting relationships. Most of the veins, however, are thought to be late-stage fracture fillings which formed during the last stages of hydrothermal alteration. If so, the temperature was probably lower than during the peak of hydrothermal activity. Although this temperature cannot be quantified, several possibilities are shown in the following table:

T	late-stage $\delta^{18}O$(qtz.vein)	qtz-Δ water	$\delta^{18}O$(water)
150°	+11.9	~ 15.0	-3.1
200°	+11.9	12.2	-0.3
250°	+11.9	9.4	+2.5

These data therefore suggest that the ocean water in the Kidd Creek area was probably not more than a few per mil different from 0, or in other words similar to seawater in other parts of the greenstone belt (See Chapter 7).

VII. SOURCE OF THE ORE-FORMING SOLUTION

Stable isotopic evidence from a number of volcanogenic massive sulfide deposits (Kuroko, Cyprus, Raul mine, Ducktown, Amulet) indicates

that they were formed from surface-derived hydrothermal fluids (typically seawater). There are no known examples, in fact, of this type of deposit having been formed from any other type of fluid such as primary magnatic water. However the data from the Amulet "A" mine (Chapter 4C) and a variety of other evidence summarized in this thesis indicate that seawater in the Archean also had $\delta^{18}O \approx 0$, in which case the Kidd Creek ores could not have been deposited directly from heated seawater.

Several processes, however, could have enriched an originally ocean-derived hydrothermal fluid in ^{18}O, including evaporation in a closed basin prior to circulating into the volcanic section, exchange with high-^{18}O country rocks (such as sediments) during circulation, and boiling during final ascent of the fluid. Two other types of fluids, metamorphic and magmatic, are also typically high in $\delta^{18}O$, and must be seriously considered. Finally, if the temperature assumptions listed above are too high by about 150°C, it is possible that the alteration was accomplished by "normal" ($\delta^{18}O \approx 0$) seawater. Each of these six possibilities are evaluated in turn.

1. Closed basin. The Kidd Creek mine is located at the present western end of the Abitibi greenstone belt. If it were also at the margin during the formation of the volcanic pile, it is possible that the geometry of the growing volcanic edifices reduced oceanic circulation and led to a localized closed basin. This basin could have then undergone rapid evaporation, enriching the water in the basin in ^{18}O. Such a model is consistent with the observation that most of the volcanic rocks in the Kidd Creek-Timmins-Kamiskotia area are anomalously high in $\delta^{18}O$ compared to the rest of the greenstone belt (Chapter 2G). Included within this area is the Dome mine, a gold-bearing quartz vein, which is also thought to

have formed from a high-^{18}O hydrothermal fluid ($\delta^{18}O \approx +10$; Kerrich and Fryer, 1979). A possible test of this model might be the presence or absence of evaporites in the geologic section, but other than carbonates (Fryer et al. 1979) and some banded iron formations (Goodwin and Ridler, 1970), none has been described.

An argument against the closed basin evaporation model is the evidence presented above which indicates that two hydrothermal fluids were active simultaneously during the deposition of the Kidd Creek ore. One of these fluids is thought to have been the local seawater, and it apparently had $\delta^{18}O$ in the vicinity of 0. According to the rapid evaporation model, however, the local seawater should have been ^{18}O-enriched.

2. Exchange with high-^{18}O country rocks. There is a large mass of sedimentary rocks in the Kidd Creek-Timmins-Kamiskotia area (Fig. 3G-1). Metagreywackes, siltstones, slates, argillites and minor pebble conglomerates outcrop over about 30-50% of this region. These rocks are presently not high in $\delta^{18}O$; a metagreywacke near Schumacher, for example has $\delta^{18}O = +9.2$ (Chapter 5). It is possible, however, that these sediments were originally higher in $\delta^{18}O$, and that they have contributed this heavy oxygen to the circulating seawater, and ultimately to the altered volcanic rocks. This model could also account for the regionally high $\delta^{18}O$-values around Timmins; sedimentary rocks are much more abundant here than they are elsewhere in the Abitibi greenstone belt.

An analagous process has been observed in the Salton Sea geothermal field. Local meteoric water ($\delta^{18} = -11$) penetrates into the sediment-filled Salton trough and is heated. This heated water then exchanges its oxygen with (and leaches certain components from) the high-^{18}O sedimentary rocks. This produces an ^{18}O-shift in the water, which emerges

in the geothermal wells with $\delta^{18}O = +3$, a 14 per mil shift (Craig, 1966). Similar shifts have been observed in six other of the world's major geothermal systems (Craig et al. 1956; Craig, 1963). In the Kidd Creek example, seawater ($\delta^{18}O$ initially = 0) could possibly have been shifted to +6 to +9 by exchange with high-^{18}O sediments.

3. Boiling in the ore fluid. Although it would have produced ^{18}O-enrichments, the possibility that boiling took place in the Kidd creek hydrothermal fluid is considered unlikely. One of the classical indications of boiling is a wide range of homogenization temperatures in the fluid inculsions, and preliminary work on the fluid inclusions at Kidd Creek indicates that they are all around 300°C (Spooner, pers. comm., 1979). Furthermore, the distribution of iron formation facies suggests that the water was relatively deep in the Kidd Creek area (Goodwin and Ridler, 1970; fig. 2). Although the depth of at Kidd Creek deposition has not been quantified, calculations by Ridge (1973) indicated that a 300°C, 5 wt. % NaCl solution exiting the seafloor will not boil unless the water depth is less than 725 m.

4. Metamorphic water. The high-^{18}O hydrothermal solution need not have been modified seawater, however. Metamorphic waters, for example, have been estimated to have $\delta^{18}O$ values between +5 and +25 (White et al. 1973; Taylor, 1974). In the case of greenstone belts it is possible that the metabasalts at the base of the volcanic pile were undergoing the transition from greenschist facies to amphibolite facies. Such a transformation involves, among other things, a replacement of chlorite (12 wt. % H_2O) with hornblende (4 wt. % H_2O) and the consequent release of a substantial amount of water. Kerrich and Fryer (1979) have invoked exactly this mechanism for deriving 90 km3 of high-180 water (+10) from

a 600 km^3 source region in the Timmins area. Although the Kidd Creek and Dome mineralizations have different ages (syngenetic vs. metamorphic) and ore types (massive sulfide vs. gold-quartz vein), it is possible that their ore fluids had similar genetic histories.

5. Magmatic water. The Kidd Creek hydrothermal solution ($\delta^{18}O$ = +6 to +9) could also have been magmatic water which exsolved from a large granitic pluton. Assuming the ore deposit contains 100 million tons of sulfides (Walker et al. 1975), and assuming an Fe solubility of 100 ppm in the hydrothermal solution (Mottl et al. 1979), the minimum amount of fluid necessary to transport the metals to the surface would be about 5×10^{11} tons. At 5 kb., granitic magmas can contain a maximum of about 10 weight percent H_2O in solution (Wyllie, 1979). Thus a pluton of at least 5×10^{12} tons would be required. This body would have a mass of 5×10^{18} gm, a volume of 2×10^{18} cm^3, and if cubic, would be about 10 km on a side. There is no evidence for a granitic (or any other type of plutonic) body this size near Kidd Creek.

It is also possible that the hydrothermal fluid is actually juvenile water which has come directly from the mantle by some means. Another possibility is subducted ocean water which equilibrated isotopically with the deep crust or mantle. In both cases, however, it is difficult to imagine a situation in which a sudden pulse of 5×10^{11} tons of water could have been produced.

6. Low-temperature alteration. An alternative interpretation of the high-^{18}O rocks in the altered zone at Kidd Creek is that the alteration took place at low temperature. As discussed above, most hydrothermal ore deposits, including the massive sulfide type, are formed at about 300-350°C. This figure is constant for a reason; it is close to the

critical point of water, and over this temperature interval many of the transport properties of water, such as the dielectric constant, change rapidly. The homogenization temperatures of the fluid inclusions at Kidd Creek are also within this range (Spooner, pers. comm., 1979). However, if the hydrothermal alteration actually took place at 150°C, the high-^{18}O rocks could have been produced by interaction with normal ($\delta^{18}O = 0$) seawater.

In summary, six possible origins for the Kidd Creek ore-bearing solution have been proposed. Only two of these possibilities adequately explain all of the observed data at the mine and are consistent with the geological and oxygen isotopic relationships elsewhere in the Abitibi greenstone belt: namely, originally normal (0 per mil) seawater that has been evaporated to a brine or that has exchanged with high-^{18}O sediments, or a metamorphic water of some sort produced by dehydration lower in the volcanic pile. Evaporation in a closed basin suffers from the apparent presence of normal-^{18}O seawater in the Kidd Creek area at the time of deposition. However, if the overall flow geometry of the fluids involves large lateral distances (10-25 km.?) this might not be an overriding constraint. Magmatic water is disfavored because there is no evidence for a nearby pluton of sufficient size and no massive sulfide deposit has yet been shown to form from magmatic water. Boiling during ore deposition runs afoul of the fluid inclusion data, and basically has little to recommend it in a submarine environment that probably involved a very high-salinity aqueous solution. The possible low temperature of formation (150°C or lower) is also very unlikely because there is a region-wide high-^{18}O zone around Timmins, and the volcanic processes and water/rock ratios are presumed to be the same throughout the Abitibi area.

Compared to the greenstone belt as a whole, the entire Timmins area is anomalously ^{18}O-rich, presumably because of wide-spread hydrothermal alteration by high-^{18}O aqueous fluids. These high-^{18}O fluids were apparently present on a regional scale, and the Kidd Creek deposit and Dome mine apparently only represent local "hot spots" where these fluids were more highly concentrated.

VIII. CONCLUSIONS

Oxygen isotopic investigation of the Kidd Creek mine indicates that all of the rocks surrounding the ore deposit have been enriched in ^{18}O in comparison to primitive magmatic values. The rhyolites underlying the ore, both massive and volcaniclastic, are not only strongly enriched in ^{18}O, they also show well-developed vertical isotopic zoning. The geologic units overlying the massive banded ore (dacite sequence, quartz porphyry) as well as the andesite/diorite, which postdates the ore, show only modest ^{18}O enrichments similar to the modest ^{18}O enrichments found in most volcanic rocks throughout the Abitibi greenstone belt.

The detailed isotopic relationships around the mine indicate that at least two distinctly different hydrothermal fluids were responsible for the alteration effects. A deep-seated isotopically heavy fluid ($\delta^{18}O$ = +6 to +9) produced the extremely ^{18}O-rich rocks in the lower stratigraphic levels. This was either a metamorphic dehydration water, an evaporated brine, or an exchanged metamorphic fluid, any or all of which could have been originally derived from seawater with $\delta^{18}O \approx 0$. A reasonable analogy might be a Salton Sea-type brine (Craig, 1963) derived from seawater rather than meteoric water. At about 200' beneath the ocean floor, this solution (high-salinity brine?) mixed with normal seawater ($\delta^{18}O \approx 0$), began precipitating sulfides, and lost its identity

as it flowed upward into the overlying ocean. Eventually, the deep-seated flow ceased, and a lower-temperature seawater hydrothermal system collapsed on the earlier system, producing retrograde alteration. Finally, this seawater-derived fluid was involved in the same type of burial metamorphism that affected the entire greenstone pile.

Because the best model for the origin of the Kidd Creek ore fluid is similar in many respects to the inferred origin of the Salton Sea brine, it is worthwhile to explore the analogy further. The Salton trough is filled with terrigenous, deltaic feldspathic sandstone and feldspathic argillaceous sandstone interbedded with lacustrine mudstone and siltstone (McDowell, 1978). These rocks are not unlike the metamorphosed greywackes and argillites to the south of Kidd Creek. Like Kidd Creek, the Salton Sea metamorphic assemblages are characterized by an abundance of layer silicates (illite, muscovite, chlorite, biotite) along with carbonates (Muffler and White, 1969; McDowell, 1978).

In contrast to the massive rhyolties at Kidd Creek, however, the altered rocks at the Salton Sea rarely contain more than 2% chlorite (McDowell, 1978; p. 8). This suggests that the Mg-contents of the two fluids were different. The Salton Sea brines contain only 10-69 ppm Mg (White, 1968) which is much less than present seawater (1350 ppm; White, 1968). If the Archean ocean had a similar concentration of magnesium, and if the Kidd Creek ore fluid was marine-derived, one might anticipate a greater abundance of chlorite in the Kidd Creek altered zone. It also seems likely that the volcanogenic sedimentary rocks near Kidd Creek were probably more Mg-rich than the terrigenous sedimentary rocks at the Salton Sea. It is important to note in this regard that high-temperatue, seawater-hydrothermal systems of all ages, including the Archean (see Chapter 4C),

are characterized by chloritization of the rocks. This might be additional evidence that the high-^{18}O, Mg-rich Kidd Creek ore fluid was in fact marine-derived.

CHAPTER 4C. THE AMULET "A" MINE

The Waite-Amulet copper-zinc mine lies astride the Duprat-Dufresnoy township boundary about 8 miles northwest of Noranda, Quebec (Fig. 4C-1). Ore was first discovered in 1924, and when operations ceased in 1962, 6,800,000 tons of ore had been produced from the Amulet group of ore bodies (Spence and de Rosen-Spence, 1975). The Amulet is a classic example of a volcanogenic massive sulfide deposit, consisting of massive, banded, stratabound sulfide ore, a peripheral pyritic chert (exhalite) horizon, and a chimney of intense alteration extending stratigraphically downward from the massive ore. Because the ore-forming solution flowed through the altered chimney, oxygen isotopic and petrologic examination of the altered rocks can give important information regarding the origin of the ore-forming solution and the nature of the ore-forming process.

I. GEOLOGY AND STRUCTURE

The Amulet group of ore bodies consists of four principal mushroom-shaped sulfide masses located with 1 km. of one another (Fig. 4C-1). Each sulfide body consists of a lens of chalcopyrite, pyrrhotite, pyrite, sphalerite and rare galena with a sulfide-bearing pipe extending downward from the massive sulfide lens. The pipe is a zone of intense alteration, recognized by the distinctive rock type dalmatianite. Spatially, this alteration has the form of "a great chimney that extends from the deepest drilling to the surface" (Suffel, 1948; p. 759), and is thought to have been the path by which the ore fluids ascended (Fig. 4C-2). The massive sulfide lenses occur along lava flow contacts, and are thought to have formed on the ocean floor as chemical precipitates from submarine fumaroles (Spence and de Rosen-Spence, 1975; Spence, 1975).

In cross section the massive sulfide lenses are locally stacked as

TABLE 1. OXYGEN ISOTOPIC AND PETROGRAPHIC DATA FROM THE AMULET "A" MINE

Sample	Location	Structure	$\delta^{18}O$ WR	$\delta^{18}O$ Min	Quartz	Biotite	Opaque	Chlorite	Albite	Calcite	Epidote	Actinolite	Anthophyllite	Sphene	Cordierite	Muscovite
AMULET "A" TRAVERSE																
Qe-25	W. end of trav.	grid fract.	4.8		X	X	X	?	?		X					
Qe-26	8 m. E. of Qe-25	grid fract.	4.0		X	X	X				X					
Qe-28	43 m. E. of Qe-25	dalmatianite	3.6		X	X	X	X	?		X		X		X	
Qe-29	52 m. E. of Qe-25	dalmatianite			X	X	X	X	?		X		X		X	
Qe-30	60 m. E. of Qe-25	dalmatianite	3.8	6.23(q) 1.56(ch)	X	X	X	X					X		X	
Qe-31	70 m. E. of Qe-25	dalmatianite			X	X	X	X					X	X	X	
Qe-32	78 m. E. of Qe-25	dalmatianite	4.6		X	X	X	X					X		X	
Qe-33	88 m. E. of Qe-25	grid fract.			X	X	X	X			X					
Qe-34	105 m. E. of Qe-25	grid fract.	4.5		X		X	?	X		X	X		X		
Qe-35	120 m. E. of Qe-25	grid fract.			X	X	X	?	?		X	X		X		
Qe-36	137 m. E. of Qe-25	grid fract.	4.7		X	X	X	X	X			X				
Qe-37	153 m. E. of Qe-25	grid fract.			X	X	X		?		X	X		X		
Qe-38	173 m. E. of Qe-25	grid fract.	6.3		X	X	X		?		X	X		X		
Qe-39	200 m. E. of Qe-25	undeformed	6.4		X		X	X	X	X	X	X		?		
NEARBY SAMPLES																
Qe-52	1560 m. E. of "A"	undeformed	6.6		X	X	X		X			X		X		X
Qe-53	1000 m. E. of "A"	undeformed	5.2	7.9(q) 5.2(a)												
Qe-54	620 m. E. of "A"	undeformed	6.7													
Qe-56	280 m. S. of "A"	undeformed	5.5		X		X	X	X	X	X	X		?		X
Qe-57	610 m. SW of "A"	undeformed	5.6		X		X	X	X		X	X				X
Qe-58	850 m. SE of "A"	undeformed	6.5		X		X	X	X	X	X	X		X		
Qe-59	1330 m. SE of "A"	undeformed	5.9		X		X	X	X		X	X				X
Qe-62	1870 m. SE of "A"	undeformed	5.9		X		X	X	X	X	X	X		?		X

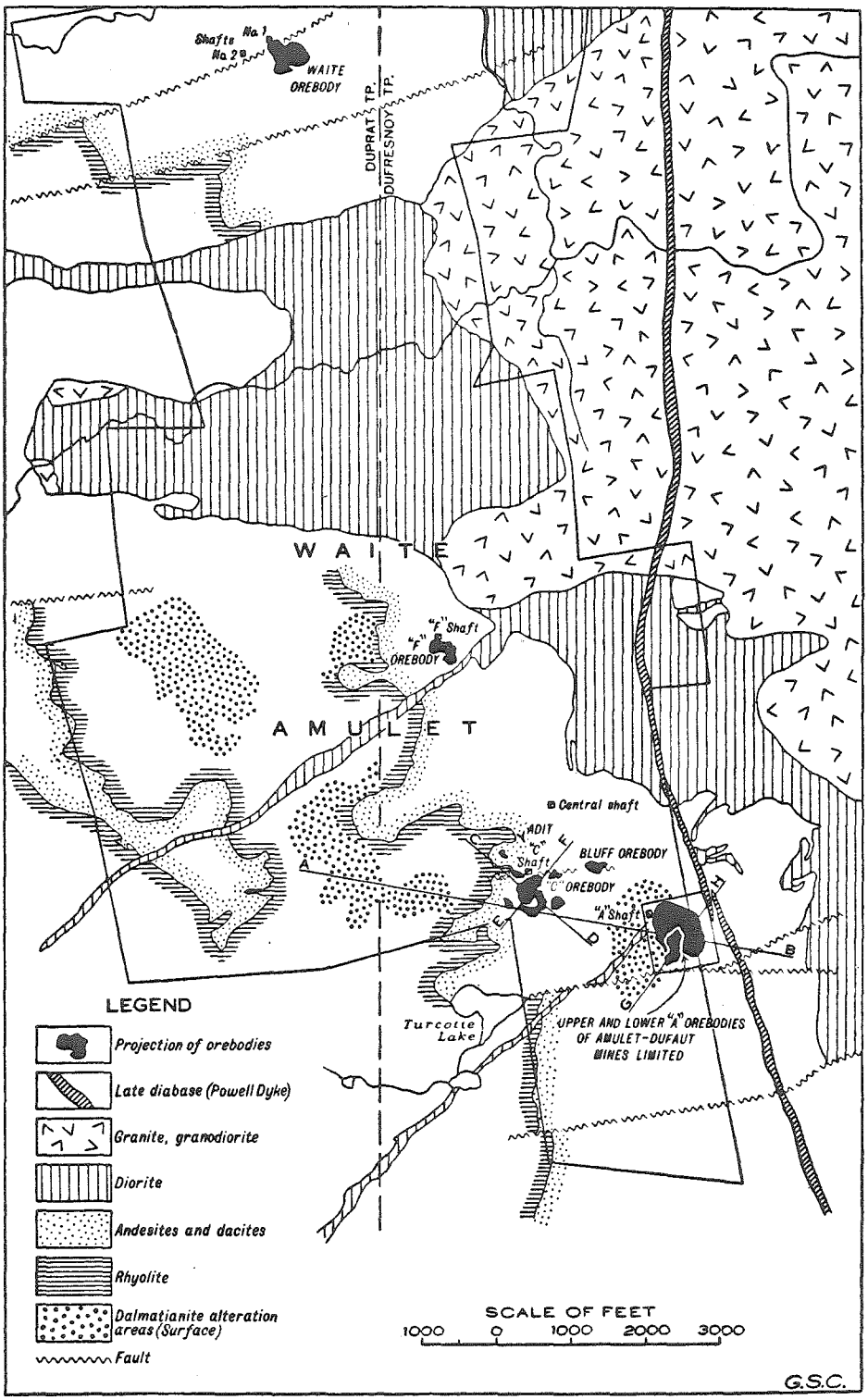

Figure 4C-1. Geologic map of the Waite-Amulet group of orebodies (from Suffel, 1948). The attention in this study is focused on the Amulet "A" deposit.

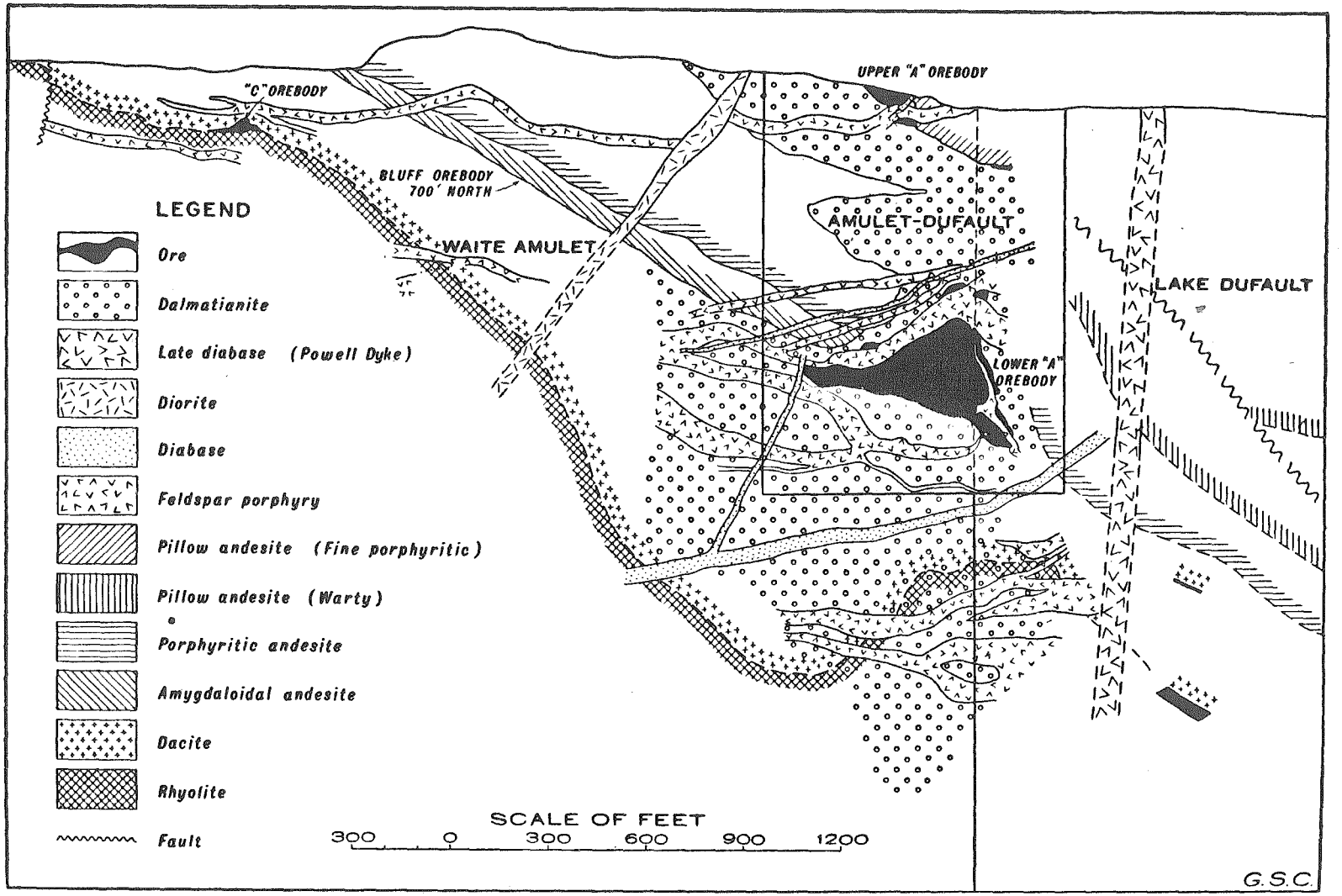

Figure 4C-2. Cross section through the Amulet "A" mine (from Suffel, 1948). The dalmatianite chimney extends through to the surface, where it was sampled.

in the case of the Lower "A" and Upper "A" orebodies. The alteration chimney passes from great depth through the Lower "A" orebody and continues upward to the Upper "A" orebody at the present surface (Fig. 4C-2). Relations such as this suggest (Spence and de Rosen-Spence, 1975) that the hydrothermal activity was episodic, and that the altered chimney of rock was in use as a fluid conduit intermittently. The surface outcrops of dalmatianite at the Amulet "A" deposit may in fact have been associated with a third sulfide lens, above the Upper "A," but now eroded (Fig. 4C-2). Although the surface outcrops of dalmatianite are not obviously related to a single sulfide lens, the altered rocks found there are typical of the alteration pipes throughout the Noranda area (W.A. Hogg, pers. comm., 1979).

In plan view the alteration chimney at the Amulet "A" consists of two concentric zones (Fig. 4C-3). The central zone consists of dalmatianite, a distinctive spotted rock (Fig. 4C-4) with large cordierite porphyroblasts (first described by Walker, 1930; Cooke et al. 1931; and Price, 1934). Surrounding that is a stockwork or zone of "grid alteration" (Fig. 4C-4), which stands out "due to differential weathering of the rock, leaving the silica-bearing joints projecting above the general surface" (Price and Bancroft, 1948; p. 756). Mineralogically, the zone of grid fracturing is a zone of biotite alteration. Beyond the grid fracturing, the Amulet andesite is regionally recrystallized to the greenschist facies.

Fifteen samples were collected along a traverse 200 meters long through the center of the dalmatianite zone (Fig. 4C-3). The traverse began at the NW edge of the outcrop on the hill above the mine (biotite zone), crossed the land bridge over the pit, and finished at the road in

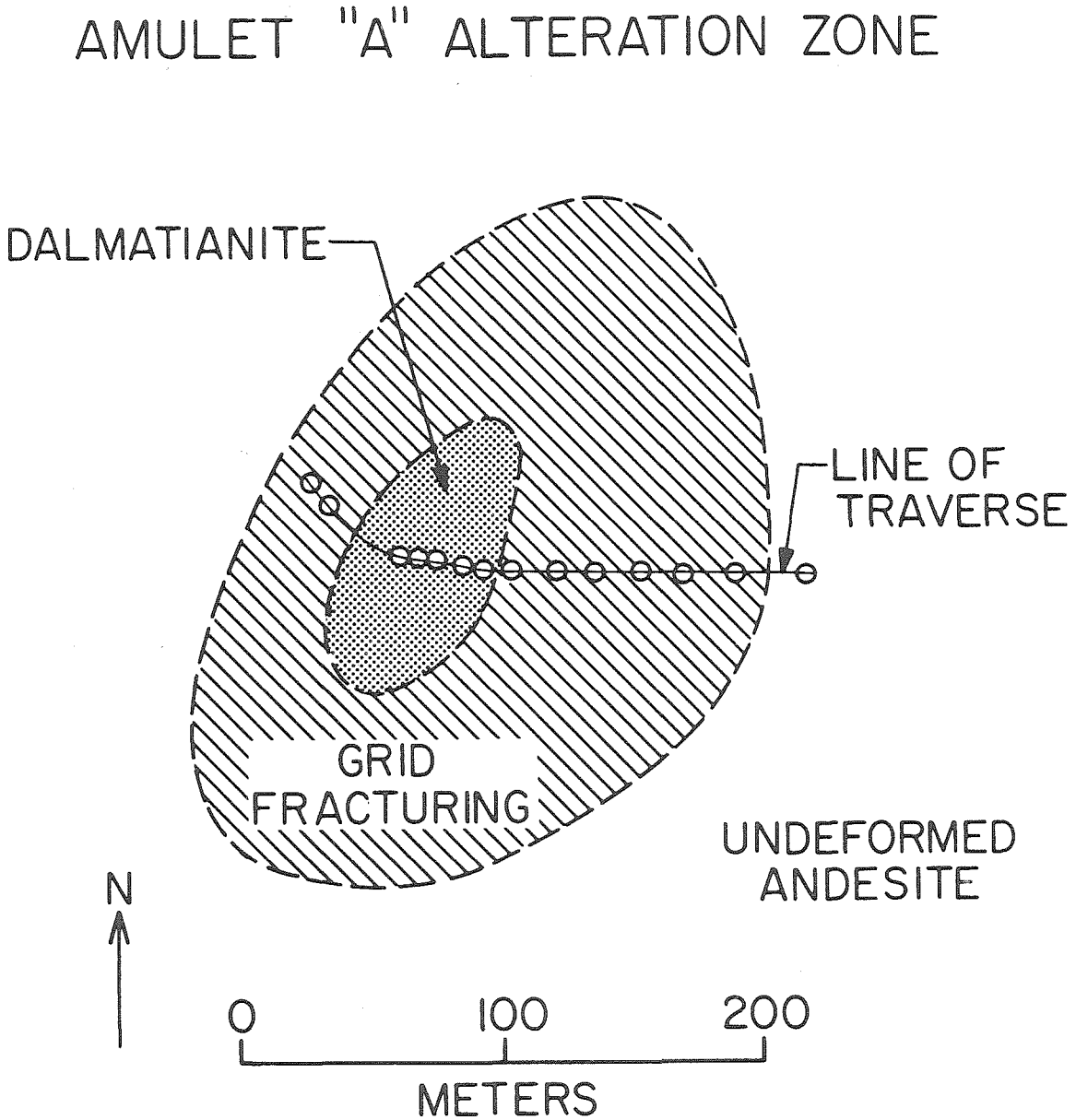

Figure 4C-3. Sketch map of the Amulet "A" alteration zone showing the sample localities. The Amulet pit lies to the NW of the sampled traverse.

Figure 4C-4. Outcrop photographs from the Amulet "A" mine.

a.) Dalmatianite from the center of the altered zone. The white spots are cordierite porphyroblasts, which are set in a matrix of quartz, chlorite and anthophyllite.

b.) The grid fracturing zone, which concentrically surrounds the dalmatianite zone. The silica-filled fractures stands out due to differential weathering.

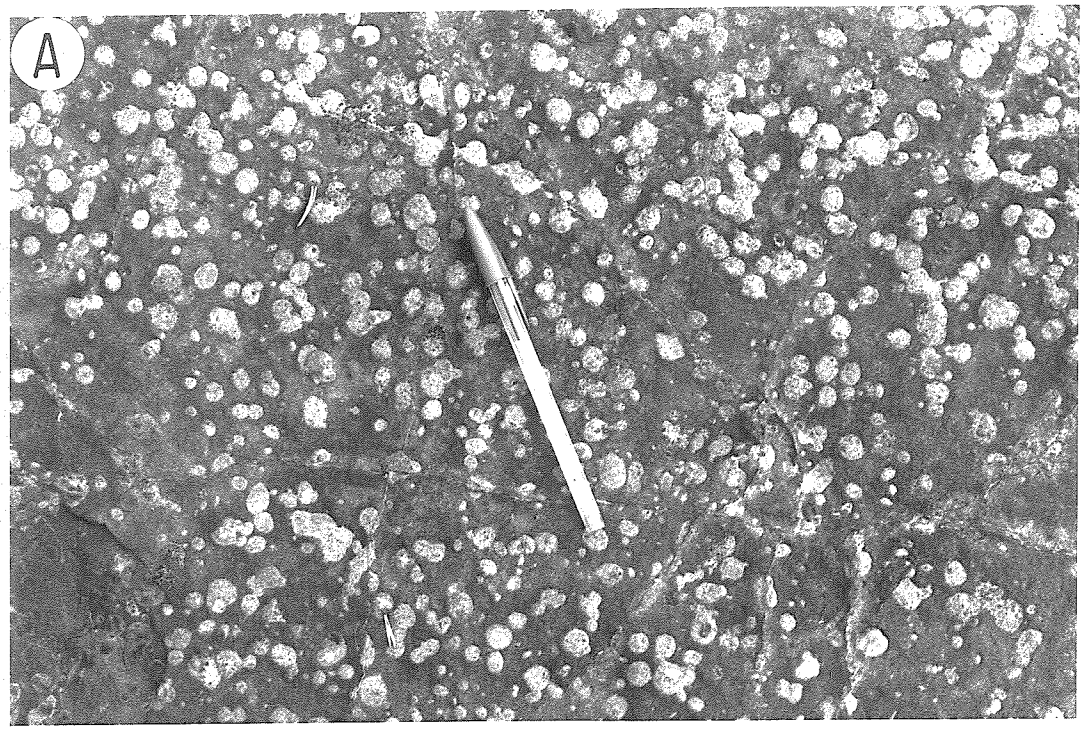

DALMATIANITE

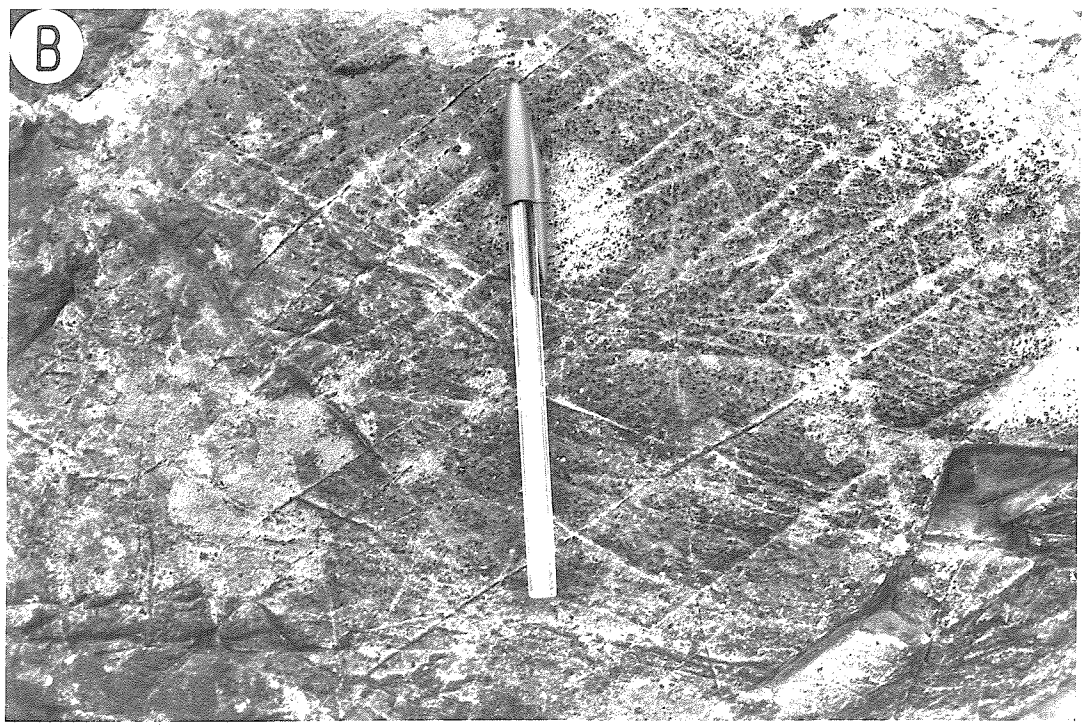

GRID FRACTURING

the valley below (beyond the limits of the altered area). To further evaluate the regional alteration effects, an additional 32 samples were analyzed from throughout the Noranda camp (Chapter 3D). Eight of these rocks are from within 1.5 km. of the Amulet "A" mine.

II. PETROLOGY

In order to interpret the oxygen isotopic data, the metamorphic petrology must be considered in detail. In the center of the altered zone recrystallization has been complete, with silicification and chloritization being the principal effects. Quartz pseudomorphs after feldspar laths are set in a matrix of chlorite plus biotite and cubic opaques (Fig. 4C-5 a,b). Large cordierite porphyroblasts and anthophyllite rosettes partially replace the chloritic groundmass, poikillitically preserving the original felted igneous texture of the rock (Fig. 4C-5 a,b). In addition, quartz fills the scattered amygdules and occupies the numerous veins which cut the rock. In the grid fracturing zone, cordierite and anthophyllite are absent, whereas actinolite and epidote are present. Biotite comprises up to 40% of the rock, and chlorite is in low abundance (<5%). Silicification remains important, with modal quartz in the range 20-40%. Outside the alteration zone the rocks consist of epidote-actinolite-albite-quartz-calcite (Table 4C-1), a typical greenschist assemblage. Although present in all samples, quartz veins are much more abundant in the dalmatianite zone. This mineralogic zonation is summarized in Figure 4C-6.

The assemblage cordierite-anthophyllite is petrologically intriguing, and an extensive literature has developed concerning the interpretation of rocks containing it (e.g. Eskola and the early Finnish petrologists, quoted in Deer et al. 1966, p.159; Tilley, 1935; Tilley, 1937; Floyd,

Figure 4C-5. Photomicrographs from the Amulet "A" mine.

a.) Qe-30, transmitted light; b.) same view, crossed polars. The original igneous texture of the rock is well preserved. In crossed polars, however, the plagioclase laths are found to be replaced by a mosaic of quartz crystals, and the groundmass is replaced by chlorite with minor biotite.

c.) Qe-30, crossed polars. A large cordierite porphyroblast (lower right) which has replaced the chlorite groundmass.

d.) Qe-30, partially crossed polars. An anthophyllite rosette.

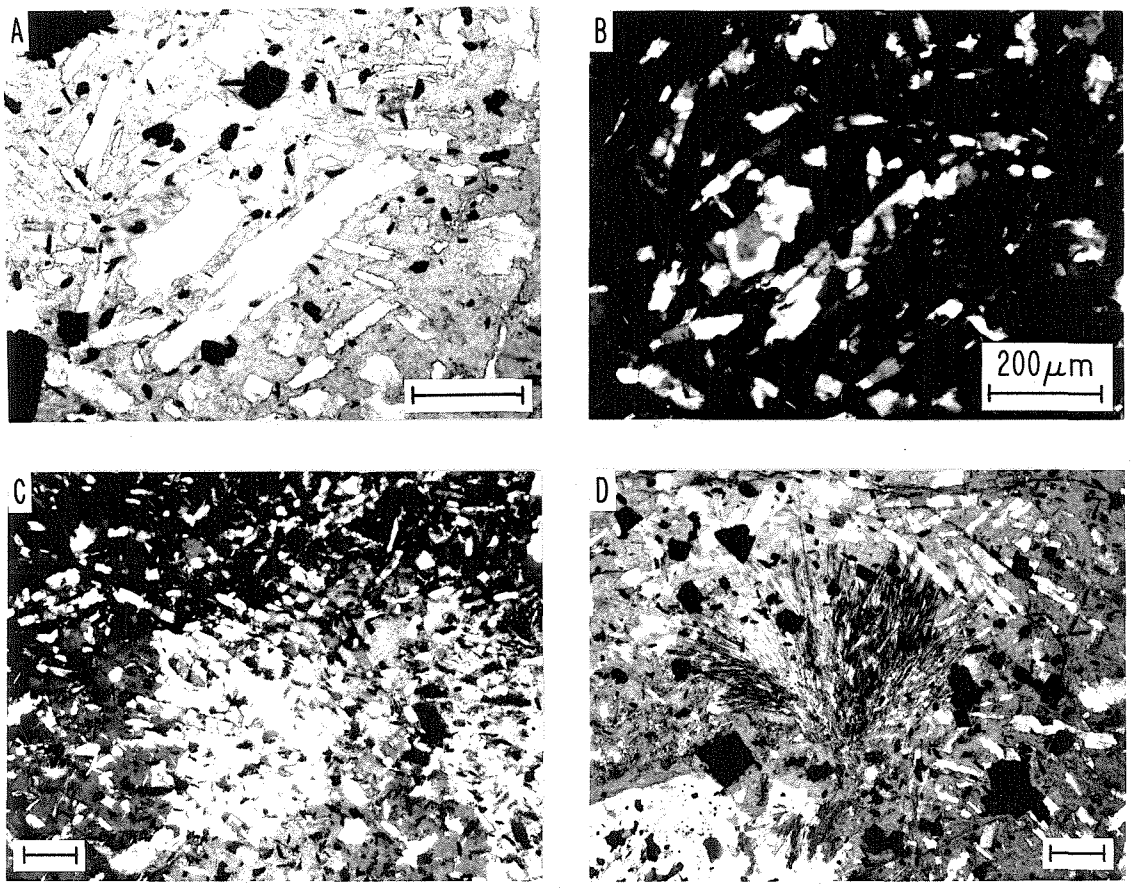
A
B
200μm
C
D

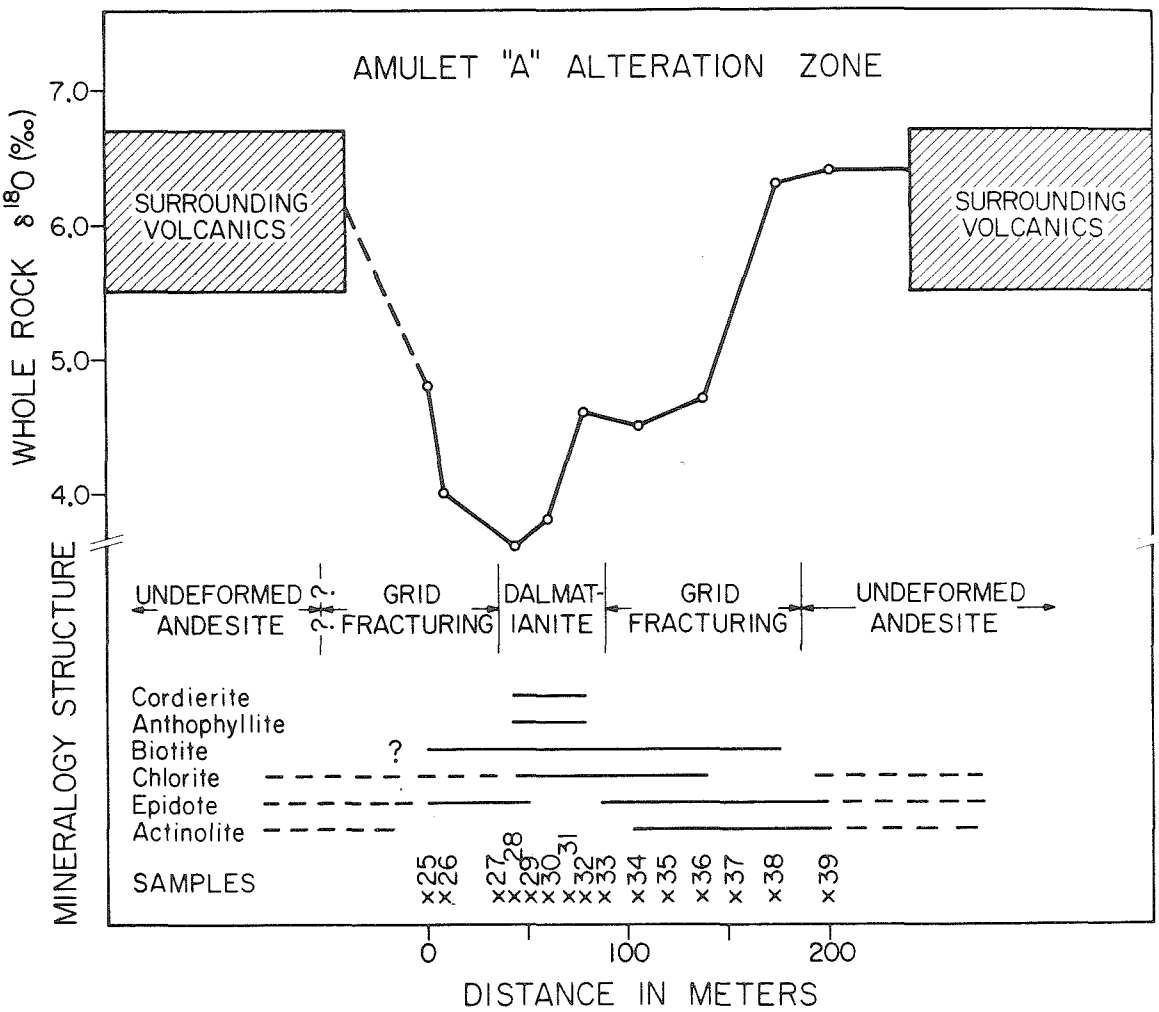

Figure 4C-6. Variations in $\delta^{18}O$, mineralogy and structure along the Amulet traverse.

1965; Vallance, 1967; Grant, 1968; Lal and Moorhouse, 1968; de Rosen-Spence, 1969; Chinner and Fox, 1974; James et al. 1978). The central argument concerns whether such Mg-rich rocks were produced by metasomatism during metamorphism or by some other means prior to metamorphism. In the Noranda case, de Rosen-Spence (1969) has argued convincingly that the dalmatianite zones formed by contact metamorphism of preexisting chloritic alteration pipes. This is based on the paragenetic relations seen in thin section combined with the fact that all of the massive sulfide deposits in the Noranda area have chemically similar chimney-shaped alteration zones beneath them, but partial recrystallization to cordierite and anthophyllite has taken place only in the 1 km. wide contact metamorphic aureole surrounding the Lake Dufault granodiorite.

The rocks at the Amulet "A" have therefore been subjected to two principal metamorphic events. First, transformation of the Amulet andesite to a quartz-chlorite-biotite rock accompanied the formation of the ore deposit. Second, partial recrystallization of the chloritic chimney to cordierite and anthophyllite accompanied the emplacement of the Lake Dufault granodiorite. The temperature of the first metamorphism was probably in the vicinity of 300-350°C, an apparently universal temperature in this type of environment. Heaton and Sheppard (1976) for example, found that the stockwork mineralization in the Cyprus massive sulfide deposits was 250-350°C. The temperature of formation of the stockwork ores of the Kuroko deposits has been estimated to be about 300° (Ohmoto and Rye, 1974; Hattori et al. 1979). Similar temperatures are present in the modern geothermal fields at the Salton Sea (Muffler and White, 1969) and Wairaki (Steiner, 1968). Finally, submarine hot springs associated with massive sulfide pinnacles and with exit tempera-

tures around 350°C have been directly sampled by ALVIN on the East Pacific Rise at 21°N (Edmond et al. 1979a).

The maximum temperature attained during the second metamorphism is probably around 550-600°C. At a pressure of 2 kb. and a chlorite composition approaching that of amesite, cordierite is first stabilized at about 550°C, and the upper stability limit of quartz + chlorite is about 600°C (Fleming and Fawcett, 1976). At 2 kb. in the iron-free system, the lower stability limit of anthophyllite is about 670°C (Schreyer, 1976). The Amulet andesite adjacent to the dalmatianite chimney contains epidote-actinolite-albite-quartz-calcite, an assemblage stable over wide range of temperatures and pressures.

III. OXYGEN ISOTOPE DATA

1. Whole-Rock Data. The whole-rock oxygen isotopic distribution along the Amulet traverse is shown in Figure 4C-6. The volcanic rocks surrounding the mine range in $\delta^{18}O$ from +5.2 to +6.7. As the biotite alteration zone is approached from either side, $\delta^{18}O$ decreases steadily to about +4.5, and then in the dalmatianite zone $\delta^{18}O$ drops as low as +3.6. Thus there is an ^{18}O-low centered on the altered zone. The significance of this ^{18}O-depleted zone is discussed in detail below, considering the two principal metamorphic events.

Although the isotopic compositions of the rocks surrounding the Amulet mine are typical for those of fresh igneous rocks (+6 to +7), the country rocks here are highly altered. These rocks, along with the rest of the Abitibi greenstone belt, have been subjected to an episode of subseafloor hydrothermal burial metamorphism (see Chapter 3). This process generally took place at about 200-300°C (producing prehnite-pumpellyite type metamorphic assemblages), and typically involved large

fluxes of water through the greenstones. Although most of the greenstone belt was enriched in ^{18}O by this process, in the area around the Amulet "A" mine the temperature was apparently such (about 300°C) that $\delta^{18}O$ did not change much. The oxygen isotopic similarity of the Amulet country rocks to fresh igneous lavas is purely coincidental--the volcanic rocks surrounding Amulet have in fact been completely exchanged and altered.

2. Mineral Data. Quartz and chlorite separates were obtained from sample Qe-30 from the center of the dalmatianite zone (Fig. 4C-6). The quartz separate is 98% pure, and has $\delta^{18}O = +6.23$. The chlorite separate ($\delta^{18}O = +2.49$) contains about 20% quartz + cordierite, which are unfortunately difficult to distinguish. Most of the impurities texturally resemble the quartz in the thin section, however, suggesting $\delta^{18}O_{chlorite} \approx +1.6$.

To first approximation Qe-30 is a binary mixture of quartz and chlorite. Using the whole rock $\delta^{18}O$ (+3.70) and the above mineral values, it is possible to calculate the mode of Qe-30 (quartz 46%, chlorite 54%). This is in good agreement with the actual point-counted mode of quartz 46%, chlorite 43%, cordierite 5%, biotite 3%, and anthophyllite 1%, and indicates that the data are internally consistent. Using $\Delta_{qtz-chl} = 2.01\ (10^6/T^2) + 1.99$ (Wenner and Taylor, 1971) the above mineral compositions indicate a temperature of about 600°C. This suggests (not surprisingly) that the constituent minerals of Qe-30 equilibrated isotopically during the high temperature contact metamorphic event which produced the cordierite and anthophyllite.

3. The Effect of Contact Metamorphism. The question of paramount importance is the extent to which the contact metamorphism has affected

the whole-rock oxygen isotopic compositions. There can be little doubt that the rock in the dalmatianite pipe was completely reconstituted during the first (hydrothermal) metamorphism. There has been a massive addition of Mg, H_2O, and Si, and a massive loss of Ca, Na, and perhaps Fe. The original igneous minerals have been completely pseudomorphed by secondary minerals.

The fact that $\delta^{18}O$ is lower in the core of the altered zone is clearly related to the fact that those rocks contain more chlorite (a low-^{18}O mineral), which was introduced during the hydrothermal event. Such low $\delta^{18}O$ values are commonly observed in chlorite-rich alteration assemblages in Phanerozoic ophiolites and massive sulfide deposits; they are to be expected because of the property that chlorite concentrates ^{16}O relative to most other minerals. In addition, the temperature of alteration in the stockwork zone was probably equal to or greater than that of the surrounding rocks (e.g. Heaton and Sheppard, 1976). This would have augmented the ^{18}O lowering in the chimney. The gross features of the oxygen isotopic distribution shown in Figure 4C-6, therefore, were undoubtedly present before the contact metamorphic event.

During the contact metamorphism the oxygen isotopes in the dalmatianite zone equilibrated at least on a hand-specimen or intergranular scale (as shown by the 600°C isotopic temperature of Qe-30). Whether they also equilibrated on a scale of meters or even hundreds of meters is difficult to evaluate. Because chlorite is a low-^{18}O mineral at 600°C as well as at 300°C, the same overall $\delta^{18}O$ profile would be expected in Figure 4C-6, regardless of the temperature. Although the magnitude of the isotopic anomaly would decrease with increasing temperature of equilibration, because chlorite was introduced prior to the

thermal metamorphism, the oxygen isotopic effect must also have been so introduced.

The degree of equilibration could be evaluated by analyzing a single mineral, such as quartz, from a number of samples. If homogenization has taken place, all of the quartz should have the same $\delta^{18}O$. Because of the fine grain size and commonly low abundance of quartz, only two such measurements were obtained: Quartz in the dalmatianite zone has $\delta^{18}O$ of +6.23, and in a nearby diorite it is +7.91. This suggests that oxygen isotopic equilibrium was attained only locally.

4. Oxygen Isotopic Effect of Dehydration. Although the specific reaction which introduces cordierite and anthophyllite to the dalmatianite has not yet been identified, it is tentatively assumed to be the following:

$$5\ Mg_3Si_2O_5(OH)_4 + 6\ Mg_2Al_2SiO_5(OH)_4 + 23\ SiO_2 \rightarrow$$

(clinochlore) (quartz)

$$3\ Mg_7Si_8O_{22}(OH)_2 + 3\ Mg_2Al_4Si_5O_{18} + 19\ H_2O.$$

(anthophyllite) (cordierite)

Note that 13% of the oxygen in the reactants of this reaction as written are lost as water. This loss would have a negligible effect on the whole-rock $\delta^{18}O$, however. The chlorite and quartz in Qe-30 are only 5-10% recrystallized to cordierite and anthophyllite. Thus, only about 1% of the oxygen in the rock is lost due to dehydration. Even if $\delta^{18}O$ of the water were 10 per mil different from the rock, only a 0.1 per mil shift would be produced. In actual fact, at 600°C $\delta^{18}O$ of the fluid would probably be about +4.4, which is only 0.7 different from the rock.

It is possible that simple dehydration was not the only contact metamorphic effect. For example, a hydrothermal convection cell driven

by the Lake Dufault granodiorite conceivably could have affected the area surrounding it (see Taylor, 1977). In the case of the Amulet, however, there is little evidence for such an event. All of the available data indicate that the oxygen isotopic distribution in the dalmatianite zone reflects its hydrothermal history, and that the whole-rock values have been little, if at all, modified by the contact metamorphism.

5. Fluid Composition. At the Amulet mine, δ^{i}_{rock} is assumed to be about +6.0 and δ^{f}_{rock} is measured at +3.7. Using the quartz-chlorite fractionation estimated by Wenner and Taylor (1971) and the abundances of quartz and chlorite in Qe-30 in the proportions 45:55, it is possible to calculate $\delta^{18}O$ of the two minerals at any given temperature. This amounts to reconstructing the rock prior to the contact metamorphic event. Then, assuming an infinite water/rock ratio (a restriction which will be relaxed later) and using the quartz-water fractionation of Clayton et al. (1972), the initial fluid can be calculated (See Chapter 1B). Several possibilities are shown in the following table, and the results are illustrated graphically in Figure 4C-7. As discussed above,

T	Δ qtz-chl	δ chl	δ qtz	Δ qtz-water	δ water
250	9.34	-0.50	+8.84	9.4	-0.6
300	8.11	+0.05	+8.16	7.4	+0.8
350	7.17	+0.47	+7.64	5.8	+1.8

the temperature of the hydrothermal alteration was probably in the range 250-350°C. This implies that the fluid composition was in the range $\delta^{18}O = +0.5 \pm 1.0$, consistent with the hydrothermal fluid being heated seawater. Alternatively, if we assume that the Amulet deposit

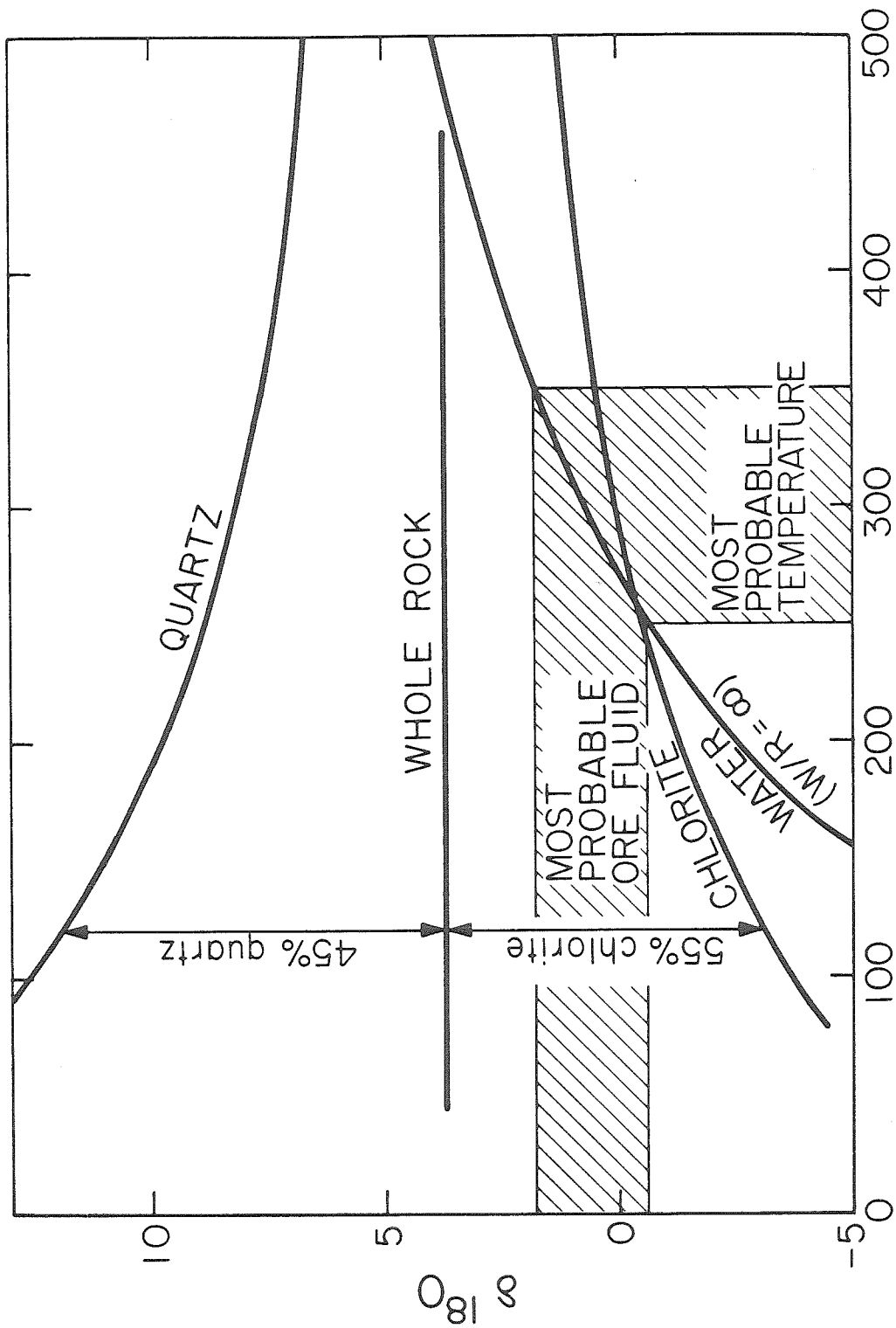

Figure 4C-7. $\delta^{18}O$ of coexisting quartz, chlorite and water in Qe-30 as a function of temperature.

had an origin similar to that of the Cyprus massive sulfide bodies, then the $\delta^{18}O$ of Archean seawater is shown to be about +0.5.

6. Water/Rock Ratio. A lower limit on the integrated water/rock ratio can be calculated by comparing the total mass of altered rock to the mass of fluid necessary to transport the sulfide ore. A total of 5,900,000 tons of ore were mined from the Amulet "A," which corresponds to about 5.4×10^{12} gm. of sulfides. The data of Mottl et al. (1979) indicate that at 400°C, seawater flowing through basalt contains about 100 ppm Fe (along with small amounts of base metals). If all of this metal were deposited in the massive sulfide lens, the mass of fluid would have been about 2.7×10^{16} gm. (only half of the ore is metal). Using an alteration zone 600 ft. in diameter and 3000 ft. deep (Fig. 4C-2), the mass of the alteration pipe is about 3.0×10^{14} gm. This indicates a minimum integrated water/rock ratio of about 100. Note, however, that because of the stacking of the orebodies the alteration pipe apparently was subject to periodic water fluxes. The deeper levels of the pipe have therefore interacted with more water than the higher levels. In particular, Qe-30 is from above the lower "A" orebody (Fig. 4C-2), so the fluid which formed the lower "A" did not actually flow through Qe-30. The overall similarity of Qe-30 with the dalmatianite which is clearly associated with sulfide mineralization, however, suggests that the water/rock ratio was large.

Figure 4C-8 shows that as long as the water/rock ratio was greater than about two, the ore-forming fluid must have had $\delta^{18}O$ close to zero in order to produce the +3.7 dalmatianite. The water/rock ratio probably decreased from the center of the dalmatianite pipe out into the country rocks, but because of the uncertainties in the temperature distribution

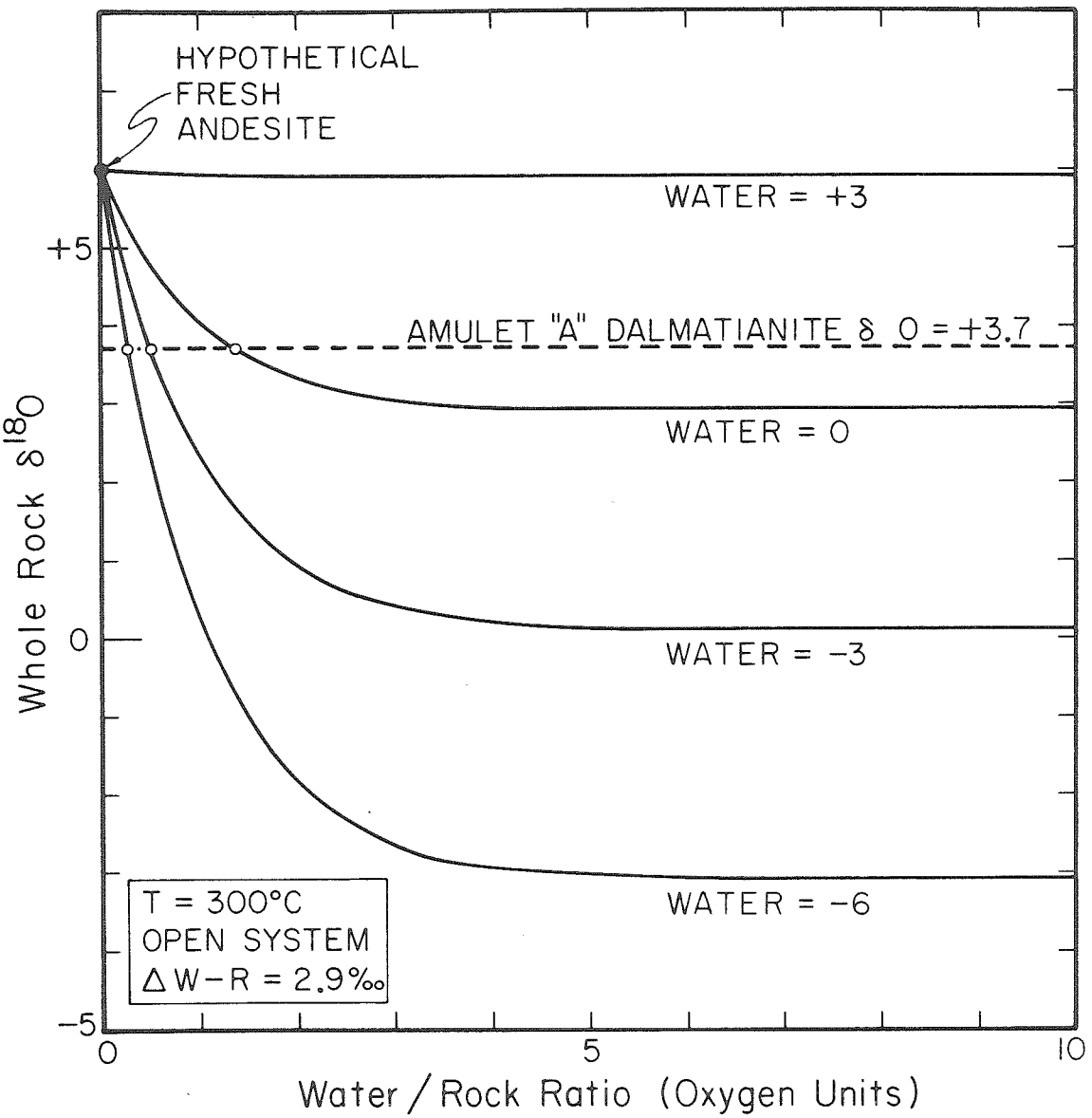

Figure 4C-8. Possible paths of alteration of a fresh andesite (+6) to dalmatianite (+3.7) through interaction with fluids of different $\delta^{18}O$. As long as W/R > 2 the water must have $\delta^{18}O$ between 0 and 1.

and the variability of the bulk compositions (which affects Δ), the detailed water/rock variations cannot be calculated.

IV. CONCLUSIONS

Whole-rock oxygen isotopic measurements across the dalmatianite chimney at the Amulet "A" mine indicate that the most altered rocks are depleted in $\delta^{18}O$ compared to the adjacent Amulet andesite (+3.7 vs. +6.0). The area has been subjected to two principal metamorphic events, the first a hydrothermal event responsible for the deposition of the sulfide ore, and the second a contact metamorphic event associated with the emplacement of the Lake Dufault granodiorite. Petrographic study indicates that only about 10% of the minerals in the alteration zone were destroyed during the second metamorphism, indicating that the ^{18}O-depletions were produced by hydrothermal activity associated with the ore-forming event. If the temperature of alteration were in the range 250-350°C, similar to that in Phanerozoic massive sulfide deposits, $\delta^{18}O$ of the fluid must have been about $+0.5 \pm 1.0$. This is consistent with the ore-forming solution being seawater which had percolated into the volcanic pile, been heated, and flowed back into the ocean as a submarine fumarole. The overall integrated water/rock ratio in the alteration pipe was almost certainly greater than two, and may have been greater than 100.

An important feature of the second (contact) metamorphism is that soon after formation, the chlorite-rich chimney was recrystallized to the coarser-grained dalmatianite. This recrystallization produced a rock that would be <u>much</u> less susceptible to later low-temperature ^{18}O exchange than the original fine-grained mineral assemblage. Thus, parenthetically, the superposition of the contact metamorphic event can be interpreted as actually favoring the oxygen isotopic preservation of the

original Archean $\delta^{18}O$ values during the subsequent 2.8 b.y. of earth history.

CHAPTER 4D. COMPARATIVE STABLE ISOTOPE GEOCHEMISTRY OF MASSIVE SULFIDE DEPOSITS

The above studies of Kidd Creek and Amulet "A" bring to six the number of volcanogenic massive sulfide deposits which have been investigated using oxygen isotopes. These six localities are, in addition to Kidd creek and Amulet "A" (this work), the Cyprus deposits (Heaton and Sheppard, 1976), the Raul mine of Peru (Ripley and Ohmoto, 1979), the Ducktown, Tenn. deposits (Addy and Ypma, 1977), and the Kuroko deposits of Japan (Ohmoto and Rye, 1974; Hattori and Sakai, 1979). A number of the important characteristics of these deposits are listed in Table 4D-1. There are some interesting and important similarities and differences among these deposits which can be used to constrain models of massive sulfide genesis.

I. OXYGEN ISOTOPES

According to the volcanogenic massive sulfide model, the ore-forming fluid passes through the submarine geologic section, emerges into the ocean, and precipitates the ore at or near the ocean/rock interface. The conduit of altered rocks along which the hydrothermal fluid ascended must inescapably have been subjected to large water fluxes, probably at temperatures of 300-350°C, producing thorough hydrothermal alteration, and hydrogen and oxygen isotopic exhange. Comparison of $\delta^{18}O$ in the highly altered zones with that in the surrounding country rocks, therefore, is the first step in comparing ore fluids. Figure 4D-1 shows how $\delta^{18}O$ varies in a generalized, schematic traverse through the altered zones of each of the six localities listed above. In each case the traverse begins and ends in the enclosing country rock, and the scale has been adjusted so that the width of each altered zone is the

TABLE 4D-1. COMPARISON OF SIX MASSIVE SULFIDE LOCALITIES.

Characteristics	Kidd Creek	Amulet	Ducktown	Cyprus	Raul	Kuroko
GEOLOGY						
Age	Archean	Archean	Late Proterozoic	Cretaceous	Cretaceous	Miocene
Geologic setting	Greenstone Belt	Greenstone Belt	Geosyncline?	Ophiolite	Island arc	Island arc
Country rocks	Andesitic to rhyolitic volcanics	Andesitic to rhyolitic volcanics	Clastic sediments intercalated with volcanic tuffs	Basaltic pillow lavas	Andesitic volcanics and marine sediments	Basaltic, andesitic and rhyolitic volcanics
Ore body size (tons)	95,000,000	6,000,000	~5,000,000	~5,000,000	not published	~5,000,000
Dominant sulfides	Py-sph-py	Py-po-cpy-sph	py-po-cpy	Py-cpy	Py-cpy	Py-cpy-sph-ga
Post-ore metamorphism	Greenschist	Amphibolite	Kyanite grade	none	Amphibolite	none
ALTERATION ZONE						
Alteration shape	uncertain shape	pipe-shaped	uncertain shape	pipe-shaped	broad, poorly defined	pipe-shaped
Protolith	Rhyolite	Andesite	Sedimentary	Basalt	Variable	Rhyolite
Alteration mineralogy	qtz,ser,chl	qtz,chl	qtz,musc,gar,bio,chl	qtz,chl	variable	qtz,ser,chl
OXYGEN ISOTOPIC DATA						
$\delta^{18}O$ altered zone	11-16	3.6-4.6	6-7	1.4-4.1	8-11	8
$\delta^{18}O$ country rocks	10-12	5.2-6.7	8-9	8-13	not known	8
Calc. $\delta^{18}O$ fluid	6-9	0.5±1	5-7 (500°C)	0±1	10±2	0±1
HYDROGEN ISOTOPIC DATA						
δD altered zone	not known	not known	-51 to -54 (musc.)	-33 to -41	-30 to -49	-35 to -47
δD country rocks	not known	not known	-49 to -50 (musc.)	-40 to -67	not known	-60 to -63
Calc. δD fluid	not known	not known	-23 to -26 (500°C)	0±5	-3 to +42	-20±10
REFERENCES	1,13	1,11,12	7,14	2,5	9,10	3,4,6,8

References: [1]This work [2]Constantinou (1976) [3]Hattori and Sakai (1979) [4]Hattori et al (1979) [5]Heaton and Sheppard (1976) [6]Lambert and Sato (1974) [7]Mauger (1972) [8]Ohmoto and Rye (1974) [9]Ripley and Ohmoto (1977) [10]Ripley and Ohmoto (1979) [11]Spence and de Rosen-Spence (1975) [12]Suffel (1948) [13]Walker et. al (1975) [14]Ypma and Addy (1977)

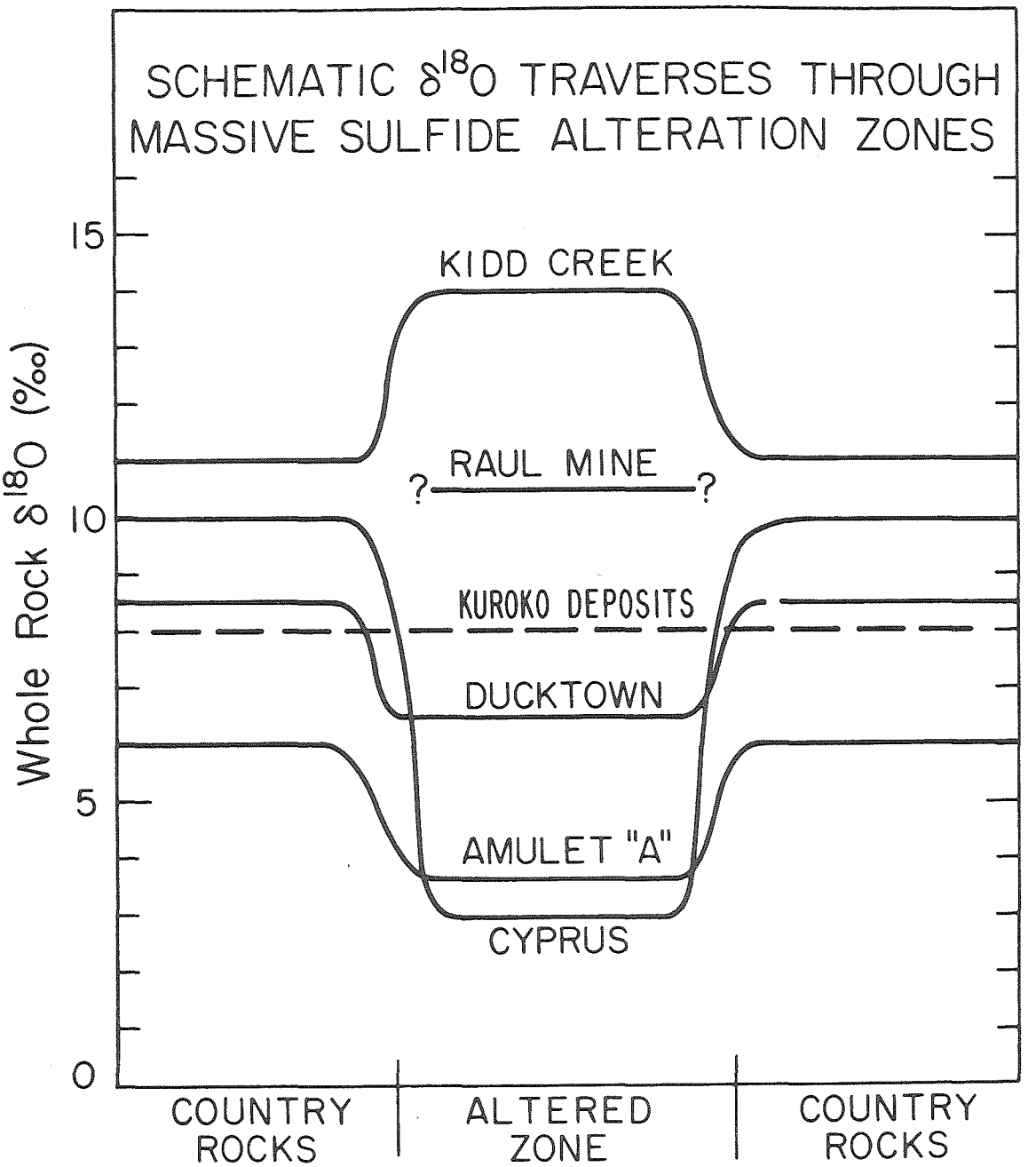

Figure 4D-1. Schematic whole-rock $\delta^{18}O$ traverses through the altered zones of six massive sulfide localities. The widths of the altered zones have been adjusted to the same value for comparison. Sources of data are listed in the text.

same.

Three of the localities have similar $\delta^{18}O$ profiles on Figure 4D-1. Ducktown, Amulet "A", and Cyprus all show a depletion in $\delta^{18}O$ in the altered zone compared to the country rocks. This has been interpreted by Heaton and Sheppard (1976) and Beaty (this work) as indicating that the fluids in the alteration zones at Cyprus and Amulet "A", respectively, were hotter than those in the surrounding rocks. At Ducktown Addy and Ypma (1977) concluded that the ^{18}O-depletion indicated formation of the altered zone by meteoric water. This interpretation has little to recommend it, however, and their data may be reinterpreted (see below) to indicate a genesis similar to that of Cyprus and Amulet "A".

Preliminary results from the Uwamuke orebody (a Kuroko-type deposit) indicate that the stockwork zone and surrounding rock are both highly altered, but are uniform in $\delta^{18}O$, $+8.0 \pm 1.2$ (Hattori et al. 1979; K. Muehlenbachs, pers. comm., 1979). In the absence of a more detailed study, it remains to be seen whether or not an ^{18}O depletion is present in the Kuroko stockworks. At the Raul mine $\delta^{18}O$ was measured in the altered zone only, but was not compared to the surrounding rock (Ripley and Ohmoto, 1979). Finally, at Kidd Creek there appears to be an ^{18}O-enrichment of about 3 per mil in the altered zone as compared to the country rocks.

Figure 4D-1 clearly shows, therefore, that a wide range of $\delta^{18}O$ is present in the alteration zones of these massive sulfide deposits. However, discounting for the moment Raul and Kuroko (for which there are insufficient data), Amulet "A" and Cyprus (and perhaps Ducktown) are rather similar to one another, while Kidd Creek is distinctly different.

II. HYDROGEN ISOTOPES

A diagram analogous to Figure 4D-1, but for δD, is presented in Figure 4D-2. There are no δD data currently available for either Kidd Creek or Amulet "A", and in any case one cannot *a priori* assume that these rocks would have preserved their original δD values during 2.8 b.y. of geologic time. In both Cyprus and Kuroko the altered zones are higher in δD than the surrounding rocks. Like the $\delta^{18}O$ data, this is consistent with a higher temperature of alteration in the stockwork. At Ducktown the country rocks have been subjected to a post-ore kyanite-grade metamorphism (500-600°C), and that may have been sufficient to homogenize any preexisting δD gradients. At Raul the sampling did not extend beyond the mine area. Note that with the exception of Ducktown, the altered rocks at these localities all have rather similar δD values, about -40 to -45. As discussed below, this is probably related to the fact that these massive sulfide deposits formed at about the same temperature (300-350°C) from a fluid with a δD value similar to seawater ($\delta D = 0$).

III. DISCUSSION

Using the above isotopic data supplemented with some fluid inclusion work (e.g. Ohmoto and Rye, 1974), it is possible to calculate δD and $\delta^{18}O$ of the various ore fluids. These results, which are in part taken from the authors cited, are shown in Figure 4D-3. The Cyprus and Kuroko ore fluids lie very close to modern seawater. The Raul mine, by contrast, apparently requires an ore fluid which is relatively rich in deuterium ($\delta D = -3$ to $+42$) and markedly enriched in ^{18}O ($\delta^{18}O = +8$ to $+12$). Ripley and Ohmoto have suggested that such a fluid could have evolved from seawater through rapid evaporation in a closed basin.

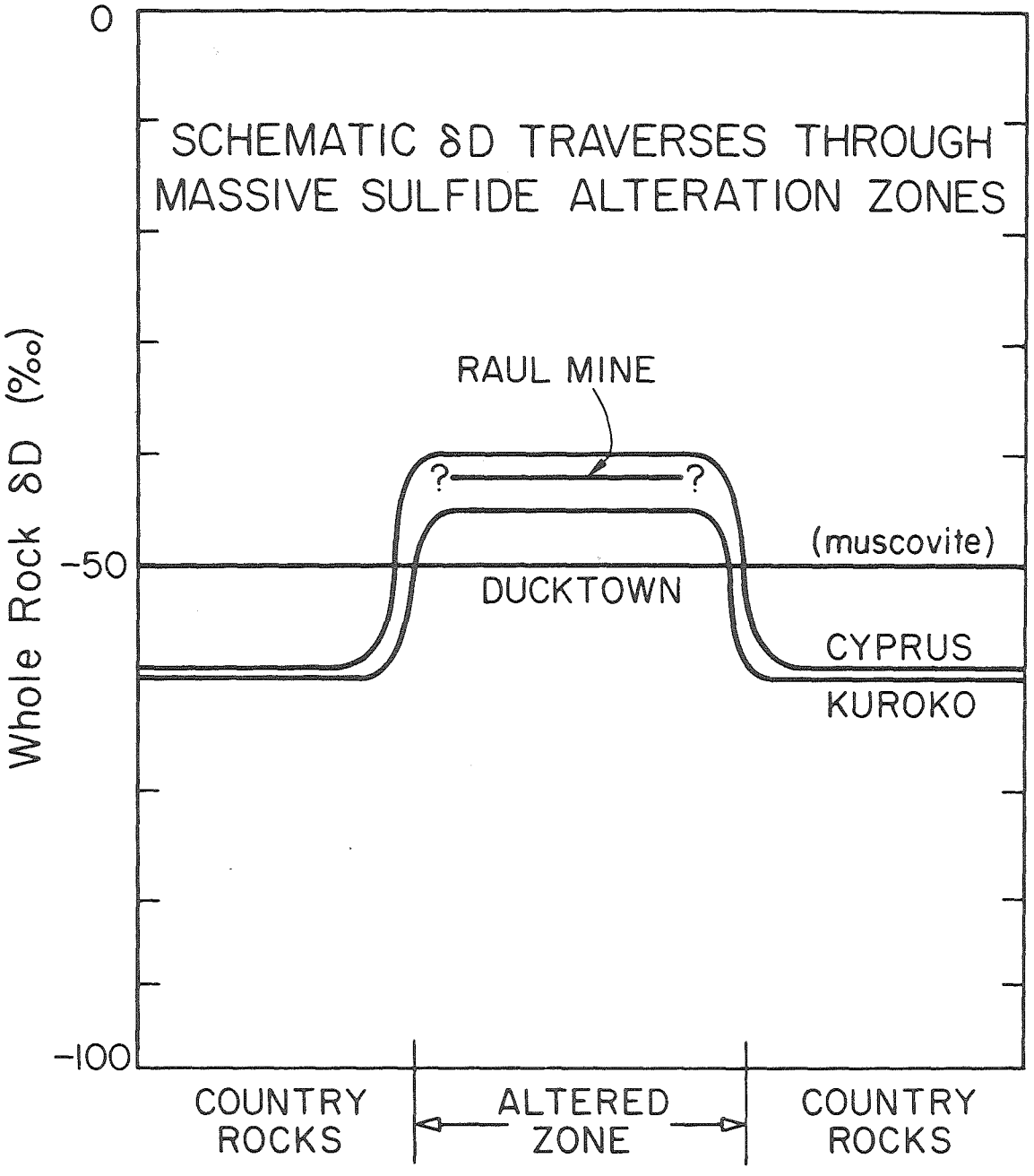

Figure 4D-2. Schematic δD traverses through the altered zones of four massive sulfide localities.

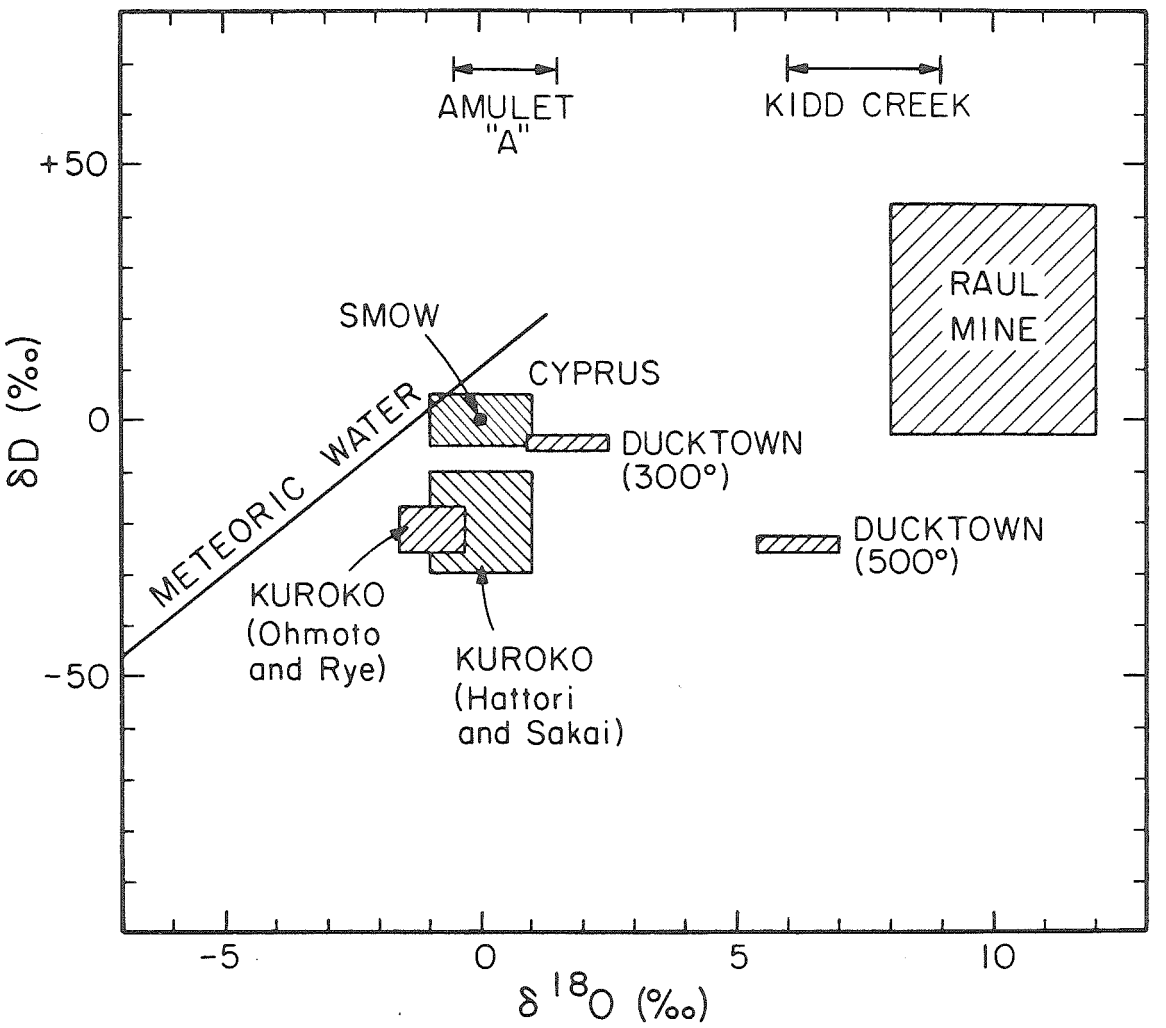

Figure 4D-3. Calculated ore fluids at six massive sulfide localities. For sources of the data, see text.

The Ducktown data are very difficult to interpret because of the extreme structural and metamorphic complexity of the deposit. No single genetic model is sufficient to explain all of the observations (for an extended discussion, see Ypma and Addy, 1977). Using an alteration temperature of 500°C (ore deposition during kyanite-grade metamorphism) the ore fluid has $\delta^{18}O \approx +6$ (Ypma and Addy, 1977). If, on the other hand, the deposit was syngenitic (e.g. Mauger, 1972), with an alteration temperature of 300°C, the $\delta^{18}O$ (ore fluid) $\approx +2$, similar to Cyprus and Kuroko.

Against this background, what is the significance of the data from Kidd Creek and Amulet "A"? The calculated Amulet "A" ore fluid has $\delta^{18}O = 0.5 \pm 1$, which is indistinguishable from the ore fluids at Cyprus, Kuroko and Ducktown (Fig. 4D-3). Because all of these more modern massive sulfide deposits are thought to have formed from seawater circulating through the rocks, a logical conclusion is that the Amulet "A" also formed from seawater and that $\delta^{18}O$ of seawater has not changed significantly since the Archean.

The origin of the Kidd Creek ore fluid is much more puzzling. As is conjectured for the Raul mine, the ore fluid might have been seawater which was modified in some way. Ripley and Ohmoto (1979) have suggested that the $\delta^{18}O = +10$ fluid at Raul originated through rapid evaporation of seawater in a closed basin, and as Fig. 4D-3 shows, the Kidd Creek and Raul ore fluids were similar in $\delta^{18}O$. The discussion in Chapter 4B indicates that there are six possible interpretations of the Kidd Creek data, of which three are preferred, but none can be eliminated. A high-^{18}O ore fluid could either have evolved from seawater (evaporation in a closed basin, exchange with high-^{18}O sediments during circulation,

or by boiling during ascent), or been a metamorphic or magmatic fluid of some sort. Alternatively, if the temperature used to calculate the $\delta^{18}O$ of the ore fluid were too high (150°C instead of 300°C), it is possible that the ore fluid was actually seawater with $\delta^{18}O \approx 0$. Considering all the different lines of evidence available, the two most plausible possibilities are (1) a metamorphic fluid of unknown origin and (2) seawater that has been enriched in ^{18}O through evaporation or interaction with high-^{18}O sedimentary rocks.

It is very obvious from the above analysis that all volcanogenic massive sulfide deposits are not alike. Many are apparently derived simply from seawater circulating through the oceanic crust. In at least two cases, however, the evolution of the ore fluid has been either more complex, or the ore fluid has had a different origin altogether. There is no obvious systematic change in the ore-forming mechanism with geologic time, however. Note that apparently normal, seawater-derived massive sulfide bodies are present from the Archean to the Cenozoic (Amulet, Ducktown, Cyprus, Kuroko), and so are the isotopically distinct high-^{18}O massive sulfides (Kidd Creek, Raul). If the metal-rich brines of the Salton Sea geothermal system were to produce a massive sulfide deposit, these "anomalous" deposits could be extended in age up to the present day.

There is, however, one possibly important difference between these two groups of ore deposits. Kidd Creek is by far the largest of the deposits listed here (Table 4D-1), and is one of the truly great mines of the world. There are no published reports of the size of Raul, but it is possible that the tremendous size and high-^{18}O characteristics of Kidd Creek are genetically related. The ore fluid at Kidd Creek

could have been chemically as well as isotopically different, and this may have led to the deposition of more sulfides. If true, this correlation (i.e. high-$^{18}O \equiv$ very large deposit) would have great significance for future exploration. A test of this model would be to study other very large massive sulfide bodies, such as the Horne Mine (Noranda, Quebec) or Kranden (Wisconsin) to see whether or not they are also very high in ^{18}O.

It is interesting to note that two of the most saline brines in nature, the Red Sea and Salton Sea brines, have the same oxygen isotopic characteristics found in the calculated ore fluids of the above six ore localities. The Red Sea brine has $\delta^{18}O$ = +1 to +2 (Craig, 1966), and is derived from ocean water ($\delta^{18}O \approx 0$). Such a fluid could easily have accounted for the hydrothermal alteration effects observed in the low-^{18}O group of massive sulfide deposits. The Salton Sea brine ($\delta^{18}O$ = +3) is derived from local meteoric ground water ($\delta^{18}O$ = -11) by exchange with high-^{18}O sedimentary rocks (Craig, 1966). If a similar ^{18}O-shift were produced in ocean water, the resultant fluid could account for the high-^{18}O alteration found at both Kidd Creek and Raul. Both the Red Sea and Salton Sea brines are extremely metal-rich, and many authors have suggested that they could represent modern ore-forming fluids.

IV. IMPLICATIONS FOR EXPLORATION

If we may regard Kidd Creek and Raul as oxygen isotopically "atypical" massive sulfide deposits, some general statements about the use of oxygen isotope data for prospecting are possible. In the "normal" case, oxygen isotopic measurements across the alteration zone beneath the massive, banded ore should produce a "bull's-eye" pattern. The intensely

altered rocks within the alteration chimney are lower in $\delta^{18}O$ than the surrounding country rocks. This gradient in $\delta^{18}O$ formed in response to gradients in water/rock ratio and temperature during hydrothermal alteration. Thus, given only the oxygen isotopic data, one could confidently outline ancient hydrothermal conduits by following the zone of ^{18}O depletion.

In general, however, the geologist also has at his disposal a variety of field and petrographical data, and such ancient hydrothermal conduits can also generally be readily identified on this basis alone. Inasmuch as alteration zones are much less widespread than are the 'normal' country rocks, a shotgun oxygen isotope approach in the absence of field studies is very likely to be fruitless. However, oxygen isotopic data might have application in the following manner. If a set of alteration zones can be mapped in a given area, $\delta^{18}O$-values might indicate which one is the most promising target or indicate the center of the conduit. Also, (see below) some rock types do not show diagnostic alteration mineral assemblages, and in addition, these assemblages may have been changed by subsequent metamorphism. As shown above, it is possible that the zones of ^{18}O depletion may survive such metamorphism.

In the "atypical" cases, Kidd Creek and Raul, the exploration potential is much greater. Because the ore-forming fluid had a distinctive isotopic composition, it left a distinctive isotopic imprint on the rocks it flowed through. The rocks procuced by the deep-seated Kidd Creek ore solution have $\delta^{18}O$ values in the range +13 to +16. This is <u>much</u> higher than the $\delta^{18}O$ values of "normal" volcanic rocks elsewhere in the Abitibi belt or, in fact, of volcanic rocks of any age throughout the world. Therefore if a high-^{18}O outcrop found, and if an extremely low-T origin

such as weathering can be excluded, there is an excellent chance that a deep-seated, high-^{18}O hydrothermal solution (evaporated brine?), has flowed through it, and thus there may be a Kidd Creek-type massive sulfide ore deposit nearby.

It is possible that there is not a one-to-one correlation between high-^{18}O outcrops and such massive sulfide deposits, because there may have been environments where such ^{18}O-rich ore-bearing solutions entered the ocean without precipitating sulfides. In general, however, the greater the increase in salinity relative to ocean water the greater is the likelihood of a strong positive ^{18}O shift in the H_2O and the greater the metal carrying capacity of the solution. Also, if the ore-bearing solution precipitated its metals at some distance from the vent (as in a distal massive sulfide deposit), there will be no associated high-^{18}O alteration zone. More detailed studies are obviously required.

It it important to note that at Kidd Creek the rhyolites which underlie the massive ore are texturally and structurally undeformed. They are obviously recrystallized, but the recrystallization is not obviously different from that found in the other rhyolites in the greenstone belt. Oxygen isotopically, however, there is a big difference: The rhyolites beneath Kidd Creek have much higher $^{18}O/^{16}O$. This alteration may be unrecognizable by any means except by using oxygen isotopes, which are an extremely sensitive indicator of the combined effects of temperature, water/rock ratio and particularly the exchange and evaporation history of the ore fluid.

Once a high-^{18}O outcrop is found, by measuring the isotopic zoning it conceivably might be possible to determine the <u>direction</u> toward the massive ore. Moreover, utilization of the isotopic reversal caused by

the mixing of seawater and the deep-seated fluid may allow an estimation of the distance to the ore. Note that using such an exploration program, the existence of the Kidd Creek orebody itself could have been predicted from studies of the surface outcrops alone. The utility of $^{18}O/^{16}O$ data at Kidd Creek is maximized by two probably anomalous conditions; the footwall does not show distinctive mineralogic alteration, and the ore fluid was very high in ^{18}O.

CHAPTER 5

NON-VOLCANIC ROCKS

This research is primarily concerned with the volcanic rocks of the Abitibi greenstone belt. The geology of the Archean involves three other important lithologies, however: granitic rocks, migmatitic gneisses and sedimentary rocks, as well as a few rare layered gabbro bodies that are intrusive into the lava pile. All of these rock types are present in the Abitibi area (Fig. 3A-1). Metasedimentary rocks are coeval with the volcanic rocks, and form part of the greenstone belt assemblage. Granitic rocks are also invariably associated with, and typically surround the greenstone belts; in fact the granites are generally more abundant in Archean terranes than the greenstones (Talbot, 1973). Finally, the oldest Archean rocks appear to be the migmatitic gneisses. A very limited amount of data was collected from the above rock types, and is discussed in the following sections.

I. GRANITIC ROCKS

According to Goodwin and Ridler (1970), at least nine major granitic plutons are present within the Abitibi orogenic belt, each of which is 40 to 100 miles in diameter. One of these "plutons" was selected for study, the Round Lake batholith south of Kirkland Lake. Additional smaller plutons are enclosed within the volcanic pile and are typically associated with felsic volcanism (e.g. at Noranda). No samples were obtained from this type of body. The Lake Dufault granodiorite and the Otto Stock, both of which were analyzed, are younger, distinctly cross-cutting plutons, with high-temperature metamorphic aureoles.

1. The Round Lake Batholith. The Round Lake batholith is a largely

TABLE 5-1. OXYGEN ISOTOPIC AND PETROGRAPHIC DATA FROM NON-VOLCANIC ROCKS

Sample	Rock Type	$\delta^{18}O$ WR	$\delta^{18}O$ qtz	$\delta^{18}O$ feld	$\delta^{18}O$ oth.	Primary Mineralogy	Secondary Mineralogy	% Rec.	Location Lat.	Location Long.
ROUND LAKE BATHOLITH										
Sk-1	granodiorite	8.0	9.8	8.0	4.4(h)	qtz,pl,mic,hbd,bi,ep	act,ep,musc,cc,chl	10	48°2.4'	80°7.1'
Sk-3	granodiorite	8.4	9.9	8.3		qtz,pl,or,hbd,?	act,musc,chl,hem	20	48°2.4'	80°7.1'
Sk-5	granodiorite	8.4				qtz,pl,mic,hbd,bi,ep	act,musc,ep,chl	8	48°2.1'	80°7.5'
Sk-10	granodiorite	8.3				qtz,pl,mic,hbd,bi,ep	act,ep,chl,musc,cc	15	48°0.5'	80°7.9'
Sk-20	granodiorite	8.1	9.6	8.9	5.8(h)	qtz,pl,per,hbd,bi,ep	act,chl,musc,cc,ep	5	47°50.4'	80°8.2'
Sk-21	tonalite	9.1			4.9(h)	qtz,pl,hbd,bi	act,chl,musc,ep,cc	40	47°47.4'	80°6.1'
Sk-22	tonalite	8.2	9.8	9.4		qtz,pl,hbd,bi	act,chl,musc,ep	30	47°46.5'	80°5.9'
Sk-23	tonalite	6.9	8.2	6.9	5.0(h) 3.4(b)	qtz,pl,hbd,bi,ep?	act,chl,musc,ep	5	47°45.9'	80°5.8'
Sk-24	tonalite	7.9	9.0	8.4	3.7(b)	qtz,pl,hbd,bi,ep?	act,chl,musc,ep	5	47°45.3'	80°5.8'
Sk-25	tonalite	8.3	9.4	8.7	4.8(b)	qtz,pl,hbd,bi,ep?	act,chl,musc,ep	15	47°45.3'	80°6.1'
Sk-30	tonalite	7.8				qtz,pl,hbd,bi	act,chl,musc,ep	10	47°55.2'	80°6.1'
Sk-17	aplite	9.6							47°54.4'	80°8.0'
Sk-20	quartz vein		10.2						47°50.4'	80°8.2'
OTTO STOCK										
Br-37	syenite			8.7		mic,per,bi,hbd,ne,pl	act,cc,musc	5	48°3.8'	80°4.4'
LAKE DUFAULT GRANODIORITE										
Qe-82	granodiorite	6.4							48°28.8'	79°1.7'
SEDIMENTARY ROCKS										
Br-26	greywacke	9.2					qtz,chl,cc,op		48°7'	79°52'
Ti-22	greywacke	11.6					qtz,pl,musc,op, hbd,chl		48°28.8'	81°13.4'
Sk-42	chert	17.4							48°4.5'	79°57.7'
GNEISSES										
Go-7	qtzofeldspathic	6.5							47°42.1'	81°44.2'

Abbreviations as in table 3B-1.

unmapped, composite mass of granitic rocks (Fig. 3B-1). In the north it consists predominantly of a distinctive hornblende granodiorite, and in the south of a presumably older quartz diorite to tonalite (Goodwin and Ridler, 1970). The geologic relations thus resemble those in South African Archean batholiths. In the Barberton Mountain Land, for example, the oldest granites consist of diapirically intrusive "tonalitic granite-gneisses" (Viljoen and Viljoen, 1969c), which are then crosscut by three younger episodes of plutonism: the "Hood granites," and two younger porphyritic series of plutons. Like the Round Lake Batholith, the South African diapiric plutons commonly possess foliated margins with aligned xenoliths and fragments of the greenstone belt (Anhaeusser, 1973).

Tonalite. Oxygen isotopic data from the Round Lake batholith are listed in Table 5-1 and displayed graphically in Figure 5-1. The tonalites show a wide range in whole-rock $\delta^{18}O$, from +6.9 to +9.1. The quartz and feldspar data also show a wide range, from +8.2 to +9.8 and +6.9 to +9.5, respectively. Hornblende from two samples has a uniform $\delta^{18}O$ = +5.0, and biotite in three samples ranges from +3.4 to +4.8. The internal relationships among the minerals in the tonalites (Fig. 5-2) suggest that the original igneous oxygen isotopic equilibrium has been only slightly disturbed. $^{18}O/^{16}O$ invariably increases in the order biotite, hornblende, feldspar, quartz. Quartz-feldspar fractionations (0.6 to 1.3) are appropriate for primary igneous assemblages. The quartz-biotite fractionations (4.6 to 5.3) indicate temperatures from 725°C to 800°C; and the quartz-hornblende fractionation (3.4) indicates a temperature of about 675°C.

Petrographically, all of the tonalites show mineralogic alteration has been partially sericitized. With increasing degree of alteration the biotite becomes pseudomorphed by chlorite + sphene, then the hornblende

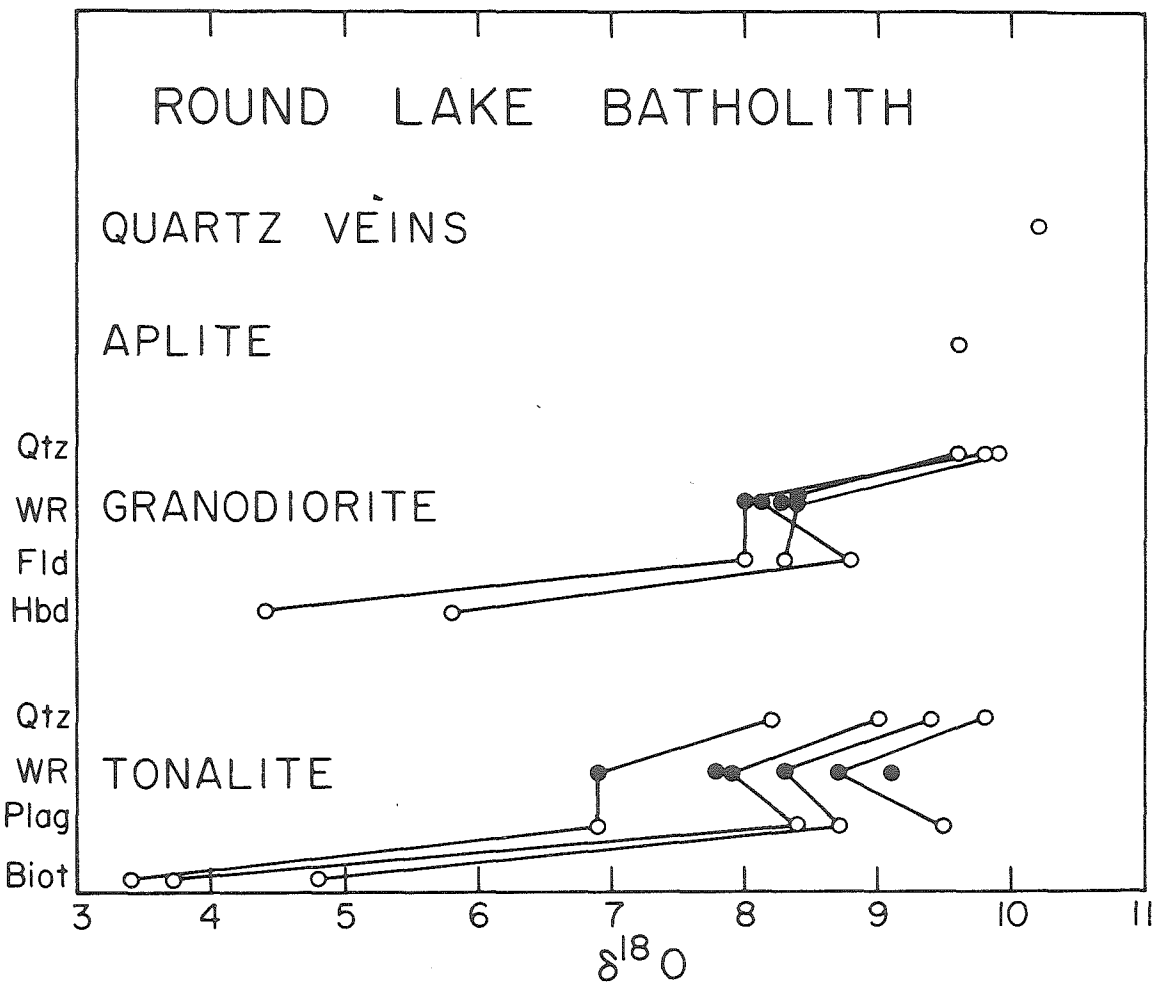

Figure 5-1. Oxygen isotopic data from the Round Lake batholith. Note the oxygen isotopic homogeneity of the granodiorites as compared to the variability of the tonalites. The mineral-mineral relationships of these rocks (Fig. 5-2) indicate that they have not undergone appreciable oxygen isotope exchange.

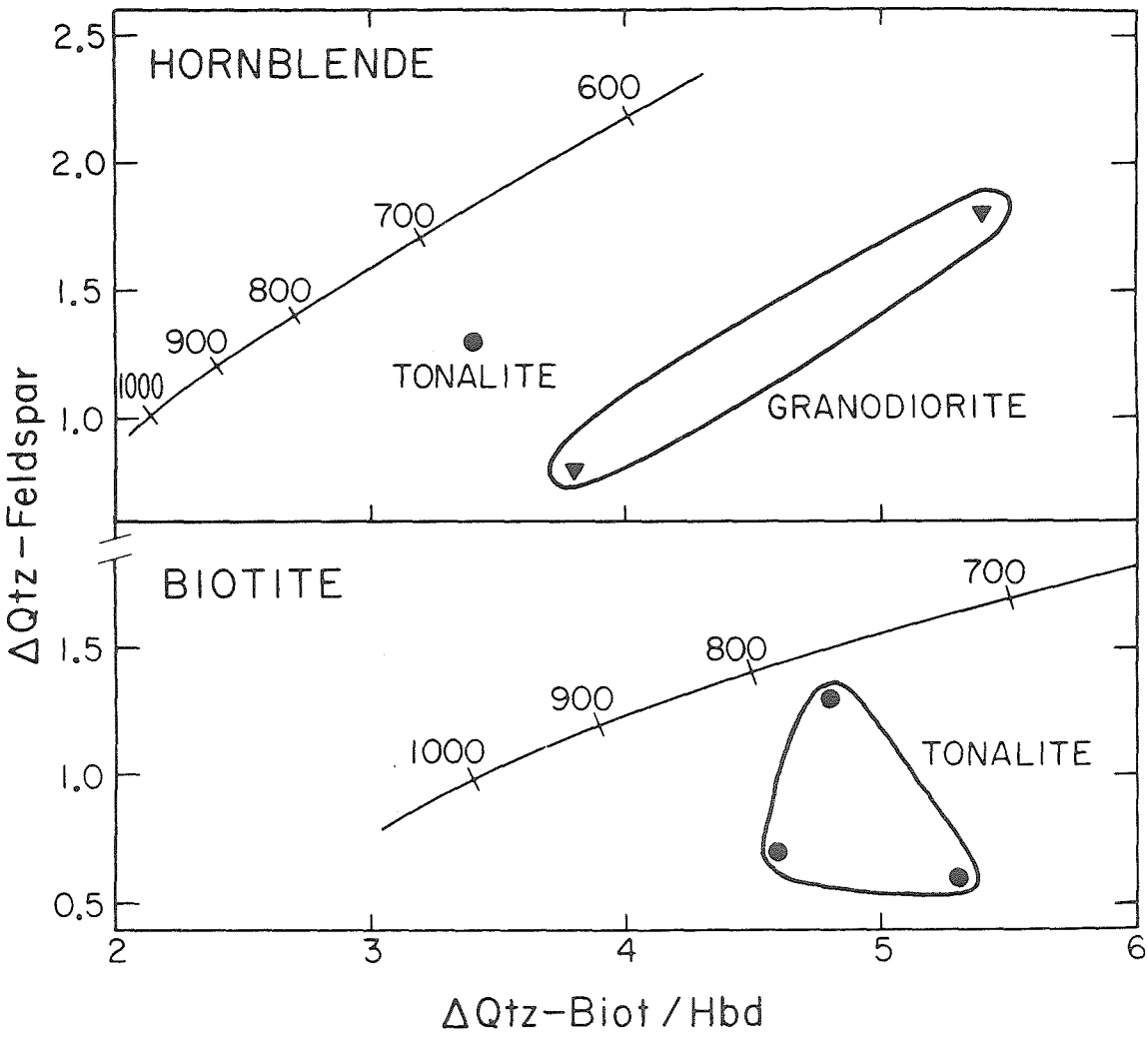

Figure 5-2. Variations between coexisting quartz, feldspar, biotite and hornblende in the Round Lake batholith. The equilibrium fractionations from Friedman and O'Neil (1977) as a function of temperature (°C) are shown for reference.

is replaced by actinolite and chlorite, and all the while turbidity and sericitization in the plagioclase becomes more intense. Quartz shows no mineralogic alteration effects.

There is a positive correspondence between the amount of alteration observed in thin section and the whole-rock $\delta^{18}O$ (Table 5-1). Whether this is a cause and effect relationship or an accident predicated by the small number of samples (5) remains open to debate. It is noteworthy, however, that the hand-picked quartz separates show nearly the same spread in $\delta^{18}O$ as the whole-rocks. Quartz is extremely resistant to hydrothermal exchange, and can be expected to have best preserved its original $\delta^{18}O$ value. This suggests that the tonalite was initially inhomogeneous in $\delta^{18}O$, which in turn suggests that the tonalite was derived from an oxygen isotopically inhomogeneous source region. Several such source regions are possible, including a (hydrothermally altered?) primordial sialic scum, and a hydrothermally altered downgoing slab. It is interesting to note in this regard that although the tonalites in the Southern California Batholith (Cretaceous) show an even wider range in $\delta^{18}O$ for quartz, the lower end of the spectrum ($\delta^{18}O \approx +7$) is identical to the Archean examples.

Granodiorite. In contrast to the $^{18}O/^{16}O$ variability of the tonalites, the granodiorites are homogeneous in $\delta^{18}O$. Whole-rock values of five samples fall between +8.0 and +8.4, quartz is +9.6 to +9.9, feldspar ranges from +8.0 to +8.8, and hornblende measures +4.4 to +5.8 Table (5-1). Biotite is present in low abundance in this rock type and was not analyzed. Like the variability of the tonalites, the constancy of the granodiorites has petrogenetic implications. The source region of the granodiorite must have been homogeneous in $^{18}O/^{16}O$. Although

they are presumed to have been derived by partial melting in the lower crust, they may have considerably post-dated the tonalites. By comparison with granitic rocks worldwide, Chappell (pers. comm. 1979) has suggested that these Archean tonalites represent an orogenic, I-type of magma, whereas the granodiorites may be alkali-rich, anorogenic A-type granites. Even if both magma types were generated there, the lower crust could have changed its oxygen isotopic distribution appreciably since production of the tonalites. Calculations by Jacobsen and Wasserburg (1979), for example, indicate that the mean age of the continental crust is about 1.5 to 1.8 b.y., so the continents must have been receiving a significant amount of material from the mantle during the Archean.

The mineral data in the granodiorites, like those in the tonalites, indicate minimal hydrothermal alteration. Quartz-feldspar fractionations (0.8 to 1.8) are mormal primary igneous values. Quartz-hornblende fractionations (3.8 to 5.4), however, indicate temperatures of 500-600°C, even though mineralogically the hornblende is quite fresh.

The principal alteration effects observed in thin section are the sericitization of plagioclase and the replacement of biotite with chlorite + sphene. In addition, in sample Sk-3, which was collected 5 feet from a 100-foot wide Keewenawan basalt dike, the hornblende is replaced with chlorite and actinolite. Epidote is present both as a fine-grained secondary mineral associated with chlorite and actinolte, and as large, well-formed interstitial crystals with symplectic intergrowths against quartz and poikilitic inclusions suggesting an igneous origin. Microcline and quartz are both petrographically unaltered. The microscopic as well as the oxygen isotopic relations of the granodiorite, therefore, indicate that the granodiorite has undergone only minor water/rock interaction.

Although the oxygen isotopic distribution in the Round Lake batholith shows some interesting variations, the hydrothermal alteration effects are minimal. In both of the major rock types the mafic minerals have equilibrated to slightly lower temperatures than the coexisting framework silicates, but this may or may not have been due to water/rock interaction. In any case, the whole-rock $\delta^{18}O$-values appear to have been essentially undisturbed since the magmas crystallized.

2. The Otto Stock and Lake Dufault Granodiorite. The Otto Stock is a circular pluton 10 km. in diameter (Fig. 3B-1) composed of syenite and nepheline syenite with local pegmatitic phases (Goodwin and Ridler, 1970). A single sample from the NW border is petrographically very fresh (minor sericitization of the feldspar) and contains perthite phenocrysts with $\delta^{18}O = +8.7$. This compares favorably with fresh, younger syenites from elsewhere in the world (Taylor, 1968), and suggests that the Otto Stock has had a simple, igneous $^{18}O/^{16}O$ history. The Lake Dufault granodiorite, on the other hand, has a whole-rock $\delta^{18}O = +6.4$. This is lower than most granodiorites (Taylor, 1968) and suggests that the intrusion may have undergone a more complicated oxygen isotopic history. The various possible mechanisms of producing low-^{18}O plutons are discussed in Taylor (1977), but cannot be evaluated in this case without additional data.

3. Comparison with other Archean Granitoids. The present study adds to the several previous studies which have been done on Archean granitoids in the North American shield. The Giants Range batholith is a typical composite Algoman batholith in northeastern Minnesota with an age of about 2700 m.y. Four principal granitic rock series have been mapped, and Viswanathan (1974) has measured $\delta^{18}O$ of the quartz in each: Tonalitic

series (+9.4 to +10.1), granodioritic series (+9.4 to +9.9), granitic series (+9.2 to +9.6), and granitoid series (+10.7 to +11.4). The first three of these series are indistinguishable from the Round Lake batholith (tonalite = +8.2 to +9.8, granodiorite = +9.6 to +9.9) while the fourth group comprises two-mica granites of apparently anatectic sedimentary origin.

In Western Ontario, Longstaffe (1979) has measured whole-rock $\delta^{18}O$-values of +7.8 to +9.3 for the Burditt Lake granodiorite, and +7.3 to +8.2 for the felsic portions (monzodiorite to granodiorite) of the Jackfish Lake Complex. Shieh and Schwarcz (1977) measured $\delta^{18}O$ ranging from +7.6 to +8.6 for a set of composite (whole-rock) granitic samples from Western Ontario, and Shieh and Schwarcz (1978) estimated that the average $\delta^{18}O$ of granitic rocks in the Slave and Superior provinces is +6.9 to +7.8, respectively. All of the above values are similar, thus it appears that the Round Lake batholith is oxygen isotopically typical of the Superior Province.

A limited amount of data are also available from the granitic rocks of the South African shield. Taylor and Magaritz (1975) found that the diapiric tonalite domes range in $\delta^{18}O$ from +6 to +8, and the tonalitic Ancient Gneiss Complex (much of which may be equivalent to the tonalitic domes according to Viljoen and Viljoen, 1969c) has $\delta^{18}O$ = +6 to +10. Barker et al. (1976) made a more detailed study of the Ancient Gneiss Complex, and found that (excluding the amphibolites) $\delta^{18}O$ ranges from +5.2 to +9.0. Care must be exercised in comparing the Ancient Gneiss Complex to the Round Lake batholith, because they are geologically dissimilar. It appears, however, that the Barberton tonalites may be slightly lower in ^{18}O than those from the Superior Province.

II. KAMISKOTIA GABBRO

1. Geology

A variety of mafic intrusives are present within the Abitibi greenstone belt, including sills, dikes and other intrusions of various geologic ages. The most prominent bodies, however, are three large (20-30 km.) layered gabbros, the Dore Lake complex, the Bell River complex, and the Kamiskotia complex (Goodwin and Ridler, 1970). The Dore Lake intrusion is exposed over a distance of 43 km., and is stratigraphically at least 20,000 feet thick. The section includes a basal anorthosite zone, a layered ultamafic zone, and finally a tonalite zone (Allard, 1970). The Bell River complex is at least 15,000 feet thick, and consists of rhythmically banded norite, anorthosite and pyroxenite (Goodwin and Ridler, 1970). The Kamiskotia complex is largely covered by glacial drift and is poorly understood. Although these gabbro bodies are intrusive into the volcanic pile, they are in turn crosscut by Kenoran granites. Their ages, therefore, are nearly the same as the volcanic rocks they intrude. Many geologists, in fact, believe that these plutons were subvolcanic magma chambers which fed the basaltic volcanism. The sizes of these differentiated complexes are comparable to that of the Skaergaard (Taylor and Forester, 1979) and perhaps the mid-ocean ridge magma chamber (Gregory and Taylor, 1980), two environments in which extensive water/rock hydrothermal interaction is known to have taken place. Anticipating similar effects in the Archean, a set of samples was collected from the Kamiskotia complex. Of all of the possible hydrothermal environments in the Abitibi greenstone belt, the alteration of this gabbro is expected to have been one of the hottest.

2. Oxygen Isotopic Data

Unfortunately the present data set is not sufficient to fully evaluate the hydrothermal effects. Two samples were analyzed for $\delta^{18}O$, one of the freshest rocks and one of the most altered rocks, along with two quartz veins. The fresher gabbro (Ti-32, Fig. 3G-2c) has +5.3 pyroxene and +5.9 plagioclase, values which are comparable to modern fresh gabbros. The altered gabbro (Ti-41, Fig. 3G-2f) contains +5.5 hornblende, +6.4 plagioclase and is cut by +9.0 quartz veins (Table 3G-1). On the outcrop three separate cross-cutting relationships are observed: 1. Short, discontinuous chlorite- or actinolite-filled fractures; 2. Aplite dikes; 3. Massive quartz veins. These features may represent, respectively, high-temperature alteration, granitic plutonism, and regional metamorphism.

3. Fluid Composition

If it is assumed that the hornblende in Ti-41 formed at about 500°C, then the fluid from which it formed must have had $\delta^{18}O \approx +7.7$ (Friedman and O'Neil, 1977). At that temperature, the quartz in equilibrium with these two phases has $\delta^{18}O = +10.5$ (Friedman and O'Neil,1977), which is close to the values measured in the quartz veins cutting the gabbro (+9.0 and +9.9). This hydrothermal fluid is more ^{18}O-rich than that which has affected most of the volcanic rocks in the Abitibi greenstone belt. The high metamorphic grade combined with the fact that the whole-rock $\delta^{18}O$ did not change during metamorphism (Ti-32 and Ti-41 have identical $\delta^{18}O$ indicating the fluid and the rock were in equilibrium) suggests that the Kamiskotia fluid underwent an ^{18}O-shift through high temperature water/rock interaction at low water/rock ratio. An alternative possibility, however, is that the fluid acquired its high-^{18}O character through one of the other possibilities discussed in connection with the nearby Timmins area.

III. MIGMATITIC GNEISSES

Among the oldest rocks exposed in all of the world's Archean cratons are migmatitic gneiss complexes. These high-grade gnessic regions typically consist of tonalitic-granodioritic gneisses whose origin is poorly understood. On the basis of bulk chemistry a variety of protoliths have been proposed (for a summary see Windley and Smith, 1976), including: andesitic-dacitic volcanic rocks, modified earlier gneisses, dioritic rocks that underplated the crust, plutonic granitic rocks in general, and igneous tonalites and granodiorites. In working with these rocks the geologist is faced with the problem that the mineralogic relations typically indicate depths of burial to 20-30 km., and the older rocks show indications of metasomatism (Windley and Smith, 1976).

The Superior Province in Western Ontario is crossed by two very long (1000 km.) gneiss belts, the English River and Quetico Gneiss Belts. In the Superior Geotraverse area these gneisses are intruded by the seas of granite which also invade the greenstones (Goodwin, 1978), and radiometric ages indicate that the gneisses are older than the greenstones (Wooden, 1978). Although neither of these belts passes close to the Abitibi greenstone belt, the smaller (60 km.) gneiss complex at the western edge of Abitibi may be the faulted extension of the English River gneisses. One sample of this complex, which is termed the Gogama gneiss complex, was analyzed in the present study (Fig. 5-3). The rock is a biotite quartzofeldspathic gneiss, probably a metamorphosed tonalite or granodiorite, and has a whole-rock $\delta^{18}O = +6.5$. In the absence of detailed geologic maps and lithologic studies it would be futile to generalize from this analysis to the entire Gogama gneiss complex. It is possible, however, to place this datum in context by reviewing the oxygen isotope geochemis-

Figure 5-3. Outcrop photographs of non-volcanic rocks.

a.) Metamorphosed greywacke (Ti-22) from the Timmins area.

b.) Migmatitic gneiss (Go-7) from the western end of the Abitibi greenstone belt, near the town of Gogama.

GREYWACKE

GNEISS

tries of the nearby English River and Quetico gneiss belts.

As part of his PhD work at McMaster, Longstaffe studied the $^{18}O/^{16}O$ distribution in several of the gneiss complexes within the Superior Geotraverse Project (summarized in Longstaffe and Schwarcz, 1977; Longstaffe, 1979). His principal results are outlined below. The Pakwash gneiss (northern English River gneiss belt) is a garnet-bearing, or more rarely, a muscovite-, sillimanite- and cordierite-bearing metasedimentary gneiss which ranges in whole-rock $\delta^{18}O$ from +6.5 to +11.7. The Footprint gneiss (western margin of the Rainy Lake batholith, Wabigoon granite-greenstone sub-Province) is a tonalitic to granitic metaigneous gneiss with whole-rock $\delta^{18}O$ = +5.9 to +8.9. The migmatized portions of the gneiss are lower in ^{18}O than the unmigmatized portions, an observation which suggests that the low-^{18}O rocks acquired that characteristic through migmatization rather than through primary igneous processes. The Cedar Lake-Clay Lake area gneisses (southern English River gneiss belt) include both metaplutonic and metasedimentary rocks, but despite their varied protoliths all have whole-rock $\delta^{18}O$-values between +7.0 and +9.3. The Kenora area (southern English River gneiss belt) contains metaplutonic gneisses ranging from tonalite to granite, with $\delta^{18}O$ = +7.3 to +8.6.

By comparing these gneisses to their more weakly metamorphosed equivalents, the oxygen isotopic effect of metamorphism can be evaluated. With the possible exception of the migmatitic portions of the Footprint gneiss, all of the orthogneisses listed above are oxygen isotopically comparable (+6 to +9) to undeformed Archean granitoids (Chapter 5A-I.). Likewise, many of the paragneisses have oxygen isotopic compositions (+9 to +12) which resemble those of undeformed Archean clastic sedimentary

rocks (Longstaffe, 1979). Some of the gneisses appear to have lost ^{18}O during metamorphism, however, a fact whose significance is discussed in detail in Chapter 7. Similar $\delta^{18}O$-values for gneisses in the Canadian shield have been obtained by Shieh and Schwarcz (1977) (+8.3) and Shieh and Schwarcz (1978) (+6.4 to +7.9). The Gogama gneiss is thus within the range of values found for gneisses elsewhere in the Superior Province.

III. SEDIMENTARY ROCKS

The sedimentary rocks of the Abitibi greenstone belt typically consist of high-energy immature clastic rocks. Local accumulations range up to 10,000 feet thick and include "greywacke, shale, lithic sandstone, conglomerate, breccia and iron formation. Identifiable clastic components compare closely in composition with nearby volcanic rocks and have obviously been derived in large part from them by rapid mechanical erosion and subaqueous deposition in nearby troughs and basins. Chaotic textures and polymictic unsorted materials are distinctive features. This facies, which is characteristic of strongly active tectonic zones, typically displays intricate soft-sediment deformational structures. Graded bedding and abrupt facies changes" (Goodwin and Ridler, 1970; p. 4-5).

Two samples of this sedimentary sequence, both greywackes, were analyzed, and have whole-rock $\delta^{18}O$ values of +9.2 and +11.6. Eleven additional samples of the sedimentary rocks near Kirkland Lake range from +9.0 to +11.9 (Longstaffe and Schwarcz, 1977). A comparison of similar sedimentary rocks of all ages throughout the world has been made by Shieh and Schwarcz (1978; Fig. 3). With the exception of some of the samples from Val d'Or, all of the Archean and Early Proterozoic metasedimentary rocks including those at Abitibi, have $\delta^{18}O$ in the range +9 to +11. The Late Proterozoic and Phanerozoic sediments and meta-

sediments of comparable metamorphic grade are about 4 per mil richer in $\delta^{18}O$, ranging from +13 to +15. Longstaffe and Schwarcz (1977) in the study of Archean clastic metasediments in Western Ontario have found that increasing $\delta^{18}O$ correlates with decreasing volcanic rock fragment content. This suggests that the low $^{18}O/^{16}O$ ratios in the early to middle Precambrian sediments are due to a high percentage of low-^{18}O igneous rock detritus. However, it is also possible that the Archean metasediments have lost their heavy oxygen through metamorphic processes. The younger +13 to +15 metasediments are not associated with greenstone belts, whereas all of the Archean +9 to +11 metasediments are.

A sample of the banded iron formation at the Adams mine was also analyzed. The iron formation consists of alternating chert and magnetite horizons, and the chert has $\delta^{18}O = +17.4$. This is comparable to the cherts which have been analyzed from several other Archean cratons. Chert in the Hamersley Range, Australia has $\delta^{18}O = +20$ to +22 (Becker and Clayton, 1976); chert from West Greenland has $\delta^{18}O = +13$ to +20 (Perry et al. 1978); and the Fig Tree chert from South Africa has $\delta^{18}O = +14$ (Perry, 1967). The significance of these values is discussed in Chapter 7.

CHAPTER 6

OTHER GREENSTONE BELTS

Although the Abitibi greenstone belt is a typical Precambrian metavolcanic pile in most respects, it must be remembered that it is also the biggest and the least metamorphosed. It is possible that this circumstance introduces some atypical oxygen isotopic effects, and that Abitibi is really not representative of all greenstone belts. Furthermore, greenstone belts are present in the geologic record from 3.4 b.y. to 1.7 b.y., which is a considerable span of earth's history. It is possible that the hydrothermal processes or effects in greenstone belts changed over that time interval. To partially evaluate these questions, a set of 15 samples from the 1.7 b.y. old Dubois greenstone belt in Colorado were analyzed. These were supplemented with 2 analyses of the 1.7 b.y. old Cape Smith fold belt in Quebec. In addition, a small amount of data from other greenstone belts are available in the literature. By comparing these data sets with the Abitibi data, the oxygen isotopic evolution of greenstone belts through time and space can be evaluated. All of the available data from other greenstone belts are listed in table 6-1, and are displayed graphically in figure 6-1.

I. DUBOIS GREENSTONE BELT

The Dubois greenstone belt is a mass of metavolcanic rocks 1-4 miles wide and 18 miles long which crops out south of the Gunnison River near the town of Gunnison. The belt contains "many large and small bodies of schist and intruded volcanic rocks. It is bounded on the north chiefly by Black Canyon schist, on the south by intrusive granitic rocks, and to the west and east it passes under younger volcanic rocks and probably

Table 6-1. OXYGEN ISOTOPIC AND PETROGRAPHIC DATA FROM OTHER GREENSTONE BELTS.

Sample	Field Description	$\delta^{18}O$ WR	$\delta^{18}O$ Min.	Microscopic Description: Texture	Ave. gr. size	Secondary Mineralogy	% Rec.
DUBOIS GREENSTONE BELT							
BCS-3	Black Canyon schist from Tomichi point	12.9					
YA-29	Amphibole schist near Yukon mine	10.0					
YA-46	Pillowed amphilobite, Cochetopa Canyon	7.8		Equigranular	20	act,ep,qtz,cc	100
DC-3	Porphyritic metadacite near Denver City mine	11.1					
DC-6	Porphyritic metadacite near Denver City mine	10.8					
DC-7	Porphyritic metadacite near Denver City mine	11.0					
DC-9	Porphyritic metadacite near Denver City mine	11.6	10.8(f)	Porphyritic	5	qtz,musc,biot	50?
DC-10	Amphibolite near Denver City mine	8.6					
DC-11(clast)	Mill breccia, 10' from Denver City hoist	12.4					
DC-11(matrix)		11.6					
DB-39	Well-foliated, siliceous schist, 20' N. of Good-Hope dump.	7.2		Foliated, veined	50	qtz,chl,act,musc	100
DB-41	Fine gr. rhyolite, N. of Good Hope dump.	7.4		Equigranular	50	qtz,act,ep,biot,chl	30
DB-51	Amphibolite along road to Vulcan	8.0		Foliated, porph.	20	qtz,musc,biot,act	95
DB-53	Amphibolite along road to Vulcan	7.7		Granular	150	chl,act,musc	15
DB-55	Amphibolite along raod to Vulcan	7.7		Equigranular	600	act,biot,musc	60
CAPE SMITH FOLD BELT							
79-18CS	Sample collected by Andrew Hynes	8.5					
78-107CS	Sample collected by Andrew Hynes	7.2					

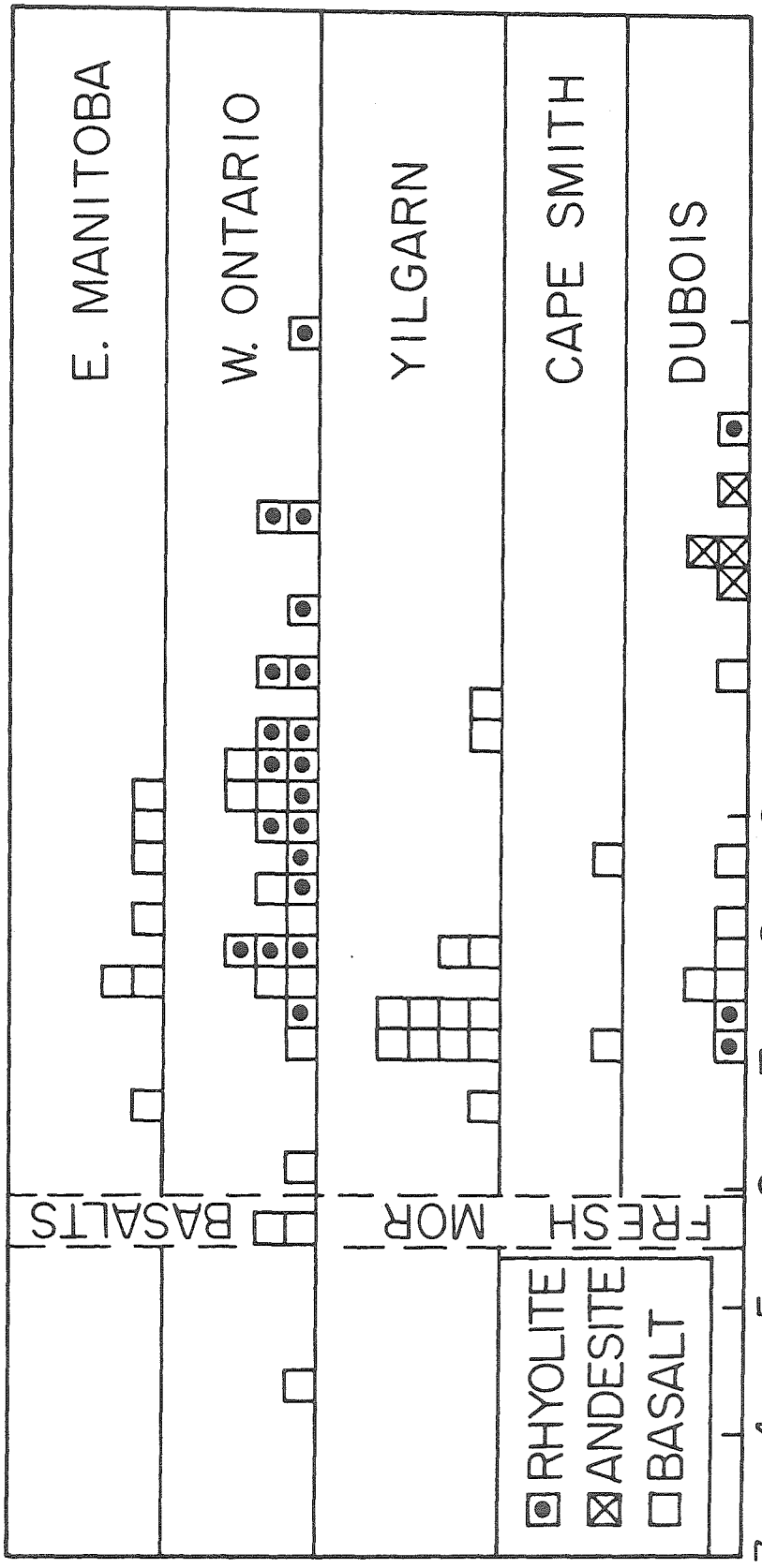

Figure 6-1. Histogram of $\delta^{18}O$-values from other greenstone belts throughout the world. The Cape Smith and Dubois data are from this work, while the rest of the data are from the literature (see text). In each locality the rocks have undergone ^{18}O enrichments relative to modern fresh basalts.

pinches out" (Larsen and Cross, 1956; p. 21). The age of the Black Canyon schist, which is interlayered with the volcanic rocks, is 1.7 b.y (Hansen and Peterman, 1968).

In sampling the Dubois greenstone belt, the author was interested not only in the volcanic pile, but in the massive sulfide ore deposits as well. Three such deposits were examined: the Vulcan, the Denver City, and the Yukon-Alaska mines. Away from these mines the basalts are recrystallized to amphibolite, and the four analyzed samples span a narrow range of $\delta^{18}O$, from +7.7 to +8.0. In thin section these metabasalts show a wide range in the degree of preservation of relic igneous minerals (Table 6-1). In sample DB-55 the pyroxene is completely replaced by fine-grained actinolite and biotite, whereas the plagiocalse is calcic, twinned, and only partially (10-20%) altered to sericite. In contrast to most of the Abitibi rocks examined, pyroxene appears to have been more susceptible to hydrothermal breakdown in this sample than the plagioclase.

At the Denver City mine (near the town of Iris) is a large mass of felsic volcanic rocks (Olson, 1976), which ranges in $\delta^{18}O$ from +10.8 to +11.6. These felsic volcanics may overlie the mafic volcanics to the north, by analogy with other chemically differentiated greenstone belts. If so, then there is an increase in $\delta^{18}O$ stratigraphically upwards in the volcanic section. Both the $\delta^{18}O$-values (+8 to +11) and the possible stratigraphic relationships, therefore, strongly resemble those in the Abitibi greenstone belt.

Immediatedly adjacent to the Denver City mine is a coarse rhyolite breccia (DC-11) which has +12.4 clasts set in a +11.6 matrix. In terms of its $^{18}O/^{16}O$ distribution, the Denver City mine resembles Kidd Creek in

two respects: The adjacent rhyolites are richer in ^{18}O than the surrounding rocks, and high-^{18}O clasts are enclosed in a lower-^{18}O matrix. Further evaluation of this interesting similarity must await further study.

Adjacent to the Good Hope mine (near the town of Vulcan) the rhyolites have $\delta^{18}O$ of +7.2 and +7.4 (Table 6-1), which is somewhat less than that of the nearby amphibolites. Although there is apparently a massive sulfide deposit present, it has been crosscut by Tertiary gold-telluride mineralization (Zahony, 1976). Among other effects, this has led to the development of three unusual copper telluride minerals, weissite (Cu_5Te_3), vulcanite (CuTe), and rickardite (Cu_4Te_3), which were first described from this locality. Clearly the hydrothermal processes are too complex to be evaluated with only two analyses.

A single sample of the Black Canyon schist was found to have $\delta^{18}O$ = +12.9. This unit is a metasedimentary sequence which originally consisted of siltstones, greywackes and other fine-grained sediments (Olson, 1976). The oxygen isotopic composition is similar to that found for metamorphosed sedimentary rocks throughout the Precambrian (Shieh and Schwarcz, 1978).

II. CAPE SMITH FOLD BELT

The Cape Smith volcanic belt extends 350 km. across the northern end of the Ungava Peninsula of Quebec. "The succession within the belt begins at the southern margin with metasedimentary rocks containing interbeds of basic to intermediate volcanic rock and minor rhyolite. These are overlain by a thick sequence of basic volcanic rocks and associated subvolcanic sills. The succession is terminated at a major east-west thrust fault" (Francis and Hynes, 1979). Two samples of this volcanic belt were provided by Dr. Andrew Hynes, and were found to have $\delta^{18}O$ of

+7.2 and +8.5. These values are similar to those from both the Abitibi and the Dubois greenstone belts.

III. YILGARN BLOCK, AUSTRALIA

As discussed above in Chapter 3F, Hoefs and Binns (1978) have reported a small amount of data for the greenstones of the Yilgarn Block, Australia. Their data show that so-called "fresh" tholeiites range in $\delta^{18}O$ from +6.7 to +7.5, and that "metamorphosed" tholeiites range from +7.1 to +9.7. One again, these values are similar to those reported above for the Abitibi greenstone belt. Relic pyroxene in two of these tholeiites has $\delta^{18}O$ of +5.3 and +5.4 (Hoefs and Binns, 1978), indicating that (like Abitibi) these rocks were not originally high-^{18}O magmas.

IV. SUPERIOR PROVINCE

Oxygen isotopic analyses of Archean metavolcanic rock are scattered throughout the literature on the Superior Province. Shieh and Schwarcz (1977) measured $\delta^{18}O$ = +7.6 on a composite volcanic sample. Shieh and Schwarcz (1978) report that the average $\delta^{18}O$ of basic igneous rocks in the Superior Province is +7.5. Felsic metavolcanics have been found to range from +7.3 to +13.0 (Longstaffe and Schwarcz, 1977) and mafic metavolcanics have been found to range from +4.4 to +9.4 (Longstaffe et al. 1977). In addition, seven unpublished analyses of the Bird River greenstone belt, S.E. Manitoba (courtesy of F.J. Longstaffe) range in $\delta^{18}O$ from +6.7 to +9.2. Similar results (Muehlenbachs, pers. comm. 1979) have been obtained from the Yellowknife greenstone belt. These values are all similar to those reported in Chapter 3 for the Abitibi greenstone belt.

V. CONCLUSIONS

From the limited data available it would appear that most if not all greenstone belts of all ages have undergone $\delta^{18}O$-enrichments of about 1

to 3 per mil relative to an original magmatic value of +5.5 to +7. In this regard the Abitibi greenstone belt is apparently representative of greenstone belts throughout the world.

CHAPTER 7

SUMMARY AND CONCLUSIONS

To tie together the various data sets presented above, the important points concerning the oxygen isotopic distribution in the Abitibi greenstone belt will be summarized. Ignoring the details for the moment, the purpose of this discussion will be to present the overall general features of the hydrothermal and oxygen isotopic history. Using this information it is possible to compare the Archean greenstone belts to Phanerozoic ophiolites and island arcs. By examining the similarities and differences in tectonic setting, associated rocks, stratigraphic section and hydrothermal style, it is possible to make an evaluation of the significance of greenstone belts.

I. SUMMARY OF THE ABITIBI GREENSTONE BELT DATA

1. General Statement

The general $^{18}O/^{16}O$ distribution within the Abitibi volcanic pile can be simply summarized with two diagrams. In each stratigraphic traverse there is a broad increase in $\delta^{18}O$ with structural height, ranging from about +6 at the base to about +10 near the top. Minor complicating features are present, as at Lavaflow Mountain, and the metamorphosed rocks around the Lake Dufault granodiorite, but most of the data can be described with the above simple statement (Skead Volcanics, Ben Nevis area, Benoit area, Noranda area, Munro Twp.). Also, although it is overall richer in ^{18}O, this generalization applies to the Timmins area as well. The process which produced this gradient in $\delta^{18}O$ therefore appears to be of fundamental geochemical importance, operative over a wide area. The origin of this general feature must be explained before considering the exceptions.

By putting together in one diagram all of these stratigraphic sections (Fig. 7-1), an interesting picture emerges. According to Jensen (1979b) there are two principal cycles of volcanism in the Abitibi area, each of which varies from komatiitic at the base through tholeiitic to calc-alkaline at the top. These two volcanic cycles are separated by a major sedimentary episode, and the total structural height is thought to be close to 40 km. (Jensen, 1979b). In a general way, both of these volcanic cycles show an upwards increase in $\delta^{18}O$, suggesting that the upper and lower portions of the greenstone belt underwent hydrothermal alteration independently. Note, however, that in the upper portion the region-wide corelation is poor, conisiting of several discontinuous segments. This may indicate that the stratigraphic section has been repeated by unrecognized structures such as folds or faults. Repetition of the section is also indicated by the fact that the metamorphic grade at the base of the pile is inconsistent with burial to a depth of 40 km (Jolly, pers. comm. 1979).

Another way to summarize the data is by contouring all of the oxygen isotopic analyses (Fig. 7-2). The concentric pattern over the Blake River syncline reflects the stratigraphic control, as do the contours through the Skead volcanics. Two features of Figure 7-2 are immediately obvious: The high-^{18}O zone around Timmins, and the low-^{18}O zone around Noranda. These two features indicate that the hydrothermal processes in these two localities were different than elsewhere in the greenstone belt. The fact that these two areas contain some of the most important hydrothermal deposits known to man may be related to these differences.

As alluded to briefly in the preceeding chapters, there are only two mechanisms which could have produced the observed gradients in $\delta^{18}O$. Either the volcanic rocks were erupted with a primary, intrinsic $\delta^{18}O$

Figure 7-1. Whole-rock $\delta^{18}O$ as a function of structural height (based on the stratigraphic work of Jensen 1979b) for all of the volcanic rocks analyzed in this study. The break in the trend at the major sedimentary episode at about 11 km. height suggests that the upper and lower portions of the pile underwent oxygen isotopic exchange independently. Alternatively, the stratigraphic section could be repeated by faulting or unrecognized folds. The data from the Noranda area plot in the same region as those from the Ben Nevis area.

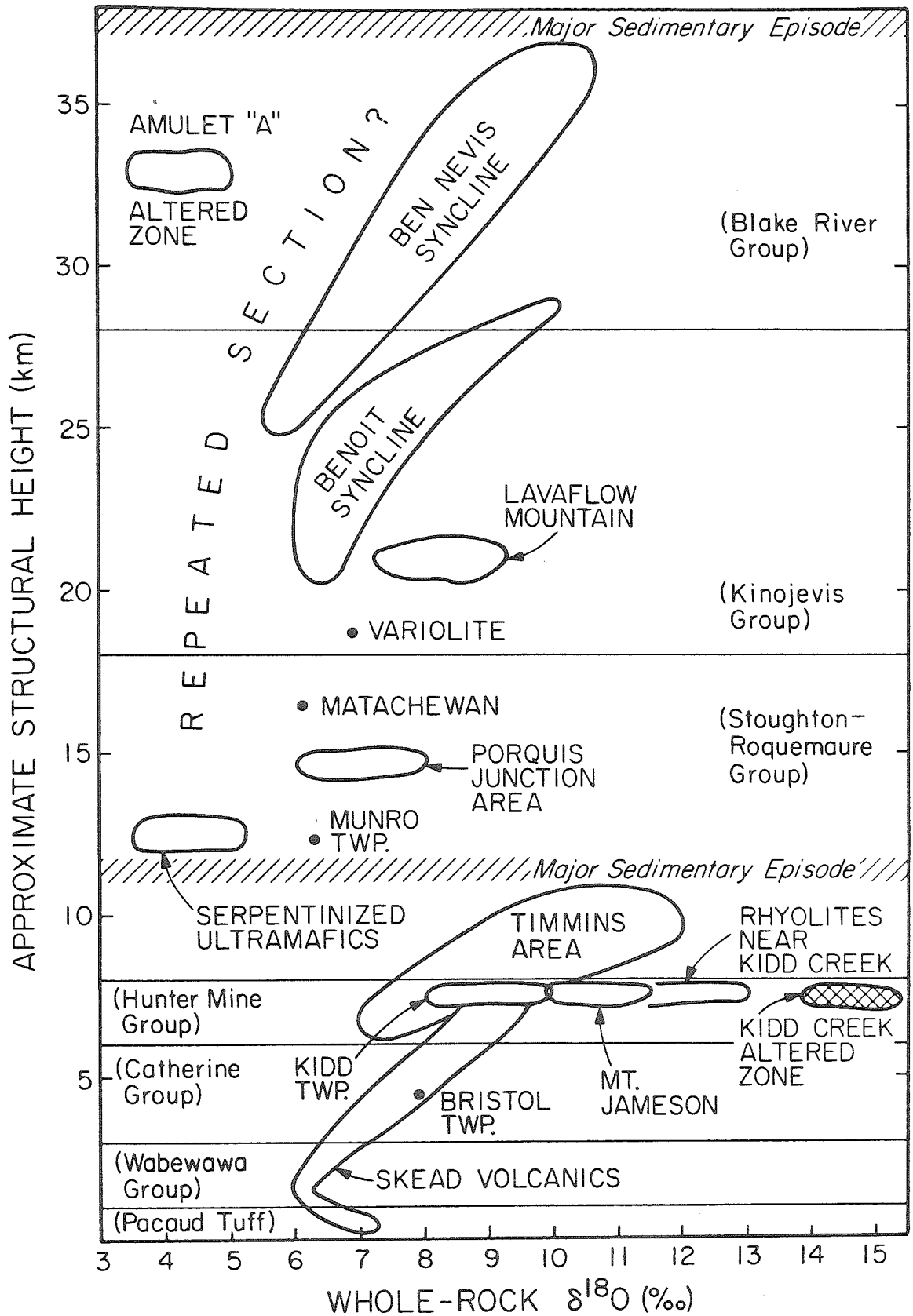
Major Sedimentary Episode
AMULET "A"
ALTERED ZONE
REPEATED SECTION?
BEN NEVIS SYNCLINE
BENOIT SYNCLINE
(Blake River Group)
LAVAFLOW MOUNTAIN
VARIOLITE
(Kinojevis Group)
MATACHEWAN
PORQUIS JUNCTION AREA
MUNRO TWP.
(Stoughton–Roquemaure Group)
Major Sedimentary Episode
SERPENTINIZED ULTRAMAFICS
TIMMINS AREA
RHYOLITES NEAR KIDD CREEK
(Hunter Mine Group)
KIDD CREEK ALTERED ZONE
(Catherine Group)
KIDD TWP.
MT. JAMESON
BRISTOL TWP.
(Wabewawa Group)
SKEAD VOLCANICS
(Pacaud Tuff)
APPROXIMATE STRUCTURAL HEIGHT (km)
35
30
25
20
15
10
5
3 4 5 6 7 8 9 10 11 12 13 14 15
WHOLE-ROCK δ18O (‰)

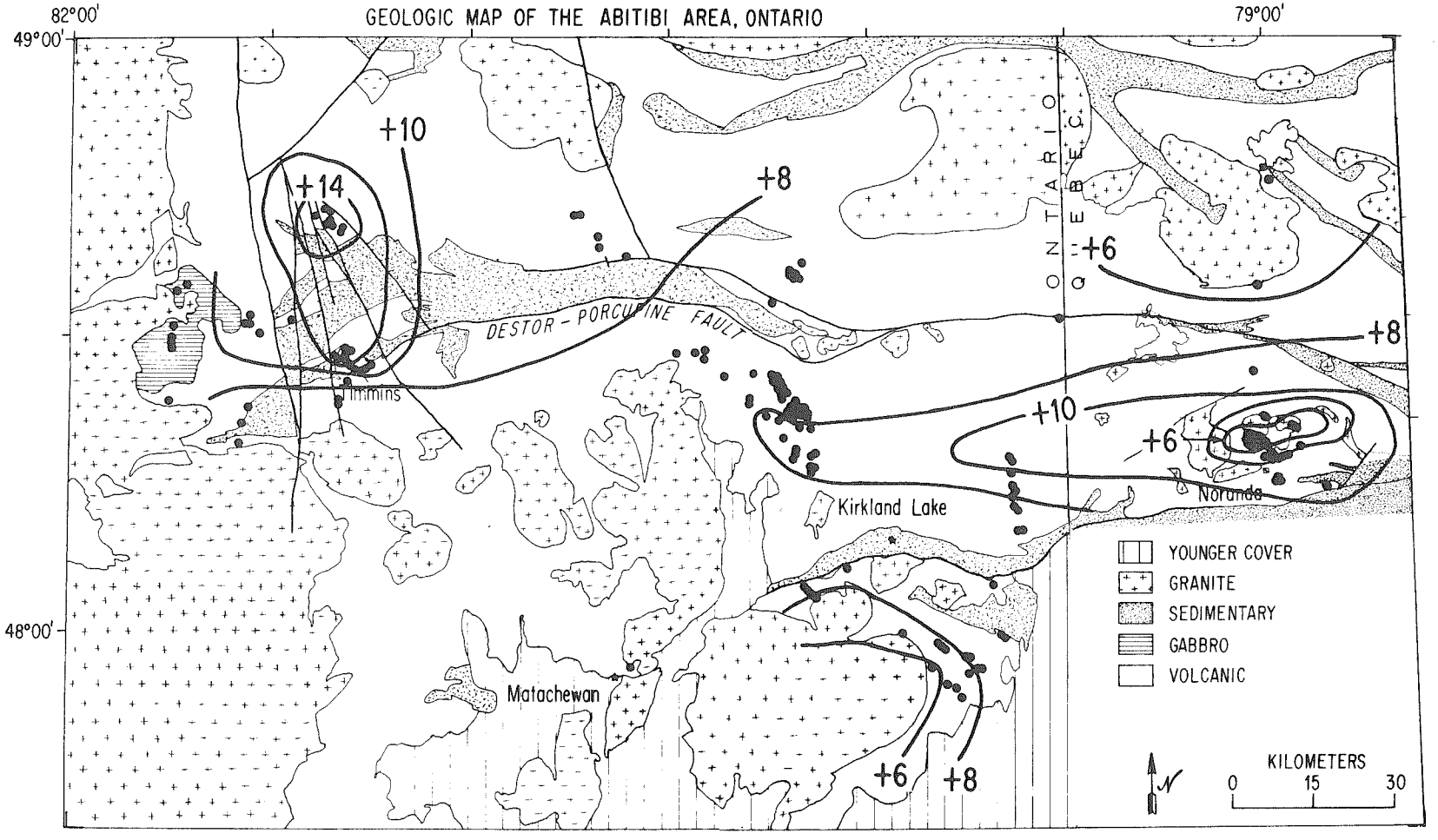

Figure 7-2. Geologic map of the western portion of the Abitibi greenstone belt, showing $\delta^{18}O$ contours of the whole-rock data. Note the high-180 zone around Timmins and the low-180 zone around Noranda.

variation, or the ^{18}O gradient was imposed on the rocks after their igneous history by hydrothermal alteration. The data from mineral separates strongly indicates that the high-^{18}O rocks in the Abitibi area principally acquired this characteristic through hydrothermal exchange. This is indicated by the fact that the relic igneous pyroxene and quartz (which are relatively resistant to hydrothermal exchange) have 'normal' magmatic $\delta^{18}O$ values, as well as by the common presence of disequilibrium isotope fractionations among the coexisting minerals. Although the possibility that high-^{18}O magmas were locally erupted within the Abitibi greenstone belt cannot be critically evaluated for each lava flow and each sill, there is no evidence that any such magmas existed. A specific search was made for such phenomena, and where it was possible to check, all of the igneous activity was apparently of the normal $\delta^{18}O$ type. It is assumed, therefore, that the generalized $\delta^{18}O$ profile in the greenstone belt is caused by subsolidus hydrothermal exchange, and that high-^{18}O magmas, if present, were of local distribution only.

The geologic history of the Abitibi area is rather complicated, due to its extreme age. There are only two geologic events which could have had an appreciable effect on the overall $^{18}O/^{16}O$ distribution, however. Because oxygen is tightly bound in silicate minerals, at relatively low temperatures the only way it can be exchanged is through recrystallization of the mineral. During recrystallization, whether it be by fine-scale solution and redeposition or by growth of a secondary mineral, the oxygen in the mineral can freely communicate and equilibrate with the oxygen in the fluid. Inasmuch as there are two region-wide recrystallization events, the prehnite-pumpellyite and greenschist facies events, they are the only contenders for the exchange role. When considered in detail,

the early, prehnite-pumpellyite facies event proves to have been by far the most important of these.

2. Seafloor Burial Metamorphism.

There are four lines of evidence which suggest that the $\delta^{18}O$-enrichments observed in the Abitibi greenstone belt were caused by seafloor burial metamorphism. These include: a. Stratigraphically controlled oxygen isotopic zoning, b. Correlation between $\delta^{18}O$ and prehnite-pumpellyite metamorphic grade, c. Spatial extent of recrystallization, d. Nature of the metamorphic events (i.e. the prehnite-pumpellyite event involved hydration, while the greenschist event involved dehydration).

a. Stratigraphic Control: The positive correlation between $\delta^{18}O$ and stratigraphic height is present in all five of the areas where the stratigraphic relations are known (Noranda, Ben Nevis, Benoit, Skead, Timmins). In a burial metamorphic environment both the temperature gradient and the proximity to the overlying seawater (and hence possibly the water/rock ratio) are controlled by the position in the stratigraphic sequence. The granitic plutons, on the other hand, crosscut the stratigraphy. Either the lower temperatures or the higher water/rock ratios (or both) would lead to high $\delta^{18}O$ values at the top of the pile.

b. Correlation With Metamorphic Grade: The correlation between high $\delta^{18}O$ values and metamorphic grade indicates that under the temperature gradient present during prehnite-pumpellyite facies metamorphism, the rocks of the volcanic pile were in oxygen isotopic communication with pore fluids. Large amounts of ^{18}O were transferred to the upper part of the pile in response to this temperature gradient. In contrast, traverses toward the contacts of some of the large granitic bodies show no clear-cut effect on $\delta^{18}O$. For example, in moving from greenschist facies

to pyroxene granulite facies towards the margin of the Otto Stock, $\delta^{18}O$ changes only slightly, from +8.8 to +7.1. Clearly these rocks were not freely communicating with respect to oxygen isotopes.

c. Spatial Extent of Recrystallization: Furthermore, the oxygen isotopic exchange process has been shown to be related to the type and degree of recrystallization (Fig. 3C-4). Prehnite-pumpellyite facies metamorphism has affected all of the volcanic rocks in the greenstone belt, producing hydrous secondary assemblages. The contact metamorphism associated with the granitic plutonism is of more local extent, however. In the central part of the Blake River Group, for example, the rocks show no obvious recrystallization due to the second metamorphism. Inasmuch as the core of the Blake River syncline is the locus of the most pronounced shifts in $\delta^{18}O$, it seems very unlikely that the greenschist facies event was responsible for those oxygen isotopic shifts.

d. Nature of the Metamorphic Events: The prehnite-pumpellyite facies event involved extensive hydration of the volcanic rocks. The mineral chlorite, for example, contains about 12 wt.% H_2O. One of the mineralogic effects of the hydrothermal recrystallization is the development in the rocks of monomineralic domains composed of pumpellyite, chlorite and epidote (Smith, 1968; Jolly and Smith, 1972; Jolly, 1980). This requires the transport of large amounts of various chemical constituents through the rocks, and suggests high water/rock ratios. By studying the mineralogic, chemical and textural characteristics of these rocks, Dimroth and Lichtblau (1979, p. 1338) concluded, "the mineralogical and chemical differentiation [introduced during the first metamorphism] is preserved during the subsequent metamorphism after deep burial, which appears to have been essentially isochemical.... It appears to us that

the metasomatic reactions can take place only when the extensive porosity permitted easy pore-fluid exchange. During seafloor metamorphism primary porosity permitted the flow of pore-fluids, during syn-kinematic dynamothermal metamorphism, pore-fluids migrated through tectonic fractures. Only minor movement of pore-fluids was possible during the load metamorphism and during phases of thermal contact metamorphism." These observations suggest that the first event involved a high water/rock ratio and that the second event involved a low water/rock ratio.

This is consistent with the dehydration character of the contact metamorphism; simple dehydration alone involves low water/rock ratios, and typically has only a negligible effect on the whole-rock $\delta^{18}O$ (see Chapter 4C). This lack of an ^{18}O effect has actually been demonstrated in a number of contact metamorphic aureoles (see Shieh and Taylor, 1969). It is not impossible, of course, for dehydration to be accomplished in the presence of large amounts of water, but it is much more likely that the large water/rock ratios indicated by the oxygen isotopic data accompanied the hydration event rather than the dehydration event.

3. Source of the aqueous fluid.

There can be little doubt that the Abitibi greenstone belt formed in a marine environment. This is indicated not only by the abundance of pillow lavas, but the presence of sedimentary rocks that include chemical precipitates such as cherts, banded iron formations, and massive sulfide deposits. Subseafloor alteration of the submarine volcanic rocks would have been an inevitable process in the Archean just as it is today (Heaton and Sheppard, 1976; Muehlenbachs and Clayton, 1976; Gregory and Taylor, 1980). Highly fractured and jointed volcanic rocks are extremely permeable

to aqueous fluids, so the volcanic pile was certainly saturated with water. In addition, the high temperature igneous activity (which is widespread) and presence of local thermal anomalies would certainly have set up hydrothermal convection cells involving these fluids. This is a general petrologic process which has now been proven to be active in both continental and oceanic environments down to depths of 5-10 km (or more). In an oceanic environment this circulating hydrothermal fluid must be the seawater itself; no other source of H_2O is feasible.

The presence of prehnite-pumpellyite associated hydrothermal alteration of the greenstone belt therefore fulfills the prediction of subseafloor water/rock interaction. The high water/rock ratios calculated from the oxygen isotopic data also support this interpretation, because in a seafloor environment large amounts of water would have access to the volcanic pile. The static, burial metamorphic style (as opposed to a dynamothermal metamorphism) involving non-hydrostatic stress is also characteristic of Phanerozoic and present-day seafloor metamorphism (e.g. Puerto Rico, Oman, Cyprus) although it also is known in other environments (e.g. the Keweenawan, which may in fact represent the transition from very shallow marine to intertidal and subaerial). It is concluded, therefore, that the hydrothermal alteration accompanying the prehnitepumpellyite facies metamorphism was accomplished by a marine pore fluid derived from seawater.

Devoloping the above conclusion further, it is possible to place limits on the oxygen isotopic composition of Archean seawater from the $^{18}O/^{16}O$ distribution in the rocks. In the preceeding chapters this calculation has been performed independently in six different areas, Ben Nevis, Benoit, Noranda, Skead, Munro, and Timmins. In five of these

areas, the fluid composition had $\delta^{18}O = 0 \pm 2$, whereas in the Timmins area, the fluid was apparently somewhat higher in $\delta^{18}O$, about 4 ± 2. This observation suggests that throughout most of the area analyzed seawater had $\delta^{18}O = 0 \pm 2$, and that in the Timmins area either the sea water was heavier (evaporation?) or the hydrothermal processes were more complex.

This suggests in turn that the calculated ore fluid for the Amulet "A" mine ($\delta^{18}O = 0.5 \pm 1.0$) was also seawater. The heated seawater convecting in the volcanic pile must have risen over the heat sources, and probably ultimately emerged from submarine fumaroles back into the ocean. It is around one of these submarine fumaroles that the Amulet "A" massive sulfide lens formed. Just as in the modern massive sulfide deposits on Cyprus and Japan, and in the sulfide pinnacles forming today on the East Pacific Rise at 21°N, the ore fluid was none other than heated, recirculated seawater. In this regard the hydrothermal processes operating in the Archean strongly resemble those operating in the Phanerozoic and in the modern ocean as documented by a number of workers using the submersible 'ALVIN' (Corliss et al. 1979).

The ore deposit at Kidd Creek, on the other hand, was apparently formed from a hydrothermal solution too rich in ^{18}O to be unmodified seawater ($\delta^{18}O \approx +8$). The various possible origins of the Kidd Creek ore fluid are discussed in detail in Chapter 4B, and the most plausible possibilities involve some form of brine or metamorphic H_2O. It is important to note, however, that the Kidd Creek ore deposit and the immediately surrounding terrain in the vicinity of Timmins, both of which are anomalously rich in ^{18}O, are located together at the margin of the greenstone belt (Fig. 7-2). By one mechanism or another the

hydrothermal fluids in this area evolved somewhat differently than the rest of the greenstone belt.

II. COMPARISON WITH OPHIOLITE COMPLEXES AND ISLAND ARCS

1. General Statement

As discussed above, greenstone belts formed as submarine plutonic-volcanic-sedimentary sequences. As such, they were a portion of the Archean oceanic crust (although they may not have been typical oceanic crust). An important comparison can be made, therefore, between greenstone belts and modern marine igneous complexes, the two most prominent examples of which are ophiolite complexes and island arcs. Ophiolites are thought to have formed by some form of seafloor spreading, and island arcs by subduction-related volcanism, but in both cases there is abundant opportunity for interaction with seawater. Comparing greenstone belts to these possible modern analogues, therefore, may lead to a more complete understanding of the geology of the Archean and of the significance of greenstone belts.

A summary of the important characteristics of greenstone belts, ophiolites and island arcs are listed in Table 7-1. As a means of indroduction, the tectonic setting, geology, and metamorphic styles are compared, and with this background, the $^{18}O/^{16}O$ data are compared.

2. Tectonic Setting

Ophiolites are found only along continental margins or along suture zones between continental plates where they are invariably associated with major decollement-type dislocations. Although originally formed at oceanic spreading centers, it is along these shallow thrust or glide faults that the ophiolites have reached their present positions. Island arcs are invariably related to subduction zones, typically occurring

TABLE 7-1. COMPARISON OF GREENSTONE BELTS WITH OPHIOLITES AND ISLAND ARCS

Characteristic	Greenstone Belts	Ophiolites	Island Arcs
Age	Archean-Proterozoic	Phanerozoic	Phanerozoic
Tectonic setting	?	Mid-ocean ridges	Subduction zones
Associated granitic rocks	"Seas" of granite (tonalite to true granite)	Plagiogranite	Calc-alkaline tonalites and granodiorite sometimes superimposed on older granitic rocks of the craton
Stratigraphic section	Clastic sediments Calc-alkaline volc. Tholeiitic volc. Komatiitic volc. Granite	Chert Tholeiitic volc. Sheeted dikes Layered gabbros Harzburgite	Clastic sediments Cacl-alkaline volc.
Strat. thickness	20-30 km.	5-10 km	10-15 km
Metamorphic style	Prehnite-pumpellyite greenschist	Zeolite greenschist amphibolite	Variable, including prehnite-pumpellyite
$\delta^{18}O$ top	+10	+12	
middle	+ 8	+ 3	?
bottom	+ 6	+ 6	

between the 100 km. and 200 km. isobaths above the Benioff zone. The original tectonic setting of greenstone belts is open to considerable debate, and a host of different possibilities have been proposed. There is no evidence, however, that greenstone belts were obducted into their present positions, so in that regard they strongly differ from ophiolites and resemble island arcs.

3. Granitic Rocks

The field evidence (Baragar and McGlynn, 1976; Viljoen and Viljoen, 1969c) suggests that the greenstone belt volcano-sedimentary piles accumulated on an older granitic crust. This density inversion (the higher greenstones were denser than the lower granites) was gravitationally unstable, leading to the diapiric rise of granitic batholiths. It is important to note that all greenstone belts were invaded by granitic diapirs shortly after their formation--the two rock types always occur together, and genetic models must account for both lithologies.

A possibly analogous phenomenon has been observed in the Japanese island arc. The present topography of the Japanese islands is the result of late Tertiary and Quaternary vertical movements (Miyashiro, 1973). The Quaternary rise alone amounts to 1200 m. Underlying the islands is a thick (30-40 km.), continental-type crust. The crust is thickest beneath the central mountains of Honshu, which is the highest part of Japan and the region with the greatest amount of Cenozoic uplift (Miyashiro, 1973). This isostatic rise may be the result of granitic diapirism at depth. In any case, the overall gravitational situation is rather similar to that governing the formation of the greenstone belts.

By contrast, granitic rocks are insignificant in the petrogenesis of an ohpiolite. The igneous rocks are almost exclusively basaltic; the only

felsic magmas present are the plagiogranites, which generally comprise only a small fraction of ophiolite complexes. Although the ophiolite plagiogranites and keratophyres are comgmatic with the basaltic volcanism, and in that regard might be considered to be analogues of the rhyolitic volcanism associated with a greenstone belt, chemically they are radically different. There is nothing in the ophiolite assemblage which resembles the seas of granite surrounding the greenstone belts, nor is there anything in the latter that resembles the harzburgite tectonite basement of the ophiolites.

4. Stratigraphy

In both greenstone belts and ophiolites a well-developed stratigraphy is present. Working from the lowermost structural levels upwards, in a greenstone belt one finds granitic batholiths overlain by a thick sequence of volcanic rocks ranging from komatiitic through tholeiitic to calc-alkaline, and capped by immature clastic sediments. In ophiolites the basement consists of harzburgite. This is overlain by a thick series of layered gabros, then isotropic, hornblende-bearing gabbros, then a sheeted dike complex, then basaltic pillow lavas, and at the top, cherts and pelagic marine sediments. In island arcs, one finds tholeiitic to calc-alkaline volcanic rocks, and immature, volcanic-derived clastic sediments. By analogy with the eastern margin of the Pacific, the deeper structural levels of island arcs probably consist of calc-alkaline plutonic complexes. Beneath the plutonic complex may lie either a pre-existing continental margin or oceanic crust.

In a broad sense, therefore, greenstone belts and island arcs have many similar features. Both contain tholeiitic to calc-alkaline volcanics and immature clastic sediments in their upper portions. At present, in

fact, calc-alkaline volcanics are distinctive and unusual rocks which are restricted to island arc environments. Beneath the volcanic piles lie granitic plutonic complexes in both cases. Komatiites were once thought to be a uniquely Archean rock type, but have now been reported from other geological environments, possibly including island arcs. Echeverria and Paris (1979) have described possible komatiites from Gorgona island, off the coast of Colombia, in what may be an island arc environment.

Greenstone belts and ophiolites, however, are stratigraphically quite dissimilar. All of the lower part of the ophiolite section, harzburgite, gabbro and sheeted dikes, is missing from greenstone belts. Although gabbros such as the Dore Lake intrusion (Allard, 1970), are present within greenstone belts, they are rare discrete plutons, not stratigraphically continuous for hundreds of kilometers along strike as found in some ophiolites. Gabbros are also rare, but ubiquitous, in plutonic calc-alkaline belts such as the west side of the Peninsular Ranges batholith (Larsen, 1948). Although komatiitic compositions have been reported in pillow lavas and sheeted dikes of the Betts Cove ophiolite (Upadhyay, 1978), and tholeiitic compositions are prevalent, ophiolite complexes are typically devoid of calc-alkaline volcanism. Thus one of the major magma series of greenstone belts is missing from ophiolites. Furthermore, the sedimentary rock associations are different. Greenstone belts do contain cherts and several types of sedimentary iron formations, but the dominant type of sedimentary rock is greywacke. In ophiolite complexes, however, cherts and pelagic sediments predominate to the virtual exclusion of clastic sediments. It is interesting to note in passing that all three geologic settings, greenstone belts,

ophiolites and island arcs, contain volcanogenic massive sulfide deposits.

5. Stratigraphic thickness

The total stratigraphic thickness of the Abitibi volcanic pile has been estimated to be about 40 km. by Jensen (1979). If the granitic basement were included, the structural thickness would be even greater. In ophiolites there is typically 6-8 km. of section above the petrologic Moho, along with up to 10 km. of harzburgite basement. In island arcs the thickness of the volcanic pile is not easy to estimate, but based on partially eroded terranes such as Puerto Rico and Baja California, 10-15 km. seems reasonable. The great thickness, and particularly the broad extent, of the greenstone belts, therefore, seems to have no modern analogue.

6. Metamorphic style

As discussed above, the Abitibi greenstone belt underwent a major metamorphic event soon after its igneous history. This subseafloor burial metamorphism produced prehnite-pumpellyite assemblages in the upper part of the pile, and probably also greenschist facies assemblages in the lower parts of the pile. In Puerto Rico (Jolly 1970), the mafic to intermediate volcanic rocks have also undergone subseafloor burial metamorphism, producing assemblages in both the zeolite and the prehnite-pumpellyite facies. In another island arc, Japan, the metamorphic style is extremely complicated. Not only are there paired metamorphic belts, but the P-T conditions and assemblages vary widely within each belt (Miyashiro, 1973). In at least two localities on Japan, the central Kii peninsula (Seki et al. 1971) and the Tanzawa Mountains (Seki et al. 1969), however, prehnite-pumpellyite facies rocks are present. The

metamorphic styles of island arcs and greenstone belts, therefore, share some similar features.

In contrast, ophiolites exhibit a very uniform metamorphic style. The upper pillow lavas are commonly in the zeolite facies, and from there the temperature steadily increases down the section. Beneath the zeolite-facies pillow lavas are greenschist-facies diabase dikes, and below that, amphibolite-facies gabbros. Pumpellyite has never been reported in an ophiolite. This circumstance is so striking that it is worth reviewing the worldwide occurrence of pumpellyite to help understand this potentially important difference between greenstone belts and ophiolites.

Prehnite-pumpellyite rocks have now been described from a variety of different localities (Winkler, 1979). Pumpellyite has been shown to develop under condition of a high geothermal gradient (Tanzawa Mtns., Japan; Seki, 1969), a "normal" geothermal gradient (New Zealand; Coombs, 1960), and a low geothermal gradient (Franciscan formation; Ernst et al. 1970). Why then, does the progressive metamorphism of ophiolites apparently bypass pumpellyite stability? 1.) Although it is possible that pumpellyite is actually present in ophiolites, but has not been observed, it is more likely that the lack of pumpellyite in such rocks is due to the extremely rapid increase in temperature with depth in a mid-ocean ridge spreading environment. In the presence of quartz, chlorite and actinolite (common secondary minerals in ophiolites), pumpellyite is stable only at pressures greater than 2 kb. (Winkler, 1979). In the absence of actinolite, however, pumpellyite is stable down to 0 kb. 2.) Pumpellyite is a very Ca-rich mineral, and is unstable with respect to calcite in the presence of a CO_2-rich fluid. 3.) Zoisite is unstable at low-T with respect to pumpellyite, but Fe-rich epidote is not (Winkler,

1979). Pumpellyite might therefore be absent under conditions of high f_{O_2}. Whatever the reason for the difference, in this regard greenstone belts resemble island arcs, and both differ from ophiolites.

7. Oxygen Isotopes

The generalized $\delta^{18}O$ profile through a section of the Abitibi greenstone belt shows a steady increase from about +6 at the base to about +10 at the top (this work). In ophiolites $\delta^{18}O$ is +6 at the base, decreases to about +3 in the layered gabbros, and then increases steadily upwards to about +12 in the upper pillow lavas (Gregory and Taylor, 1980). The ophiolite initially had a uniform $\delta^{18}O$ of about +5.7, so the hydrothermal alteration has produced both ^{18}O-enrichments and ^{18}O-depletions, a fact which is discussed in more detail below. In the greenstone belt virtually all of the rocks show ^{18}O enrichments, and only a tiny fraction (komatiities and stockwork zones) show ^{18}O depletions. Detailed oxygen isotopic data are currently not available for island arcs. However, reconnaissance $^{18}O/^{16}O$ and D/H data along the western side of the Peninsular Ranges batholith south of Ensenada show that ^{18}O enrichments in both the plutonic and the country rocks are observed, and the range of $\delta^{18}O$ is from +6 to +11 (Taylor and Silver, 1978). This is very similar to the observed variation in the greenstone belts; in neither case are ^{18}O depletions found.

The ^{18}O distribution in ophiolites is easy to understand. The liquidus temperatures of mid-ocean ridge tholeiites is about 1200°C. The contact temperature of the wall rocks adjacent to the mid-ocean ridge magma chamber is at least half that, 600°C or more (assuming the top of the oceanic crust is held at 0°C). Thus a strong geothermal gradient from 0° to 600°C is imposed on the uppermost 3 km. of oceanic crust, and

it is within this gradient that the hydrothermal alteration takes place. The $\delta^{18}O$ profile described above, roughly speaking, is the result of all of the basaltic rocks equilibrating with ocean water at these various temperatures. The heat engine driving the hydrothermal convection cells is, of course, the mid-ocean magma chamber.

The ^{18}O distribution in greenstone belts was apparently produced in a different way. Like ophiolites, the observed profile indicates equilibration of the igneous section with seawater under a certain temperature distribution. The temperatures, however, are much different from those in ophiolites. From base to top, the total range in temperature was apparently only about 350-200°C. The absence of high-temperature effects is compatible with the absence of large plutonic intrusive bodies, suggesting either that the hydrothermal systems were not driven by large mafic magma chambers, or that the lower part of the section has not been preserved. The absence of extreme low-temperature effects suggests that the top of the pile has not been analyzed (or else the upper part was sedimentary).

These observations suggest that the mechanism of hydrothermal alteration in the greenstone belts simply involved burial metamorphism and the circulation of marine pore fluids through the rocks without any great abundance of local "heat-engines" in the form of igneous plutons. This raises an important question: What was the energy source which powered the hydrothermal system? Some mechanism was apparently able to drive large amounts of water through the volcanic pile. Although this question cannot be definitively answered, a model can be proposed. All of the volcanic rocks in the greenstone belt were erupted onto the earth's surface. The mechanism of those eruptions has not yet been

fully established, but it appears that some were fed from high-level magma chambers, others from dikes. Whatever the geometry, numerous very small, scattered magma sources must have been present as feeders to the pile. These may have been sufficient to induce hydrothermal circulation in a myriad of small convection cells or in a few broad, slowly convecting cells, without heating a significant fraction of the country rocks to temperatures as high as 500°C.

In any case, the detailed mechanisms and styles of hyrdothermal alteration were dramatically different in greenstone belts and ophiolites. The end result was similar, however; both were thoroughly altered by seawater. Whether or not this same phenomenon will be demonstrated with more detailed work in deeply eroded island arcs awaits future study.

III. IMPLICATIONS FOR THE EVOLUTION OF THE OCEANIC CRUST

The $\delta^{18}O$ distribution in ophiolites is such that the initially homogeneous section ($\delta^{18}O \approx +5.7$) has undergone both ^{18}O-enrichments and ^{18}O-depletions (Gregory and Taylor, 1980). The weighted average amount of ^{18}O-enrichment is indistinguishable from the amount of ^{18}O-depletion, so the overall rock sequence has undergone no net change in $\delta^{18}O$. The heavy oxygen has been redistributed, but considering the ophiolite as a whole, has been conserved. The lack of change, coupled with the extensive seawater alteration which as affected the rocks, indicates that this hydrothermal alteration of the oceanic crust section is in fact controlling the oxygen isotopic composition of seawater (Muehlenbachs and Clayton, 1976; Gregory and Taylor, 1980). Integrating the fractionation factor Δ over all of the temperatures of alteration, one finds that the overall material balance value of $\Delta_{ophiolite\text{-}water} \approx 6$. The facts that fresh basalts are erupted at $\delta^{18}O = +5.7 \pm 0.2$ and that

seawater has $\delta^{18}O = 0$ are a consequence of this fractionation. The ocean equilibrates with the oceanic crust via hydrothermal alteration, emerging from the reaction with a $\delta^{18}O$-value which is 6 per mil lighter than the rocks (Gregory and Taylor, 1980).

The mantle is the major reservoir of oxygen on earth, and it appears to have a fairly uniform $\delta^{18}O$ of about +6. Basaltic crust (also $\delta^{18}O = +6$) is presently being derived form the mantle and being formed under the ocean at an enormous rate. This new crust exchanges continually with the seawater. The amount of oxygen introduced by this magmatism is so large compared to the amount of oxygen in the ocean that $\delta^{18}O$ of the seawater is controlled by that of the rock. As long as fresh, mantle-derived basalts have been interacting with the ocean at great rates and in great abundance, the $\delta^{18}O$ of seawater will be 'buffered' at a value close to 0. Calculations by Gregory and Taylor (1980), for example, indicate that even if the ocean were instantaneously shifted to $\delta^{18}O = +8$, the present tectonic regime would return it to 0 within a few hundred million years. As long as plate tectonics in its present form has been active, it is very unlikely that seawater was any different than 0.

The present study of the Abitibi greenstone belt indicates that Archean seawater (2.85 b.y. before present) also apparently had $\delta^{18}O$ close to 0. The preliminary data from the Cape Smith fold belt and the Dubois greenstone belt suggest that the Proterozoic seawater (1.7 b.y. ago) was in the same range. The ophiolite data extend from the Ordovician to the Cretaceous, also indicating seawater with $\delta^{18}O = 0$. The evidence therefore suggests that the oxygen isotopic composition of seawater has remained virtually constant through geologic history at

least as far back as 2.85 b.y ago.

This conclusion is consistent with a variety of oxygen isotopic data on other Precambrian rocks. Taylor (1977), through a detailed study of granitic batholiths that have interacted with meteoric waters found evidence that $\delta^{18}O$ of the hydrosphere (and hence of ocean water) has remained relatively constant over the last 2.5 b.y. The considerable amount of data that have been collected on Precambrian cherts (Perry, 1967; Perry et al. 1978; Oskvarek and Perry, 1976; Chase and Perry, 1972; Becker and Clayton, 1976; Knauth and Epstein, 1976; Yeh and Epstein, 1978) indicates that the Archean cherts tend to be isotopically lighter than Phanerozoic cherts. These data have been interpreted in three ways, hotter Archean oceans, lighter Archean seawater and post-crystallization exchange and lack of $\delta^{18}O$ preservation in the cherts. However, in the absence of an independent test, these three possibilities cannot be resolved. The present study provides such a test, suggesting that the second possibility should be ruled out, thus perhaps favoring the idea that Archean ocean water was somewhat warmer than at present, as proposed by Knauth and Epstein (1976).

The fact that the oxygen isotopic composition of seawater has not changed noticeably with time suggests that the physical processes operating on the earth's surface in the Archean were basically similar to those operating today. All of the major crustal processes, including weathering, sedimentation, plutonism, volcanism and metamorphism, interact in one way or another with the hydrosphere. If the relative rates of these processes were vastly different in the Archean, an effect of some sort might be anticipated in the hydrosphere. At present, most of the water/rock interactions in the Earth's crust take place via submarine

volcanism and plutonism. Thus it seems inevitable that volcanism and plutonism in the Archean ocean were also the dominant forms of water/rock interaction in the Archean (contrary to the conclusions of Chase and Perry, 1972 and Perry and Tan, 1972, who suggested that sedimentation was dominant). Although submarine volcanism and plutonism are known through numerous geologic studies to have been widespread in the Archean (perhaps much more voluminous than at present considering the much greater abundance of heat-producing elements such as ^{235}U and ^{40}K), is there any assurance that such volcanism took the same form it does today, i.e. mid-ocean ridge seafloor spreading plate tectonics?

During the early Precambrian there was a great deal more heat production within the earth than there is today. At present this heat is lost primarily through the process of plate tectonics, suggesting that in the Archean either the plates were smaller, or that the plate motion was faster (McKenzie and Weiss, 1975). Because of the higher heat flow, it seems inevitable that some form of (rapid?) seafloor spreading was active in the Archean. From the geologic constraints and oxygen isotopic data, it is equally clear that greenstone belts were not created at those hypothetical ancient mid-ocean ridges.

The average $\delta^{18}O$ of the Abitibi greenstone belt appears to be around +7 to +8. This indicates an average ^{18}O-enrichment in the rocks of 1 to 2 per mil during the hydrothermal alteration process. Similar results are found in the Yilgarn block, the Yellowknife greenstone belt, and the Dubois greenstone belt and Cape Smith; all have experienced an addition of heavy oxygen. If the only volcanic process active in the Precambrian ocean was greenstone belt formation, these data imply that there would have been a continuous transfer of ^{18}O from the ocean

water into the rocks. This would have reduced the $\delta^{18}O$ of the ocean by an amount which depends on the rate of production of greenstone belts. It is difficult to estimate the amount and time scale of this lowering, but the amount of oxygen in the Abitibi greenstone belt alone is 1/500 of that in the modern oceans. If the whole surface of the earth were made of greenstone belts, their oxygen content would far outweigh that of the ocean, and the corresponding $\delta^{18}O$ depletions in the ocean would have taken place very rapidly.

Within the resolution of the present data, it is possible to calculate the $\delta^{18}O$ of ocean water at best only to within 1 or 2 per mil, so such an ^{18}O depletion might go unnoticed. Note, however, that all of the greenstone belts, including the younger ones, have apparently been enriched in ^{18}O. This shows that the expected complementary shift in $\delta^{18}O$ in the ocean water had not taken place by 1.7 b.y. This requires either that light oxygen was also continously being removed from the ocean during the period 3.4 - 1.7 b.y. ago, or the total volume of greenstone belts amounted to only a fraction of the volume of ocean (in which case there obviously must also have been some other type of oceanic crust). This idea is illustrated schematically in Figure 7-3. To fully evaluate all of the possible complementary reservoirs of light oxygen, it is necessary to consider all of the Archean crustal rocks, including the granites and gneisses, because they have all probably interacted with the hydrosphere.

Granites. The data summarized in Chapter 5A show that the Archean granitic rocks in the Superior province have $\delta^{18}O = +7$ to $+10$. Modern granitoids with similar chemical composition have comparable $\delta^{18}O$-values. Thus there is no evidence that the Archean granites have

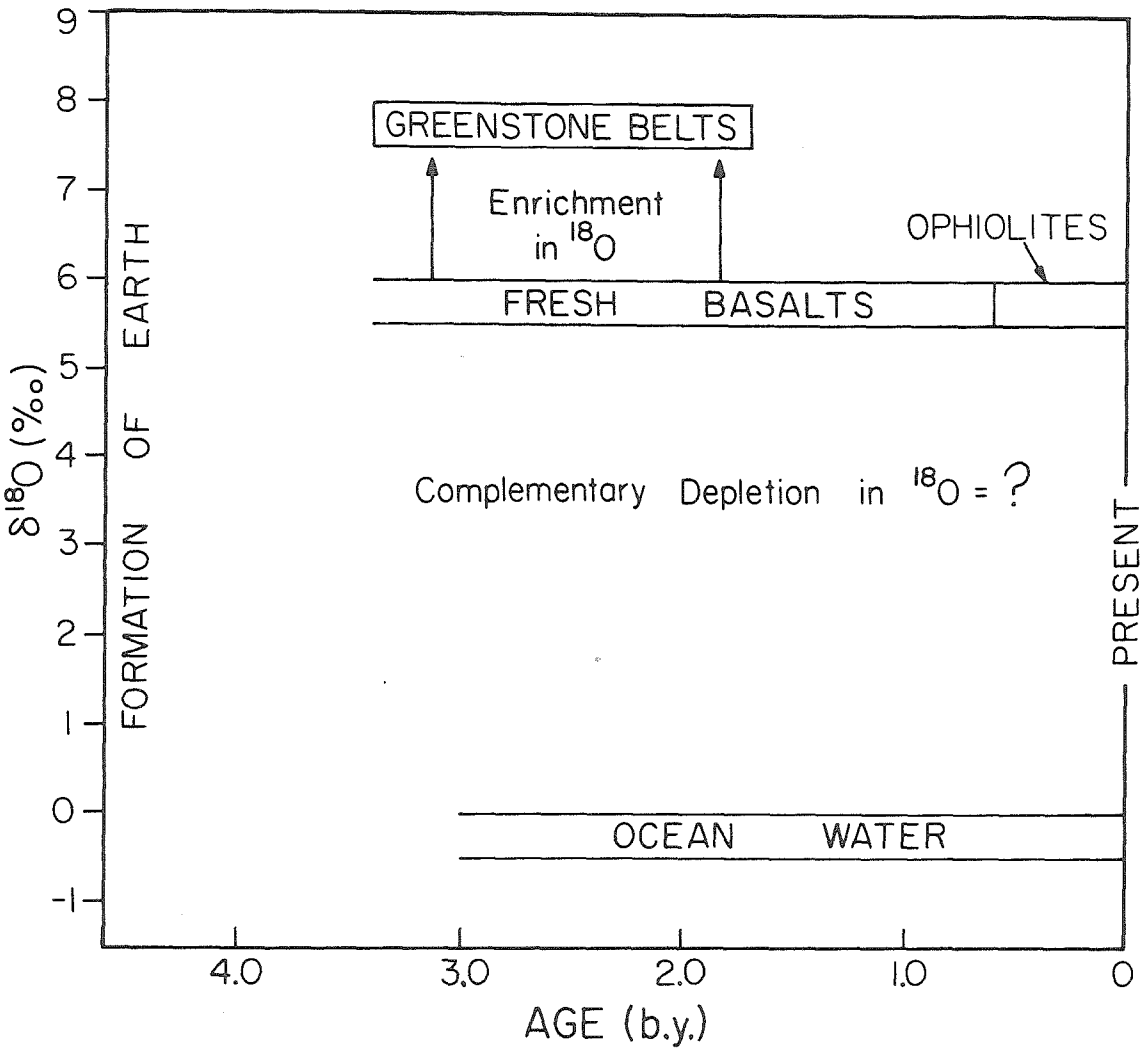

Figure 7-3. Schematic representation of the oxygen isotopic evolution of seawater, greenstone belts, and fresh basaltic magmas. The enrichment in ^{18}O observed in greenstone belts requires a complementary depletion in ^{18}O in some other reservoir.

undergone an ^{18}O-depletion. Furthermore, the detailed study of the Round Lake batholith indicates that hydrothermal effects of any sort are rare. In the Barberton Mountain Land the tonalitic domes range in $\delta^{18}O$ from +6 to +10 (Taylor, 1977). Although these data indicate local ^{18}O-depletions, further study is needed to evaluate the extent and significance of these +6 tonalites. The overwhelming majority of Archean granitoids, however, apparently have normal $\delta^{18}O$-values.

Gneisses. With the possible exception of the migmatized portions of the Footprint gneiss, all of the orthogneisses discussed in Chapter 5B are oxygen isotopically comparable to undeformed Archean granitoids. Likewise, the $\delta^{18}O$ values of many of the paragneisses resemble those of undeformed Archean clastic sedimentary rocks. Some of the paragneisses, however, appear to have lost ^{18}O during metamorphism. The total abundance of these low-^{18}O gneisses is not clear, and is a subject for further study. In all, the Superior Geotraverse area contains 14% paragneiss and 36% orthogneiss (Goodwin, 1978), so most of the gneisses are presumed to have maintained their $\delta^{18}O$-values through metamorphism. The overall abundance of low-^{18}O Archean gneisses, however, is an important unanswered question.

Sedimentary rocks. The metamorphosed clastic sedimentary rocks in the Archean are typical of those throughout the Precambrian in terms of their oxygen isotopic ratios (Chapter 5C). Longstaffe and Schwarcz (1977) have reported that increasing $\delta^{18}O$ correlates with decreasing content of volcanic clastic material, which suggests that the whole-rock $\delta^{18}O$ values have not changed through metamorphism.

It appears that in the present geologic record, therefore, only the greenstones and some of the paragneisses have undergone obvious ^{18}O-shifts

during metamorphism. Although the direction of ^{18}O-shift was opposite in these two reservoirs, it seems unlikely that they balance one another. Although the metasedimentary Pakwash gneiss ranges in $\delta^{18}O$ from +6.5 to +11.0 (Longstaffe, 1979), 75% of the analyses lie between +9 and +11, values comparable to those from the sedimentary rocks. 80% of the five analyses from the Twilight paragneiss range from +8.3 to +9.3, with the remaining sample being +7.3. The present, admittedly incomplete, data set therefore suggests that about one-fourth of the paragneisses may have undergone depletions of as much as 1 to 3 per mil in $\delta^{18}O$. The Abitibi greenstone belt, on the other hand, has been enriched in ^{18}O by 0 to 7 per mil, with an average of about +2.

In order to compare these two reservoirs properly their original masses in the Archean must be estimated, a nearly hopeless task. In the Superior Geotraverse area, however, greenstones and paragneisses each comprise 14% of the outcrop (Goodwin, 1978). If this area were typical of the Archean crust, therefore, the greenstones are about a factor of four too abundant to be balanced in terms of oxygen isotopes by the gneisses. Thus, either there were more gneiss belts present in the Archean (which have not been preserved), or there was another reservoir of light oxygen to complement the greenstone belts.

If this reservoir of light oxygen were the ocean, then the greenstone belts could not have comprised the entire oceanic crust. In that case the amount of oxygen in the greenstone belts would have greatly exceeded the amount of oxygen in the water, and the exchange process would have buffered itself through time. Although the resolution of the data (0 ± 2) is not such that we can be certain that seawater has not changed slightly in $\delta^{18}O$ with time, it is clear that greenstone belts are uniformly

enriched in ^{18}O through geologic history (Fig. 7-3). Thus greenstone belts did not buffer $\delta^{18}O$ of the ocean, and some other type of oceanic crust must also have been present. If this postulated second type of oceanic crust did not interact strongly with the ocean, then seawater itself must have been the low-^{18}O reservoir. Seawater might, for example, have changed in $\delta^{18}O$ from +2 at 3 b.y. ago to 0 today. To balance this change, all of the greenstone belts ever created throughout history sum to only about 1/6 of the surface area of the earth, which means that at least 1/2 of the surface area of the earth was covered by the second oceanic crustal type. Alternatively, if this second type of oceanic crust interacted with seawater at high temperature, it could represent the low-^{18}O reservoir. In any case, greenstone belts could not have been typical Precambrian oceanic crust.

An obvious, geologically reasonable process which satisfies these constraints is plate tectonics. If new oceanic crust were being formed and altered at spreading centers, but at slightly higher temperatures than at present, then the integrated fractionation factor Δ (see p. 440) may hae been about 5. If the ocean had $\delta^{18}O = 0$, this would have caused an overall ^{18}O depletion in the (initially +5.7) basalt, and a complementary ^{18}O enrichment in the ocean water. In this example, the ocaen would eventually have been buffered at $\delta^{18}O = +0.7$, neglecting all other water/rock interactions. If the amount of mid-ocean ridge basalt was much larger than the amount of greenstone belts, the magnitude of this ^{18}O-depletion could have been very small. This hypothetical ^{18}O-depleted basalt would then have to have disappeared from the geologic record (lost down the subduction zones?).

This model is attractive for two reasons. First of all, oceanic

volcanism was apparently extensive in the Archean. This is required to explain the constant $\delta^{18}O$ of seawater with time. Greenstone belts apparently could not have been typical oceanic crust, however, because of the observed problem with the ^{18}O balance. Some other type of oceanic crust must also have been present. If this second crustal type were present in great abundance it could have had a nearly "normal" oxygen isotopic distribution (the altered crust overall having nearly the same $\delta^{18}O$ as the fresh crust, i.e. $\approx +6$). If it were present in low abundance it would have to exhibit an overall $\delta^{18}O$ significantly less than +5.7. This second hypothetical type of Archean oceanic crust has not been preserved in the geologic record. The only logical mechanism for quantitatively destroying such crust is by seafloor spreading plate tectonics. This could also account for the apparent destruction of the necessary low-^{18}O reservoir - the downgoing slab could perfectly balance the global ^{18}O distribution but be completely eliminated by the tectonic process.

If seafloor spreading were in fact taking place in the Archean, then this low-^{18}O reservoir would have been continuously recycled back into the mantle throughout geologic history. At the present rate of seafloor spreading the total amount of oceanic crust subducted over the past 3 b.y. would amount to about 1/6 of the mass of the upper mantle. Whether or not this would produce an ^{18}O-shift in the mantle depends on the rates of all of the other crustal processes (which will determine $\delta^{18}O$ of seawater, and consequently $\delta^{18}O$ of the downgoing slab). The actual observation, however, that newly erupted basaltic magma has not noticeably changed in $\delta^{18}O$ through geologic time is consistent with this idea.

IV. THE SIGNIFICANCE OF GREENSTONE BELTS

The numerous published models for the origin of greenstone belts can be divided into two classes, those which attempt to apply modern plate tectonic theory, and those which attempt to deduce a uniquely Archean tectonic setting. Virtually all of the modern tectonic environments have been suggested for the formation of greenstone belts, including midocean ridges, marginal basins, and island arcs. The presence of extensive calc-alkaline volcanism is a powerful argument in favor of the island arc model, which is championed by Goodwin and Anhausser. On the other hand, Hargraves and Baragar are impressed by the ubiquitous association of greenstone belts and seas of granite. They favor some sort of downwarp model in which a volcanic pile forms on a thin sialic crust. Isostatic equilibrium forces the sial beneath the pile into the mantle, where it heats up above its solidus and intrudes the volcanic pile. Note that the two models are not exclusive - island arcs may have formed in downwarps located on sialic crust.

The oxygen isotopic data are consistent with either model with an added bonus: By considering the total ^{18}O budget of the early ocean it is possible to draw conclusions about the entire oceanic crust. These results suggest that greenstone belts were not typical oceanic crust, and that massive volcanism and marine hydrothermal interactions must have been going on in some other structural setting elsewhere in the ocean. This, combined with the numerous geological similarities between greenstone belts and island arcs, suggests that greenstone belts were the Archean equivalent of island arcs. Some form of seafloor spreading tectonics was therefore taking place elsewhere in the Earth's crust. It would, of course, be extremely important if remnants of such spreading could be

identified somewhere in the Precambrian crust, but this may be possible only in (eclogite?) fragments accidentally brought upward from the upper mantle.

REFERENCES

Addy, S.K. and P.J.M. Ypma (1977) Origin of massive sulfide deposits at Ducktown, Tennessee: An oxygen, carbon and hydrogen isotope study. Econ. Geol., 72, 1245-1268.

Allard, G.O. (1970) The Dore Lake complex, Chibougamau, Quebec -- A metamorphosed Bushbeld-type layered intrusion. Geol. Soc. S. Afr. Spec. Publ. 1, 477-491.

Anderson, A.T., R.N. Clayton and T.K. Mayeda (1971) Oxygen isotope geothermometry of mafic igneous rocks. Jour. Geol., 79, 715-729.

Anhaeusser, C.R. (1973) The evolution of the early Precambrian crust of southern Africa. Phil. Trans. R. Soc. Lond., 273, 359-388.

Arndt, N.T. (1976) Melting relations of ultramafic lavas (komatiites) at 1 atm. and high pressure. Ann. Rept. Dir. Geophys. Lab., 555-562. Carnegie Inst. of Washington Yearbook 75.

Arndt, N.T., A.J. Naldrett and D.R. Pyke (1977) Komatiitic and iron-rich tholeiitic lavas of Munro Township, northeast Ontario. Jour. Petr., 18, 319-369.

Baragar, W.R.A. and J.C. McGlynn (1976) Early Archean Basement in the Canadian shield: A review of the evidence. Geol. Sur. Canada Paper 76-14.

Barker, F., I. Friedman, D.R. Hunter and J.D. Gleason (1976) Oxygen isotopes of some trondjemites, siliceous gneisses, and associated mafic rocks. Precambrian Res., 3, 547-557.

Beaty, D.W. and H.P. Taylor, Jr. (1979) Oxygen isotope geochemistry of the Abitibi greenstone belt, Ontario: Evidence for seawater/rock interaction and implications regarding the isotopic composition and evolution of the ocean and oceanic crust. (abs.) Geol. Soc. Amer. Abs. w. Progs., 11, 386.

Becker, R.H. and R.N. Clayton (1976) Oxygen isotope study of a Precambrian banded iron-formation, Hamersley Range, western Australia. Geochem. et Cosmochim. Acta, 40, 1153-1165.

Berry, L.G. (1941) Geology of the Bigwater Lake area. 48th Rept. Ont. Dept. Mines, 48, pt. 12, 1-9.

Chase, C.G. and E.C. Perry, Jr. (1972) The oceans: Growth and oxygen isotope evolution. Science, 177, 992-994.

Chinner, G.A. and J.S. Fox (1974) The origin of cordierite-anthophyllite rocks in the Land's End aureole. Geol. Mag., 111, 397-408.

Clayton, R.N., J.R. O'Neil and T.K. Mayeda (1972) Oxygen isotope exchange between quartz and water. Jour. Geophys. Res., 77, No. 17, 3057-3067.

Constantinou, G. (1976) Hydrothermal alteration of the basaltic lavas of the Troodos Ophiolitic Complex associated with the formation of the massive sulfide deposits. in Volcanic processes in ore genesis (London: Inst. Min. Metall. and Geol. Soc.), 77.

Cooke, H.C., W.F. James and J.B. Mawdsley (1931) Geology and ore deposits of the Rouyn-Harricana region, Quebec. Geol. Sur. Can. Mem. 166.

Coombs, D.S. (1960) Lower grade mineral facies in New Zealand. Int. Geol. Cong. 21st Sess. Rept., Part 13, 339-351. Copenhagen.

Corliss, J.B. et al. (1979) Submarine thermal springs on the Galapagos Rift. Science, 203, 1073-1083.

Craig, H. (1963) The isotopic geochemistry of water and carbon in geothermal areas. in Nuclear Geology and Geothermal Areas, (E. Tongiorgi, ed) (Consiglio Nazionale delle Ricerche, Rome, 1963) 17-53.

Craig, H. (1966) Isotopic composition and origin of the Red Sea and Salton Sea geothermal brines. Science, 154, 1544-1548.

Craig, H., G. Boato and D.E. White (1956) in "Nuclear processes in geologic settings" Nat. Acad. Sci. Nat. Res. Council Publ., 400, 29.

Criss, B.C. and H.P. Taylor, Jr. (in prep.) An oxygen, hydrogen and argon isotopic study of the Idaho batholith.

Davies, J.F. (1977) Structural interpretation of the Timmins mining area, Ontario. Can. Jour. Earth Sci., 14, 1046-1053.

Dimroth, E. and A.P. Lichtblau (1979) Metamorphic evolution of Archean hyaloclastites, Noranda area, Quebec, Canada. Part I: Comparison of Archean and Cenozoic sea-floor metamorphism. Can. Jour. Earth Sci., 16, 1315-1340.

Echeverria, L.M. and G. Paris (1979) Tertiary komatiites of Gorgona Island, Columbia: Their field occurrence and geochemistry. Geol. Soc. Amer. Abs. w. Progs., 11, 419.

Edmond, J.M., H. Craig, L.I. Gordon and H.D. Holland (1979a) Chemistry of hydrothermal waters at 21°N on the East Pacific Rise (abs.) EOS Trans. Amer. Geophys. Union, 60, 864.

Edmond, J.M., C. Measures, B. Mangum, B. Grant, F.R. Sclater, R. Collier, A. Hudson, L.I. Gordon and J.B. Corliss (1979b) On the formation of metal-rich deposits at ridge crests. Earth and Planet. Sci. Lett., 46, 19-30.

Ernst, W.G., Y. Seki, H. Onuki and M.C. Gilbert (1970) Comparative study of low-grade metamorphism in the California Coast Ranges and the outer metamorphic belt of Japan. Mem. Geol. Soc. Amer., 124,1-276.

Evans, B.W. and V. Trommsdorff (1970) Regional metamorphism of ultramafic rocks in the central Alps: Parageneses in the system CaO-MgO-SiO_2-H_2O.

Schweiz. Miner. Petrol. Mitt., 50, 481-492.

Faure, G. (1977) Principles of Isotope Geology. John Wiley & Sons, New York. 464 p.

Fleming, P.D. and J.J. Fawcett (1976) Upper stability of chlorite + quartz in the system MgO-FeO-Al_2O_3-SiO_2-H_2O) at 2 kb. water pressure. Am. Min., 61, 1175-1193.

Floyd, P.A. (1965) Metasomatic hornfelses of the Land's End aureole at Tater-du, Cornwall. Jour. Petrol., 6, 223-245.

Forester, R. W. and H.P. Taylor, Jr. (1972) Oxygen and hydrogen isotope data on the interaction of meteoric ground waters with a gabbro-diorite stock, San Juan Mountains, Colorado. 24th Int. Geol. Cong., 10, Geochemistry, 254-263.

Francis, D.M. and A.J. Hynes (1979) Proterozoic volcanic rocks of the Cape Smith fold belt, Quebec. Unpub. report, Penrose Conf. on komatiites, Val d'Or, Que., August 1979.

Friedman, I. and J.R. O'Neil (1977) Compilation of stable isotope fractionation factors of geochemical interest. U.S.G.S. Prof. Paper. 440-kk.

Fryer, B.J., R. Kerrich, R.W. Hutchinson, M.G. Peirce and D.S. Rogers (1979) Archean precious-metal hydrothermal systems, Dome Mine, Abitibi greenstone belt. I. Patterns of alteration and metal distribution. Can. Jour. Earth Sci., 16, 421-439.

Garlick, D.G. and S. Epstein (1966) The isotopic composition of oxygen and carbon in hydrothermal minerals at Butte, Montana. Econ. Geol., 61, 1325-1335.

Gelinas, L. and C. Brooks (1974) Archean quench-texture tholeiites. Can. Jour. Earth Sci., 11, 324-340.

Gelinas, L., C. Brooks, G. Perrault, J. Carignan, P. Trudel and F. Grasso (1977) Chemo-stratigraphic divisions within the Abitibi volcanic belt, Rouyn-Noranda district, Quebec. Geol. Assoc. Can. Spec. Pap., 16, 265-295.

Goodwin, A.M. (1977) Archean volcanism in Superior Province, Canadian Shield. Geol. Assoc. Can. Spec. Pap., 16, 205-242.

Goodwin, A.M. (1978) Archean crust in the Superior geotraverse area: Geologic overview. in Proc. 1978 Archean Geochem. Conf. (Smith and Williams, eds.), 73-106.

Goodwin, A.M. and R.H. Ridler (1970) The Abitibi orogenic belt. Can. Geol. Sur. Paper 70-40.

Graham, C.M., S.M.F. Shepard and T.H.E. Heaton (1980) Experimental hydrogen isotope studies -- I. Systematics of hydrogen isotope fraction-

ation in the systems epidote-H_2O, zoisite-H_2O, and AlO(OH)-H_2O. Geochim. et Cosmochim. Acta, 44, 353-364.

Grant, J.A. (1963) Geology of Catharine and Marter Townships. Ont. Dept. of Mines Geol. Rept. No. 18.

Grant, J.A. (1968) Partial melting of common rocks as a possible source of cordietite-anthophyllite bearing assemblages. Amer. Jour. Sci., 266, 908-931.

Gregory, R.T. and H.P. Taylor, Jr. (1980) An oxygen isotope profile in a section of Cretaceous oceanic crust, Samail ophiolite, Oman: Evidence for $\delta^{18}O$-buffering if the oceans by deep (>5 km.) seawater-hydrothermal circulation at mid-ocean ridges. Submitted to Jour. Geophys. Res.

Hansen, W.R. and Z.E. Peterman (1968) Basement-rock geochronology of the Black Canyon of the Gunnison, Colorado. U.S.G.S Prof. Pap. 600-C, p. C80-C90.

Hargraves, R.B. (1976) Precambrian geologic history. Science, 193, 363-371.

Hattori, K. and H. Sakai (1979) D/H ratios, origins, and evolution of the ore-forming fluids for the Neogene veins and Kuroko deposits of Japan. Econ. Geol., 74, 535-555.

Hattori, K., T. Urabe and K. Muehlenbachs (1979) $\delta^{18}O$ and δD study of Kuroko ores (abs.). EOS Trans. Amer. Geophys. Union, 60, 425.

Heaton, T.H.E. and S.M.F. Sheppard (1976) Hydrogen and oxygen isotope evidence for sea-water-hydrothermal alteration and ore deposition, Troodos complex, Cyprus. Volcanic Processes in Ore Genesis, Geol. Soc. Lond. Spec. Pub. No. 7, 42-57.

Hoefs, J. and R.A. Binns (1978) Oxygen isotope compositions in Archean rocks from Western Australia, with special reference to komatiites. U.S.G.S. Open-file Rept. 78-701, 180-182.

Hogg, W.A. (1964) Arnold and Katrine Townships. Ont. Dept. Mines Geol. Rept. No. 29.

Jackson, M.C. (1980) The geology and petrology of Lavaflow Mountain. Unpub M.S. thesis, University of Toronto.

Jacobsen, S.B. and G.J. Wasserburg (1979) The mean age of mantle and crustal reservoirs. Jour. Geophys. Res., 84, 7411-7428.

James, R.S., R.A.F. Grieve and L. Pauk (1978) The petrology of cordierite-anthophyllite gneisses and associated mafic and pelitic gneisses at Manitouwadge, Ontario. Amer. Jour. Sci., 278, 41-63.

Javoy, M. (1977) Stable isotopes and geothermometry. Jour Geol Soc., 133, 609-636.

Javoy, M. (1978) $^{18}O/^{16}O$ and D/H ratios in high temperature peridotites. U.S.G.S. Open-file Rept. 78-701, 202.

Jensen, L.S. (1975) Geology of Clifford and Ben Nevis Townships. Ont. Div. Mines Geoscience Rept., 132 p.

Jensen, L.S. (1979a) Archean komatiitic, tholeiitic, calc-alkalic and alkalic volcanic sequences in the Kirkland Lake area. in Toronto '78 Field Trips Guidebook (A.L. Currie and W.O. Mackasey, eds.), Geol. Soc. Amer. Ann. Meeting 1978, Toronto, 237-259.

Jensen, L.S. (1979b) Komatiitic volcanic rocks in the Kirkland Lake portion of the Abitibi belt. Unpub. report, Penrose Conf. on komatiites, Val d'Or, Que., August 1979.

Jolly, W.T. (1970) Zeolite and prehnite-pumpellyite facies in South Central Puerto Rico. Contr. Min. Petrol., 27, 204-224.

Jolly, W.T. (1974) Regional metamorphic zonation as an aid in study of Archean terrains: Abitibi region, Ontario. Can. Min., 12, 499-508.

Jolly, W.T. (1980) Development and degradation of Archean lavas, Abitibi area, Canada, in light of major element geochemistry. Submitted to Jour. Petrol.

Jolly, W.T. and R.E. Smith (1972) Degradation and metamorphic differentation of the Keweenawan tholeiitic lavas of Northern Michigan, U.S.A. Jour. Petrol., 13, 273-309.

Kerrich, R. and B.J. Fryer (1979) Archean precious-metal hydrothermal systems, Dome mine, Abitibi greenstone belt. II. REE and oxygen isotope relations. Can. Jour. Earth Sci., 16, 440-458.

Knauth, L.P. and S. Epstein (1976) Hydrogen and oxygen isotope ratios in nodular and bedded cherts. Geochim. et Cosmochim. Acta, 40, 1095-1108.

Kyser, T.K. (1979) The temperature dependence of oxygen isotope distributions and the origin of basalts and ultramafic nodules. Geol. Soc. Amer. Abs. w. Progs., 11, 462.

Kyser, T.K. and J.R. O'Neil (1978) Oxygen isotope relations among oceanic tholeiites, alkali basalts, and ultramafic nodules. U.S.G.S. Open-file Rept. 78-701, 237-240.

Lajoie, J. and L. Gélinas (1978) Emplacement of Archean peridotitic komatiites in La Motte Township, Quebec. Can. Jour. Earth Sci., 15, 672-677.

Lal, R.K. and W.W. Moorhouse (1969) Cordierite-gedrite rocks and associated gneisses of Fishtail Lake, Harcourt Township, Ontario. Can. Jour. Earth Sci., 6, 145-165.

Lambert, I.B. and T. Sato (1974) The Kuroko and associated ore deposits

of Japan: A review of their features and metallogenesis. Econ. Geol., 69, 1215-1236.

Larsen, E.S., Jr. (1948) Batholith and associated rocks of Corona, Elsinore, and San Louis Rey quadrangles, southern California. Mem. Geol. Soc. Amer., 29, 182 p.

Larsen, E.S., Jr. and W. Cross (1956) Geology and petrology of the San Juan region, southwestern Colorado. U.S.G.S. Prof. Pap. 258, 303 p.

Longstaffe, F.J. (1979) The oxygen isotope geochemistry of Archean granitoids. in Trondhjemites and Related Rocks (F. Barker, ed.), Elsevier Press, Amsterdam, 363-399.

Longstaffe, F.J. and H.P. Schwarcz (1977) $^{18}O/^{16}O$ of Archean clastic metasedimentary rocks; a petrogenetic indicator for Archean gneisses? Geochim. Cosmochim. Acta, 41, 1303-1312.

Longstaffe, F.J., R.H. McNutt and H.P. Schwarcz (1977) Geochemistry of Archean rocks from the Lake Despair Area, Ontario: A preliminary report. Geol. Sur. Can., Paper 77-1A, 169-178.

Magaritz, M. and H.P. Taylor, Jr. (1974) Oxygen and hydrogen isotope studies of serpentinization in the Troodos ophiolite complex, Cyprus. Earth and Plan. Sci. Lett., 23, 8-14.

Margaritz, M. and H.P. Taylor, Jr. (1976a) $^{18}O/^{16}O$ and D/H studies along a 500 km. traverse across the Coast Range batholith and its country rocks, central British Columbia. Can. Jour. Earth Sci., 13, 1514-1536.

Margaritz, M. and H.P. Taylor, Jr. (1976b) Oxygen, hydrogen and carbon isotope studies of the Franciscan formation, Coast Ranges, California. Geochim. et Cosmochim. Acta, 40, 215-234.

Matulich, A., A.C. Amos, R.R. Walker and J.J. Watkins (1974) The Ecstall story: The geology department. Con. Min. Metall. Bull., 67, No. 745, 56-63.

Mauger, R.L. (1972) A sulfur isotope study of the Ducktown, Tennessee district, U.S.A. Econ. Geol., 67, 497-510.

McCulloch, M.T., R.T. Gregory, G.J. Wasserburg and H.P. Taylor, Jr. (1980) A neodymium, strontium, and oxygen isotopic study of the Cretaceous Samail ophiolite and implications for the petrogenesis and seawater-hydrothermal alteration of oceanic crust. Earth and Planet. Sci. Lett., 46, 201-211.

McDowell, S.D. (1978) Layer silicate minerals in borehole Elmore #1, Salton Sea Geothermal field, California, U.S.A. Univ. Calif. Riverside/IGPP-78/15, 66 p.

McDowell, Douglas and M. McCurry (1977) Active metamorphism in the Salton Sea geothermal field, Calif: Mineralogical and Mineral chemical changes with depth and temperature in sandstone. Geol. Soc. Amer. Abs.

w. Progs., 9, 1088.

McKenzie, D. and N. Weiss (1975) Speculations on the thermal and tectonic history of the earth. Geophys. J.R. astr. Soc., 42, 131-174.

Miyashiro, A. (1973) Metamorphism and Metamorphic Belts. John Wiley & Sons, New York. 492 p.

Mottl, M.J., H.D. Holland and R.F. Corr (1979) Chemical exchange during hydrothermal alteration of basalt by seawater - II. Experimental results for Fe, Mn, and sulfur species. Geochim. et Cosmochim. Acta, 43, 869-884.

Muehlenbachs, K. and R.N. Clayton (1976) Oxygen isotope composition of the oceanic crust and its bearing on seawater. Jour. Geophys. Res., 81, 4365-4369.

Muffler, L.J.P. and D.E. White (1969) Active metamorphism of Upper Cenozoic sediments in the Salton Sea geothermal field and the Salton Trough, southeastern Calif. Bull. Geol. Soc. Amer., 80, 157-182.

Nitsch, K.H. (1971) Stabilitatsbeziehungen von Prehnit - und Pumpellyit-haltigen Paragenesen. Contr. Min. Petrol., 30, 240-260.

Norton, D. and H.P. Taylor, Jr. (1979) Quantitative simulation of the hydrothermal systems of crystallizing magmas on the basis of transport theory and oxygen isotope data: An analysis of the Skaergaard intrusion. Jour. Petrol., 20, 421-486.

Ohmoto, H. and R.O. Rye (1974) Hydrogen and oxygen isotopic compositions of fluid inclusions in the Kuroko deposits, Japan. Econ. Geol., 69, 947-53.

Olson, J.C. (1976) Geologic map of the Iris guadrangle, Gunnison and Saguache Counties, Colorado. U.S.G.S. Quad. Map GQ-1286.

O'Neil, J.R. (1977) Stable isotopes in mineralogy. Phys. Chem. Minerals, 2, 105-123.

O'Neil, J.R. (1979) Stable isotope geochemistry of rocks and minerals. in Lectures in Isotope Geology (E. Jager and J.C. Hunziker, eds.), Springer-Verlag, New York.

O'Neil, J.R. and Y.K. Kharaka (1976) Hydrogen and oxygen isotope exchange reactions between clay minerals and water. Geochim. et Cosmochim. Acta, 40, 241-246.

Ontario Division of Mines Map 2205, Timmins-Kirkland Lake.

Onuma, N., R.N. Clayton and T.K. Mayeda (1970) Apollo 11 rocks: Oxygen isotope fractionation between minerals, and an estimate of the temperature of formation. Proc. Apollo 11 Lunar Sci. Conf., 1429-1434.

Oskvarek, J.D. and E.C. Perry, Jr. (1976) Temperature limits on the early Archean ocean from oxygen isotope variations in the Isua supracrustal

sequence, West Greenland. Nature, 259, 192-194.

Perry, E.C., Jr. (1967) The oxygen isotope chemistry of ancient cherts. Earth and Planet. Sci. Lett., 3, 62-66.

Perry, E.C., Jr. and F.C. Tan (1972) Significance of oxygen and carbon isotope variations in early Precambrian cherts and carbonate rocks of southern Africa. Bull. Geol. Soc. Amer., 83, 647-664.

Perry, E.C., Jr., S.N. Ahmad and T.M. Swulius (1978) The oxygen isotope composition of 3,800 m.y. old metamorphosed chert and iron formation from Isudasia, West Greenland. Jour. Geol., 86, 223-239.

Price, P. (1934) The geology and ore deposits of the Horne Mine, Noranda, Quebec. Can. Inst. Mining Met. Trans., 37, 108-140.

Price, P. and W.L. Bancroft (1948) Waite Amulet Mine: Waite section. in Structural Geology of Canadian Ore Deposits: Can. Inst. Mining Metall., Geol. Div., 748-756.

Pyke, D.R. (1975) On the relationship of gold mineralization and ultramafic volcanic rocks in the Timmins area. Ont. Div. Mines Miscellaneous Paper, 12, 1-23.

Ridge, J.D. (1973) Volcanic exhalations and ore deposition in the vicinity of the seafloor. Mineralium Deposita, V. 8, 332-348.

Ridler, R.H. (1970) Relationship of mineralization to volcanic stratigraphy in the Kirkland-Larder Lakes area, Ontario; Proc. Geol. Assoc. Can., 21, 33-42.

Ripley, E.M. and H. Ohmoto (1977) Mineralogic, sulfur isotope, and fluid inclusion studies of the stratabound copper deposits at the Raul mine, Peru. Econ. Geol., 72, 1017-1041.

Ripley, E.M. and H. Ohmoto (1979) Oxygen and hydrogen isotopic studies of ore deposition and metamorphism at the Raul mine, Peru. Geochim. et Cosmochim Acta, 43, 1633-1643.

Roberts, R.G., J. Carnevali and J.D. Harris (1978) The volcanic-tectonic setting of gold-quartz vein systems in the Timmins district, Ontario. Geol. Sur. Can. Car. Res. Part B, Paper 78-1B, 187-190.

Rosen-Spence, A.F. de (1969) Genèse des roches a cordierite-anthophyllite des gisements cupro-zincifères de la région de Rouyn-Noranda, Quebec, Canada. Can. Jour. Earth Sci., 6, 1339-1345.

Schreyer, W. (1976) Experimental metamorphic petrology at low pressures and high temperatures. in The Evolution of the Crystalline Rocks (D.K. Bailey and R. MacDonald eds.), Academic Press. 261-331.

Seki, Y., Y. Oki, T. Matsuda, K. Mikami and K. Okumura (1969) Metamorphism in the Tanzawa Mountains, central Japan. J. Jap. Assoc. Mineral. Petrol. Econ. Geol., 61, 1-29, 50-75.

Seki, Y., H. Onuki, T. Oba and R. Mori (1971) Sanbagawa metamorphism in the central Kii Peninsula. Jap. J. Geol. Geogr., 41, 65-78.

Sheppard, S.M.F. and H.P. Taylor, Jr. (1974) Hydrogen and oxygen isotope evidence for the origins of water in the Boulder batholith and the Butte ore deposits, Montana. Econ. Geol., 69, 926-946.

Sheppard, S.M.F., R.L. Nielson and H.P. Taylor, Jr. (1971) Hydrogen and oxygen isotope ratios in minerals from porphyry copper deposits. Econ. Geol., 66, 515-542.

Shieh, Y.N. and H.P. Taylor, Jr. (1969) Oxygen and hydrogen isotope studies of contact metamorphism in the Santa Rosa range, Nevada, and other areas. Contr. Mineral. Petrol., 20, 306-356.

Shieh, Y.-N. and H.P. Schwarcz (1977) An estimate of the oxygen isotope composition of a large segment of the Canadian Shield in northwestern Ontario. Can. Jour. Earth Sci., 14, 917-931.

Shieh, Y.-N. and H.P. Schwarcz (1978) The oxygen isotope composition of the surface crystalline rocks of the Canadian Shield. Can. Jour. Earth Sci., 15, 1773-1782.

Smith, R.E. (1968) Redistribution of major elements in the alteration of some basic lavas during burial metamorphism. Jour. Petrol., 9, 191-219.

Spence, C.D. (1975) Volcanogenic features of the Vauze sulfide deposit, Noranda, Quebec. Econ. Geol., 70, 102-114.

Spence, C.D., and A.F. de Rosen-Spence (1975) The place of sulfide mineralization in the volcanic sequence at Noranda, Quebec. Econ. Geol., 70, 90-101.

Steiner, A. (1968) Clay minerals in hydrothermally altered rocks at Wairakei, New Zealand. Clays and Clay Min., 16, 193-213.

Suffel, G.G. (1948) Waite Amulet mine: Amulet section. in Structural Geology of Canadian Ore Deposits: Can. Inst. Mining Metall., Geol. Div., 757-763.

Talbot, C.J. (1973) A plate tectonic model for the Archean crust. Phil. Trans. R. Soc. Lond., 273, 413-427.

Taylor, H.P., Jr. (1968) The oxygen isotope geochemistry of igneous rocks. Contr. Min. Petrol., 19, 1-71.

Taylor, H.P., Jr. (1971) Oxygen isotope evidence for large-scale interaction between meteoric ground waters and Tertiary granodiorite intrusions, western Cascade range, Oregon. Jour. Geophys. Res., 76, 7855-7874.

Taylor, H.P., Jr. (1973) $^{18}O/^{16}O$ evidence for meteoric-hydrothermal alteration and ore deposition in the Tonopah, Comstock Lode, and Gold-

field mining districts, Nevada. Econ. Geol., 68, 747-764.

Taylor, H.P., Jr. (1974) The application of oxygen and hydrogen isotope studies to problems of hydrothermal alteration and ore deposition. Econ. Geol., 69, 843-883.

Taylor, H.P., Jr. (1977) Water/rock interactions and the origin of H_2O in granitic batholiths. Jour. Geol. Soc., 133, 509-558.

Taylor, H.P., Jr. (1978) Oxygen and hydrogen isotope studies of plutonic granitic rocks. Earth and Planet. Sci. Lett., 38, 177-210.

Taylor, H.P., Jr. and S. Epstein (1962) Relationships between $^{18}O/^{16}O$ ratios in coexisting minerals of igneous and metamorphic rocks. Bull. Geol. Soc. Am., 73, 461-480, 675-694.

Taylor, H.P., Jr. and S. Epstein (1970) $^{18}O/^{16}O$ ratios of Apollo 11 lunar rocks and minerals. Proc. Apollo 11 Lunar Sci. Conf., 1613-1626.

Taylor, H.P., Jr. and R.W. Forester (1971) Low-^{18}O igneous rocks from the intrusive complexes of Skye, Mull, and Ardnamurchan, western Scotland. Jour. Petrol., 12, 465-497.

Taylor, H.P., Jr. and R.W. Forester (1979) An oxygen and hydrogen isotope study of the Skaergaard intrusion and its country rocks: A description of a 55-m.y. old fossil hydrothermal system. Jour. Petrol., 20, 355-419.

Taylor, H.P., Jr. and M. Magaritz (1975) Oxygen and hydrogen isotope studies of 2.6-3.4 b.y. old granites from the Barberton Mountain Land, Swaziland, and the Rhodesian craton, southern Africa (abs.), Geol. Soc. Am. Abs. w. Progs., 7, 1293.

Taylor, H.P., Jr. and M. Magaritz (1978) Oxygen and hydrogen isotope studies of the Cordilleran batholiths of western North America. in Stable Isotopes in the Earth Sciences (B.W. Robinson, ed.), DSIR Bulletin 220, 151-173.

Taylor, H.P., Jr. and L.T. Silver (1978) Oxygen isotope relationships in plutonic igneous rocks of the Peninsular Ranges batholite, southern and Baja California. U.S.G.S. Open-File Rept. 78-701, 423-426.

Taylor, H.P., Jr. B. Giannetti and B. Turi (1979) Oxygen isotope geochemistry of the potassic igneous rocks from the Roccamonfina volcano, Roman comagmatic region, Italy. Earth and Planet. Sci. Lett., 46, 81-106.

Tilley, C.E. (1935) Metasomatism associated with the greenstone-hornfelses of Kenidjack and Botallack, Cornwall. Min. Mag., 24, 181-202.

Tilley, C.E. (1937) Anthophyllite-cordierite-granulites of the Lizard. Geol. Mag., 74, 300-309.

Upadhyay, H.D. (1978) Phanerozoic peridolitic and pyroxenitic komatiites from Newfoundland. Science, 202, 1192.

Vallance, T.G. (1967) Mafic rock alteration and isochemical development of some cordierite-anthophyllite rocks. Jour. Petrol., 8, 84-96.

Viljoen, M.J. and R.P. Viljoen (1969a) Evidence for the existence of a mobile intrusive peridotite magma from the Komati Formation of the Onverwacht Group. Upper Mantle Project. Spec. Publs. Geol. Soc. S. Afr., 2, 87-112.

Viljoen, M.J. and R.P. Viljoen (1969b) The geology and geochemistry of the lower ultramafic unit of the Onverwacht Group and a proposed new class of igneous rock. Upper Mantle Project. Spec. Publs. Geol. Soc. S. Afr., 2, 221-244.

Viljoen, M.J. and R.P. Viljoen (1969c) The geochemical evolution of the granitic rocks of the Barberton region. Upper Mantle Project. Spec. Publs. Geol. Soc. S. Afr., 2, 189-219.

Viswanathan, S. (1974) Oxygen isotope studies of Early Precambrian granitic rocks from the Giants Range batholith, northeastern Minnesota, U.S.A. Lithos, 7, 29-34.

Walker, R.R. and G.W. Mannard (1974) Geology of the Kidd Creek mine - A progress report. Can. Min. Metall. Bull., 67, No. 752, 41-57.

Walker, R.R., A. Matulich, A.C. Amos, J.J. Watkins and G.W. Mannard (1975) The Geology of the Kidd Creek mine. Econ. Geol., 70, 80-89.

Walker, T.L. (1930) Dalmatianite, the spotted greenstone from the Amulet mine, Noranda, Quebec. Univ. Toronto Studies, Geol. Ser., 29, 10.

Wenner, D.B. and H.P. Taylor, Jr. (1971) Temperatures of serpentinization of ultramafic rocks based on $^{18}O/^{16}O$ fractionation between coexisting serpentine and magnetite. Contr. Min. Petrol., 32, 165-185.

Wenner, D.B. and H.P. Taylor, Jr. (1973) Oxygen and hydrogen isotopic studies of the serpentinization of ultramafic rocks in oceanic environments and continental ophiolite complexes. Amer. Jour. Sci., 273, 207-239.

White, D.E. (1968) Environments of generation of some base-metal ore deposits. Econ. Geol., 63, 301-335.

White, D.E., I. Barnes and J.R. O'Neil (1973) Thermal and mineral waters of non-meteoric origin, California coast ranges. Geol. Soc. Amer. Bull., 84, 547-560.

White, W.S. (1968) The native-copper deposits of northern Michigan. in Ore Deposits of the United States (J.D. Ridge ed.), 303-325. Am. Inst. Mining, Metall. and Petroleum Engn., N.Y.

Williams, H., F.J. Turner and C.M. Gilbert (1954) Petrography: An Introduction to the Study of Rocks in Thin Section. W.H. Freeman and

Company, San Francisco. 406 p.

Windley, B.F. and J.V. Smith (1976) Archean high grade complexes and modern continental margins. Nature, 260, 671-675.

Winkler, H.G.F. (1979) Petrogenesis of metamorphic rocks, 5th ed., 348 p, Springer-Verlag, N.Y.

Wooden, J.L. (1978) Rb-Sr isotopic studies of the Archean rocks of the eastern Lac Seul and Kenora areas, English River Subprovince, Ontario. Proc. 1978 Archean Geochem. Conf. (Smith & Williams, eds.), 131-149.

Wyllie, P.J. (1979) Magmas and volatile components. Am. Min., 64, 469-500.

Yeh, H.-W. and S. Epstein (1978) D/H and $^{18}O/^{16}O$ ratios of Precambrian cherts of Swaziland sequence and others (abs.). EOS, 59, 386.

Zahony, S.G. (1976) Final geological report on the Vulcan property, Domingo mining district, Gunnison County, Colorado. Unpub. company report, Noranda Exploration, Denver, Colorado.